

This PDF was created from the British Library's microfilm copy of the original thesis. As such the images are greyscale and no colour was captured.

Due to the scanning process, an area greater than the page area is recorded and extraneous details can be captured.

This is the best available copy

"THE ELECTROCHEMICAL BEHAVIOUR OF ZINC-CADMIUM BASED ANODE MATERIALS IN POTASSIUM HYDROXIDE."

by

Shaikh Abdul Salam, BTech(Hons), MSc, MIMF, AMICorrT

Thesis submitted in partial fulfilment to the requirements of the degree of

DOCTOR OF PHILOSOPHY

to the

COUNCIL FOR NATIONAL ACADEMIC AWARDS.

Sponsoring Establishment:

Department of Metallurgy and Materials Engineering
City of London Polytechnic
Central House
Whitechapel High Street
London E1 7PF.

Collaborating Establishment:

Procurement Executive
Ministry of Defence
Royal Armament Research Development Establishment
Fort Halstead
Kent TN14 7BP.

May 1981

ABSTRACT

A review is presented on the historical background to the development of primary cells, their performance characteristics and their fundamental electrochemistry. A series of carefully characterised Zn-Cd alloys was prepared, from which metallography has shown them to be prone to structural changes and work hardening during normal surface preparations. Limitations imposed by the phase diagram have been examined. The influence of composition and structure on the corrosion behaviour of these alloys and the distribution of Hg in Zn-Cd-Hg ternary alloys has been studied.

Corrosion of homogenised Zn-Cd-Hg alloys in 6 mol dm^{-3} KOH at room temperature was studied by measuring the volume of hydrogen evolved and comparison made with results obtained in an earlier study. It was found that the two phase alloys suffered more corrosion than the pure metals or single phase alloys. The alloys can be arranged in the increasing order of corrodibility as follows:

Cd, Zn-0.05Cd, Zn-0.2Cd, Zn-1Cd, Zn-2Cd, Zn, Zn-25Cd, Zn-5Cd.

Amalgamation nearly halves the corrosion rates of the binary alloys. Addition of ZnO in the electrolyte reduces the corrosion still further.

Detailed studies of the anodic polarisation characteristics of these alloys as rotating disc electrodes in plain and ZnO saturated 6 mol dm^{-3} KOH showed that two different kinds of films are produced. The mechanism of film formation appeared to be dissolution of the metal and precipitation of the anodic products on the surface. The film formation process is diffusion controlled. The first film is adherent, transparent and a few molecular layers thick. The overlying film is non-stoichiometric and semiconducting because of the presence of excess interstitial metallic zinc. X-ray diffraction studies confirm that both films contain hydrated oxides.

Cathodic polarisation studies to measure Tafel slopes for hydrogen evolution on the alloys in KOH solutions confirmed a mechanism involving a fast charge transfer, endothermic adsorption and electrochemical desorption. The Tafel slope and exchange current density are influenced by the Cd content.

Long term constant current discharge behaviour of the alloys was studied. It was found that the presence of more than 2% Cd either changes the mechanism of passivation or influences the critical concentration and nature of the anodic oxidation products at the surface, as corroborated by RDE studies. The transition time depends upon the magnitude of applied current density and the alloy composition. The presence of mercury does not affect this parameter.

Finally, alternative means of producing single phase, homogeneous alloys were considered. Electrodeposition proved to be a viable proposition. Conditions are defined for producing homogeneous, microcrystalline Zn-Cd or Zn-Cd-Hg alloys in powder or plated form. These studies have established an improved anode material for primary alkaline cell development.

LIST OF SYMBOLS

A	area, m^2
a	length of a side in hexagonal close packed crystal structure, nm intercept of Tafel straight line on current axis $mV\ dec^{-1}$ activities
b	angular width of X-ray diffraction curve, radians
B	width of X-ray peak at the base, nm
c	length of axis in hexagonal close packed crystal, nm
C	total differential capacity, farads
C_{dl}	differential capacity of the double layer, farads
C_G	differential capacity contribution from Gouy layer, farads
C_H	differential capacity contribution from Helmholtz layer, farads
C^b	bulk concentration of ions, $mol\ dm^{-3}$
C^s	surface concentration of ions, $mol\ dm^{-3}$
C^E	surface concentration of ions at a given potential E, $mol\ dm^{-3}$
d	distance between crystal planes, nm
D	diffusion coefficient, m^2s^{-1}
E	potential, Volt
E^\ominus	standard potential, Volt
E_r	reversible or equilibrium potential, Volt
E_c	rest or corrosion potential, Volt
E_{ir}	i-R or ohmic potential drop, Volt
f	rotation frequency, Hz
F	Faraday constant, Coulombs mol^{-1}
G	Gibbs free energy, Joules
ΔG	change in free energy, Joules
ΔG^\ominus	standard free energy change, Joules
ΔH	enthalpy change, Joules
ΔH^\ominus	standard enthalpy change, Joules
h,k,l	Bragg indices of a crystal plane,

I	current, Amperes
i	current density, $A\ m^{-2}$
i_L	limiting current density, $A\ m^{-2}$
i_c	critical current density, $A\ m^{-2}$
i_{corr}	corrosion current density "
i_0	exchange current density "
i_p	peak current density "
i_{ss}	steady state current density "
i_∞	current density at infinite rotation speed, $A\ m^{-2}$
i_t	threshold current density, $A\ m^{-2}$
J	diffusion flux
K	rate constant for forward reaction
K_b	rate constant for backward reaction
n	number of moles of electrons taking part in a reaction
N	crystallite size, nm
P_0	intensity of incident wavelength, candela
P	intensity of emergent wavelength, "
r	radius, mm
R	gas constant, $8.3143\ J\ k^{-1}mol^{-1}$
Re	Reynolds number
Sc	Schmidt number
ΔS	entropy change, $J\ k^{-1}$
ΔS^\ominus	standard entropy change, $J\ k^{-1}$
S.E.P.	standard electrode potential, Volt
t	time, second
t_p	passivation time, transition time, second
t_i	transference no. of i_{th} component,
T	absolute temperature, Kelvin
α	transfer coefficient
$\beta_{\frac{1}{2}}$	width of X-ray peak at half height, radians
γ_i	activity coefficient of i_{th} component

γ_{\pm}	mean ionic activity coefficient
δ_0	diffusion boundary layer thickness, mm
δ_H	hydrodynamic boundary layer thickness, mm
	overpotential, volts
η_a	activation overpotential, volts
η_c	concentration overpotential, volts
ν	kinematic viscosity, m^2s^{-1}
θ	angle of reflection from a crystal plane, radians
μ	chemical potential, Joules mol^{-1}
μ^\ominus	standard chemical potential, Joules mol^{-1}
K	conductivity, $\Omega^{-1}\text{m}^{-1}$
σ	charge, Coulombs
ϕ_m	electrode potential, volts
ϕ_s	potential of bulk of solution, volts
$\Delta\phi_H$	potential drop across Helmholtz plane, volts
ψ_1	potential in the plane of hydronium ion centres, volts
ψ	potential drop across diffuse layer, volts
ω	rotation speed, angular velocity, radians s^{-1}
λ	wave length, nm

CONTENTS

Page No.

CHAPTER I

1.1	Historical Background to Primary Cells.	1
1.2	Performance Characteristics.	5
1.2.1	Energy per unit volume or weight.	5
1.2.2	Discharge Characteristics.	5
1.2.3	Shelf life and kinetics of self discharge.	5
1.3	Modern Electrochemical Systems.	6
1.3.1	Fuel Cells.	6
1.3.2	Non-aqueous Cells.	7
1.3.3	Solid State Cells.	7
1.3.4	Alkaline Cells.	8
1.3.4.1	Anodes.	8
1.3.4.2	Cathodes.	10
1.3.4.3	Electrolyte.	11
1.3.4.4	Cadmium-mercuric oxide cell.	12
1.3.4.5	Zinc-mercuric oxide cell.	14
1.4	Fundamental Aspects.	16
1.4.1	Thermodynamics.	16
1.4.2	Potential - pH Equilibrium Diagrams.	20
1.4.2.1	Zinc - water system.	20
1.4.2.2	Cadmium - water system.	25
1.4.2.3	Mercury - water system.	29
1.4.3	Electrode Kinetics.	32
1.4.3.1	Activation Polarisation.	33
1.4.3.2	Concentration polarisation.	36
1.4.3.3	Resistance Polarisation.	37
1.4.3.4	Passivation.	38
1.4.3.5	Chronopotentiograms and Transitions Times	38
1.4.4	Anodic Behaviour of Zinc.	40
1.4.5	Anodic Behaviour of Cadmium.	43
1.4.6	The Role of Mercury.	45
1.5	Investigations at the City of London Polytechnic.	46
1.6	Object of the present investigations.	50

/...

	<u>Page No.</u>
CHAPTER 4	
The Electrochemical Behaviour of Zn-Cd Alloys.	125
4.1 Introduction.	125
4.2 Experimental.	128
4.2.1 Potentiostats.	128
4.2.1.1 Potential Control Amplifier.	128
4.2.1.2 Voltage Scan Generator.	128
4.2.1.3 Precision Potential Meter.	128
4.2.2 Electrochemical Cell.	129
4.2.3 Electrode Holder.	131
4.2.4 Maintaining an inert atmosphere.	134
4.2.5 Reference Electrode.	136
4.2.5.1 Systems.	136
4.2.5.2 Construction.	138
4.2.6 Rotating Disc Assembly.	139
4.2.6.1 Introduction.	139
4.2.6.2 Theory.	139
4.2.6.2 Description.	143
4.2.7 Preelectrolysis of the Solution.	149
4.3 Anodic Polarisation.	149
4.4 Results.	151
4.5 Discussion.	265
4.6 Conclusions.	271
CHAPTER 5	
Hydrogen Overpotential on the Alloys in Alkaline Solutions.	274
5.1 Introduction.	274
5.2 Experimental.	284
5.3 Results and Discussion.	290
5.4 Conclusions.	290
CHAPTER 6	
Constant Current Discharge Behaviour.	291
6.1 Introduction.	293
6.2 Experimental.	297
6.3 Results and Discussion.	321
6.4 Conclusions.	321

	<u>Page No.</u>
CHAPTER 7	
Studies on Electrodeposition of Zn-Cd and Cd-Zn-Hg Alloys.	323
7.1 Introduction.	323
7.2 Practical Considerations in Alloy Electrodeposition.	323
7.2.1 Thermodynamic Aspects.	323
7.2.2 Complex formation.	324
7.2.3 Influence of current density.	326
7.2.4 Addition Agents.	326
7.3 Experimental.	326
7.3.1 Apparatus and Circuit Diagram.	326
7.3.2 Pretreatment and cleaning of the substrate.	328
7.3.3 Electrodeposition Conditions.	328
7.3.4 Bath Composition.	329
7.3.5 Analysis of Electrodeposited Alloys.	333
7.4 Results	333
7.4.1 Influence of Addition Agent.	333
7.4.2 Influence of Current Density.	335
7.4.3 Influence of pH.	335
7.4.4 Influence of Metal Content of Bath.	336
7.4.5 Influence of temperature.	336
7.4.6 Influence of mercury ion concentration and the current density on the composition of deposit for ternary baths.	342
7.5 X-ray diffraction studies.	342
7.5.1 General.	342
7.5.2 Results.	343
7.5.3 Discussion.	347
7.6 Electron Microscopy.	348
7.7 Discussion.	348
7.8 Conclusions.	356
CHAPTER 8	
General Discussion and Conclusions.	357
Recommendation for Further Work.	361
ACKNOWLEDGEMENTS.	363
REFERENCES.	364

1.1 HISTORICAL BACKGROUND TO PRIMARY CELLS

A new era in the history of electricity began around 1796, when Volta¹ constructed the first electric battery of cells capable of delivering a current of several amperes, which was a hundred times more than that generated by other known cells at that time. The cells of the early nineteenth century suffered from the detrimental effects of polarisation, local action and general corrosion, due to the lack of fundamental knowledge of cell processes.

In 1836 Daniell² invented the cell named after him which was based on a zinc anode and copper cathode separated by an animal membrane and immersed in dilute sulphuric acid and saturated copper sulphate solution respectively. Zinc sulphate was removed and fresh dilute sulphuric acid added from time to time. Grove³ designed a cell using an amalgamated zinc anode dipped in strong nitric acid inside a clay bowl which was inside a vessel containing sulphuric acid. Platinum sheet was used as a cathode. Bunsen later on substituted carbon for platinum to reduce the cost. The cell suffered from poor shelf life because of wasteful corrosion caused by strong nitric acid and evolution of noxious fumes of nitric oxides.

In 1842 Poggendorff⁴ substituted chromic for nitric acid. This proved to be an important heavy-duty battery in its day. A reserve type cell was also designed. This cell was used for military applications and saw active war service. Another heavy duty cell invented in 1843⁵ utilised a zinc anode in sulphuric acid and a cathode assembly consisting of a porous cup containing grains of lead peroxide packed around a platinum collector. Lalonde and Chaperon⁶ developed an alkaline copper oxide, zinc cell which displaced the Daniell cell and was used by the telegraph companies from 1881 onwards. It consisted of a horizontal positive plate

with copper oxide as the active material. The parallel negative electrode was zinc, placed above the positive electrode; an alkaline electrolyte based on potassium hydroxide was used for the first time.

Another important landmark during this period was the invention of the widely used Leclanché cell.⁷ This consisted of an amalgamated zinc rod dipped in saturated ammonium chloride solution and a carbon cathode in a graphite and manganese dioxide mix contained in a porous pot which acted as a separator. This cell was later on also produced in a dry form as described below. It was rugged and cheap, contained no highly corrosive electrolyte and gave minimum self discharge and a good shelf life. Gassner⁸ takes the credit for designing a commercially successful dry cell that had an impact on modern battery technology as prototype of the conventional dry battery. He used the zinc anode as the cell container and gelatin as an electrolyte immobiliser. Later on gelatin was replaced by paste coated paper which reduced wasteful corrosion of zinc. In the mid 1960's the production of these cells in the U.S.A. alone approached two billion.

The science and technology of alkaline batteries is now well developed.⁹ It embraces various scientific disciplines such as chemistry, physics and metallurgy, as well as the interdisciplinary field of interfacial phenomena. The application of these sciences has resulted in a vast improvement in performance characteristics for practical applications. From the very beginning of battery development, zinc was used as an anode because of its ready availability and low cost. Amalgamation was practical as early as 1828¹⁰ and was used as a beneficial modification for eliminating wasteful corrosion and avoiding irregular dissolution of zinc with the reservation that incorporation of mercury was accompanied by an implicit toxicity hazard and embrittling tendency.

Figures 1 and 2 show sectional drawings of a modern cylindrical and flat cell respectively.

A brief description is now presented of the various electrochemical systems widely used as power sources.

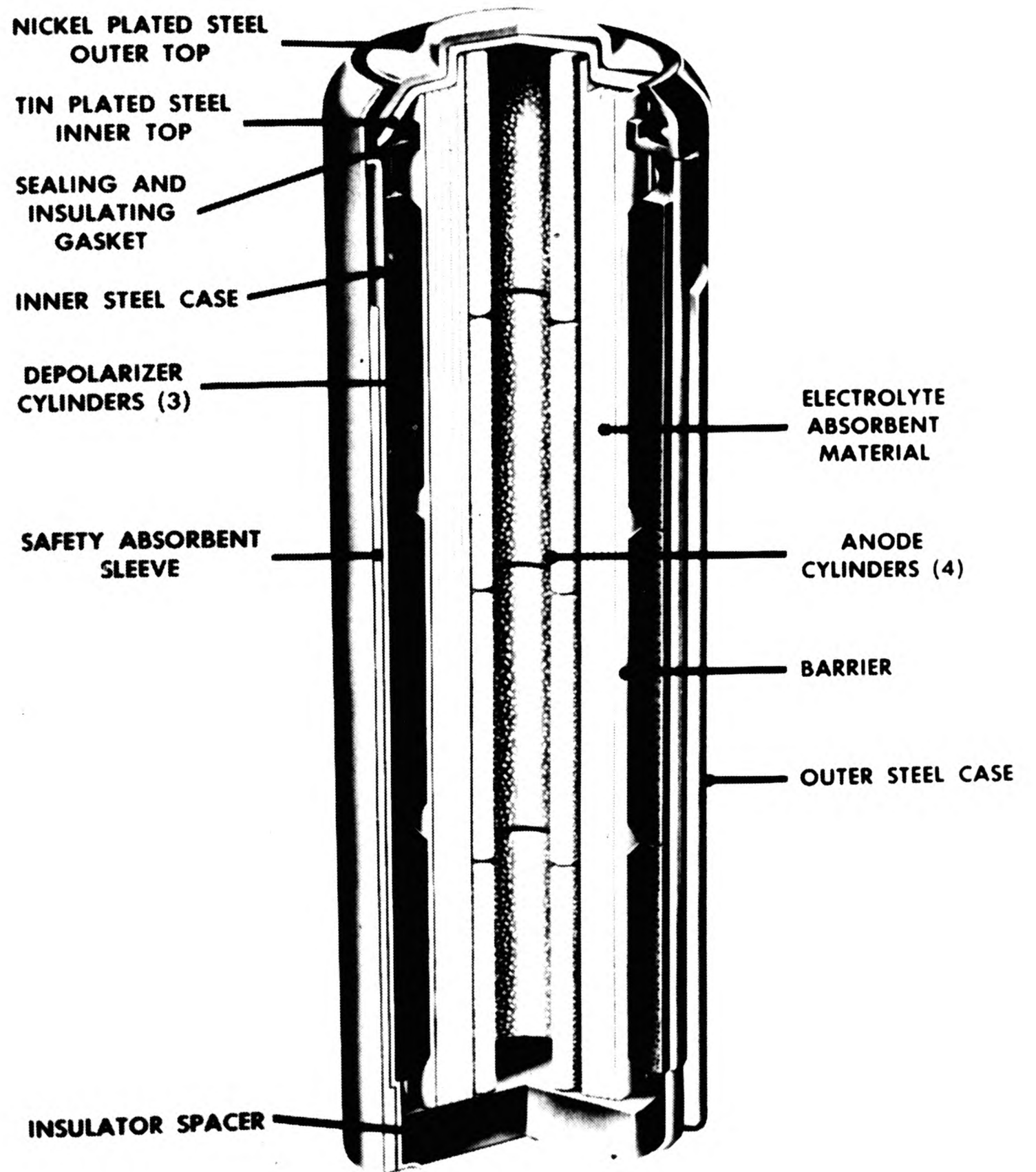


Figure 1. Pressed-powder cylindrical cell.

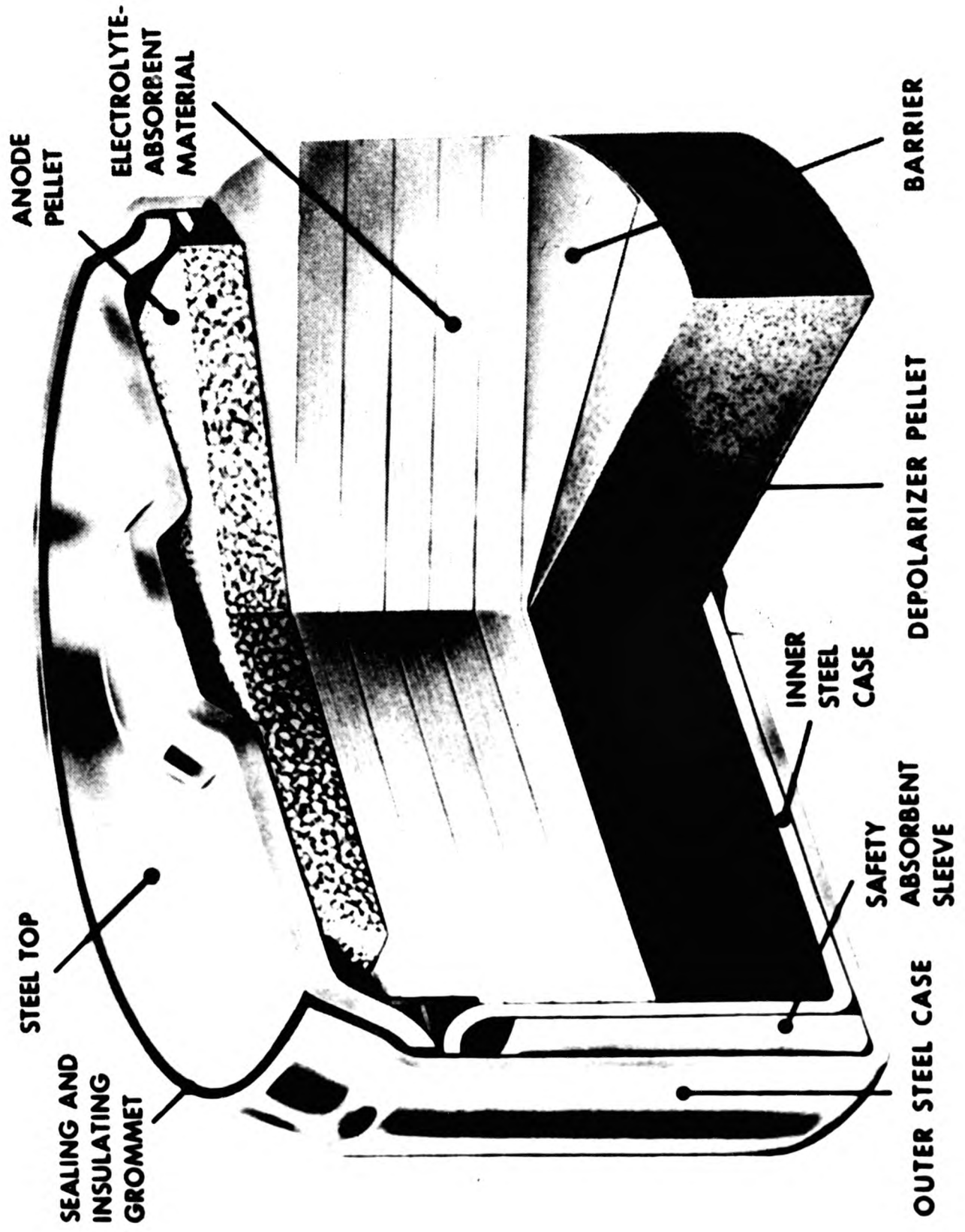


Figure 2. Pressed-powder flat cell.

1.2 PERFORMANCE CHARACTERISTICS

Battery properties of general importance are energy density per unit volume or weight, discharge characteristics at different rates and temperatures, internal resistance, shelf life and efficiency.

1.2.1 Energy per unit volume or weight. This is always less than the theoretical value because of the need of an appropriate container, connectors etc. which add on to "dead" volume and weight. Usually wet cells have lower values than those for dry or sealed cells because of the extra "head space" needed in the former. The theoretical energy density for the mercuric oxide-zinc system is 240 W h kg^{-1} and that for manganese dioxide-zinc systems is 191 W h kg^{-1} .

1.2.2 Discharge characteristics. The magnitude of current drawn and the ambient temperature are the two most important variants influencing the performance of a cell. When large currents are drawn, the diffusion limited electrochemical reactions cannot cope and the cell voltage diminishes dramatically, resulting in a drastic loss in power output. The general effect of ambient temperature is that with decreasing temperatures the cell voltage and therefore cell output power decreases, because temperature adversely affects the physical properties of electrolyte etc.

1.2.3 Shelf life and kinetics of self discharge. Shelf life is limited because of wasteful corrosion reactions taking place. This may be due to electrode instability associated with local action and impurities in the electrolyte. Again the amount and rate of these reactions would depend on the ambient temperature. Fortunately in alkaline electrolytes this is very slow compared with acid electrolytes. A very small amount of hydrogen gas is evolved which decreases with increasing electrolyte concentration. In addition to this a slow oxidation may take place as a result of reduction of oxygen. The classical Arrhenius equation $K = Ae^{-\frac{\Delta G}{RT}}$ may be applied to calculate the rate of self-discharge, because it has been found that the

capacity decay curve is logarithmic in nature. Measurements of potential decay on open circuit for several of the alkaline cell systems have been reported. Milner¹¹ gives a general interpretation which is suitable for most systems, i.e.

$$E = E_i - b \log \left(\frac{1+t}{bt} \right);$$

where E is electrode potential at time ' t ', E_i is the initial potential, b is Tafel slope $-2.3RT/n\alpha F$.

1.3 MODERN ELECTROCHEMICAL SYSTEMS

1.3.1 Fuel Cells. Up to the time of the second world war practically usable fuel cells had not been developed. Since then some advances have been made in their electrochemistry and engineering. Worthy of mention are hydrogen-oxygen cells with concentrated potassium hydroxide electrolyte operating between 70 and 250°C and at elevated pressure.¹² Both hydrogen and oxygen electrodes were made of porous carbon impregnated with catalysts. Since alkali electrolytes react with carbon dioxide, decreasing the cell output, efforts were directed to use phosphoric acid¹³ and also to find an alternative to hydrogen. Hydrocarbons, ammonia and hydrazine were used with success. With the use of hydrocarbons it was found that the operating temperature could rise to within the ranges 550-700°C. Advantage has been taken of bio-oxidation and bio-reduction by microbes to provide electrical energy.¹⁴ The metabolic activity could take place inside the cell at anodes and cathodes, or more practically external to the cell to generate hydrogen from carbohydrate for example, the action of *clostridium welchii* or *escherichia coli* on glucose.

Fuel cells have been used in the Gemini and Apollo space-craft missions, for load-levelling, and hold a promise as an energy supplier of the future when petrol may be in short supply. So far, the cost and technological difficulties have been the major drawbacks to more widespread utilisation.

1.3.2 Non-aqueous cells. These cells are specifically intended for very low temperatures (-40°C or less), where water which is cheap, abundant, and an extremely good solvent for conducting solutions, suffers from freezing, low conductivity, rapid polarisation, etc. Non-aqueous solvents¹⁵ such as acetonitrile, liquid ammonia and sulphur dioxide cells have been made. These liquids have properties well suited to the requirements of battery technology. For example anhydrous ammonia has abnormally high boiling and freezing points, heats of fusion and vaporisation, heat capacity and dielectric constant. It has low viscosity and density, is a better proton acceptor and its degree of dissociation is small. The electrochemical behaviour of anodes such as lead, magnesium and zinc in anhydrous ammonia is similar to that in water allowing for the difference in solvation energy, solubility of salts etc. Manganese dioxide has been selected as cathode largely because of its ready availability than anything else. Cells using organic solvents such as propylene carbonate have been designed. It seems likely that these cells might out-perform aqueous cells on the basis of energy density, low temperature performance, and good shelf life.

1.3.3 Solid State Cells. The drastic miniaturisation that has taken place in the electronics industry has called for a corresponding miniaturisation in their power packs because now they have to deliver only a few microwatts. Miniature semi-dry, dry, and sealed cells have been commercially produced using trace amounts of electrolyte impregnated in a separating membrane. These have very long shelf life, but suffer from high internal resistance and large polarisation losses. Batteries with lattice immobilised ions using ion-exchange membranes or resins have also been developed.¹⁶⁻¹⁹ Grubb²⁰ has done most extensive work in this field. Some solids, for example silver iodide, barium permanganate, silver mercury iodide etc., are electrically conductive, specially at high temperatures. Batteries have been constructed using these substances as electrolytes by the General Electric Company,²¹ Mallory Co.,²² Union Carbide Co.,²³ Patterson-Moos Co.,²⁴

and Sprague Electric Co.²⁵ Thin film batteries for use with silicon chip circuits have been made. In this construction the power source is an integral part of the integrated circuit and is therefore rechargeable. The components, that is, anode, electrolyte, cathode, connectors etc. are deposited on a substrate by evaporation. Film thicknesses can be controlled and may range from 5nm to 20µm. Sator and Perrot²⁶ developed the first thin film cell based on Pb/PbCl₂/AgCl/Ag system. For such a cell the charge discharge reaction could be represented by the equation:

$$\text{Pb} + 2\text{AgCl} \rightleftharpoons \text{PbCl}_2 + 2\text{Ag}.$$
Moulton, HacsKaylo and Feldman²⁷ improved this cell and used the system Pb/PbBr₂/AgBr/Ag. Later on some systems²⁸⁻³⁰ were found to possess certain properties and could find uses as a humidistat, strain gauge, pressure and temperature sensors - with possible applications in diagnosis of diseases, ionic balancing devices, and memory element capable of reading in and out and erasing.

1.3.4 Alkaline cells. Alkaline electrolyte based cells offer distinct advantages over acid electrolyte cells and have become increasingly popular in the consumer market. For example nitric acid has a higher wasteful corrosion rate and gives noxious fumes, hydrochloric acid is volatile and corrosive, sulphuric acid gives insoluble reaction products. The acids are bulky and inconvenient to handle in contrast to sodium or potassium alkalis, which are available in dry form and easy to handle. The alkali cells have advantage over dry Leclanche type cells which suffer from pH and concentration changes at electrodes upon drawing current, thus cell voltage drops which is more pronounced at heavier drains. Some of the merits of alkaline cells include stable conductive solutions over a wide range of temperature, slight wasteful attack, compatibility with many cathodes and better discharge characteristics.

1.3.4.1 Anodes. The principal anode metals for primary alkaline cells are sodium, aluminium, indium, cadmium and zinc. Their theoretical potentials and Faraday equivalents are given below.

Table 1: Reaction equation, SEP, and theoretical capacity of some anode materials

Metal	Reaction	Potential ³¹ SEP/V	Theoretical capacity $\times 10^5 \text{As kg}^{-1}$
Sodium	$\text{Na} + 4\text{OH}^- = \text{NaOH} + 2\text{e}$	-2.71	41.94
Indium	$\text{In} + 3\text{OH}^- = \text{In}(\text{OH})_3 + 3\text{e}$	-1.00	25.2
Aluminium	$\text{Al} + 4\text{OH}^- = (\text{H}_2\text{AlO}_3)^- + \text{H}_2\text{O} + 3\text{e}$	-2.35	107.34
Cadmium	$\text{Cd} + 2\text{OH}^- = \text{Cd}(\text{OH})_2 + 2\text{e}$	-0.81	17.34
Zinc	$\text{Zn} + 4\text{OH}^- = \text{Zn}(\text{OH})_4 + 2\text{e}$	-1.22	29.52
	$\text{Zn} + 2\text{OH}^- = \text{Zn}(\text{OH})_2 + 2\text{e}$	-1.25	29.52

Sodium appears theoretically attractive in view of its high potential, but its extreme reactivity excludes it from use unless amalgamated with mercury. An amalgam containing 0.60 w/o sodium is fluid at room temperature. Combination of this with an active carbon-oxygen electrode in 5-6 mol.dm⁻³ sodium hydroxide electrolyte gives an open circuit potential of about 2.05V, and 1.6-1.8V at current densities of 750-1000 Am⁻².^{1(b)}

Indium is stable at room temperature, a silvery white metal softer than lead and ductile, is oxidised to indium trioxide on heating. It has a high hydrogen overvoltage. However, it suffers from excessive polarisation and a voluminous anodic product. Indium-bismuth alloy anodes have been used with success. Aluminium is soft, ductile, malleable and silvery white. At room temperature it develops a thin, adherent film of aluminium oxide. It acquires passivity in alkaline or neutral environment or the attack is highly local. It is an amphoteric metal and therefore it has not gained wide useage despite its low cost, light weight, high potential and capacity. Aluminium anodes require air to be excluded during idle periods or storage to avoid excessive corrosion. Like indium, aluminium gives a voluminous aluminium hydroxide precipitate during service which for small or dry cells is undesirable. To obtain good output this precipitate must be removed continuously.

Cadmium is a malleable, ductile, silvery white, soft metal. Tarnishing occurs at room temperature in moist air; oxidises at elevated temperature. It is embrittled by heating to 80°C. Its compounds and the metal is toxic. It has a high hydrogen overvoltage and is very stable in alkaline solutions. Cadmium cells therefore have very long shelf life. Cost is a disadvantage, but where cost can be spread, as in rechargeable systems, such as the Ni/Cd alkali cell, cadmium has found widespread application.

Zinc is a silvery white, malleable, ductile metal, slightly harder than cadmium and has a higher melting point. It is cheaper than cadmium and widely available in massive and powder form. It amalgamates easily and does not passivate readily. Its standard electrode potential is -1.22V which is higher than that of cadmium (-0.81V). It tarnishes at room temperature in moist air.

1.3.4.2 Cathodes. Oxides of silver, manganese, mercury and copper have found wide usage. Iron oxide, a low cost material, suffers from low potential and significant solubility. Lead dioxide is even more soluble. Nickel oxide is suitable only for reversible systems. Given below is the potential and capacity of cathodes used commercially, with their reaction schemes.³¹

Table 2: Reaction equation, S.E.P. and theoretical capacity for some cathode materials

Material	Reaction	S.E.P.	Theoretical capacity Askg ⁻¹ x 10 ⁵
Cupric oxide	$\text{CuO} + 2\text{H}_2\text{O} + 2\text{e} = \text{Cu}_2\text{O} + 2\text{OH}^-$	-0.159	24.36
Cuprous oxide	$\text{Cu}_2\text{O} + \text{H}_2\text{O} + 2\text{e} = \text{Cu} + 2\text{OH}^-$	-0.357	12.18
Manganese dioxide	$\text{MnO}_2 + \text{H}_2\text{O} + \text{e} = \frac{1}{2}\text{Mn}_2\text{O}_3 + \text{H}_2\text{O} + \text{OH}^-$	+0.188	11.10
Mercuric oxide	$\text{HgO} + \text{H}_2\text{O} + 2\text{e} = \text{Hg} + 2\text{OH}^-$	+0.098	8.88
Silver peroxide	$2\text{AgO} + \text{H}_2\text{O} + 2\text{e} = \text{Ag}_2\text{O} + 2\text{OH}^-$	+0.570	15.60
Silver oxide	$\text{Ag}_2\text{O} + \text{H}_2\text{O} + 2\text{e} = \text{Ag} + 2\text{OH}^-$	+0.344	8.34

Of these, HgO and MnO₂ have found the most widespread commercial use.

Mercuric oxide operates at substantially constant voltage since only one reduction step is involved. Its solubility in alkaline electrolytes is low and any mercury deposited simply improves cell conductance and amalgamates with zinc. Thus the cell using this cathode displays long shelf life, high output and constant voltage. The high cost of mercury and its compounds is a deterrent, but for miniature cells where fabrication cost overshadows material cost it is gainfully employed.

Manganese dioxide is an important cathode because of its low cost, stability, capacity and temperature range. It has the additional advantage in combination with a zinc anode of providing an e.m.f. of 1.5V, exactly comparable with the traditional dry cell.

1.3.4.3 Electrolyte. The alkali electrolytes e.g. sodium or potassium hydroxide are distinguished by high conductivity over a wide range of concentrations, thus contributing to the low impedance of the cell. They are also cheap and readily available in bulk, dry and pellet form so that handling is easy. Because of its lower freezing point and higher conductivity potassium hydroxide is preferred over sodium hydroxide, which offsets the higher cost of the former in cells where low temperature operation and low electrolyte volumes are needed. The normal concentrations used in wet cell are 6-7.5 mol dm⁻³ as a compromise in conductivity and freezing point. In dry cells 8-10 mol dm⁻³ solutions are used to achieve ZnO precipitation necessary for operation of this type of cell. The ampere-hour capacity of commercial alkaline primary cells is a function of the solubility of the complexes formed by anodic dissolution of Zn and of the physical form of the solid by-products crystallising from these solutions when saturation is reached. The freezing point is minimum (-66°C) at 31 w/o solution, below and above this concentration f.p. is higher. The viscosity η , for concentrations up to 8 mol dm⁻³ can be calculated by the equation $\log \eta / \eta_0 = \left(\frac{0.0476C}{1-0.0199C} \right)$ at 25°C; where C is the molarity and η_0 is the viscosity of pure water. The viscosity increases with decreasing temperature, and there is a marked increase below -10°C. The conductivity varies with temperature,

concentration and the amount of additives. Concentration has a smaller effect on conductivity compared to temperature. Maximum conductivity occurs at 31 w/o at room temperature.⁴¹ ZnO additions or presence of carbonates decrease conductivity. The transference number⁴² of hydroxyl ions is between 0.74 and 0.78, and that of potassium ion is between 0.2 and 0.3 depending upon concentration. The activity coefficient⁴³ is less than one below 2.8 mol dm^{-3} , one at 2.8 mol dm^{-3} and rapidly increases after this concentration. These values have been determined experimentally for purely academic reasons and presented here for information. Figure 3 is a nomogram for expressing electrolyte concentration in various units.

1.3.4.4 Cadmium-mercury oxide cell. A primary mercuric oxide-cadmium cell is commercially made for exclusive use of military applications. The cells are made in button, prismatic or cylindrical shape. As there are no gases evolved during storage and discharge, the cell can be encapsulated or hermetically sealed. However, the open circuit voltage of 0.93V is significantly less than that of the comparable Zn-HgO cell (1.35V). Cathodes for these cells are made of pressed mercuric oxide mixed with graphite or silver on a nickel mesh, while the anodes are made of pressing electro-deposited cadmium powder on a nickel mesh. This cell is characterised by exceptional storage capability, a wider operating temperature range, a very stable operating voltage. The stability of the mercuric oxide and cadmium electrodes gives this couple the best storage capability of all aqueous electrolyte cells with actual tests validating 9 years at room temperature storage resulting in a 22% loss in capacity. Since the electrodes evolve no gas, the small loss in capacity is due to two factors; solubility of the mercuric oxide in the electrolyte and reduction of the soluble species at the cadmium electrode, thus decreasing the capacity of the anode and cathode. At higher drains, the cause of loss in capacity is slight crystal growth of cadmium resulting in increased current density. Partial discharge or low rate discharge will give full capacity. The cell can operate at as low as -54°C at high efficiency. Very constant voltage levels are a feature

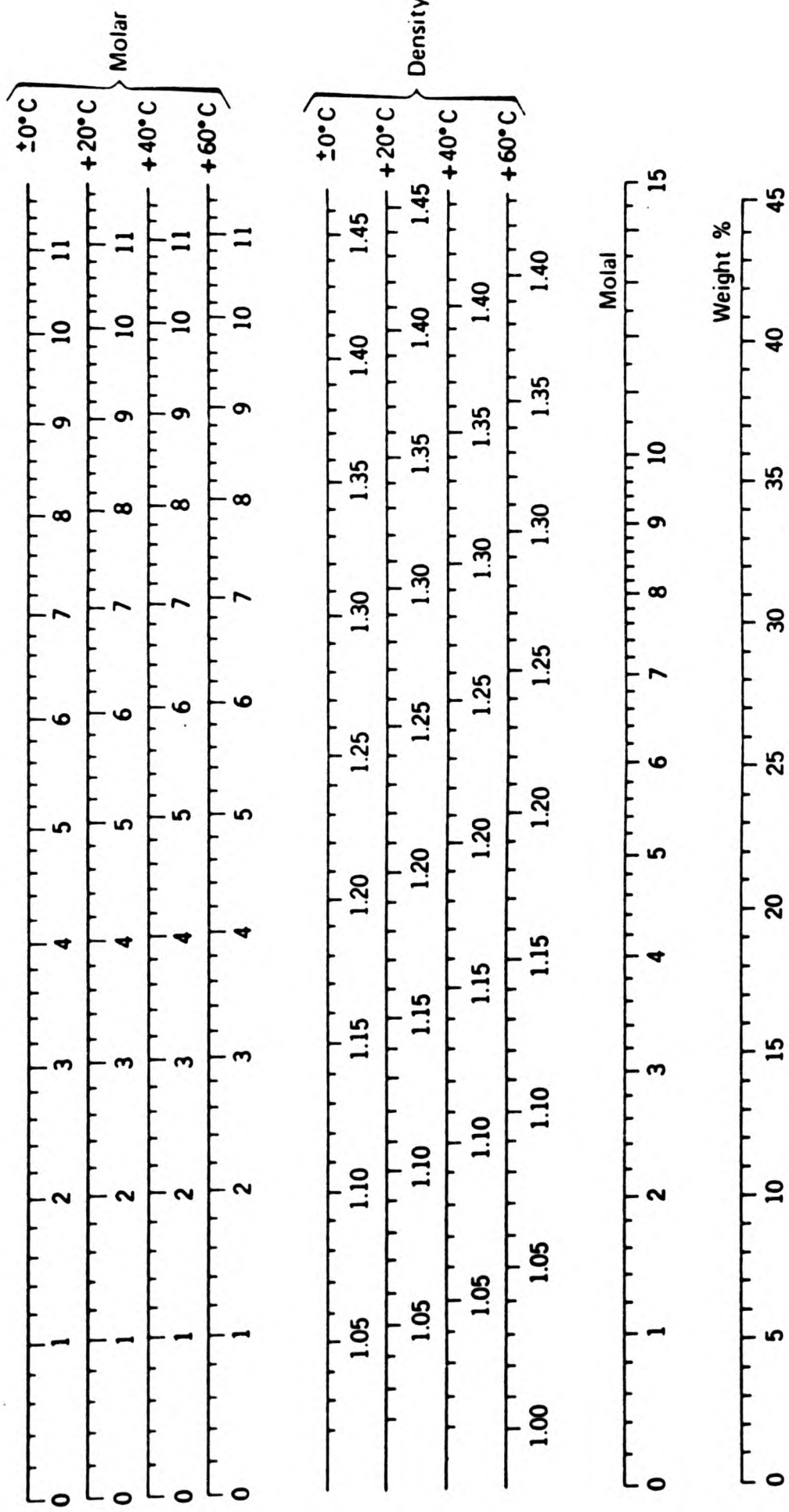


Figure 3. Conversion diagram for various expressions of KOH concentration.

of this cell, so that even though the open circuit voltage is low at 0.93V, the capacity obtained to a cut off of 0.8V may be 100%, due to the very low polarisation of the electrodes throughout the course of the discharge.

1.3.4.5 Zinc-mercuric oxide cell. Zinc is by far the most widely used anode in the aqueous alkaline cells where it is used in massive or plate form. In the dry cells it is as an amalgamated powder either compacted or gelled. The porous structure is of particular advantage in cells for which high current density and maximum ampere and watt hour capacity per unit of weight and volume are desired. Zinc of high purity 2N or 3N is customary for these cells, with the addition of 0.04-0.06 w/o Pb in the case of powder metal, for greater resistance to corrosion. It increases the normally high hydrogen ^{over} voltage of zinc and provides a means of obtaining an equipotential surface. During discharge the mercury concentrates mainly on the surface, thereby increasing protection effectiveness. Great care is exercised in the manufacture of the cells to avoid contaminants that accelerate corrosion. High quality separators are used to minimise diffusion of dissolved species and shorting out of the electrodes. As a further protection against corrosion and gas generation in the dry type cells, substantial amounts of zinc oxide are added initially to the electrolyte, this decreases the rate of self corrosion. Sealed cells are also made but gas vents are provided as protection against inadvertent pressure build-up. Figure 4 shows a sectional drawing indicating gas path by the arrows. Potential measurements show the electrode voltage to be 1.3 V for amalgamated zinc (1% Hg) in 6 mol dm⁻³ KOH and 1.3317V for amalgamated zinc (10% Hg) in 8 mol dm⁻³ zincate saturated KOH. The measured potential of the HgO electrode is 0.018V, thus the cell voltage is 1.35V. The cells are made in flat, button or cylindrical form. The cathode and anode are made as described before. For dry sealed cells and for complete utilisation of the zinc, cathode is made of greater coulombic capacity than the anode. For applications in which initial voltage is not critical, addition of MnO₂ results in excess capacity (which raises the o.c. voltage to 1.4V). The separators play an important role. There may be several layers performing

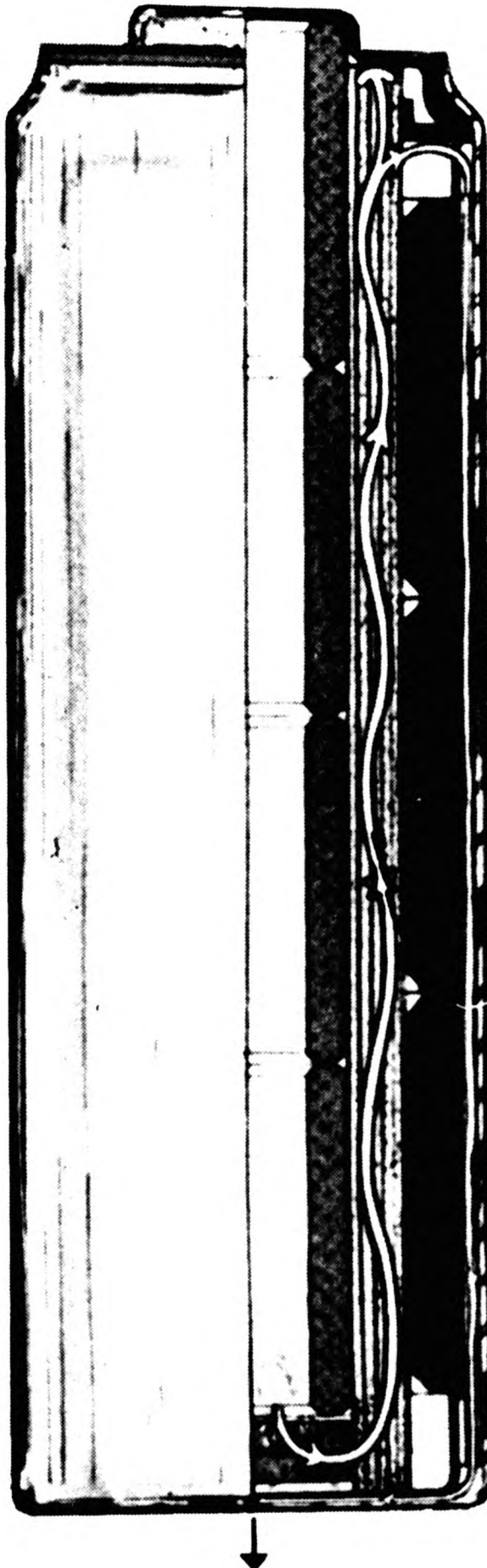


Figure 4. Automatic venting of mercury cells.

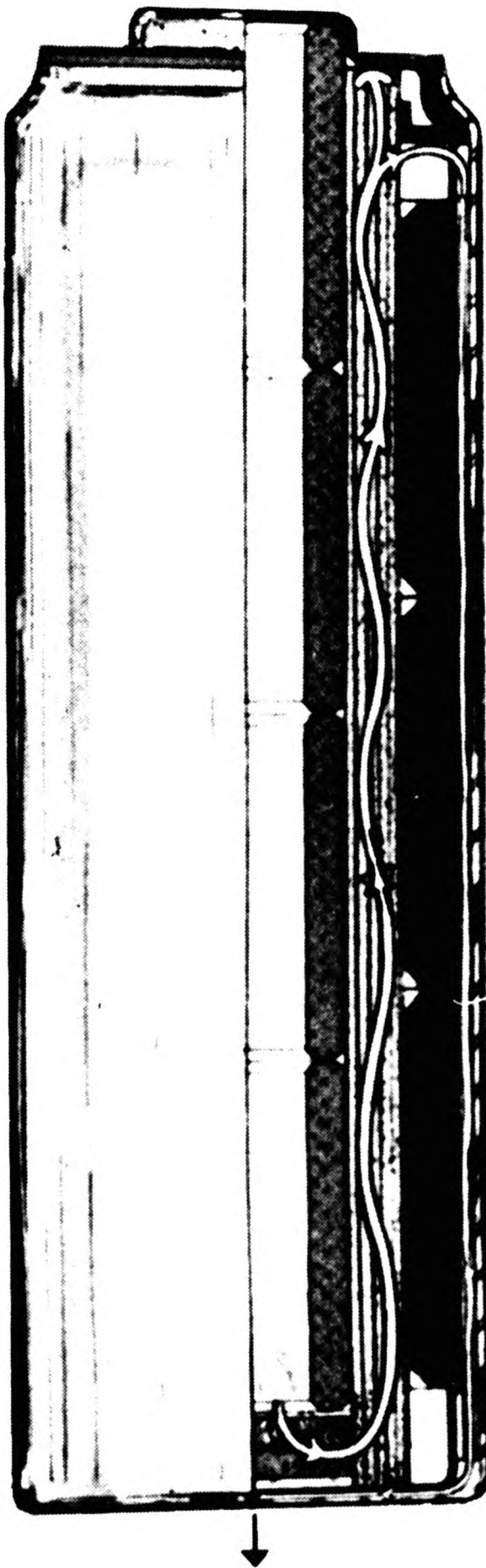


Figure 4. Automatic venting of mercury cells.

different functions e.g. immobilisation of electrolyte, diffusion barrier to dissolved species, prevention of short circuiting due to bridging materials. Anodes are also made in a wound form (Figure 5) that is a flat spiral of corrugated metal and an absorbent paper strip as separator. The corrugations provide enough space for zinc oxide formed during discharge, and paths for electrolyte despite accumulation of reaction product.

1.4 FUNDAMENTAL ASPECTS

1.4.1 Thermodynamics. Many charge transfer reactions initially appear suitable for use as electrochemical cells. Irreversibility and gassing reactions rule many of them out. Increasing importance is being given to the fundamental understanding of the thermodynamics and kinetics of the electrochemical processes in the exploration of the new systems and the improvement of the existing systems. Electromotive force or the open circuit voltage may be calculated using thermodynamic properties of reactants and products, employing the Nernst equation, thus

$$E = E^{\ominus} - \frac{RT}{nF} \ln \left(\frac{a_{\text{prod.}}}{a_{\text{react.}}} \right)$$

During discharge the open circuit voltage may or may not drop considerably, this fact can be ascertained for a given system from thermodynamic considerations. Thus if the activities of the reactants and products do not change appreciably, then the open circuit voltage will remain unchanged during the useful life as for example in the case of the mercuric oxide zinc cell or the lead-acid cell. On the other hand the manganese dioxide cell or Leclanche cell show a continuous drop of voltage during their useful life because during partial discharge the activities of OH^- and H^+ ions change by several powers of ten. If the cathodic material exists in two different valency states for example silver oxide and manganese oxide, then the cell voltage would change during partial discharge according to the state of oxidation involved. This can take the form of a clear change if the two oxides are not soluble in each other e.g. silver oxides or a more or less unmarked continuous change e.g. in the case of manganese oxides. The temperature

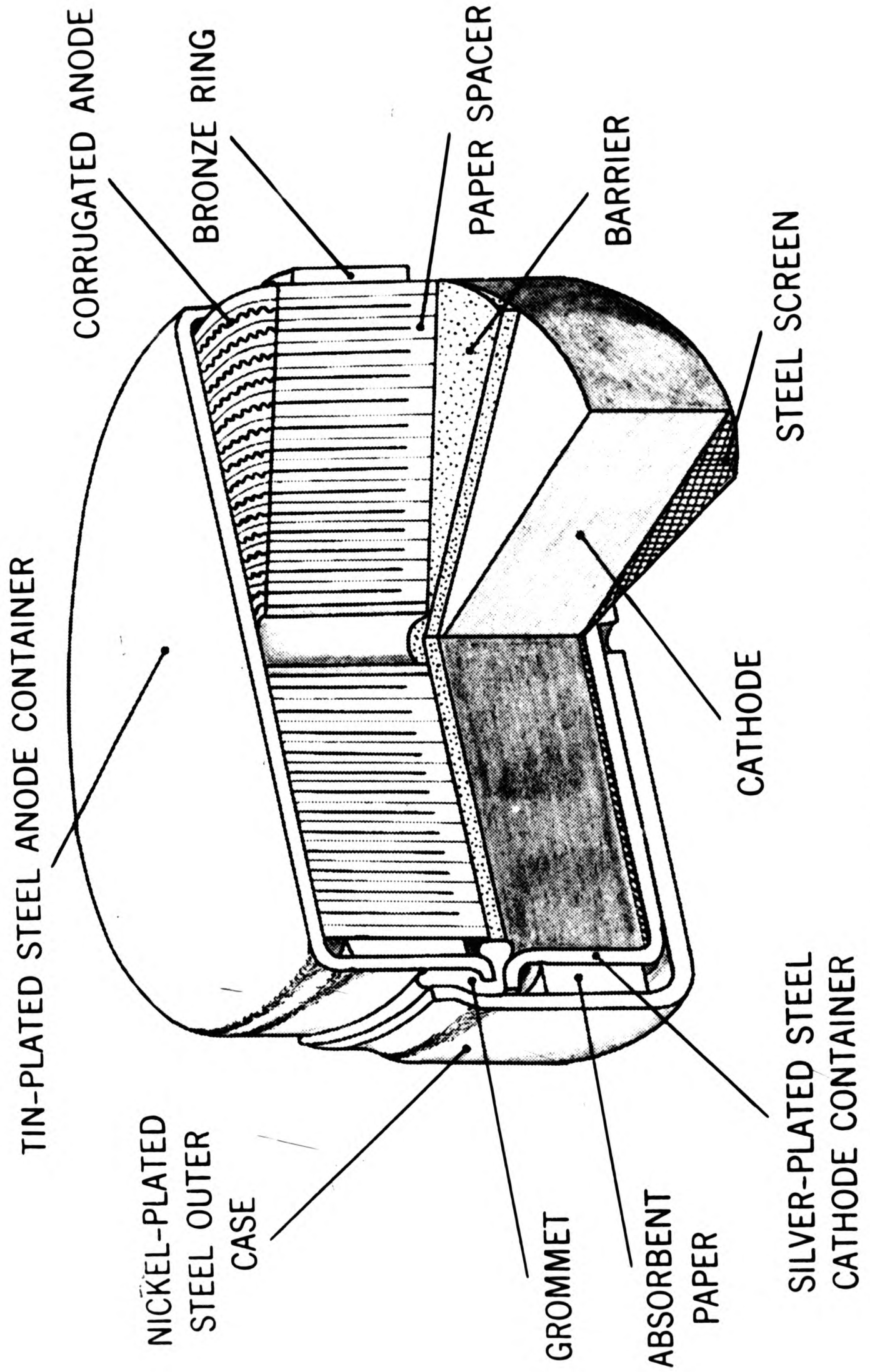


Figure 5. Internal structure of wound anode zinc-mercuric oxide cell.

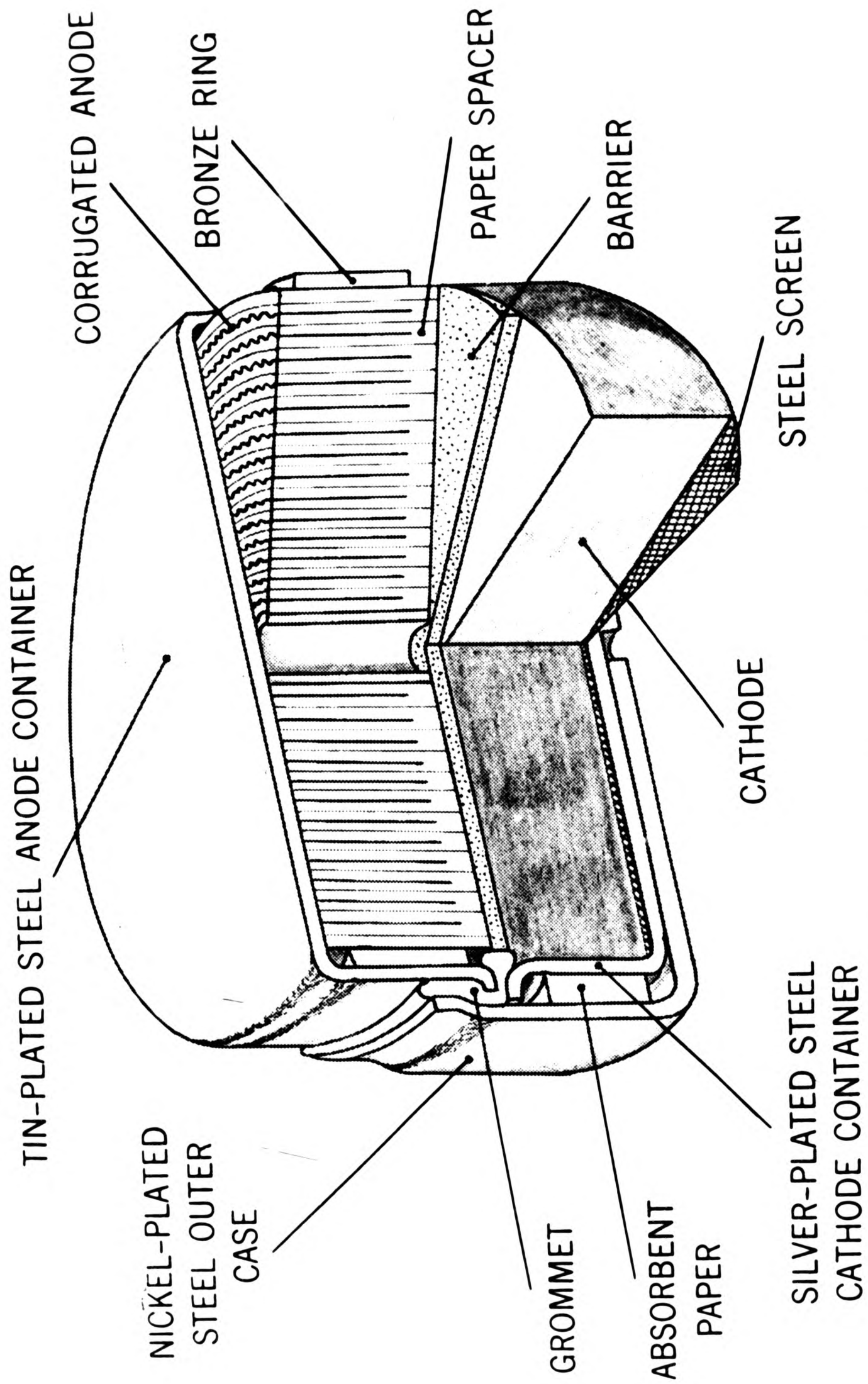


Figure 5. Internal structure of wound anode zinc-mercuric oxide cell.

coefficient of the cell voltage may be calculated from the Gibbs-Helmholtz equation:

$$\left(\frac{\partial E}{\partial T}\right) \text{ at constant pressure} = \frac{\Delta S}{nF}$$

$$= \frac{(\Delta H/nF + E)}{T}$$

The overall efficiency ϵ of a cell is defined as:

$$\epsilon = - \frac{\int_{\sigma=0}^{\sigma=q} E d\sigma}{\Delta G}$$

The Coulombic efficiency ϕ of an electrode is defined as:

$$\phi = \frac{q}{nF}$$

The thermal efficiency θ is defined as:

$$\theta = - \frac{\int_{\sigma=0}^{\sigma=q} E d\sigma}{\Delta H}$$

The chemical reactions occurring in a cell are heterogeneous processes occurring at the interface between electrolyte and electrodes and on the surface of the electrodes. The structure of the interface is thus very important. The electrical double layer at the electrode consists of a layer of ions of charge opposite to that of the electrode. This is the Helmholtz layer and the plane through the centre of the ions is known as the Helmholtz plane. This plane corresponds to the distance of closest approach of the ions to the electrode surface. The distance of closest approach depends upon the type of ion, the potential of the electrode relative to the ionic solution, and the interaction of ions with solvent dipoles. The ions may be said to be specifically adsorbed when no solvent is interposed between the electrode and the ions. In some cases e.g. with most electrolytes over some range of potentials, two Helmholtz planes are encountered designated as inner and outer, the outer plane consists of ions that have water of hydration interposed between them and the electrode surface. Extending from the solution side of the Helmholtz layer is the Gouy diffuse layer. As shown in Figure 6 the potential in this layer decreases nonlinearly and asymptotically approaches that of the bulk of the solution. For the

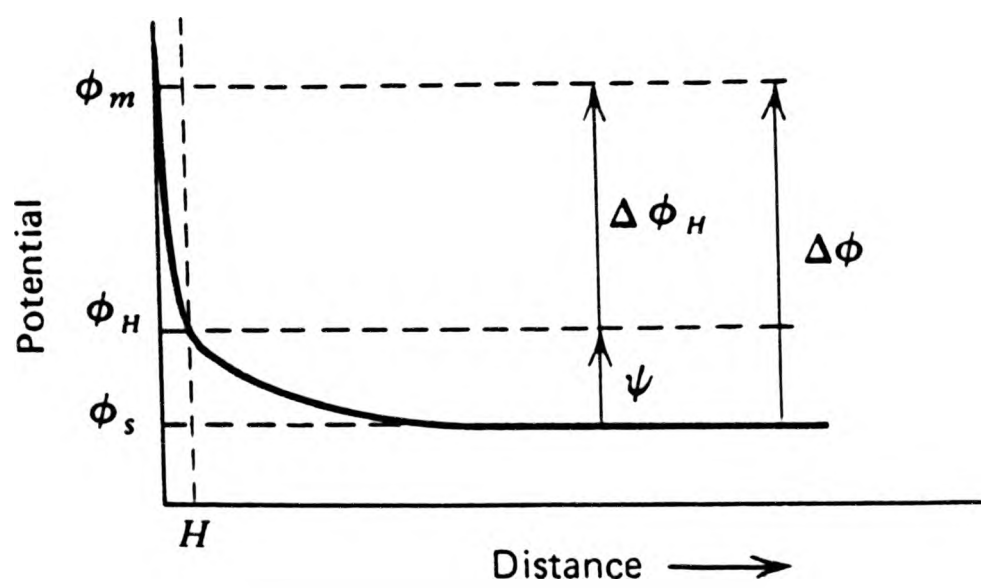
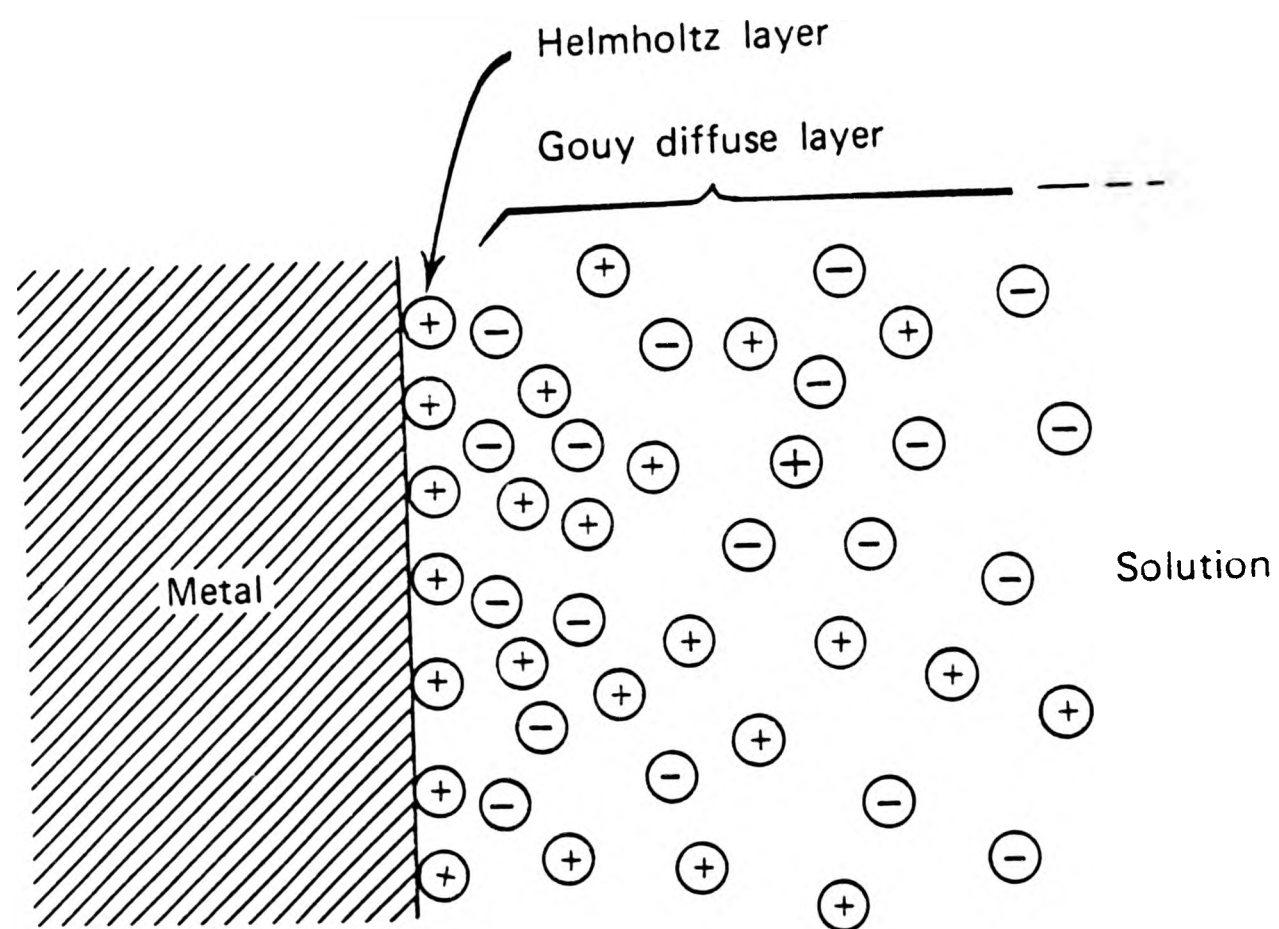


Figure 6. Schematic representation of the electrical double layer and the potential distribution.

concentrated electrolyte of the alkaline cell this diffuse layer is of the order of 10^{-7} cm or a few hydrated ionic diameters. The ionic double layer at an electrode-solution interface gives rise to a considerable capacitance component, C_{dl} given by $C_{dl} = d\sigma/dE$ and is related to the contributions from Helmholtz and diffuse layers thus $\frac{1}{C_{dl}} = \frac{1}{C_H} + \frac{1}{C_G}$. The double layer capacity is sensitive to organic impurities in the electrolyte at potentials where these impurities are adsorbed on the electrode surface. The concentration of an impurity in the solution need be sufficient only to support the formation of a reasonable fraction of a mono-layer on the electrode surface for the C_{dl} to be changed. With a semiconductor as an electrode, the equivalent of the Gouy diffuse layer exists in the electrode in addition to the Helmholtz and Gouy layers in the solution. The diffuse layer within the semiconductor contributes to the overall capacity of the semiconductor-solution interface as a series component. Measurement of C_{dl} as a function of electrode potential can be used to determine the carrier concentration in the semiconductor. Trace elements in the semiconductor can produce major changes in the carrier concentration and can have a large effect on C_{dl} . The semiconductor properties of oxides are of some importance because they are used as cathodes in aqueous and fuel cells. The phenomenon of passivation caused by anodic films can also be interpreted in terms of film's semiconducting properties.

1.4.2 Potential-pH Equilibrium Diagrams. Pourbaix³² and his co-workers described the various equilibria existing between a metal and water or aqueous solutions as a function of pH and potential. These diagrams provide a thermodynamic basis to a fundamental study of cell reactions, although their shortcomings and limitations must not be overlooked. Here only Zn, Cd and Hg will be considered as being particularly relevant to the present study.

1.4.2.1 Zinc-water system. Figure 7 illustrates Zn-H₂O diagram³² showing the zones of corrosion, passivation and immunity. The zone of corrosion is defined as one where the activity of metal cations, anions or complexes is greater than 10^{-6} gdm⁻³. Similarly the zone of immunity is one where

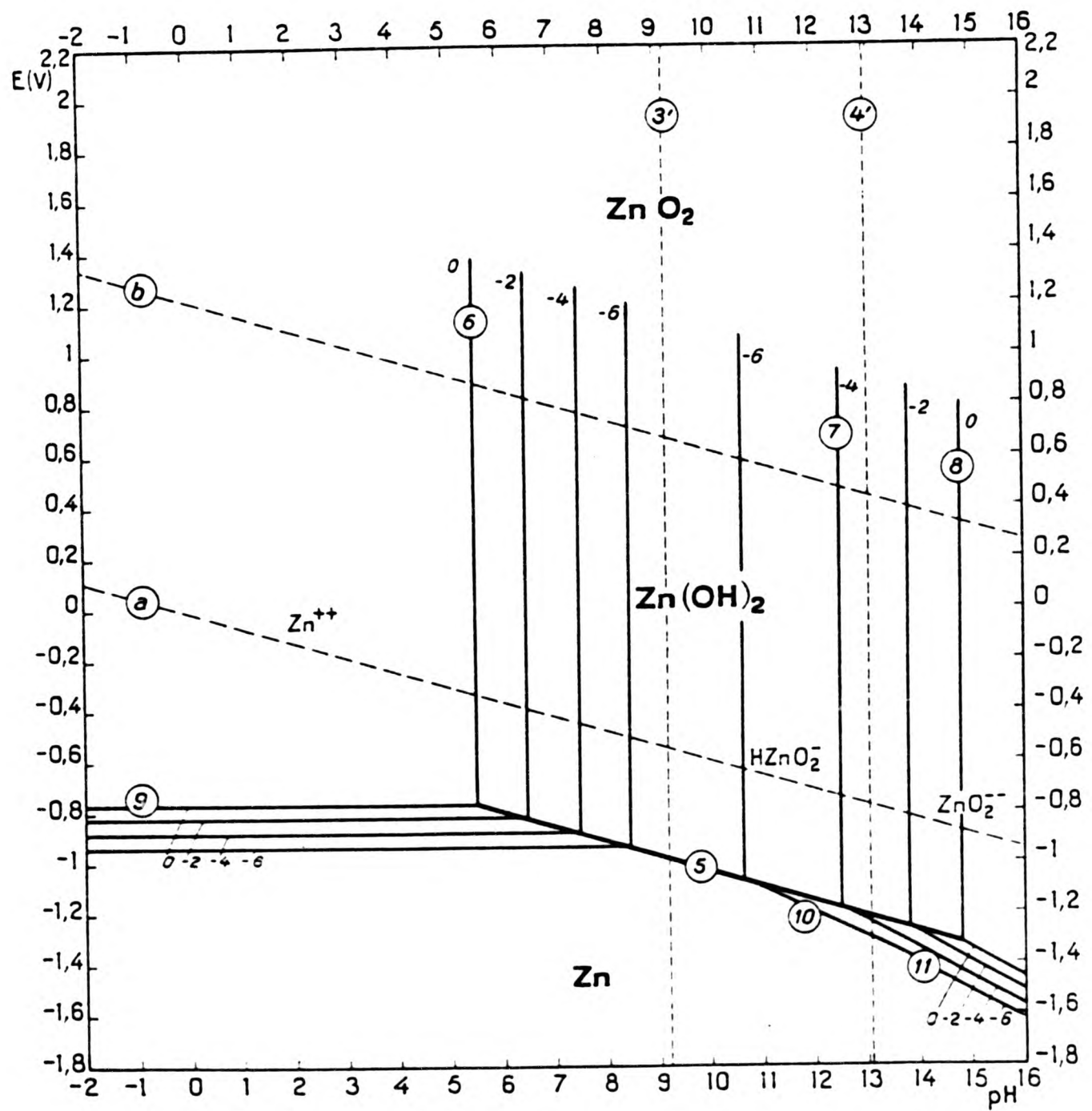


Figure 7. Potential pH equilibrium diagram for the system zinc water, at 25 C. [Established by considering $\Delta Z\text{n(OH)}_2$]

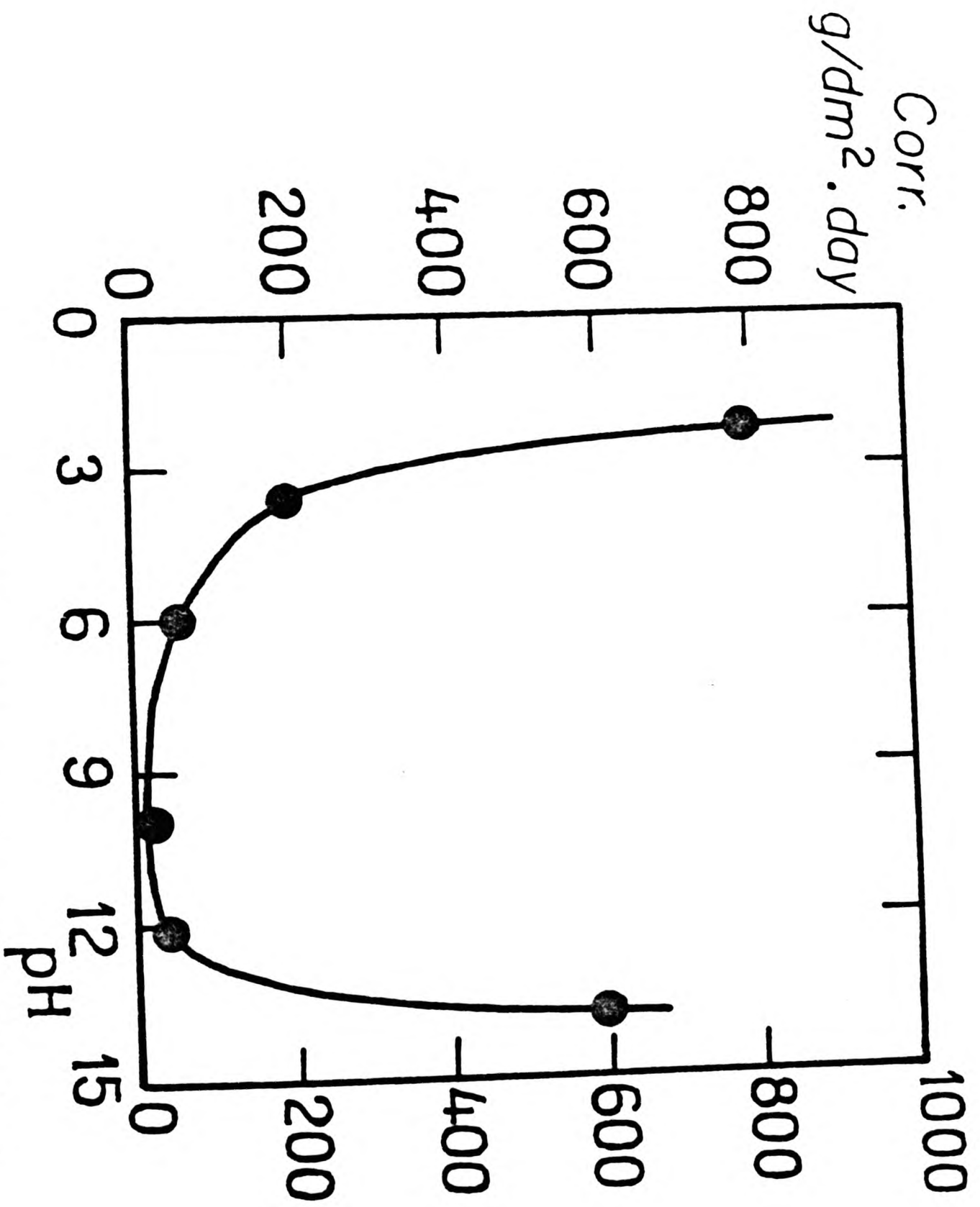


Figure 8. Influence of pH on the corrosion rate of zinc (Chatalov).

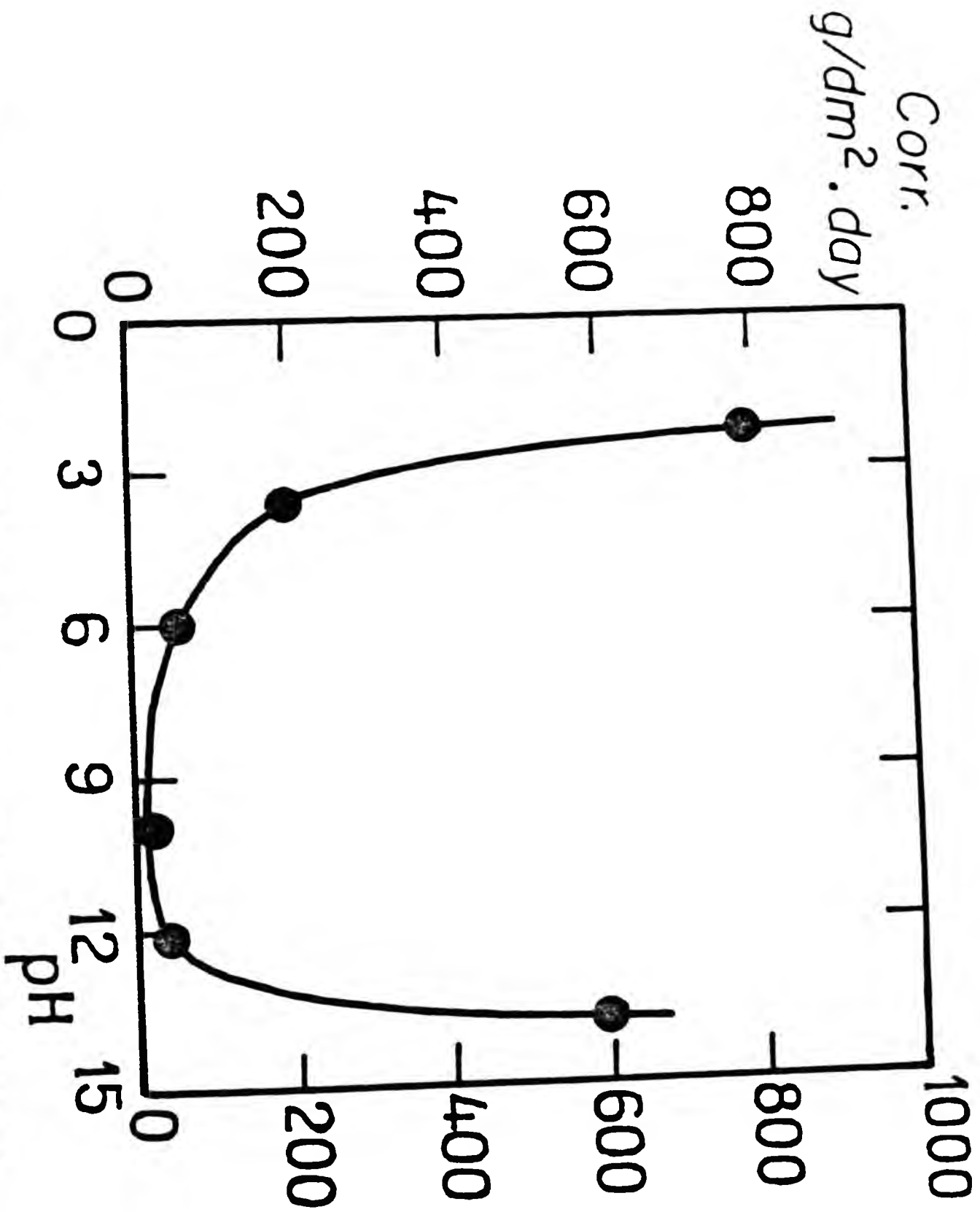


Figure 8. Influence of pH on the corrosion rate of zinc (Chatalov).

activity of metal ions is less than 10^{-6}gdm^{-3} . Here the oxides, hydroxides etc. are thermodynamically unstable with respect to uncombined metal. Similarly the zone of passivity is one where a solid metal compound is thermodynamically stable and is in equilibrium with less than 10^{-6}gdm^{-3} concentration of metal ions. The metal would be thermodynamically unstable. The Pourbaix diagrams represent the equilibria between the metal, metal ions, solid or dissolved oxides and hydroxides for systems in which reactants are metal, water and OH^- ions. In real solutions a change of pH can be affected only by additions of acids or alkalis and in the case of the former the anion may have a profound effect e.g. complex formation. Only in dilute perchloric acid and to a lesser extent in sulphate and nitrate solutions are complexes unlikely to form. Anions like Cl^- , CN^- , citrate, tartrate etc. which tend to form soluble complexes may thus extend the zone of corrosion; on the other hand PO_4^{3-} , CO_3^{2-} , SiO_4^{2-} etc. which tend to form insoluble basic compounds, may increase the extent of the zone of passivity.

Zn is thermodynamically unstable in the presence of water and aqueous solutions and dissolves with the evolution of hydrogen in acid, neutral or alkaline solutions. The rate may be slow if the metal is very pure because then the H_2 overvoltage is high. The attack is rapid if it is coupled with a metal of low H_2 overvoltage such as platinum. In the presence of moderately alkaline solutions of pH between 8.5 and 10.5 Zn would be covered by a film of $\text{Zn}(\text{OH})_2$. Corrosion is minimal in the pH range of 6 to 12 (see Figure 8). Batteries using Zn anodes cannot tolerate contamination from carbonates. $\text{Zn}(\text{OH})_2$ is amphoteric in nature dissolving in acid solutions to give bizincate HZnO_2^- or zincate ZnO_2^{2-} ions. $\text{Zn}(\text{OH})_2$ has been identified in seven modifications. The solubility products of each are given below;³⁴⁻³⁶ See also Figure 9.

$\epsilon\text{-Zn}(\text{OH})_2$	8.41×10^{-18}	$= 10^{-17.075}$
inactive ZnO	9.21×10^{-18}	$= 10^{-17.036}$
$\gamma\text{-Zn}(\text{OH})_2$	1.4×10^{-17}	$= 10^{-16.854}$

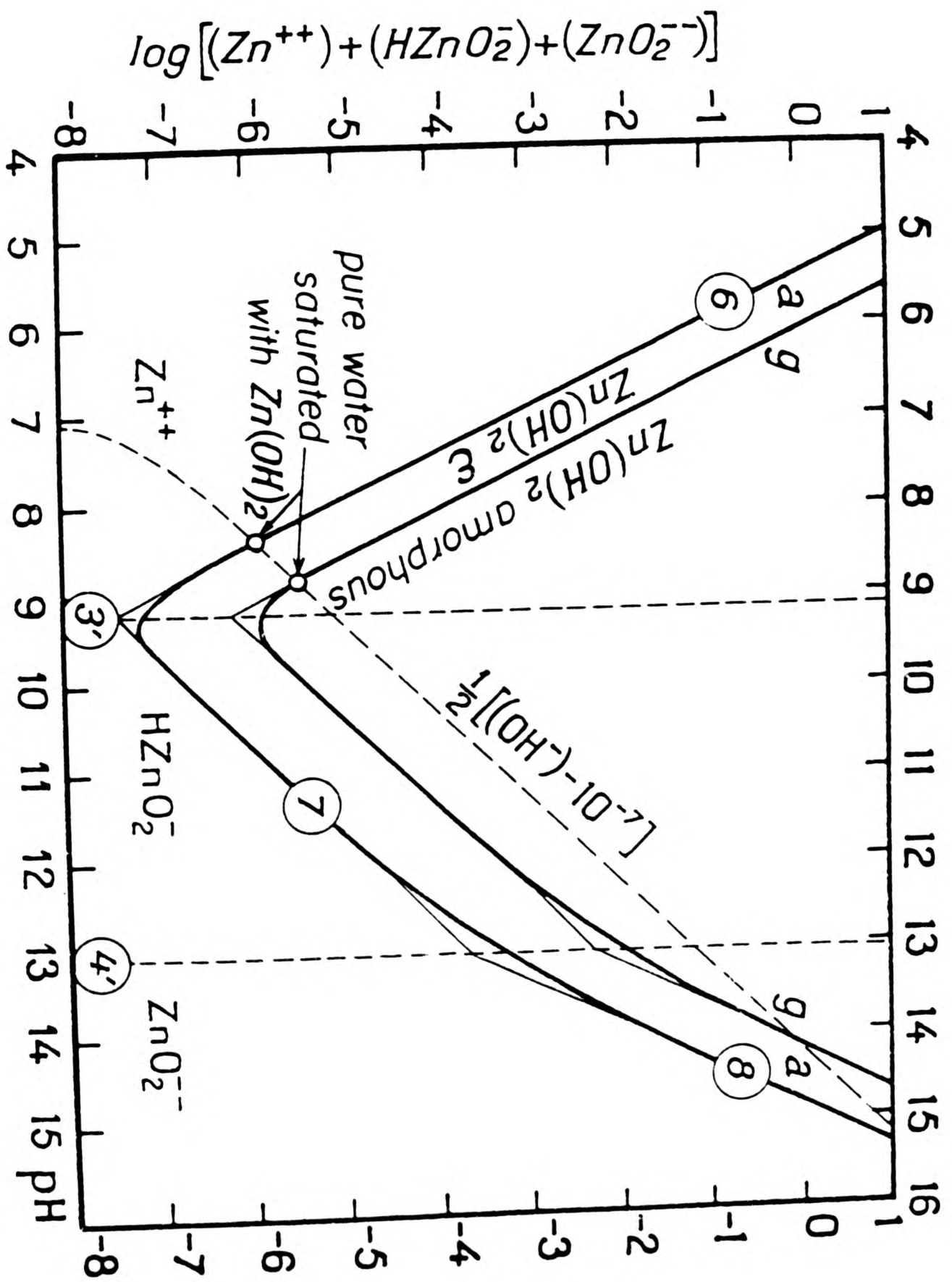


Figure 9. Influence of pH on the solubility of the zinc hydroxides, at 25 C.

β -Zn(OH) ₂	$1.9 \times 10^{-17} = 10^{-16.722}$
active ZnO	$6.86 \times 10^{-17} = 10^{-16.164}$
α -Zn(OH) ₂	$1.43 \times 10^{-16} = 10^{-15.845}$
amorphous Zn(OH) ₂	$1.66 \times 10^{-16} = 10^{-15.780}$

Only at higher alkali concentrations and pH the precipitation of these compounds takes place. The minimum solubility occurs at 9.3 pH, this value is 0.0882 mgdm⁻³Zn for the amorphous variety and 0.0041 mgdm⁻³Zn for ϵ variety. The α variety is formed by the incomplete precipitation of a zincic solution at a neutral pH of 7. The product of the complete precipitation of a solution of a zinc salt by a base is the unstable amorphous variety, resulting from the transformation of the alpha variety. The amorphous variety in turn converts into a beta variety or an oxide, depending upon the operating conditions in a slightly alkaline or neutral solution. In very alkaline solutions amorphous Zn(OH)₂ is rapidly converted into a gamma variety, which has not been observed in the corrosion products. The allotropic beta form can also be obtained from a very dilute zincate solution. The epsilon variety is the most stable of the system, Zn-H₂O at 25°C. It is formed by a slow separation from a zincate solution. Zinc oxide appears in various, more or less, active forms. The most inactive forms are prepared by the high temperature calcination of zinc carbonate or zinc hydroxide. Spontaneous dehydration of the amorphous hydroxide produces the active oxides. A zinc peroxide of composition ZnO₂ has been prepared by the action of 1 mol dm⁻³ sodium hydroxide on an aqueous mixture of zinc hydroxide and hydrogen peroxide³⁰ and also by the action of concentrated hydrogen peroxide on an ammoniacal solution of zinc sulphate or nitrate.

1.4.2.2 Cadmium-water system. Figure 10 shows cadmium-water system³² at 25°C outlining zones of corrosion, passivation and immunity. Cadmium hydroxide is the most stable form. The corrosion zones will be extended if soluble complexes are formed in the presence of ions such as chloride,

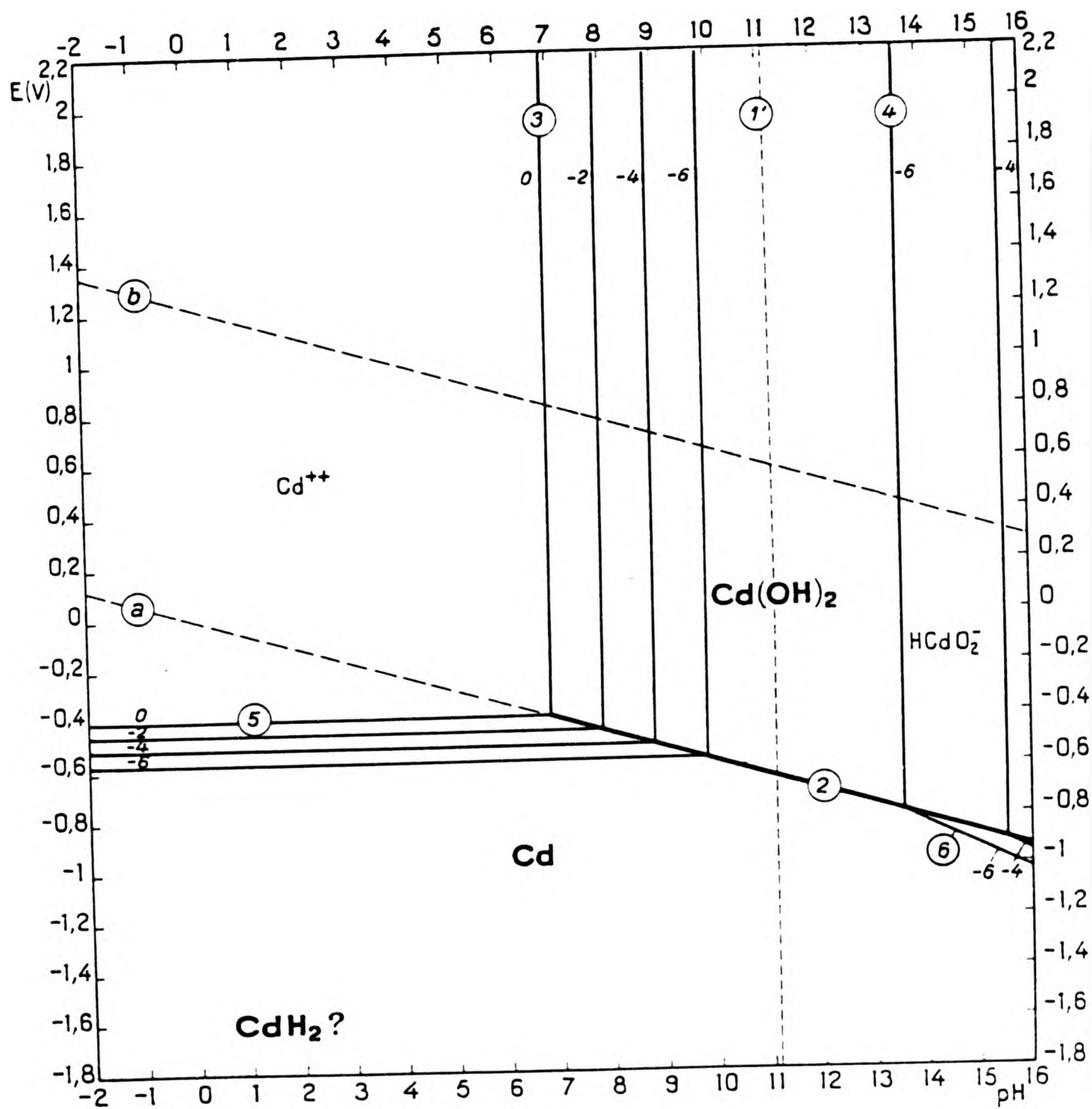


Figure 10. Potential pH equilibrium diagram for the system cadmium-water, at 25°C.

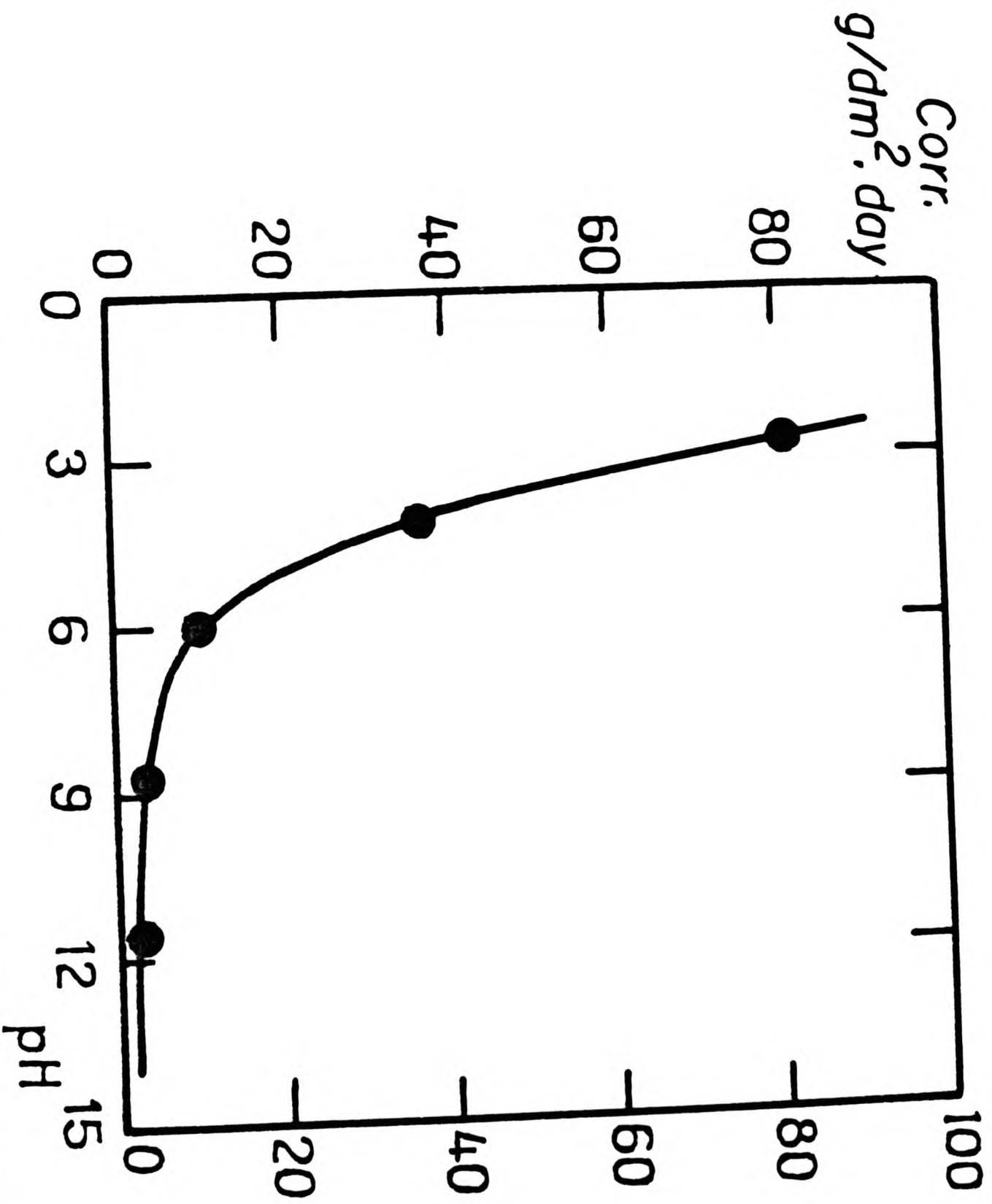


Figure 11. Influence of pH on the corrosion rate of cadmium (Chatalov).

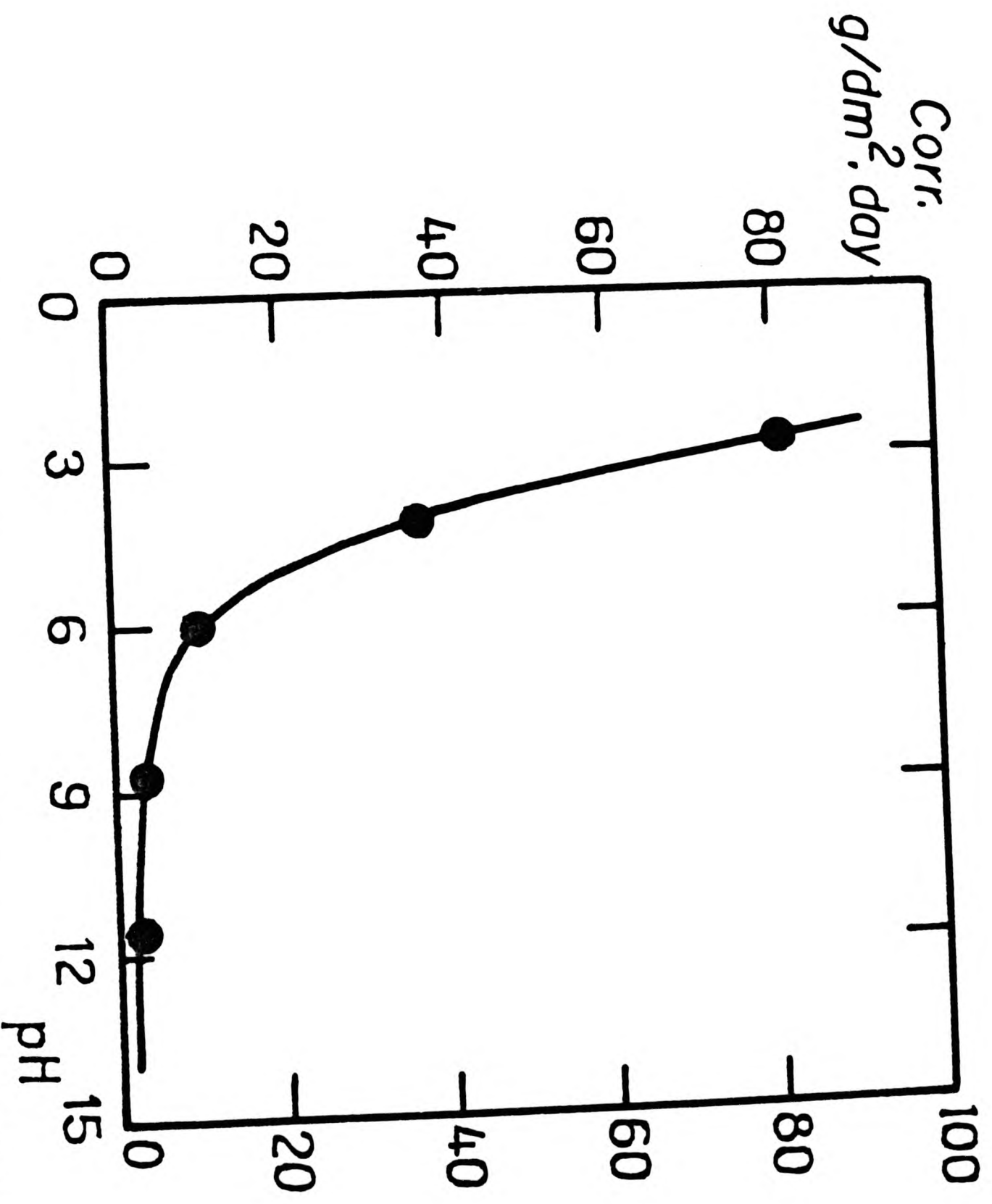


Figure 11. Influence of pH on the corrosion rate of cadmium (Chatalov).

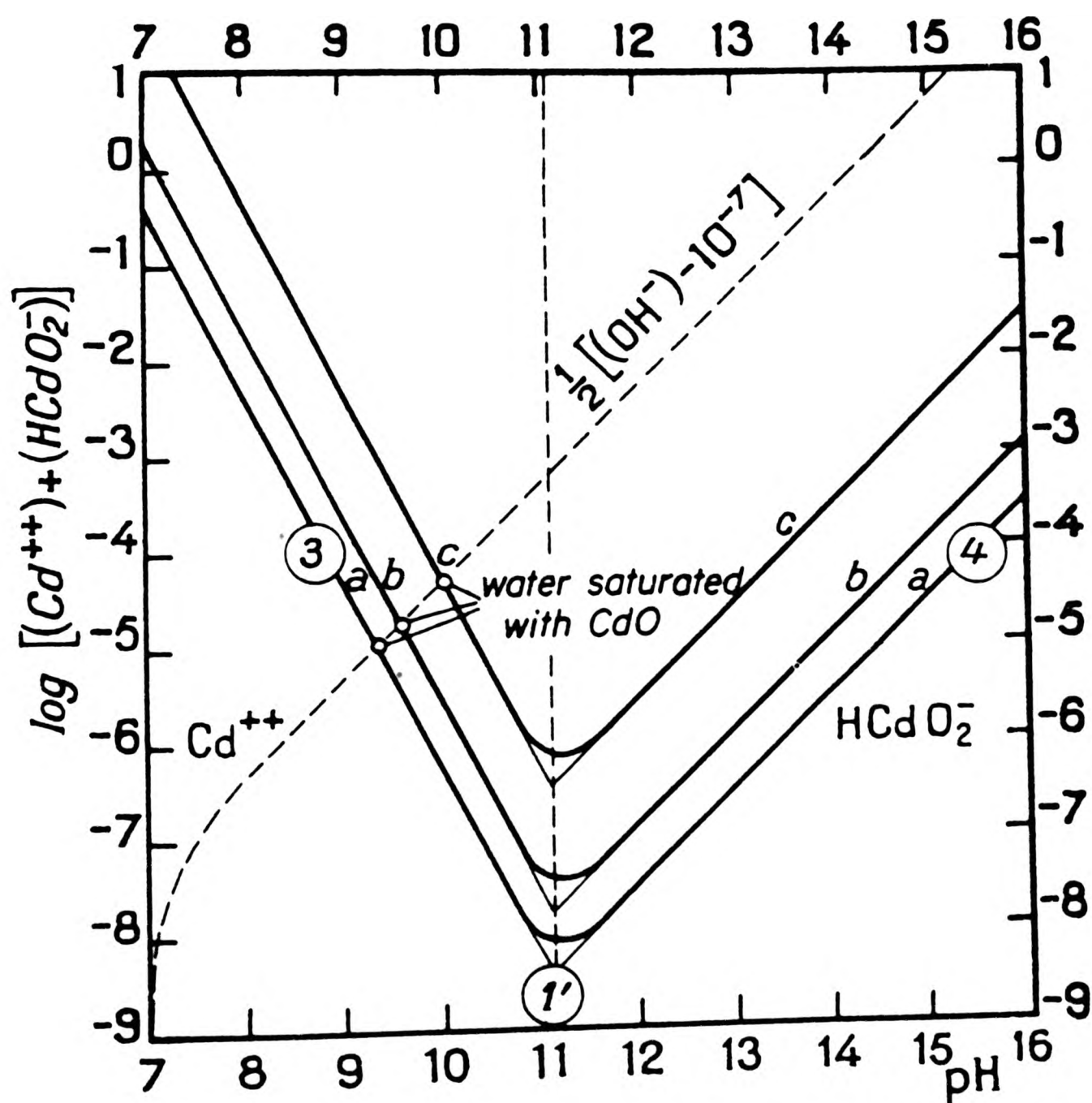


Figure 12. Influence of pH on the solubility of cadmium, at 25°C.
 (a, "inactive" $Cd(OH)_2$; b, "active" $Cd(OH)_2$; c, anhydrous CdO .)

bromide, iodide, nitrate, sulphate, ammonium, cyanide etc.³⁶ In general, cadmium complexes are not very stable. A large number of cadmium salts are sparingly soluble, e.g. carbonates, cyanides, phosphate and sulphides. Figure 11 shows the influence of pH on the solubility of anhydrous and hydrated oxides of cadmium. The upper limit of the domain of stability of cadmium practically coincides with the lower limit of the domain of stability of water at ambient and atmospheric pressures. This, coupled with the higher hydrogen overvoltage of cadmium, makes it stable in aqueous media. Cadmium can therefore be considered as being at the dividing line between noble and base metals; it is less noble than lead, appreciably more noble than zinc and slightly more noble than iron. The action of aqueous solutions on cadmium is qualitatively similar to their action on zinc, although cadmium has a slightly better resistance to general corrosion, it is appreciable only in the presence of oxidising or complexing substances, for example, ammonia, cyanides. At a current density of 1 A dm^{-2} zinc has an over potential of 0.746V, that of Pb 1.090V and that of Cd is 1.134V. In alkaline solutions cadmium is covered by a film of hydroxide, the formation of this film is easier at pH's of 10-13. This hydroxide constitutes a passive, protective layer at pH of 11. In other pH mediums it is soluble (see Figure 12).

1.4.2.3 Mercury-water system. Figure 13 shows the mercury-water system³² at 25°C in the absence of ions which form soluble complexes or insoluble salts, the mercuric cation Hg^{2+} forms a large number of complexes which are often quite stable. The monovalent mercury halides, the chromates (red), the iodide (green), and the sulphide (black) are sparingly soluble, and so are the divalent compounds, the iodide (red),³⁸ the sulphide, and thiocyanide. The presence of these would increase the passive zone. It appears that mercury is a noble metal since its domain of thermodynamic stability has a large area in common with the domain of thermodynamic stability of water. Mercury is practically unaffected by non-oxidising aqueous solutions of all pH's (provided that they are free from complexing

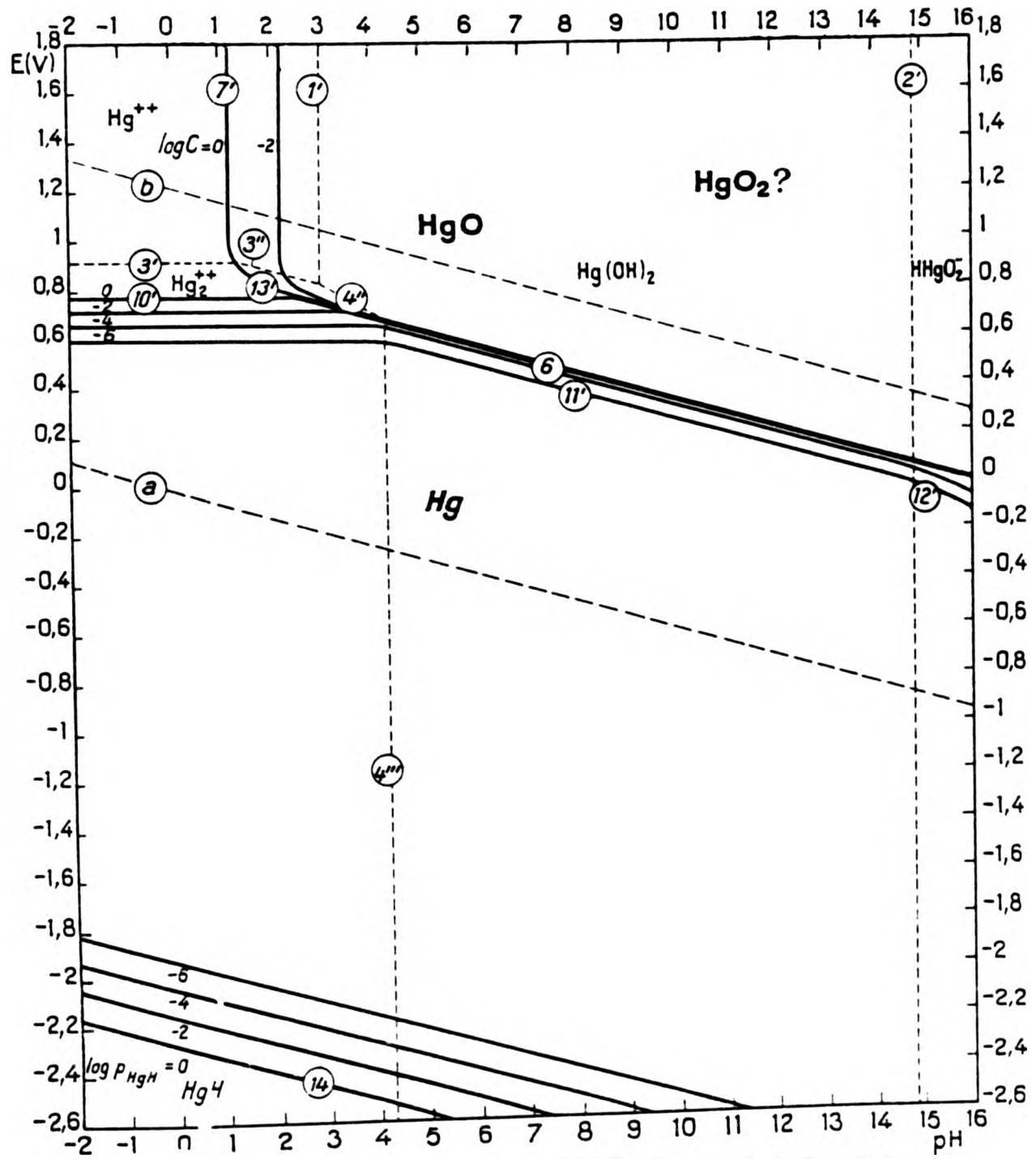


Figure 13. Potential-pH equilibrium diagram for the system mercury-water at 25°C. The part of the diagram inside the line $\log C = 0$ refers to solutions saturated with mercury or red HgO; the part outside this line concerns non-saturated solutions containing 1 g-at of dissolved mercury per litre (200 g l⁻¹) in the form of Hg²⁺ and Hg⁺.

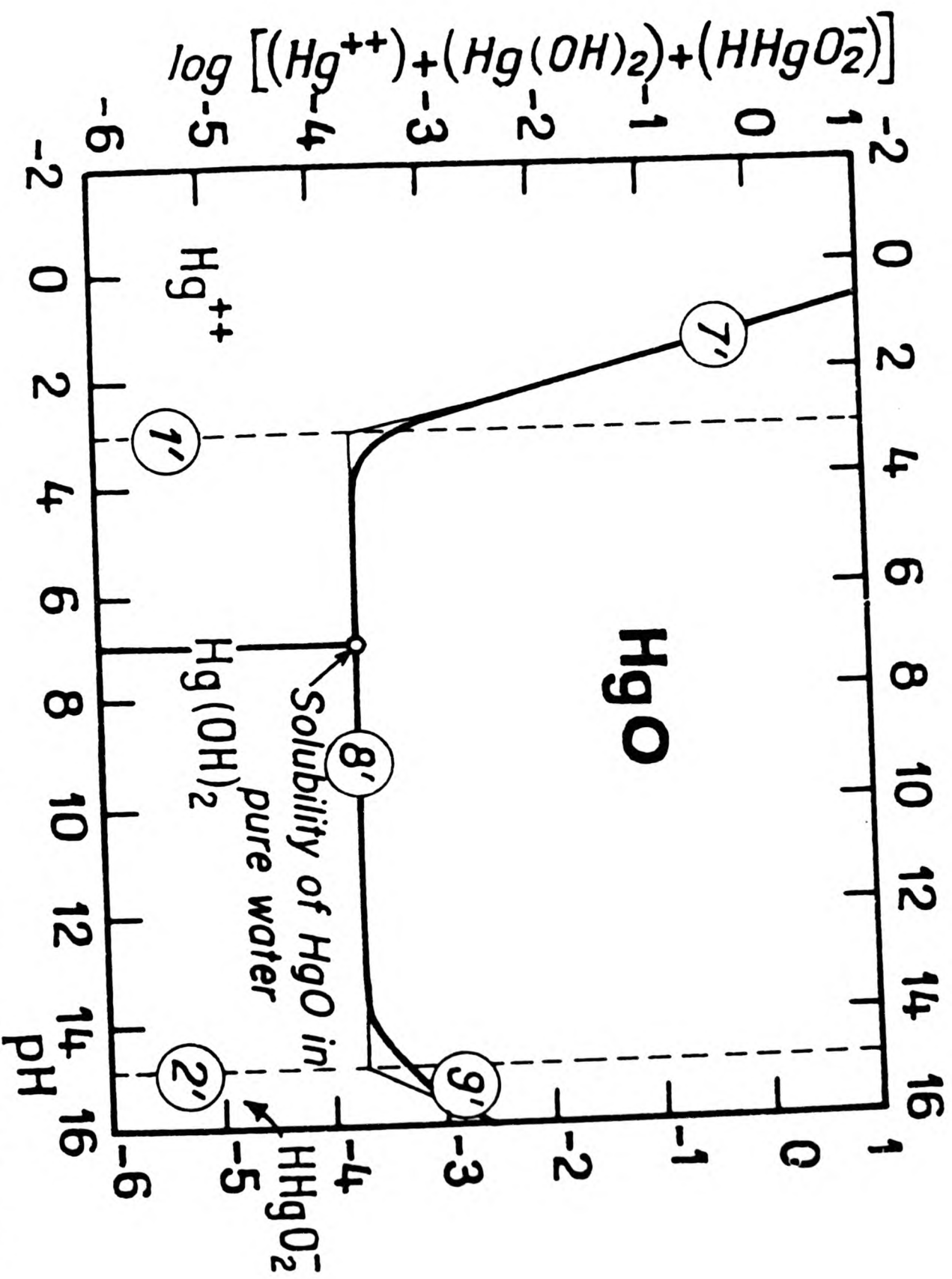


Figure 14. Influence of pH on the solubility of red HgO, at 25°C.

agents notably ammonia and ammonium salts) e.g. dilute solutions of sulphuric and hydrochloric acids, sodium and potassium hydroxides if free from oxygen. In neutral or alkaline solutions mercury is oxidised directly to the mercuric state with the formation of relatively soluble mercuric oxide. For example mercury is dissolved by nitric acid at 25°C to give mercurous nitrate, it is also dissolved by acid solutions of ferric chloride, it becomes covered with HgO in the presence of water and alkaline solutions containing oxygen. The formation of mercuric oxide is very rapid in the presence of ozone or permanganates. The large hydrogen over voltage enables many reduction reactions to be effected on the surface e.g. as in polarography. Mercury forms amalgams with many metals, some of which have reducing properties making them useful in analytical applications. It is not yet known whether the red and yellow form of mercuric oxide are allotropes or just differ in grain size. It is an amphoteric oxide and an oxidising agent. Mercurous oxide does not exist.³⁹ Figure 14 shows the influence of pH on the solubility of mercuric oxide at 25°C.

1.4.3 Electrode Kinetics. This is concerned with the processes taking place at the electrode electrolyte interface. These processes are responsible for the deviations from the thermodynamic equilibrium potentials and are referred to as "over potentials". The over potential ' η ' is related to the actual electrode potential E and the reversible thermodynamic value E_r by the equation: $\eta = E - E_r$. η will be positive for an anode where oxidation is occurring and negative for a cathode where reduction takes place. The factors contributing to the over potential may be classified as follows:

- (i) Activation over potential. The deposition or dissolution of an atom involves the transfer of electrons between ion and atom. The electron must overcome an activation energy barrier.
- (ii) Concentration over potential. This is associated with the decrease

in the concentration of reactants and increase in the concentration of products at the electrode interface because of the limited rate of transport of these components to and from the interface.

(iii) Resistive over potential. This does not include the ohmic potential drop due to the bulk solution and electrode phases, but is due to the interface and any film present on the electrode.

1.4.3.1 Activation over potential. In many cell reactions this is not very large, usually, and therefore does not contribute so much towards the departure of cell terminal voltage from the thermodynamic value. Over potential arising from the irreversibility of a charge transfer step is one of the most common types of activation over potential.

The activation component is represented by the well-known Tafel equation:

$$\eta = a - b \log i$$

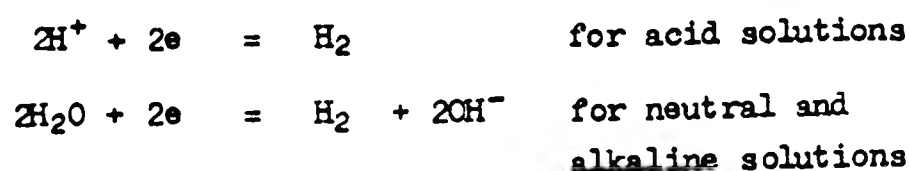
where η is the activation over potential in volts:

$$a \text{ is } \left(\frac{2.303RT}{\alpha nF} \right) \log i_0;$$

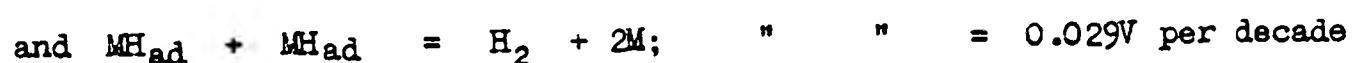
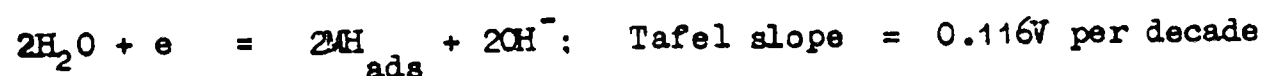
$$b \text{ is } \frac{2.303RT}{\alpha nF}; \quad \text{with the usual notation}$$

The exchange current density i_0 is defined as the internal current density in anodic or cathodic direction under reversible conditions. The transfer coefficient α represents the fraction of the potential difference between the metal and the Helmholtz plane ($\phi_m - \phi_H$) capable of changing the activation energy for the reactions. The transfer coefficient is relatively constant over a wide range of potentials for many processes provided the Helmholtz layer does not undergo any major changes. Hydrogen evolution reaction is quite an important electrochemical reaction.

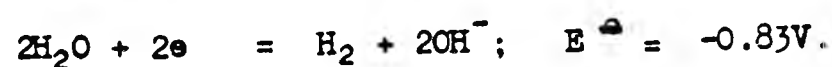
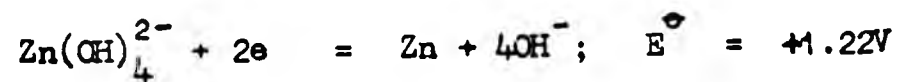
Hydrogen could evolve in two overall schemes:



The overall reactions can be broken down to a sum of individual sub-reactions consisting of charge transfer, adsorption, desorption, simple chemical recombination or electrochemical reduction. Either of these sub-reactions may become rate controlling depending upon the conditions of reaction. Certain metals for example platinum and palladium have very low hydrogen evolution over potential and have high exchange current densities of the order of a few mA per cm², whereas certain other metals for example mercury, lead, gallium etc. have high hydrogen over potential and very much lower exchange current densities of the order of a few picoamperes per cm². Thus hydrogen evolution will be efficient and quicker on platinum and palladium but much slower and irreversible on mercury, lead etc. On zinc and cadmium these values lie in between these extremes. The overall reaction for hydrogen evolution in alkaline or neutral solution may be written as



Some evidence also exists in favour of a more complex electrochemical desorption, that is $\text{MH}_{\text{ads}} + \text{H}^+ + e = \text{M} + \text{H}_2$. The discharge step involves the incorporation of hydrogen ion in the lattice of the metal or adsorption on available sites on the metal surface. Here again different metals show a preference for one or the other depending upon the conditions. The practical significance of hydrogen overvoltage can be realised while considering zinc deposition and dissolution reactions.



At first it may seem that it is not possible to deposit zinc from aqueous solutions because the reduction potential for hydrogen deposition is lower than that for zinc deposition, so that cathodic reduction in a zincate solution will only result in hydrogen evolution. However, because

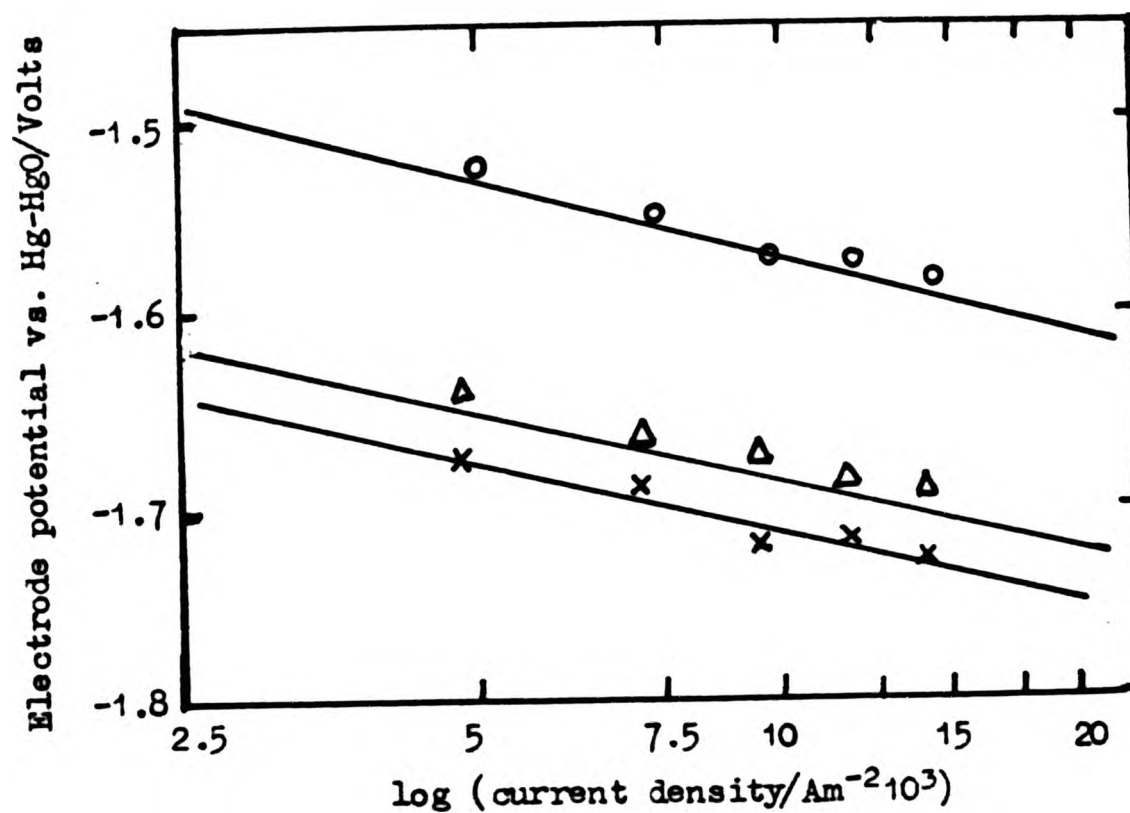


Figure 15. Tafel plots for hydrogen overvoltage on Zn-Hg electrodes in 1 mol dm⁻³ KOH at 25°C

Zinc ○
5 w/o Hg-Zn △
8 w/o Hg-Zn ×

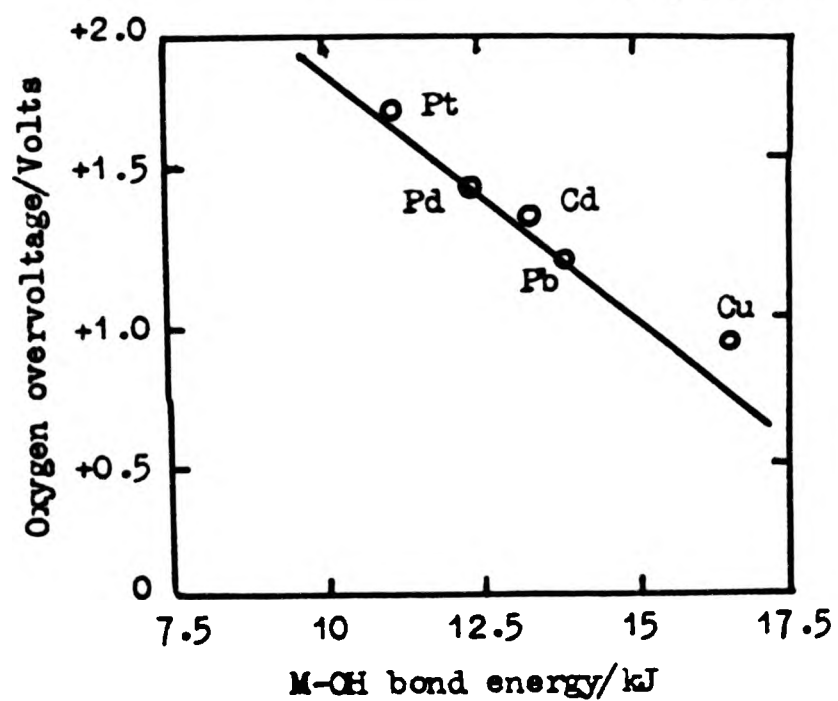
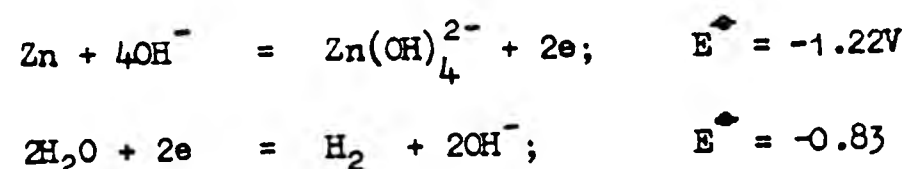


Figure 16. Oxygen overvoltage data at 25°C in 1 mol dm⁻³ KOH at 10⁻⁴Am⁻².

of this hydrogen overvoltage it is possible in practice to deposit zinc from aqueous solution. During zinc dissolution process represented by equation



The difference of potential as indicated by the above values would mean that thermodynamically the reaction should be driven by a large e.m.f. but this is not so because of the high hydrogen overvoltage on zinc this corrosion is decreased to a considerable extent. Any addition of mercury should further increase the hydrogen overvoltage as indicated in Figure 15.

Oxygen overvoltage also varies according to the metal. Rüttschi and Delahay⁴⁰ proposed that the overvoltage variation results from differences in the bond energy of M-OH bond. The overvoltage decreases approximately linearly with increasing bond energy. The correlation is shown in Figure 16.

1.4.3.2 Concentration polarisation. This is associated with the mass transport of ions. As an example, consider a common cell reaction



Hydroxyl ions will reach the zinc surface by two mechanisms: migration and diffusion. The former is the result of a voltage gradient in the cell, the latter is the result of a concentration gradient set up at the reaction interface. From Fick's law of diffusion the diffusion current can be calculated and is given by the equation:

$$i = \frac{DnF}{\delta_0(1-t_i)} \times (C^b - C^s), \quad \text{with usual notations,}$$

The value of t_i will approach zero if the solution contains another type of ion which has the same polarity as the ion being discharged. Otherwise t_i will remain finite, even though the concentration of the i th ion approaches zero at the electrode surface. The value for the effective

thickness of the diffusion layer δ_0 depends on the type of convection and the configuration of the electrode. On vertical flat electrodes δ_0 is of the order of 10^{-4} m. For many simple solutes in aqueous solutions, the diffusion coefficients D fall in the range 10^{-10} - 10^{-9} m² per second. With forced convection, δ_0 decreases and is of the order of 10^{-5} m now.

Increasing the rate of reaction by increasing the current results in less time for new dischargeable ions to arrive by diffusion replacing the ions used up by the reaction. Thus C^s decreases with increasing current. When the rate of charge transfer is much greater than the diffusion rate, C^s becomes zero, and we arrive at a maximum diffusion limited current.

$$i_{lim} = \frac{DnF}{\delta_0(1-t_i)} C^b.$$

The difference in concentration existing between the reaction interface and the bulk of the electrolyte result in a potential and concentration gradient. The concentration potential acts in opposition to the electrode potential and is therefore termed as the concentration polarisation. This is related to the limiting current density, i_l , by the

equation:
$$\eta = \frac{2.303RT}{nF} \log \left(1 - \frac{i}{i_l} \right).$$

A relatively large change in the concentration of a component at the electrode interface is required to produce a significant concentration overpotential. For example, a tenfold change in the concentration will produce only ± 60 mV change in overpotential for a one electron process at room temperature.

1.4.3.3 Resistance polarisation. This is the result of a potential drop due to sum of resistances of the electrolyte, oxide films, gas layers, separating membranes, contact resistances etc. This component is time-independent and is zero when the current is zero. The activation and concentration polarisation terms are time-dependent and exhibit build-up and decay on switching on and switching off. This fact may be utilised

to separate the linear and non-linear components of voltage loss associated with chemical reaction. If an oxide film is monolayer thick, the distinction between activation overpotential and ohmic overpotential becomes superficial. Even with films many layers thick, it is difficult to establish adequate experimental criteria for distinguishing between activation and ohmic overpotentials.

1.4.3.4 Passivation. It occurs under certain circumstances, as the potential of a dissolving metal electrode is shifted to more positive values, the current passes through a maximum and then decreases to low values rather than increasing. In the range of potentials where the dissolution is negligible, the electrode is described as passive. Passivity is conferred by a covering of a mono or multilayer film of oxide or hydroxide or some similar species. The movement of cations or anions through this layer is very slow even with large potential gradients at room temperatures. The stability, adherence, and resistivity of passive films usually depends on minor components and impurities present in the metal as well as the solution. Passivation sets an upper limit to the current that can be drawn from a cell and has been encountered in alkaline cells using zinc anodes. Passivation is not always an undesirable phenomenon in batteries. In dry cells using magnesium anodes, the alloying elements and the electrolyte composition are chosen such that anodes are passive under open circuit conditions, becoming active rapidly when current is drawn. In this way self discharge through anode corrosion is minimised.

1.4.3.5 Chrono-potentiograms and Transition Times

Sometimes it may be advantageous to apply a current step or galvanostatic method to study passivation. The principal advantage is the ease of measuring the charge supplied. The inherent disadvantage is that the double layer charging interferes as it proceeds at the same time as the electrode reaction. The form of a typical chronopotentiogram is illustrated in Figure 17. Such chronopotentiograms can be divided into three

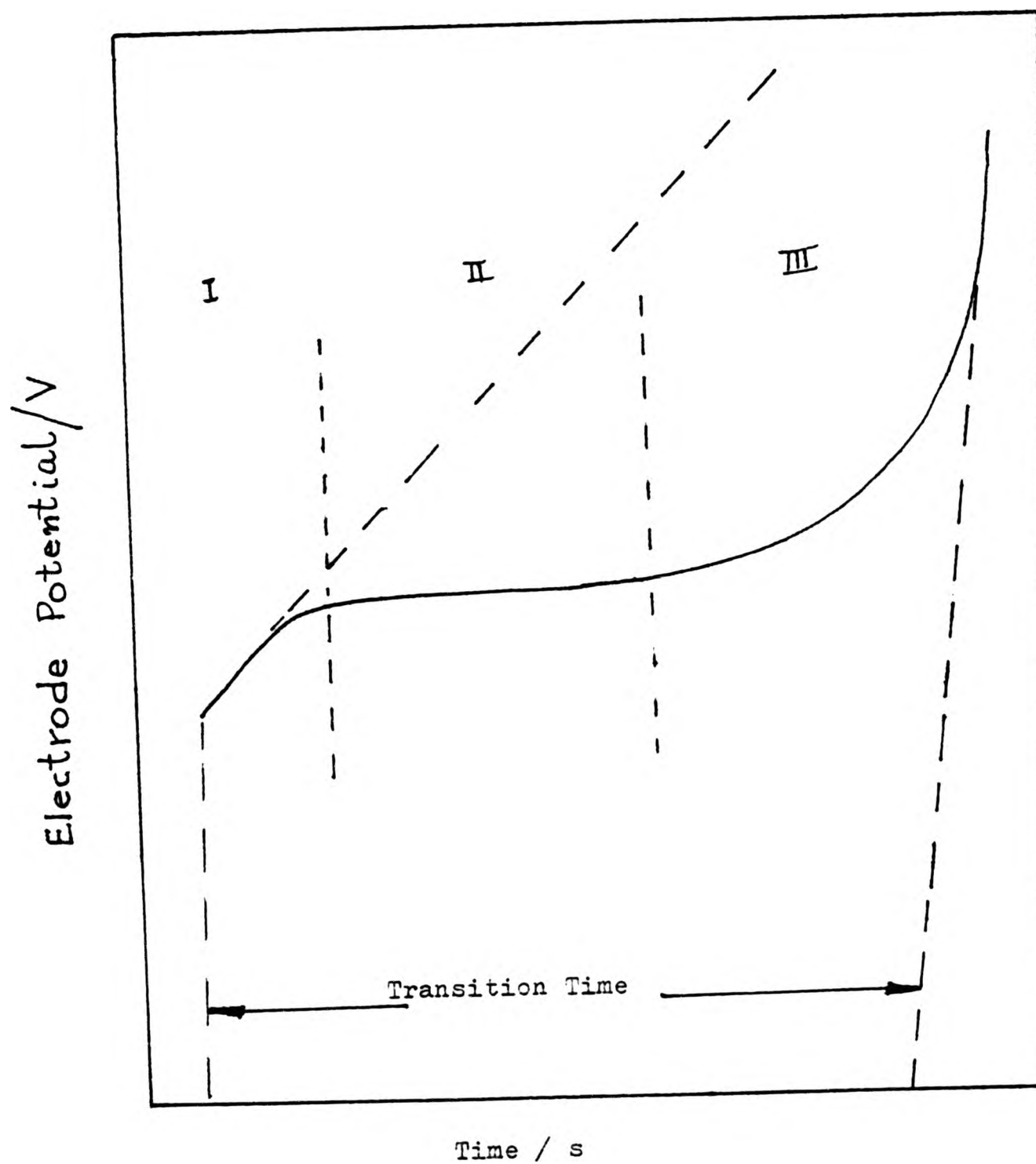


Figure 17. A schematic representation of a typical chronopotentiogram. Part I is the effect of double layer charging. Part II is the effect of a slow electrochemical step. Part III is the effect of onset of passivation.

parts. The first curve in the beginning shows the effect of double layer charging, where the potential rises with time. This is completed in a short duration of time, after which the potential assumes a steady value. This straight line part represents a slow electrochemical step for a simple redox reaction. The third part is a steep curve representing a sudden or abrupt rise of potential with time, which is caused by the onset of passivity, the passive film being a barrier to the diffusion of ions, resulting in the steep rise of potential. The time to passivation or the transition time can be measured as the time interval between the tangents drawn to the curved parts where the potential is at the rest potential and at the part where the potential has attained a value such that the curve is now almost a straight line parallel to the potential axis. The transition time is a characteristic quantity inversely proportional to the square of the applied current density. As stated earlier this relationship can be represented by the formula below where i represents the current density associated with the electroactive species.

$$i t_p^{\frac{1}{2}} = \frac{n F A^{\frac{1}{2}} D^{\frac{1}{2}} (C^b - C^s)}{2}$$

The notation in this formula has the usual meaning. See the list of symbols. With certain electrode configuration a critical current density has been observed below which no passivation is observed. This fact modifies the above formula to the following:

$$(i - i_c) = \text{constant}$$

1.4.4 Anodic Behaviour of Zinc. Zinc is thermodynamically unstable in air and in many aqueous electrolytes. In air it is covered with a thin oxide layer or tarnish. It is amphoteric in nature so it can corrode in alkaline, neutral or acidic media by hydrogen evolution or oxygen reduction with precipitation of oxide on the surface. Depending upon the conditions the latter may form a passive, protective

27

layer on the surface thus diminishing the corrosion rate to a great extent. The realisation that the rate of deterioration of cells utilising zinc is closely related to its rate of hydrogen evolution has led a number of workers to investigate this problem in detail by means of the measurement of the hydrogen evolved in alkaline solutions. Bobker⁹ has reviewed the status of zinc in alkali system covering the science and technology. Snyder and Lander⁴⁴ found that the amount of hydrogen evolved from commercial amalgamated zinc specimens:

- (i) increased in the presence of zincate ions in the electrolyte,
- (ii) decreased with decreasing temperature,
- (iii) decreased with increasing alkali concentration,
- (iv) decreased in the presence of amalgamated mercury.

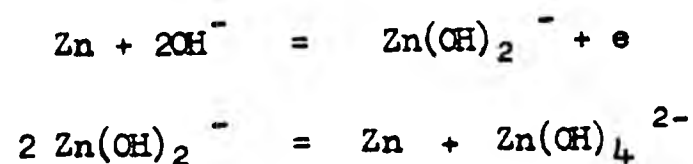
Rüetschi⁴⁵ carried out experiments on amalgamated zinc powder in potassium hydroxide obtaining different results from those found by the above authors. He found the corrosion rate to increase with increasing alkali concentration as was also found by Jofa, Komlev and Bogotski.⁴⁶ There was agreement in results over the influence of temperature. Dirkse and Trimmer⁴⁷ attributed the conflicting results of these workers to their method of obtaining the data. They performed similar experiments, but their results were not in full agreement with either worker, but agreed partly with either on the influence of certain variables. Gregory, Jones and Redfearn⁴⁸ conducted their experiments over a few weeks rather than over a few minutes or hours. They found that the corrosion rate of zinc amalgams decreased rapidly for the first few days and attained a steady value over a month. The corrosion rate of zinc and zinc containing lead decreased initially with increasing potassium hydroxide concentration and then increased with further increase in concentration. The corrosion rate from zinc amalgam was a minimum at 5-6 mol dm⁻³ concentration. In zincate containing solutions the rate of corrosion decreased initially and then increased, the minimum being at the same concentration. Vorkapic et al⁴⁹ carried out volumetric measurements of the rate of hydrogen evolution

42

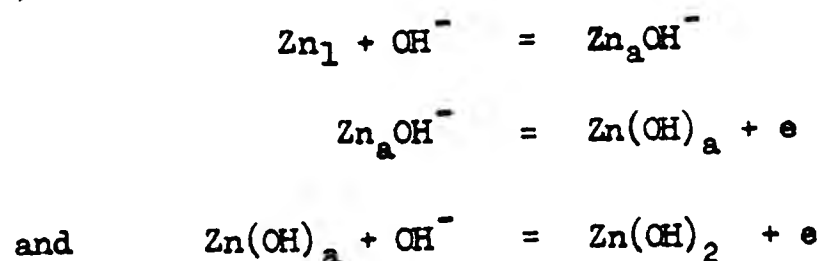
and polarisation studies and found that rate of hydrogen evolution was dependent upon time and concentration of electrolyte. Moshtev and Stoicheva⁵⁰ used a spongy alloy of zinc and lead, containing 0.2 to 0.5% lead, produced by co-deposition at an appropriate current density. De Pauli et al⁵¹ using cyclic voltammetry studied the effect of phosphate ions on this system. They attributed the observed decrease of zinc dissolution rate in the presence of phosphate ions to the formation of an insoluble complex.

Depending upon the applied current density, temperature, concentration of hydroxyl ions, a complete discharge of all available capacity can be achieved or passivation may occur after partial discharge or at higher current drains the anode may passivate with total loss of capacity. The passivation has been found to be a reversible process. The applied current density is inversely proportional to the square root of the time to passivation, i.e. $it_p^{\frac{1}{2}} = \text{constant}$ for vertical electrode with no stirring. With horizontal electrodes and stirring $(i - i_c)t_p^{\frac{1}{2}} = \text{constant}$, where i_c is a critical current density and t_p is time to passivation. The E-i curve shows the presence of two different types of oxide films. There are distinct signs of two types of anodic films.⁵³ In the absence of stirring a thick flocculent layer forms. When properly stirred a tough, transparent, adherent film forms. During anodic polarisation experiments conducted at low sweep rates⁵⁴ in unstirred solutions, hydrogen gas bubbles disrupted the oxide film exposing fresh metal to attack. Passivation occurs at lower voltages with porous electrodes,⁵⁵ although peak current obtained is higher. Nikitina⁵⁶ obtained zinc hydroxide crystals from spent solution at -15°C , but for higher temperatures and concentrations of greater than 5 mol dm^{-3} he found zinc oxide on the surface as well as in the solution. X ray diffraction⁵⁴ and electron diffraction⁵⁷ studies show that the passive surface is composed of zinc oxide whereas the non passive state is composed of epsilon zinc hydroxide. Popova⁵⁸ and co-workers, during their measurements on

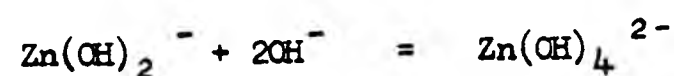
rotating disc electrodes found that the current density at the onset of passivation was affected by the zinc oxide content of electrolyte and was about $10,000 \text{Am}^{-2}$ in a 10 mol dm^{-3} solution and 3200Am^{-2} for zinc oxide saturated solutions. The blackening of the zinc surface often observed is due to the elemental zinc formed by a disproportionation⁵³ reaction as under:



The mechanism of zinc dissolution in an alkaline system is thought to be as follows,⁵⁵

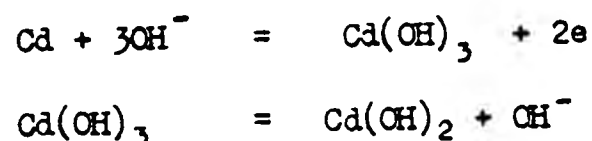


where 'l' indicates an atom in the metal lattice at a kink site, 'a' indicates an adsorbed ion on the kink site. An alternative⁵⁹ reaction scheme has been suggested when a soluble species forms:

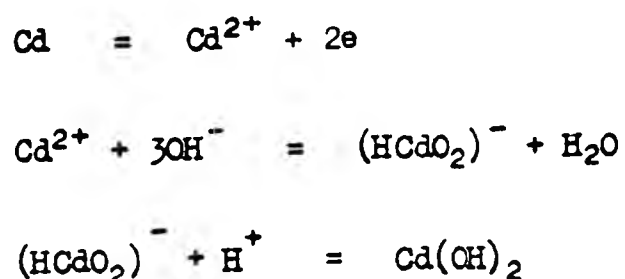


1.4.5 Anodic Behaviour of Cadmium. Cadmium in strongly alkaline solutions behaves similarly to zinc except in the pH range 12-14 where the passive film is not soluble to any significant extent. In spite of much effort by a number of workers, the reaction mechanism is not agreed upon. A dissolution-precipitation mechanism⁶⁰ and an alternative solid-state oxidation mechanism involving ionic transport⁶¹ through the Cd(OH)_2 film have been proposed. Some authors⁶²⁻⁶⁴ found no evidence of CdO formation but others^{87, 65-67} reported experimental results of cadmium oxide formation. It has been suggested⁶⁸ that cadmium oxide is formed as a primary product before its conversion to cadmium hydroxide or as a result of a secondary reaction that occurs after it has formed. Some

authors^{66,69} suggest that it is the cadmium oxide layer and not cadmium hydroxide layer that causes the passivation which limits the extent of anodic oxidation of cadmium metal. Using ring disc electrode technique,⁶¹ formation of a soluble intermediate species has been demonstrated, during anodic polarisation, thus:



Lytner et al⁷⁵ found that the polarisation curves in the region of active dissolution of cadmium had small Tafel slopes (10-12mV per decade) suggesting that hydroxide ions were adsorbed on the surface. Hampson and Latham⁷⁶ used the a.c. impedance method and a double-pulse galvanostatic technique to study the charge transfer reaction at polycrystalline cadmium specimens. They found the charge transfer process to be very rapid and adsorbed hydroxide or oxide film present. Bro and Kang⁷⁷ measured discharge profiles in porous electrodes by chemical analyses of thin sections and found that the extent of discharge was strongly dependent on current density. $\text{Cd}(\text{OH})_2$ the product of dissolution remained inside the electrode and caused eventual choking of the porous structure. Yoshizawa and Takehara⁷⁸ proposed a reaction sequence as follows:



When the solution is saturated with $(\text{HCdO}_2)^-$, cadmium oxide forms on the electrode surface which dissolves in the electrolyte, if the rate of formation of CdO is greater than its dissolution rate it accumulates on the surface. The findings of Armstrong et al⁷⁹ on porous electrodes were similar to those of Bro and Kang. It has generally been concluded that anodic passivation proceeds through steps and ranges from -0.9 to 1.0 volts. Passivation times are strongly dependent on temperature and

current density. Armstrong and West⁸⁰ using a linear sweep on the ring disc systems into the region of film formation found, in agreement with Okinaka,⁶¹ that a small fraction of the disc current was consumed in the formation of a solution-soluble cadmium species. Linear sweeps at different rotation speeds showed that (within experimental error) a change in the rotation speed did not change the *i*-*E* relation, indicating that the solid-state mechanism was operative, in disagreement with Okinaka. They considered that Okinaka's reasons for the dissolution-precipitation mechanism could equally well be explained by a nucleation overvoltage due to a solid-state mechanism together with parallel metal dissolution.

1.4.6 The Role of Mercury. Mercury has been used as a constituent of cell anodes since 1828. It was generally adopted from 1910. As an anode material it acts as a rather noble metal. It does not get 'attacked' in the presence of base metals such as zinc, cadmium, lithium, sodium etc. A 0.60 w/o sodium-mercury alloy has been used, as cited earlier. Up to 10 w/o mercury-zinc alloy is used in the alkaline cells. In all these cases mercury simply acts as a check on wasteful corrosion in the following ways:

(i) It provides a smooth surface that minimises high energy points such as kink, step and dislocation sites, thus reducing the possibility of wasteful corrosion.

(ii) Mercury serves as a solvent for small amounts of certain heavy metal impurities such as lead, copper and nickel. These metals are then not capable of acting as cathodes for local galvanic couples at the electrode surface.

(iii) Mercury increases the hydrogen overvoltage above that of the unamalgamated metal. Davies¹¹² quotes the following values of overpotential in aqueous HCl solutions at 0.001 and 0.10A cm⁻²; 1.04V, 1.21V, exchange current density 6 x 10⁻¹³A cm⁻² and transfer coefficient 0.50. Krishtalik¹¹³ considers the discharge of hydrogen on mercury as a

"barrierless" process at low current density. The theory predicts that for this mode, overvoltage should be practically independent of the solution composition and $\alpha = 1$ and $b = 59\text{mV}$. This is proved by a sharp inflection in the curves of $\log i$ vs. η indicating a change from barrierless to ordinary discharge. These curves were plotted for acidified solutions of potassium iodide at 25°C . Barrierless discharge is independent of ψ_1 potential and the concentration of hydronium ions. A change in double layer structure affects the barrierless discharge strongly.

Data on h.e.r. on mercury in acid solutions is accurate and there is agreement amongst workers¹¹⁴ but that in alkaline solutions is scarce and discrepant. Thus in 0.1 mol dm^{-3} KOH at 25°C at $10^{-5} \text{ A cm}^{-2}$, η can be from 0.965 to 1.15V.^{115,116}

1.5 INVESTIGATIONS AT THE CITY OF LONDON POLYTECHNIC

1.5.1 Introduction. The zinc electrode is subject to self-discharge in aqueous KOH electrolyte as discussed in section 1.4.2.1. Hydrogen is evolved as a result. The reaction is pH dependent. The rate of gassing will depend on kinetic factors discussed earlier in section 1.4.3. The reaction causes a loss in capacity, loss in water from the electrolyte, and also necessitates incorporating a system to vent hydrogen from the cell. These factors influence the shelf life capacity in service. Amalgamation reduces self-corrosion but it increases the cell cost and reduces the capacity as zinc is displaced. Amalgamation with 10 w/o Hg is equivalent to a reduction in capacity of nearly 40%. An interest in these aspects of cell development led to a programme of research sponsored by the Procurement Executive, Ministry of Defence at the City of London Polytechnic to investigate these problems.

The possibilities of modifying the nature of the anode material to improve its long term stability on open circuit without losing performance

under normal discharge conditions were particularly of interest. In many potential service applications a single discharge mode of operation could be envisaged.

The first investigation started in 1973 when Ramanathan⁷⁰ studied the corrosion properties of cadmium and gallium plated sheet zinc in potassium hydroxide with a view to examining improved 'open-circuit' stability of zinc through the interaction of a surface coating of a more corrosion resistant metal with a higher hydrogen overvoltage characteristic. He also reviewed the literature on indium and indium-bismuth alloys. He concluded that the rate of hydrogen evolution in potassium hydroxide of commercial grade zinc sheet is both concentration and time dependent. It exhibits a maximum in 3.5 mol dm^{-3} KOH concentration. Cadmium coated zinc exhibited a decreased rate of hydrogen evolution at initial times with increasing KOH concentration. The maximum was at 5 mol dm^{-3} concentration. The presence of small amounts of dissolved cadmium in the solution markedly increased the corrosion rate of zinc. The rate of corrosion was lower in concentrations greater than 2 mol dm^{-3} for cadmium coated zinc as compared to that of uncoated zinc. Gallium coated zinc suffered from grain boundary embrittlement and increased the corrosion rate tenfold. Adding dissolved gallium to the solution increased the corrosion rate of zinc. From electrochemical polarisation studies Ramanathan concluded that zinc oxide formed as a product of anodic dissolution, which thickened and spread skimming the surface, was bluish black in colour and peeled off leaving a transparent passive film of oxide. The critical current density was seen to increase with increasing KOH concentration. During cathodic sweep, the peak current was lower and the break from passivation occurred at a lower potential. Current oscillations observed just before the onset of passivation were seen only in KOH of higher concentrations. Reversibility of passivation phenomenon, was exhibited by the observed current oscillations at the same potential during the anodic and cathodic sweep. From the review on the behaviour

of indium Ramanathan concluded that indium dissolved as a trivalent species and passivation was caused by an insoluble $\text{In}(\text{OH})_3$ film. The initial formation of a soluble trivalent species occurred at around the same value for all current densities, whereas formation of insoluble film occurred at increasingly positive values and at current densities in excess of 8mA cm^{-2} disappeared and was followed by oxygen evolution. In 8.5 mol dm^{-3} KOH, a loose white gelatinous deposit of $\text{In}(\text{OH})_3$ forms at -1.11V which flakes off at potentials between -1.10V and -1.06V . At more positive potentials an In_2O_3 deposit was formed.

Alloying indium with bismuth increases its hardness, counters the deleterious effects of impurities, enables it to maintain its voltage, imparts protective properties to the passivating film and causes disruption of In_2O_3 deposits. He suggested that performance of zinc anodes may be improved by incorporating a surface coating of cadmium or indium imparting superior corrosion resistance. This project was taken up by Carew⁷¹ who succeeded in producing electrodeposits of cadmium and indium on zinc and then studied corrosion properties of these combinations. He concluded that thin, coherent, non-porous deposits of cadmium and indium can be plated onto zinc substrates if the coating thickness was over $6\text{ }\mu\text{m}$. Cadmium coatings produced by variation of current during deposition, showed better stability and corrosion behaviour. The rate of hydrogen evolution was sharply lowered, over the test period, for deposits of cadmium thicker than $8\text{ }\mu\text{m}$ as compared to that of pure zinc. Indium coated zinc showed superior corrosion resistance to that of pure zinc, pure cadmium and cadmium coated zinc. He suggested that there was scope for improving the electroplating process so that non-porous, adherent and thin coatings were produced and also conducting long term corrosion tests on the corrosion behaviour as opposed to the short-period tests conducted so far.

Russ⁷² took up these suggestions and attempted to produce better electrodeposits on zinc substrates, but he did not succeed in producing

thin, adherent and non-porous coatings. However, he did conduct long term corrosion tests and anodic polarisation studies. His conclusions were as follows: Cyclic potentiodynamic scans of electrodeposited cadmium on zinc showed that the cadmium could not be readily dissolved to expose the zinc substrate, due to the highly passivable nature of cadmium. It is not possible to produce porosity free cadmium coating and therefore its protective value is nil at thicknesses less than 2-3 μ m. Hydrogen evolution studies showed the catastrophic effect of porosity on the corrosion rates. It was evident from his investigations that the potential benefits initially considered possible in using coated anode material in a cell to improve long term corrosion resistance were unlikely to be achieved.

It was thought that instead of using a coating, alloying with cadmium would be more beneficial. Manohar⁷³ and Shaikh⁷⁴ prepared zinc-cadmium alloys containing 0.2, 1.0, 2.0, 5.0 and 25% cadmium. They conducted long term hydrogen evolution experiments, anodic polarisation and galvanostatic discharge studies on these alloy specimens. Alloy amalgams were also made and similar long term experiments were carried out in addition to the electrochemical polarisation. The following conclusions were reached. One thousand hour tests confirmed that an alloy composition of 0.2 to 1.0 w/o cadmium appeared to exhibit the best corrosion resistance. Short galvanostatic discharge tests indicated that a 1.0 w/o alloy performed as well as a comparable commercially amalgamated porous anode (ex Mallory). Open circuit corrosion potentials are little changed by alloy composition or temperature. Potentiostatic polarisation at 1mV per second shows that the slope of the active dissolution region is little influenced by composition up to 5% Cd or by temperature. The critical current density for passivation is progressively increased by temperature, barely changed by alloy composition but suppressed by ZnO additions to the electrolyte.

These investigations have continued to support the development

potential of the cadmium-zinc alloys. It was suggested that future work should include evaluation of discharge performance after long exposures.

1.6 THE OBJECT OF THE PRESENT INVESTIGATIONS

The present studies represent an extension of the author's previous work from which it was concluded that homogeneous zinc-cadmium alloys and their amalgams could yield improved anode material as assessed by their self-corrosion behaviour. This work has been consolidated.

To characterise the electrochemical behaviour of these thermally prepared alloys in more detail anodic polarisation experiments employing a rotating disc electrode assembly have been carried out. Some data on long term galvanostatic discharge characteristics has also been collected and examined. This has been complemented by a study of the hydrogen evolution reaction and the associated overpotential phenomena in the same system.

It was also considered desirable to examine alternative methods of preparation of such alloys in a form more suitable for battery anode fabrication. This has led to an investigation of the possibilities of employing the principles of alloy electrodeposition for the production of microcrystalline binary zinc-cadmium and ternary zinc-cadmium-mercury alloys. The conditions necessary to achieve the required range of compositions have been delineated, the structure of the material has been examined and by X-ray diffraction studies the electrodeposit has been proved to be an alloy and that it is not simply just an intimate mixture.

CHAPTER TWO

PREPARATION OF ALLOYS2.1 INTRODUCTION

Alloying additions of cadmium to zinc have been found to be very promising with regard to the self corrosion and discharge rates of the battery anodes.⁷⁴ These alloys were prepared in the laboratory from 99.99% purity zinc and cadmium rods supplied by Metals Research Ltd. It was thought that amalgamation may also have some additional beneficial effect and therefore a series of amalgamated alloys was also produced.

It had been found in earlier studies on the preparation of these alloys that other methods had inherent disadvantages. For example, casting in a steel or graphite mould increases the risk of contamination with iron and carbon respectively. Both these impurities have a harmful effect of increasing the hydrogen evolution rate. On the other hand approaching the problem from a powder metallurgical route by compacting a mix of powders resulted in a porous electrode. Subsequent sintering at 200°C gave coarse grain material with considerable retained porosity. In view of the nature of this process there are more chances of the introduction of contaminants and impurities and for oxidation to take place.

To avoid oxidation, ingress of impurities and contamination vacuum induction melting was finally adopted. This gave a good clean melt. Induction heating is based on the fact that eddy currents are induced in the work piece if it is kept inside a conductor coil carrying an alternating current. The frequency of alternating current determines the depth of heat penetration in the specimen. Thus a low frequency induces heating to a significant depth, whereas a high frequency may heat only the surface layers.

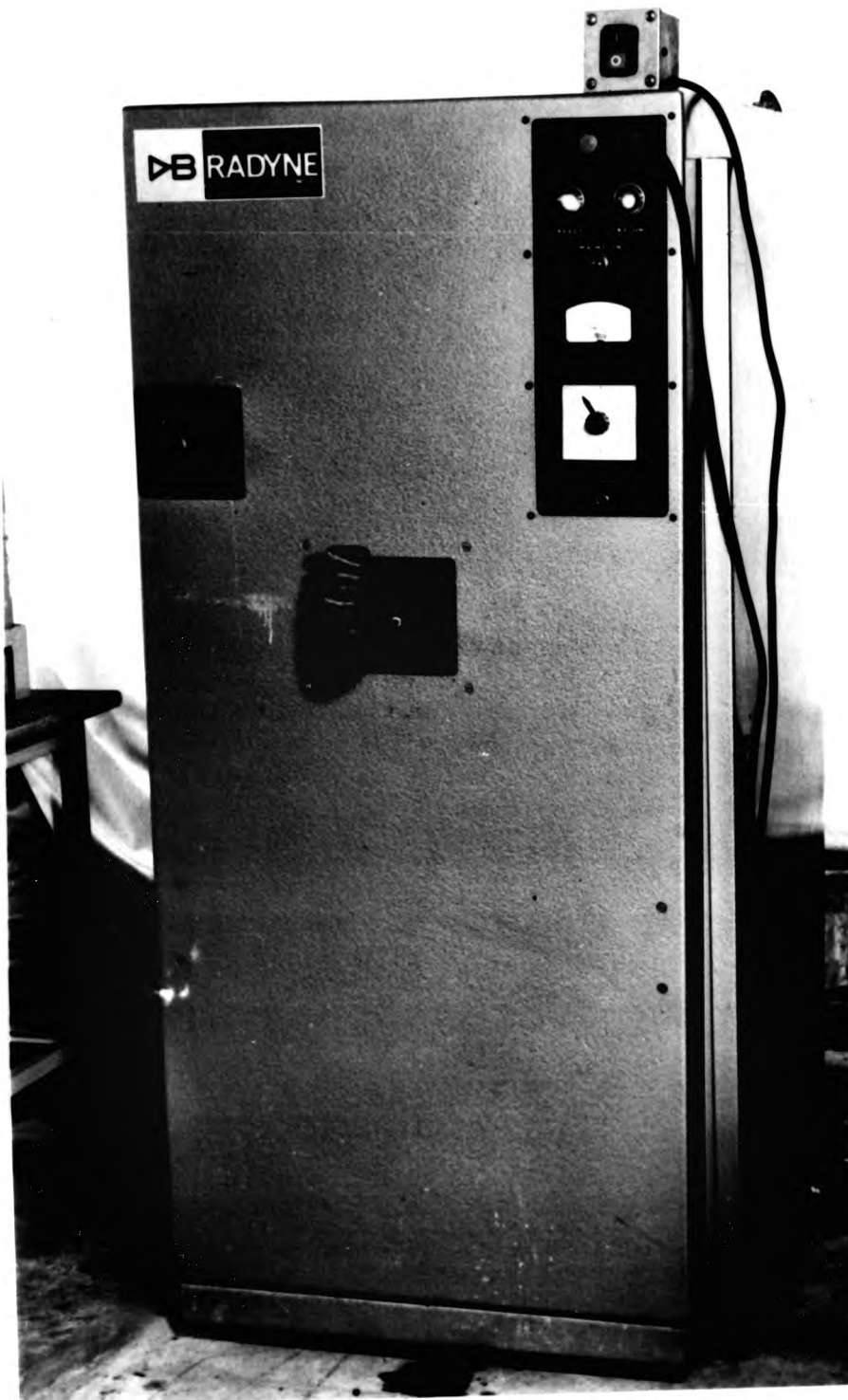


Figure 18. A view of the low frequency induction heating
and melting unit

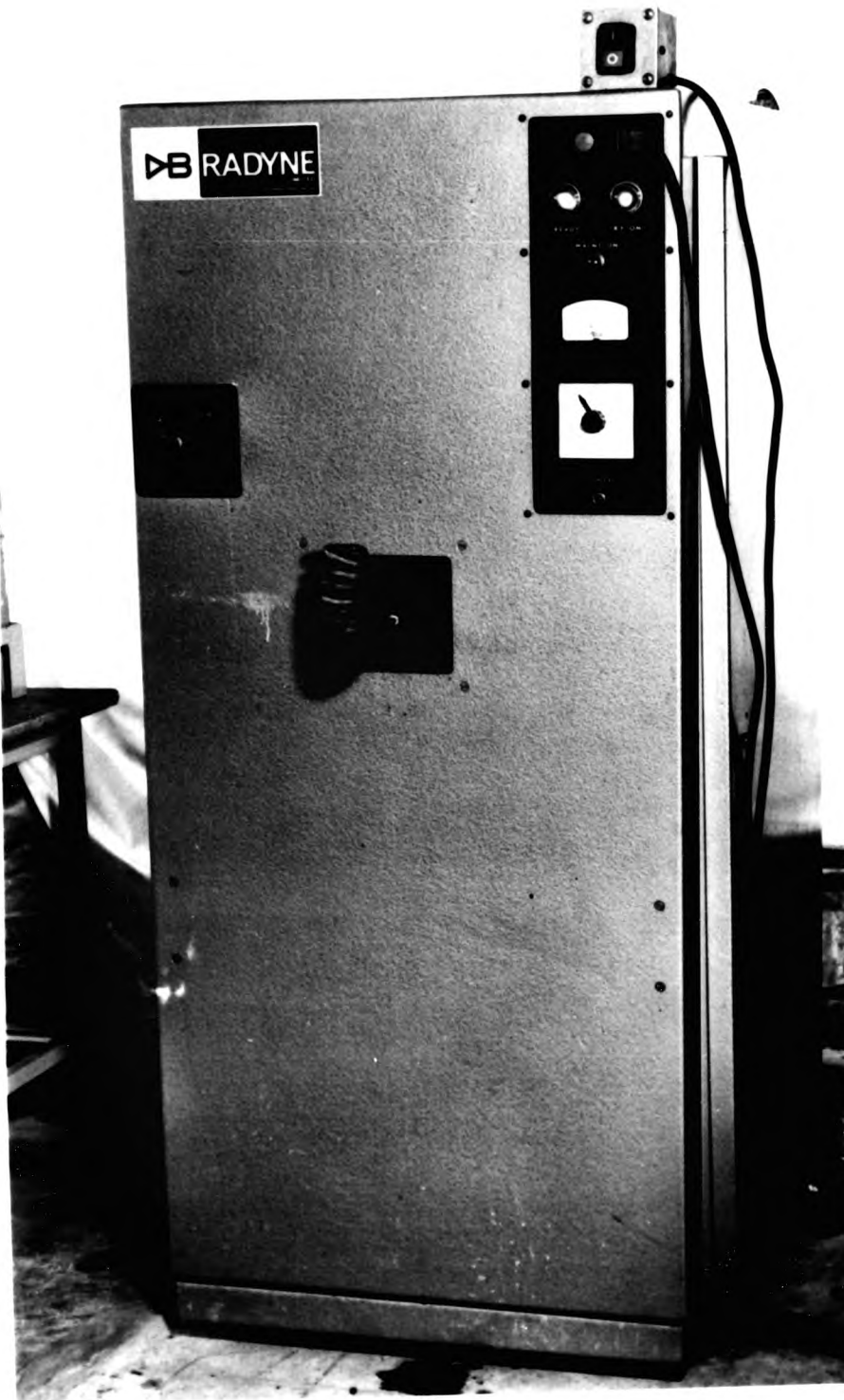


Figure 18. A view of the low frequency induction heating
and melting unit

2.2 EXPERIMENTAL

2.2.1 Equipment. A 'Radyne' induction heater model R503 was used (see Figure 18). This has a water cooled coil of an optimum inductance of $20\mu\text{H}$, a power rating of 50kW and an operating frequency range of 100-200 kHz.

2.2.2 Procedure. Special glass tubes were made. The alloy components were mixed and put into the tubes and the open end was sealed. The tubes were evacuated for several hours and then the side tube was sealed under vacuum. Good coupling between the induction coil and glass tube was obtained by using a graphite tube as a coupler and a narrow diameter induction coil. The molten mix of zinc and cadmium had the tendency to segregate under gravity, this was minimised partly by the stirring effect of eddy currents and partly by turning the tubes upside down and shaking them. The coil current was controlled manually while observing the state of the melt. Fast cooling after melting was achieved by air blown from a dryer, when an outer hard skin has formed the tube was quenched in water upon which the glass shattered and the alloy rod was recovered. Two master alloys of composition 2% and 10% cadmium were prepared. From these alloys of different compositions varying from 0.05% to 25% cadmium were prepared.

The amalgamation was carried out as follows. 0.2g of $\text{Hg}(\text{NO}_3)_2 \cdot \text{H}_2\text{O}$ was dissolved in 100 cm^3 of doubly distilled water. To help dissolution, a few drops of nitric acid were added. A clear solution was thus obtained. Specimens of cylindrical shape 3-4mm long and diameter 7.14mm were cut from the alloy rods. After cleaning (see below) the specimens were immersed completely for about thirty minutes, by that time there was a visible mobile layer of mercury on the surface. At room temperature it takes a long time for the surface mercury to penetrate the interior of the specimens.⁷³ For this reason a "homogenisation" operation was carried out, which consisted of keeping the specimens in an air circulatory oven

maintained at 50°C. To avoid oxidation the specimens were individually sealed in small evacuated glass tubes. The tubes were removed after 72 hours, which was found to be ample time to allow mercury to diffuse into the interior of the specimens. The specimens were recovered by breaking the glass and were polished using standard metallographic techniques. Cleaning prior to amalgamation was carried out as follows:

- (a) a preliminary wash in dilute nitric acid and methanol mixture,
- (b) four or five rinses in methanol.
- (c) after amalgamation, four or five rinses in water followed by two rinses in acetone,
- (d) dry over silica gel in a desiccator for several hours.

2.3 ANALYSIS

Zinc, cadmium and mercury which belong to the same group of periodic table, have very similar physical and chemical properties, so that they form analogous chemical compounds and often coexist in many natural materials, for example, cadmium can replace zinc in sphalerite and other naturally occurring ores. They also replace each other in biological systems.⁸¹ In these investigations it was necessary to determine simultaneously the amount of the metals in one sample, not readily carried out by conventional chemical analysis. Neutron activation⁸² and polarography⁸³⁻⁸⁶ have been employed. The former is superior as far as high sensitivity and low interference are concerned but is less satisfactory for reproducibility.

2.3.1 Colorimetry. Colorimetric methods, usually superior in reproducibility, are likely to suffer from mutual interference of the three metals reducing selectivity, because the method is based on the formation of complexes. This is usually overcome by sequential extraction. The method adopted is due to Kayoko Nakamura and T. Ozawa.⁸⁷ First the anionic halides are formed and selectively extracted in a sequence by tribenzylamine.

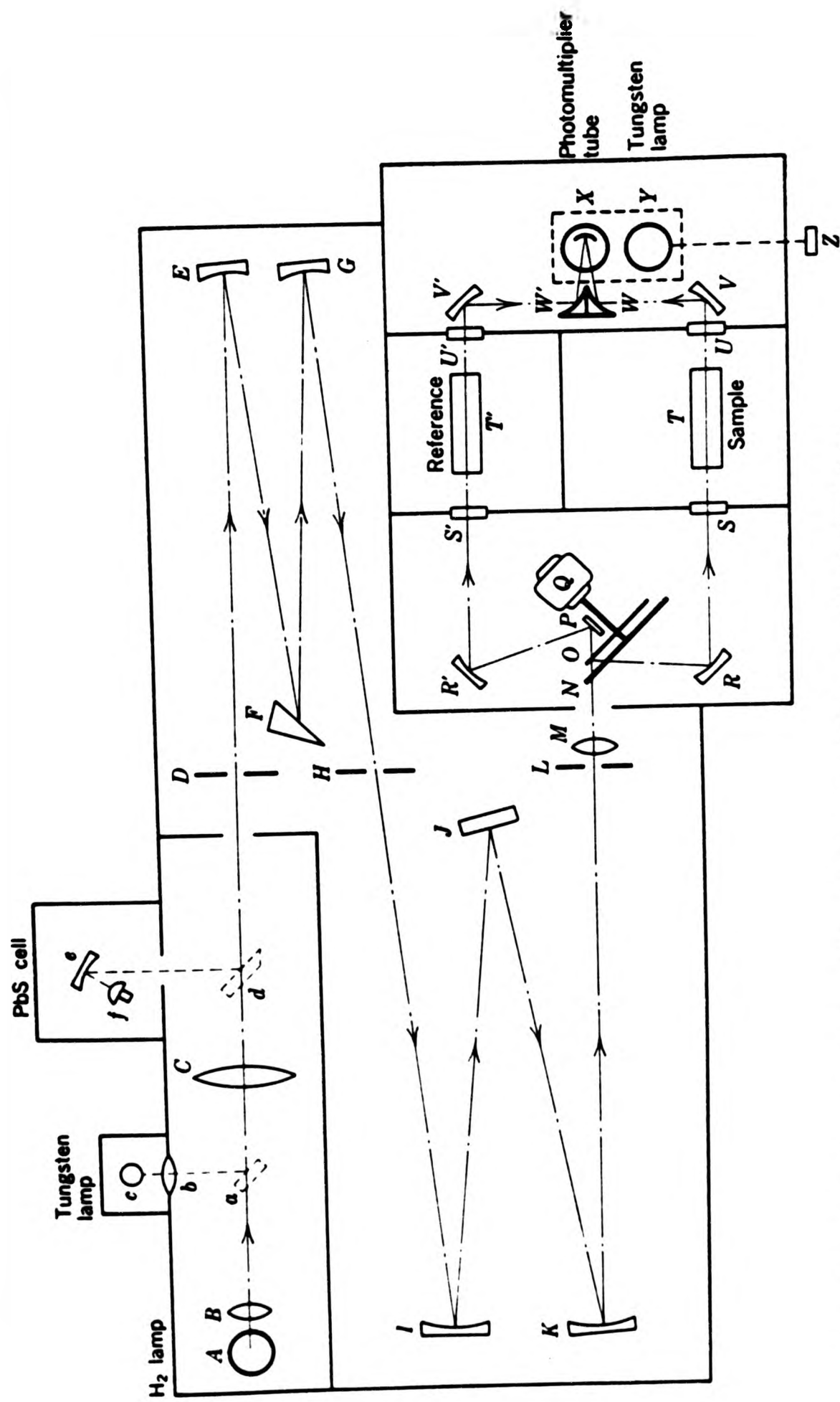


Figure 19. Optical system of the PYE-UNICAM SF 1800 spectrophotometer.

2.3.2 Experimental. Instruments for the measurement of the selective absorption of radiation by solutions are known as colorimeters, absorption meters or spectrophotometers. The term colorimeter is generally restricted to the simpler visual and photoelectric devices for the visible region. However, no sharp demarkation line is drawn to distinguish between them. All forms must have certain features and components in common e.g. a source of radiation, an intensity control, a wavelength control, a sample holder, a photomultiplier and a pen recorder. A Pye-Unicam SP 1800 ultra-violet visible spectrophotometer, covering the wavelength range 190nm to 700nm was used. A schematic optical system of the instrument is shown in Figure 19.

All chemicals used were of analytical grade. A series of reagent solutions were made as indicated below.

(i) Standard cadmium stock solution, concentration 1000 ppm, was made by dissolving 1g cadmium metal of 6N purity in 50 cm³ of 10 mol dm⁻³ nitric acid. Nitrogenous oxides were expelled by boiling and the solution then diluted to 1dm³ with redistilled water.

(ii) Standard zinc stock solution, concentration 1000 ppm, was made by dissolving 1g zinc metal of 6N purity in 50cm³ of 10 mol dm⁻³ nitric acid. Nitrogenous oxides were expelled by boiling and diluted to 1dm³ with redistilled water.

(iii) Standard mercury stock solution, concentration 1000 ppm was made by dissolving 0.84g of hydrous mercuric nitrate in redistilled water, acidified with nitric acid and diluted to 1dm³, standardised by titration with EDTA.

(iv) Pre-equilibration of tribenzylamine with hydrobromic acid was done by shaking 100cm³ of 2.5% tribenzylamine solution in chloroform with 100cm³ of 0.5 mol dm⁻³ hydrobromic acid and the aqueous layer was discarded.

(v) Dithizone solution was prepared by dissolving 0.25g of dithizone in 500cm³ of carbon tetrachloride, and filtering through medium pore filter paper. The filtrate was shaken with four 50cm³ portions of pure

0.1 mol dm⁻³ aqueous ammonia solution. The combined aqueous solution was washed with chloroform twice with 10cm³ portions, and neutralised with 3 mol dm⁻³ HCl. Dithizone was extracted with chloroform twice using 125cm³ portions. This solution was stored while covered with sodium bisulphite solution in a brown bottle in a refrigerator.

(vi) The washing solution was prepared by dissolving 8.4g of potassium iodide and 0.5g of sodium hydrogen sulphite in 100cm³ of 0.15 mol dm⁻³ sulphuric acid. This solution was used to wash the organic phase after extraction of cadmium iodide.

2.3.3 Procedure. A solution was prepared by mixing quantities equivalent to 1-30µg Hg²⁺, 1-25µg Cd²⁺ and 10-250µg Zn²⁺ ions from the standard solutions prepared as above. This was taken in a 100cm³ separating funnel and aqueous solutions of KOH and KBr were added. The pH was adjusted to 4, if necessary, by adding drops of dilute HNO₃. The bromide concentration was also adjusted to 0.05 mol dm⁻³. This mixture was well shaken with 8cm³ of 0.088 mol dm⁻³ of TBA.HBr to extract mercuric bromide. When the two layers had separated, the organic layer was transferred to a 25cm³ glass stoppered tube. A 2cm³ portion of 1 x 10⁻³ mol dm⁻³ dithizone in chloroform and 10cm³ of alkaline EDTA solution (5 x 10⁻³ mol dm⁻³ EDTA in 1 mol dm⁻³ KOH) was added. The mixture was shaken vigorously by hand, and the absorbance was measured for the organic layer for mercury against chloroform at 490nm. (Transmittance is the ratio of the intensities of the emergent and incident beams.)

To the aqueous solution free from mercury, 1cm³ each of 10% sodium hydrogen sulphite, 6 mol dm⁻³ potassium iodide, and 1.5 mol dm⁻³ sulphuric acid was added. This gave a pH of 1.5 and an iodide concentration of 0.5 mol dm⁻³. The addition of sodium hydrogen sulphite prevented the oxidation of dithizone by iodine. This solution was shaken with 8cm³ of 0.088 mol dm⁻³ TBA.HBr for 3 minutes to extract cadmium. The organic layer was transferred to a 25cm³ glass tube and 2cm³ of 1.0 x 10⁻³ mol dm⁻³ dithizone in chloroform and 10cm³ of 1 mol dm⁻³ KOH were added. The mixture was

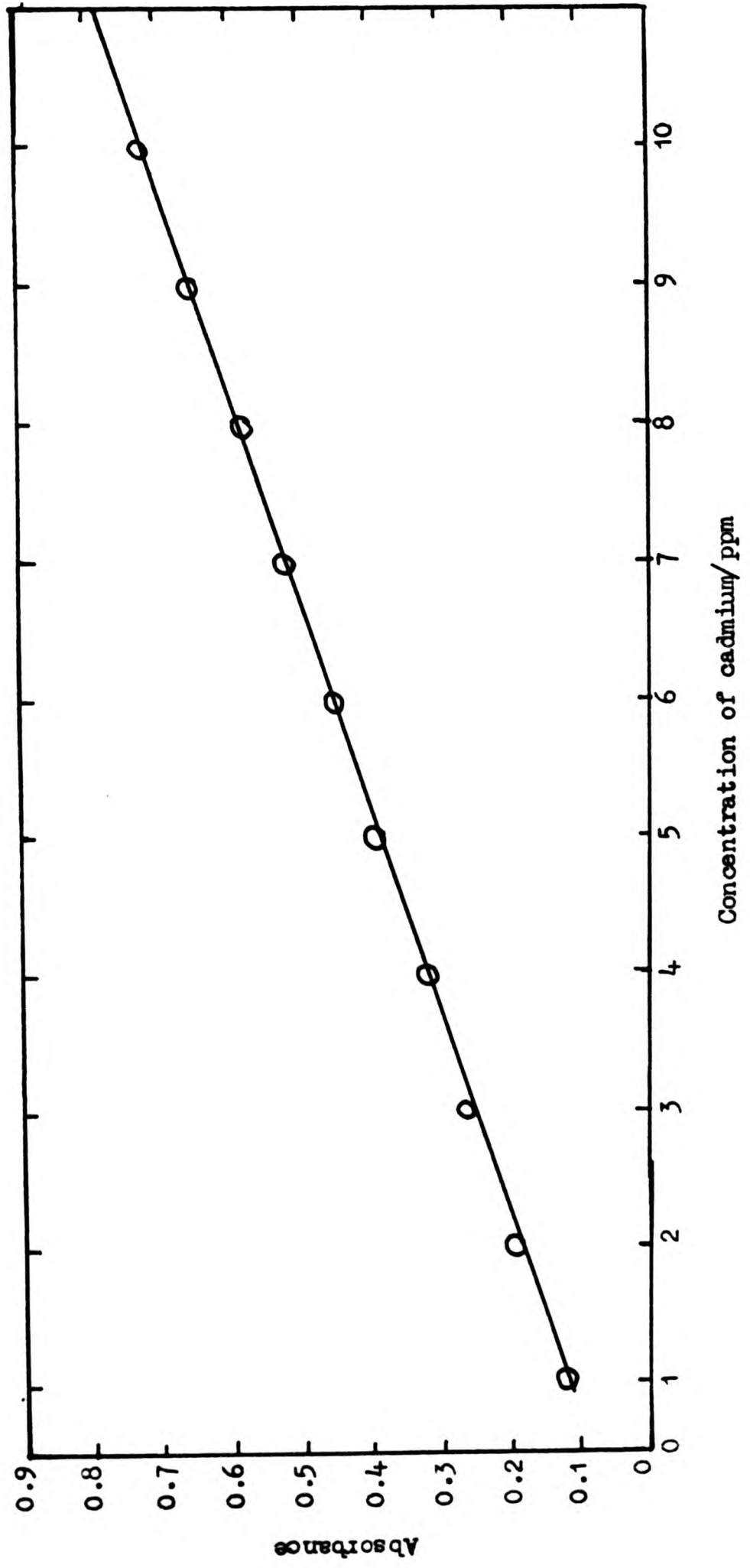


Figure 20. Calibration curve for cadmium as determined by colorimetry.

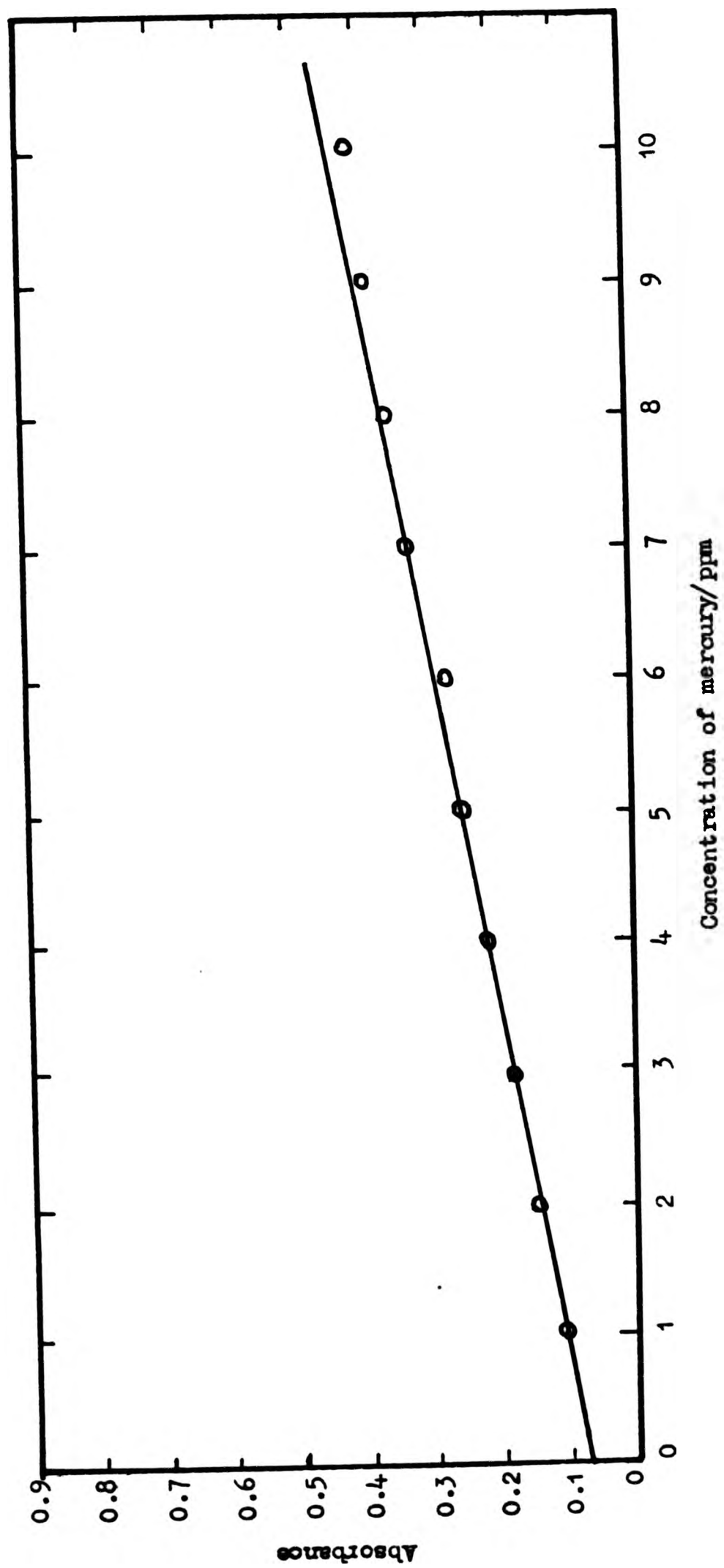


Figure 21. Calibration curve for mercury as determined by colorimetry.

shaken vigorously by hand, and the absorbance of the organic layer for cadmium against chloroform was measured at 510nm.

2.3.4 Results. The calibration graphs shown in Figures 20 and 21 were obtained by the procedure described above, with standard solutions of mercury and cadmium. The graphs show a good linear relationship with relative standard deviation of 0.2% and 0.5% for cadmium and mercury respectively, for ten replicate measurements.

Table 3: Standardisation of mercury and cadmium.

ppm Cd	Absorbance	ppm Hg	Absorbance
1	0.170	1	0.110
2	0.240	2	0.150
3	0.320	3	0.180
4	0.375	4	0.215
5	0.445	5	0.250
6	0.500	6	0.275
7	0.570	7	0.330
8	0.630	8	0.360
9	0.709	9	0.380
10	0.775	10	0.410

Table 4: Cadmium analysis for binary alloys

Nominal Composition w/o Cd	Dilution Ratio	Absorbance	Actual Composition (avg. of 10 measurements) w/o Cd
0.05	100	0.450	0.05
0.20	1000	0.180	0.24
1.00	1000	0.760	0.96
2.00	2500	0.642	1.96
5.00	25000	0.250	4.96
10.00	25000	0.398	10.50
25.00	50000	0.490	28.00

Table 5: Analysis of amalgamsMercury Analysis

Alloy	Dilution ratio	Absorbance	w/o mercury avg. of 10 measurements
pure zinc	250	0.260	2.60
0.05% Cd-Zn	250	0.250	2.40
0.20 "	250	0.260	2.60
1.00 "	250	0.250	2.50
2.00 "	250	0.250	2.50
5.00 "	250	0.250	2.50
10.00 "	250	0.265	2.55
25.00 "	250	0.265	2.60
pure cadmium	250	0.265	2.60

Table 6: Analysis of amalgams

pure zinc	250	0.352	9.5
0.05% Cd+Zn	250	0.358	9.6
0.20 "	250	0.365	9.9
1.00 "	250	0.360	9.7
2.00 "	250	0.368	10.0
5.00 "	250	0.361	9.8
10.00 "	250	0.368	10.0
25.00 "	250	0.381	10.5
pure cadmium	250	0.398	11.0

The analysis of the zinc and cadmium rods as supplied by Metal Research Ltd. was as follows.

Table 7: Analysis of as received material.

Element	Zinc rod w/o	Cadmium rod w/o
Magnesium	0.0001	0.0001
Aluminium	0.0001	0.0001
Iron	0.0002	0.0002
Nickel	0.0002	0.0002
Copper	0.0020	0.0020
Silver	0.0001	0.0009
Cadmium	0.0100	99.9567
Tin	0.0040	0.0028
Lead	0.0430	0.0320
Zinc	99.9403	0.0050

These results were obtained by emission spectroscopy, X-ray fluorescence and atomic absorption spectrometry.

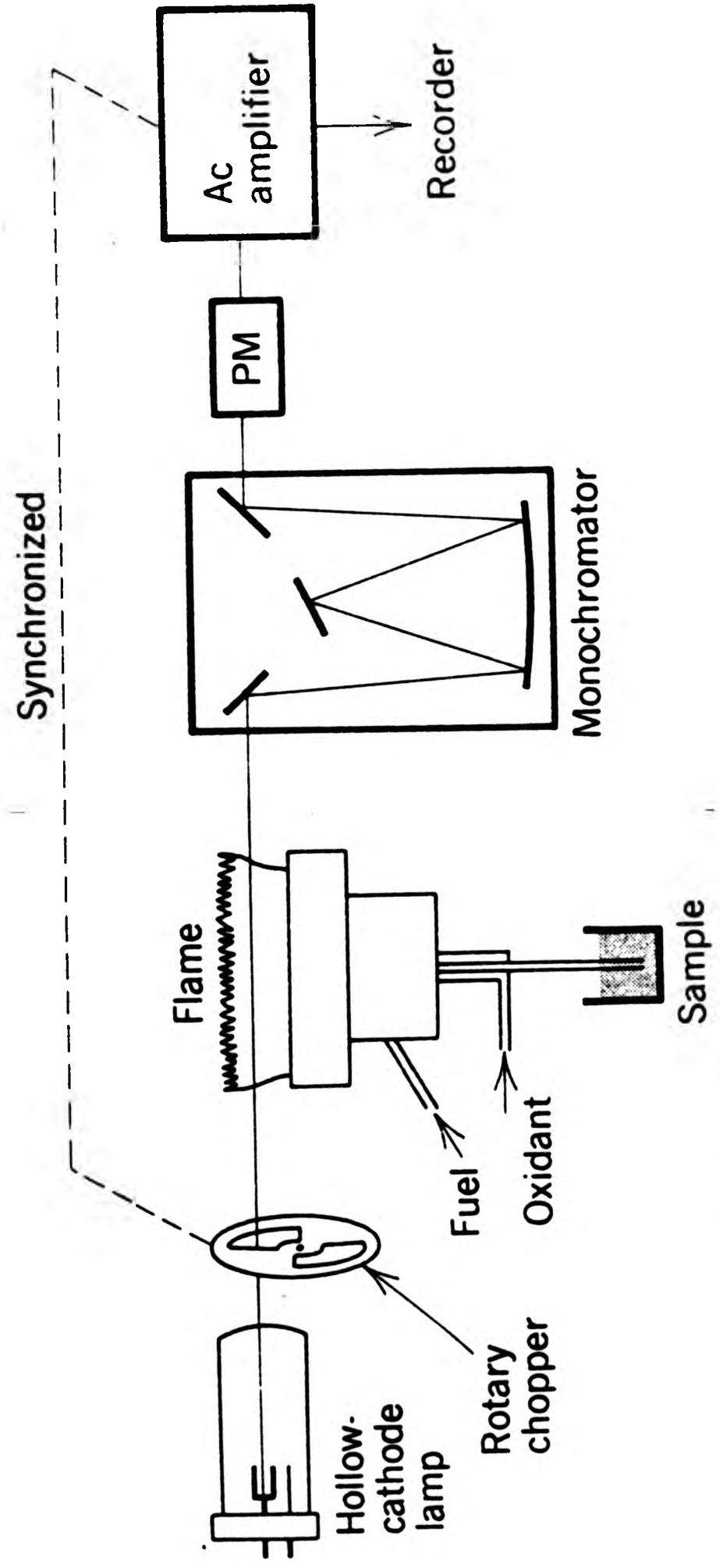


Figure 22. A schematic diagram of an atomic absorption spectrometer.

2.4 ATOMIC ABSORPTION SPECTROSCOPY

2.4.1 Introduction. Atomic absorption spectroscopy or flame spectroscopy is a versatile analytical tool. The flame serves effectively as a source of atomic emission lines and also as an absorbing medium for these lines. In the presence of sufficient available energy - say a very hot flame - the metal atoms are raised to a higher energy level upon which a characteristic radiation is emitted. However, only a very small fraction of the metal atoms of the entrained salt becomes activated, the rest remaining in their ground state. The unexcited atoms are able to absorb radiation from an external source and this absorbance is measured and correlated to the concentration, as indicated in Figure 23 by the ratio P/P_0 .

2.4.2 The Instrument. A Perkin-Elmer X90 series 103 single beam instrument was available for use. This early model suffered from lamp and detector fluctuations. There was also a delay time involved of up to half an hour due to warming up of the hollow cathode lamp. This instrument provided modulation by chopping the light beam with a rotary shutter and by supplying the lamp a pulsed current. Figure 22 shows a schematic diagram of this instrument. Figures 23(a), (b) and (c) illustrate the theoretical principle.

2.4.3 Procedure. A standard stock solution of 1000 ppm zinc was prepared by dissolving 1g of pure 6N zinc in a minimum volume of 1+1 HCl and diluted to 1 dm³ with 1 v/o HCl. Working solutions of 10, 5, 3, 2 and 1 ppm were prepared by appropriate dilution of the stock solution. Cadmium stock and working solutions were prepared similarly. The instrument was set up as follows.⁸⁸ After switching on the power, air, and acetylene supplies, in that order, the flame was lit and adjusted to a lean blue flame. This was achieved with oxygen supply control vernier knob at 182.5 and acetylene knob at 398. The slit width required was 0.7nm. The wave length used for cadmium absorption was 229 nm, for mercury

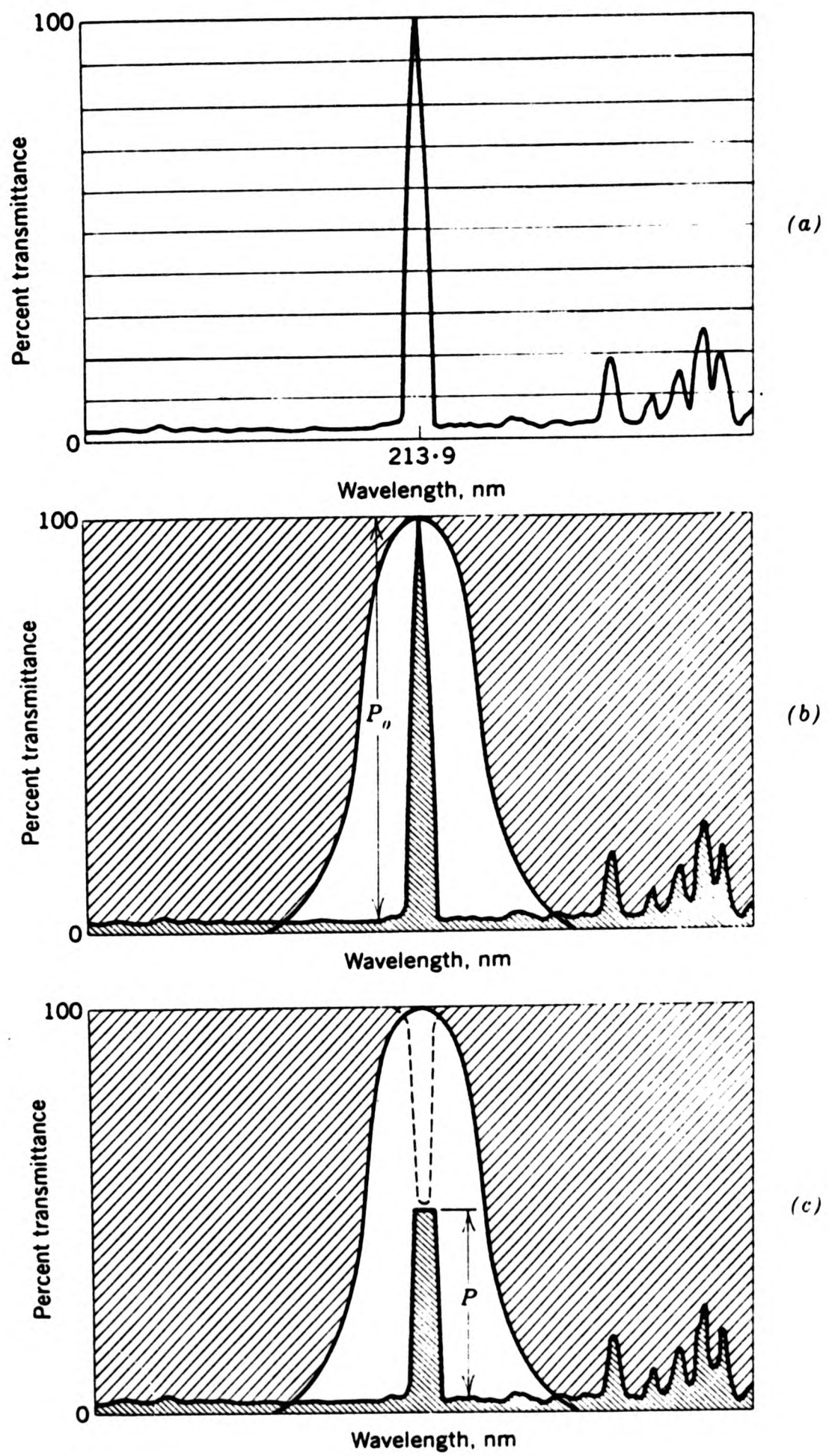


Figure 23. (a) The spectrum of zinc emission.
(b) Elimination of extraneous lines by a monochromator.
(c) Absorption effect of zinc atoms in the flame.

absorption 254nm and for zinc it was 214nm. The absorbance scale was frequently checked and set to zero with blank solution (triply distilled water) being sucked through the flame.

2.4.4 Results. As this method of analysis required comparison with a standard a calibration curve was plotted for the unknown metal by feeding known concentrations of metal ions through the flame. The graph in Figure 24 shows a linear relationship up to a concentration of 5 ppm. At greater concentrations the relation is non linear. Ten replicate measurements were made. The sensitivity for the standard conditions is about 0.025 ppm for 1% absorption.

Table 8: Calibration of Cadmium Content

Amount of Cd ppm	1	2	4	5
Absorbance	0.17	0.33	0.61	0.76

Table 9: Cadmium Analysis of Binary Alloys

Nominal Composition w/o Cd	Dilution Ratio	Absorbance	Actual Composition w/o Cd
0.05	1	0.08	0.05
1.00	2	0.58	1.08
2.00	3	0.40	1.95
5.00	7	0.71	4.70
25.00	200	0.24	27.00

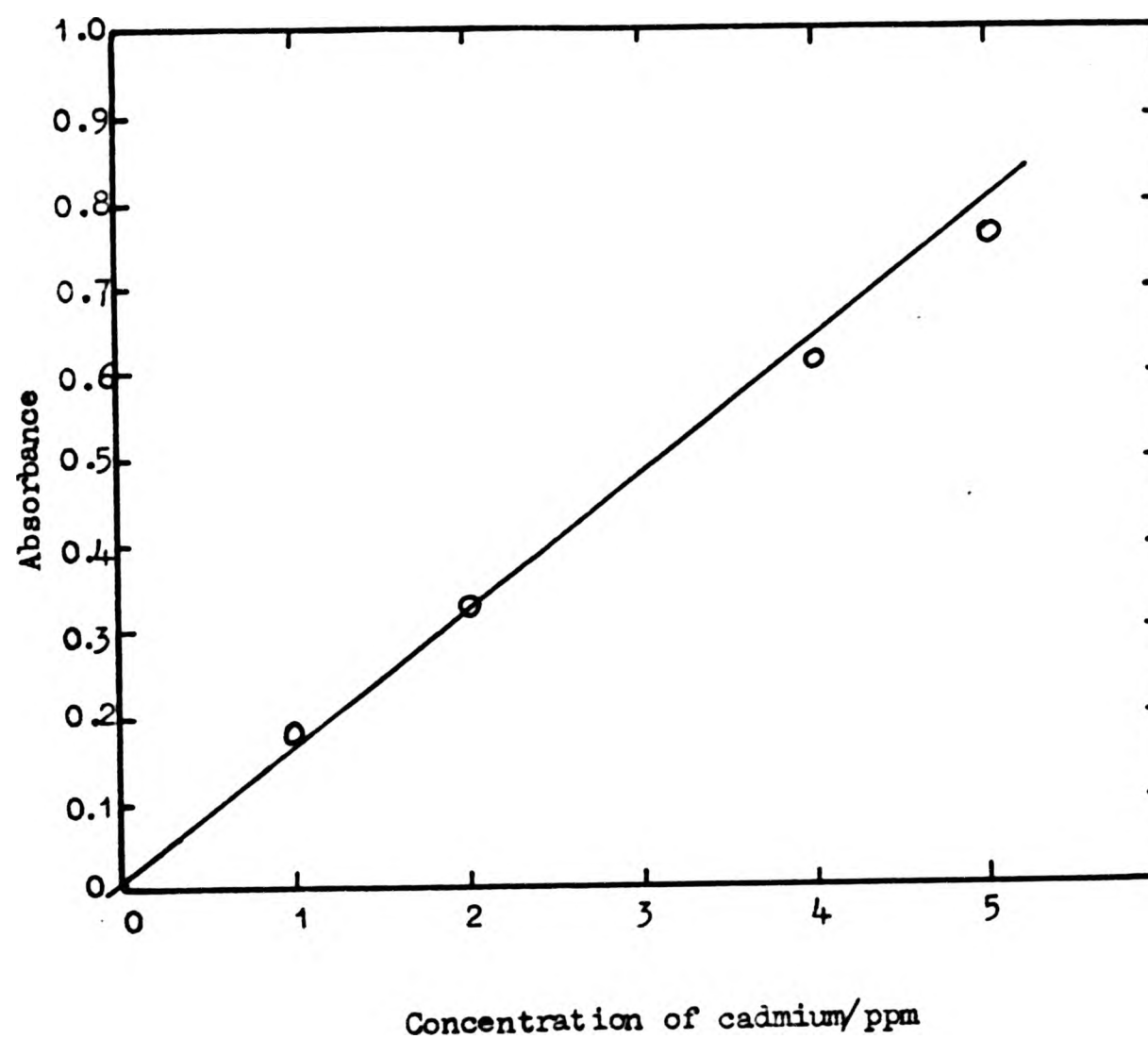


Figure 24. Calibration curve prepared by measuring absorbance of standard known concentrations of cadmium by atomic absorption spectrometry.

2.5 ATOMIC VAPOUR ABSORPTION SPECTROMETRY

2.5.1 Introduction. This technique can be employed when it is possible to produce a vapour of metal atoms by means other than a flame.⁸⁹ Thus it is possible to determine very minute concentrations of the order of a few nanograms. In this respect, this technique provides a quick and easy way of determining an alloying component, and is beyond doubt quite extensively employed. In the case of mercury, at very low concentrations, it is possible to produce "vapours" in solution, thus minute quantities of mercury reduced from the ionic state are not visible as metallic particles and have been shown to be in a "vapour" state. This 'vapour' can be aspirated into the stream of an inert carrier gas such as Argon; leading to a transparent glass tube where the concentration can be estimated by measuring absorbance at 254nm resonance line emitted by a quartz lamp. Other metals may be treated in a similar way by means of an electric discharge at radio frequency⁹⁰ or after vaporisation by a laser beam.⁹¹

2.5.2 Apparatus. A PYE-UNICAM SP90, single beam atomic absorption instrument was used. This instrument needed to be switched on half an hour earlier to allow the mercury lamp to stabilise. It suffered from the drawback that with time there was a pronounced drift in the source, which showed up on the chart recorder as a positive shift in the zero base line. An allowance was made for this when measuring the absorbance from the chart recorder tracings. Care was taken that under no circumstances water entered the absorption tube, which renders the instrument inoperable until dismantled and cleaned.

2.5.3 Procedure. A stock solution of mercury of 1000 ppm concentration was prepared as described earlier. A working solution containing 1 ppm mercury was prepared by a thousand fold dilution. From this 50, 100, 150, 200 and 250 μdm^3 were withdrawn each time and transferred into a 200 cm^3 conical flask containing 15 cm^3 distilled water. Before applying the flask

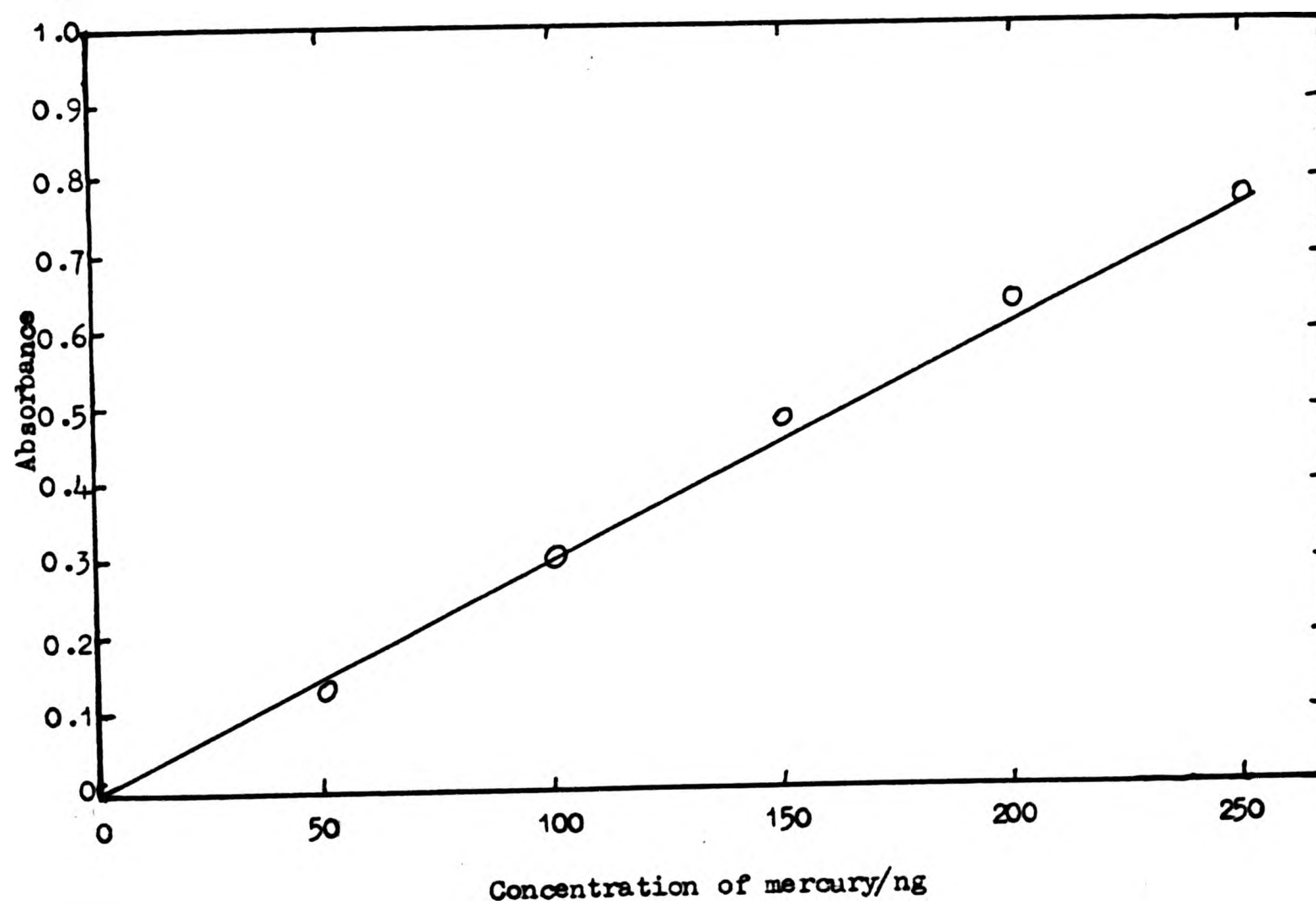


Figure 25. Calibration curve prepared by measuring absorbance of known standard concentrations of mercury by vapour atomic absorption spectrometry.

to the instrument, 4cm^3 of stannous chloride was added and quickly covered by a Dreschel cap and shaken well and carefully for about 3 minutes. The flask was pressurised by admitting water from a tap, this action displaced the mercury (which was in 'vapour' form after reduction by stannous chloride), into the absorption tube of the spectrometer. This procedure was repeated until reproducible results were obtained. A plot of absorbance against known mercury concentrations is shown in Figure 25.

Representative samples from the ternary alloys were cut and dissolved in just enough dilute nitric acid to make up 1 dm^3 by adding doubly distilled water. A dilution of 500-1000 times was found necessary in order to be able to keep the absorbance in the linear region of the calibration curve. Mercury concentration could thus be read off the curve from the absorbance value thus obtained.

2.5.4 Results.

Table 10: Calibration for mercury (plotted in Fig.25)

Concentration of mercury ng	0	50	100	150	200	250
Absorbance	0	0.13	0.31	0.49	0.64	0.77

Table 11: Analysis of amalgam series

Alloy	w/o Hg	w/o Hg
Pure zinc	2.50	9.50
0.05 w/o Cd+Zn	2.60	9.70
0.20 "	2.40	9.80
1.00 "	2.45	9.50
2.00 "	2.50	10.00
5.00 "	2.50	10.00
10.00 "	2.50	10.00
25.00 "	2.60	10.50
Pure cadmium	2.60	10.75

The results of the chemical analysis show that the intended compositions were achieved within close limits. Some of the alloy samples were also checked by the same technique for the presence of heavy metals like iron and lead, but these were not found in any detectable amounts.

2.6 METALLOGRAPHY

2.6.1 Introduction. The purpose of metallography is to reveal the structure of transparent or opaque substances. It can also be used for many other purposes in electrochemical and corrosion research. For metals and alloys it is invariably necessary to "etch" them with a chemical or a mixture of chemicals which attack the various constituents at different rates or are selective in nature. Etching solutions are thus in use which attack one constituent to a greater extent than others or leave it un-attacked. A similar effect may sometimes be obtained without resorting to chemical or electrochemical etching,⁹² by simply polishing so that the hard and soft constituents or phases stand out in relief having been abraded to different extents.

2.6.2 Procedure: The specimens were selected from the centre of the rods so that they were a representative sample. The specimens were about 6-8mm in diameter and about 10-12mm long. These were mounted in a cold setting epoxy resin "Metset SW" type obtained from Metaserv Ltd. Although the cold setting reaction is exothermic, the resultant heat release was rather small and did not raise the temperature of the system appreciably. Thus there was no risk of changing specimen structure in contrast to the risks with thermosetting resins. The cold setting resin was allowed to stand for 36 hours after which time the moulds were ejected. The castings were deburred and bevelled. Polishing⁹³ was carried out mechanically on wet emery papers. Water was used as a coolant and lubricant so that overheating did not occur during abrasion. Starting from the coarsest grade 320, polishing was done in opposite directions alternatively through 400, 500 and 600 (17 μ m) grades.

Further polishing was carried out on motorised lapping wheels covered with chamois leather, using 6 μ m, 1 μ m and finally $\frac{1}{2}$ μ m diamond paste, care being taken not to use high speeds and pressures. The specimens were degreased in Teepol and rinsed with cold water and finally well rinsed with distilled water. The specimens were observed under the microscope at various magnifications. Chemical etching was carried out when necessary. Pure zinc, cadmium and alloys low in cadmium needed etching but alloys high in cadmium hardly needed any. A dilute solution of nitric acid in alcohol (2-5% Nital) was used as an etchant. For the amalgams dilute hydrochloric acid (1%) gave good results.

2.6.3 Results and Discussion. Photomicrographs of pure zinc and cadmium (see figures 26-37 inclusive) show their polycrystalline nature. Some micrographs show polishing artefacts. In zinc and cadmium (both of these have hexagonal close packed crystal structure) deformation by 'slip' is limited to the basal planes. Both the metals recrystallise on deforming at room temperature. The recrystallisation temperature is between 0.4 and 0.5m.pt.(K). This gives rise to some trouble during metallographic examination, where mechanical polishing produces spurious recrystallised surface structures. Mechanical twins are also sometimes visible. Figure 38 shows the phase diagram of the cadmium-zinc binary alloy system. This is clearly a simple eutectic system. The two metals are completely miscible in the liquid state, but as the alloy cools, a zinc rich phase (which is really a solid solution of cadmium in zinc) separates out. The two metals are not miscible in the solid state. This equilibrium diagram is valid for very slow equilibrium cooling rates. Faster cooling rates bring about different composition ranges than predicted by the diagram. About 3 w/o zinc dissolves in cadmium and about 2.15 w/o cadmium dissolves in zinc at the eutectic temperature. On rapid cooling this quantity of elements can remain in solid solution, but if very slowly cooled (so that the equilibrium is not disturbed), then as the solubility is almost nil below 150°C, the metals

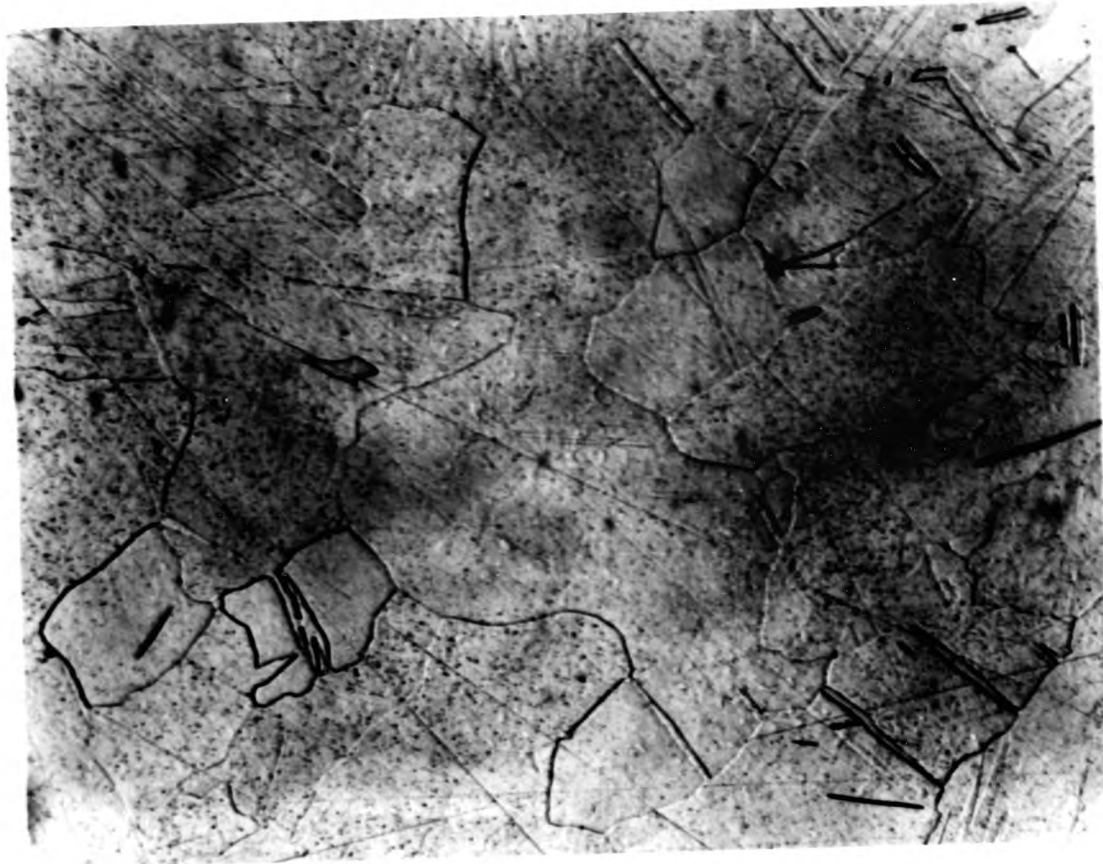


Figure 26. Photomicrograph of pure zinc, in as received condition. Etched with 5% Nital for 60s to reveal the structure. Magnification 200.

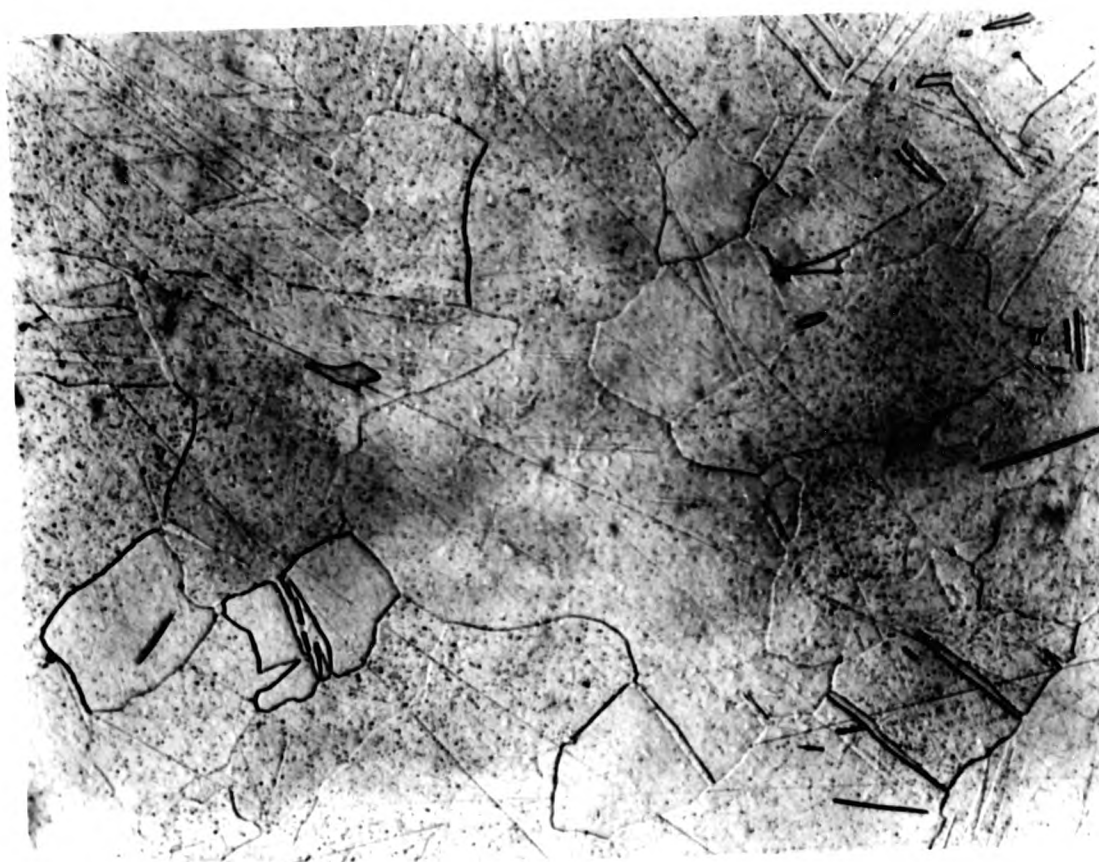


Figure 26. Photomicrograph of pure zinc, in as received condition. Etched with 5% Nital for 60s to reveal the structure. Magnification 200.

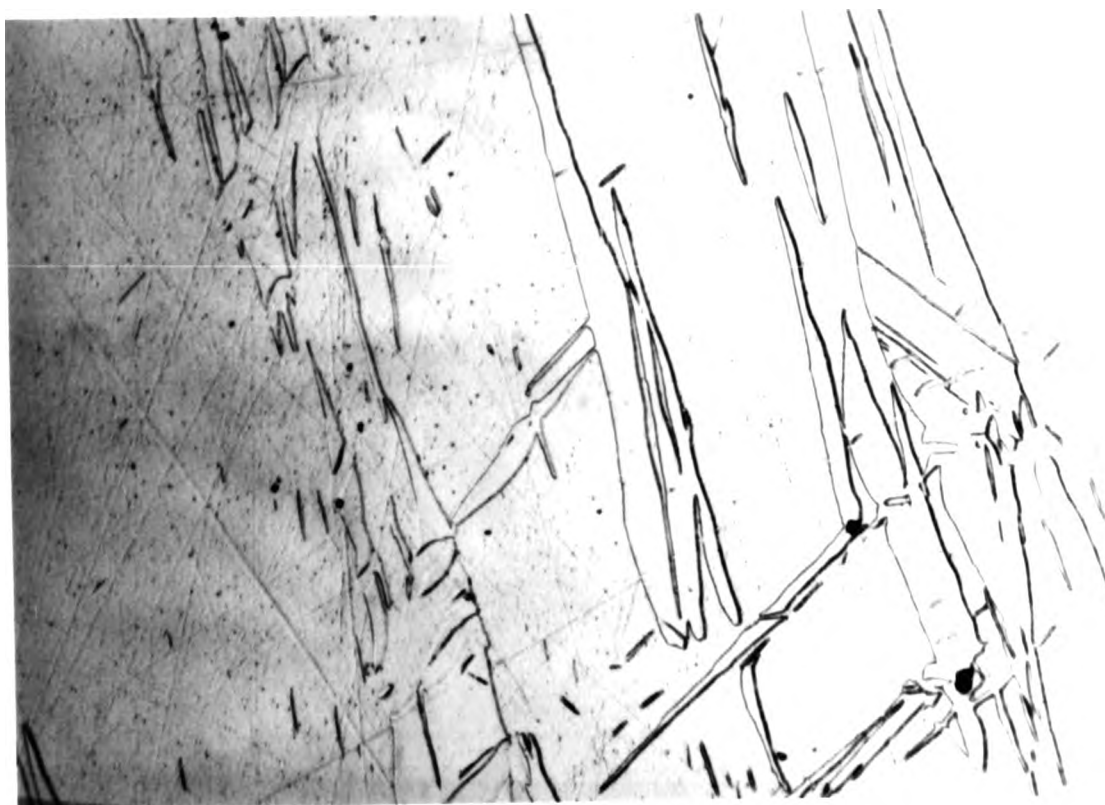


Figure 27. Photomicrograph of 0.05 w/o Cd-Zn binary alloy in as cast condition. Etched with 5% Nital for 60s to reveal the structure. Magnification 200.

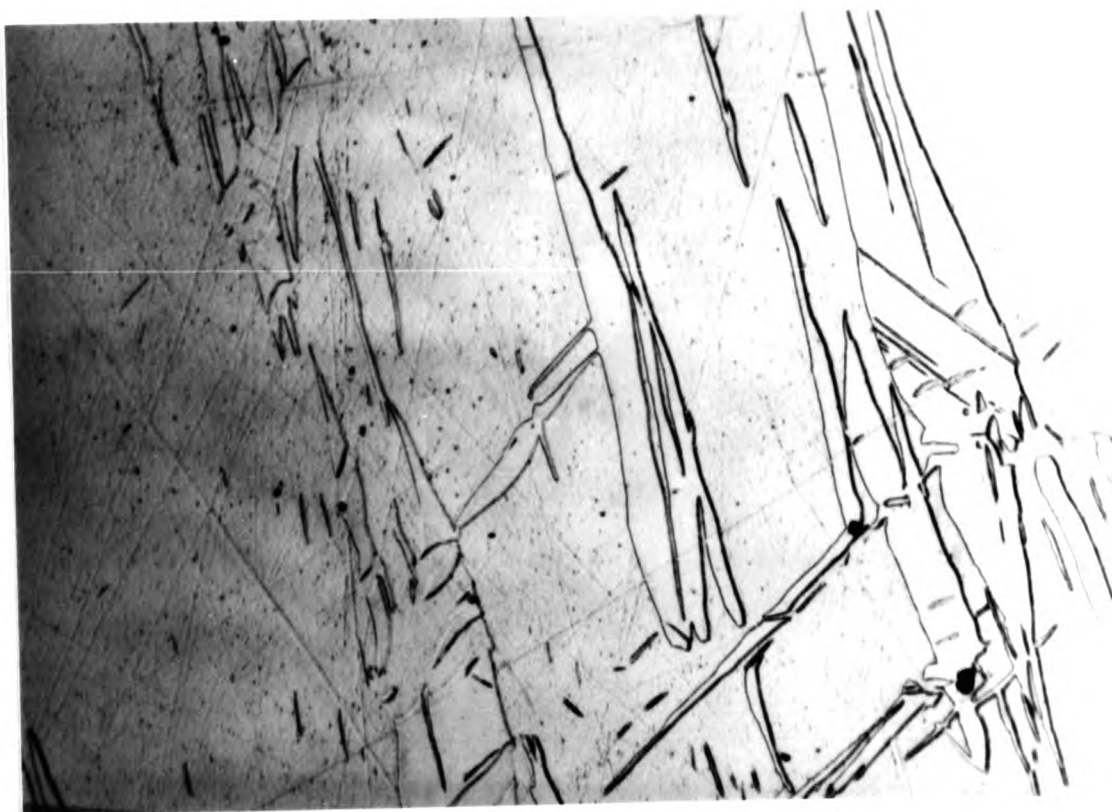


Figure 27. Photomicrograph of 0.05 w/o Cd-Zn binary alloy in as cast condition. Etched with 5% Nital for 60s to reveal the structure. Magnification 200.



Figure 28. Photomicrograph of 0.20 w/o Cd-Zn binary alloy in as cast condition. Etched with 5% Nital for 70s to reveal the structure. Magnification 200.

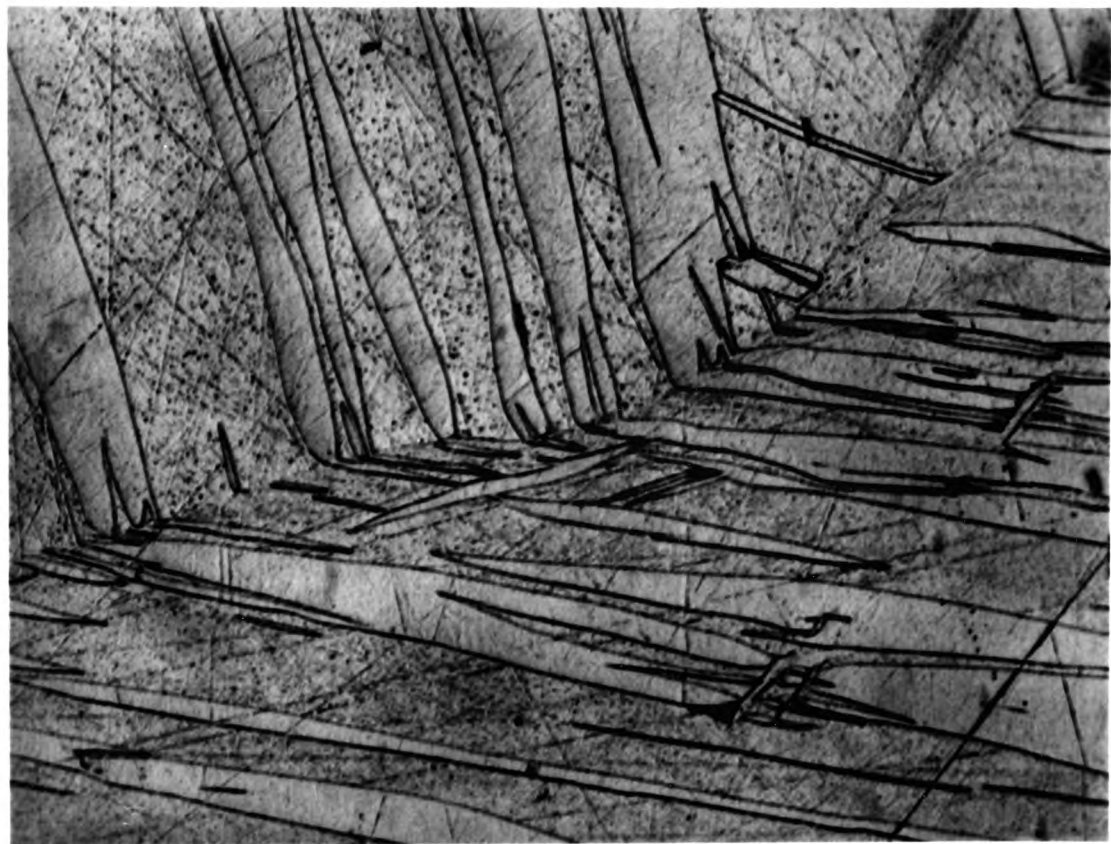


Figure 28. Photomicrograph of 0.20 w/o Cd-Zn binary alloy in as cast condition. Etched with 5% Nital for 70s to reveal the structure. Magnification 200.



Figure 28. Photomicrograph of 0.20 w/o Cd-Zn binary alloy in as cast condition. Etched with 5% Nital for 70s to reveal the structure. Magnification 200.

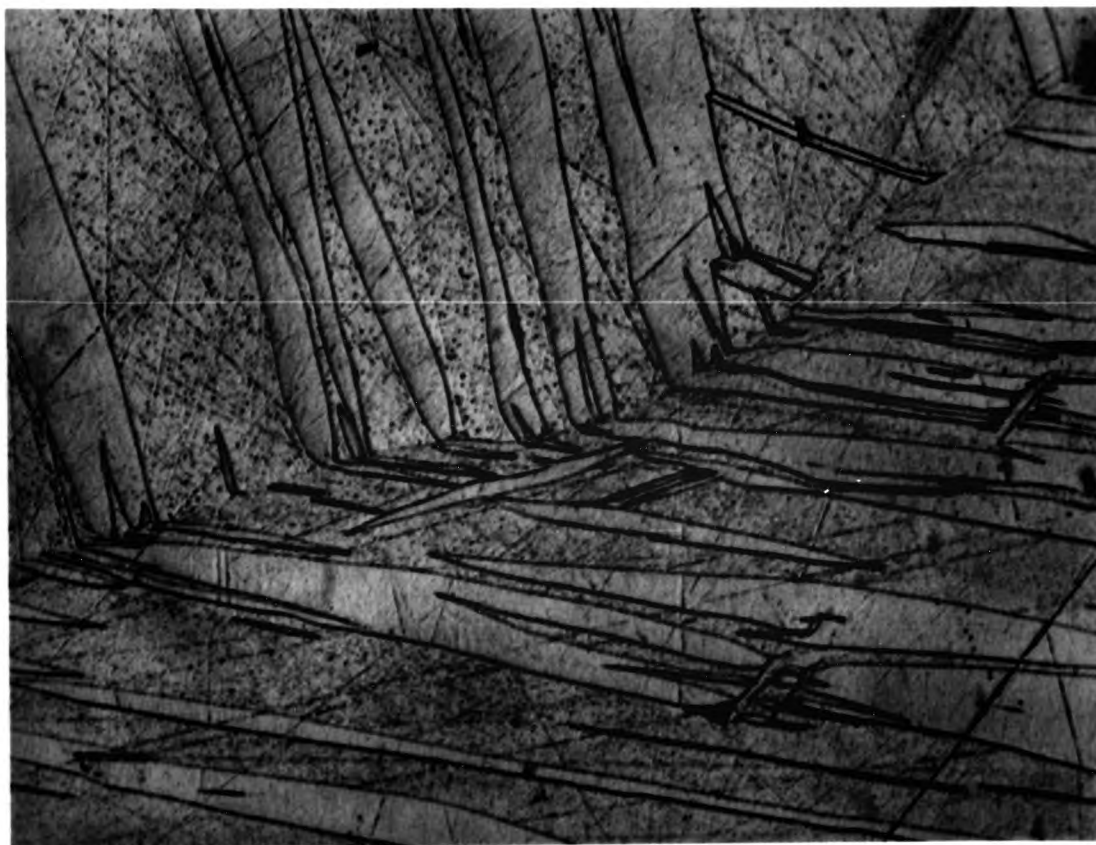


Figure 28. Photomicrograph of 0.20 w/o Cd-Zn binary alloy in as cast condition. Etched with 5% Nital for 70s to reveal the structure. Magnification 200.



Figure 29. Photomicrograph of 1.0 w/o Cd-Zn binary alloy in as cast condition. Etched with 2% Nital for 70s to reveal the structure. Magnification 200.

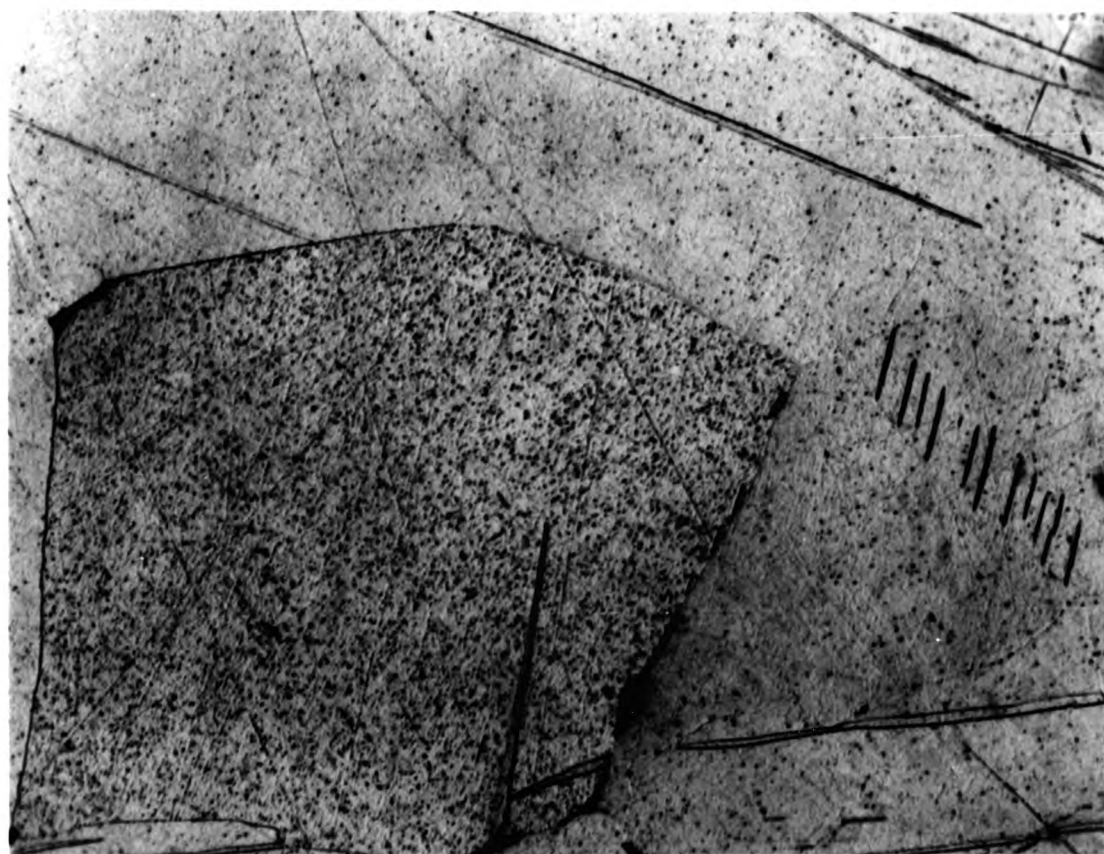


Figure 29. Photomicrograph of 1.0 w/o Cd-Zn binary alloy in as cast condition. Etched with 2% Nital for 70s to reveal the structure. Magnification 200.

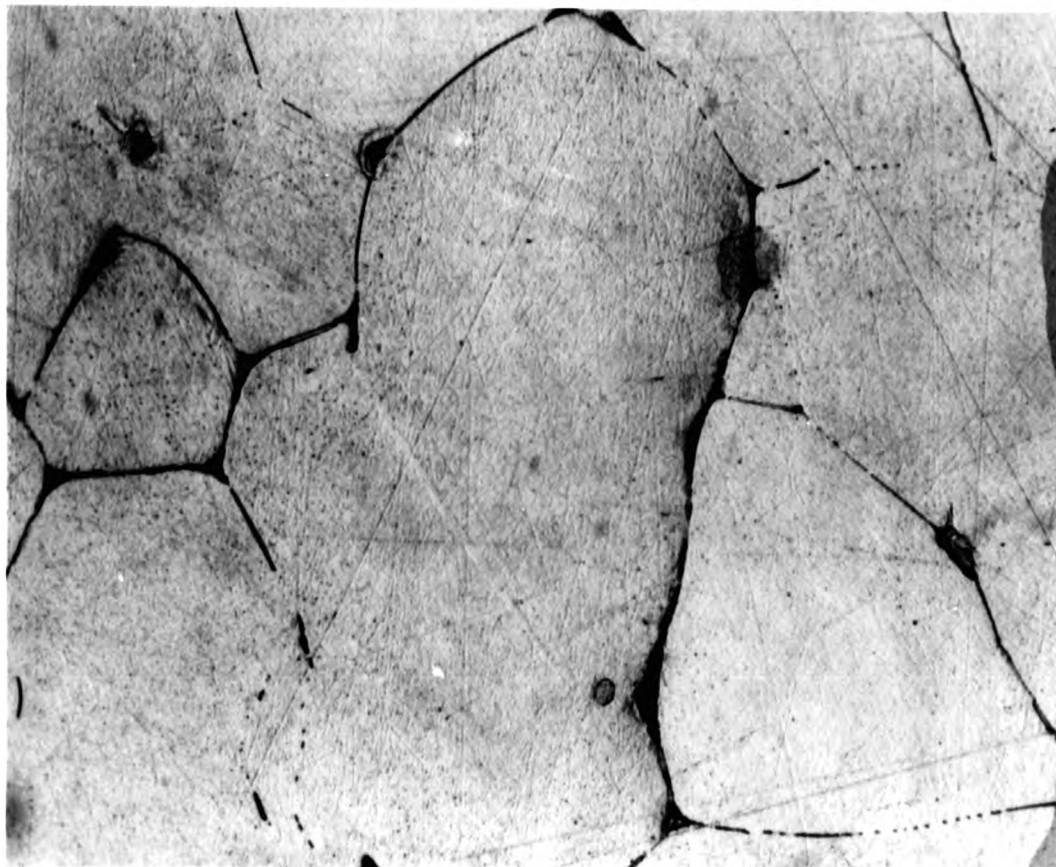


Figure 30. Photomicrograph of 2.0 w/o Cd-Zn binary alloy in as cast condition. Etched with 2% Nital for $1\frac{1}{2}$ minutes to reveal the polygrain structure. Eutectic at the grain boundary appears as a dark phase - preferentially attacked by the etchant. Magnification 200.



Figure 30. Photomicrograph of 2.0 w/o Cd-Zn binary alloy in as cast condition. Etched with 2% Nital for $1\frac{1}{2}$ minutes to reveal the polygrain structure. Eutectic at the grain boundary appears as a dark phase - preferentially attacked by the etchant. Magnification 200.

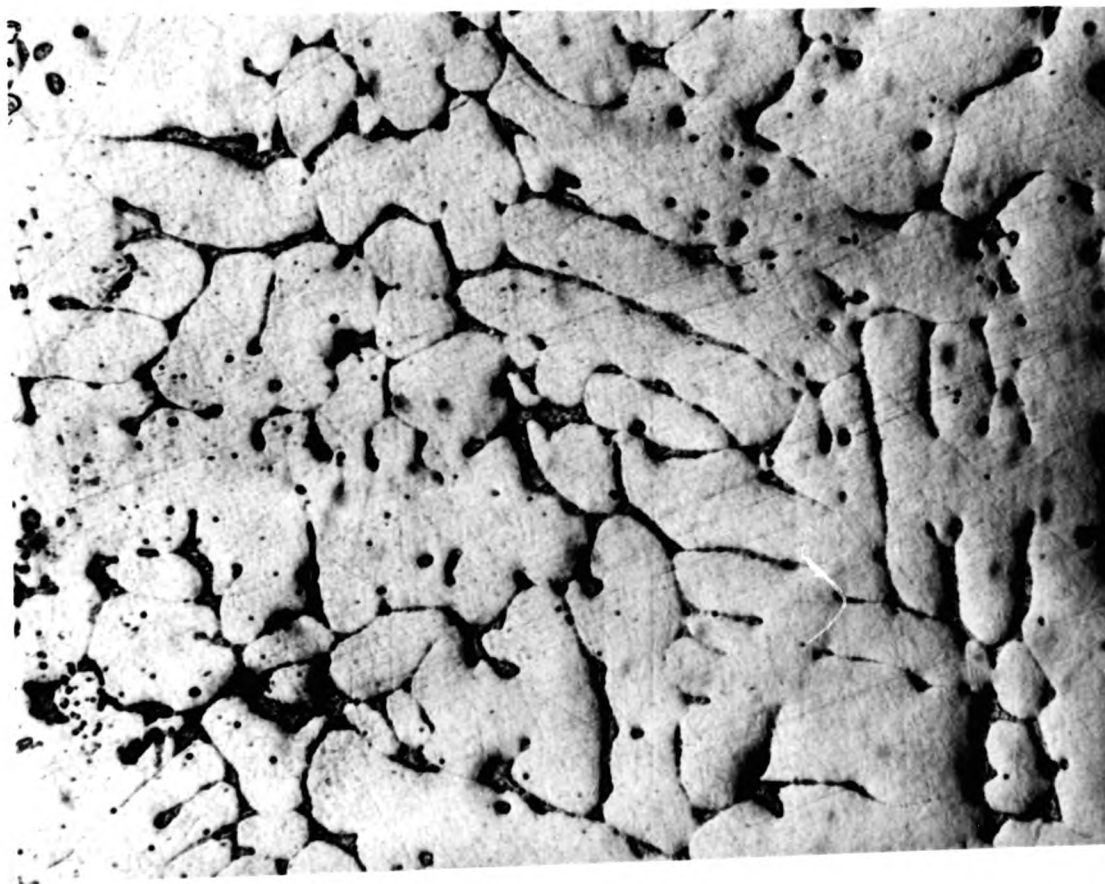


Figure 31. Photomicrograph of 10 w/o Cd-Zn binary alloy. Etched with 2% Nital for 30s to reveal the structure. Magnification 200.

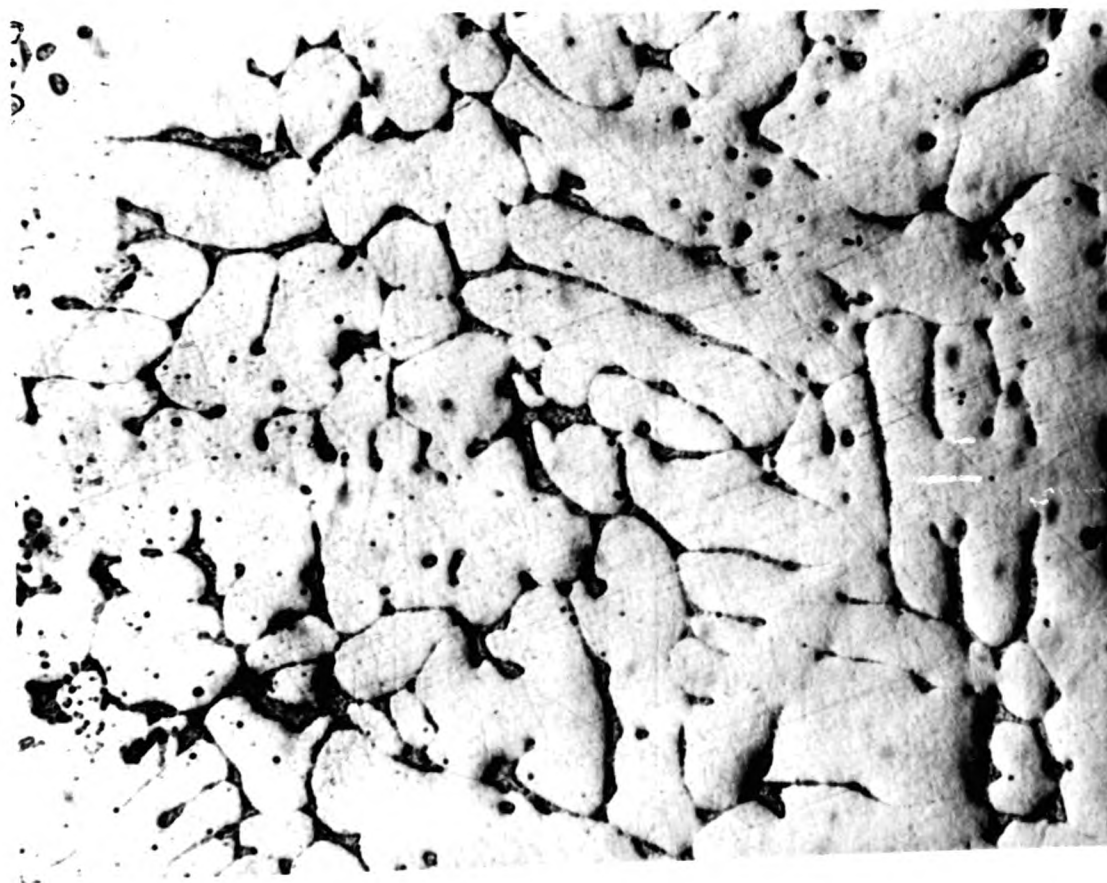


Figure 31. Photomicrograph of 10 w/o Cd-Zn binary alloy. Etched with 2% Nital for 30s to reveal the structure. Magnification 200.

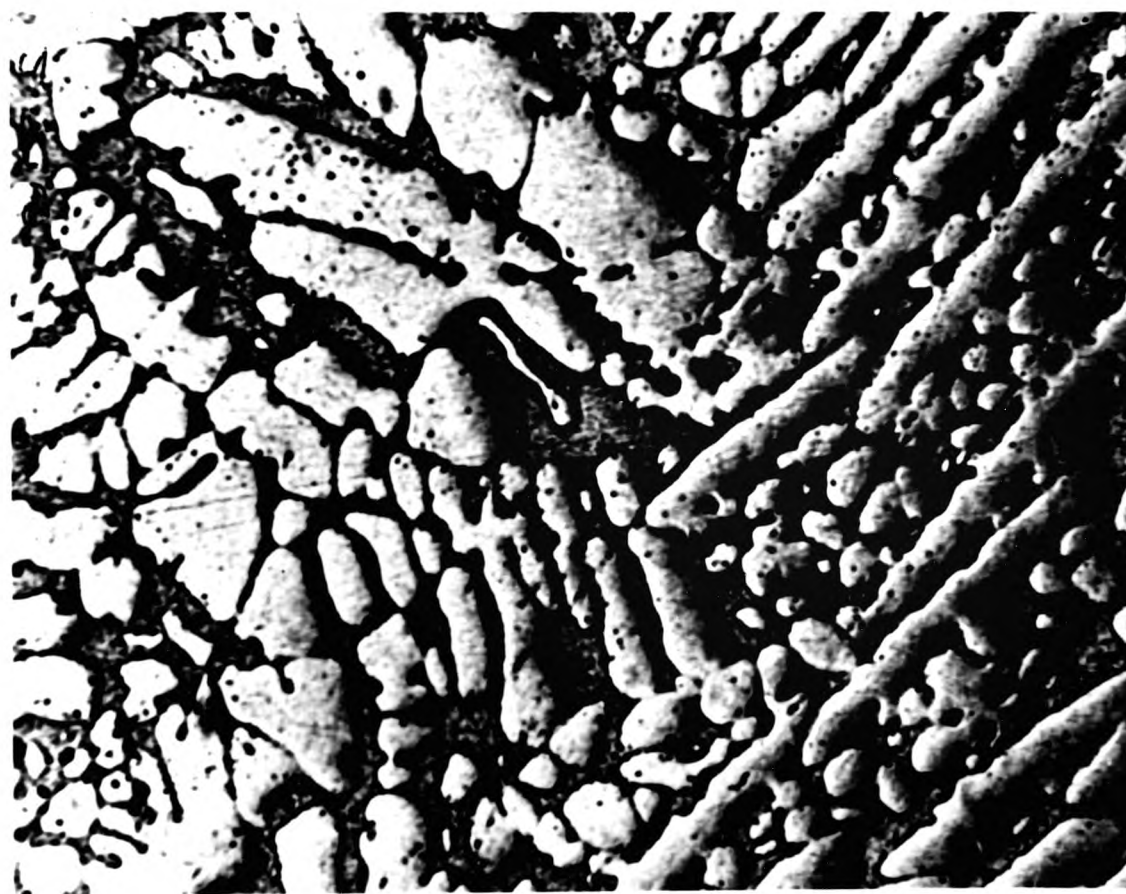


Figure 32. Photomicrograph of 25.0 w/o Cd-Zn binary alloy in as cast condition.
Magnification 200.
Unetched.
Zn rich eutectic islands embedded in the cadmium rich solid solution forming the matrix or background.

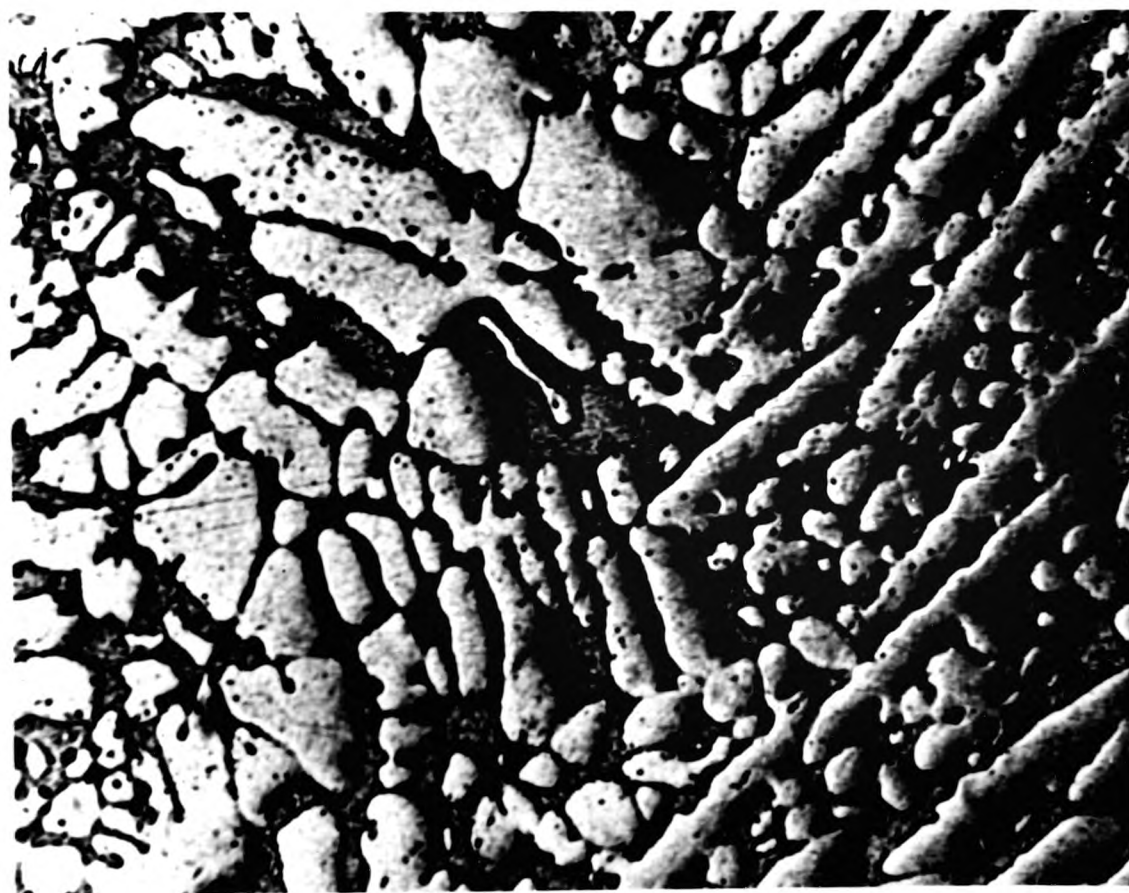


Figure 32. Photomicrograph of 25.0 w/o Cd-Zn binary alloy in as cast condition.
Magnification 200.
Unetched.
Zn rich eutectic islands embedded in the cadmium rich solid solution forming the matrix or background.



Figure 33. Photomicrograph of 5.0 w/o Cd-Zn binary alloy in as cast condition. Etched with 2% Nital to reveal the structure. Magnification 200.

The structure shows very fine grains due to chill casting in graphite moulds. Showing finer grains and eutectic at the grain boundaries.

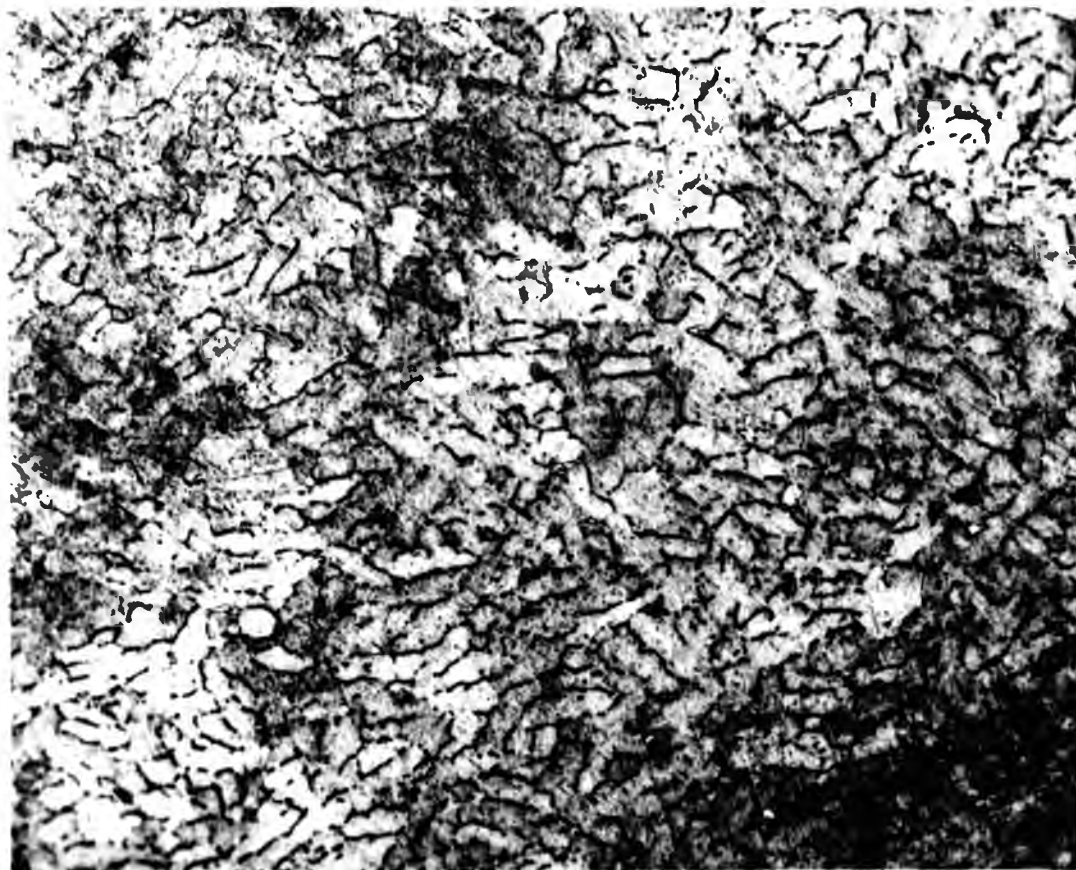


Figure 33. Photomicrograph of 5.0 w/o Cd-Zn binary alloy in as cast condition. Etched with 2% Nital to reveal the structure. Magnification 200.

The structure shows very fine grains due to chill casting in graphite moulds. Showing finer grains and eutectic at the grain boundaries.

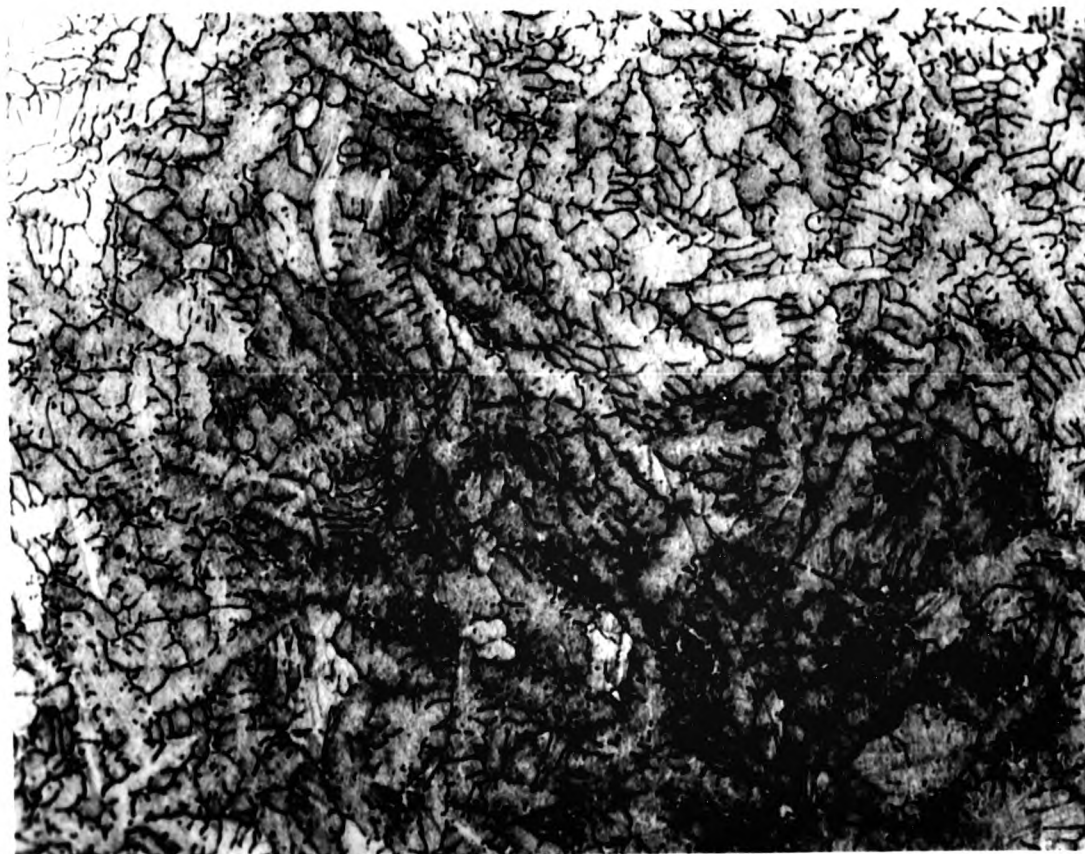


Figure 34. Photomicrograph of 10 w/o Cd-Zn binary alloy chill cast in graphite mould. Shows effect of fast cooling. Dendrite or islands clearly visible. Etched in 2% Nital for 10s to reveal structure. Magnification 200.

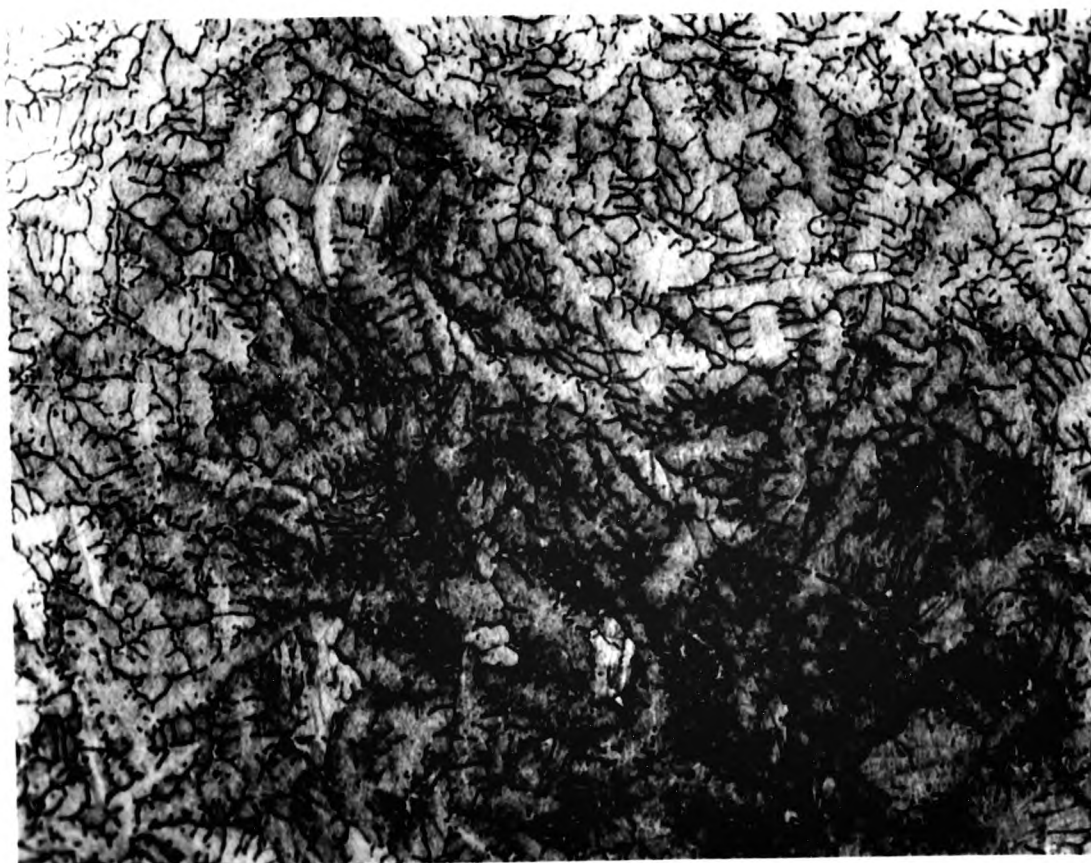


Figure 34. Photomicrograph of 10 w/o Cd-Zn binary alloy chill cast in graphite mould. Shows effect of fast cooling. Dendrite or islands clearly visible. Etched in 2% Nital for 10s to reveal structure. Magnification 200.

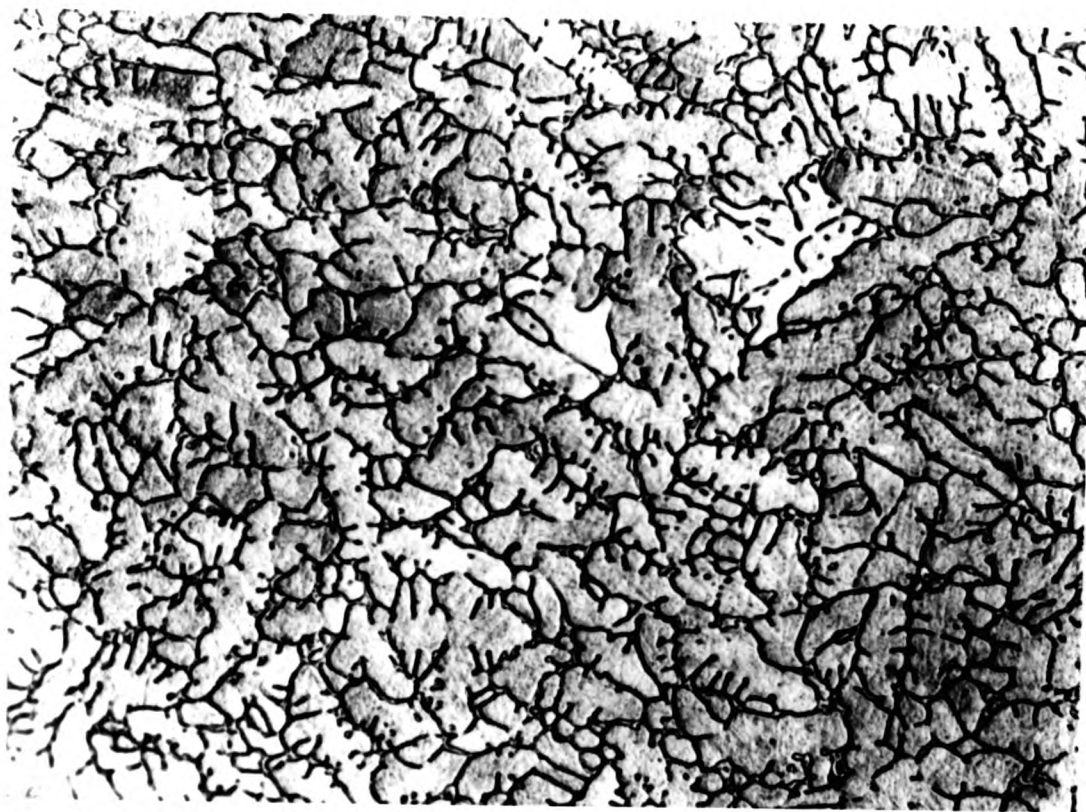


Figure 35. Photomicrograph of 25.0 w/o Cd-Zn binary alloy. Chill cast in graphite mould showing islands or dendrites formation. Magnification 200.

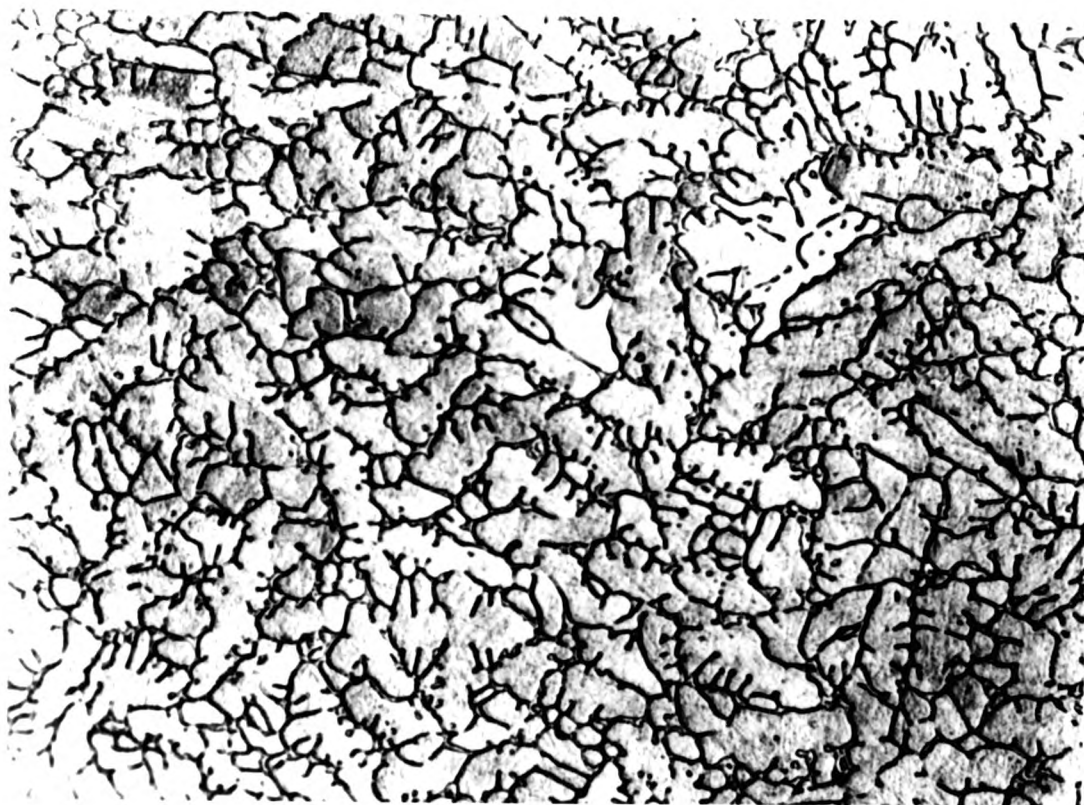


Figure 35. Photomicrograph of 25.0 w/o Cd-Zn binary alloy. Chill cast in graphite mould showing islands or dendrites formation. Magnification 200.

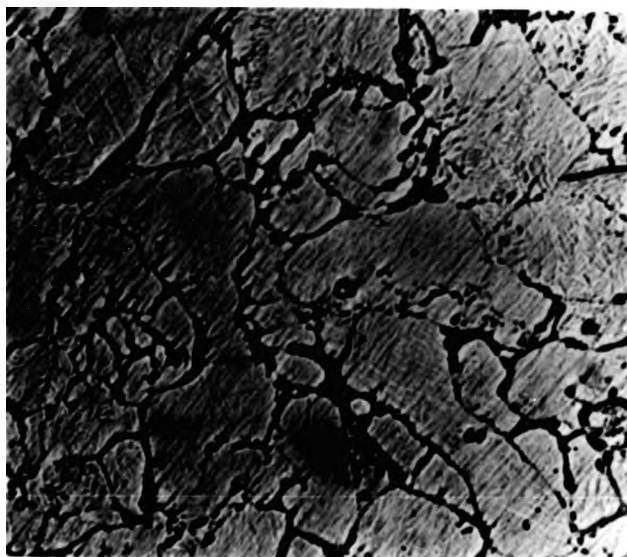


Figure 36. Photomicrograph of 10 w/o Cd-Zn binary alloy as made by compaction of powder at high pressure. Etched with 2% Nital for 15s. Magnification 250.

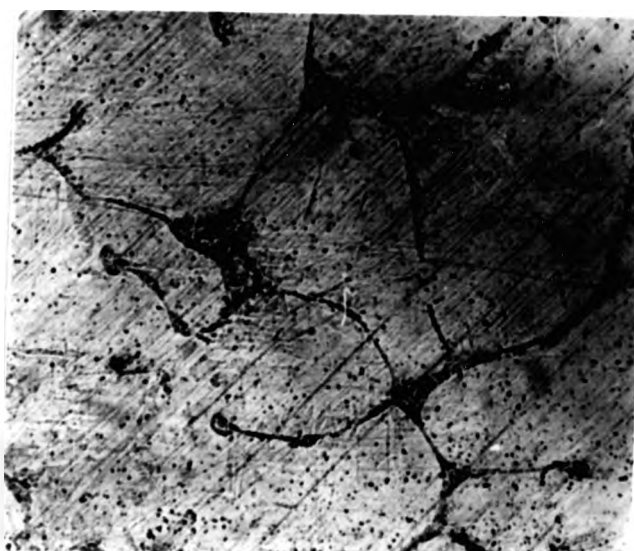


Figure 37. Photomicrograph of 10 w/o Cd-Zn binary alloy as made by compaction of powder at high pressure and then sintered at 200°C for 3 hours. Etched with 2% Nital for 15s. Magnification 250.

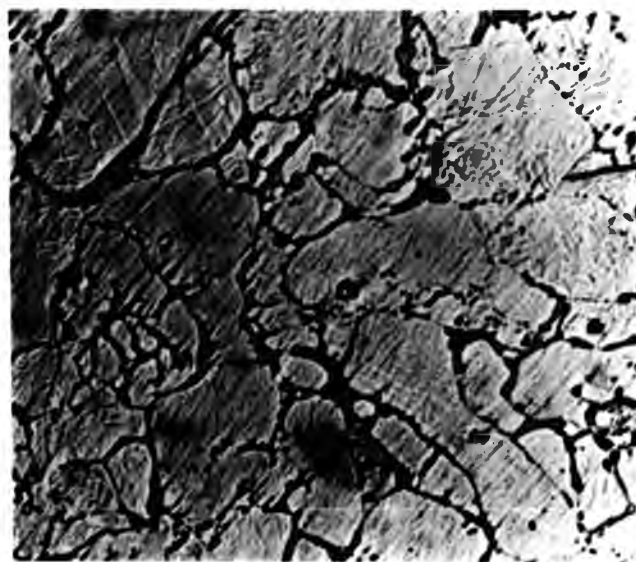


Figure 36. Photomicrograph of 10 w/o Cd-Zn binary alloy as made by compaction of powder at high pressure. Etched with 2% Nital for 15s. Magnification 250.



Figure 37. Photomicrograph of 10 w/o Cd-Zn binary alloy as made by compaction of powder at high pressure and then sintered at 200°C for 3 hours. Etched with 2% Nital for 15s. Magnification 250.

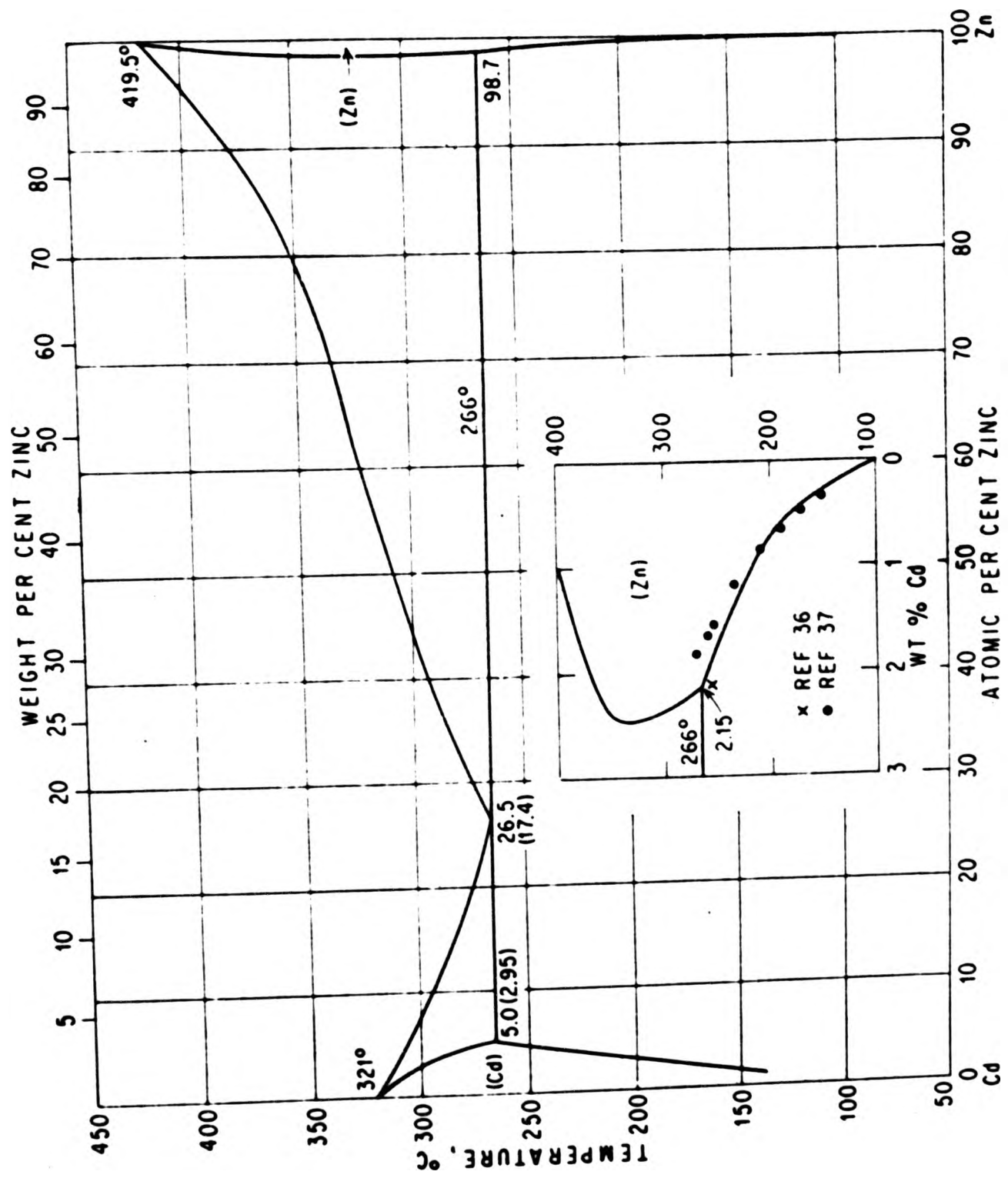


Figure 38. Equilibrium phase diagram of zinc and cadmium

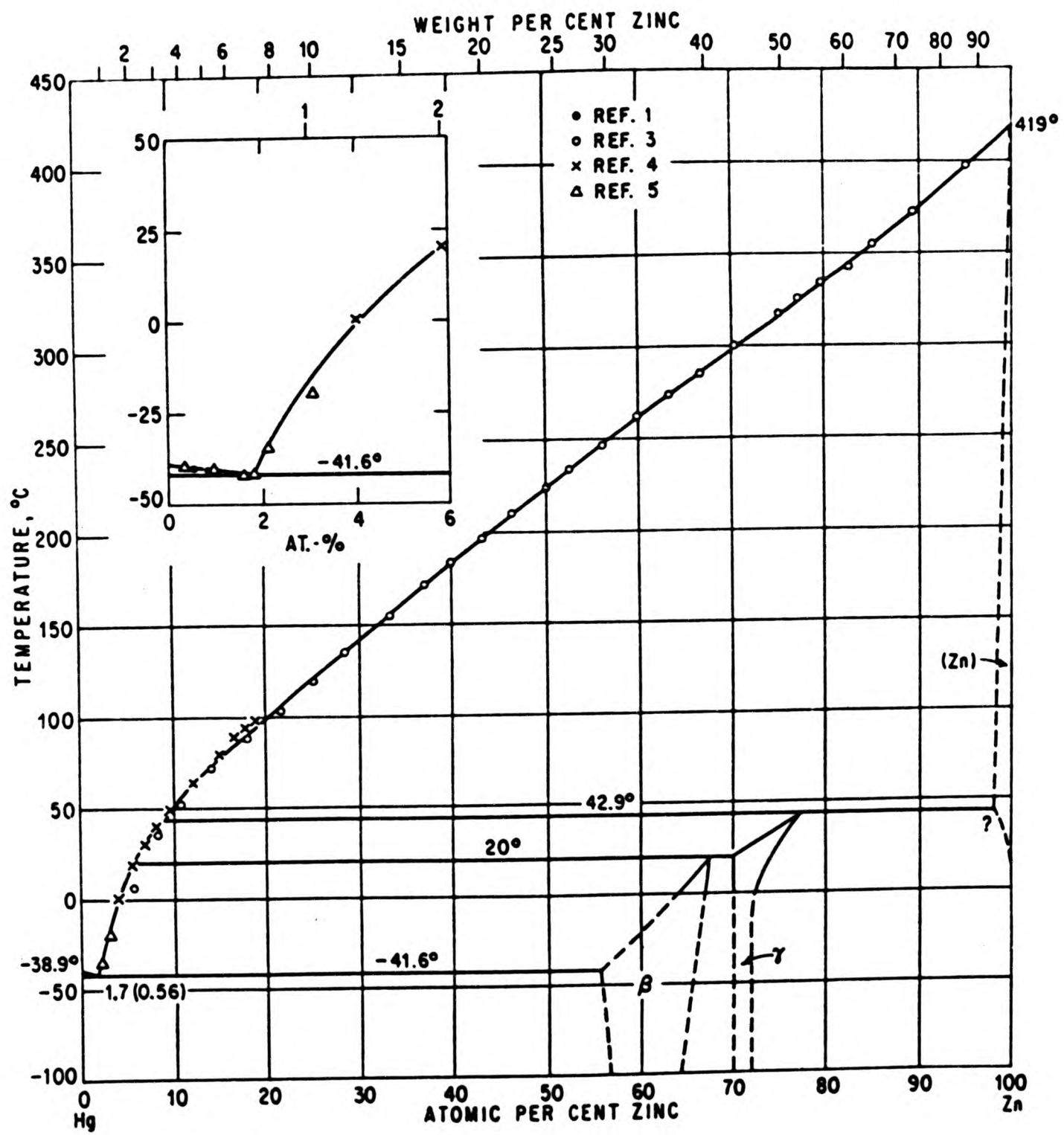


Figure 39. Hg-Zn equilibrium phase diagram.

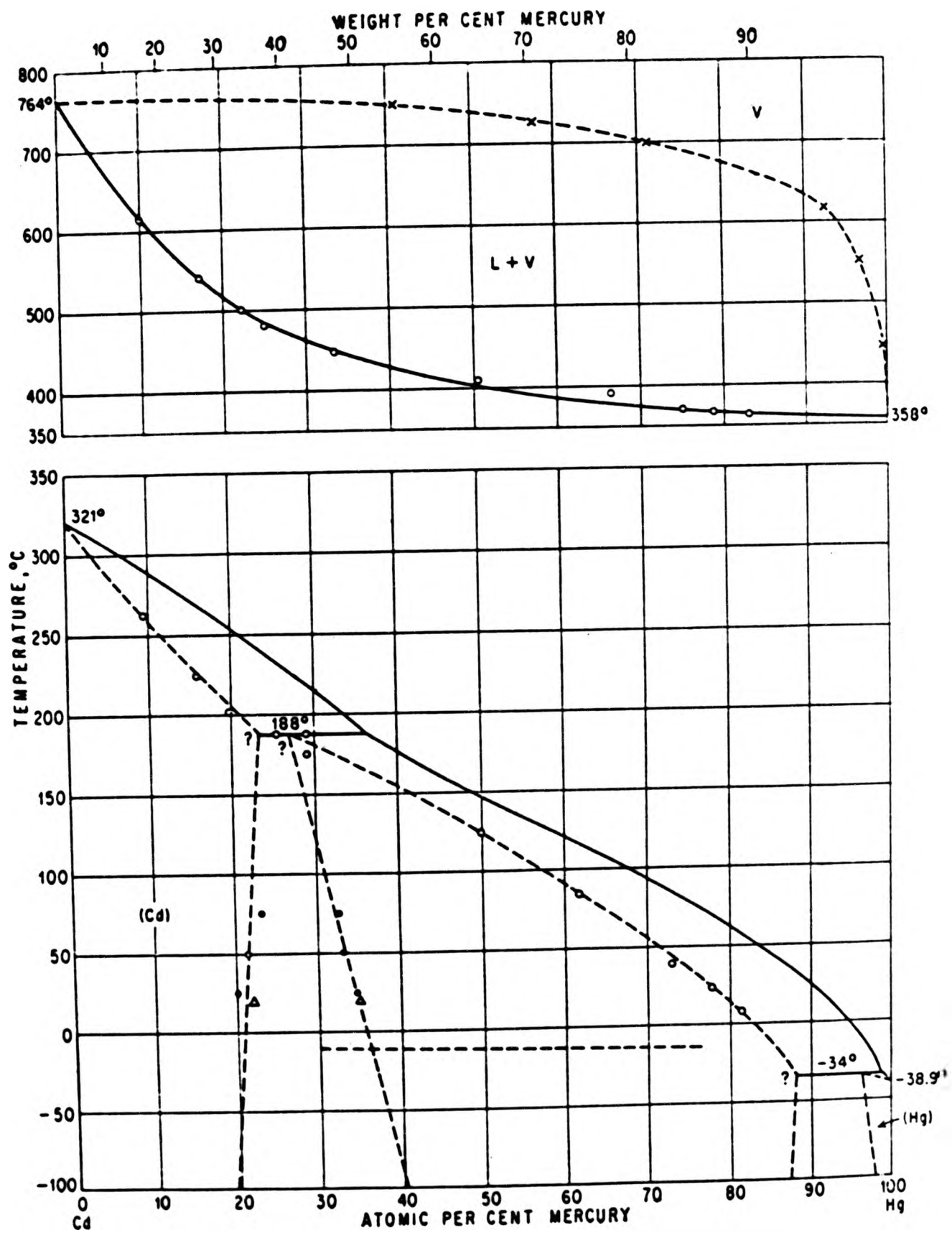


Figure 40. Hg-Cd equilibrium phase diagram.

separate out as confirmed by the decreasing slope of the solubility lines. The eutectic composition at the equilibrium cooling rate is 26.5 at/o. The alloys used in these investigations do not contain more than 25 w/o cadmium. However under certain cooling conditions, they can show the equilibrium structure. The effect of cooling rate becomes clear when microstructures of slowly cooled and fast cooled (cast in graphite moulds) alloys are compared. Fast cooling brings out smaller grains and does not allow enough time for the constituents to separate out completely, as would happen during slow cooling. Slow cooling also allows time for grains to grow and hence coarser grain size will be obtained. Increasing the amount of cadmium in the alloy would mean more possibility for eutectic phase to separate out as it is present in larger amounts. The 25 w/o cadmium alloy (which is the largest amount of cadmium added), shows the Zn rich solid solution embedded in Cd rich solid solution because the former solidifies earlier than the latter.

Figures 41 to 45 show ^{micro} photographs of amalgams of zinc-cadmium alloys and zinc and cadmium metals. With pure zinc mercury forms amalgams which can be liquid at room temperature if mercury is in excess, as it would be on the surface of the specimen being amalgamated. As the mercury diffuses through the specimen the amalgam becomes poorer in mercury and richer in zinc. The main dissolution and incorporation is at the high energy areas such as grain boundaries. At a certain distance from the surface a solid solution of formula Hg_2Zn_3 or $HgZn_2$ that is intermetallic compounds are formed. About 2 w/o Hg is completely soluble in zinc at $40^\circ C$. Any excess mercury would separate out if an equilibrium cooling rate is allowed to take place. However, in the case of cadmium about 30 w/o Hg is soluble in cadmium at around $40^\circ C$. Any excess mercury would separate out as Cd_3Hg an intermetallic compound of stoichiometric composition containing 37.3 w/o Hg. See Figures 39 and 40 for Zn-Hg and Hg-Cd phase diagrams. However commercially so much mercury is not used because of the high cost. This for the alloys means that there would be more mercury in the cadmium



Figure 41. Photomicrograph of pure Zinc Amalgam etched with 1% HCl for 15s to show the presence of Hg.
Magnification 200.
Shows preferential mercury attack at grain boundaries. Also shows mercury distribution in the grains.

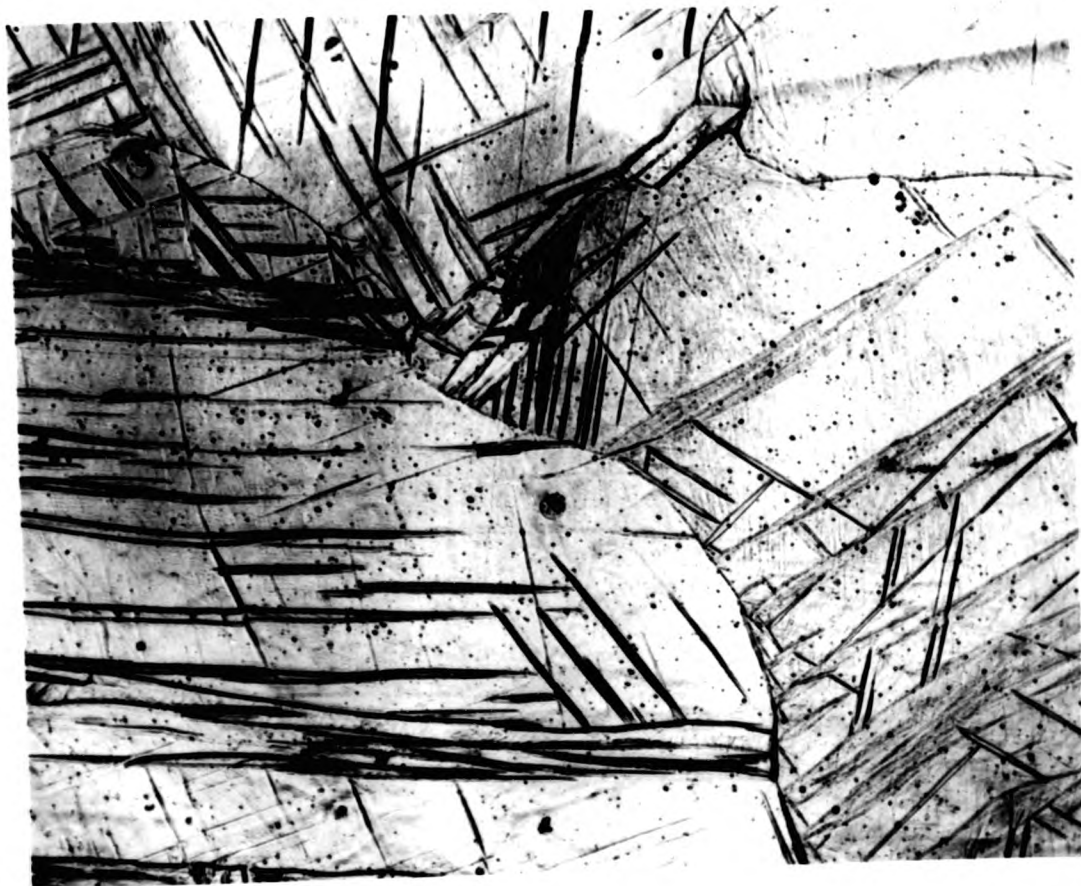


Figure 42. Photomicrograph of 0.2 w/o Cd-Zn amalgam ternary alloy. Etched with 1% HCl for 15s to show the presence of mercury. Magnification 200. Shows preferential mercury attack on the areas of high strain energy.

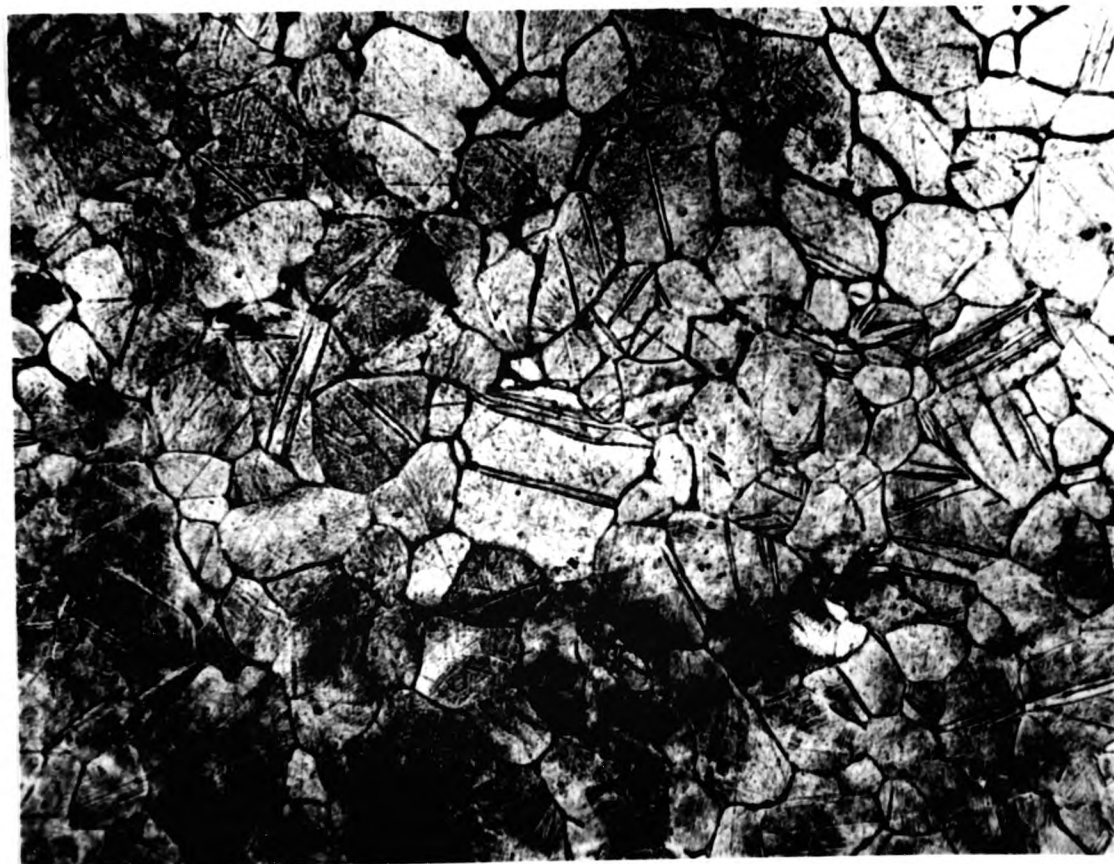


Figure 43. Photomicrograph of 5 w/o Cd-Zn amalgam ternary alloy. Etched with 1% HCl for 15s to reveal the presence of mercury. Magnification 100. Recrystallisation has occurred as evidenced by the presence of twin grains.

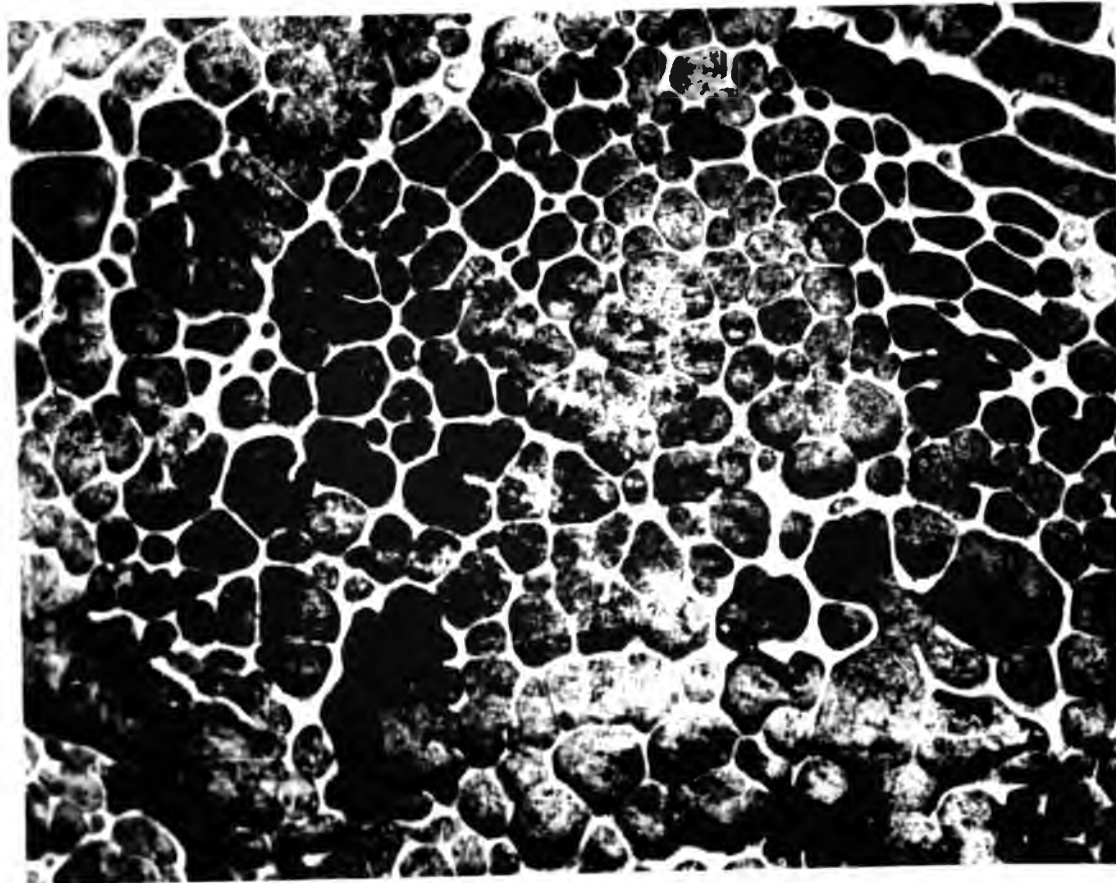


Figure 44. Photomicrograph of 25.0 w/o Cd-Zn amalgam ternary alloy. Etched in 1% HCl to show presence of Hg. Dark areas are Hg rich. Magnification 100.

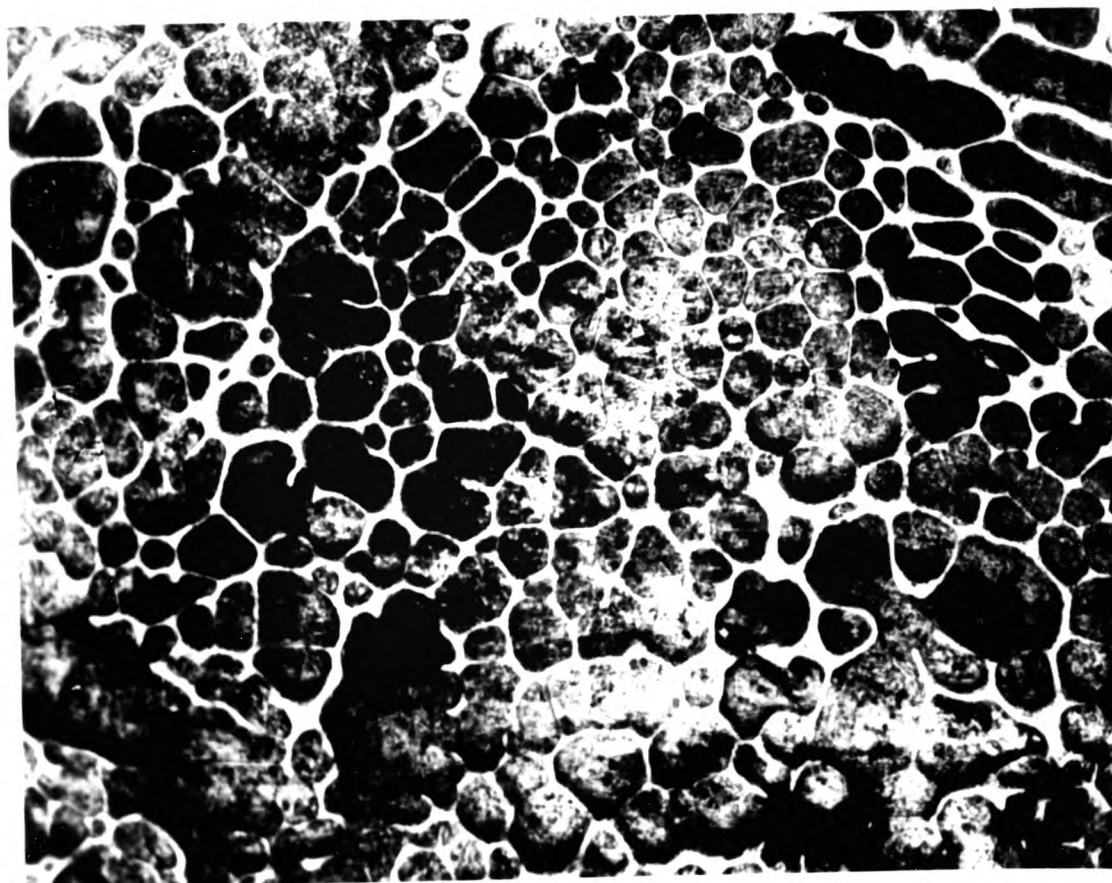


Figure 44. Photomicrograph of 25.0 w/o Cd-Zn amalgam ternary alloy. Etched in 1% HCl to show presence of Hg. Dark areas are Hg rich. Magnification 100.

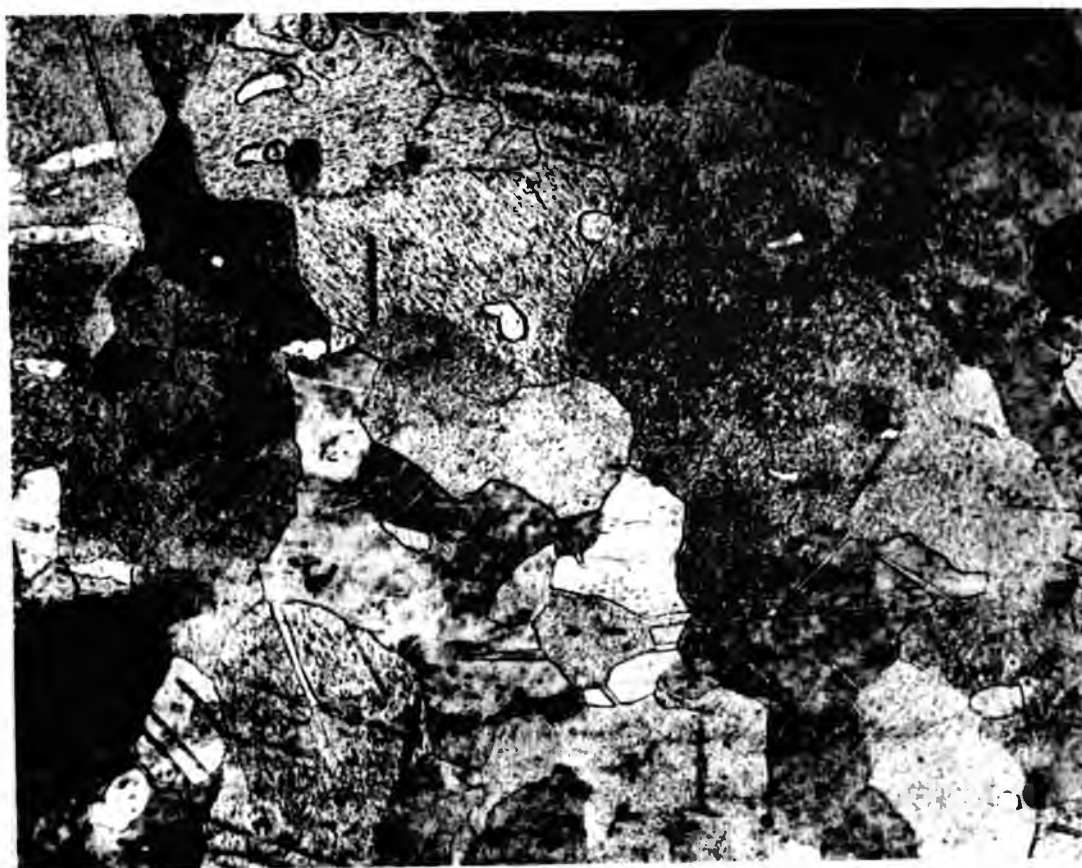


Figure 45. Photomicrograph of pure Cd amalgam at 200 magnification. Etched with 1% HCl to reveal the presence of mercury. Compared with pure Zn, cadmium has much more affinity for Hg than Zn as evidenced in the above picture. Dark areas are mercury.

rich phase and less mercury in the zinc rich phase. This is borne out by the microphotographs and later by the electronmicrographs.

2.7 SCANNING ELECTRON MICROSCOPY AND ELECTRON MICROPROBE ANALYSIS

2.7.1 Introduction. Interest in using characteristic X-rays for chemical analysis arose as a result of Moseley's work in 1913 on the relationship between an element's characteristic wavelength and atomic number. The electron microprobe has been engineered as an analytical X-ray instrument incorporating up to four or five wavelength spectrometers for the simultaneous chemical analysis of several elements. Electron beam scanning is added to the microprobe to facilitate faster specimen surveying for element distributions and higher point to point resolution by detecting backscattered electrons. It has the advantage of having a greater depth of field (20 times) and higher resolution (100-500 times) than the optical (light) microscope and without the elaborate specimen preparation as required for the transmission electron microscope.

2.7.2 Equipment. The instrument can be divided into three parts, each with a distinct function:

- (a) electron beam forming,
- (b) specimen handling,
- (c) signal detection and recording.

The first part consists of an electron gun generating an electron beam of sufficient current and potential in a vacuum better than 10^{-5} torr. This beam can be used in two modes, stationary (point) or scanning. The use of a stationary beam is for quantitative elemental analysis. Approximate element concentrations are calculated by comparing the specimen's characteristic X-ray line intensities with those of standards of known composition. The operating conditions can be generalised as:

- (a) an accelerating potential between 5-30kV, which is about 1.5-2 times the critical excitation energy of the measuring line,

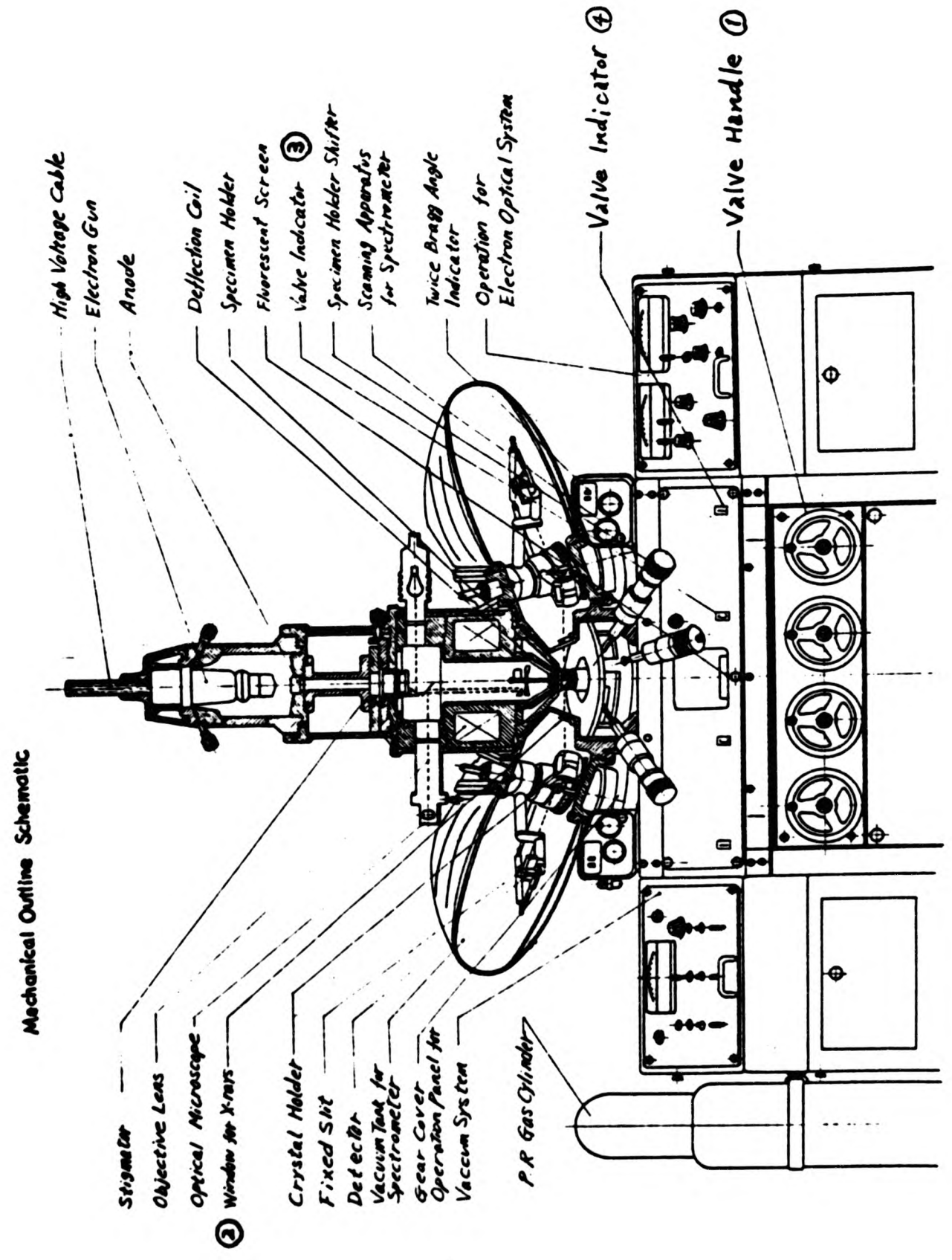


Figure 46. Schematic mechanical outline of the electron microprobe analyser.

- (b) incident specimen current of 10^{-9} to 10^{-7} A,
- (c) beam diameter of greater than or equal to $0.5\mu\text{m}$.

The stationary beam is also used to obtain a complete X-ray spectrum by scanning the wavelength spectrometers through their entire range. The X-ray intensity as a function of wave length is usually recorded on a strip chart recorder. Besides generating two dimensional images for photographing, the scanning mode is extremely useful for guiding the stationary beam to an exact point on the specimen. First a backscattered electron image is viewed to determine the point of analytical interest. Then switching to the stationary mode, the beam is directed on to the spot. The specimen handling section includes a specimen chamber vacuum interlock valve, a specimen stage and the visual light optics. The specimen is introduced to the stage through a port in the chamber. The stage can be moved by manual controls outside the chamber. The third part which does the signal detection and recording consists of five basic channels; 3 for electron and 2 for photon signals. Each channel consists of a detector and a collector, amplifying, display and recording facilities. Additionally there may be on-line direct computer interfacing.

Most solids can be used as specimens. The metals having a high electrical and thermal conductivity, can conduct away the heat generated by the beam impact and the resulting temperature rise may be just a few $^{\circ}\text{C}$. For minerals, ceramics and organics which are bad conductors the temperature rise may be as high as 500°C . Therefore ceramic materials are coated with 10-30nm thick conducting film of gold, carbon or aluminium. These elements have low secondary electron yield and low absorption characteristics for generated X-rays.

A secondary electron image is formed by electrically scanning the electron beam across the specimen surface and detecting secondary electrons. These have low energies and therefore they may be gathered by an applied electrostatic field and accelerated towards the detector. These electrons are released from a shallow depth (~ 1 nm deep) of specimen surface. This image

produces topographic features such as cracks, holes, ridges etc. and has good depth of field. The backscattered electron image is composed of elastically scattered electrons from the specimen's atomic nuclei and therefore have high energy as opposed to the previous case where electrons were produced from inelastic collisions with electrons in the specimen atoms.

Characteristic X-rays are produced when the incident beam excites electrons from K, L, M, N etc. shells after which atoms return to their normal state. This provides the basis for quantitative chemical analysis. However, a background X-ray radiation is also unavoidably obtained which limits the minimum amount of an element that can be detected. Figure 46 is a diagrammatic representation of a scanning electron microscope.

2.7.3 Results and Discussion. Figures 47-52 show electron micrographs of some selected alloys. The backscattered secondary electron image for the pure metals, alloys and amalgams resembles the optical photomicrographs. The mercury, zinc and cadmium X-ray images indicate the degree of inhomogeneity of these alloys. There is more mercury associated with cadmium and less with zinc. Similarly zinc rich solid solution is embedded in the cadmium rich eutectic. This is so because the former has a higher melting point while the latter has a lower melting point.

2.8 CONCLUSIONS

From the chemical analysis of the bulk material it can be inferred that preparation of alloys was a successful operation. This was double checked by colorimetric and atomic absorption spectrophotometric techniques. However, metallography and electron microscopy revealed that, in spite of the care taken, the distribution of cadmium and therefore mercury was far less homogeneous than ideally desired. Mercury formed continuous solutions with either metal upon amalgamation. Intermetallic compounds $HgZn_2$ and Cd_3Hg have also been detected by X-ray diffraction. Cadmium dissolves more

Figure 48. Electron micrographs of 5 w/o Cd-Zn binary alloy at 1200 magnification (selected area from Fig.47)

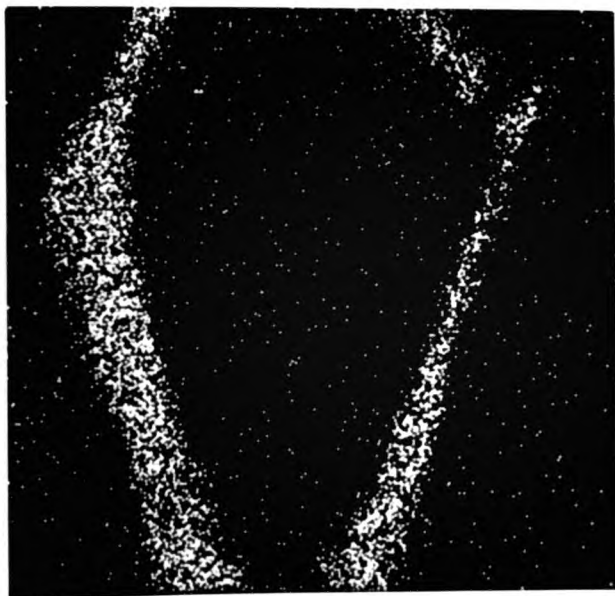
(a) Electron image (b) Cd K_{α} X-ray image

(c) Zn K_{α} X-ray image

(a)

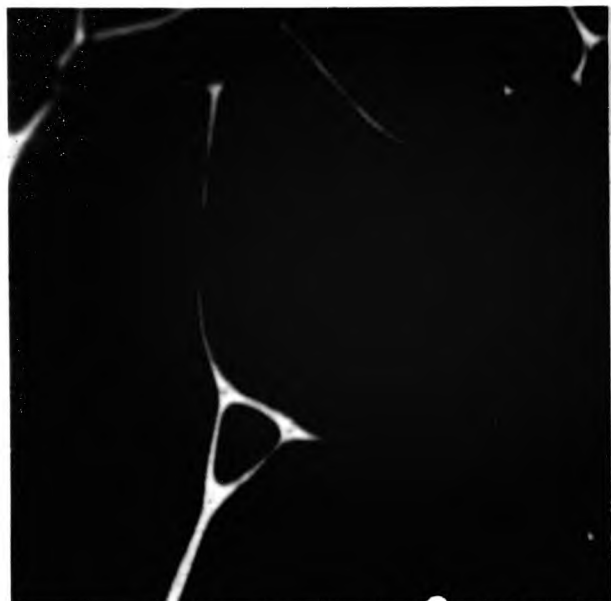


(b)

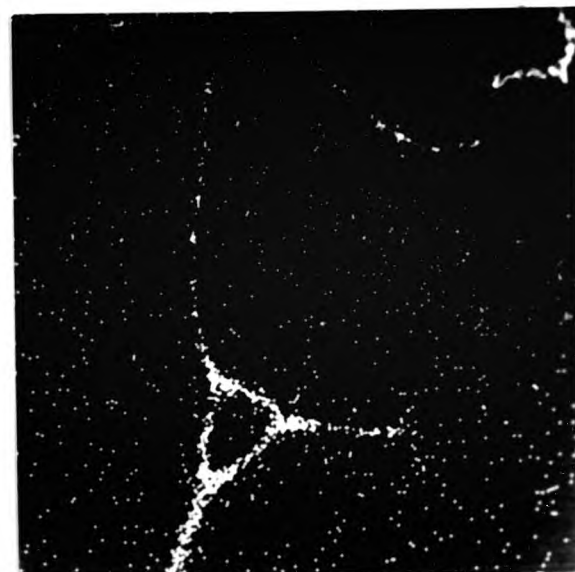


(c)





(a)

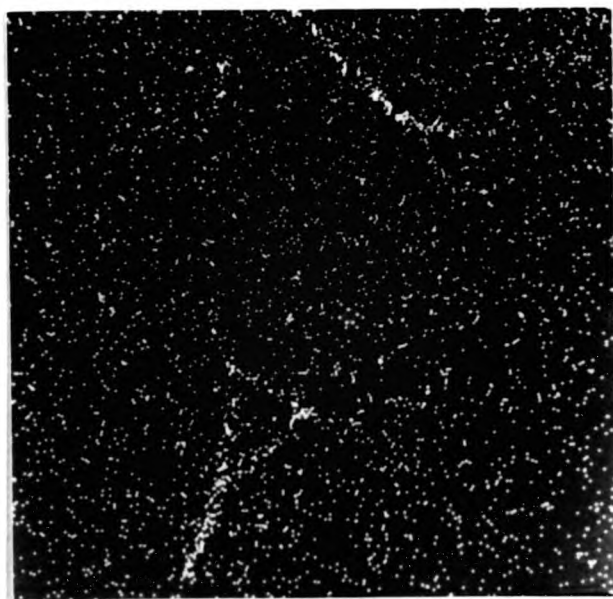


(b)

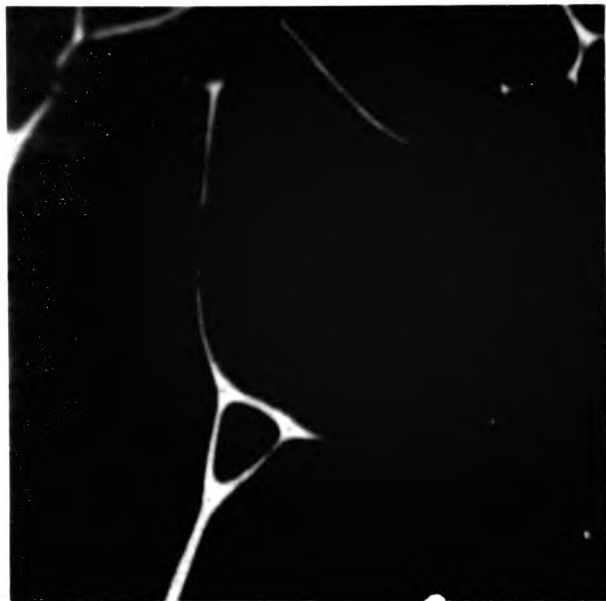
Figure 49. Electron micrographs of 10 w/o Cd-Zn amalgam containing 2.5 w/o Hg at 300 magnification.

(a) Electron image (b) Cd K α X-ray image

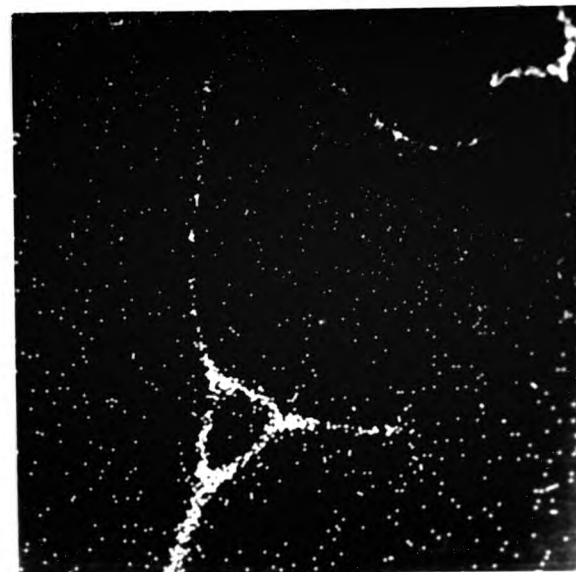
(c) Hg K α X-ray image



(c)



(a)

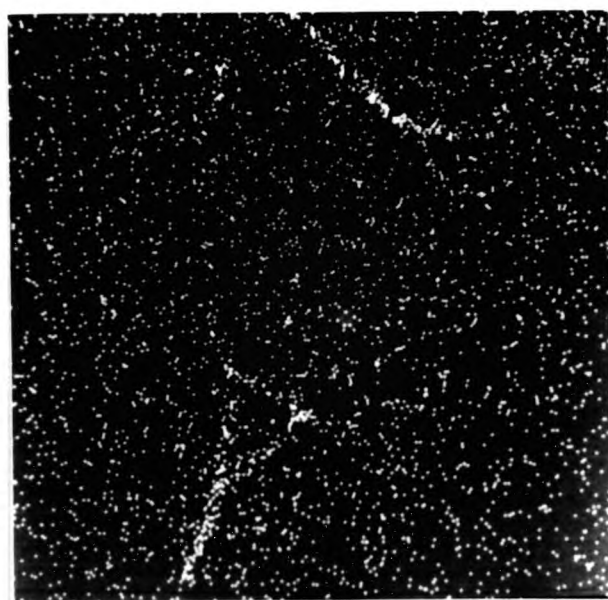


(b)

Figure 49. Electron micrographs of 10 w/o Cd-Zn amalgam containing 2.5 w/o Hg at 300 magnification.

(a) Electron image (b) Cd K α X-ray image

(c) Hg K α X-ray image



(c)

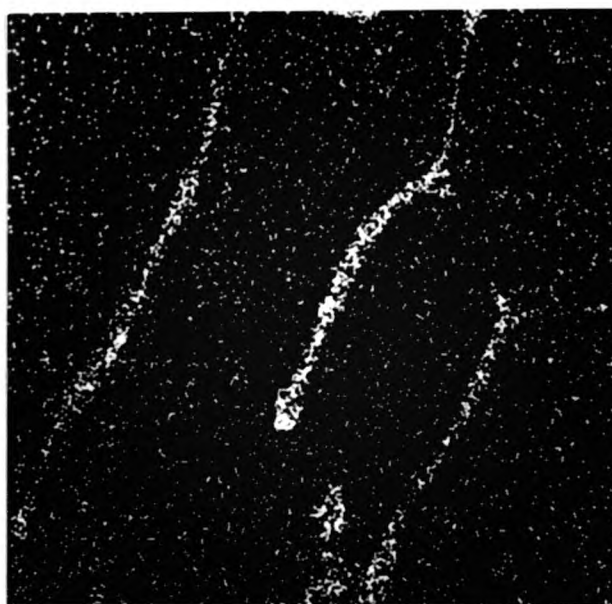
(a)



Figure 50. Electron micrographs of 10 w/o Cd-Zn binary alloy at 300 magnification.

(a) Electron image (b) Cd K_{α} X-ray image

(b)



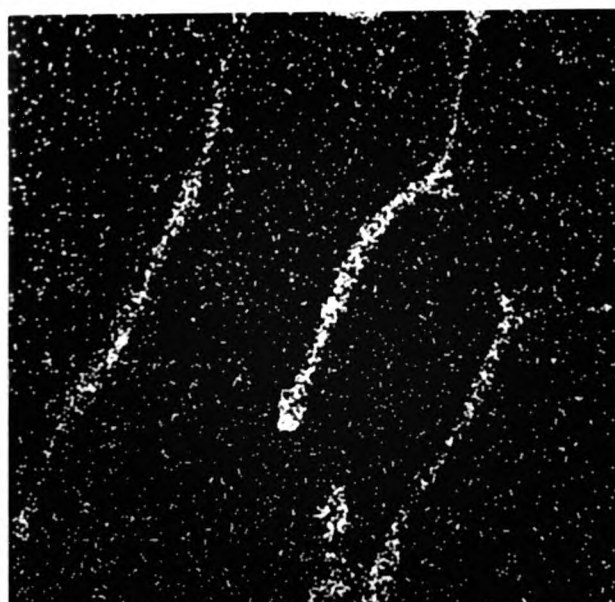
(a)

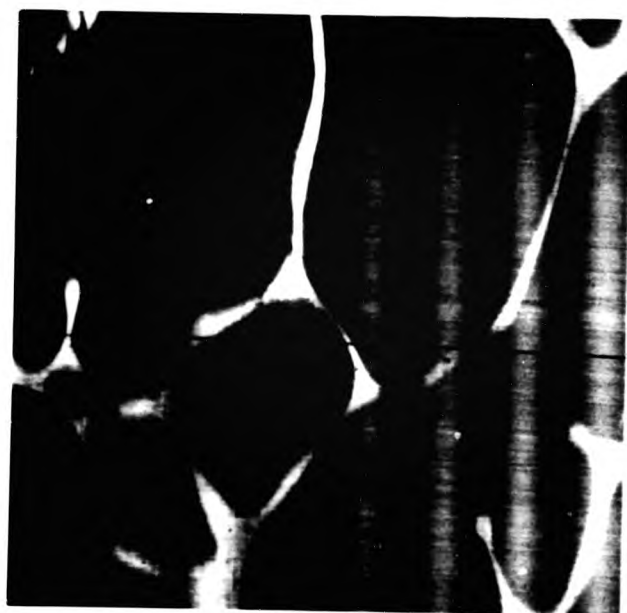


Figure 50. Electron micrographs of 10 w/o Cd-Zn binary alloy at 300 magnification.

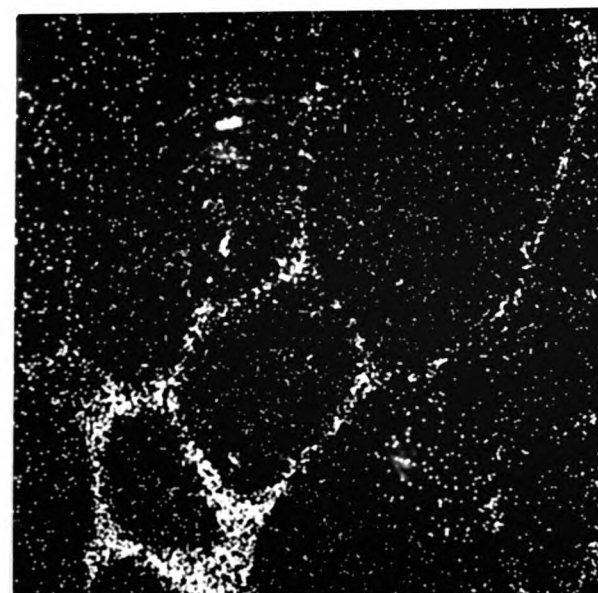
(a) Electron image (b) Cd K_{α} X-ray image

(b)





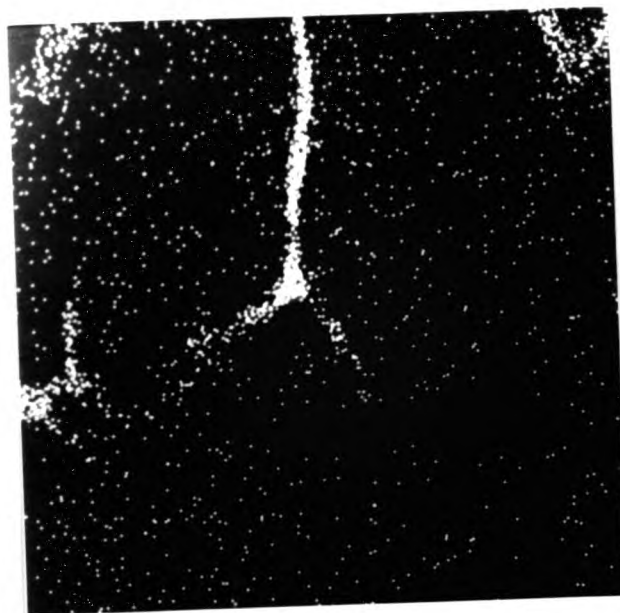
(a)



(b)

Figure 51. Electron micrographs of 5 w/o Cd-Zn amalgam containing 10.0 w/o Hg at 300 magnification.

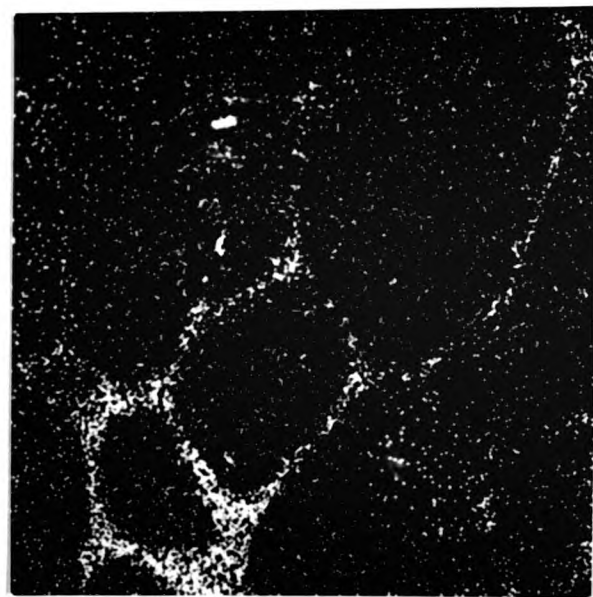
(a) Electron image (b) Cd K α X-ray image (c) Hg K α X-ray image



(c)



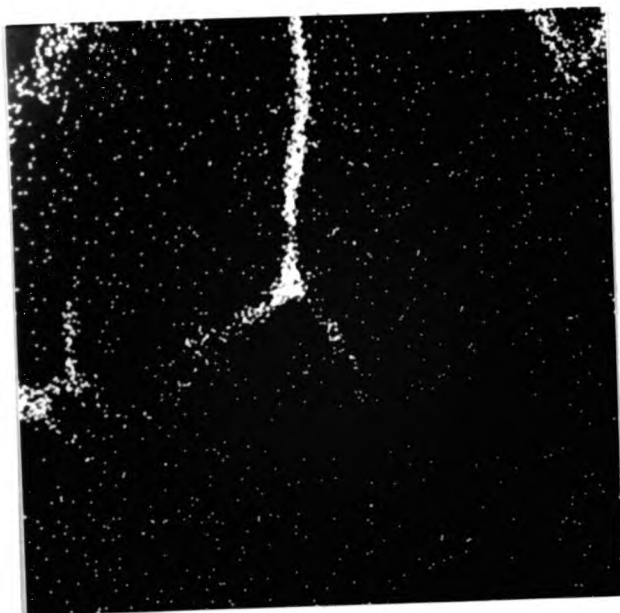
(a)



(b)

Figure 51. Electron micrographs of 5 w/o Cd-Zn amalgam containing 10.0 w/o Hg at 300 magnification.

(a) Electron image (b) Cd K_{α} X-ray image (c) Hg K_{α} X-ray image



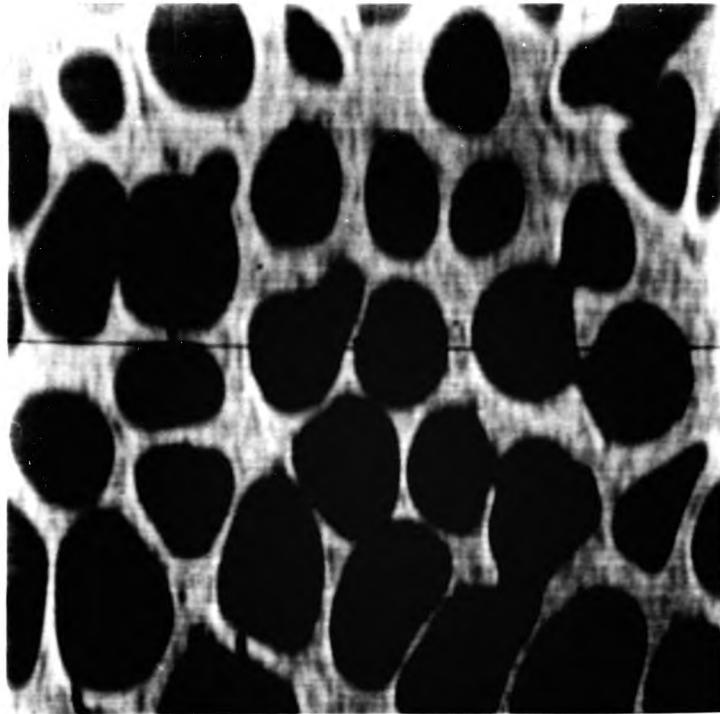
(c)

Figure 52. Electron micrographs of 25 w/o Cd-Zn binary alloy at 300 magnification.

(a) Back scattered electron image

(b) Cd K_{α} X-ray image

(a)



(b)

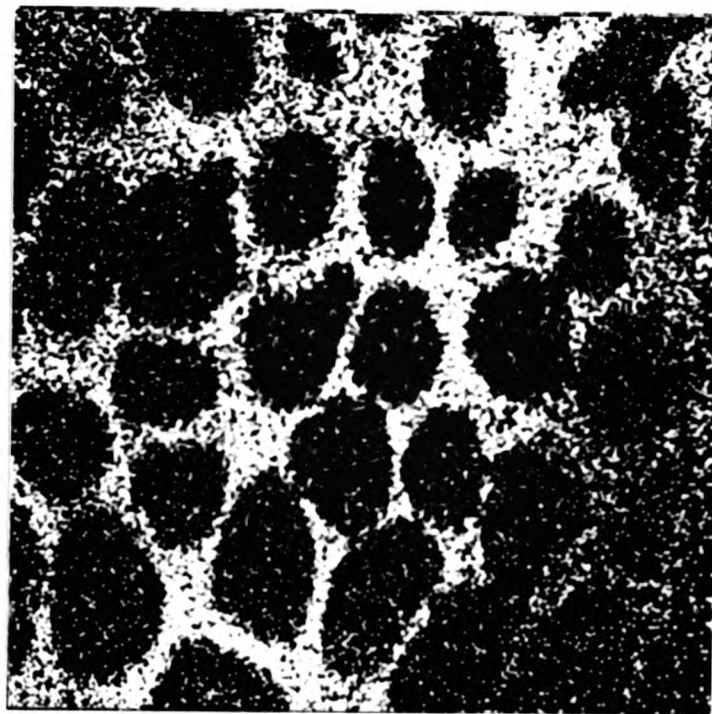
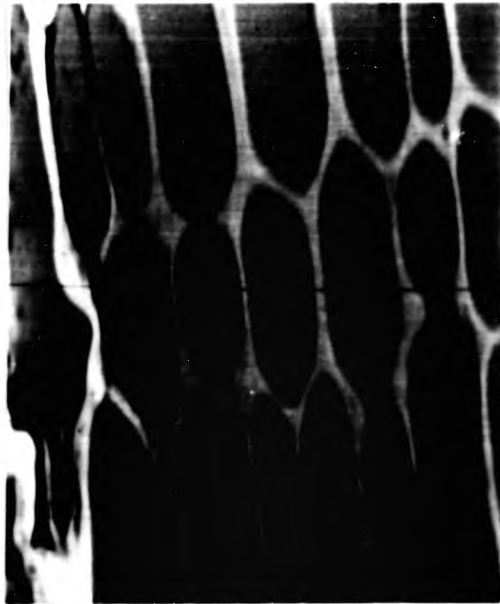
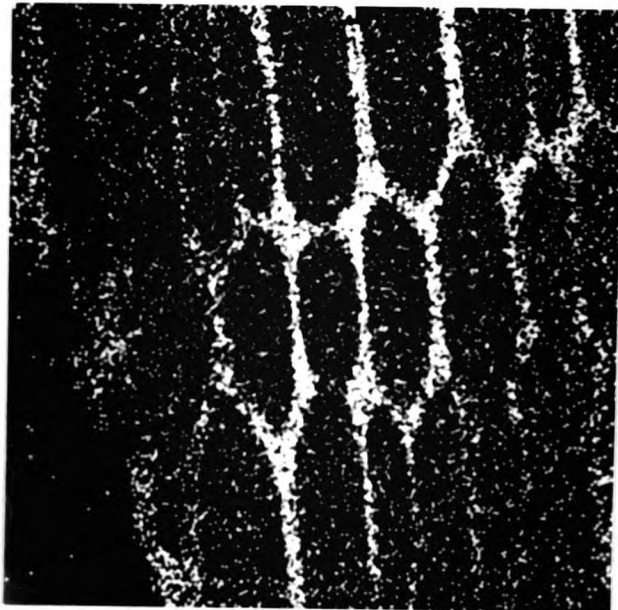


Figure 53. Electron micrographs of 25 w/o Cd-Zn amalgam containing 2.5 w/o Hg at 300 magnification. (a) Electron image (b) Cd K_{α} X-ray image (c) Hg K_{α} X-ray image

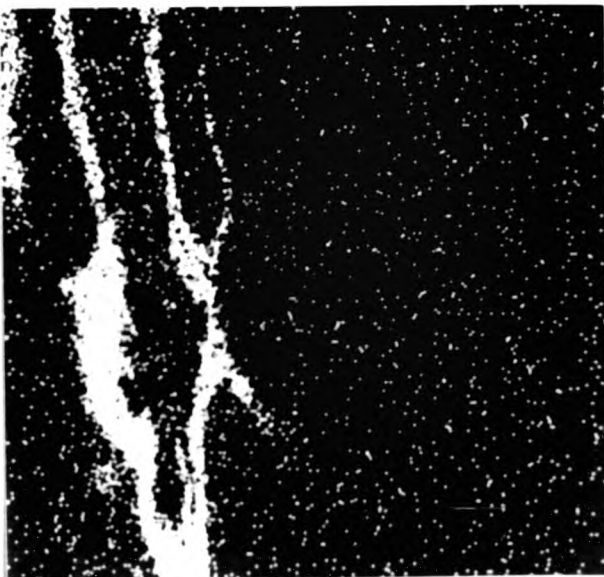
(a)



(b)



(c)



mercury than does zinc and the solubility of mercury in the former is 30 w/o as compared to 2 w/o in the latter at the same temperature. This inevitably results in mercury rich areas in the eutectic phase containing cadmium.

The zinc-cadmium equilibrium diagram is a simple eutectic type. The two metals are completely miscible in the liquid state, but not in the solid state. This is why, when the two are mixed in different proportions to make alloys, unless the cooling rate is extremely fast, the solid solution phase rich in zinc will separate out from the cadmium rich eutectic because the former freezes first having a higher melting point. The equilibrium phase diagram also makes it possible to understand the fact that these alloys do not lend themselves to a "homogenising treatment" as would other systems, because of their limited mutual solubility.

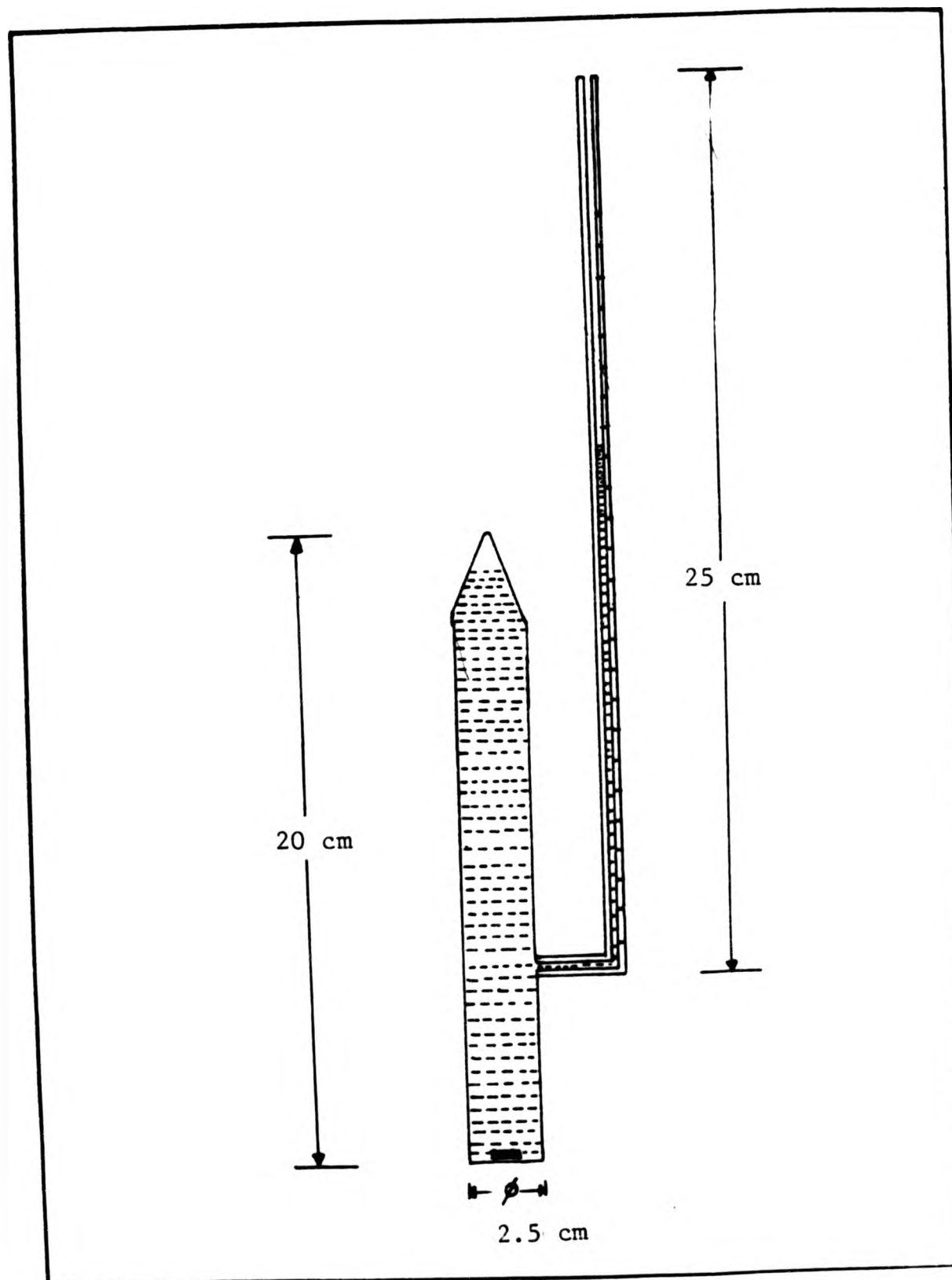


Figure 53. Corrosion cell for hydrogen evolution studies.

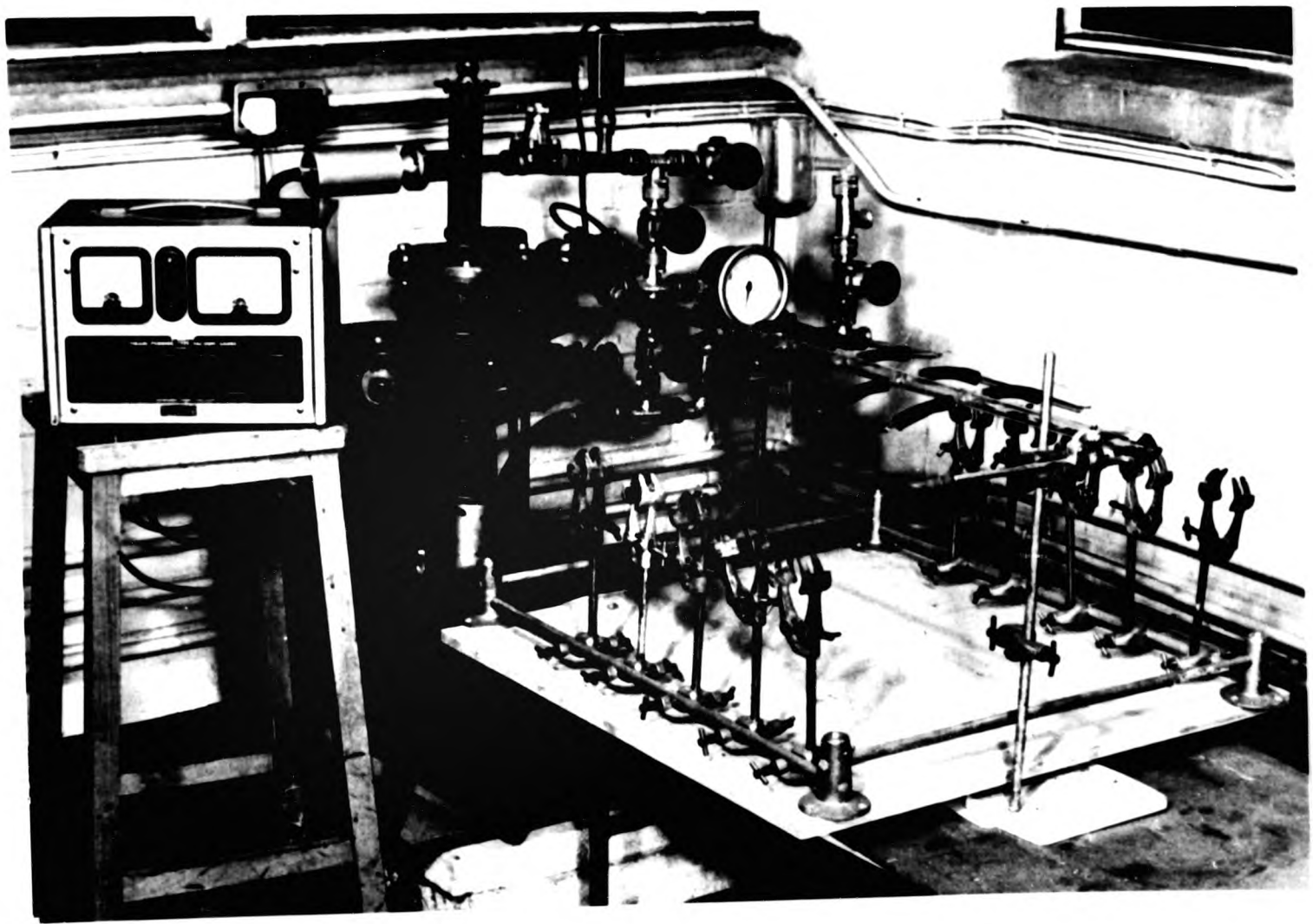


Figure 54. Edwards high vacuum pump with central glass stem

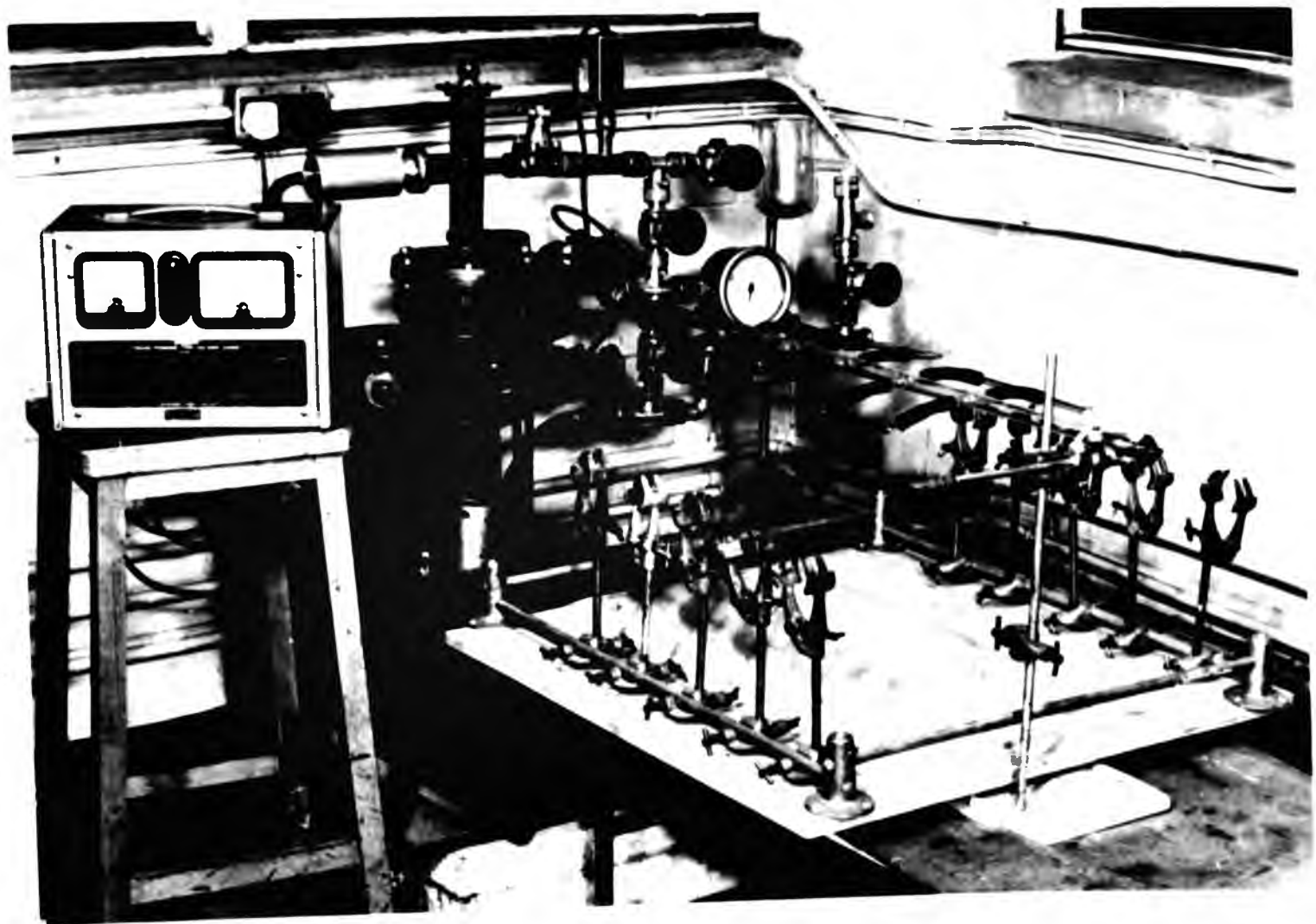


Figure 54. Edwards high vacuum pump with central glass stem

Carew. This essentially consists of a sealed bulb 20cm long and 2.5cm in diameter with a graduated metric scale side arm capillary, 25cm long. This design has several advantages. It is simple to make by normal glass blowing techniques, leak proof, allows easy monitoring of the gas evolved without cumbersome calculations. The capillary internal diameter was 2mm \pm 0.5mm. Each capillary was calibrated for volume by injecting a known amount of liquid through a syringe and noting the height. The cells were cleaned with doubly distilled water and acetone and dried in an air oven at 80°C. One specimen was introduced into each cell, which was then marked. The open end was then sealed using a glass blowing torch. Experiments were conducted in batches of ten. Ten cells were fixed at a time to the central evacuation arm (see Figure 55) attached to an Edwards high vacuum rotary diffusion pump unit, as shown in Figure 54. High vacuum silicone grease and pressure tubes were used at all the joints to prevent leaks and for ease during the fitting and removal of the cell to the central arm. With only the rotary pump switched on, the cells were evacuated down to a pressure of 10^{-1} torr. The cells were then flamed twice with a gas torch to remove any adsorbed gas adhering to the glass walls of the cells. The diffusion pump was then switched on and the cells evacuated to a pressure of 10^{-4} torr. The pressure measurements were carried out using a conventional Pirani-Perming vacuum gauge. The diffusion pump was kept running for over six hours after the gauge had registered a pressure of 10^{-4} torr to ensure complete evacuation of the cells, necessitated owing to the possible reduction in efficiency of evacuation due to the long capillary arm. The electrolyte used was 6 mol dm⁻³ KOH saturated with zinc oxide. The solution was prepared by dissolving accurately weighed amounts of Analar grade KOH pellets in doubly distilled water, in a vessel with a narrow opening covered by a stopper to minimise absorption of carbon dioxide by the KOH solution. The solution was cooled to 25°C; saturated zinc oxide solution was prepared by dissolving small quantities of oxide at a time, until such time that no more would go into solution. This process took a

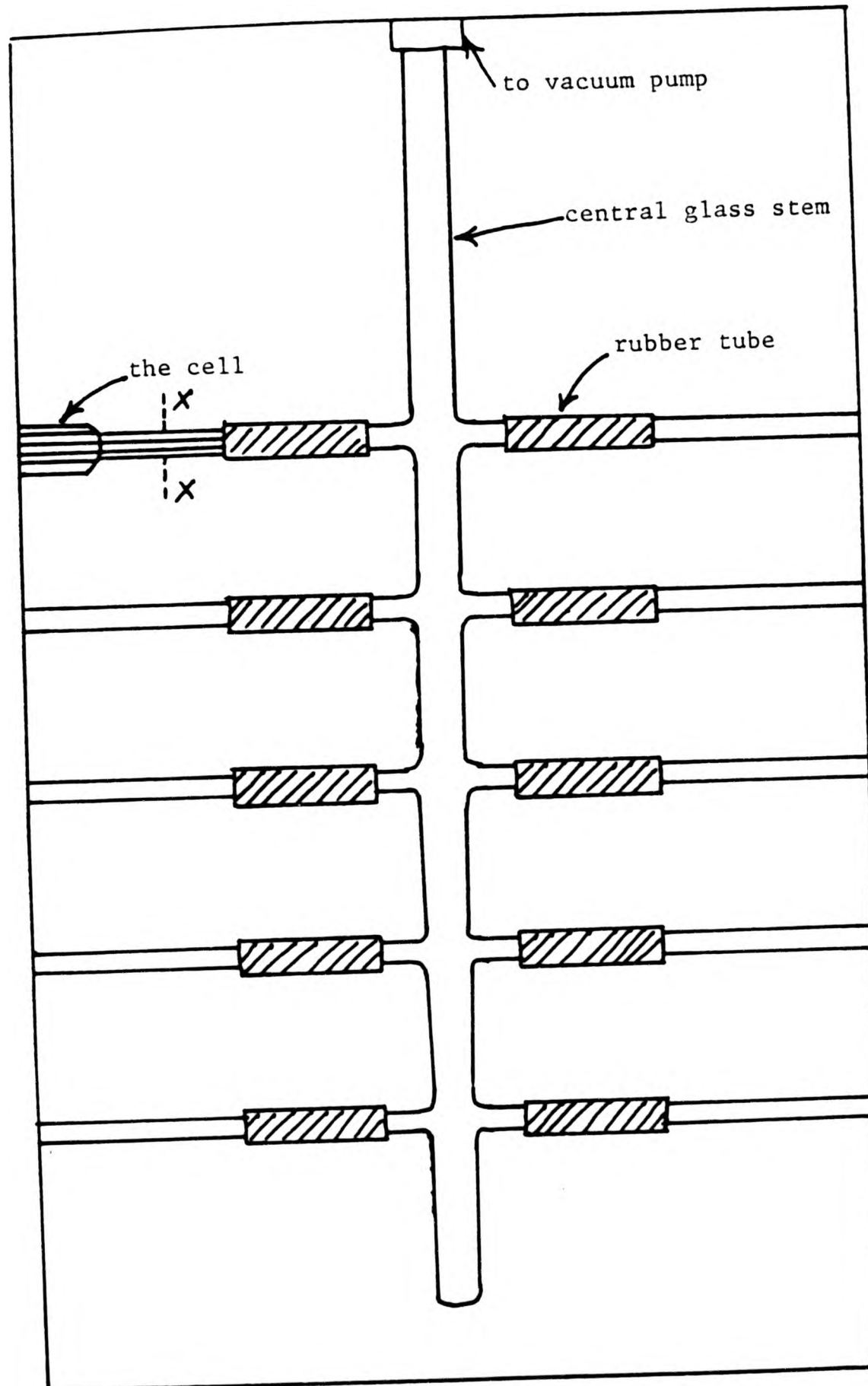


Figure 55. Set-up for evacuating cells

couple of days. The operation was carried out in a closed vessel to prevent ingress of air. Stirring was carried out by a magnetic follower, the vessel being placed on a magnetic hot plate. During the dissolution the solution was bubbled with argon and a positive pressure of argon was maintained on the surface of the solution.

Specimens 3mm thick were cut from 6mm diameter rods and cast into cold setting resin. The final casting was machined to 5mm or less thick and 10mm diameter. Each casting was marked by a label inserted in the resin. Resin was allowed to set at room temperature for 72 hours. Polishing was carried out on wet emery papers, using plenty of free running water, on 320, 400, 500 and 600 grades successively. Further polishing was done on lapidary wheels using diamond paste. Specimens were finished at $\frac{1}{4}\mu\text{m}$. The specimens were washed, degreased thoroughly, washed in double distilled water, dried in acetone and hot air and stored in a desiccator ready to be inserted in the cells.

The evacuated cells were filled with solution presaturated with hydrogen gas to minimise any initial error associated with the solubility of the gas evolved during self-discharge. The filled cells were placed in the thermostated water bath maintained at $25^{\circ}\text{C} \pm 0.1^{\circ}\text{C}$. The tubes were hung from side walls by specially made clamps. To reduce evaporation the bath was covered with $\frac{1}{2}$ " diameter polyethylene hollow spheres. Topping up of baths was done from time to time by using quantities of water brought to 25°C . It was ensured that cells were always immersed in water. The cells were allowed to equilibrate overnight in the bath and the readings were begun by zeroing each capillary arm. Fluctuations in the atmospheric pressure were taken into account by incorporating a blank cell filled with the solution. The experiments were carried out in duplicate and for a duration of 1100 hours.

3.3 RESULTS AND DISCUSSION

The amount of hydrogen gas measured every day at the interval of twenty four hours, was corrected for pressure and converted to volume per unit area of the specimens. The cumulative amount was plotted against time for 2.5 w/o Hg amalgams and 10 w/o Hg amalgams. The rate of gas evolution was also plotted separately for the two amalgams. The self corrosion rates are tabulated for both the amalgams at intervals of 100 hours. Table 12 lists some earlier results. Table 13 lists present results and Tables 14 and 15 list the rates of corrosion on amalgamated alloys.

Figures 56-63 show the data in plotted form. The amount of corrosion and the rate of corrosion have been plotted against time. Information extracted from these curves has been presented in Tables 12-16.

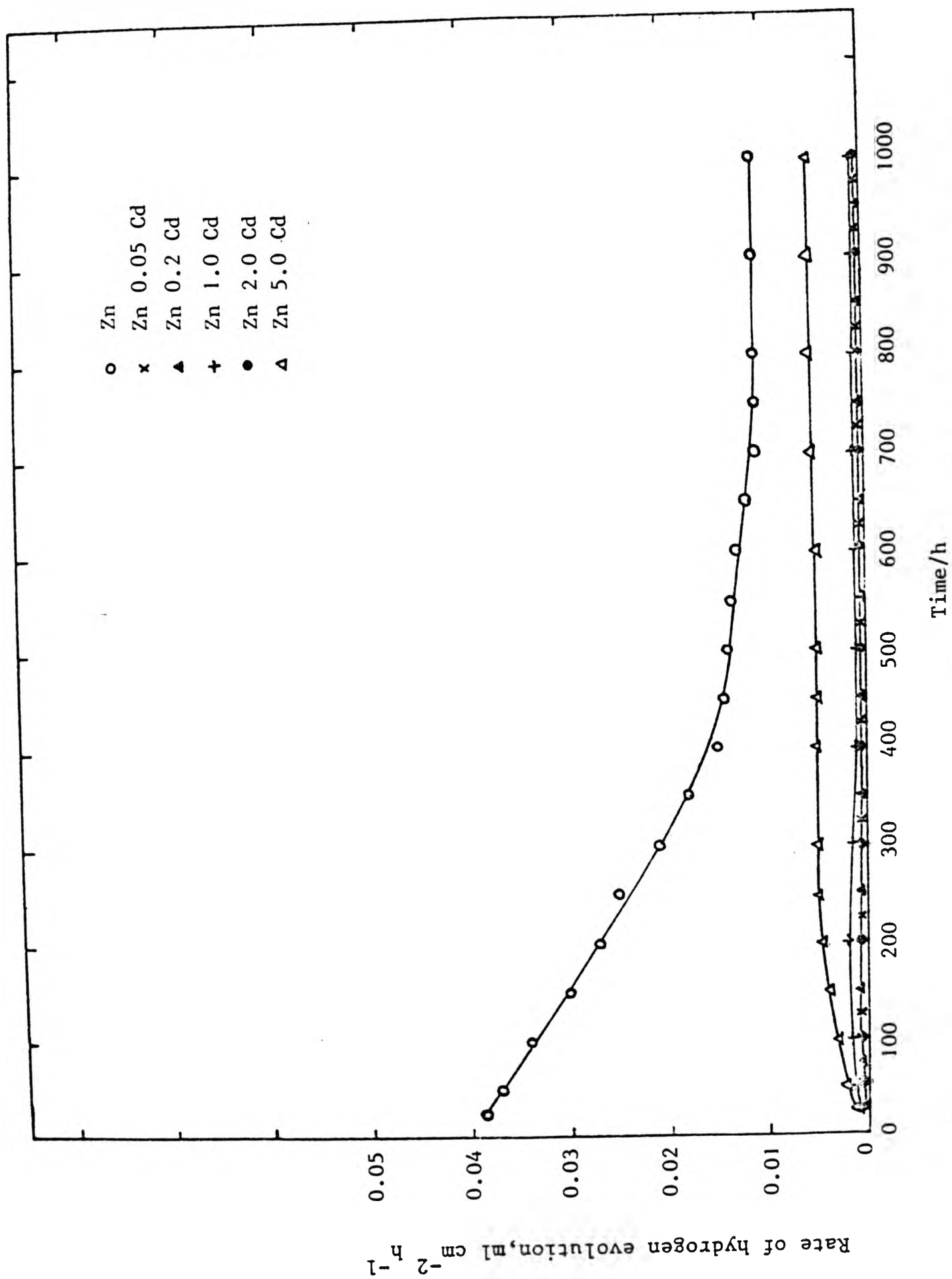


Figure 57. Comparison of corrosion rates for pure zinc and Zn-Cd alloys at 25°C. Electrolyte: ZnO saturated 6 mol dm⁻³ KOH.

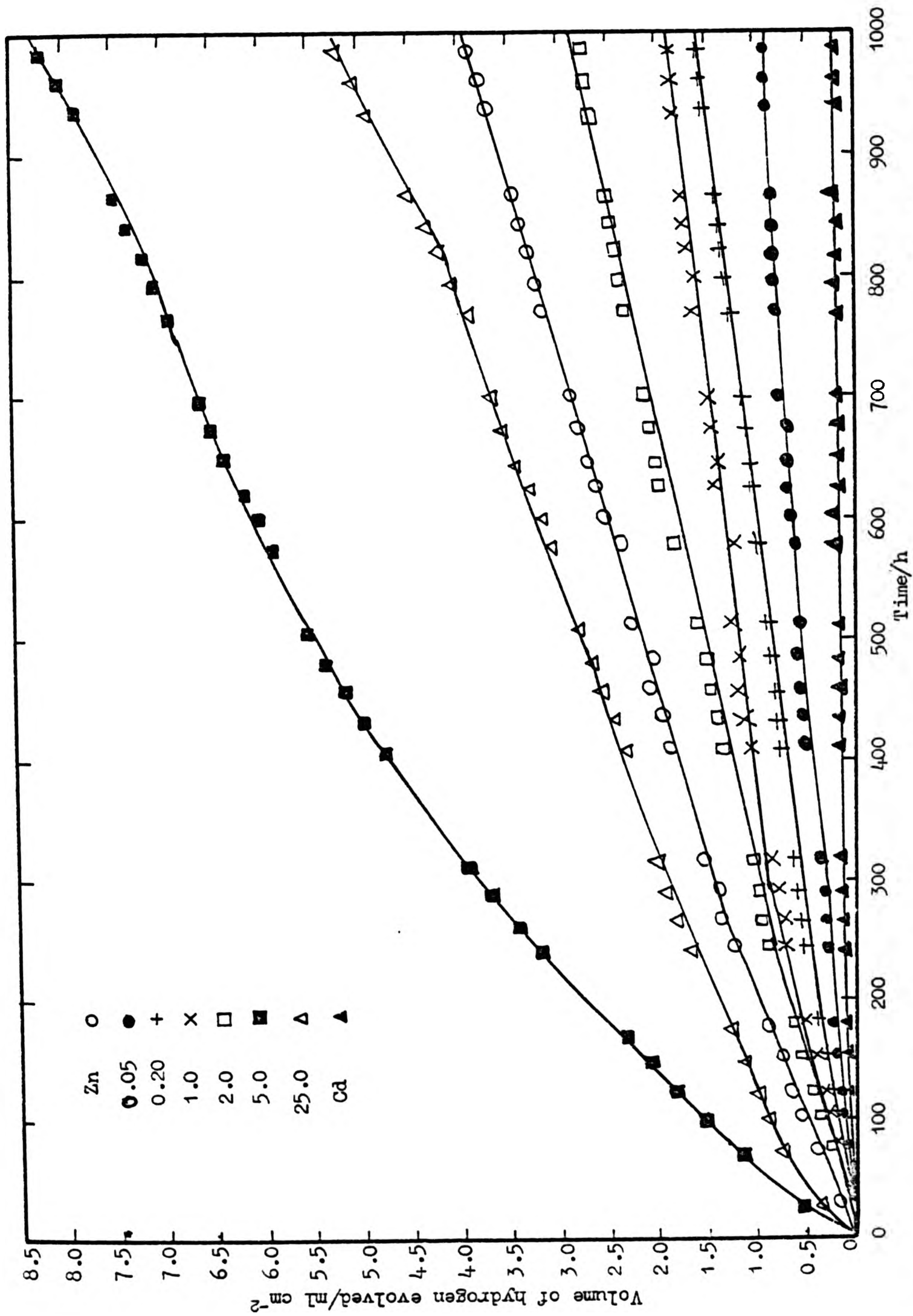


Figure 58. Comparison of amounts of hydrogen evolved on Zn-Cd alloys amalgamated with 2.5 w/o Hg, at 25°C in ZnO saturated 6 mol dm⁻³ KOH.

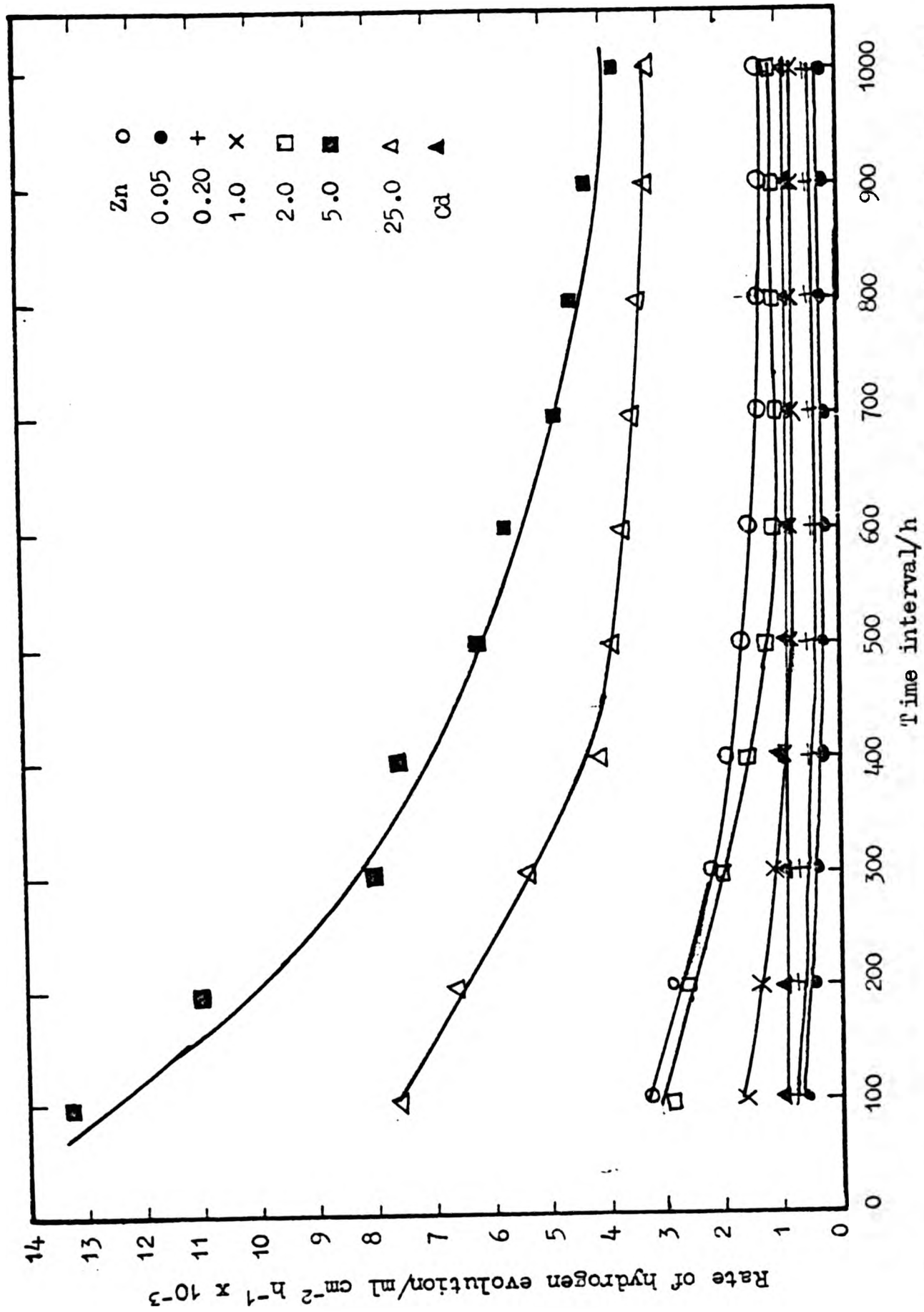


Figure 60. Comparison of corrosion rates for Zn-Cd alloys amalgamated with 10 w/o Hg in ZnO saturated 6 mol dm⁻³ KOH at 25 °C.

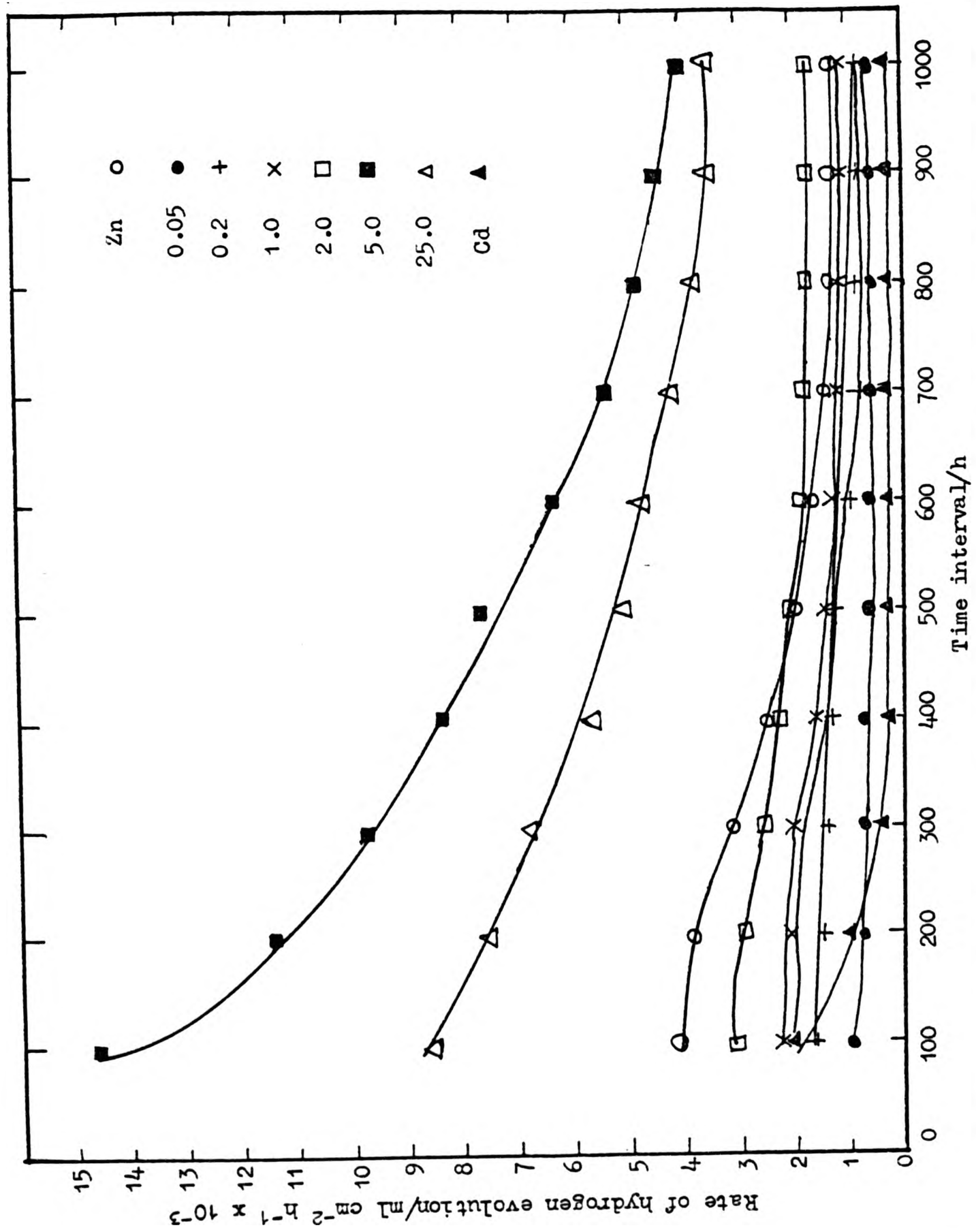


Figure 61. Comparison of corrosion rates for Zn-Cd alloys amalgamated with 2.5 w/o Hg in ZnO saturated 6 mol dm⁻³ KOH at 25°C

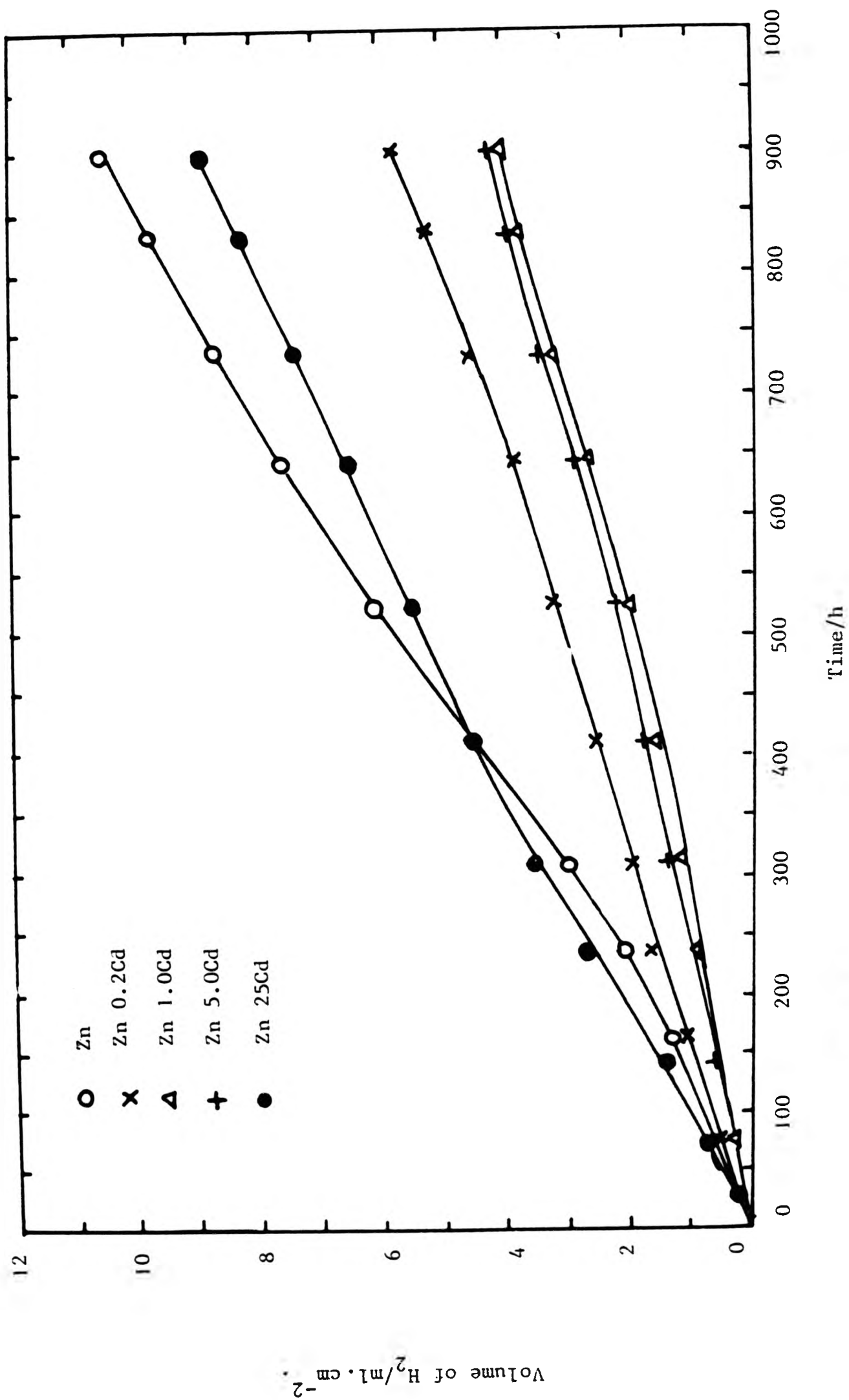


Figure 62. Variation of amounts of hydrogen evolved on pure Zn and Zn-Cd alloys, with time.

Table 12. Comparison of hydrogen evolution data for Zn-Cd alloys at 25°C

Conditions	Duration h	Hydrogen evolved ml cm ⁻²	Alloy Composition w/o cadmium							Cd
			Zn	0.05	0.2	1.0	2.0	5.0	25.0	
6 mol dm ⁻³ KOH	200	1.80	1.65	1.35	0.75	0.80	0.85	2.10	0.42	
	400	4.90	4.72	2.60	1.50	1.69	1.80	4.35	0.44	
	800	10.40	9.80	5.70	3.90	3.99	4.20	7.95	0.46	
6 mol dm ⁻³ KOH saturated with ZnO	200	6.80	4.91	0.10	0.35	0.1	0.70	0.68	0.20	
	400	11.00	8.10	0.20	0.65	0.20	1.75	1.60	0.23	
	800	16.20	12.22	0.40	1.20	0.40	3.70	3.30	0.25	
6 mol dm ⁻³ KOH 1% Hg amalga- mated specimens	200	0.60	0.53	0.35	0.35	0.38	2.80	1.30	0.21	
	400	1.70	1.62	1.45	1.25	1.38	4.90	2.80	0.24	
	800	3.85	3.58	3.20	2.65	3.08	8.75	4.85	0.26	

Table 13. Comparison of H₂ evolution data for amalgamated Zn-Cd alloys at 25°C in 6 mol dm⁻³ saturated with ZnO

Conditions	Duration h	Hydrogen evolved ml cm ⁻²	Alloy Composition in w/o cadmium							Cd
			Zn	0.05	0.2	1	2	5	25	
6 mol dm ⁻³ KOH saturated with ZnO; 2.5% Hg	200	0.95	0.22	0.33	0.51	0.6	2.75	1.4	0.10	
	400	1.84	0.42	0.73	1.07	1.45	4.75	2.4	0.15	
	800	3.5	0.83	1.27	1.6	2.35	7.1	4.1	0.17	
6 mol dm ⁻³ KOH saturated with ZnO; 10% Hg	200	0.65	0.15	0.27	0.4	0.5	2.65	1.0	0.10	
	400	1.1	0.17	0.43	0.66	0.9	4.53	2.0	0.13	
	800	1.75	0.37	0.8	1.02	1.35	7.08	4.0	0.15	

Table 14. Comparison of hydrogen evolution rates for 10 w/o Hg amalgams at 25°C in 6 mol dm⁻³ KOH saturated with ZnO

Duration h	Rate of H ₂ evolution ml cm ⁻² h ⁻¹ x 10 ⁻³							
	Zn	0.05	0.2	1	2	5	4	Cd
100	3.25	0.69	0.79	1.67	2.98	13.3	7.6	0.917
200	2.9	0.67	0.75	1.4	2.78	11.1	6.7	0.917
300	2.2	0.56	0.7	1.2	2.08	8.04	5.4	0.917
400	2.0	0.43	0.58	1.0	1.6	7.7	4.2	0.917
500	1.67	0.34	0.46	.83	1.25	6.25	3.9	0.917
600	1.5	0.34	0.46	.83	1.1	5.87	3.75	0.917
700	1.4	0.34	0.46	0.83	1.1	4.86	3.5	0.917
800	1.25	0.34	0.46	0.83	1.1	4.58	3.4	0.917
900	1.25	0.34	0.46	0.83	1.1	4.4	3.2	0.917
1000	1.25	0.34	0.46	0.83	1.1	3.75	3.2	0.917

Table 15. Comparison of H₂ evolution rates for 2.5 w/o Hg amalgams at 25°C in 6 mol dm⁻³ KOH saturated with ZnO

Duration h	Rate of H ₂ evolution ml cm ⁻² h ⁻¹ x 10 ⁻³							
	Zn	0.05	0.2	1	2	5	25	Cd
100	4.2	0.83	1.7	2.3	3.1	14.6	8.6	2.17
200	3.9	0.79	1.5	2.1	2.9	11.2	7.6	1.05
300	3.13	0.75	1.45	2.08	2.5	9.8	6.8	0.42
400	2.5	0.73	1.36	1.34	2.3	8.3	5.6	0.375
500	2.0	0.66	1.25	1.25	2.08	7.7	5.0	0.375
600	1.8	0.66	1.10	1.25	1.9	6.25	4.8	0.375
700	1.5	0.66	0.98	1.25	1.7	5.3	4.2	0.375
800	1.25	0.66	0.83	1.25	1.7	4.8	3.8	0.375
900	1.25	0.66	0.83	1.25	1.7	4.5	3.5	0.375
1000	1.25	0.66	.83	1.25	1.7	4.0	3.5	0.375

At the end of the tests spent electrolyte was collected from each cell and was analysed for the presence of mercury and cadmium. No detectable amount of mercury was found in any of the solutions. Cadmium was found in various amounts ranging from 2.5 ppm to 6 ppm as tabulated below.

Table 16. Analysis of 'spent' electrolyte

Cell	ppm Cd	Cell	ppm Cd
2.5 Hg 1 Cd	2.5	10 Hg 5 Cd	3.8
10 Hg 1 Cd	2.5	2.5 Hg 25 Cd	5.0
2.5 Hg 2 Cd	3.0	10 Hg 25 Cd	4.5
10 Hg 2 Cd	3.0	2.5 Hg Cd	6.0
2.5 Hg 5 Cd	4.0	10 Hg Cd	5.8

5 w/o cadmium-zinc amalgam produces more hydrogen at any time, and at the end of the test, than any other alloy amalgam or pure zinc amalgam. Pure zinc amalgam (10 w/o Hg) produced nearly a quarter of the gas produced by 5 w/o Cd alloy amalgam in ZnO saturated KOH solution, whereas 2.5 w/o Hg pure zinc amalgam produced nearly half of the gas produced by the 2.5 w/o Hg 5 w/o cadmium alloy amalgam. The least gas was produced in both the cases by the cadmium amalgam (2.5 and 10 w/o Hg). The alloys can be put in the increasing order of gas evolution as follows:- Cd < 0.05 w/o Cd < 0.20 w/o Cd < 1.0 w/o Cd < 2.0 w/o Cd < Zn < 25.0 w/o Cd < 5.0 w/o Cd.

The initial corrosion rates were very high for 5 w/o, 25 w/o Cd alloys and zinc. For the other alloys, the initial corrosion rates were comparatively low. The rates fell off as time passed. After 400-500 hours the rate levelled off; 0.05 and 0.20 w/o Cd show the least initial corrosion rates which were approximately 1/10th of that of 5.0 w/o Cd alloy. At the end of the test duration all the alloys were corroding at uniform rate. The amount of corrosion suffered by the 0.20, 1.0 w/o Cd alloys is

nearly half that suffered by zinc amalgam, but the final rates were not much different, the initial rates were slightly more different. A comparison between 2.5 w/o Hg and 10.0 w/o Hg shows that the higher amalgam is slightly better. When the costs are compared this advantage will be marginal. A comparison between various conditions under which self corrosion is conducted, for example with and without ZnO in the electrolyte and with or without amalgamation of the specimens indicates that self corrosion is least when amalgamated alloys are used in ZnO saturated solution. It is widely accepted that cadmium is more corrosion resistant in strong alkali than zinc because of the much lower solubility of the passive anodic film. This is generally considered to consist of a thin continuous film of the oxidation products, that is cadmium oxide and hydroxide. Amalgamation halves the corrosion rate and so does addition of ZnO to the electrolyte. Employing both expedients reduces the corrosion rate to one quarter of what it would otherwise be. The general reduction in the corrosion rates of Zn-Cd alloys may be expected because the Tafel slope for hydrogen evolution (as discussed in Chapter 5) on the alloys is nearer in value to that of cadmium, and exchange current densities are nearer to that of zinc, but in any case much higher than that for cadmium which is $8-9 \times 10^{-1} \text{ A m}^{-2}$. Thus the actual corrosion rates may be similar to that of cadmium, the cumulative values are higher than that of cadmium and lower than that of zinc. Additionally the stability of the passive film changes as cadmium is added as an alloying element to zinc. This effect explains why alloys should be better than either pure zinc or cadmium alone. However, with a 25 w/o Cd alloy, the duplex structure results in a consequential increase in the corrosion rate. Amalgamation and ZnO additions individually and in concert seem to be very effective in reducing self corrosion of zinc and the alloys. For primary cell applications up to 10 w/o Hg is beneficial. Mercury raises the hydrogen overvoltage to about -2.0V with respect to the normal hydrogen electrode.

This means self corrosion is slowed down considerably. The mercury surface layer also covers impurity sites in the electrode thereby reducing local galvanic action. However, amalgamation produces grain boundary embrittlement and consequent disintegration, thus reducing the fabrication capability. However, cadmium alloying produces no such adverse mechanical disadvantage.

3.4 CONCLUSIONS

- (1) 1000 Hour tests confirm that an alloy composition 0.20 to 1.0 w/o Cd appears to exhibit the best corrosion resistance.
- (2) These tests confirm the development potential of a binary and ternary alloy system as primary battery anodes.
- (3) Amalgamation alone or addition of zinc oxide alone halve the corrosion rates. Both together reduce it to a quarter.
- (4) The total cumulative corrosion and the rate of corrosion are time dependent.
- (5) Initial corrosion rates are high, they decrease as time goes on and stabilise to a constant value after approximately 500 hours.
- (6) Highest corrosion rates and amounts are exhibited by two phase alloys. These are nearly double the values exhibited by pure zinc.
- (7) 0.20 and 1.0 w/o Cd alloys show half the amount of self corrosion shown by pure zinc.

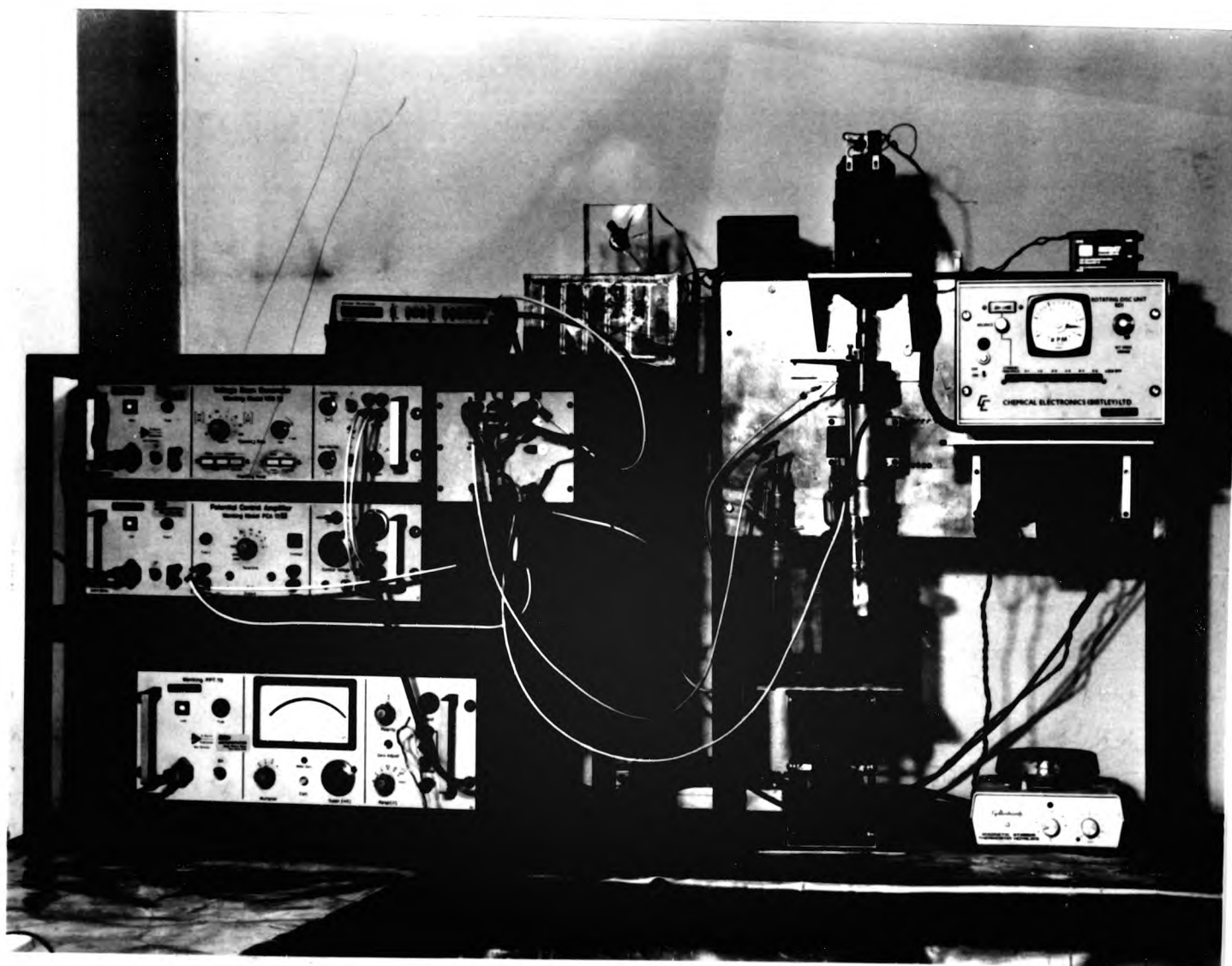


Figure 64. Assembly of apparatus for potentiodynamic polarisation experiments on rotating disc electrode specimens

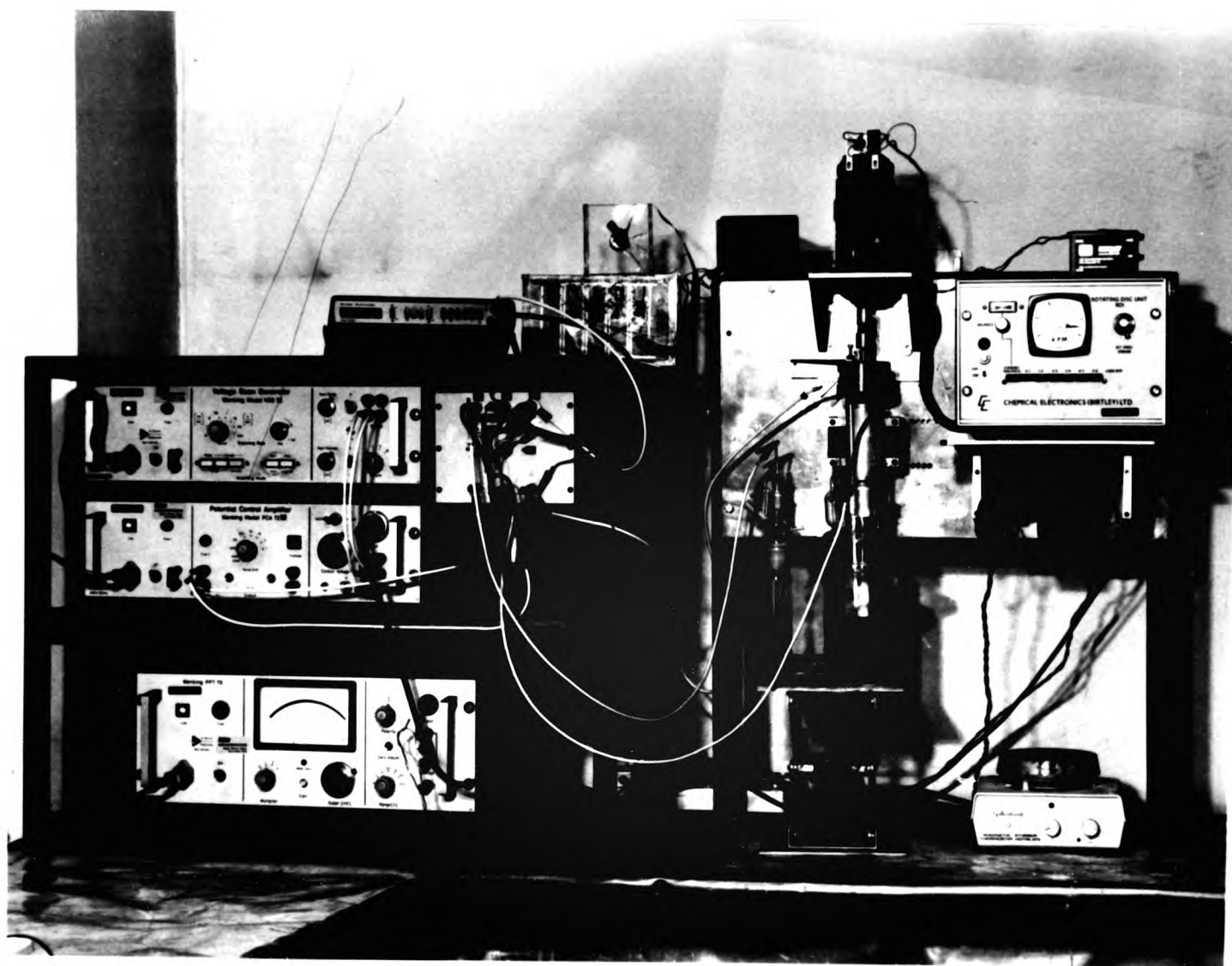


Figure 64. Assembly of apparatus for potentiodynamic polarisation experiments on rotating disc electrode specimens

4.2.1 Potentiostats. The basic potentiostat consists of three units, (i), (ii) and (iii) mentioned above.

4.2.1.1 Potential Control Amplifier. This unit is not only capable of supplying constant stabilised potentials but can also be used as a constant current source. Figure 65 gives a block circuit diagram of the instrument. The specifications are as follows:

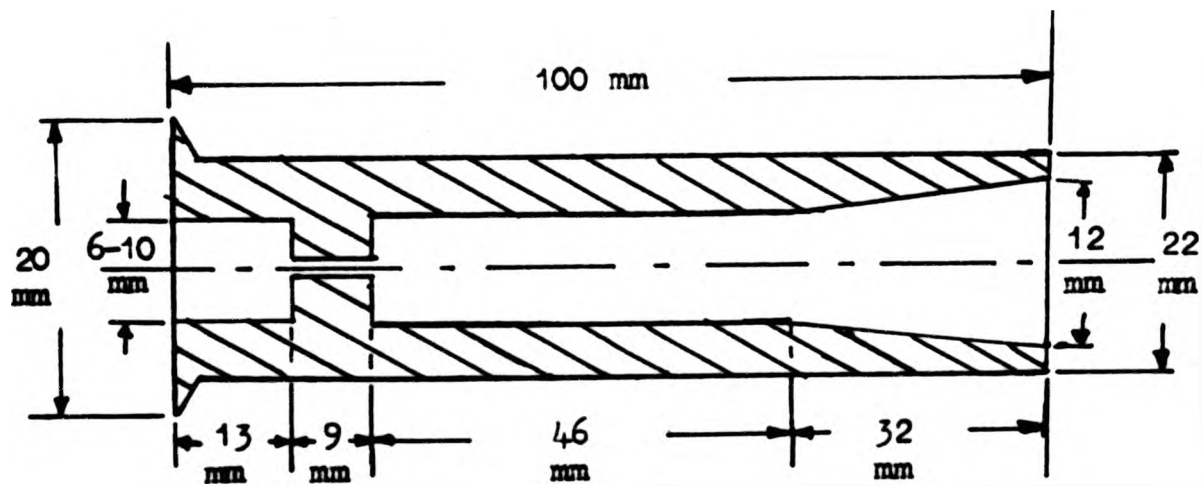
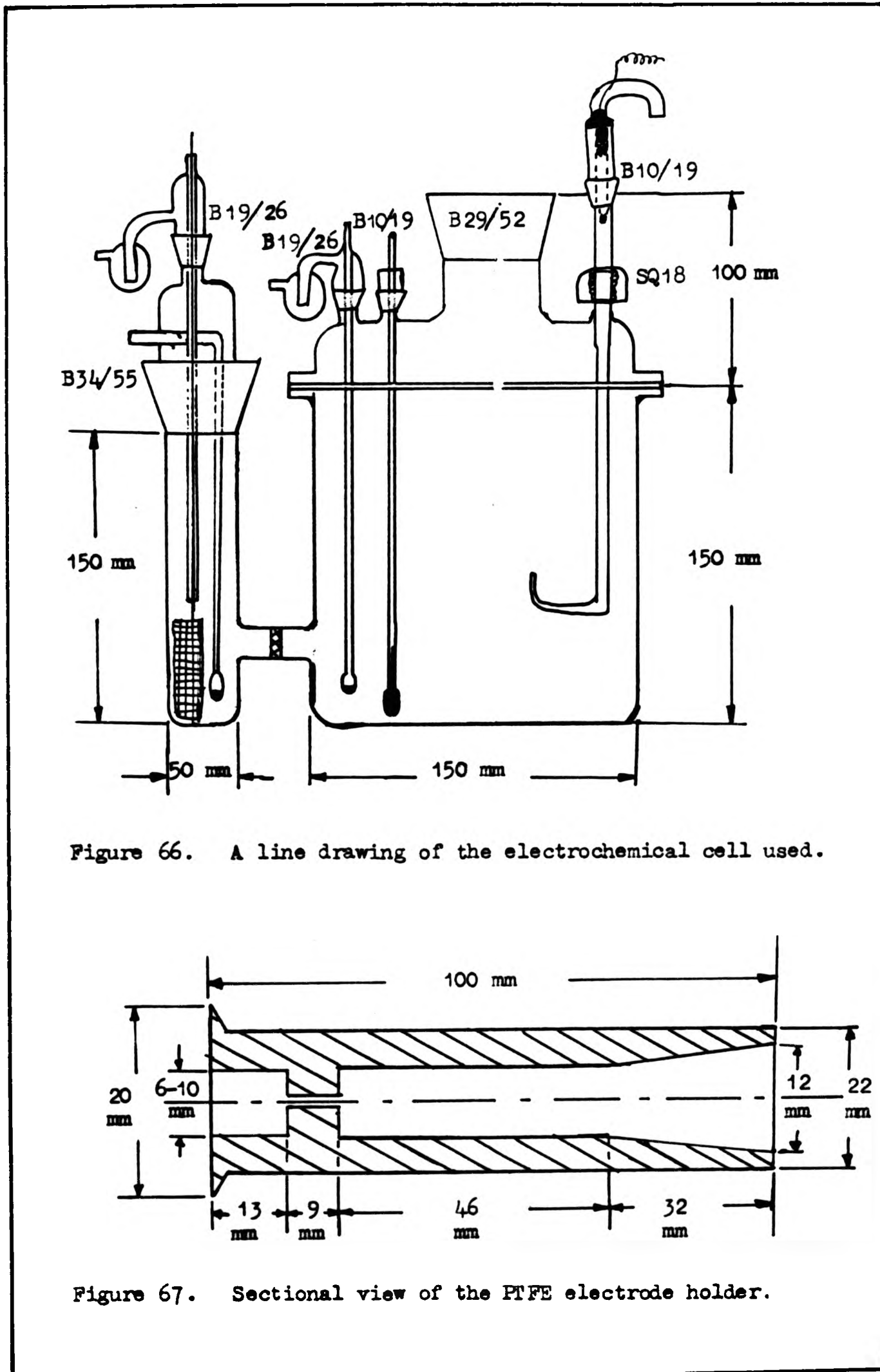
Maximum output	$\pm 40V$, $\pm 1.2A$
Power	25W
Input impedance	10^{11} ohm
Input bias current	10^{11} A
Bandwidth	3 MHz
Rise time	$2 \times 10^{-7}s$ and $2 \times 10^{-6}s$
Slew rate	$10V \mu s^{-1}$ and $1V \mu s^{-1}$
Open loop gain	500K

4.2.1.2 Voltage Scan Generator. This is capable of delivering a voltage ramp, a single triangle or a periodic triangle. Scanning rates available range from $0.1 mVs^{-1}$ to $1.0 kV$ per second. Polarity is selectable. Very low scanning rates permit the recording of stationary current vs potential characteristics. Potentiodynamic investigations can be accomplished in the faster ranges. Transient responses are recorded in the high speed position of scanning rate.

Specifications:	Stability	$\pm 1mV$
	Drift	0.01%
	Signal to noise ratio	80 dB
	Output resistance	1 ohm

4.2.1.3 Precision Potential Meter. This high impedance precision instrument is intended for measuring potentials at electrode-electrolyte interface using a Luggin probe. The low input currents prevent polarisation or potential drops at the electrode.

Specifications:	Input impedance	10^{12} ohm
	Input current	10^{-12} A



Some comment on the hydrodynamic restrictions imposed by a rotating electrode system will be appropriate here. The theory of the rotating disc was, strictly speaking, developed for an infinite volume of solution. The hydrodynamic conditions near the surface of the disc remain virtually unchanged by placing a stationary solid body at a distance of a few centimeters. For precise measurements, cells of not too small dimensions are required. Moreover a small volume of solution may result in errors connected with the decrease of reactant concentration during electrolysis. Similarly other items such as thermometer, gas bubbling frit should also be a few centimeters away from the r.d.e. The Luggin capillary cannot be, however, kept that far away from the electrode surface. The proximity of a Luggin probe is tolerable if it does not disturb the hydrodynamic boundary layer. Zhaludev and Stender⁹⁴ suggested that the counter electrode and reference electrodes be placed on two opposite sides of the disc. Theoretically, due to the non equipotentialities of the disc (see Figure 68), surface potential measurement at a given point does not represent the exact potentials at all other points. Experimental evidence suggests that it is enough to place the tip of the probe 1mm away from the surface vertically along the rotation axis.

4.2.3 Electrode Holder. The working electrode is a specimen of button shape of 8-10mm thick and 7.14mm diameter and is embedded in a synthetic polymer. The best choice is the non-stick PTFE which is a white opaque and chemically resistant polymer. It is inert up to 200°C to practically all aqueous chemicals. It is relatively soft and needs very light finishing cuts during machining to achieve good tolerances and a smooth finish. Use of force fits or shrink fits avoids crevices which could affect the results adversely. A sectional drawing of the electrode holder is shown in Figure 67. The following considerations helped in⁹⁵ designing its shape and the dimensions. In practice the diameter of disc, r_0 , should be at least an order of magnitude of the thickness of the

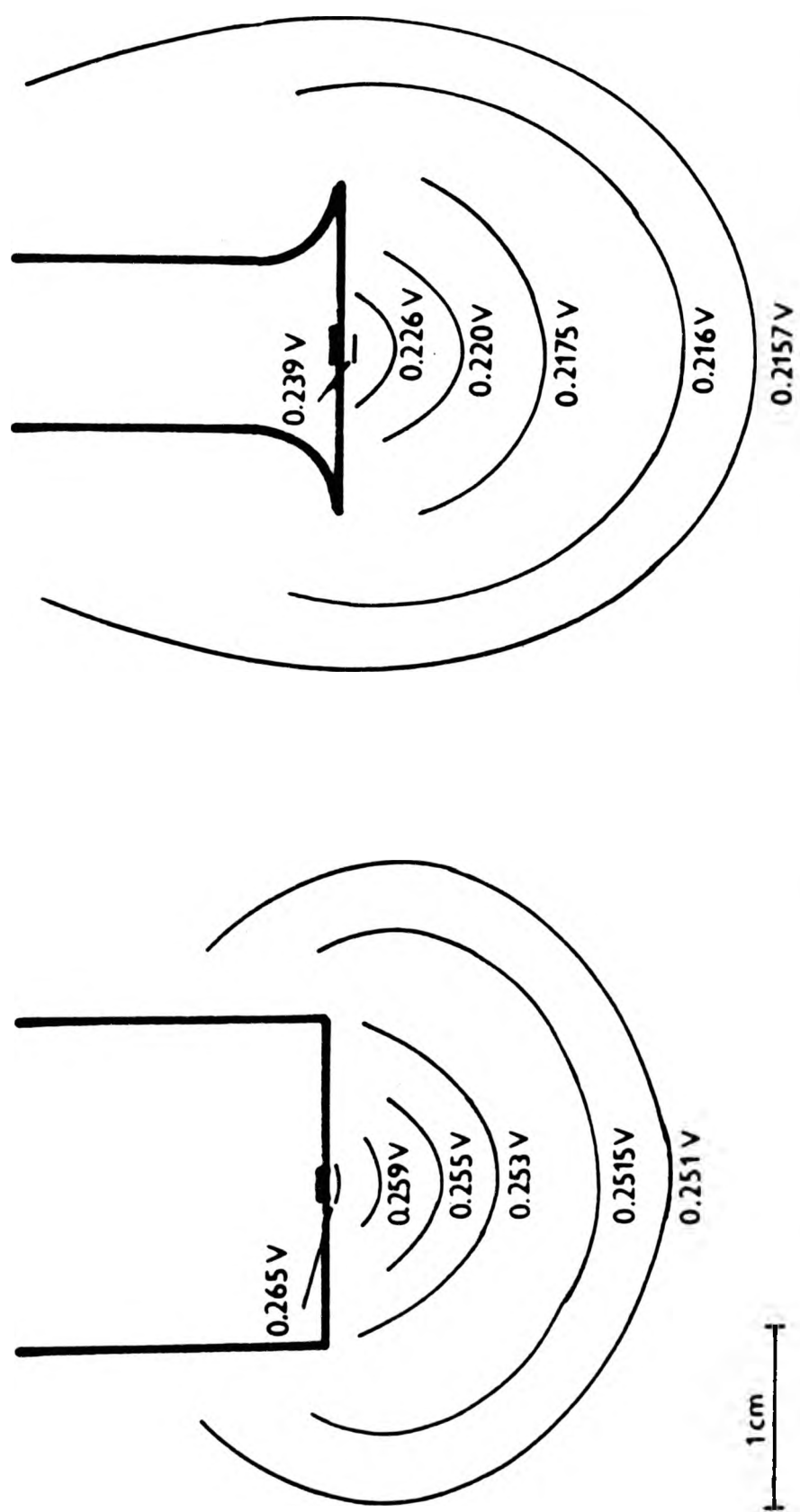


Figure 68. Potential distribution profiles on rotating disc electrodes of two different shapes.

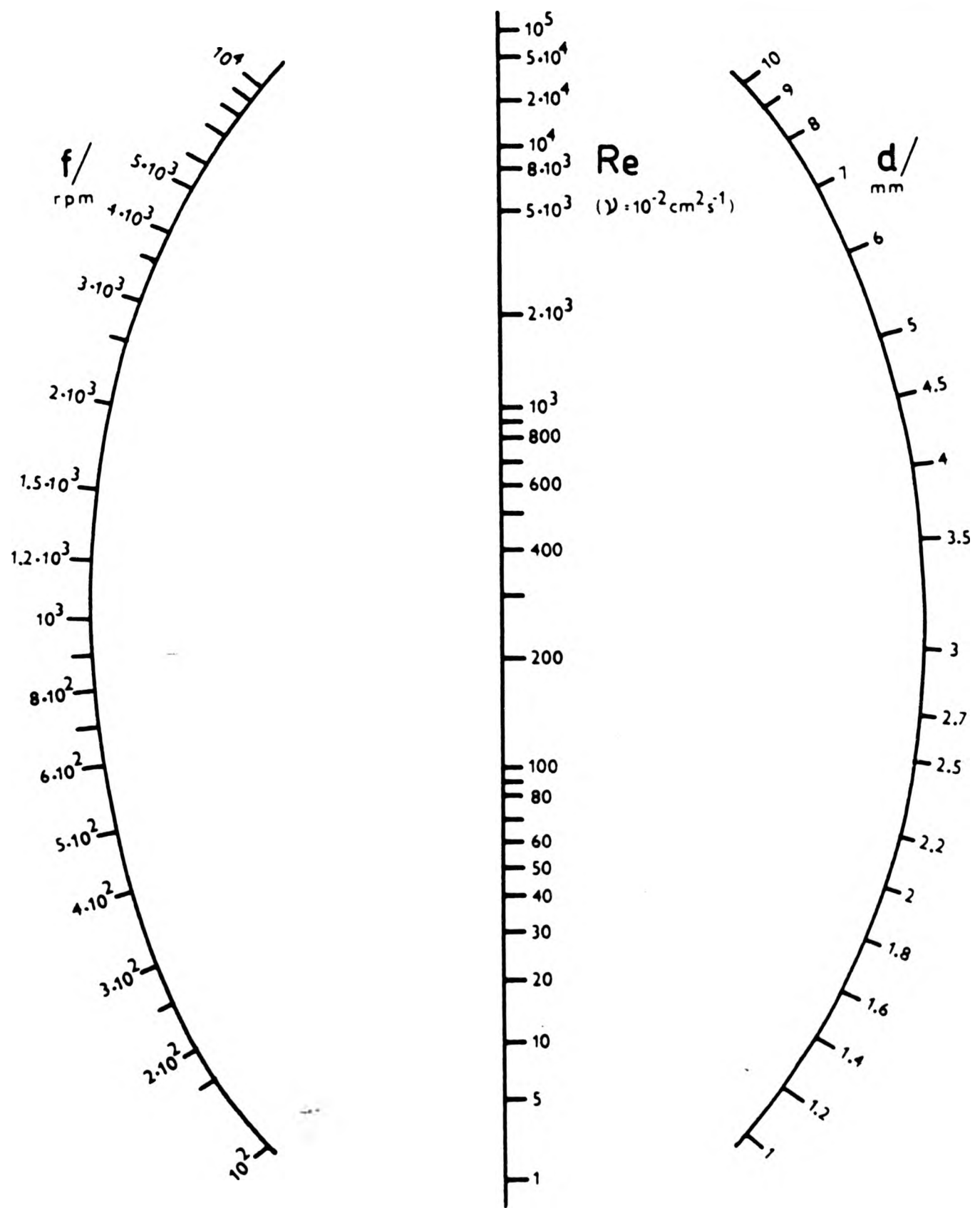


Figure 69. A nomogram for calculating Reynolds number for a given rotation speed and electrode diameter.

hydrodynamic boundary layer δ_H . The diameter of the electrode holder should be much greater than $2\delta_H$. A practical size is between 1 and 10mm. Earlier workers⁹⁶ used large discs of up to 10cm diameter. Another important factor requiring consideration in relation to the choice of the disc diameter and range of rotation speeds is the necessity of maintaining laminar conditions of liquid flow. Refer to the nomogram in Figure 69. The transition to turbulent-flow occurs, for a well centred disc with a smooth surface, at a Reynolds number

$$Re = \frac{r_0^2 \omega}{\nu} \approx 10^5$$

where r_0 is the disc diameter, ω is the disc rotation speed in radian per second, ν is the kinematic viscosity (m^2s^{-1}) of the electrolyte. The shape of the holder should be chosen to minimise the additional stirring caused by the rotation. Riddiford et al^{96,97} carried out a special study aimed at optimisation of the shape of the holder (refer to Figure 70). They employed discs of 3mm diameter and holder diameters of 15-30mm. Flow stream lines were observed by using coloured electrolyte. It was shown that limiting currents closest to the theoretical values were obtained with electrodes of shape B. Therefore this shape was adopted. Types A and C gave a large deviation and type D and E were unsatisfactory. A rigid, demountable and leak-proof electrode was designed.

4.2.4 Maintaining an inert atmosphere. Oxygen from the atmosphere is chemically reactive with many substances and electrochemically reducible. It must be excluded from the system of reactants. This was achieved by purging the electrolyte with a flow of nitrogen, argon, or hydrogen. 'Whitespot' nitrogen from British Oxygen Company was used. This usually has less than 20ppm oxygen, which is sufficient to take part in reactions and therefore must be removed. Argon, hydrogen and helium are available in very high purity. Argon being denser than air also covers the solution with an inert blanket. Residual oxygen can be removed from 'white spot'

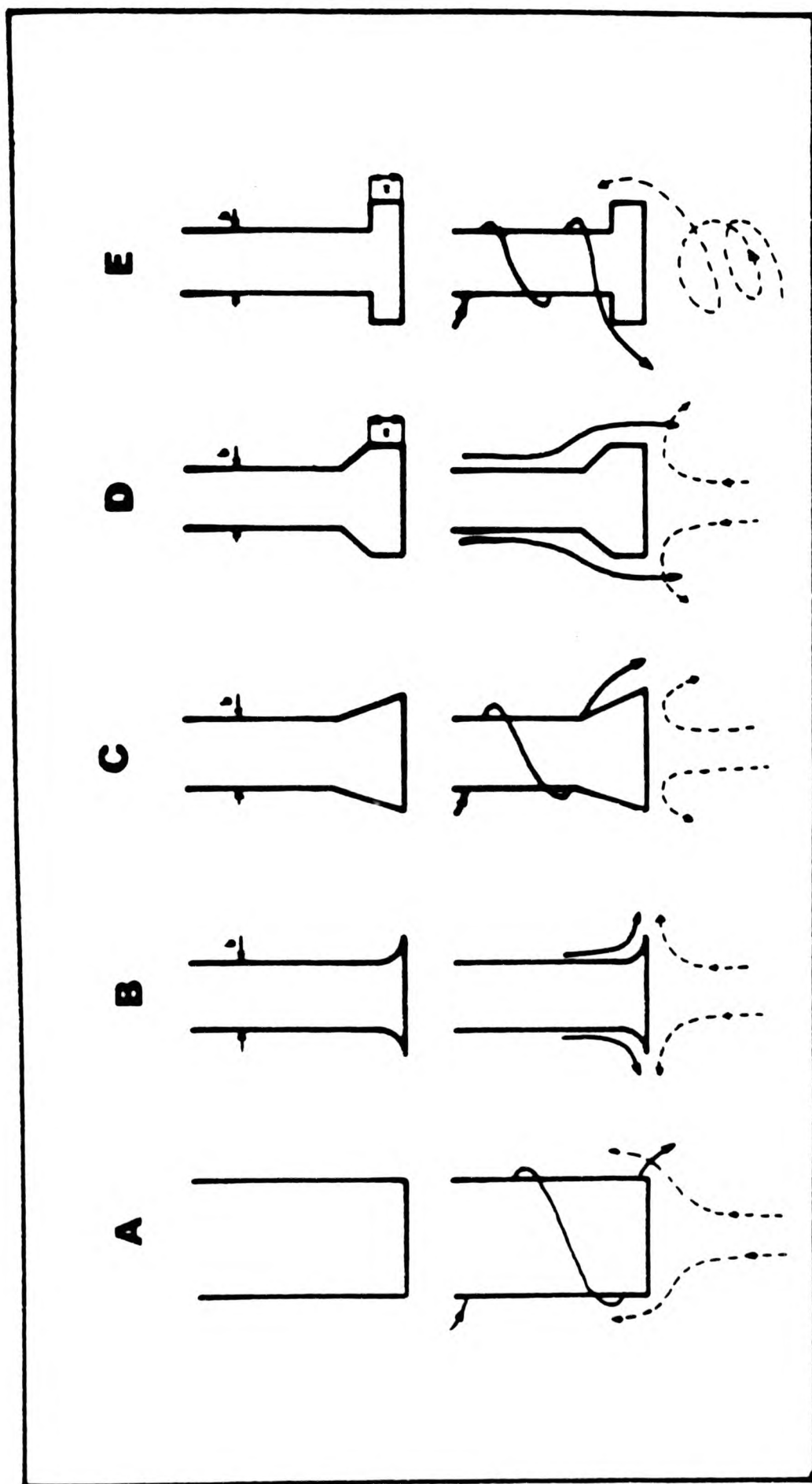


Figure 70. The most common shapes of disk electrode insulating mantles and a scheme of steady-state fluid flow around these electrodes. From ref. 96; flow at 25 rad s^{-1} .

nitrogen by bubbling through an aqueous solution of vanadous or chromous ions contained in a scrubbing column.¹²² The reducing ions are continuously regenerated through contact with amalgamated zinc. The amalgam is prepared by immersing 170g zinc granules in a solution of acidified mercuric nitrate (4.5g per 250 cm³). After fifteen minutes with occasional stirring with a glass rod the solution can be drained off. The zinc amalgam rinsed thoroughly in distilled water after which the granules may be transferred into a Nylox scrubber column. A chromous sulphate solution was freshly prepared by dissolving 70g hydrated chromous sulphate salt in 150ml doubly distilled water acidified with 8ml of concentrated sulphuric acid. Two or three drops of Teepol were added to the solution to increase its surface wetting power and flow. This solution should be poured into the scrubber without delay and the scrubber sealed air tight to prevent air ingress as this will eventually deactivate the solution. Connections of the gas train should be made with thick walled pressure tubing as thin wall PVC tubing is highly permeable to gases. It is estimated that up to 0.8 ppm oxygen may get in through permeable tubing. A common practice is to saturate the purified, oxygen-free, gas with solvent in a gas dispersion Dreschel bottle that is filled with a solution identical to the test solution. This avoids the evaporation of the solvent or the differential evaporation of a volatile constituent of the test solution that would otherwise accompany the continuous purging of the system. The other Dreschel bottles are simply filled with distilled water, or any reactant to remove a specific ion such as lead acetate for removing sulphides. The arrangement described is shown in Figure 71.

4.2.5 Reference Electrode.³⁹

4.2.5.1 Systems. Reference electrodes are non-working auxiliary electrodes used in characterising the levels of electrode potential of the working electrodes in electrochemical measurements. The practical applications of reference electrodes in alkaline electrolytes is limited

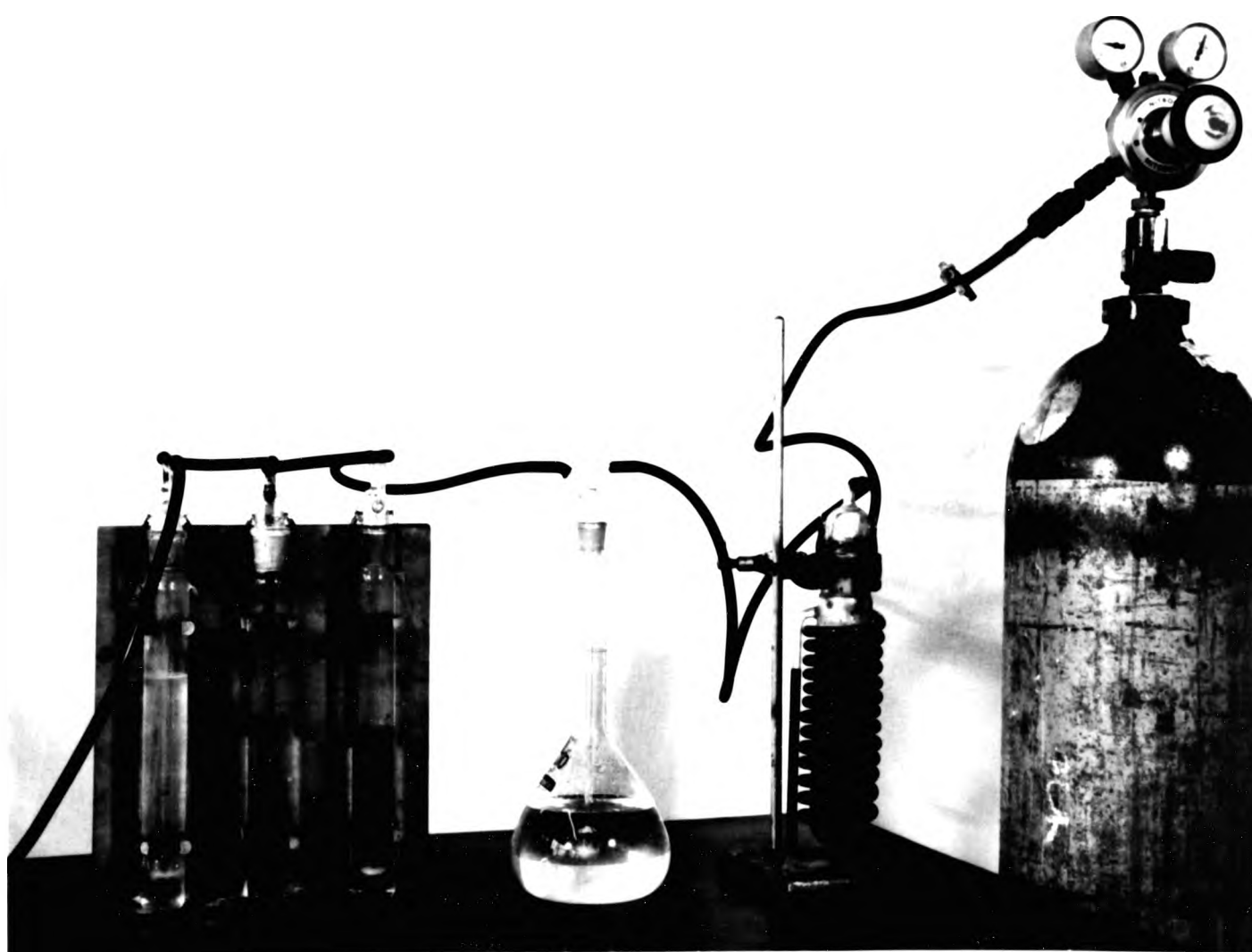


Figure 71. Arrangement of apparatus for removal of residual oxygen from gases

to a few systems. In general, the material used for a reference electrode should be a stable oxide of low solubility in the alkaline electrolyte. The tendency of metals such as zinc and cadmium to react with oxygen makes them unsuitable for measurements where oxygen is present. Hydrogen bubbling over platinum has been used as a prime reference, but suffers from several disadvantages such as being bulky, non-portable, prone to contamination etc. Mercuric oxide-mercury system has been used in this work. Although mercuric oxide is very slightly soluble in alkali, it has never been reported that the working electrode was amalgamated; this may be due to a good design and construction of the electrode. This electrode has the advantages of a highly reproducible standard state for the metallic phase and complete freedom from any disturbing effects due to variable valency of oxide. The differences between red and yellow oxide forms is thermodynamically insignificant, and the potential over a wide range of temperature and electrolyte concentration has been well established.³⁹ A summary of thermodynamic data of this electrode is as follows:

$$\begin{aligned} \text{e.m.f. at } 25^\circ\text{C} & 0.9258\text{V}; & dE/dt \text{ at } 25^\circ\text{C} & 0.000288 \text{ V per } ^\circ\text{C} \\ \Delta G \approx & 10.2 \text{ kJ} & \Delta S \approx & -13.27 \text{ e.u.} \end{aligned}$$

Table 17. Potentials of H₂O-Hg reference electrodes vs. SHE at 25°C in KOH solutions

w/o KOH	Potential/V
18	+0.929 ± 0.001
26	+0.931 ± 0.001
35	+0.936 ± 0.001

Table 17 lists potential of this electrode with different concentration of electrolyte.³⁹

4.2.5.2 Construction. The blank glass tube closed at one end where a 2 cm long platinum wire 2 mm diameter is sealed in is first cleaned in aqua regia for 5 minutes, thoroughly washed with distilled water and then with acetone, being finally dried in hot air at 80°C. Purified mercury

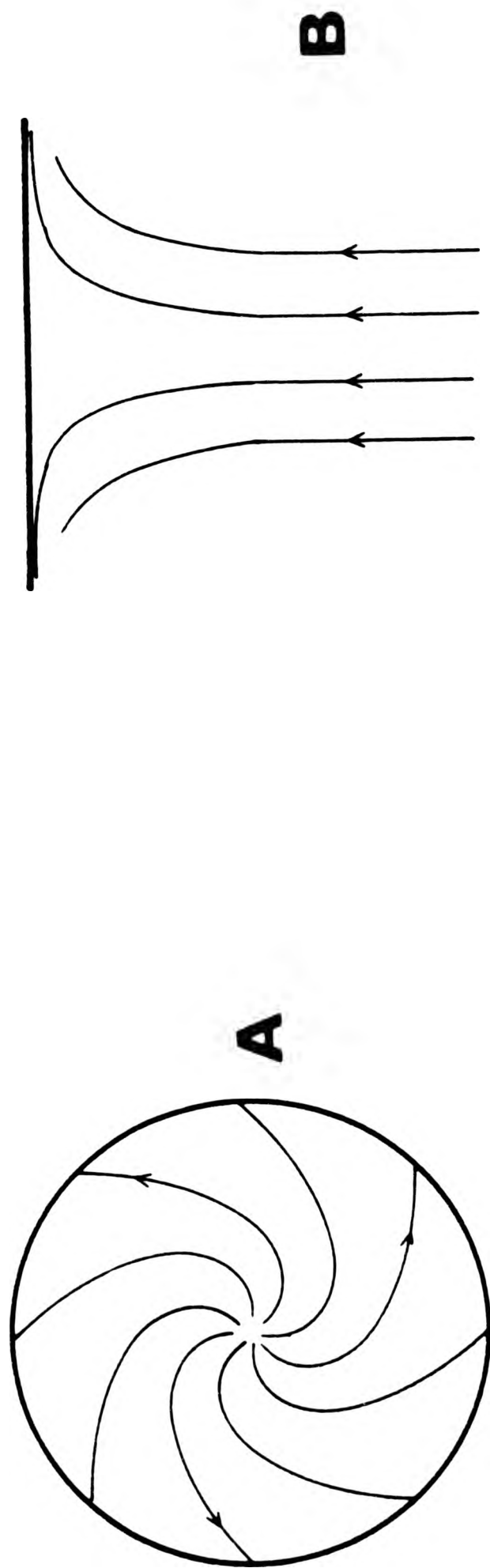


Figure 72. Mode of fluid flow at a rotating disc electrode in plan and elevation views.

in an incompressible fluid, in a non-turbulent and stationary state, the thickness of the hydrodynamic boundary layer is identical over the entire surface of the electrode and is given by

$$\delta_H = 2.8 \left(\frac{\nu}{\omega} \right)^{\frac{1}{2}};$$

where ν is the kinematic viscosity m^2s^{-1} , ω is the rotation speed or angular velocity in radians per second. Thus for aqueous solutions it is 2.8 mm at $\omega = 1 \text{ rads}^{-1}$; 1.1 mm at 10 rads^{-1} ; 0.36 mm at 100 rads^{-1} and 0.11 mm at 1000 rads^{-1} . The fluid flows at right angles to the surface of the disc at a constant velocity, at a large distance from the disc. Refer now to Figure 72. At a certain distance from the surface of the disc the fluid begins to be carried tangentially, its angular velocity increases with decreasing distance from the surface, and at the surface of the disc equals its maximum value. The mode of fluid flow may be characterised by various dimensionless quantities, one of them is the Reynolds number, $\text{Re} = \omega r_0^2 / \nu$. At a certain critical value the fluid flow changes gradually from laminar to turbulent through a transition state. First the edge of the disc is affected by turbulence, which spreads to the centre. A critical value is of the order of 10^5 . Another extreme occurs at $\text{Re} \approx 10$, whence the thickness of the boundary layer is comparable to the dimensions of the disc and natural convection sets in. Under laminar flow conditions, ignoring ionic migration, the thickness of the diffusion boundary layer is given by

$$\delta_0 = 1.61 D^{\frac{1}{3}} \nu^{\frac{1}{6}} \omega^{-\frac{1}{2}}.$$

The Schmidt number relates the thicknesses of the hydrodynamic and diffusion boundary layers. Thus $\delta_0 = 0.5 \delta_H / S_c^{\frac{1}{3}}$; where $S_c = \nu / D$. Normally the Schmidt number is 10^3 for aqueous solutions. Thence typical values for diffusion boundary layer are $150 \mu\text{m}$ at 1 rad s^{-1} , $50 \mu\text{m}$ at 10 rad s^{-1} , $15 \mu\text{m}$ at 100 rad s^{-1} and $5 \mu\text{m}$ at 1000 rad s^{-1} . The rotating disc electrode is particularly suitable for studying various electrochemical

problems because of uniform accessibility of the disc surface. An expression for the diffusion limited current density has been developed using Eukens⁹⁹ analysis.

$$i_d = \pm 0.620 nF D^{2/3} \nu^{-1/6} \omega^{1/2} C^b = \pm B \omega^{1/2}$$

where n is number of moles of electrons taking part in the reaction,

F is Faraday constant, 96500 coulombs mol⁻¹,

D is diffusion coefficient, m² s⁻¹,

ν is kinematic viscosity, m² s⁻¹,

ω is rotational velocity radians per second ($2\pi f$),

C^b is bulk concentration of the species.

The current is proportional to the square root of the rotation velocity. More rigorous treatment,^{100,101} by taking into account higher terms in the expansion may be achieved. The difference between the two values amounts to about 3-5%, which is nullified to a large extent by a number of other error factors such as edge effect, contribution from natural convection, local non-uniformities, and migration of species. The significance of the correction increases for Schmidt numbers in the interval, $10 < Sc < 100$, where the difference reaches up to 17%.¹⁰² The flux of a species towards a rotating disc under laminar flow can be expressed by the dimensionless quantity called the Sherwood number, $Sh = 0.62 Re^{1/2} Sc^{1/3}$. If charged ions are present, the migration component contributes to the mass transport. Using the Eukens⁹⁹ procedure, the solution in terms of limiting current density is:-

$$i_d = F Z_+ D_+ \left(1 - \frac{z_+}{z_-} \right) \frac{C_b^+ \omega^{1/2}}{1.61 D_{eff}^{1/3} \nu^{1/6}} ;$$

Resistive voltage drop appearing in the vicinity of the rotating disc electrode is a linear function of the distance from the disc. The potential distribution close to a disc held in an insulating holder was calculated by Newman.¹⁰³ The equipotential planes under the electrode were experimentally determined by Angell¹⁰⁴ (see Figure 68). The current density is not uniform on the disc surface.¹⁰⁵⁻¹⁰⁹

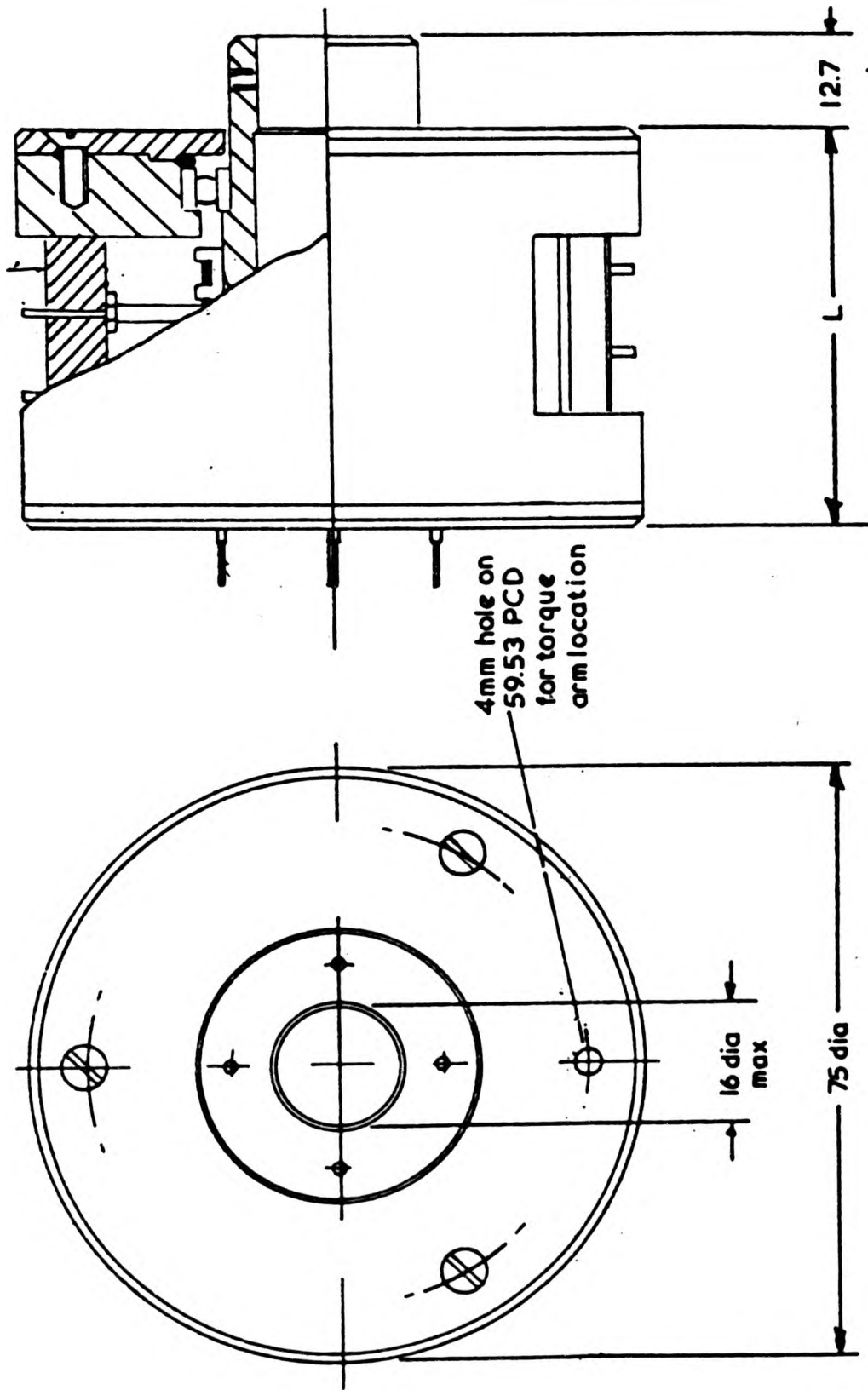
4.2.6.3 Description. The salient features of the assembly are:-

- (i) the main frame,
- (ii) the shaft,
- (iii) the bearing housing,
- (iv) the coupling,
- (v) the slipring and brush assembly,
- (vi) the drive,
- (vii) the controls.

(i) The main frame. The main frame was constructed from 38 mm angle iron welded together and subsequently painted. This frame was suitably fixed by nuts and bolts to the wall and the bench. An aluminium plate $\frac{1}{4}$ " thick and 650 x 380 mm was fitted onto the frame. The aluminium plate was suitably drilled with appropriate holes at several locations to take up the assembly components. Subframes were constructed from aluminium plate to hold various components such as control units, electric motor, shaft, blower etc.

(ii) The shaft. The main feature of the assembly is this carefully machined stainless steel shaft made from a hollow tube of outer diameter 12 mm and inner diameter 4 mm. One end of the shaft was tapered to take the demountable PTFE electrode holder, the other was fixed to a flexible rubber coupling attached to the electric motor. The tapered holder provided an easy means of interchanging and centering the electrode. The run-out of the electrode tip was measured by a micrometer dial gauge. It was easy to achieve an accuracy of ± 0.0005 inch. A small aperture was machined in the shaft to bring out the electrical connections from the electrodes and connect them to the brush terminals. The shaft rotates inside two light self-centering ball bearings accommodated in a bearing housing.

(iii) The bearing housing. This was machined out from an aluminium rod of 45 mm outer diameter. The ends were machined to take two lightweight self-aligning ball bearings. A through hole was drilled, this was big enough to allow the shaft to rotate freely. The ends of the housing were



Dims in mms.

Figure 73. A drawing of slip ring and brush assembly showing plan and elevation views.

fitted with end caps. The housing was fixed to the frame by a bracket mounted on rubber pads to absorb vibrations.

(iv) The flexible coupling. The driven shaft was coupled to the drive shaft of the electric motor by a flexible rubber coupling. This has two merits. First it can take up slight misalignment, if any, and second, being made of solid rubber, electrically insulates the driven shaft from the motor. The rubber piece is $\frac{3}{4}$ " in diameter and two inches long, fitted with aluminium caps which take up the respective shafts.

(v) The Slipring and brush assembly. Brushes were made of silver plated silver graphite composite and mounted on springy bronze strips. The slip-rings were made of silver plated copper. The whole assembly was fully enclosed with only the connecting terminals coming out. The outer casing of the assembly was screwed to an angle bracket fixed to the main frame, to stop it from rotating along with the shaft. Figure 73 shows an engineering drawing of the unit.

(vi) Drive unit. The motor and control unit was supplied by Chemical Electronics Ltd., Birtley, Washington, U.K. The electric motor is a D.C. shunt wound type capable of providing a maximum torque of 1000 g-cm, fitted with an integral tachogenerator for constant speed control. The tachogenerator signals are fed back to a differential amplifier in the control unit where it is compared with a reference voltage and the difference, if any, appears across the field windings of the motor correcting its speed. The stabilisation accuracy is about 1%. The motor was mounted on a bracketed aluminium frame which was bolted to the main frame on rubber pads.

(vii) Control unit and frequency meter. The control unit consisted of a dial indicator for rotation speed in r.p.m., and speed selector push buttons. The control unit circuitry generated sufficient heat to warrant an air blower to be fitted subsequently to cool it. The frequency meter is a digital unit indicating the speed in r.p.m. and was constructed from components bought from Radio Spares Ltd., and circuit supplied by the electronics department. The instrument is based on the stroboscope

fitted with end caps. The housing was fixed to the frame by a bracket mounted on rubber pads to absorb vibrations.

(iv) The flexible coupling. The driven shaft was coupled to the drive shaft of the electric motor by a flexible rubber coupling. This has two merits. First it can take up slight misalignment, if any, and second, being made of solid rubber, electrically insulates the driven shaft from the motor. The rubber piece is $\frac{3}{4}$ " in diameter and two inches long, fitted with aluminium caps which take up the respective shafts.

(v) The Slipring and brush assembly. Brushes were made of silver plated silver graphite composite and mounted on springy bronze strips. The slip-rings were made of silver plated copper. The whole assembly was fully enclosed with only the connecting terminals coming out. The outer casing of the assembly was screwed to an angle bracket fixed to the main frame, to stop it from rotating along with the shaft. Figure 73 shows an engineering drawing of the unit.

(vi) Drive unit. The motor and control unit was supplied by Chemical Electronics Ltd., Birtley, Washington, U.K. The electric motor is a D.C. shunt wound type capable of providing a maximum torque of 1000 g-cm, fitted with an integral tachogenerator for constant speed control. The tachogenerator signals are fed back to a differential amplifier in the control unit where it is compared with a reference voltage and the difference, if any, appears across the field windings of the motor correcting its speed. The stabilisation accuracy is about 1%. The motor was mounted on a bracketed aluminium frame which was bolted to the main frame on rubber pads.

(vii) Control unit and frequency meter. The control unit consisted of a dial indicator for rotation speed in r.p.m., and speed selector push buttons. The control unit circuitry generated sufficient heat to warrant an air blower to be fitted subsequently to cool it. The frequency meter is a digital unit indicating the speed in r.p.m. and was constructed from components bought from Radio Spares Ltd., and circuit supplied by the electronics department. The instrument is based on the stroboscope

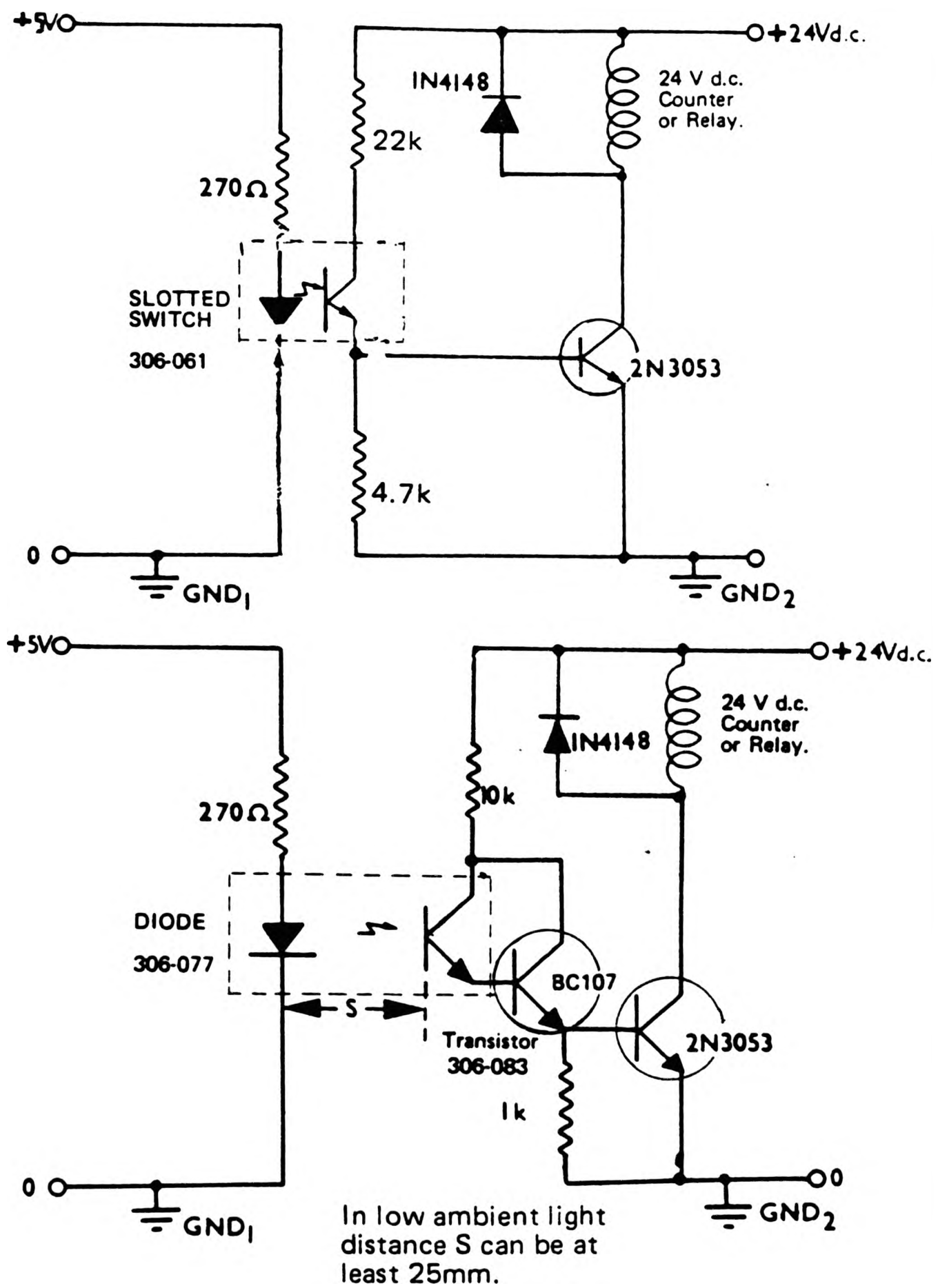
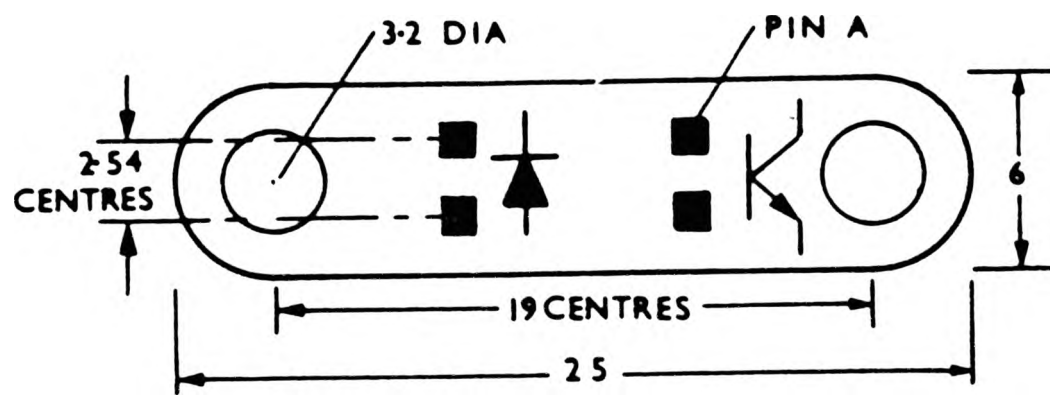
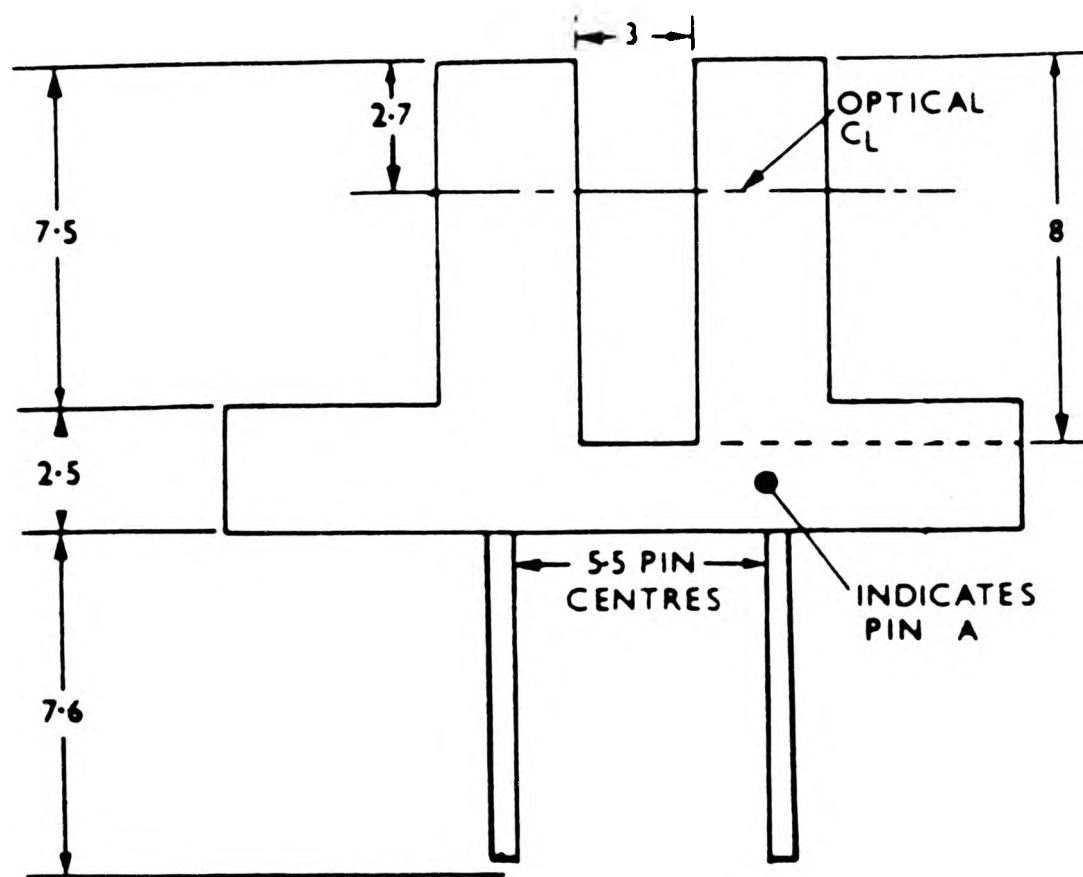


Figure 74. Schematic circuit diagram of interface between the photo diode and the counting circuit.



PIN VIEW

Figure 75. Plan and elevation views of the photo-sensitive diode used to measure rotation speed.

principle. A slotted disc fitted to the drive shaft, at the upper end of the motor revolves within a pair of optical diodes which change the varying light intensity into a voltage signal, this is interfaced with a revolution counting circuit Zn 1040 B microchip capable of digital read out. This is interfaced with an oscillator circuit capable of summing the counts over 6 seconds, 60 seconds or 6 minutes. See Figures 74-76 for circuit details.

4.2.7 Pre-electrolysis of the solution. Pre-electrolysis of the electrolyte prepared by dissolving Analar grade chemicals in doubly distilled water, is carried out to remove heavy metal impurities. This is done simply by using a two compartment cell provided with gas dispersion frits, connected to a stabilised direct current power supply with an ammeter to measure the electrolysis current. The heavy metal impurities deposit on to a large platinum cathode. This solution is emptied and used when needed. A continuous stream of inert gas keeps oxygen out. The cell is flat bottomed, made of glass. The two compartments are separated at the top by a glass frit of very fine porosity preventing free intermixing of anolyte and catholyte. The electrolysis is carried out for several days at a low current 3-6 mA. The capacity of anolyte compartment was 100 cm³ and that of catholyte compartment was 2000 cm³. In the pre-electrolysed solution lead and iron could not be detected at all. Figure 77 shows the arrangement of the apparatus.

4.3 ANODIC POLARISATION

Prior to the experiments the glass cell was cleaned by steeping overnight in freshly prepared solution of chromic acid. It was then washed thoroughly in doubly distilled water and dried. It was then filled with 700 cm³ of inert gas saturated, pre-electrolysed solution. The zinc oxide saturated solution was made as follows. About 36 g of zinc oxide Analar grade was dissolved in 1000 cm³ of pre-electrolysed 6 mol dm⁻³ KCl by adding bit by bit at a time. Initially the dissolution rate was fast, but as the

saturation point drew nearer it took longer to dissolve a given quantity. The process took two or more days. During this period a tightly fitting lid was used on the vessel, it was continually purged with nitrogen purified as described previously and stirred by a magnetic follower. The electrochemical cell was similarly purged at all times, except during the actual experiment. The temperature was maintained at $25 \pm 0.1^\circ\text{C}$ by a water bath. The specimen was a disc of 7.14 mm diameter, shrunk fit into the holder, polished to a $0.25 \mu\text{m}$ finish. The specimen was thoroughly degreased, cleaned ultrasonically, dried and fitted onto the shaft. The polarisation curves were recorded on the X-Y chart recorder. To observe the surface of the specimen during the experiment a plane mirror at an angle was placed below the cell for observations on selected occasions.

4.4 RESULTS

The i-E curves thus obtained are shown in Figures 78-185 attached. Tables 18 and 19 summarise the data contained in the curves. The curves clearly show the following features:-

- (i) A region of active dissolution, an initial steep rise in potential and current showing an exponential relation (Tafel behaviour).
- (ii) Region of the onset of passivity, where the current rises slowly with potential and then decreases suddenly to a very low value.
- (iii) Passive region, where the current is more or less constant at this low value while the potential is raised.

The visual changes occurring have been observed. In the active region uniform dissolution takes place, forming soluble species and resulting in an etched surface because dissolution depends on the crystal face exposed to the solution. Nearer to the point of maximum current density nucleation of insoluble oxidation products takes place. These form clumps and grow until the surface is covered. This sometimes occurs in a "skin" effect, the film spreading from one corner to cover the entire surface area. Colour changes occurring are as follows: the brightly polished surface changes to light

Table 19. R.D.E. anodic polarisation data for 2.5 w/o Hg-Cd-Zn ternary alloys

Alloys	Rotation Speed rad s ⁻¹	Electrolyte									
		6 mol dm ⁻³ KOH					6 mol dm ⁻³ KOH ZnO to saturation				
		Rest Pot. mV	Pass. Pot. mV	Break Pot. mV	Peak C.D. 10 ³ Am ⁻²	Passivation C.D. Am ⁻²	Rest Pot. mV	Pass. Pot. mV	Break Pot. mV	Peak C.D. 10 ³ Am ⁻²	Passivation C.D. Am ⁻²
0.05	0	1425	940	1020	4.75	90	1385	930	1035	4.40	50
	10	1410	890	1000	6.00	145	1385	875	1030	5.30	75
	50	1410	640	980	10.50	180	1385	670	1000	9.50	140
	100	1410	470	980	13.40	230	1385	490	990	12.30	175
0.2	0	1410	920	960	3.88	60	1375	920	980	3.70	40
	10	1410	900	950	4.46	80	1375	890	970	4.50	80
	50	1410	640	930	8.00	150	1375	650	960	8.20	150
	100	1410	520	920	9.86	210	1375	500	950	10.50	250
1.0	0	1395	930	930	4.15	70	1370	910	920	3.70	40
	10	1395	860	900	4.90	100	1370	880	910	4.00	50
	50	1395	620	880	8.00	200	1370	670	890	7.77	100
	100	1395	480	860	9.60	250	1370	530	880	9.50	150
2.0	0	1385	920	1020	4.80	80	1365	940	950	3.90	40
	10	1385	885	980	5.60	100	1365	880	930	5.00	50
	50	1385	640	900	9.50	150	1365	650	920	8.50	100
	100	1385	510	870	11.25	200	1365	510	900	10.00	150
5.0	0	1390	890	950	4.33	40	1360	950	980	4.60	45
	10	1390	850	940	5.30	60	1360	900	960	6.00	60
	50	1390	770	930	8.65	80	1360	790	950	9.50	80
	100	1390	690	920	10.33	110	1360	680	930	11.50	90
10.0	0	1390	880	960	4.00	50	1355	1000	1000	3.90	40
	10	1390	830	930	4.70	60	1355	980	990	4.30	50
	50	1390	670	910	7.15	110	1355	900	970	5.00	60
	100	1390	580	900	8.25	130	1355	690	950	8.00	90
25.0	0	1380	940	980	3.60	45	1350	1000	1000	3.75	35
	10	1380	950	960	4.15	60	1350	980	980	4.25	40
	50	1380	800	930	7.60	75	1350	850	960	7.40	60
	100	1380	750	930	9.00	80	1350	730	950	9.00	70

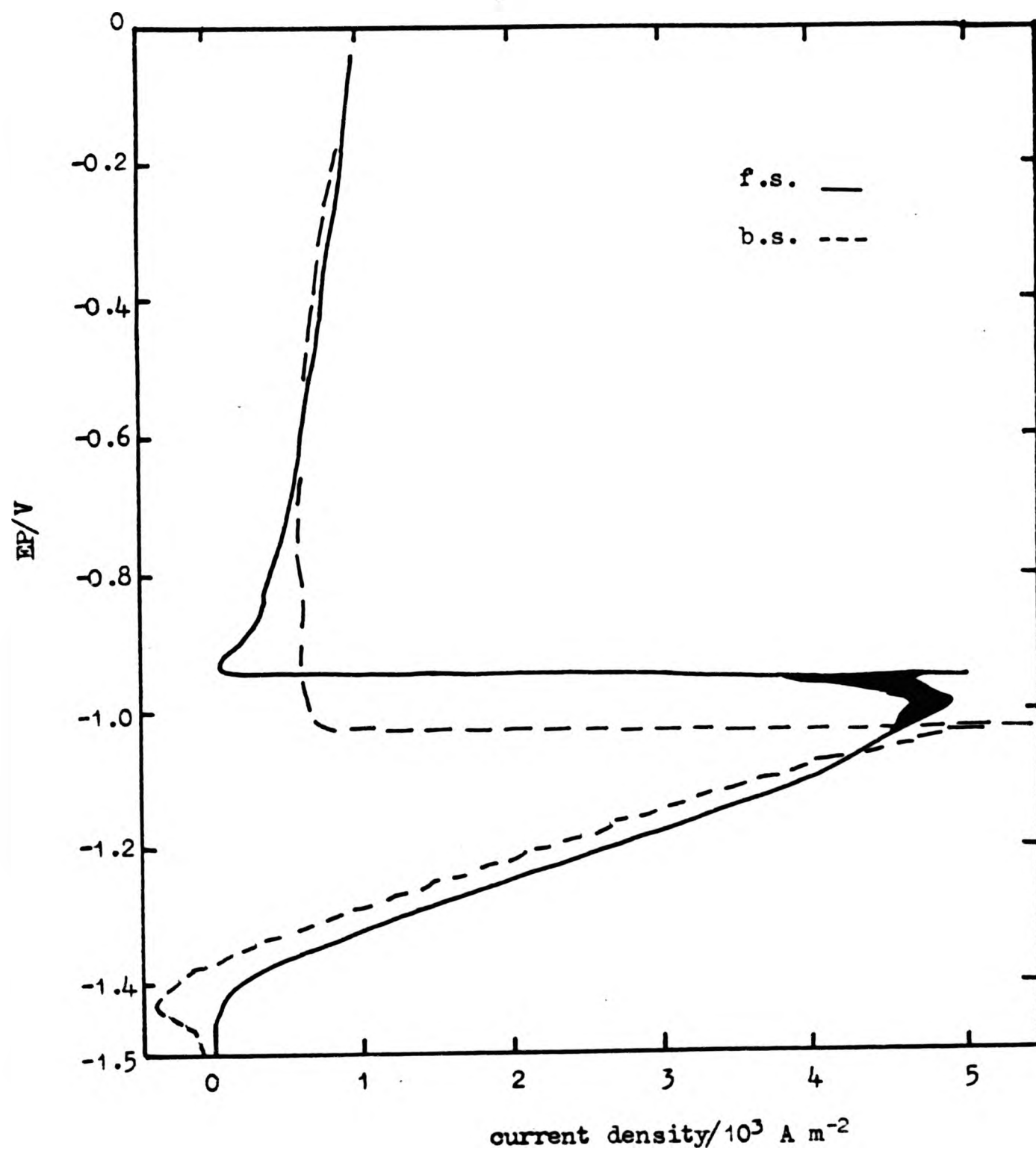


Figure 78. Anodic polarisation curves for Zn-.05 Cd-2.5 Hg alloy in 6 mol dm^{-3} KOH on a stationary electrode.

Note: In the following Figures Nos. 78 to 185 the abbreviation EP/V along the ordinate denotes the "Electrode Potential vs Hg/HgO reference electrode in volts"
 f.s. stands for "forward sweep"
 b.s. stands for "backward sweep"

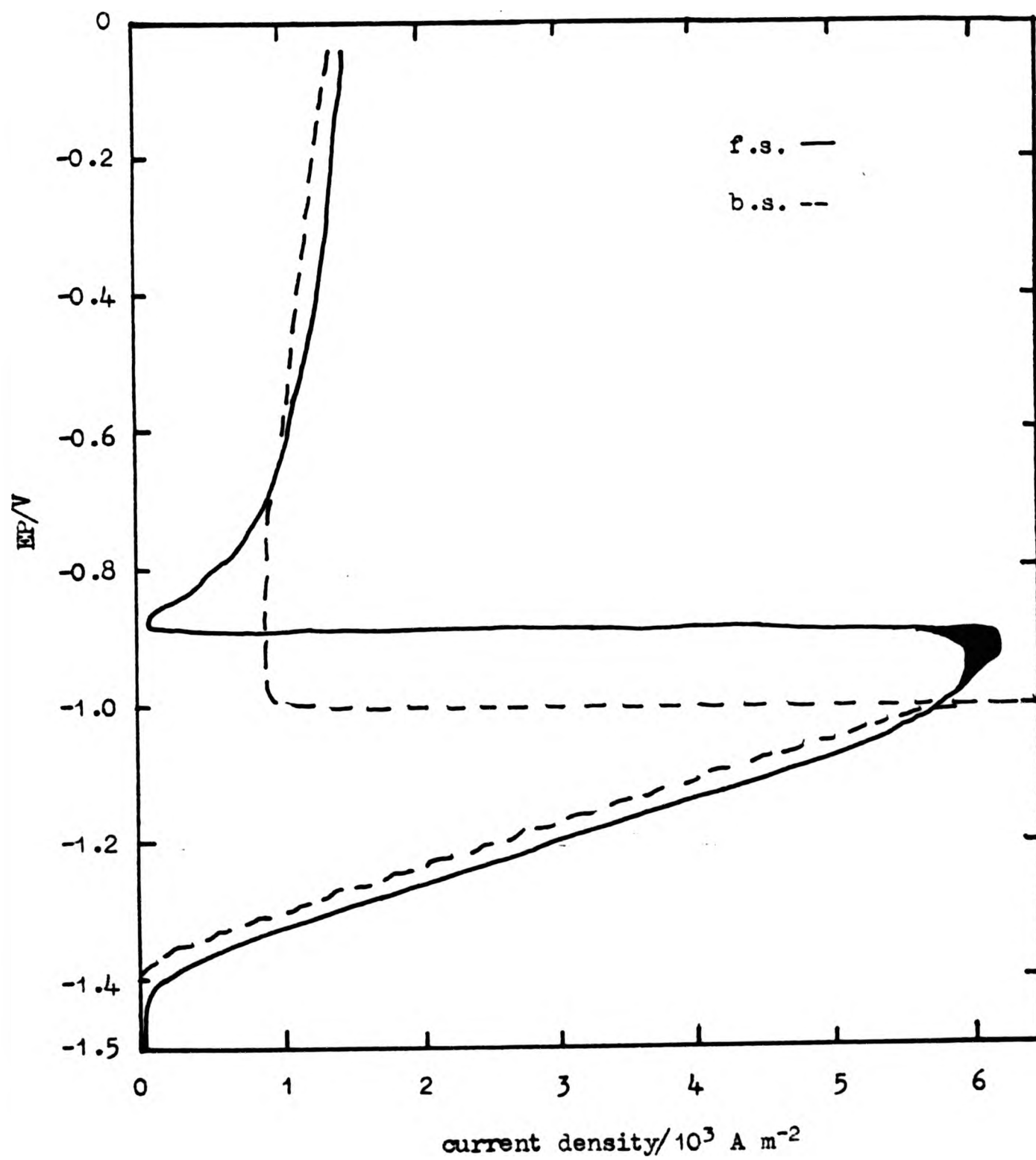


Figure 79. Anodic polarisation curves for Zn-.05 Cd-2.5 Hg alloy in 6 mol dm⁻³ KOH at 10 rad s⁻¹ rotation speed.

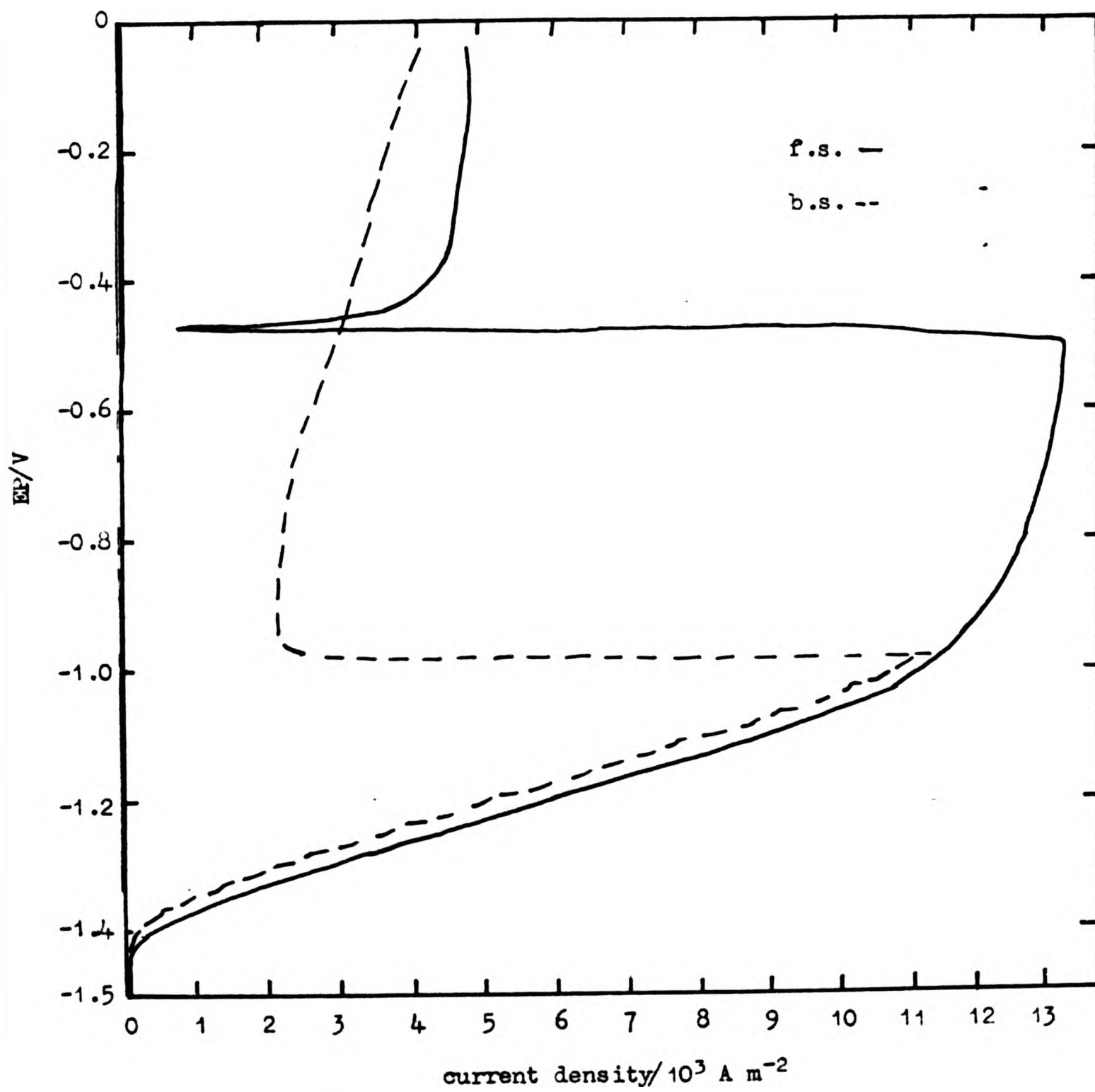


Figure 81. Anodic polarisation curves for Zn-.05 Cd-2.5 Hg alloy in 6 mol dm^{-3} KOH at 100 rad s^{-1} rotation speed.

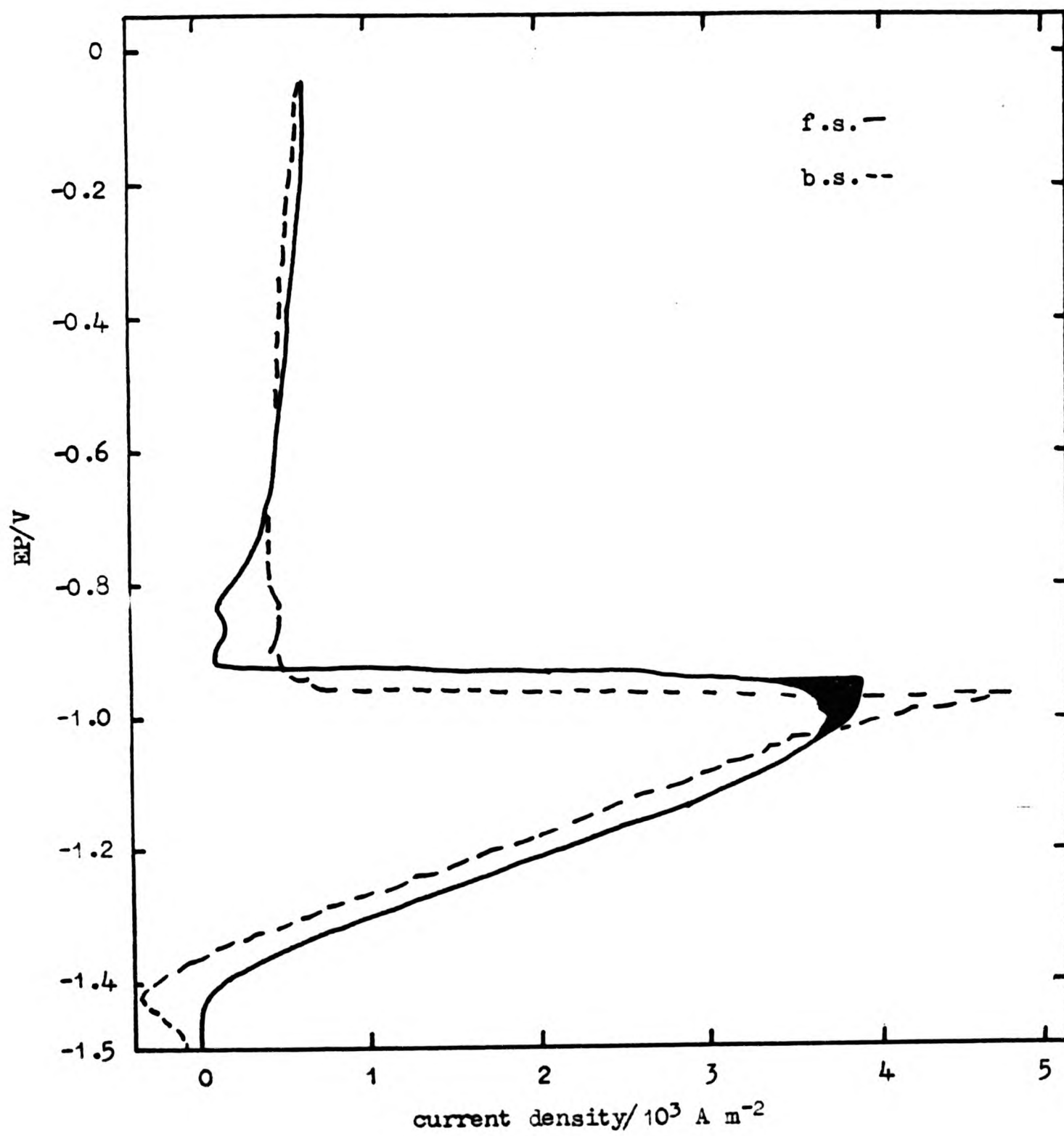


Figure 82. Anodic polarisation curves for Zn-.2 Cd-2.5 Hg in $6 \text{ mol dm}^{-3} \text{ KOH}$ on a stationary electrode.

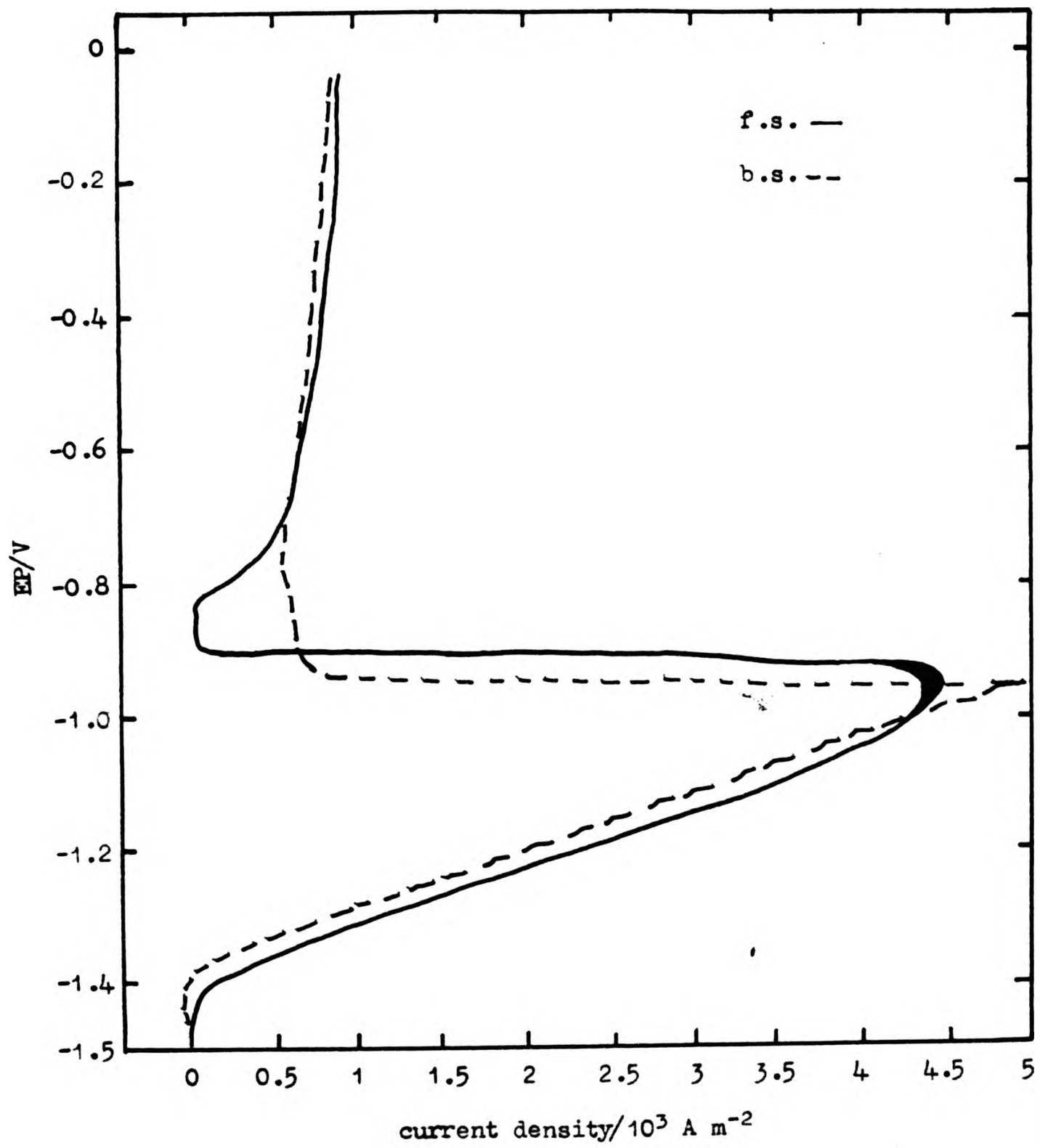


Figure 83. Anodic polarisation curves for Zn-.2 Cd-2.5 Hg alloy in 6 mol dm⁻³ KOH at 10 rad s⁻¹ rotation speed.

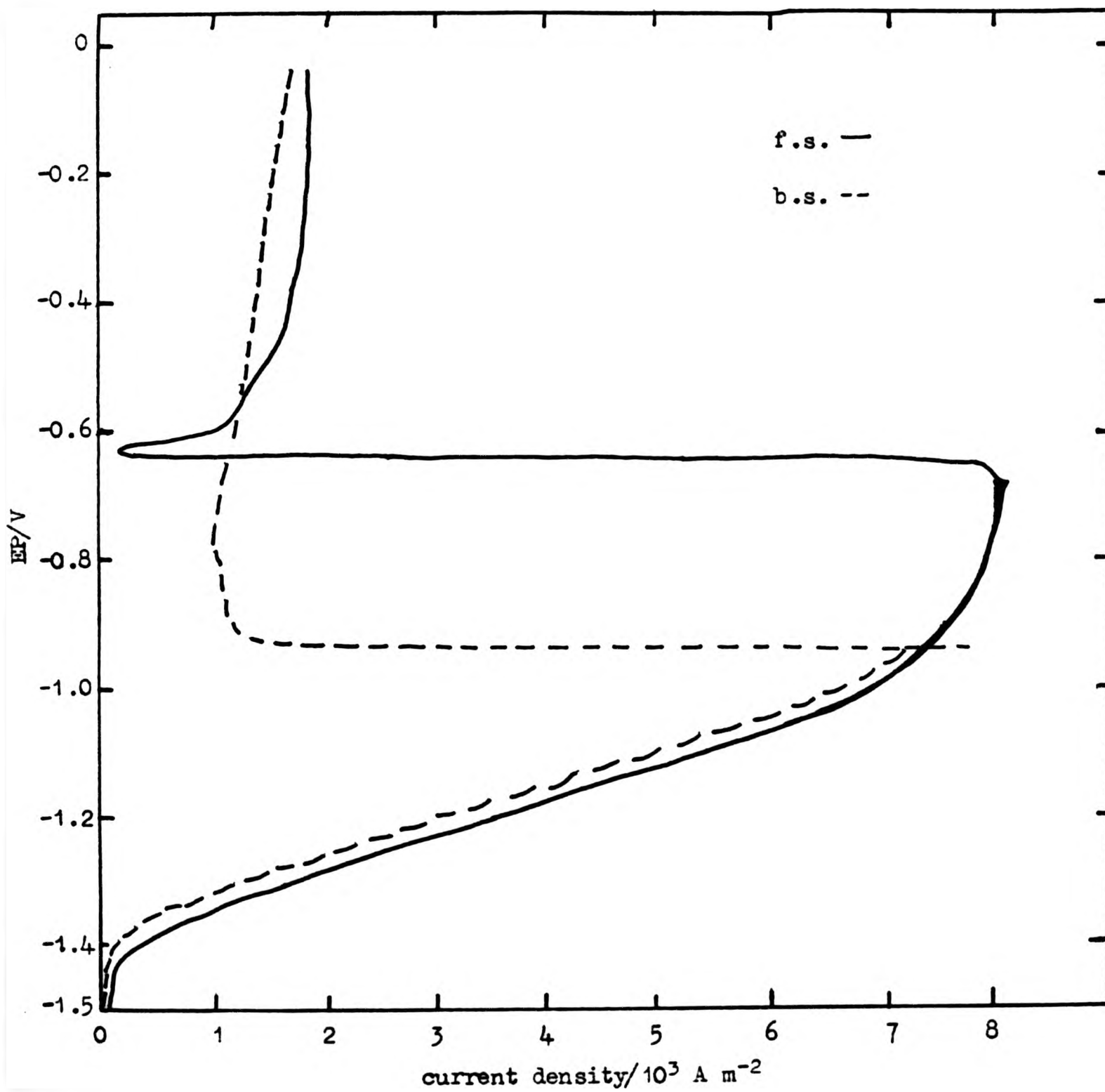


Figure 84. Anodic polarisation curves for Zn-2 Cd-2.5 Hg alloy in 6 mol dm⁻³ KOH at 50 rad s⁻¹ rotation speed.

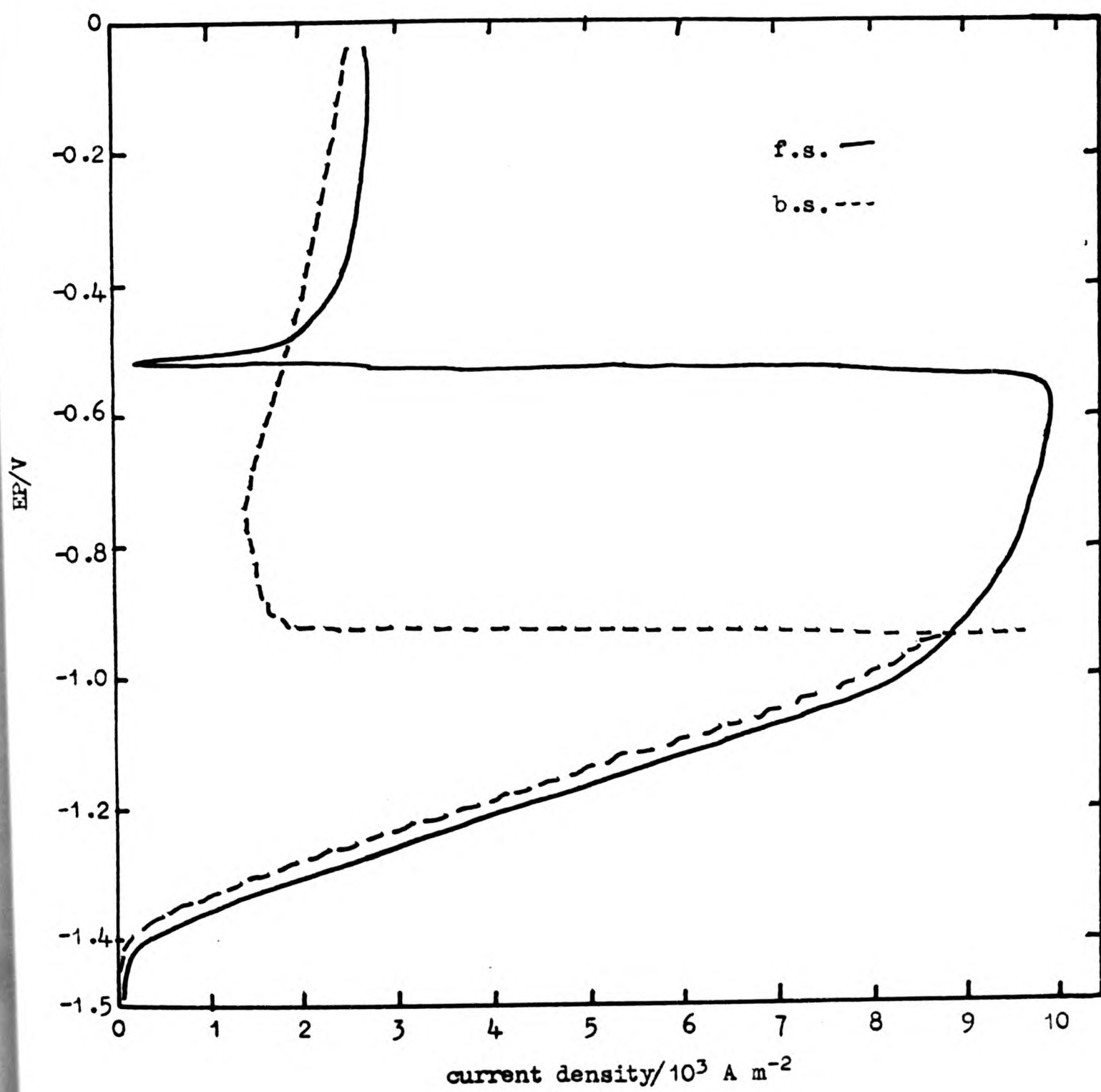


Figure 85. Anodic polarisation curves for Zn-2 Cd-2.5 Hg alloy
in 6 mol dm⁻³ KOH at 100 rad s⁻¹ rotation speed.

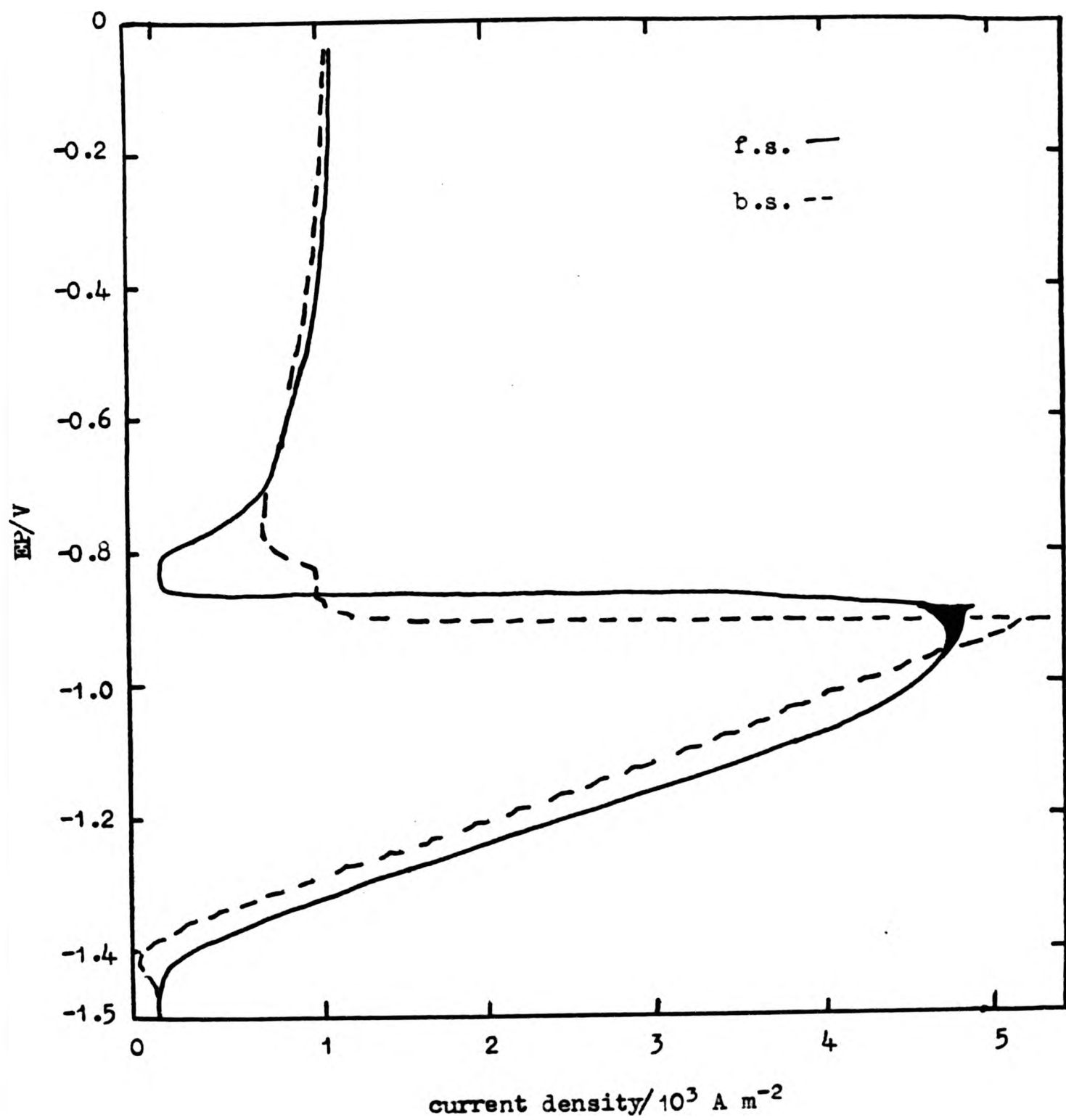


Figure 87. Anodic polarisation curves for Zn-1 Cd-2.5 Hg alloy in 6 mol dm⁻³ KOH at 10 rad s⁻¹ rotation speed.

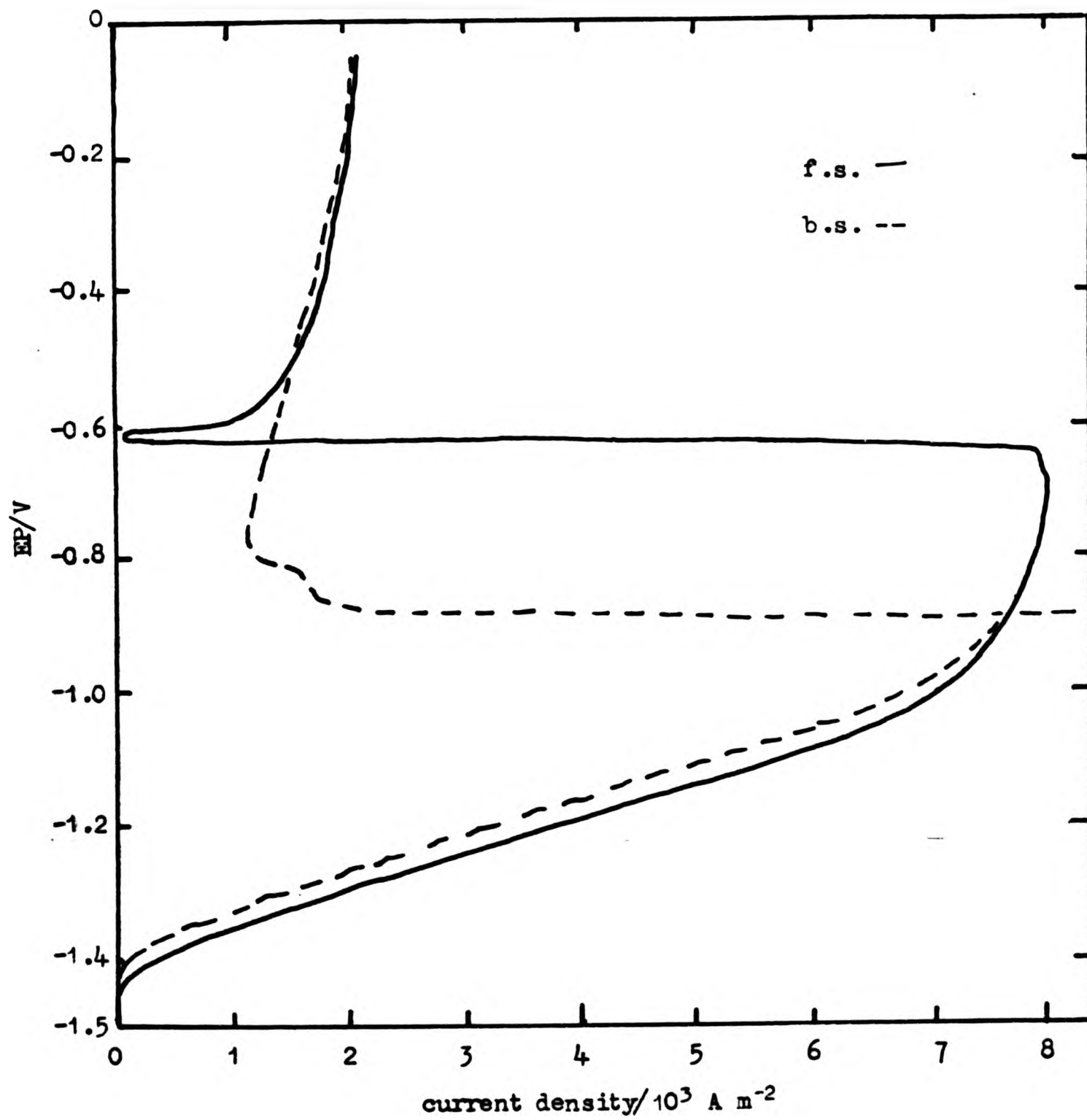


Figure 88. Anodic polarisation curves for Zn-1 Cd-2.5 Hg alloy in 6 mol dm⁻³ KOH at 50 rad s⁻¹ rotation speed.

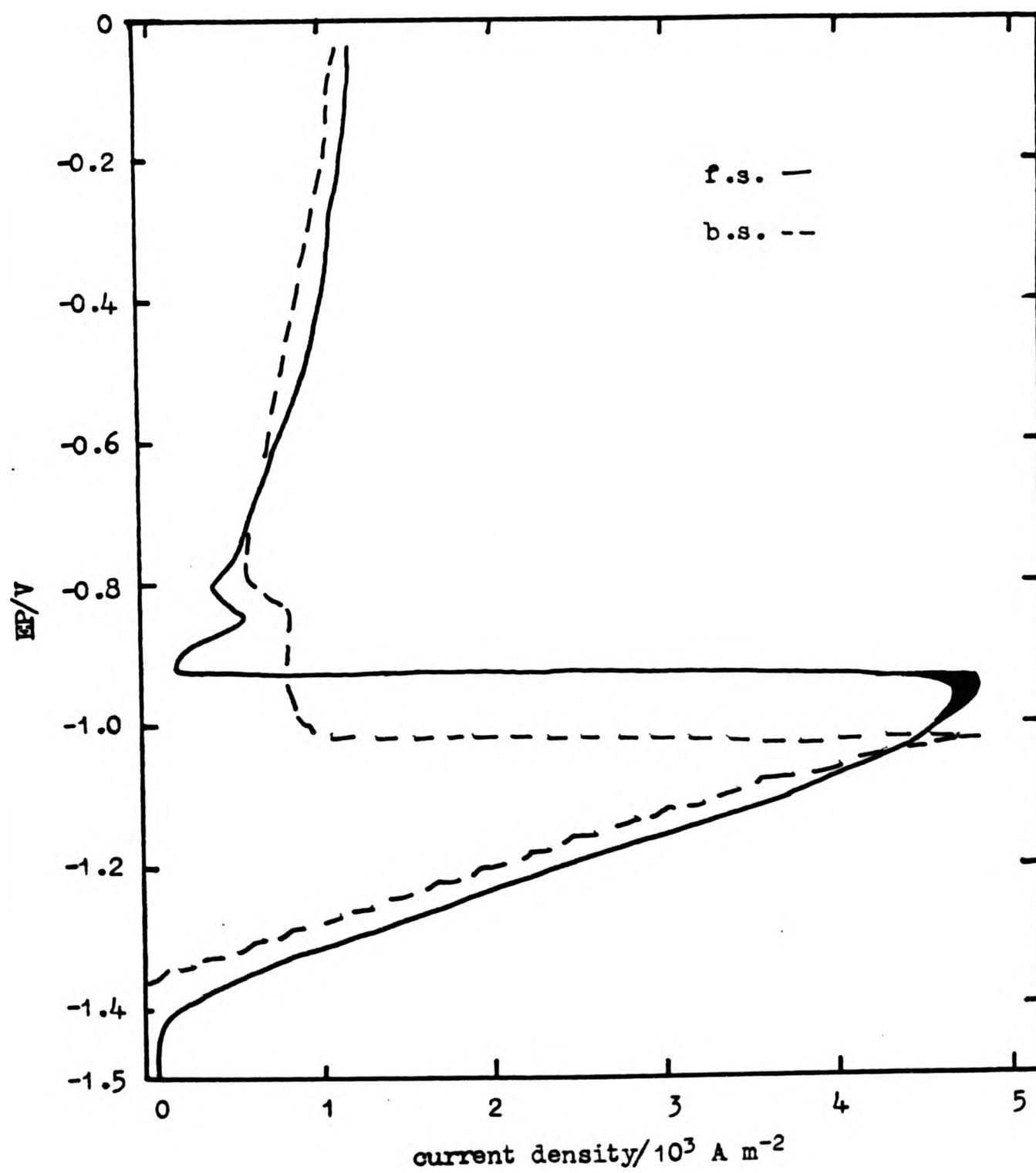


Figure 90. Anodic polarisation curves for Zn-2 Cd-2.5 Hg alloy
in 6 mol dm⁻³ KOH on a stationary electrode.

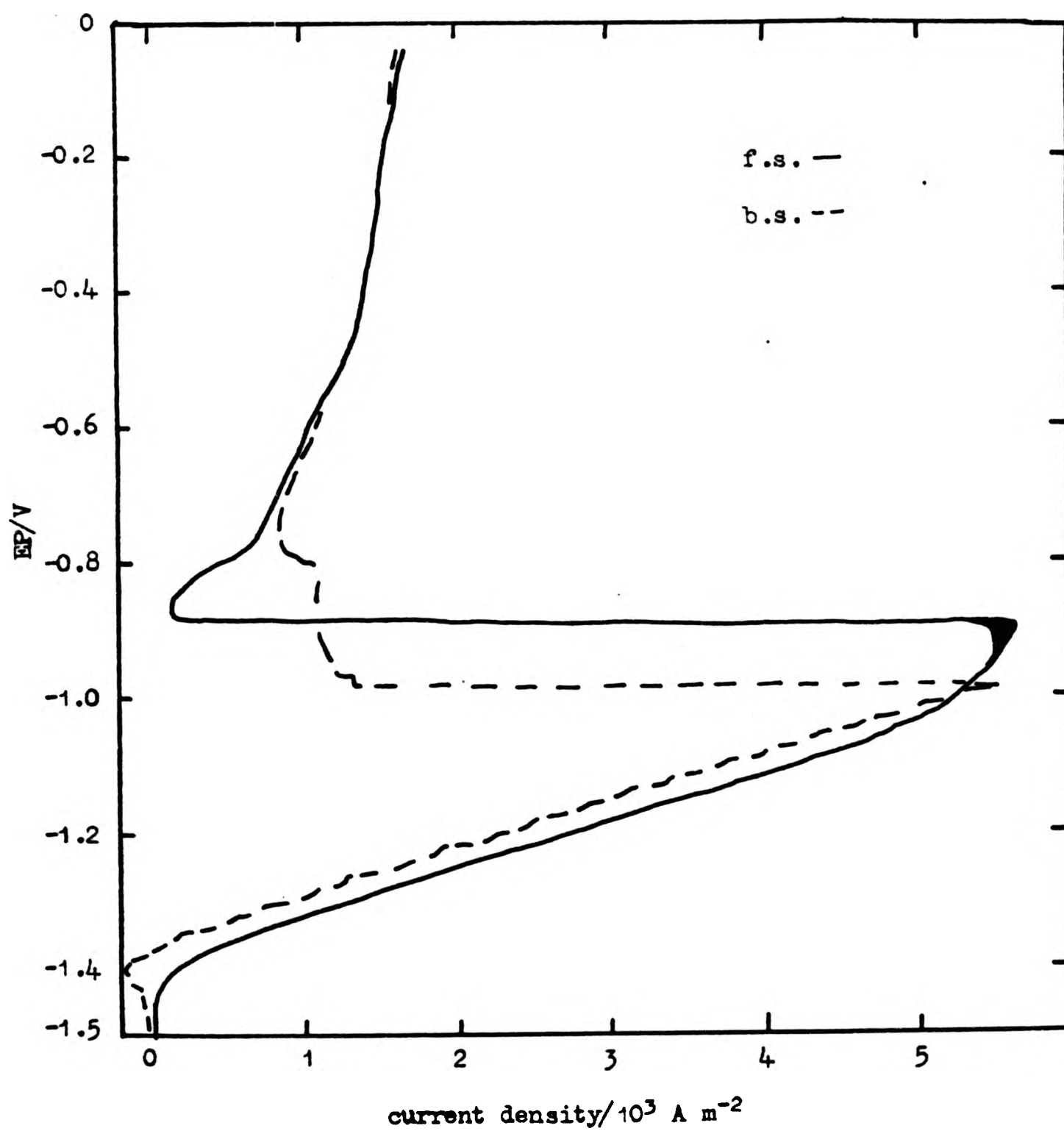


Figure 91. Anodic polarisation curves for Zn-2Cd-2.5 Hg alloy
in 6 mol dm⁻³ KOH at 10 rad s⁻¹ rotation speed.

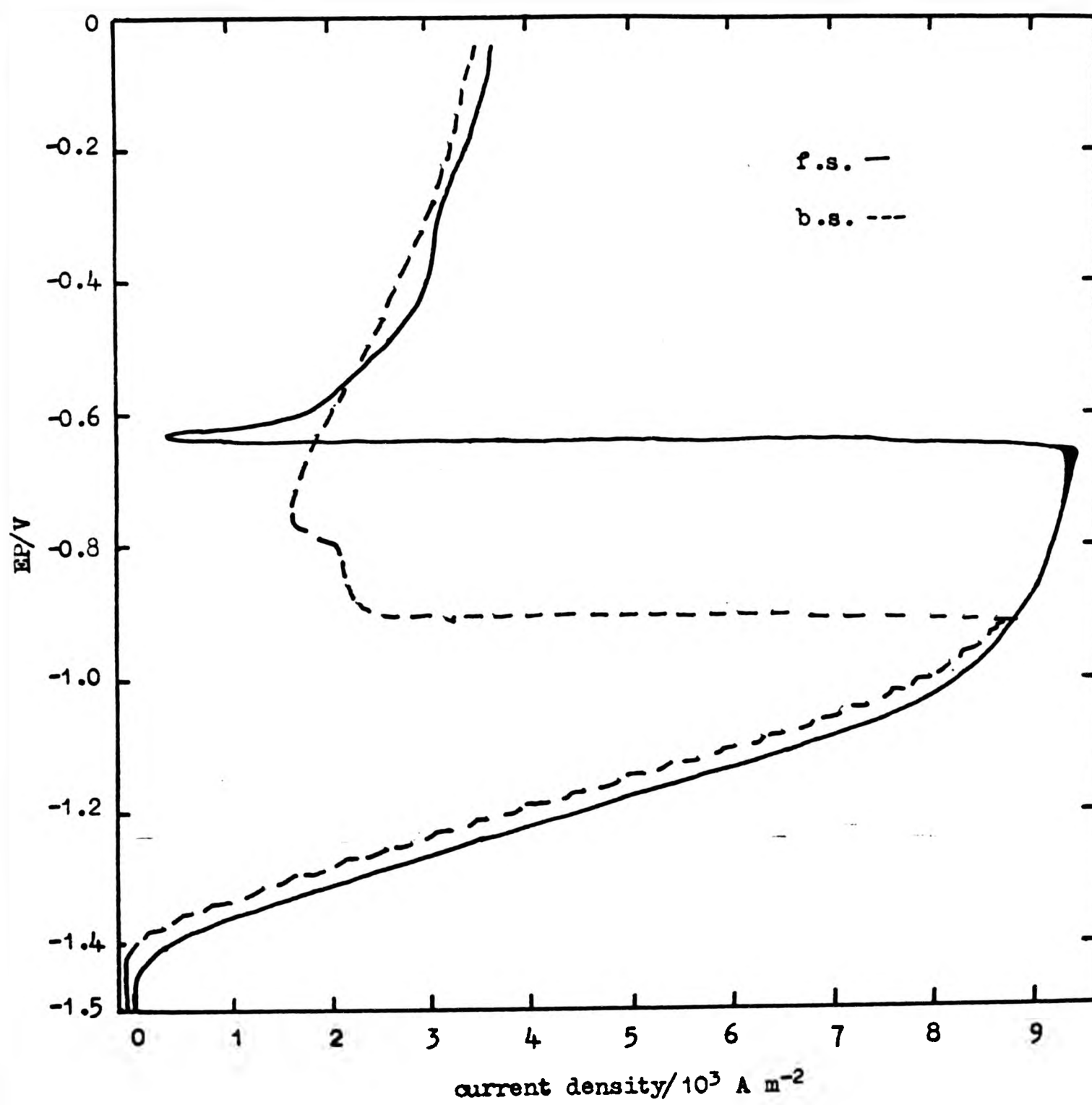


Figure 92. Anodic polarisation curves for Zn-2Cd-2.5 Hg alloy in 6 mol dm³ KOH at 50 rad s⁻¹ rotation speed.

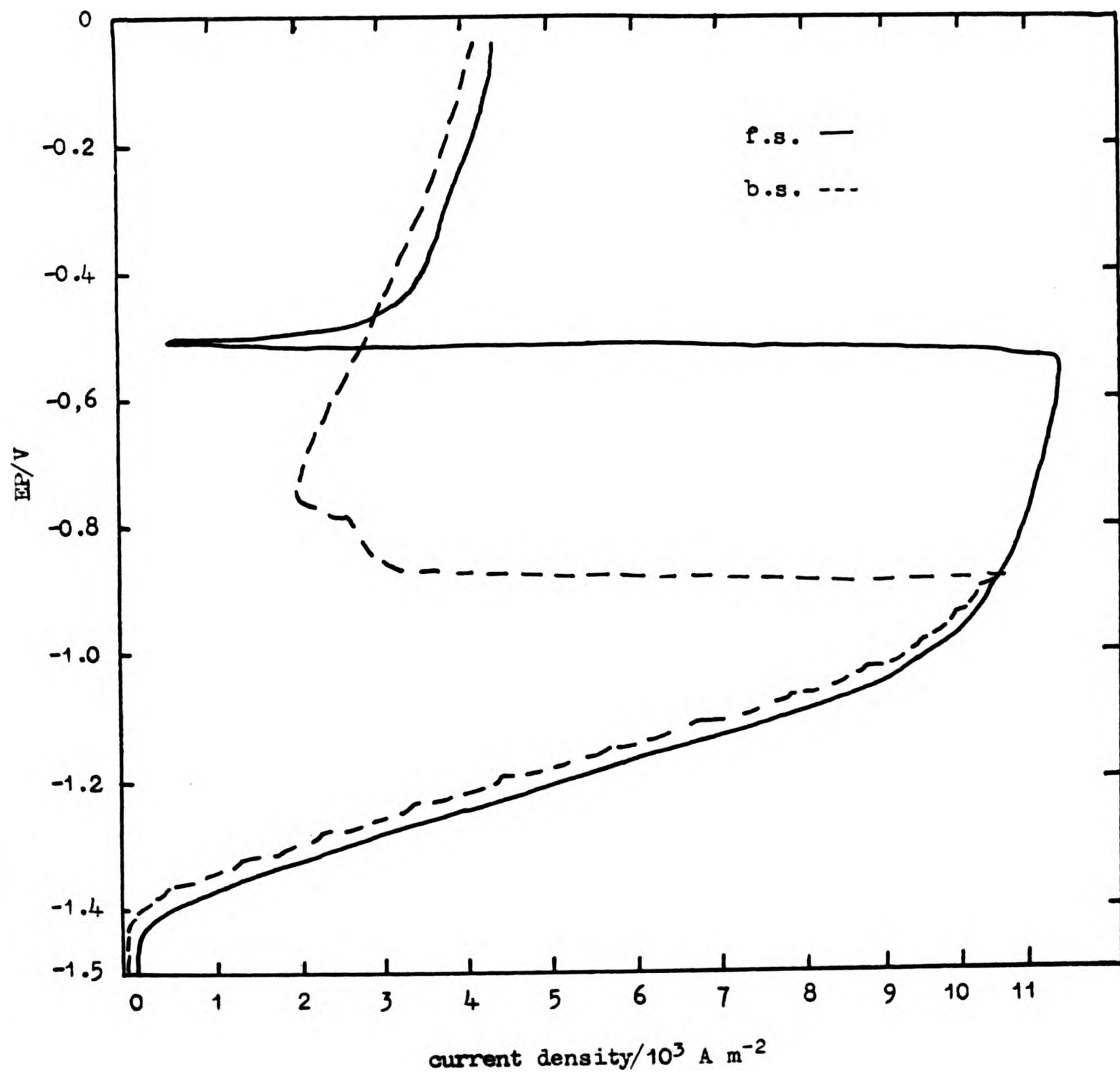


Figure 93. Anodic polarisation curves for Zn-2 Cd-2.5 Hg alloy in 6 mol dm⁻³ KOH at 100 rad s⁻¹ rotation speed.

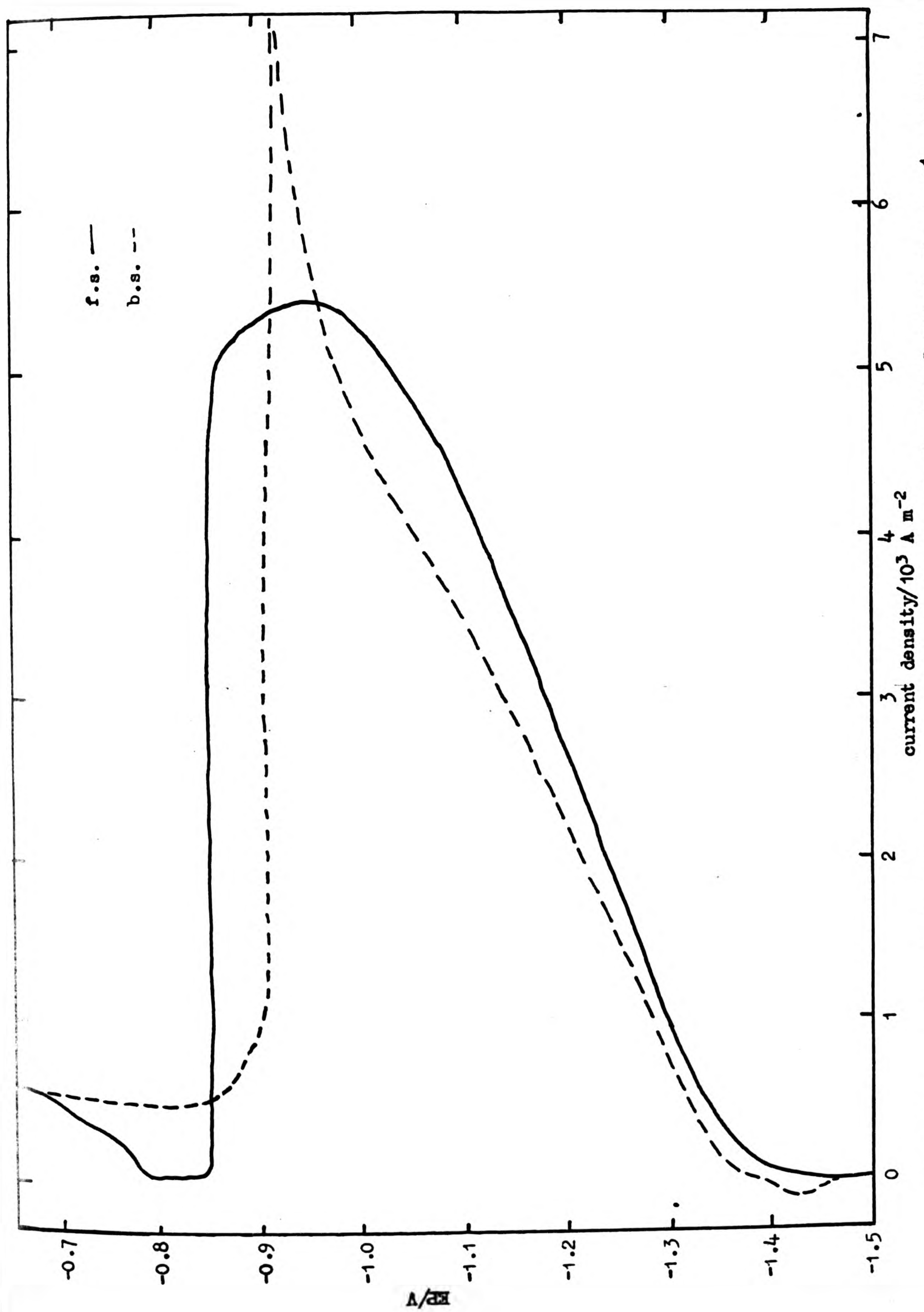


Figure 95. Anodic polarisation curves for Zn-5 Cd-2.5 Hg alloy in $6 \text{ mol dm}^{-3} \text{ KOH}$ at 10 rad s^{-1} rotation speed.

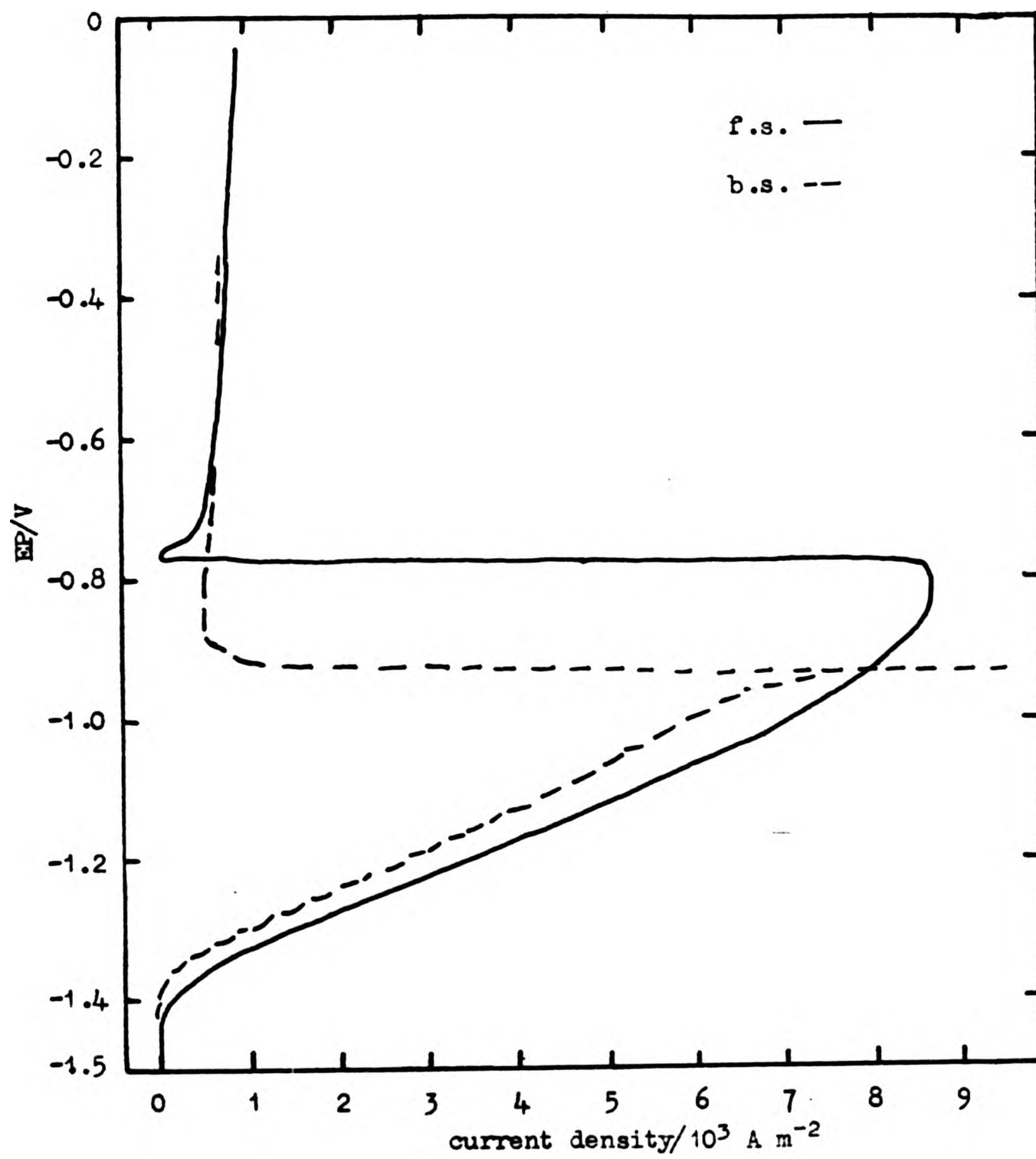


Figure 96. Anodic polarisation curves for Zn-5 Cd-2.5 Hg alloy in 6 mol dm⁻³ KOH at 50 rad s⁻¹ rotation speed.

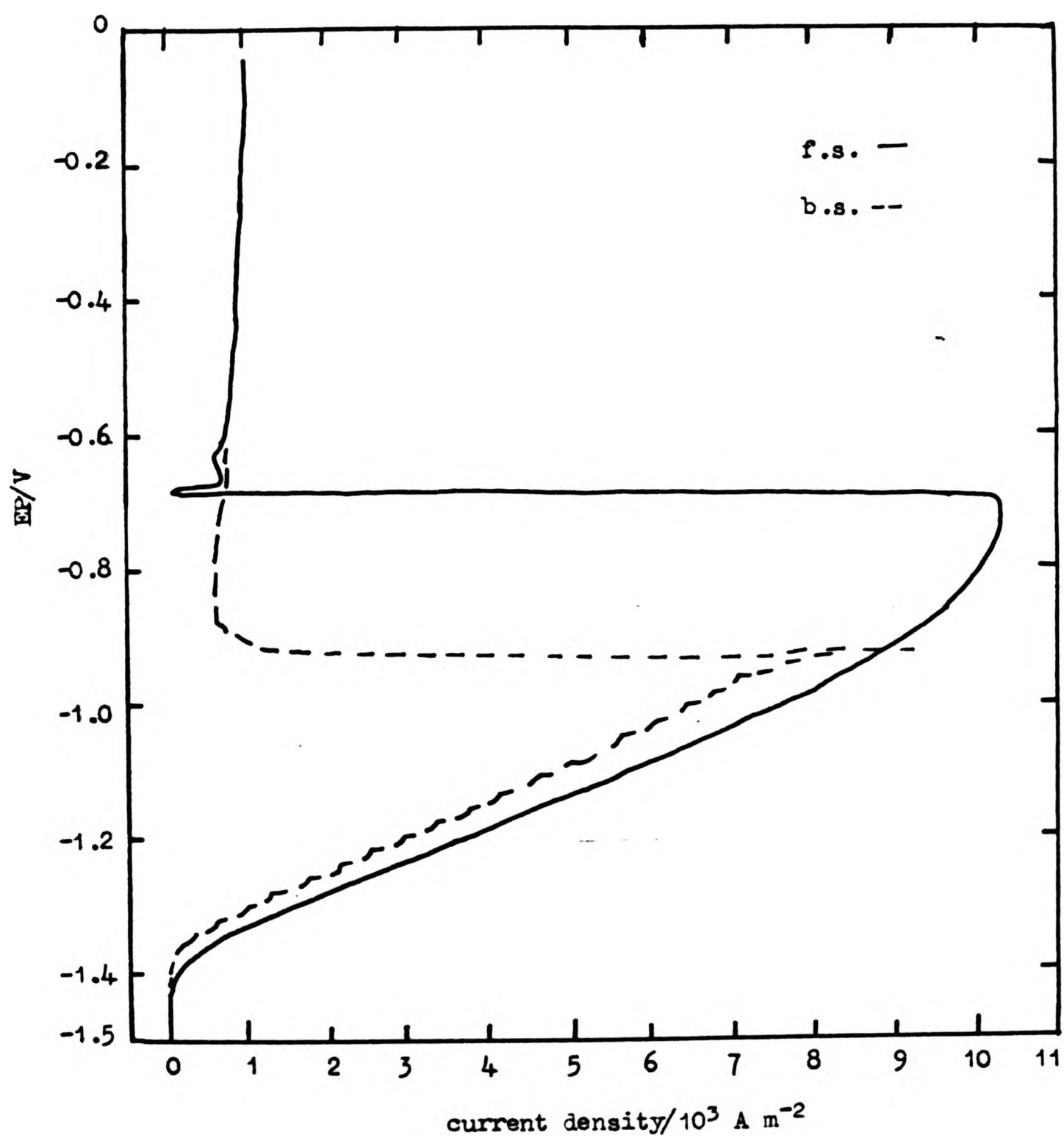


Figure 97. Anodic polarisation curves for Zn-5 Cd-2.5 Hg alloy in 6 mol dm⁻³ KOH at 100 rad s⁻¹ rotation speed.

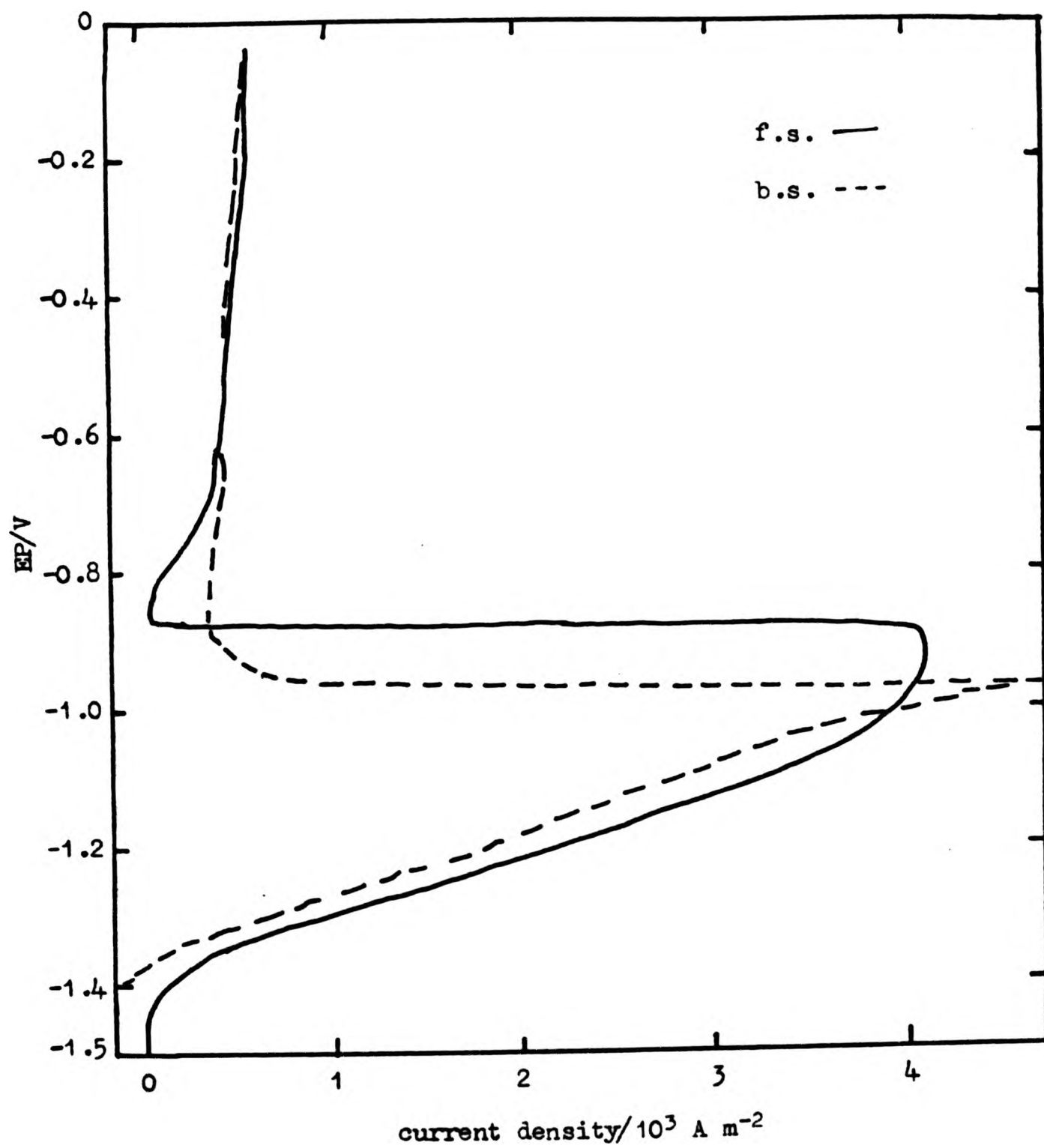


Figure 98. Anodic polarisation curves for Zn-10 Cd-2.5 Hg alloy in 6 mol dm^{-3} KOH on stationary electrode.

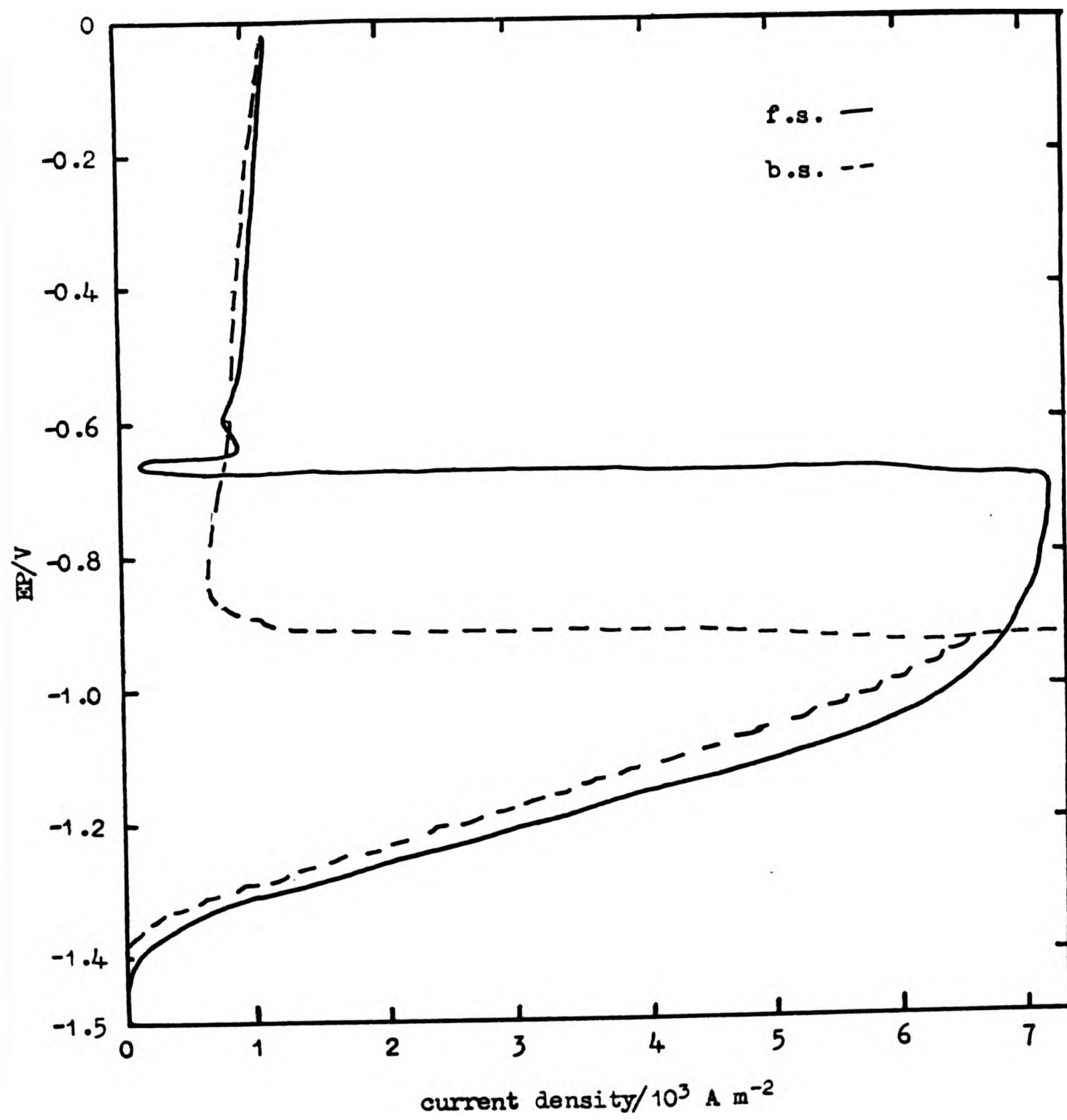


Figure 100. Anodic polarisation curves for Zn-10 Cd-2.5 Hg alloy in 6 mol dm⁻³ KOH at 50 rad s⁻¹ rotation speed.

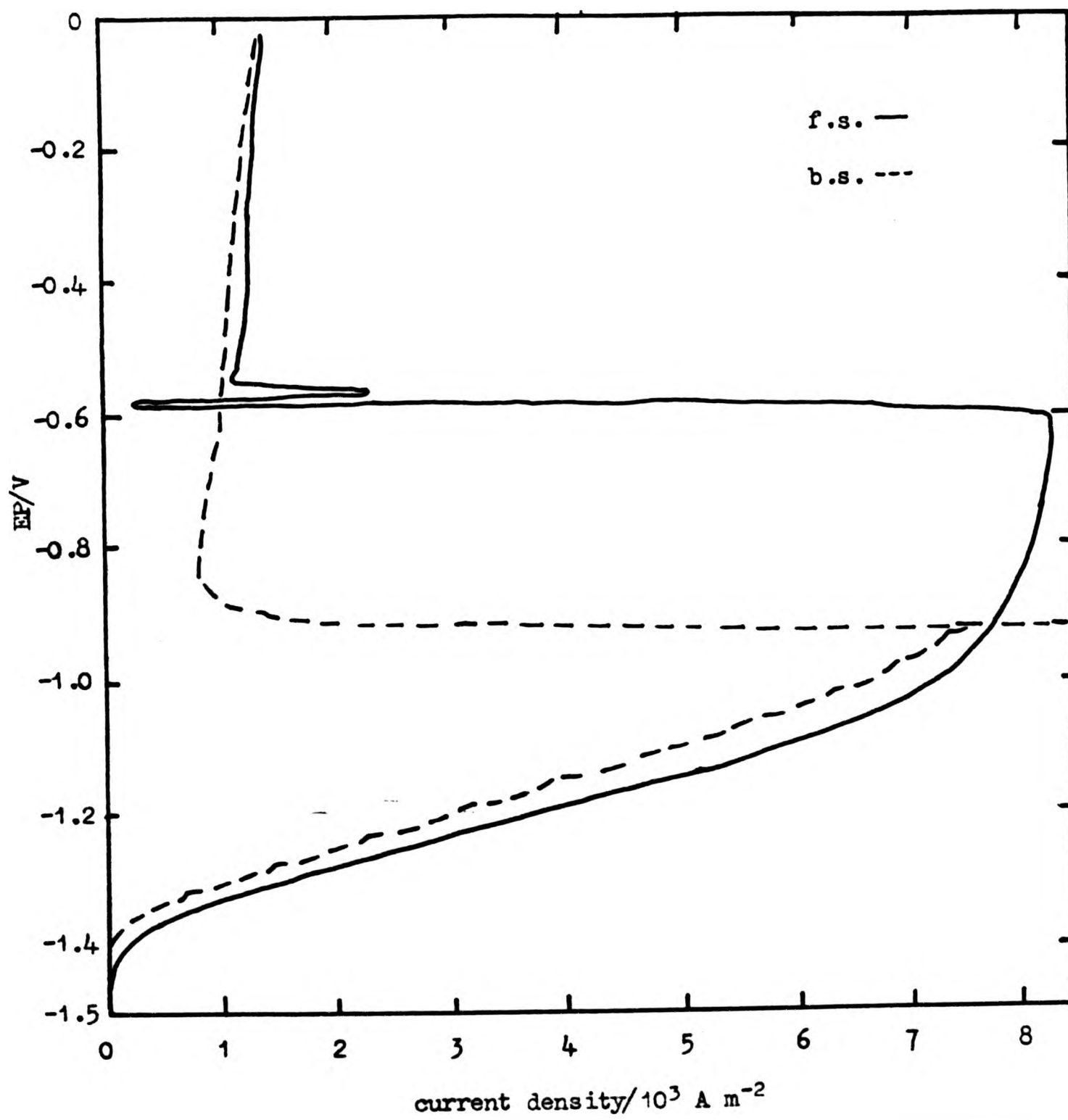


Figure 101. Anodic polarisation curves for Zn-10 Cd-2.5 Hg alloy in 6 mol dm⁻³ KOH at 100 rad s⁻¹ rotation speed.

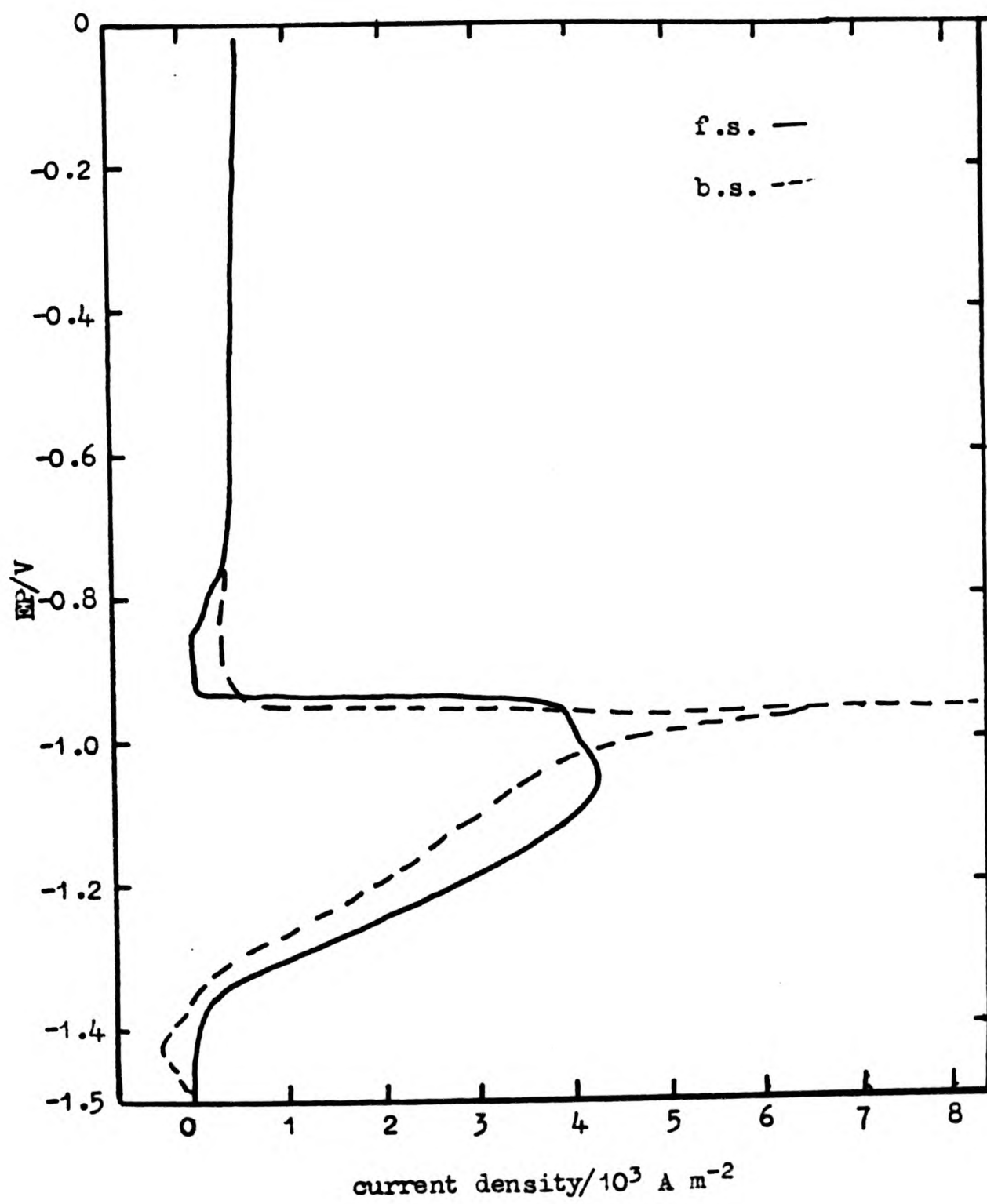


Figure 103. Anodic polarisation curves for Zn-25 Cd-2.5 Hg alloy in 6 mol dm⁻³ KOH at 10 rad s⁻¹ rotation speed.

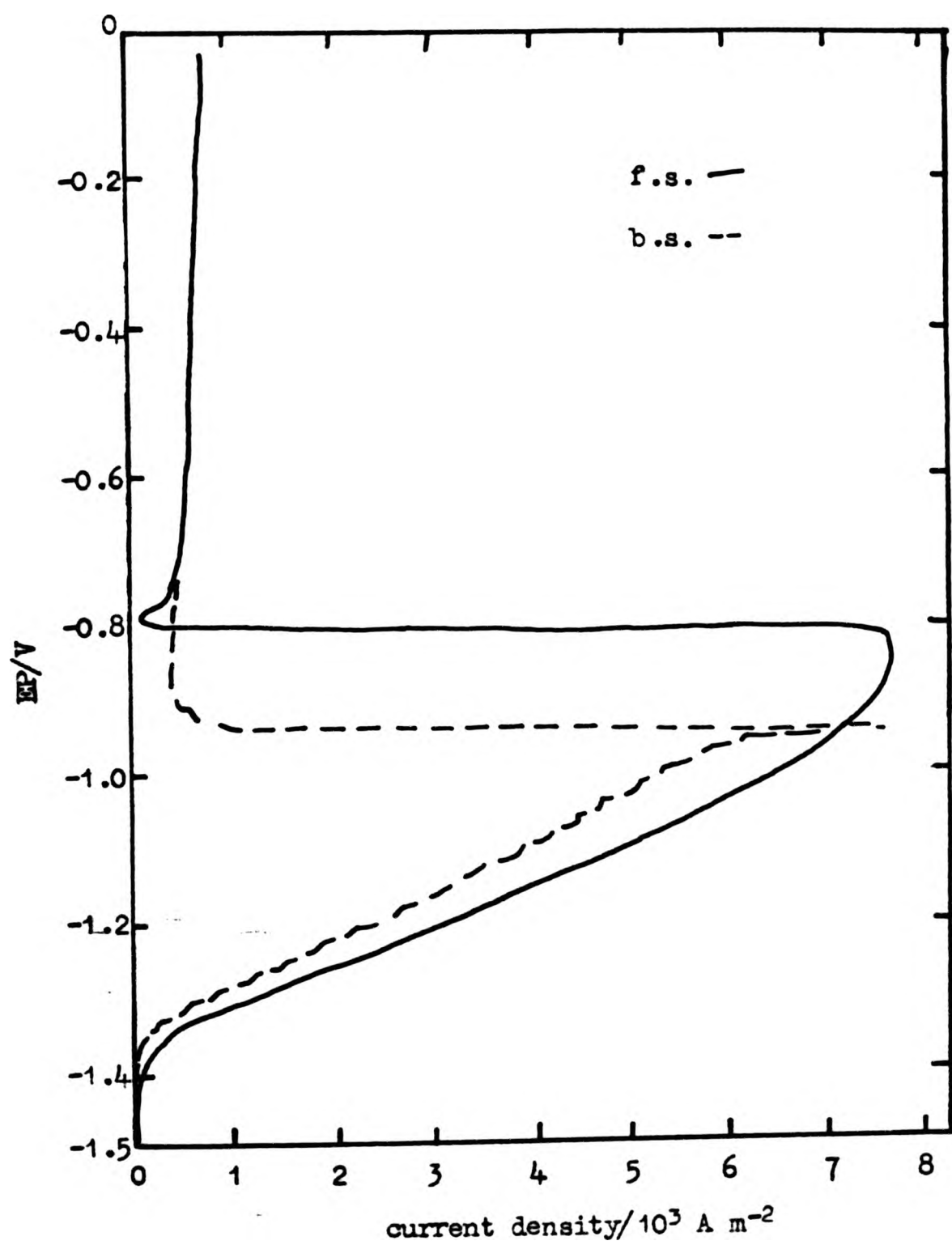


Figure 104. Anodic polarisation curves for Zn-25 Cd-2.5 Hg alloy in 6 mol dm⁻³ KOH at 50 rad s⁻¹ rotation speed.

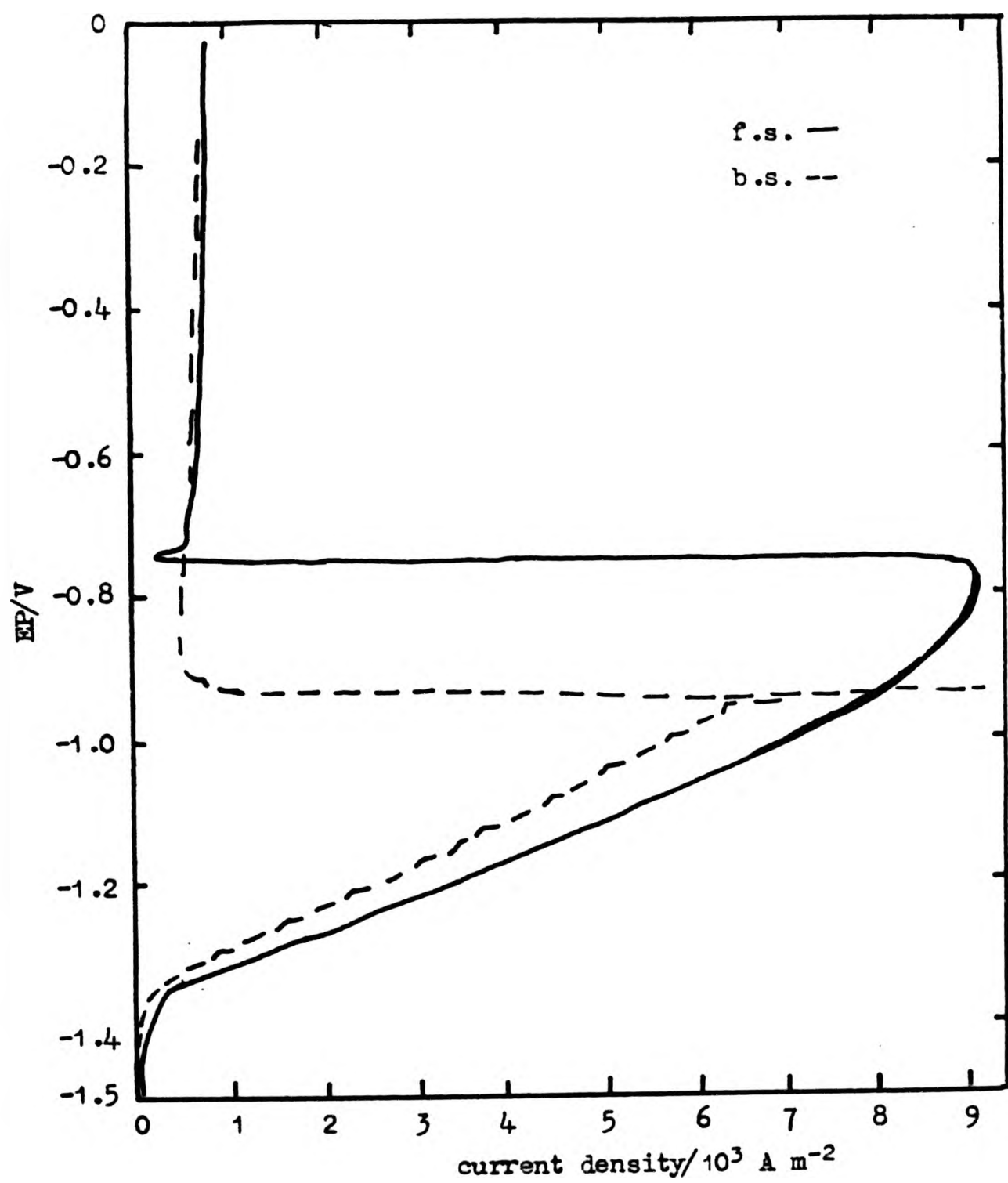


Figure 105. Anodic polarisation curves for Zn-25 Cd-2.5 Hg alloy in 6 mol dm⁻³ KOH at 100 rps rotation speed.

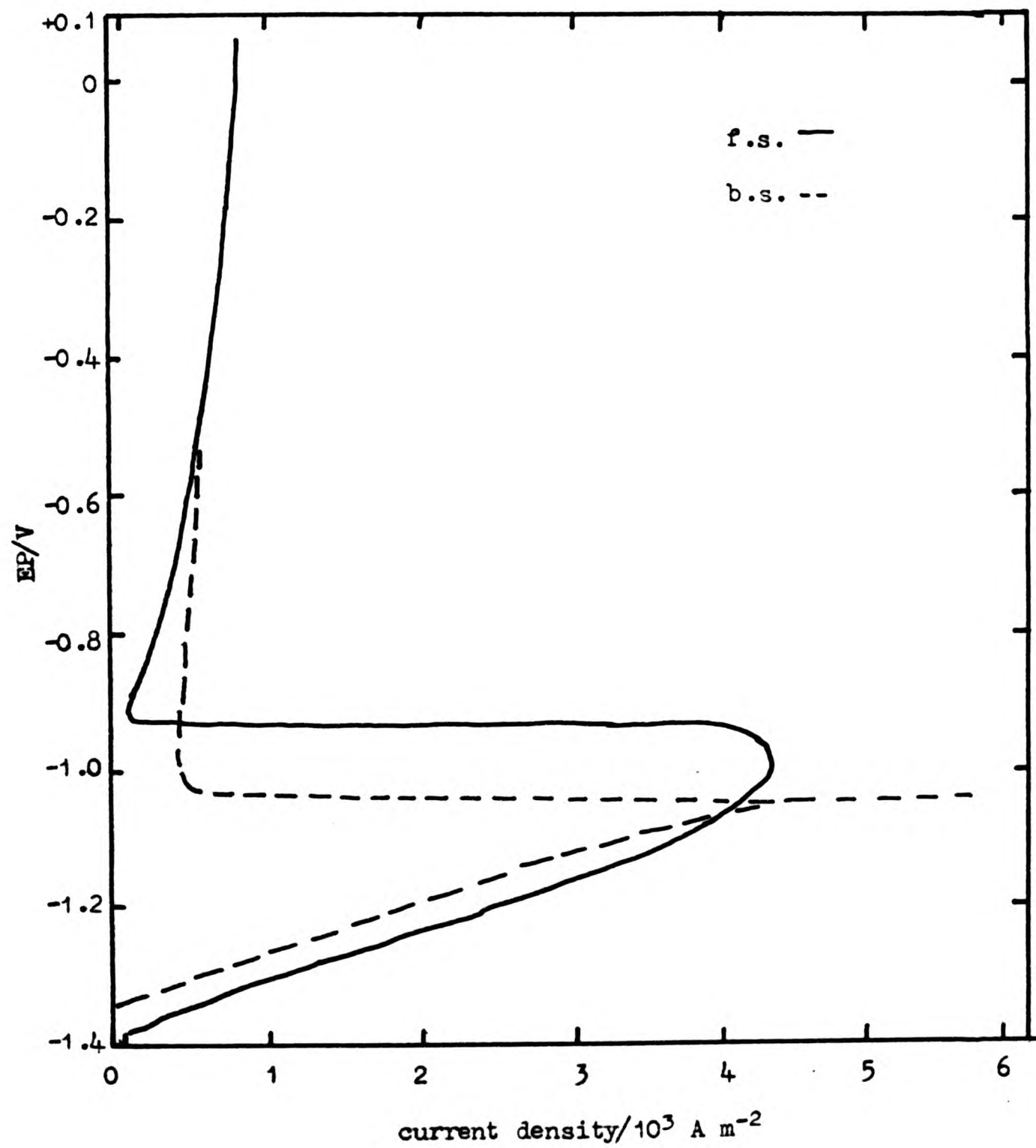


Figure 106. Anodic polarisation curves for Zn-.05 Cd-2.5 Hg alloy in ZnO saturated 6 mol dm⁻³ KOH on a stationary electrode.

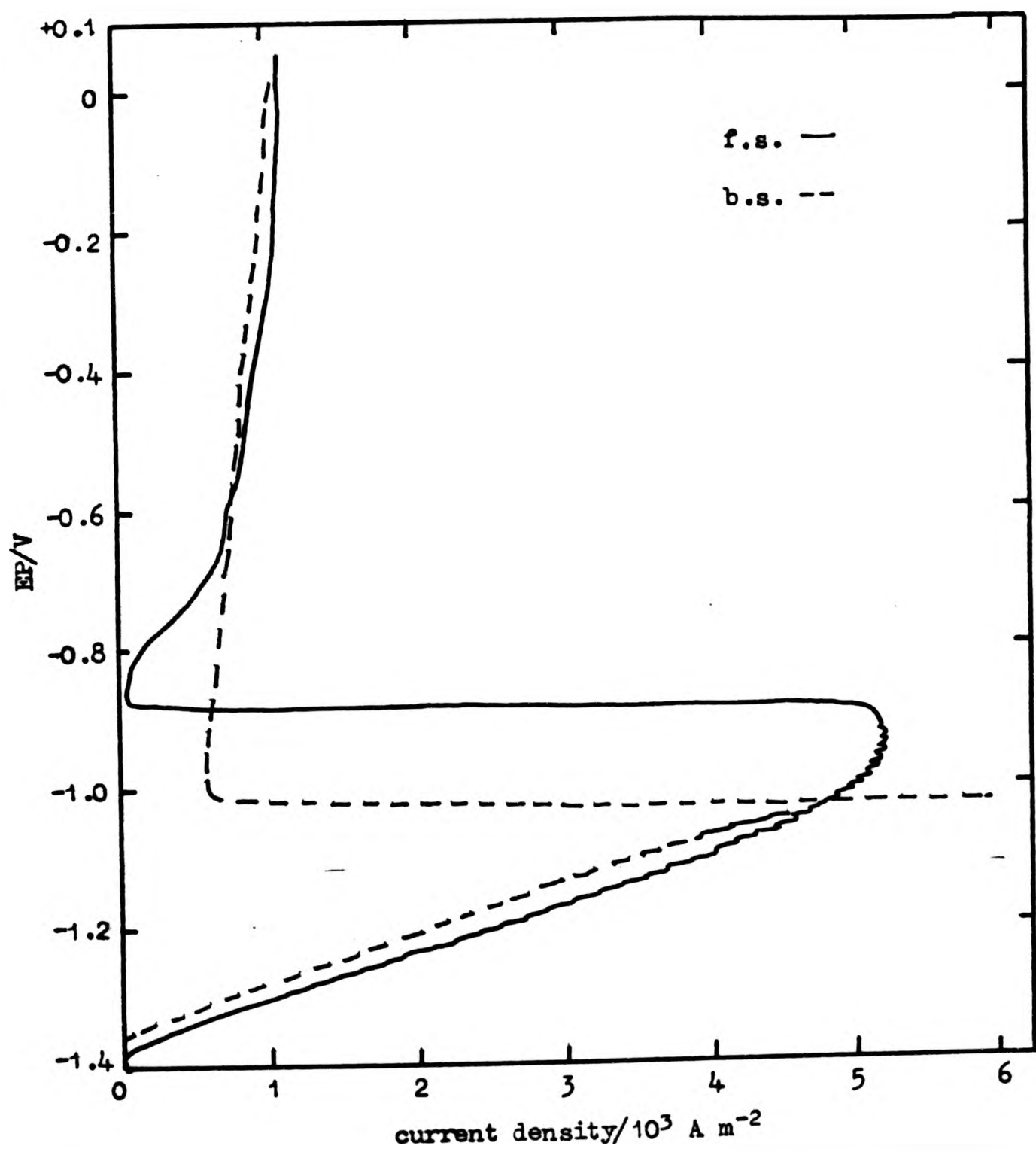


Figure 107. Anodic polarisation curves for Zn-.05 Cd-2.5 Hg alloy in ZnO saturated 6 mol dm⁻³ KOH at 10 rad s⁻¹ rotation speed.

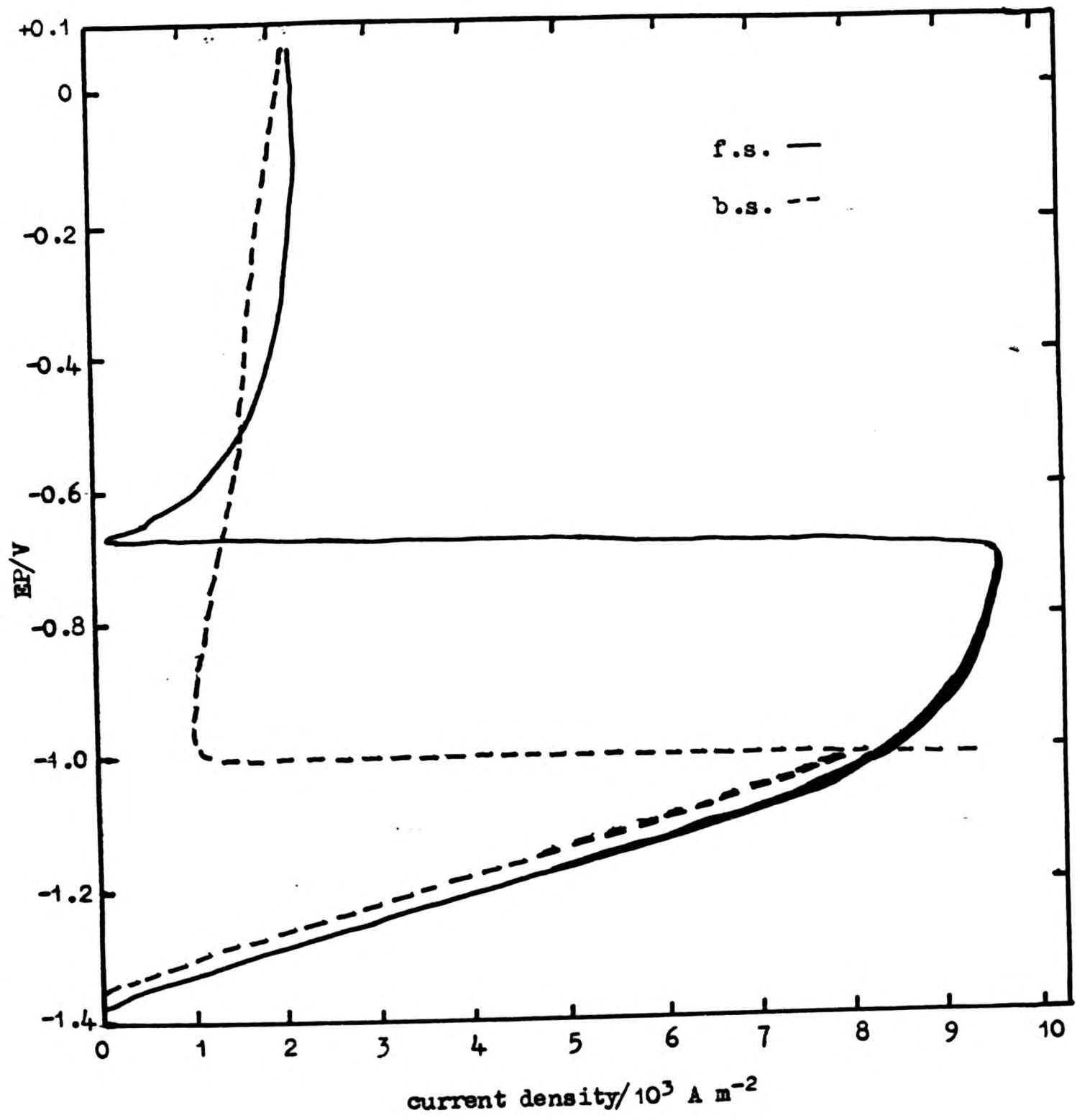


Figure 108. Anodic polarisation curves for Zn-.05 Cd-2.5 Hg alloy in ZnO saturated 6 mol dm⁻³ KOH at 50 rad s⁻¹ rotation speed.

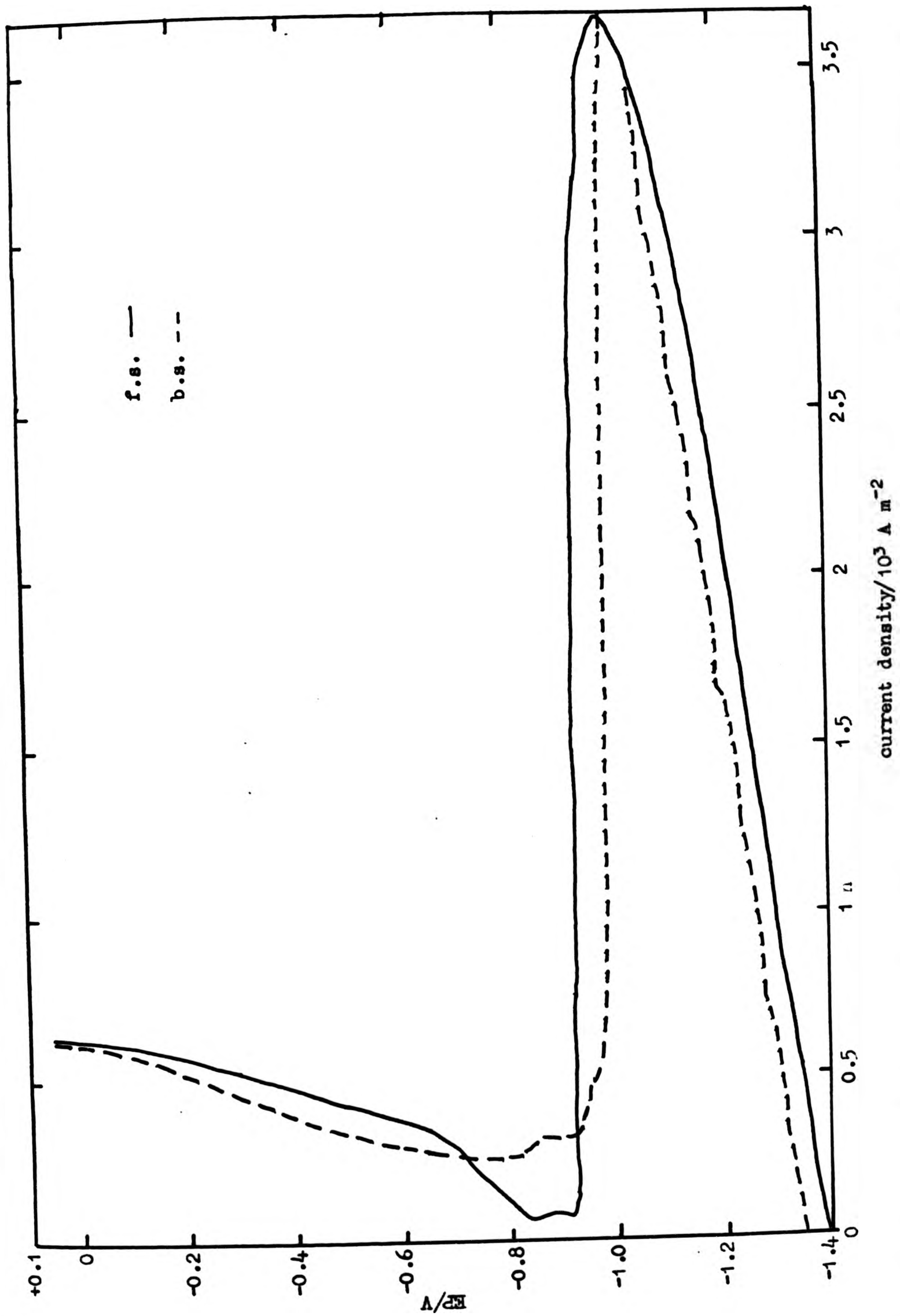


Figure 110. Anodic polarisation curves for Zn-0.2 Cd-2.5 Hg alloy in ZnO saturated 6 mol dm⁻³ KOH on stationary electrode.

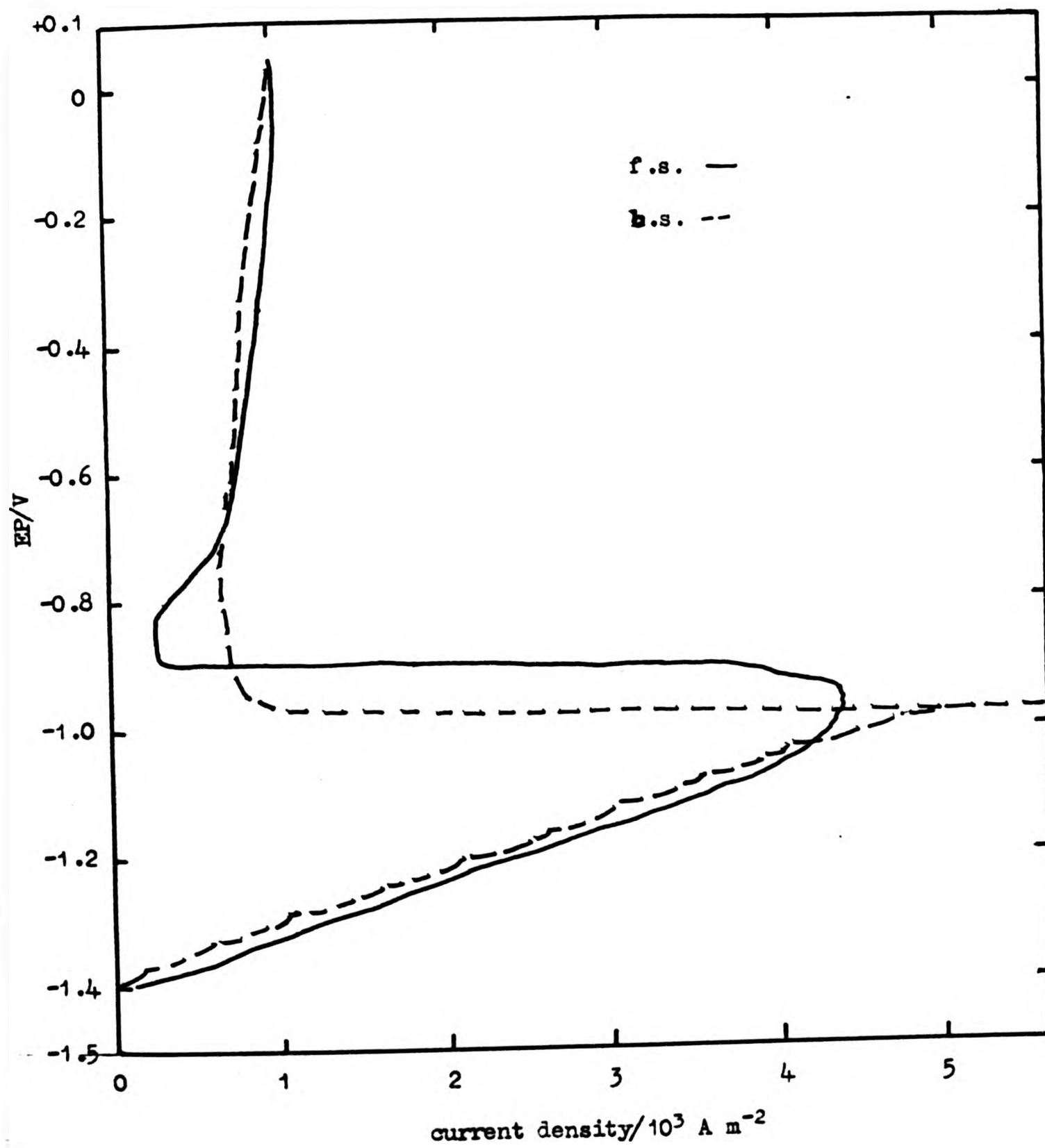


Figure 111. Anodic polarisation curves for Zn-0.2 Cd-2.5 Hg alloy in ZnO saturated 6 mol dm⁻³ KOH at 10 rad s⁻¹ rotation speed.

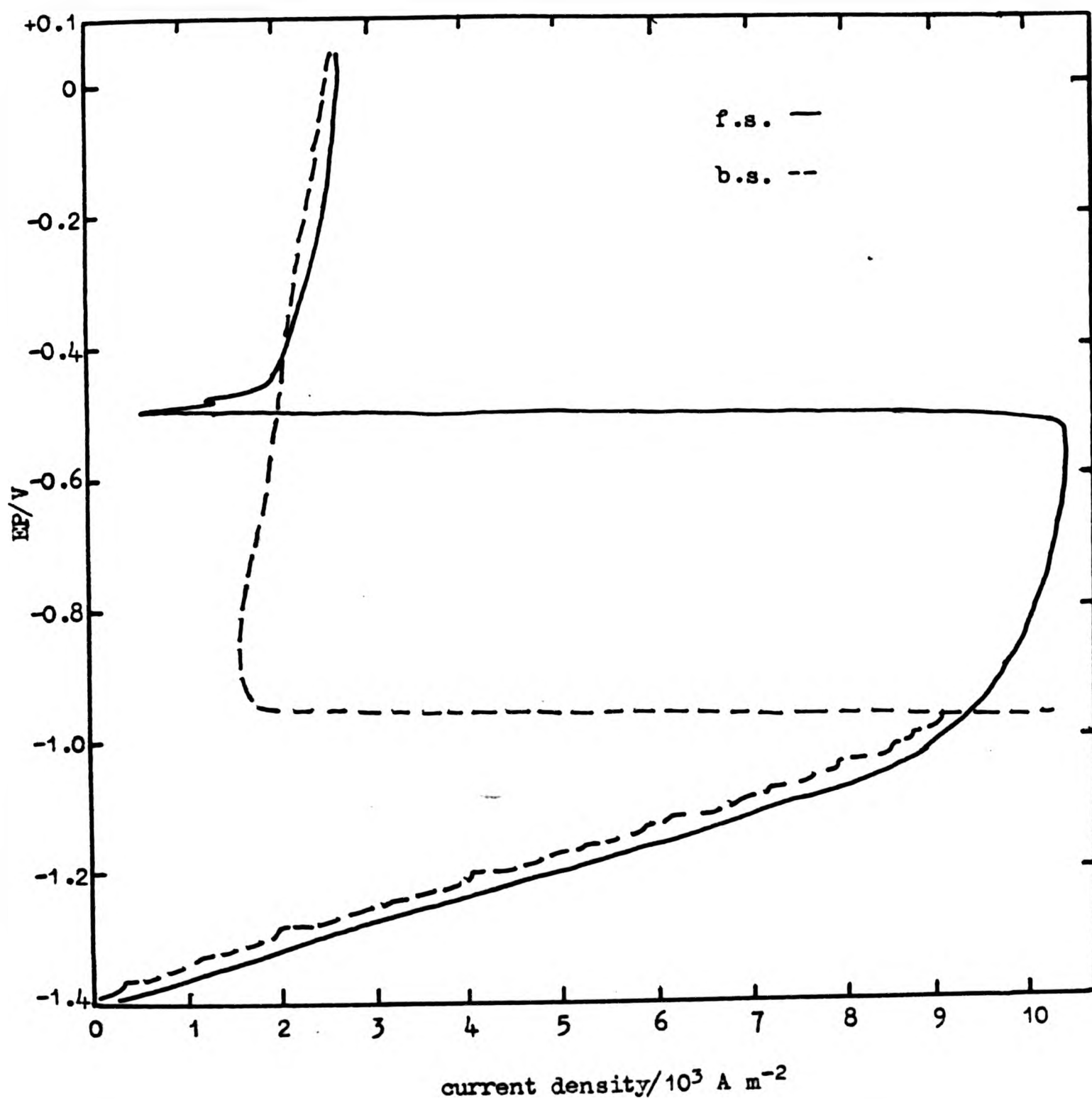


Figure 113. Anodic polarisation curves for Zn-0.2 Cd-2.5 Hg alloy in ZnO saturated 6 mol dm³ KOH at 100 rad s⁻¹ rotation speed.

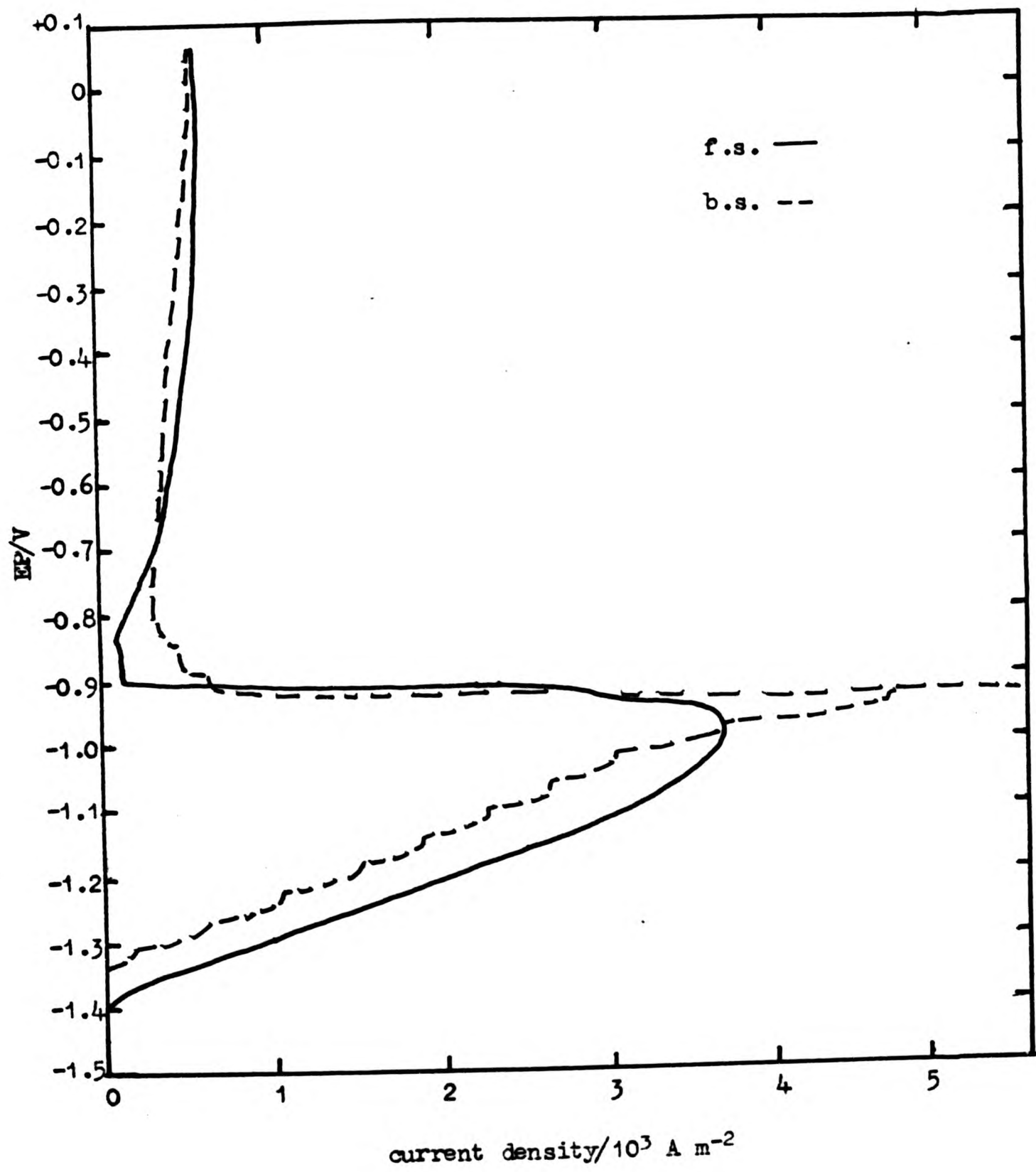


Figure 114. Anodic polarisation curves for Zn-1 Cd-2.5 Hg alloy in ZnO saturated 6 mol dm⁻³ KOH on a stationary electrode.

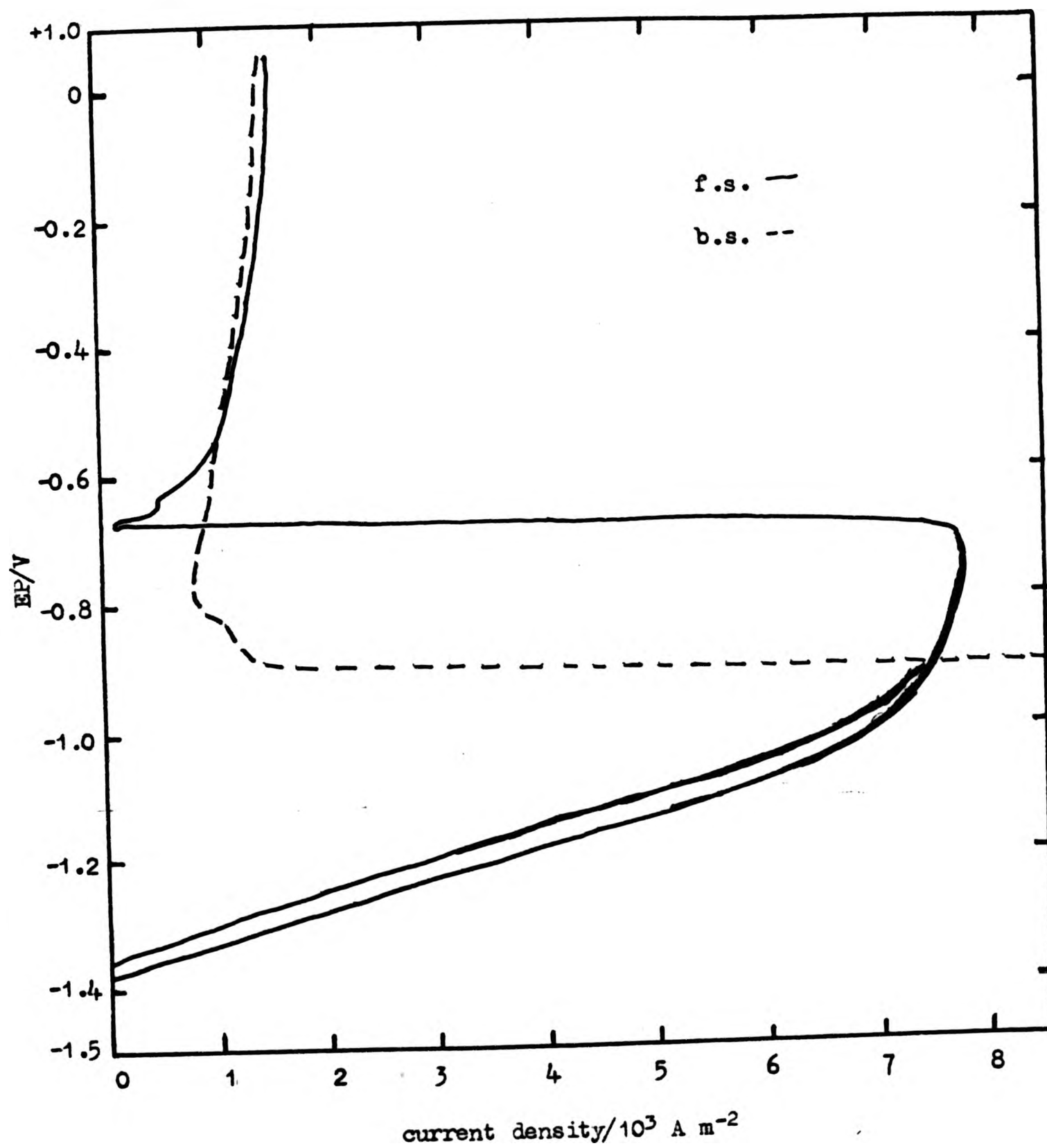


Figure 116. Anodic polarisation curves for Zn-1 Cd-2.5 Hg alloy in ZnO saturated 6 mol dm^{-3} KOH at 50 rad s^{-1} rotation speed.

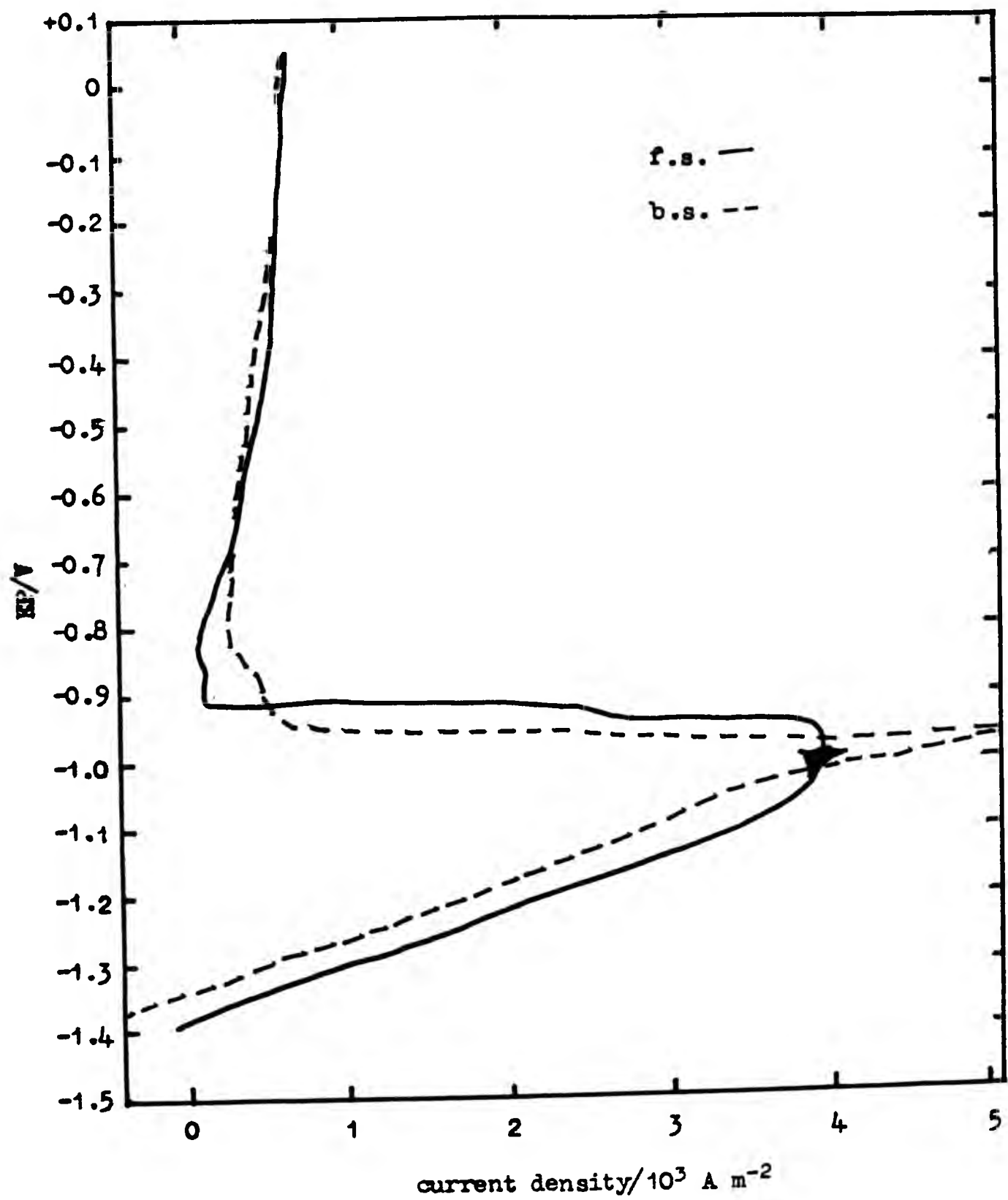


Figure 118. Anodic polarisation curves for Zn-2 Cd-2.5 Hg alloy in ZnO saturated 6 mol dm⁻³ KOH on a stationary electrode.

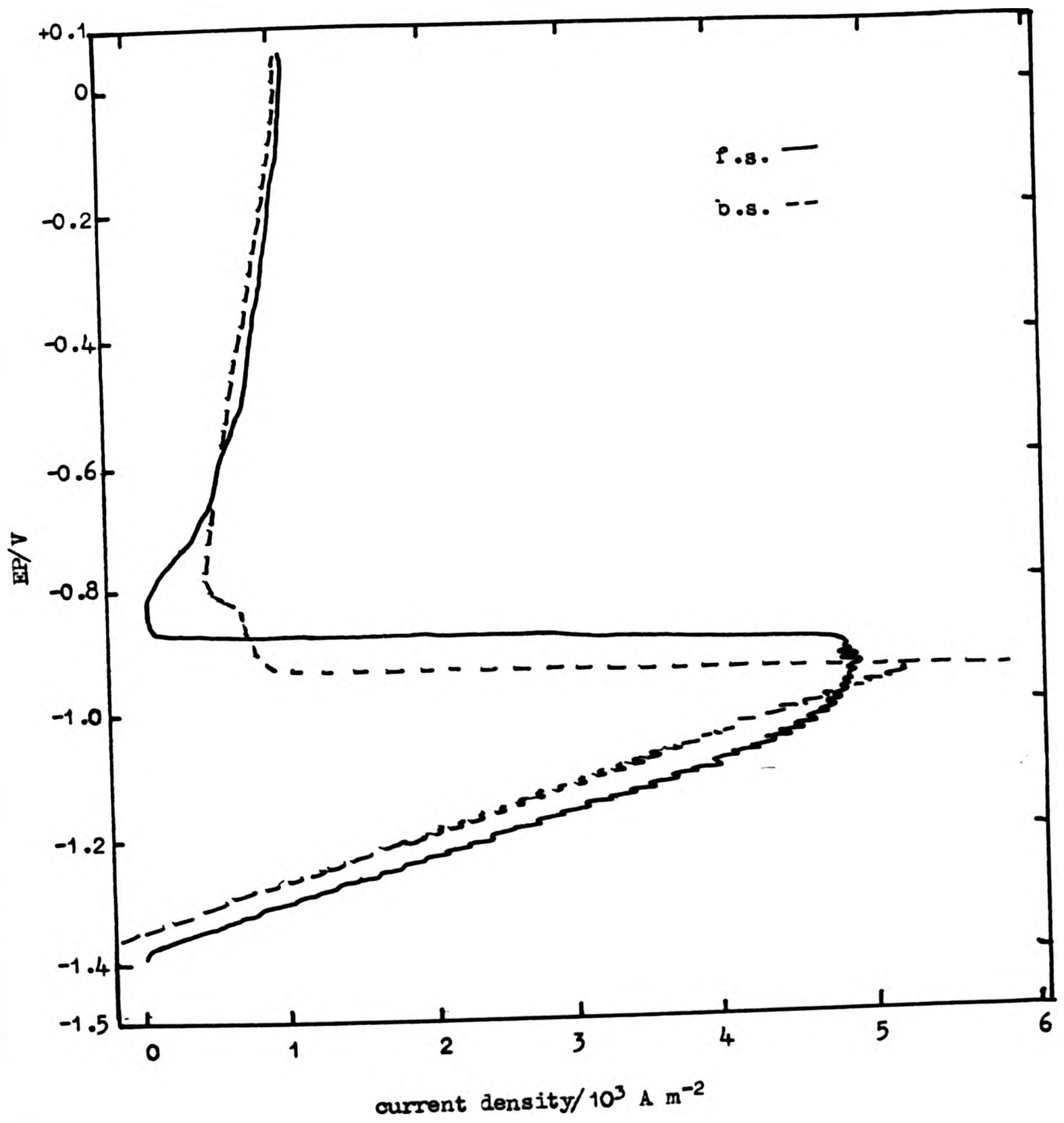


Figure 119. Anodic polarisation curves for Zn-2 Cd-2.5 Hg alloy in ZnO saturated 6 mol dm⁻³ KOH at 10 rad s⁻¹ rotation speed.

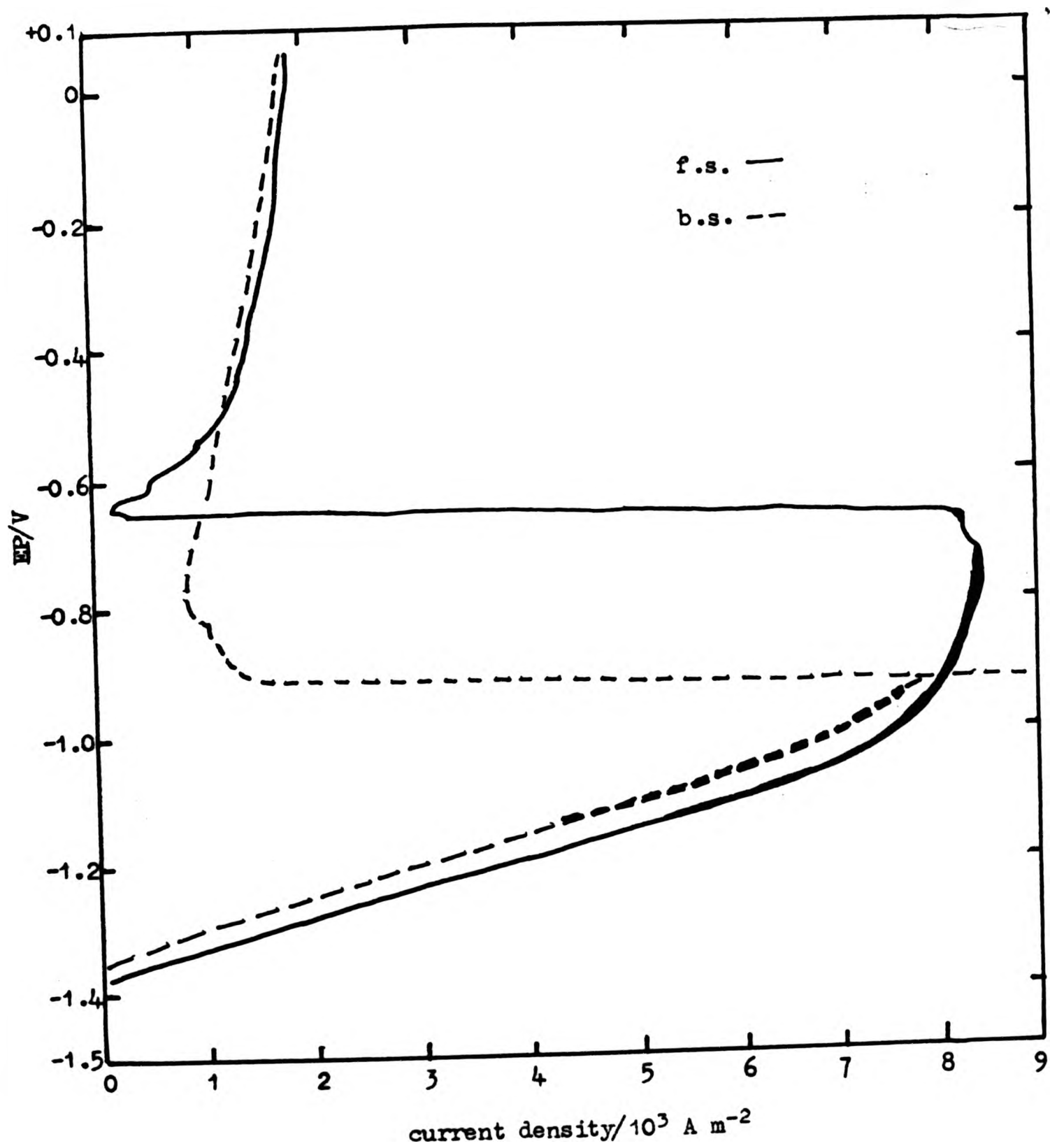


Figure 120. Anodic polarisation curves for Zn-2 Cd-2.5 Hg alloy in ZnO saturated 6 mol dm^{-3} KOH at 50 rad s^{-1} rotation speed.

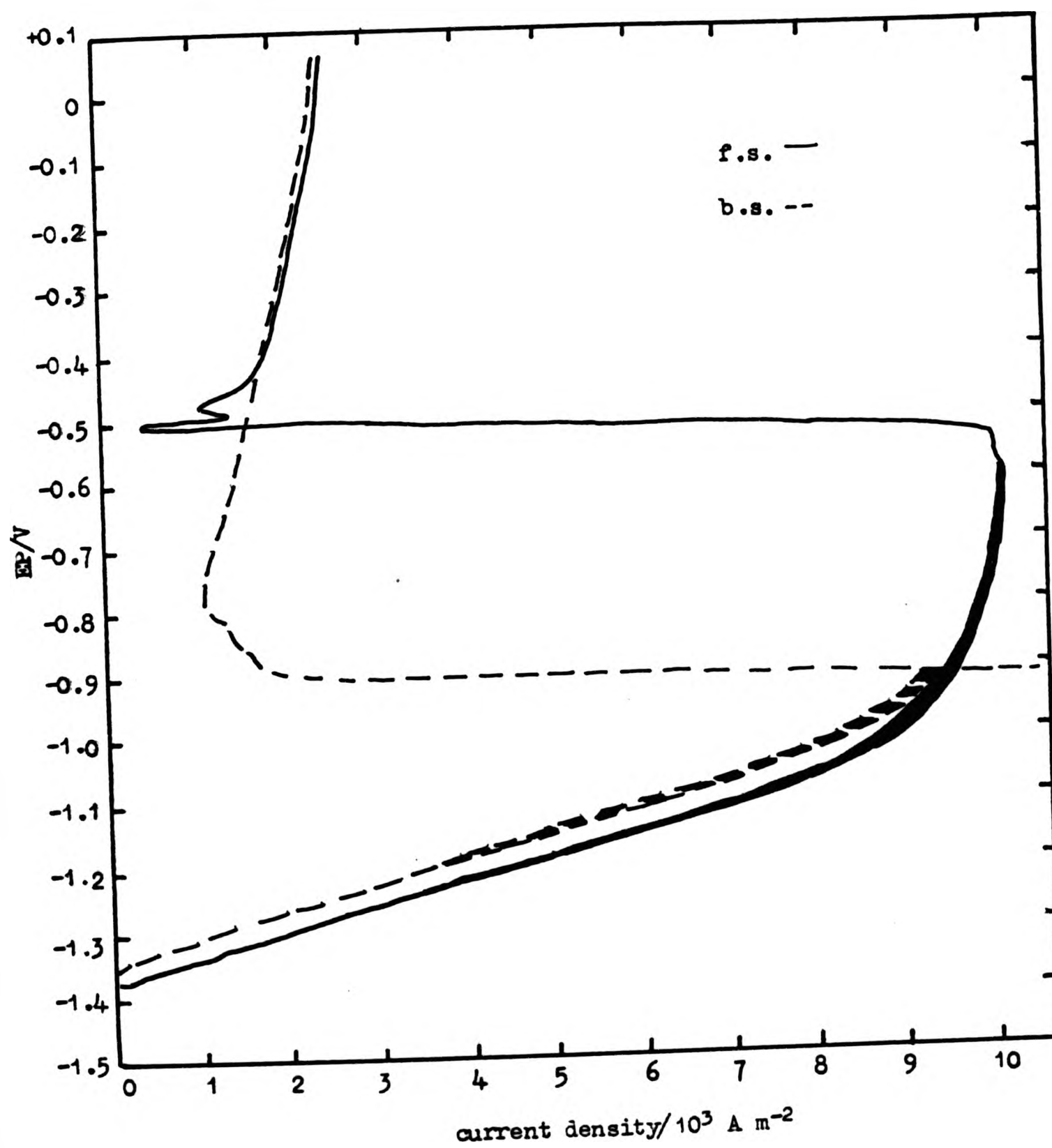


Figure 121. Anodic polarisation curves for Zn-2 Cd-2.5 Hg alloy in ZnO saturated 6 mol dm⁻³ KOH at 100 rad s⁻¹ rotation speed.

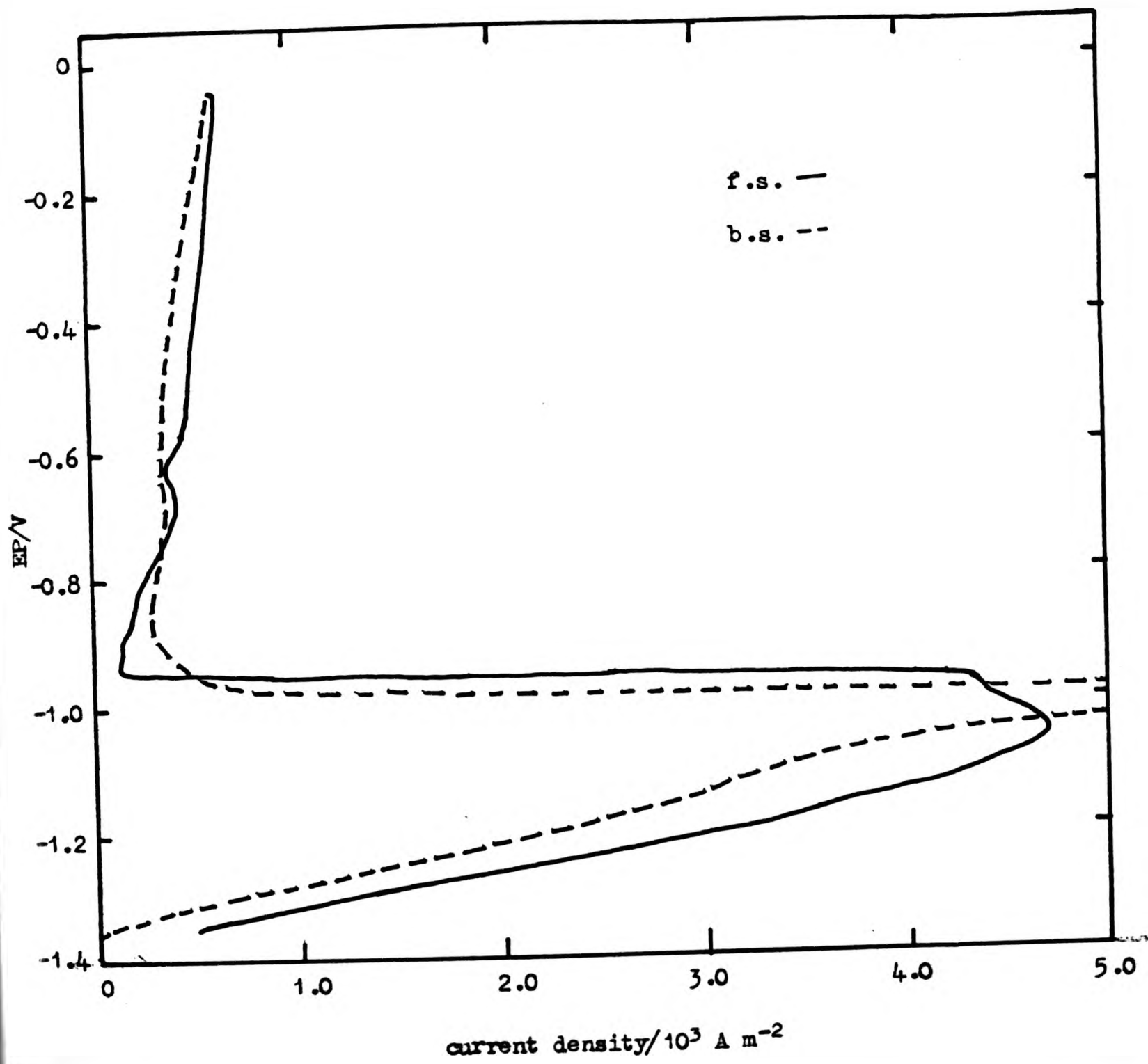


Figure 122. Anodic polarisation curves for Zn-5 Cd-2.5 Hg alloy in ZnO saturated 6 mol dm⁻³ KOH on a stationary electrode.

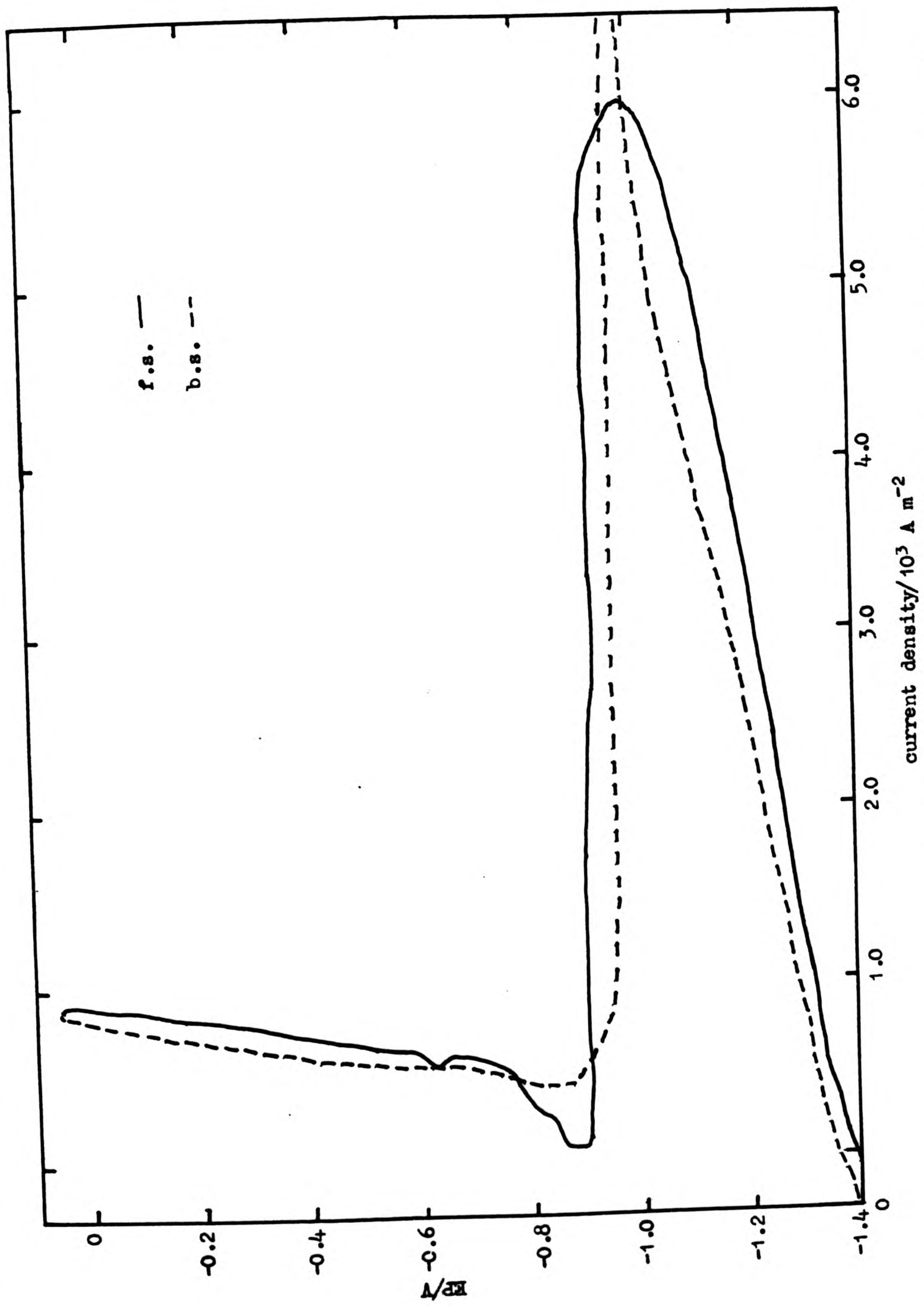


Figure 123. Anodic polarisation curves for Zn-5 Cd-2.5 Hg alloy in ZnO saturated 6 mol dm⁻³ KOH at 10 rad s⁻¹ rotation speed.

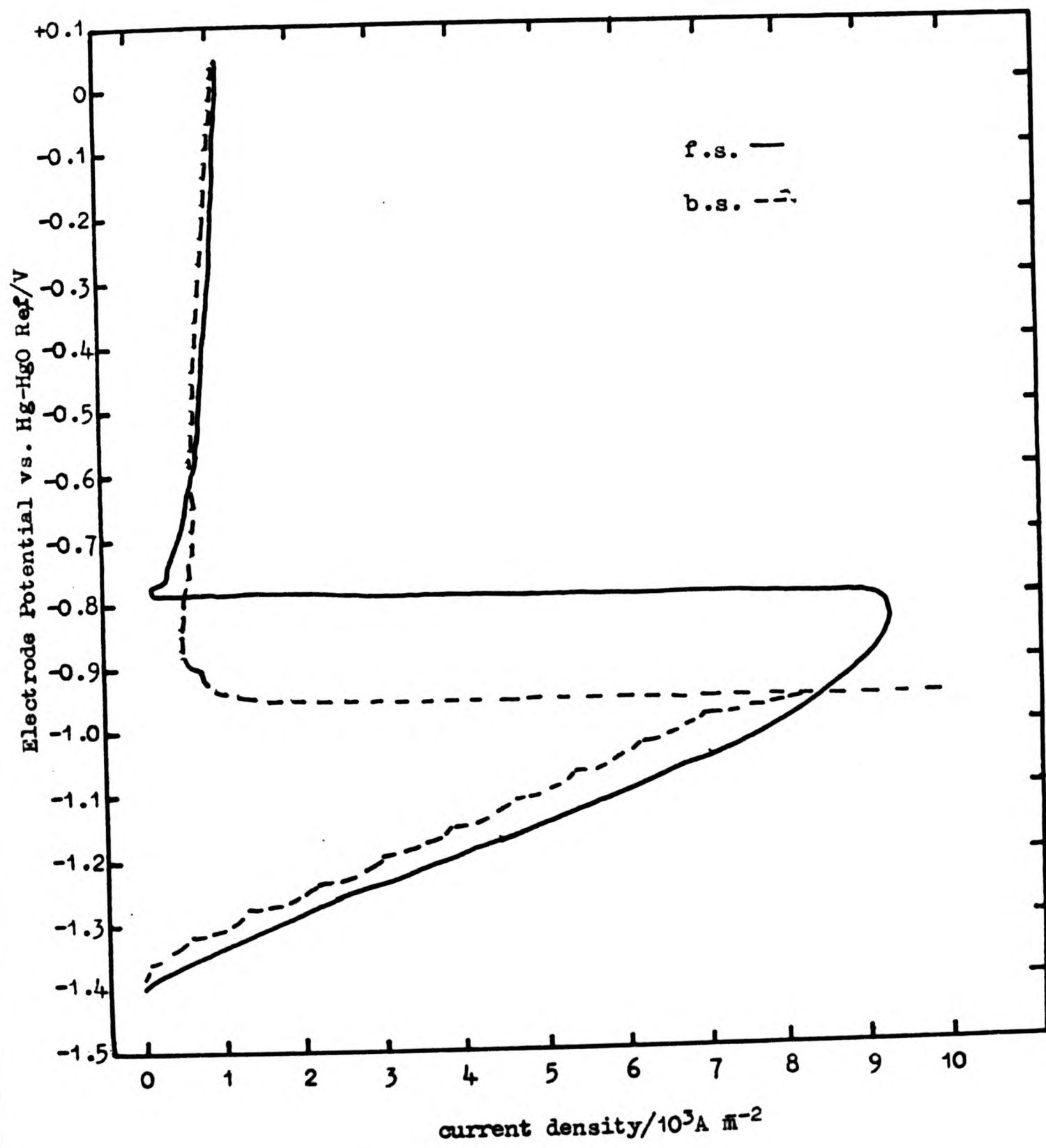


Figure 124. Anodic polarisation curves for Zn-5 Cd-2.5 Hg alloy in ZnO saturated 6 mol dm⁻³ KOH at 50 rad s⁻¹ rotation speed.

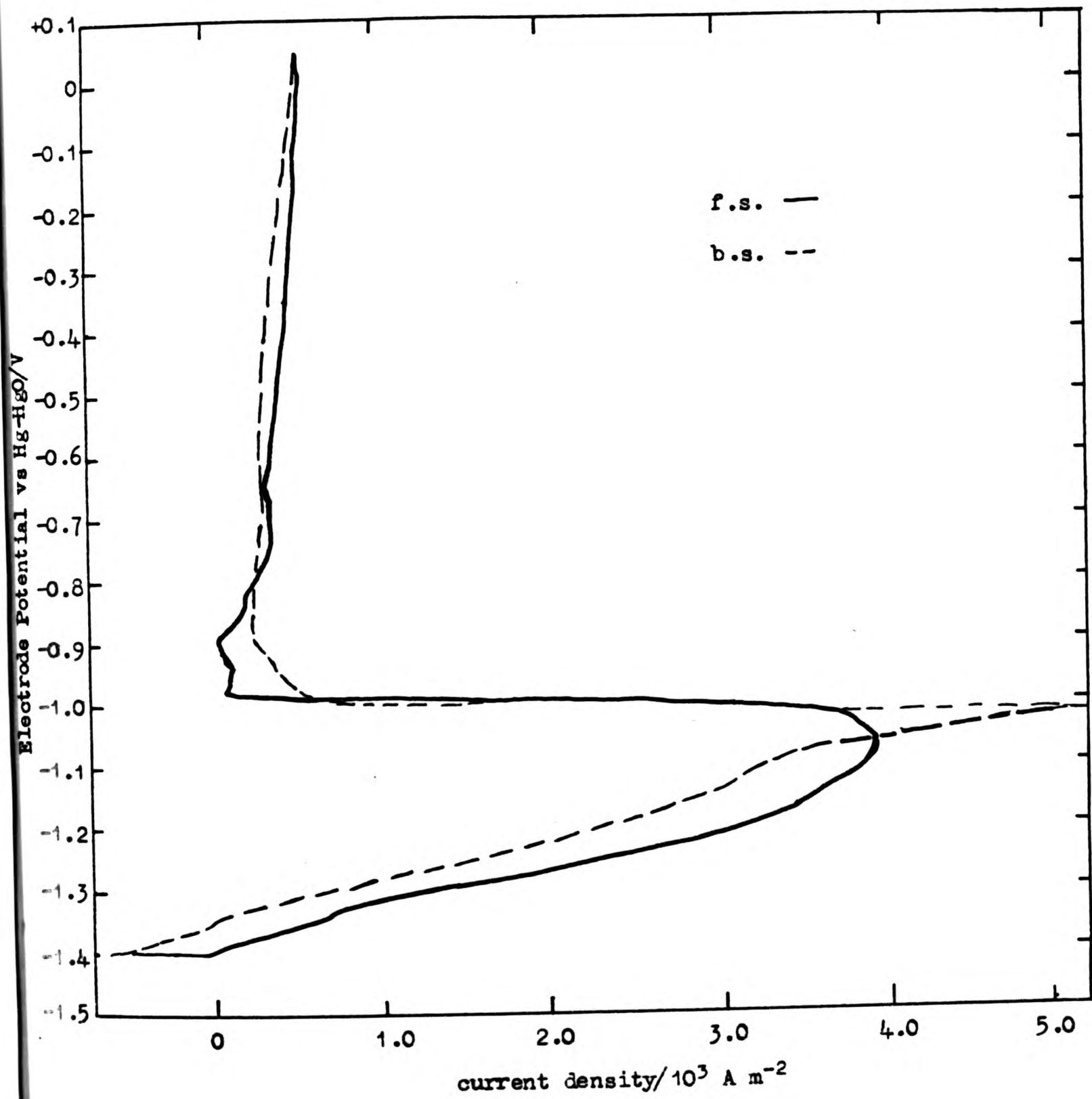


Figure 126. Anodic polarisation curves for Zn-10 Cd-2.5 Hg alloy in ZnO saturated 6 mol dm⁻³ KOH on a stationary electrode.

**TIGHTLY
BOUND
COPY**

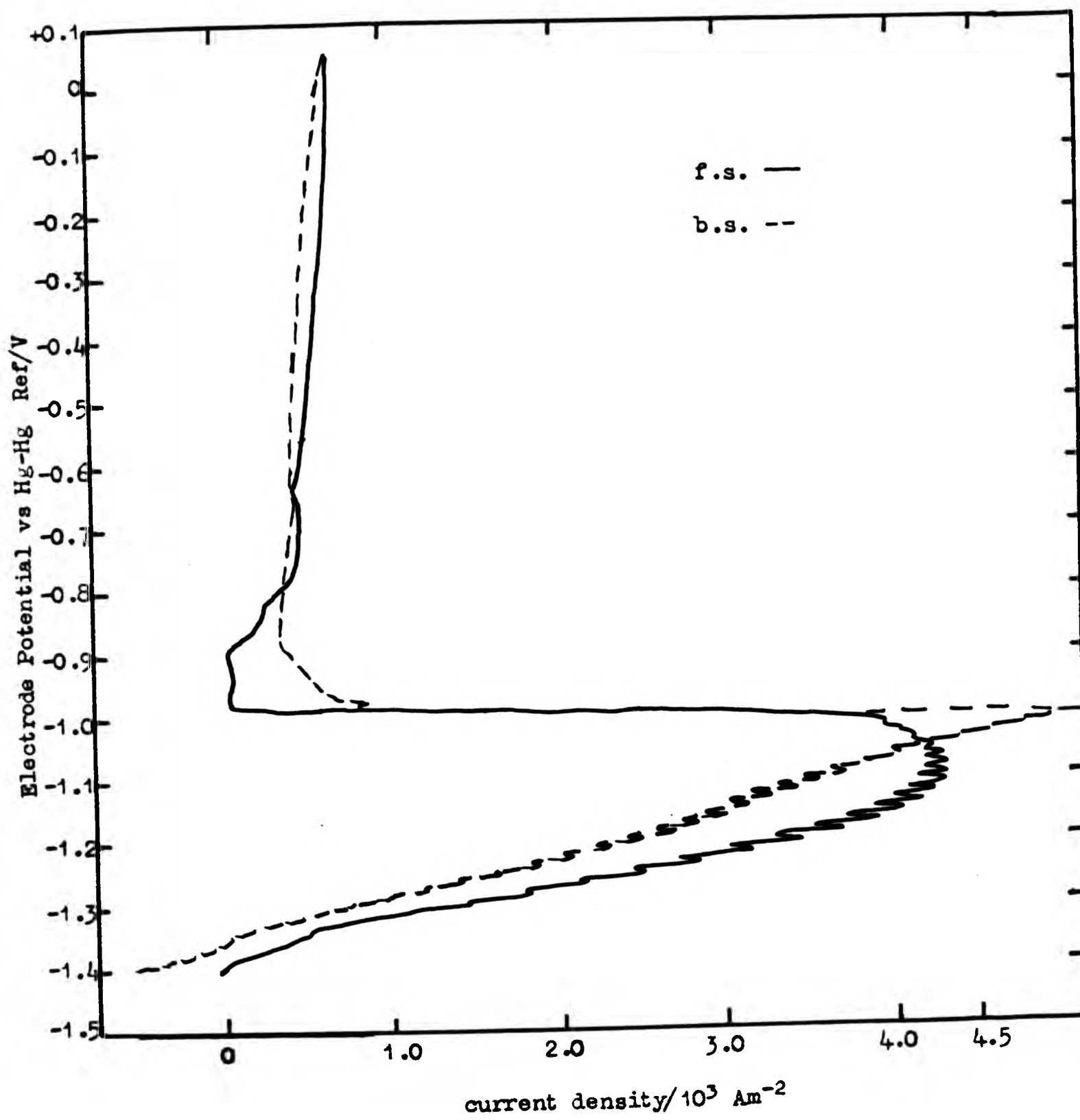


Figure 127. Anodic polarisation curves for Zn-10 Cd-2.5 Hg alloy in ZnO saturated 6 mol dm⁻³ KOH at 10 rad s⁻¹ rotation speed.

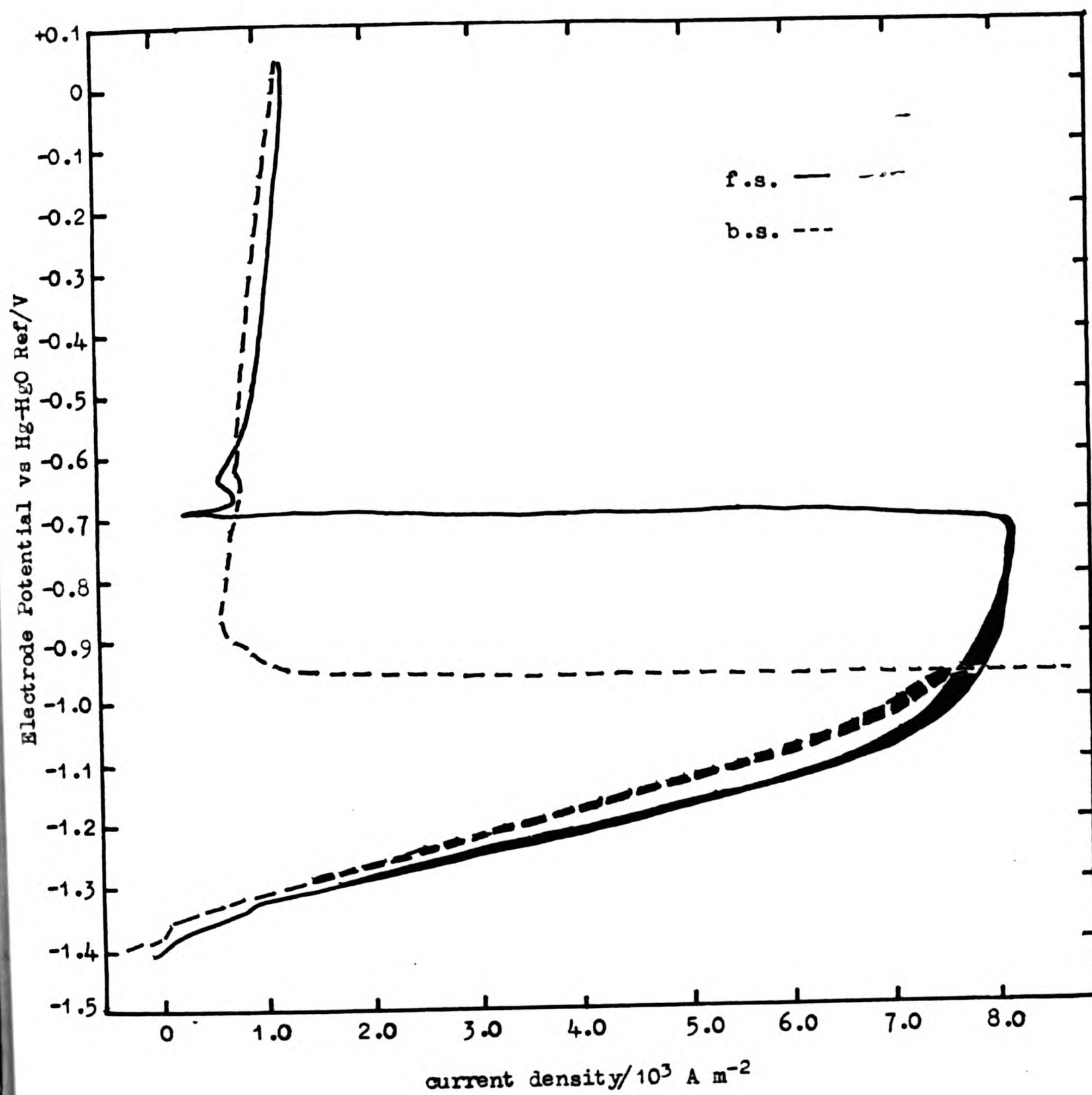


Figure 129. Anodic polarisation curves for Zn-10 Cd-2.5 Hg alloy in ZnO saturated 6 mol dm⁻³ KOH at 100 rad s⁻¹ rotation speed.

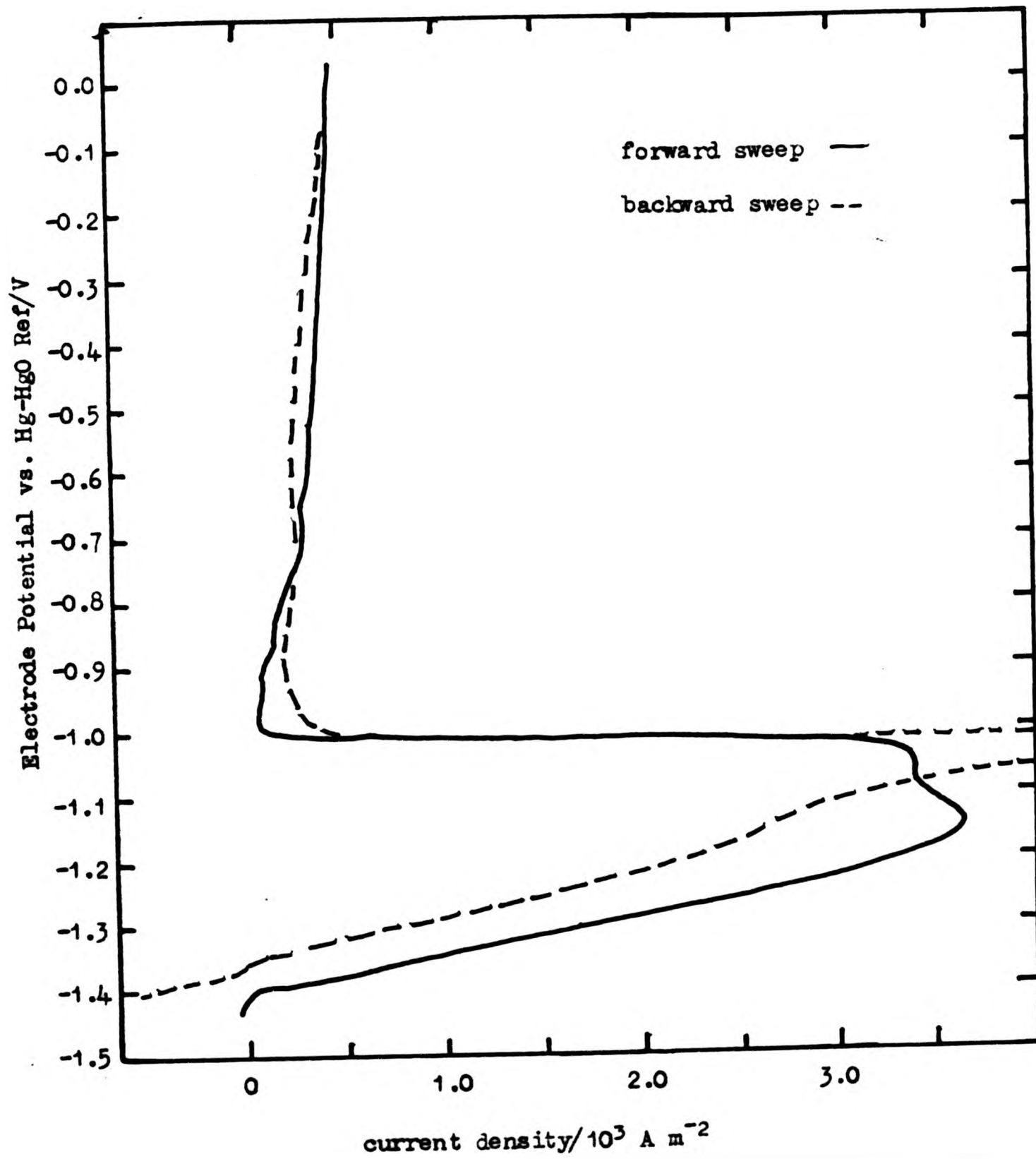


Figure 130. Anodic polarisation curves for Zn-2.5 Cd-2.5 Hg alloy in ZnO saturated 6 mol dm⁻³ KOH on a stationary electrode.

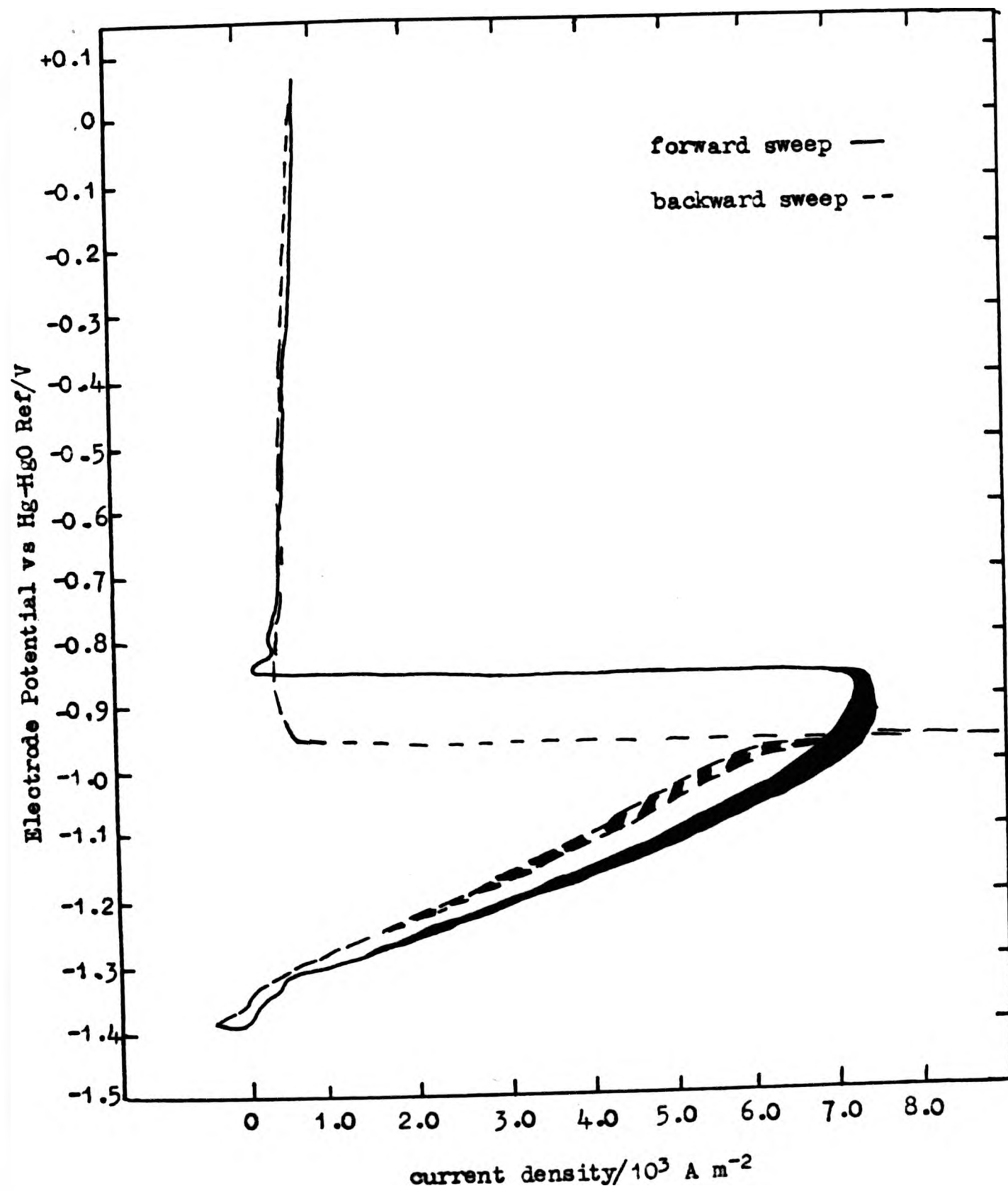


Figure 132. Anodic polarisation curves for Zn-25 Cd-2.5 Hg alloy in ZnO saturated 6 mol dm⁻³ KOH at 50 rad s⁻¹ rotation speed.

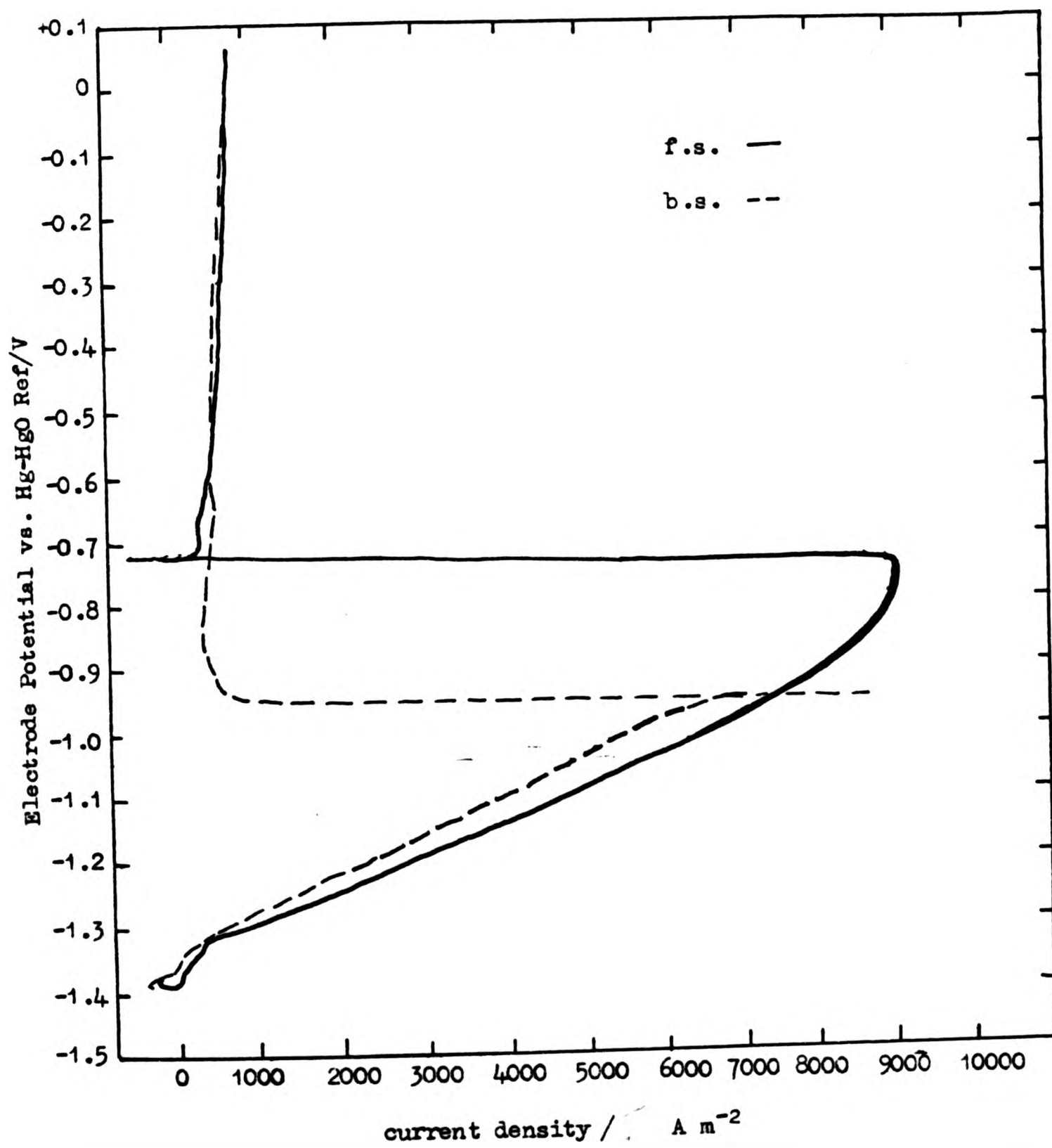


Figure 133. Anodic polarisation curves for Zn-25Cd-2.5 Hg alloy in ZnO saturated 6 mol dm⁻³ KOH at 100 rad s⁻¹ rotation speed.

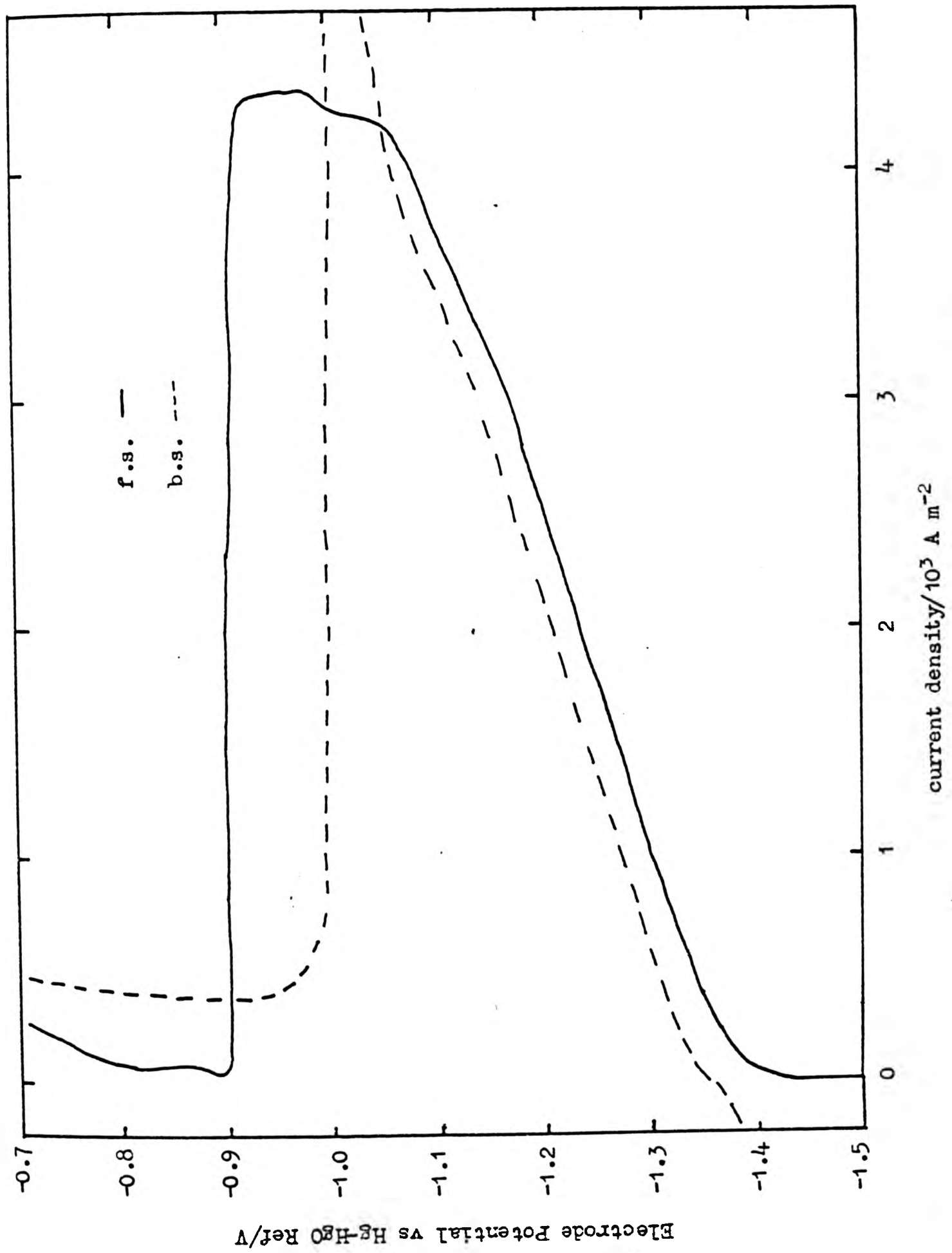


Figure 134. Anodic polarisation curves for Zn-0.05 Cd alloy in 6 mol dm⁻³ KOH on stationary electrode.

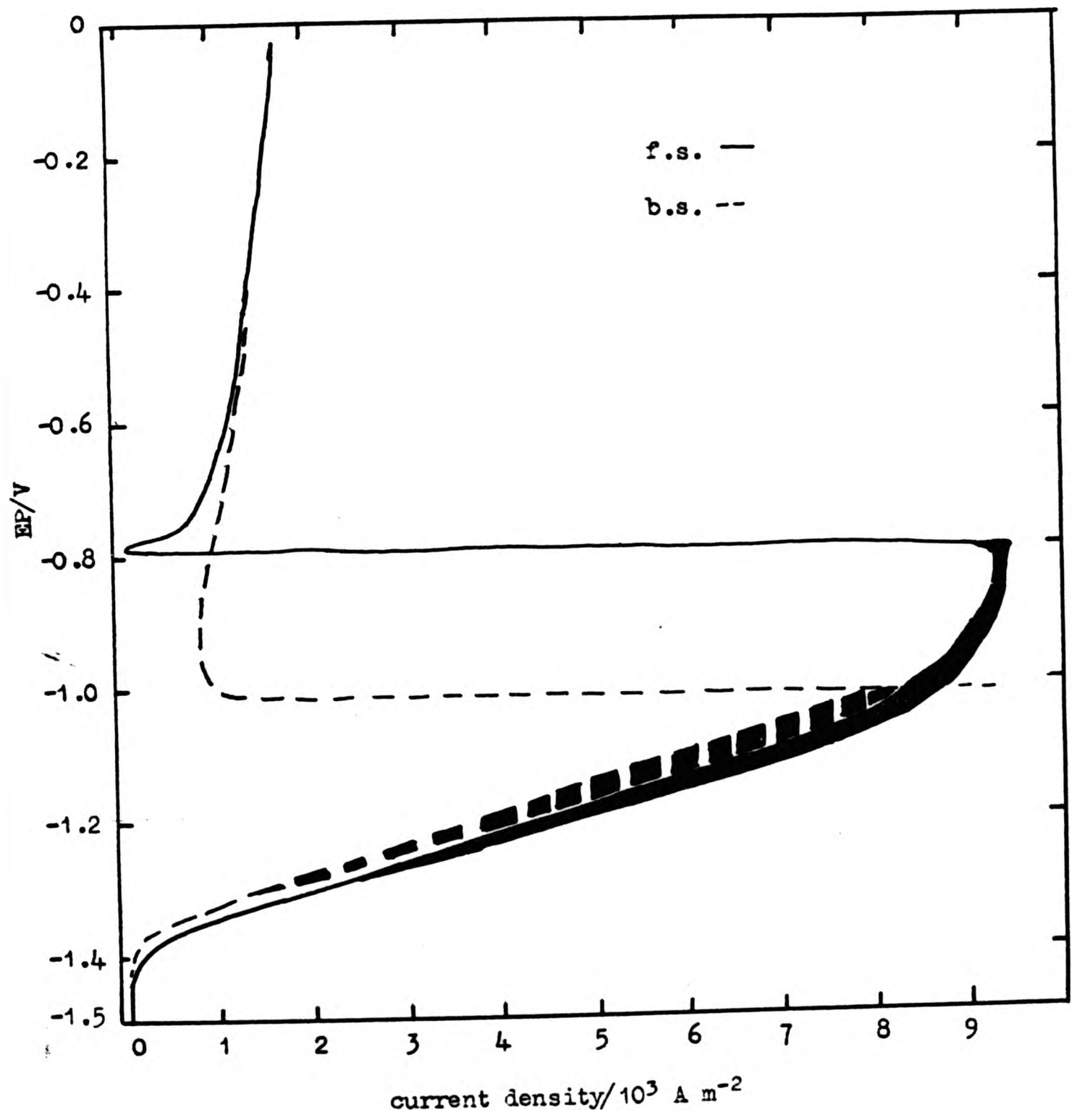


Figure 136. Anodic polarisation curves for Zn-.05 Cd alloy in
6 mol dm⁻³ KOH at 50 rad s⁻¹ rotation speed.

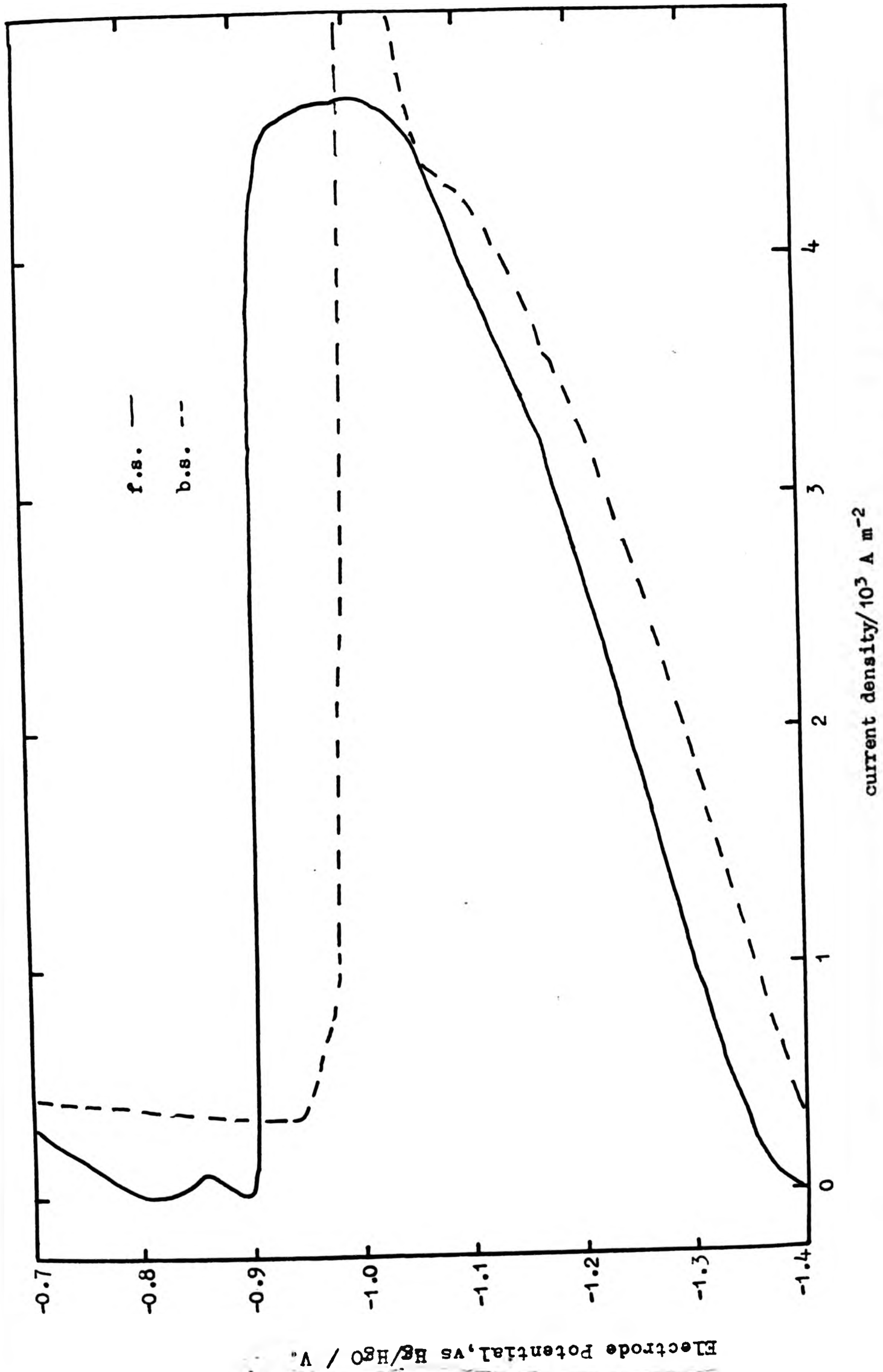


Figure 138. Anodic polarisation curves for Zn-2 Cd alloy in 6 mol dm³ KOH on a stationary electrode.

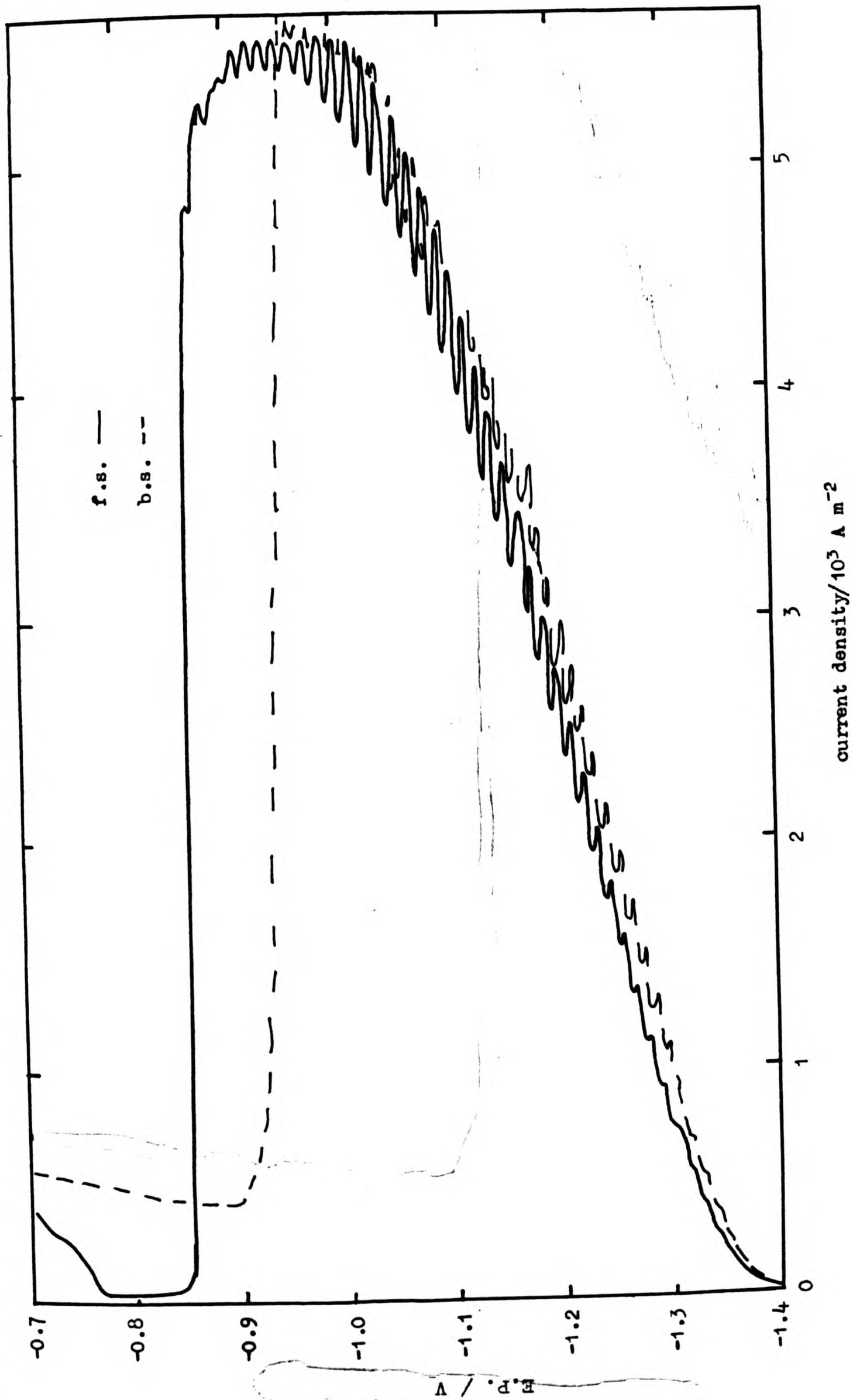


Figure 139. Anodic polarisation curves for Zn-2 Cd alloy in 6 mol dm⁻³ KOH at 10 rad s⁻¹ rotation speed.

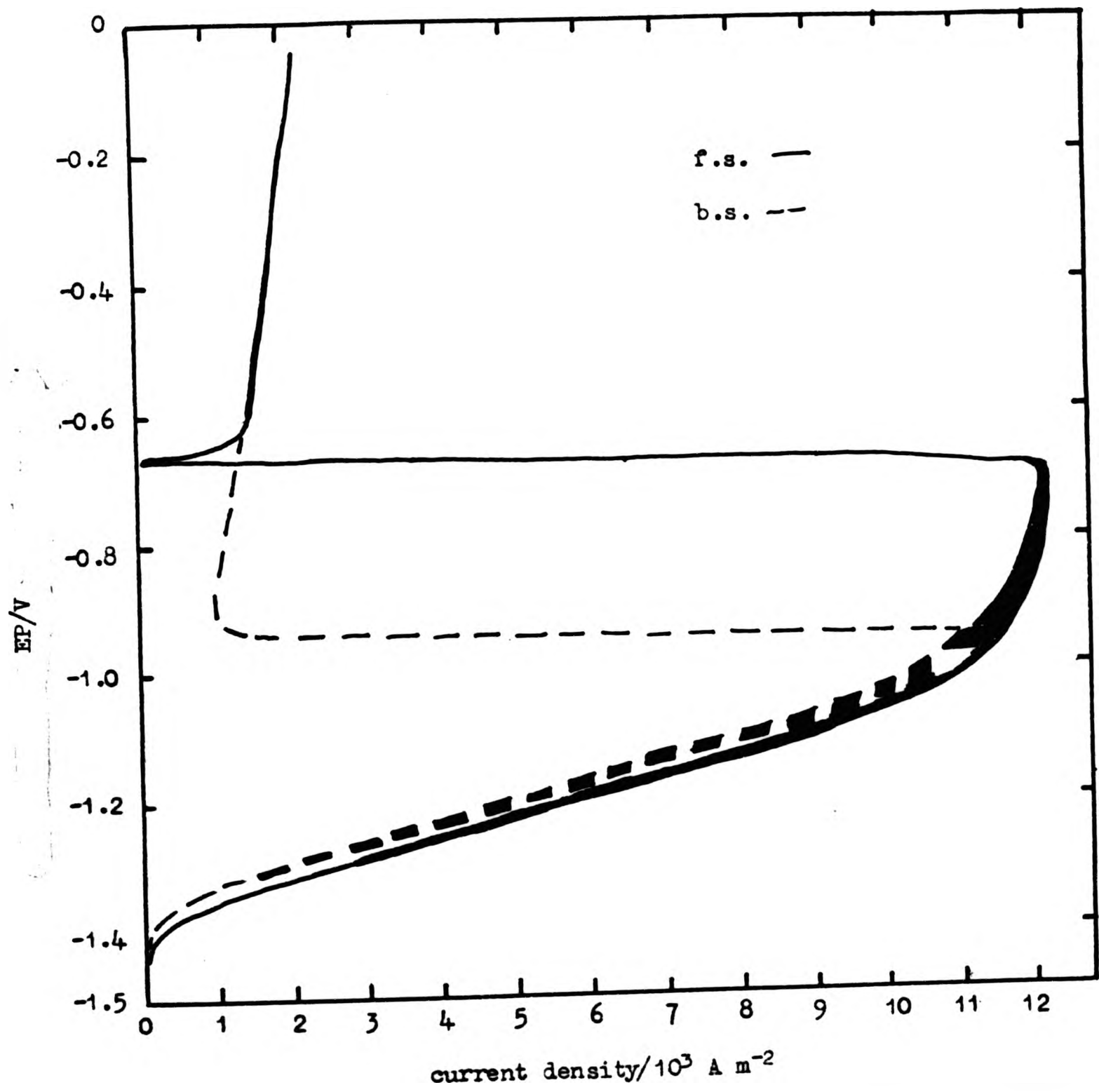


Figure 141. Anodic polarisation curve for Zn-.02Cd alloy in 6 mol dm⁻³ KOH at 100 rad s⁻¹ rotation speed.

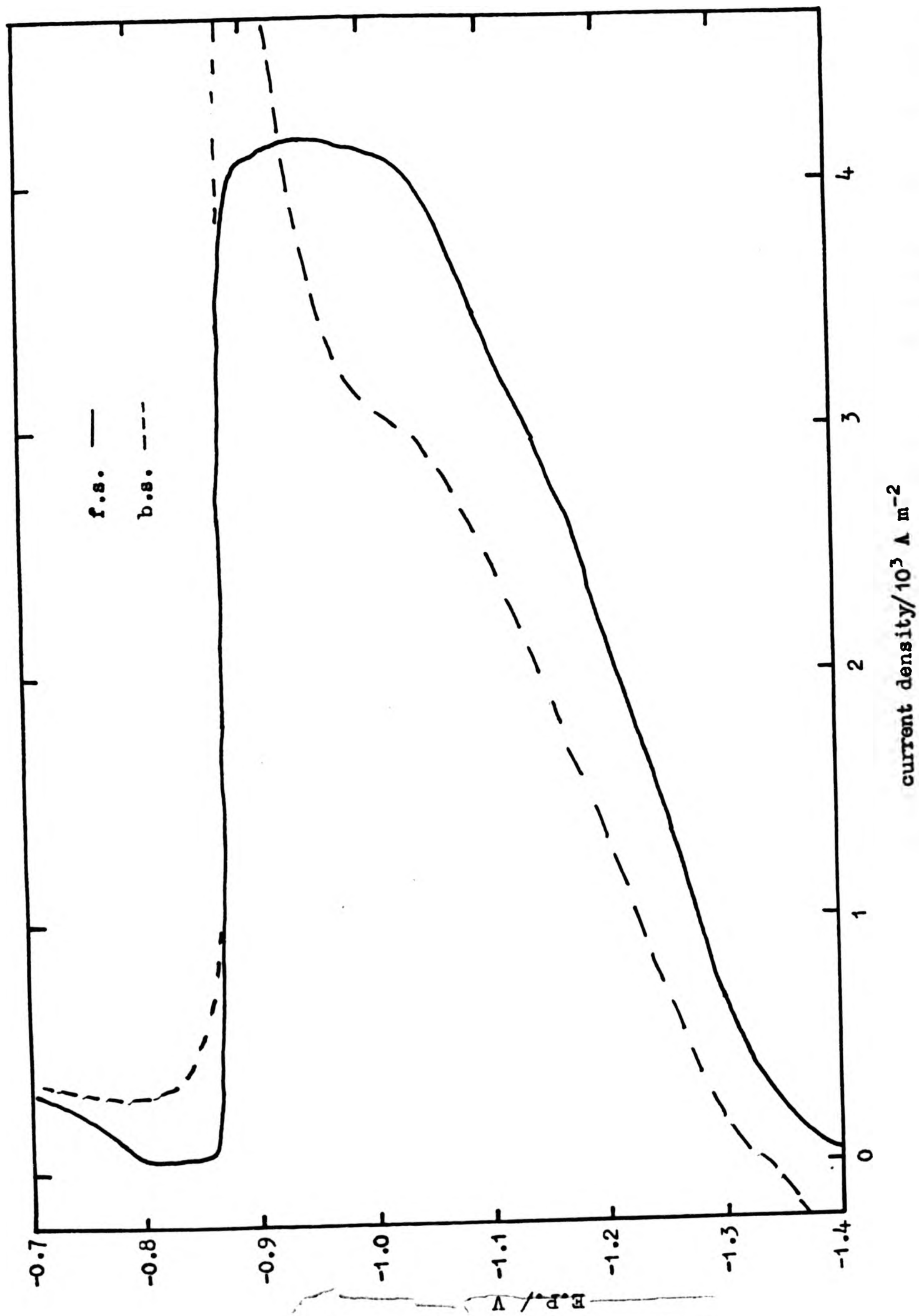


Figure 142. Anodic polarisation curves for Zn-1 Cd alloy in 6 mol dm⁻³ KOH on a stationary electrode.

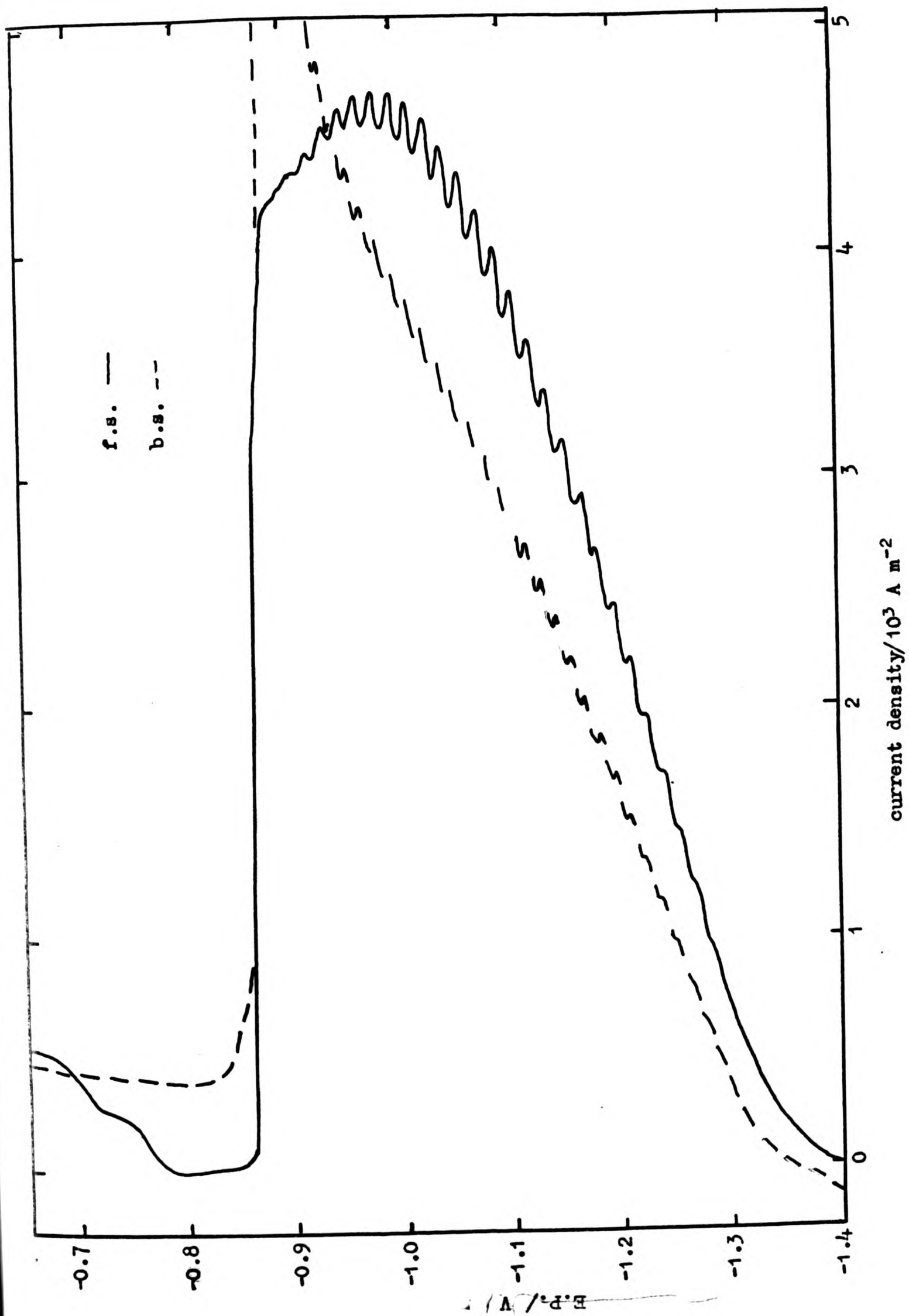


Figure 143. Anodic polarisation curves for Zn-1 Cd alloy in 6 mol dm⁻³ KOH at 10 rad s⁻¹ rotation speed.

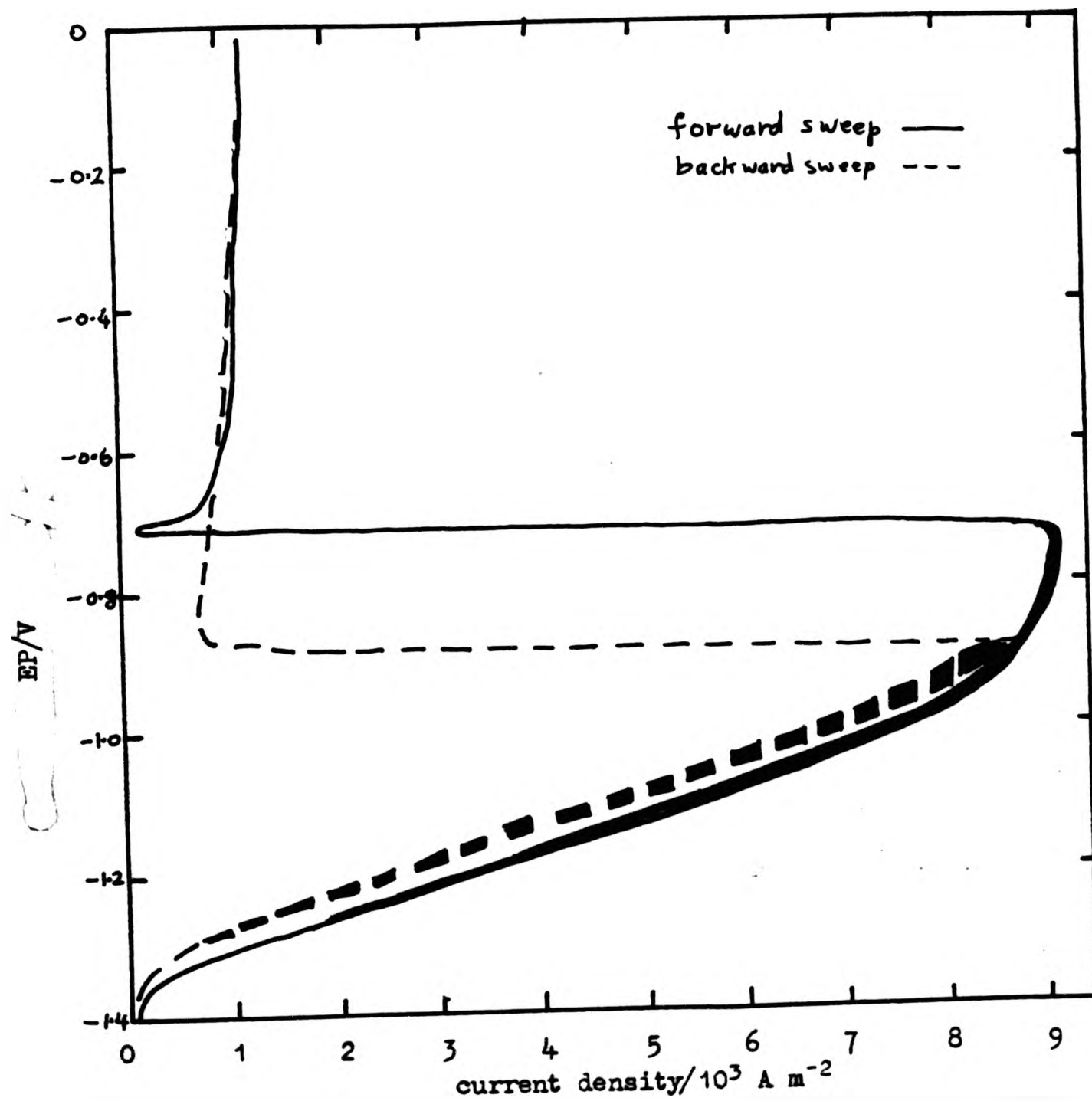


Figure 144. Anodic polarisation curves for Zn-1 Cd alloy in 6 mol dm^{-3} KOH at 50 rad s^{-1} rotation speed.

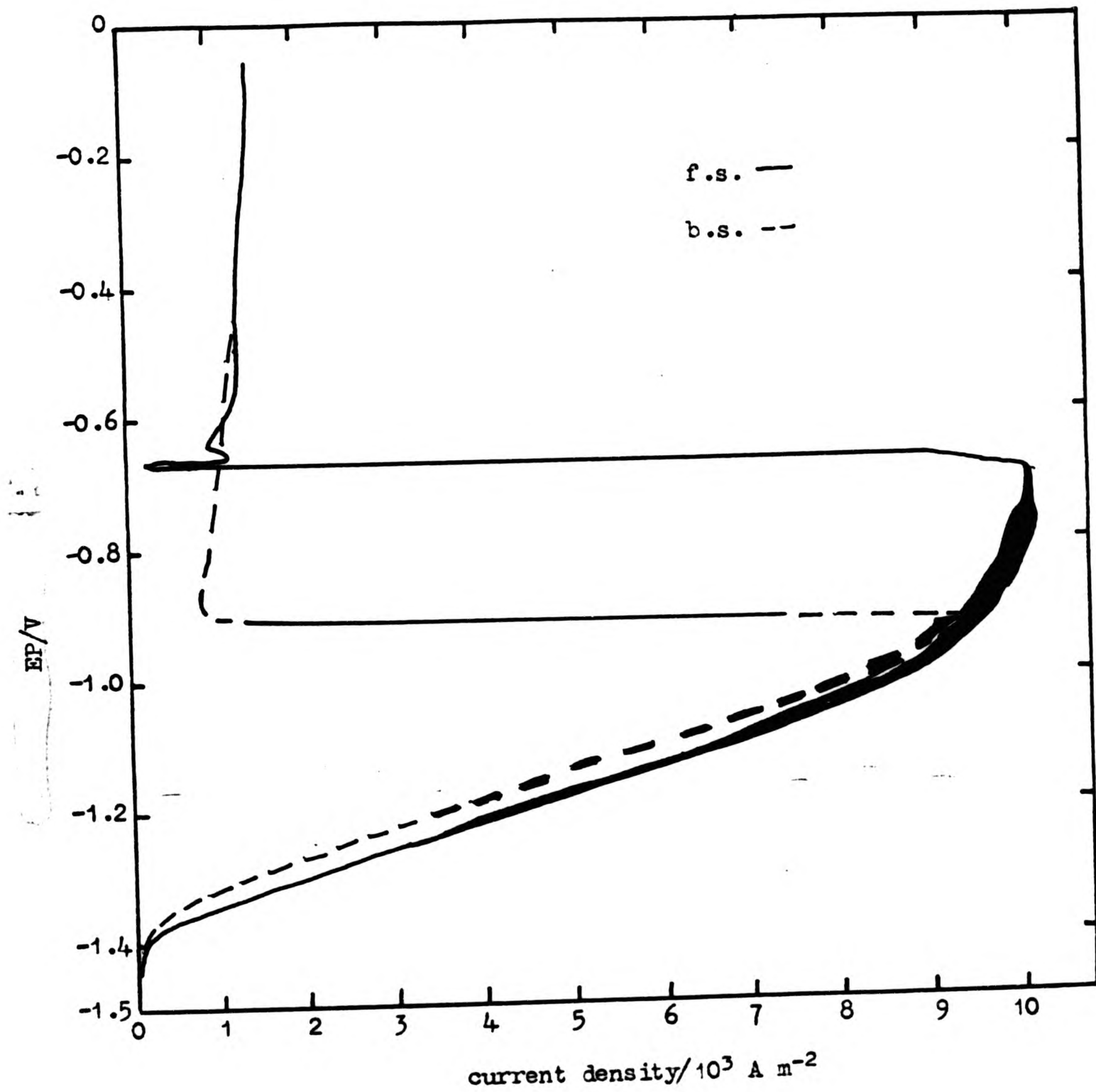


Figure 145. Anodic polarisation curves for Zn-1 Cd alloy in 6 mol dm^{-3} KOH at 100 rad s^{-1} rotation speed.

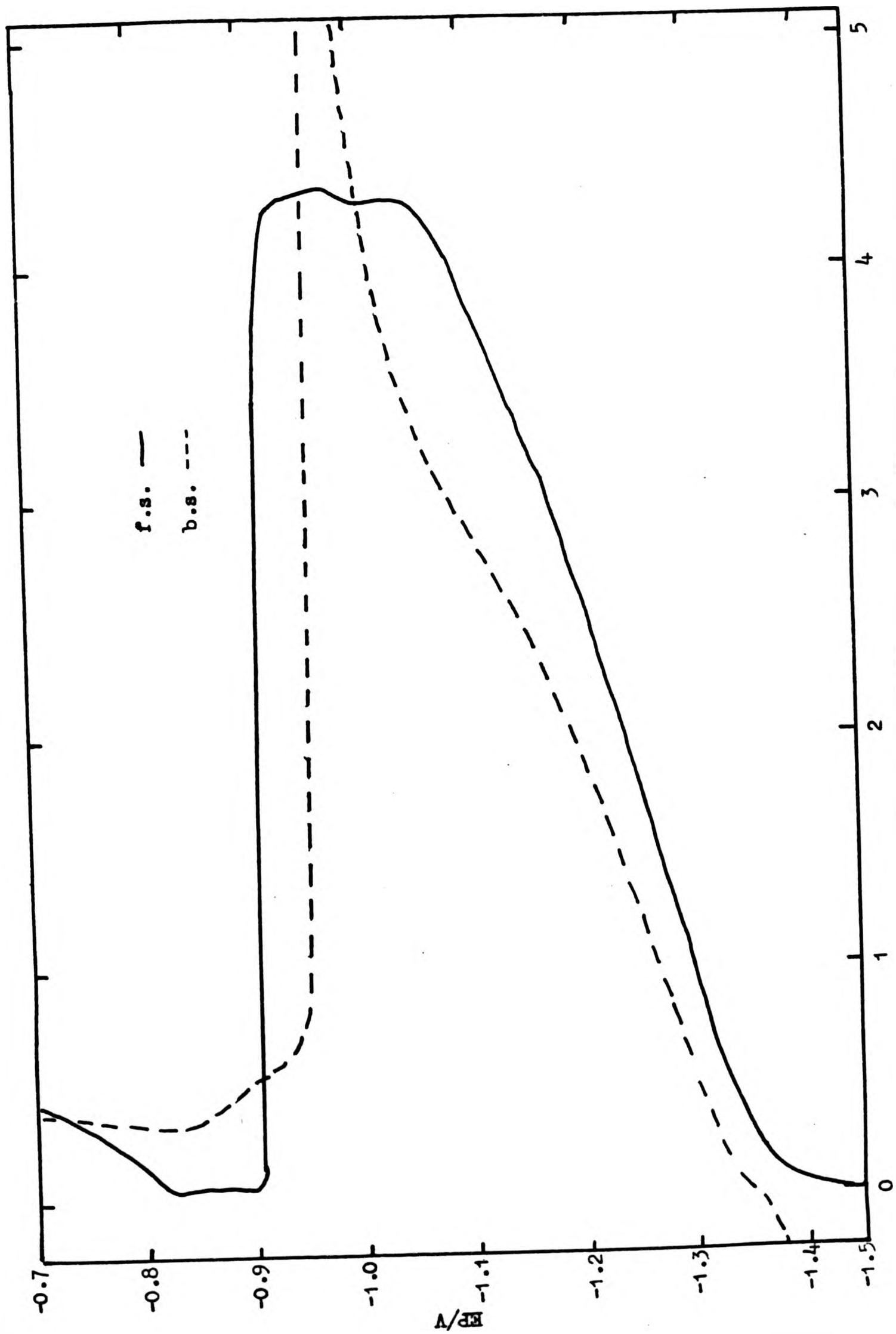


Figure 146. Anodic polarisation curves for Zn-2 Cd alloy in 6 mol dm^{-3} KOH on a stationary electrode.
current density/ 10^3 A m^{-2}

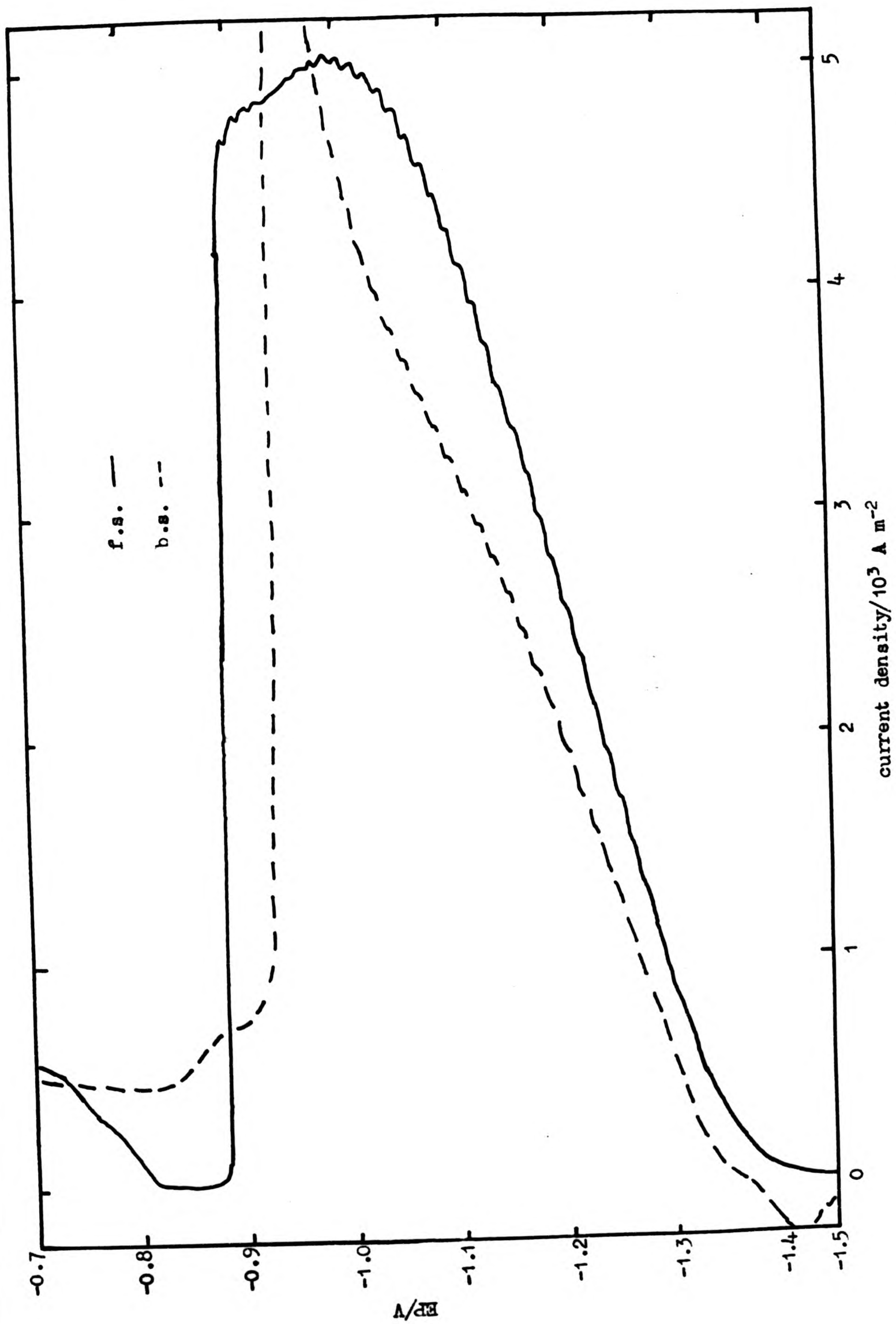


Figure 147. Anodic polarisation curves for Zn-2 Cd alloy in 6 mol dm⁻³ KOH at 10 rad s⁻¹ rotation speed.

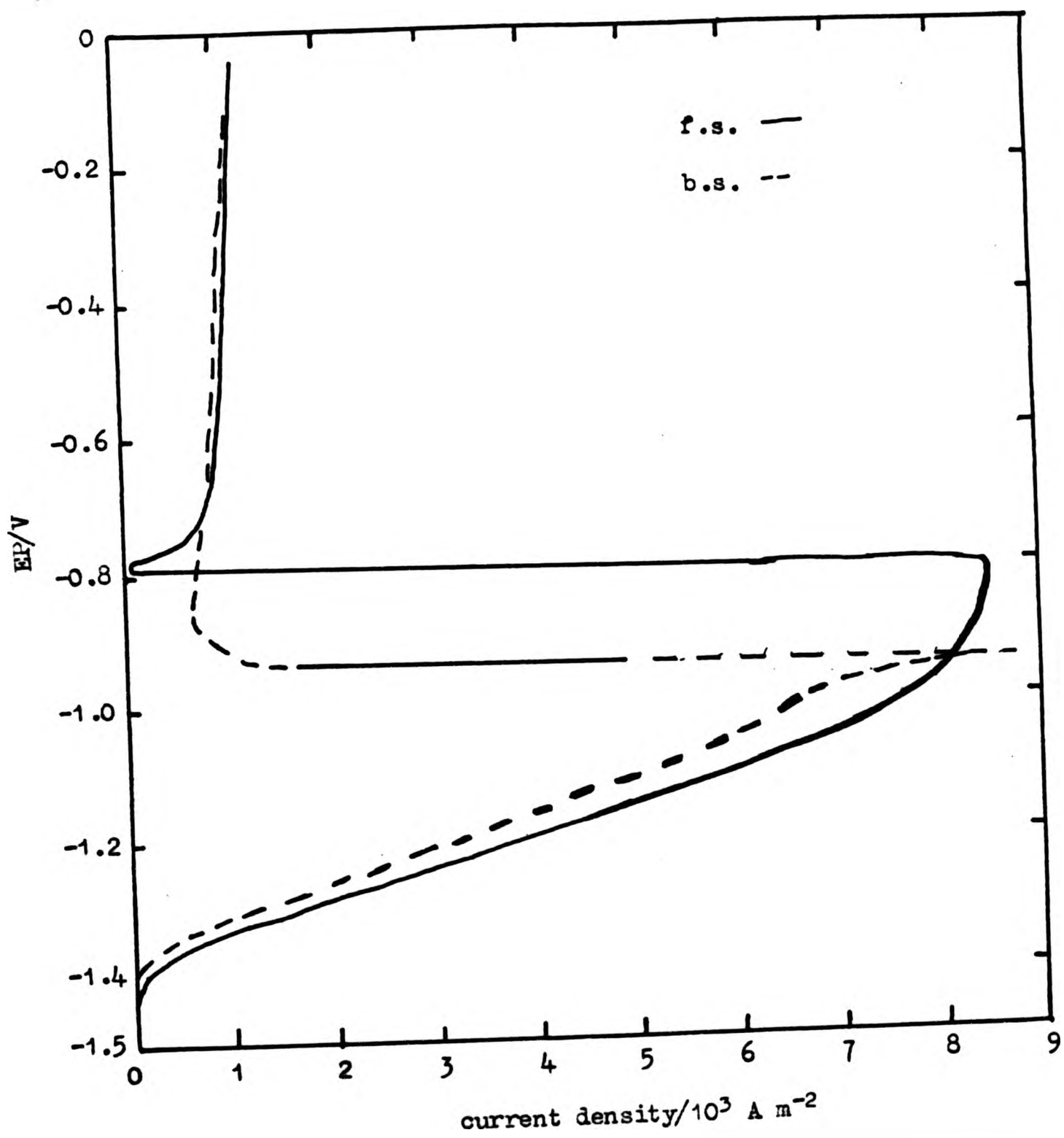


Figure 148. Anodic polarisation curves for Zn-2 Cd alloy in 6 mol dm⁻³ KOH at 50 rad s⁻¹ rotation speed.

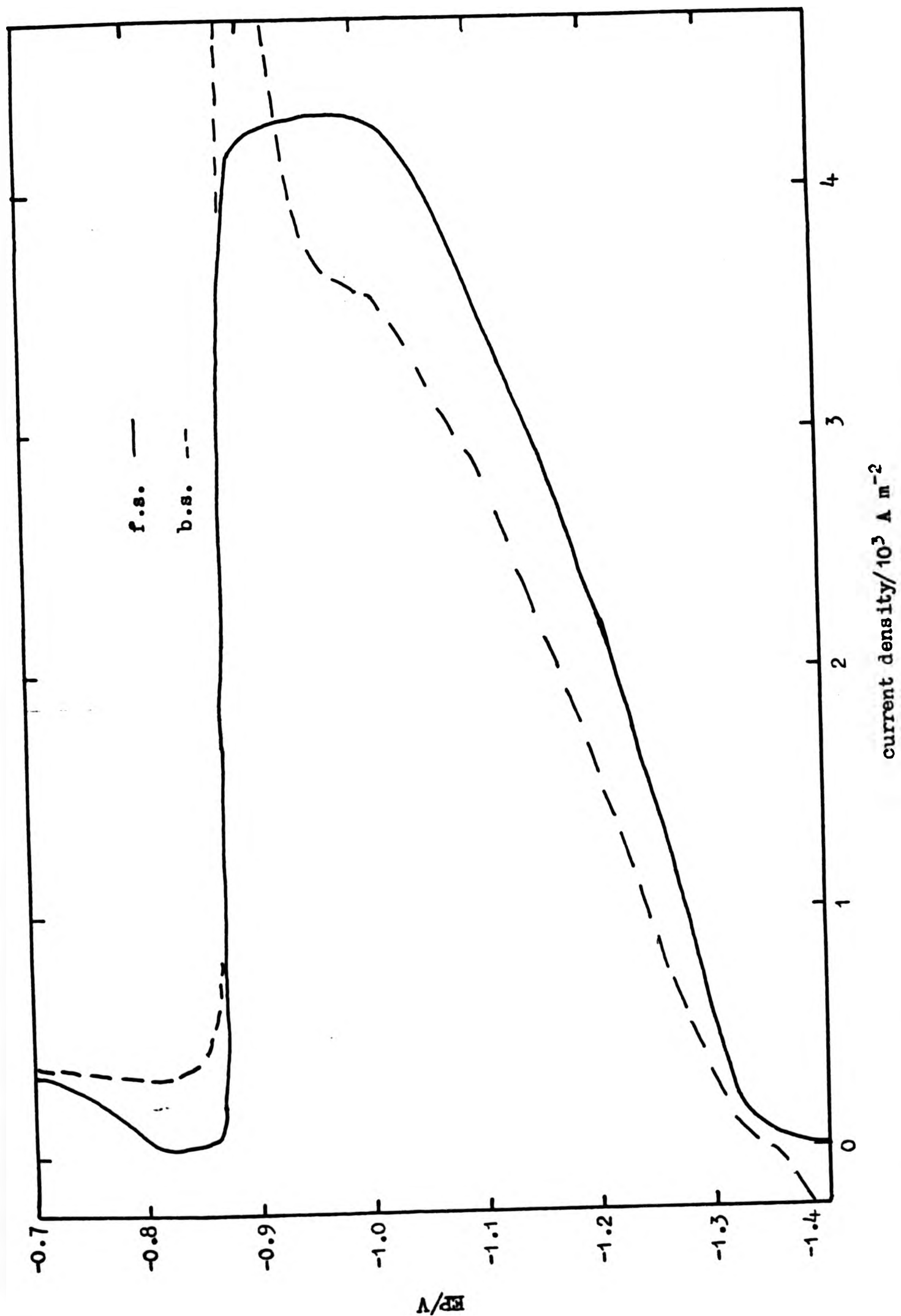


Figure 150. Anodic polarisation curves for Zn-5 Cd alloy in 6 mol dm^{-3} KOH on a stationary electrode.

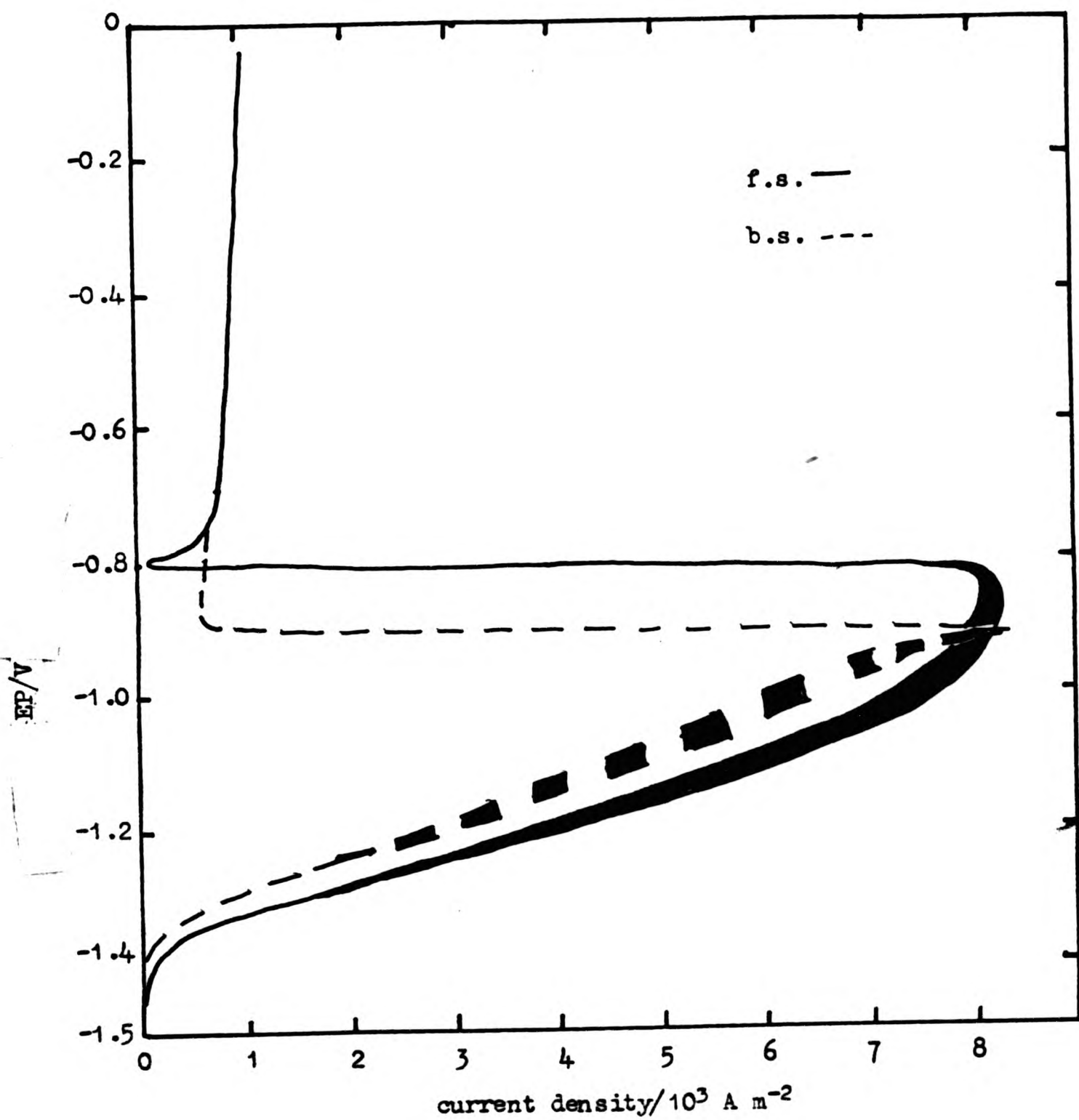


Figure 152. Anodic polarisation curve for Zn-5 Cd alloy in 6 mol dm⁻³ KOH at 50 rad s⁻¹ rotation speed.

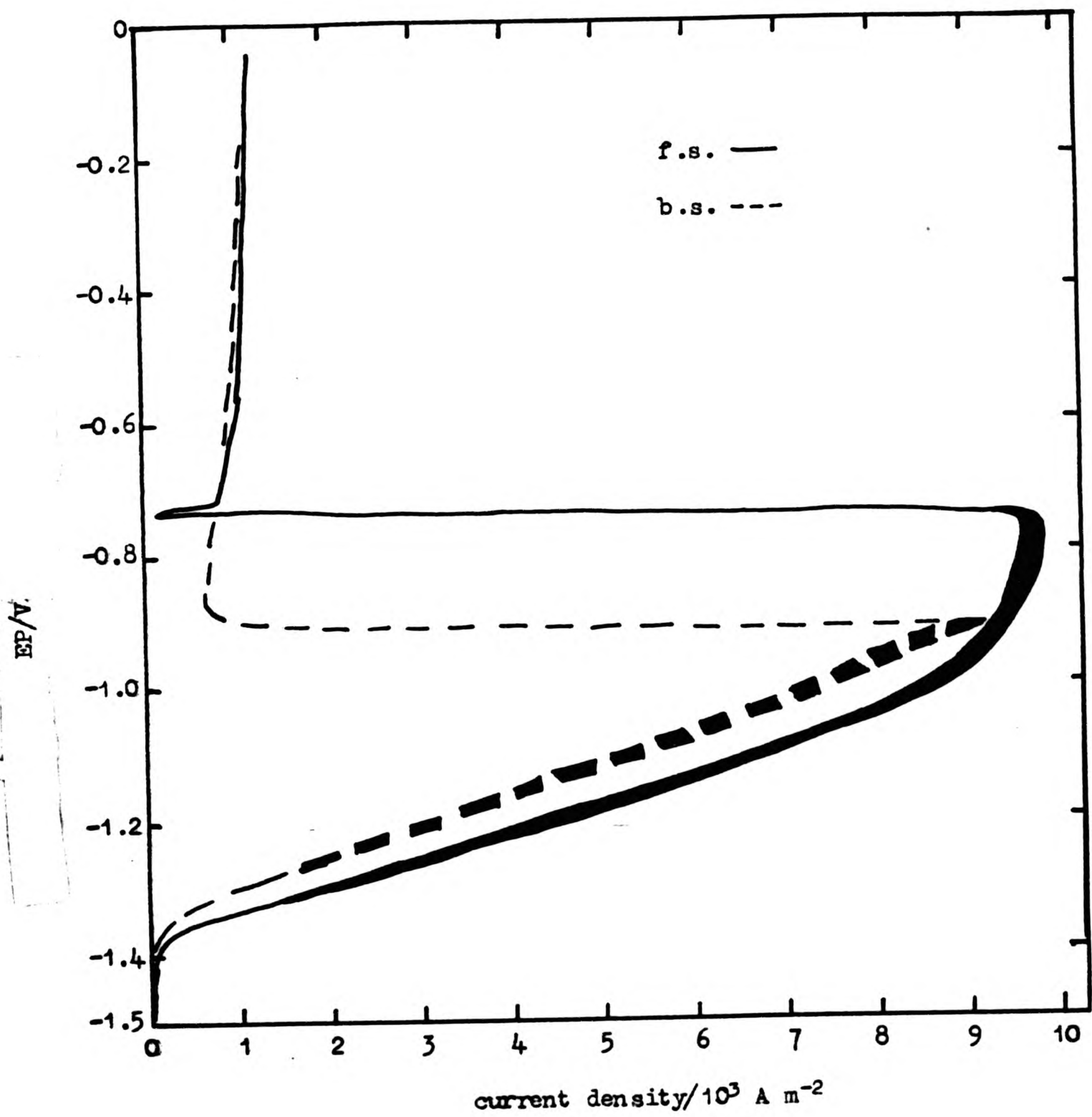


Figure 153. Anodic polarisation curves for Zn-5 Cd alloy in 6 mol dm⁻³ KOH at 100 rad s⁻¹ rotation speed.

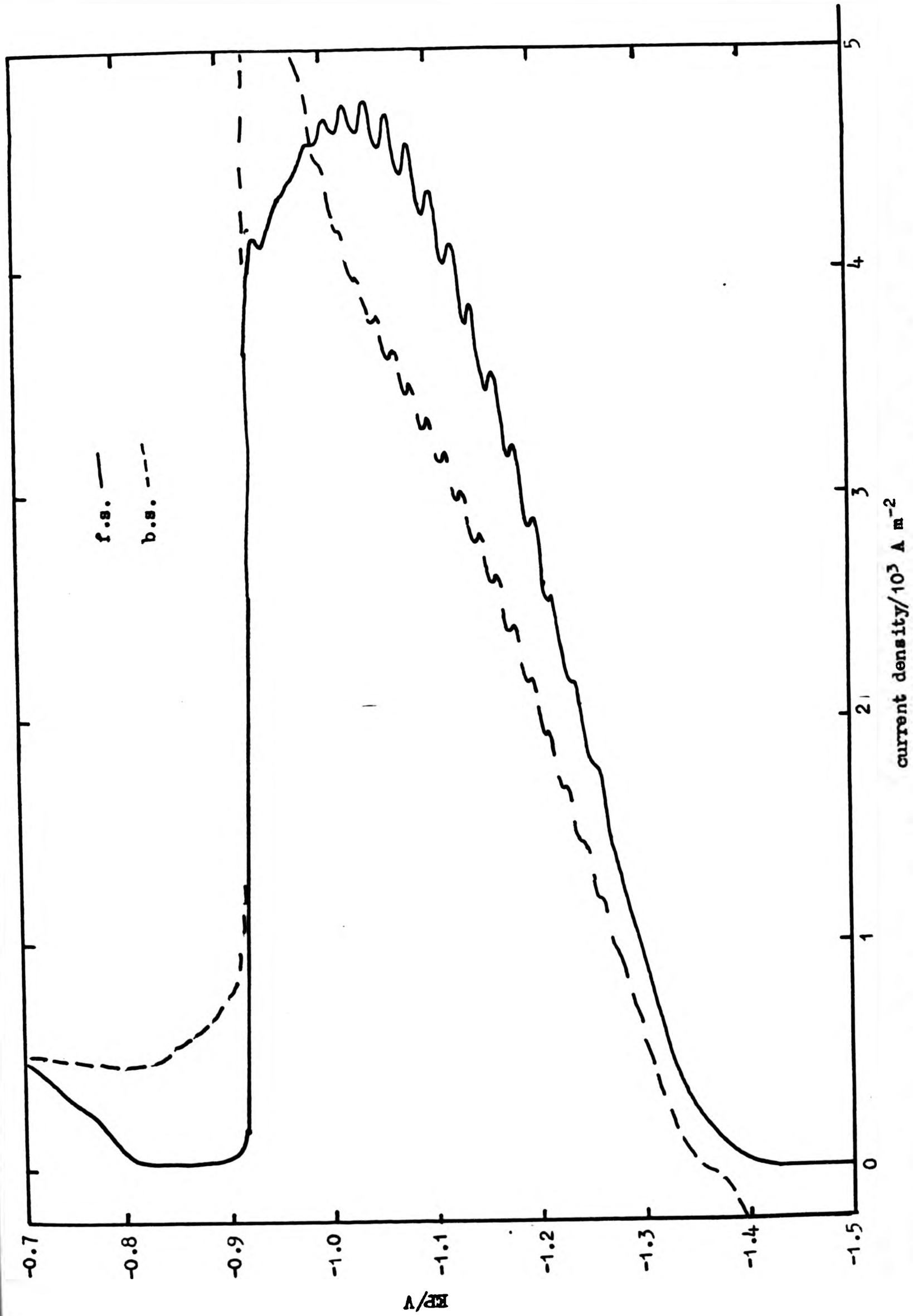


Figure 155. Anodic polarisation curves for Zn-10 Cd alloy in 6 mol dm⁻³ KOH at 10 rad s⁻¹ rotation speed.

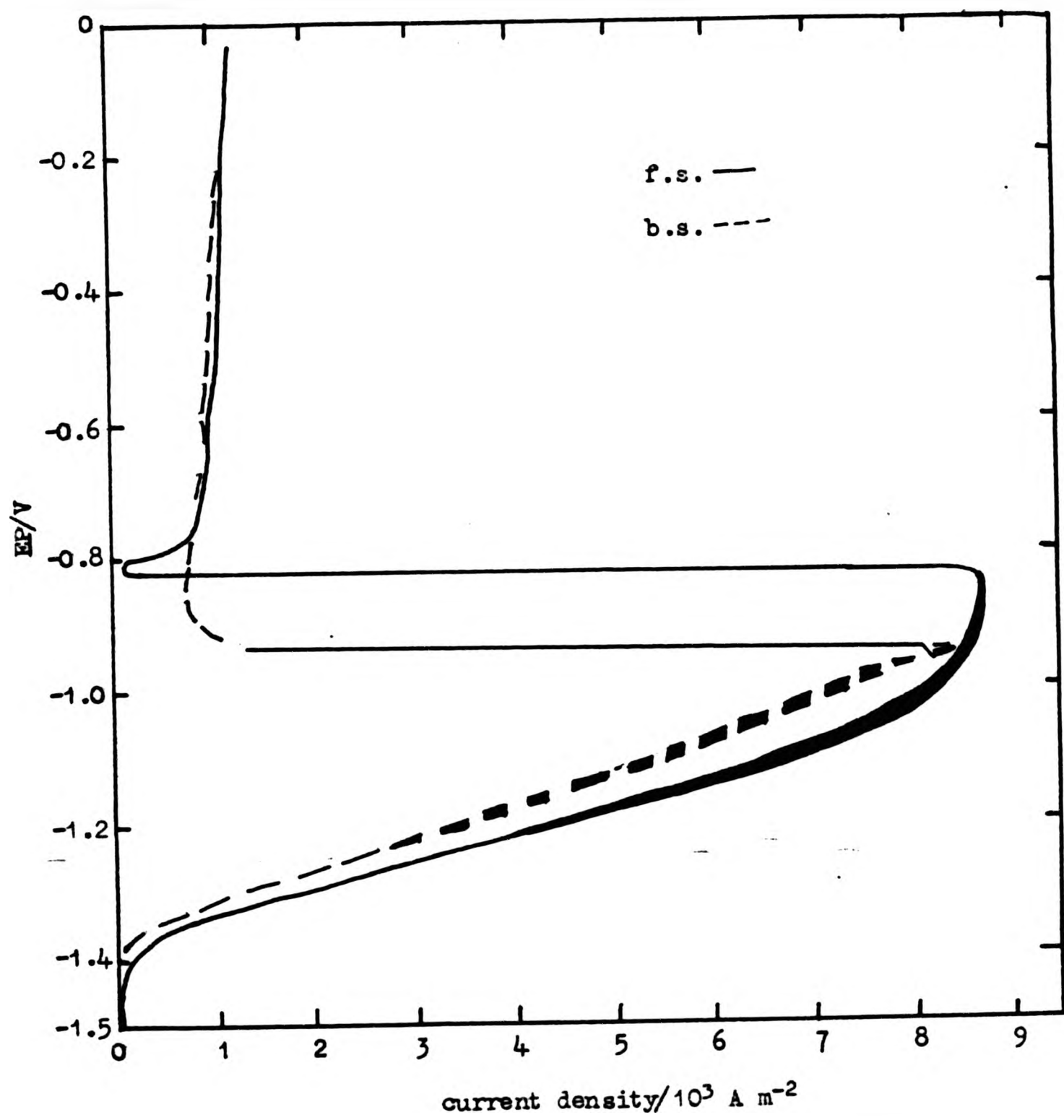


Figure 156. Anodic polarisation curves for Zn-10 Cd alloy in 6 mol dm^{-3} KOH at 50 rad s^{-1} rotation speed

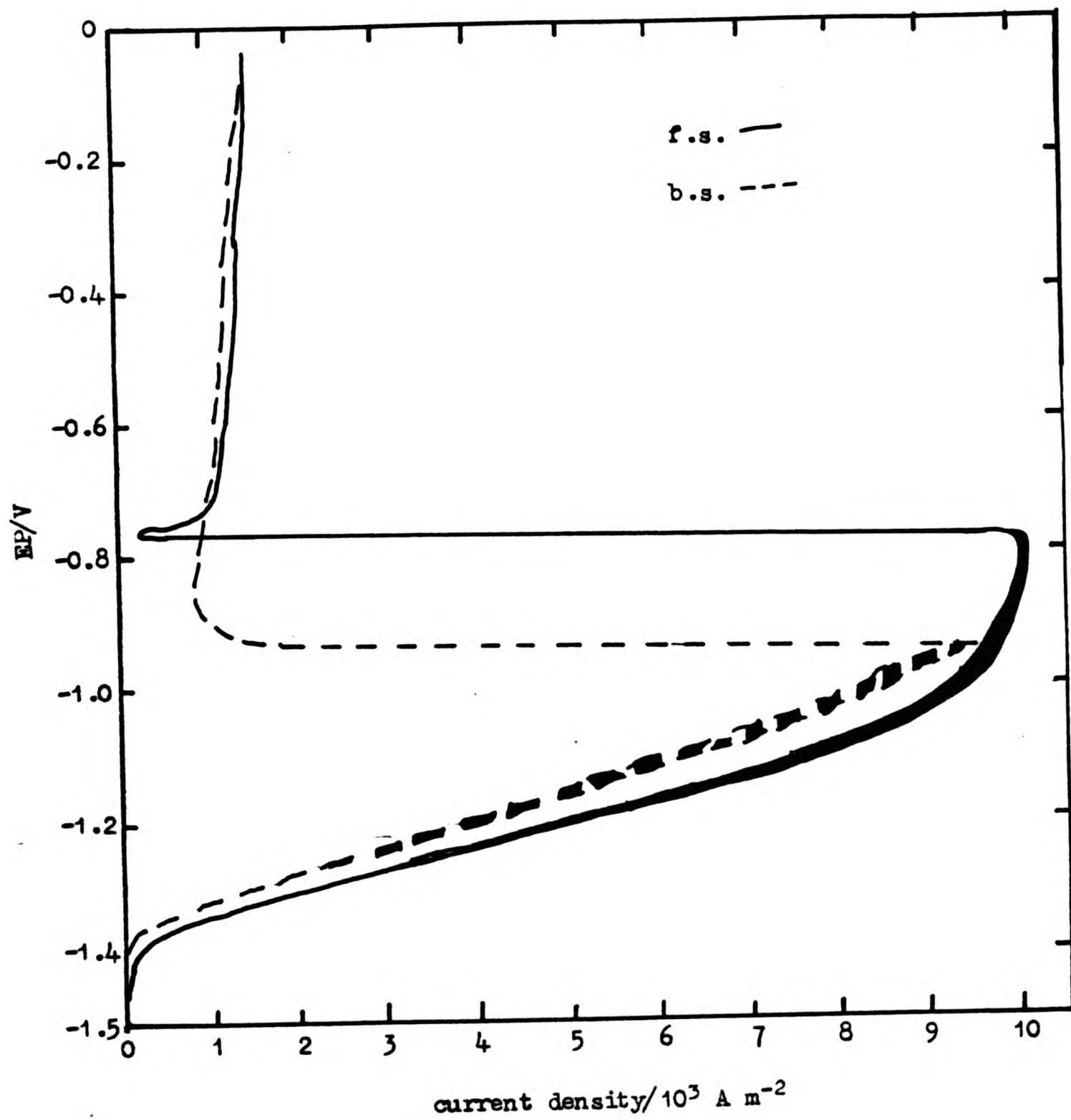


Figure 157. Anodic polarisation curves for Zn-10 Cd alloy in 6 mol dm⁻³ KOH at 100 rad s⁻¹ rotation speed.

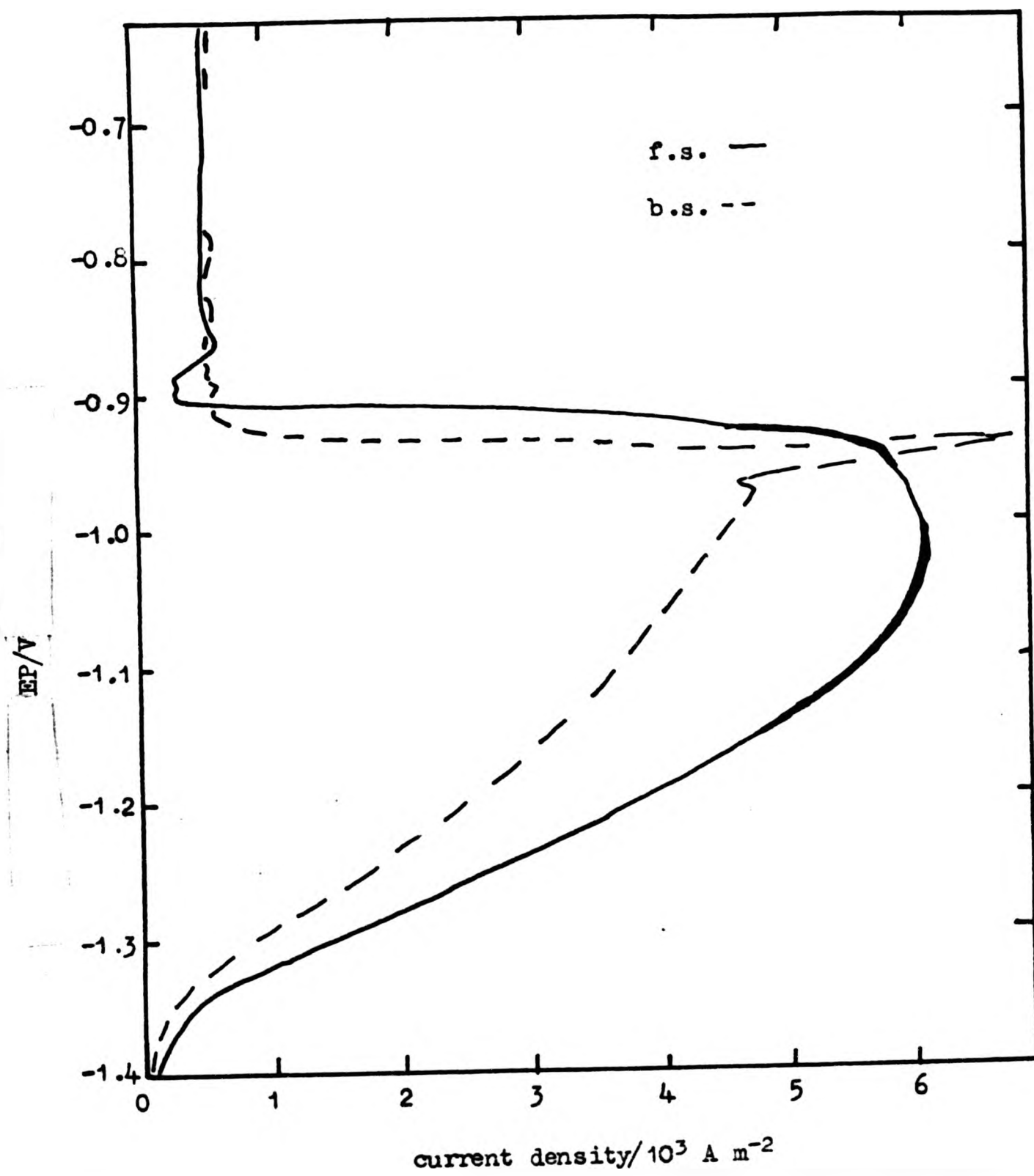


Figure 159. Anodic polarisation curves for the Zn-25 Cd alloy in 6 mol dm⁻³ NaOH at 50 rad s⁻¹ rotation speed.

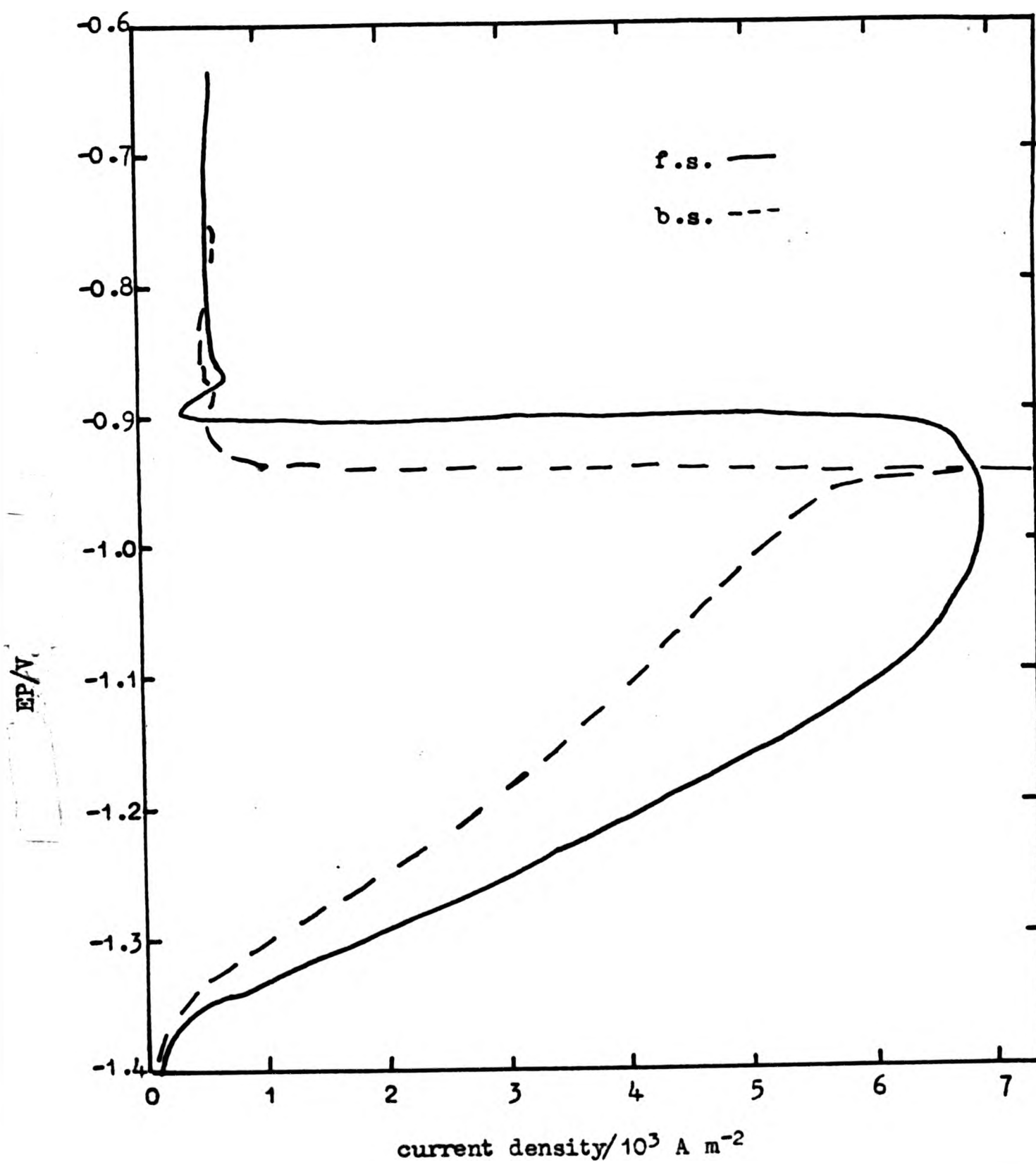


Figure 160. Anodic polarisation curves for the Zn-25 Cd alloy in 6 mol dm⁻³ KOH at 100 rad s⁻¹ rotation speed.

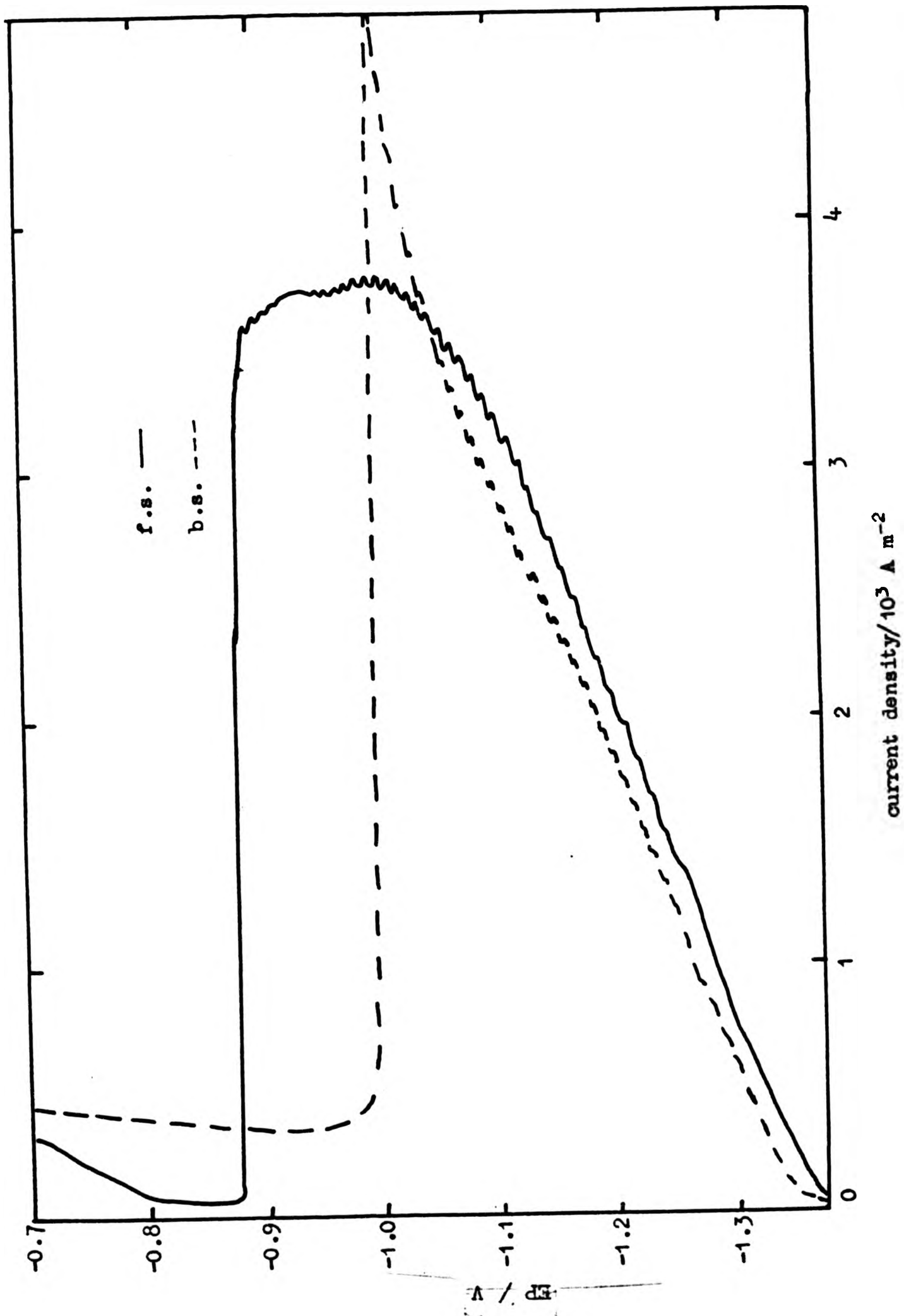


Figure 161. Anodic polarisation curves for Zn-0.05 Cd alloy in ZnO saturated 6 mol dm⁻³ KOH on a stationary electrode

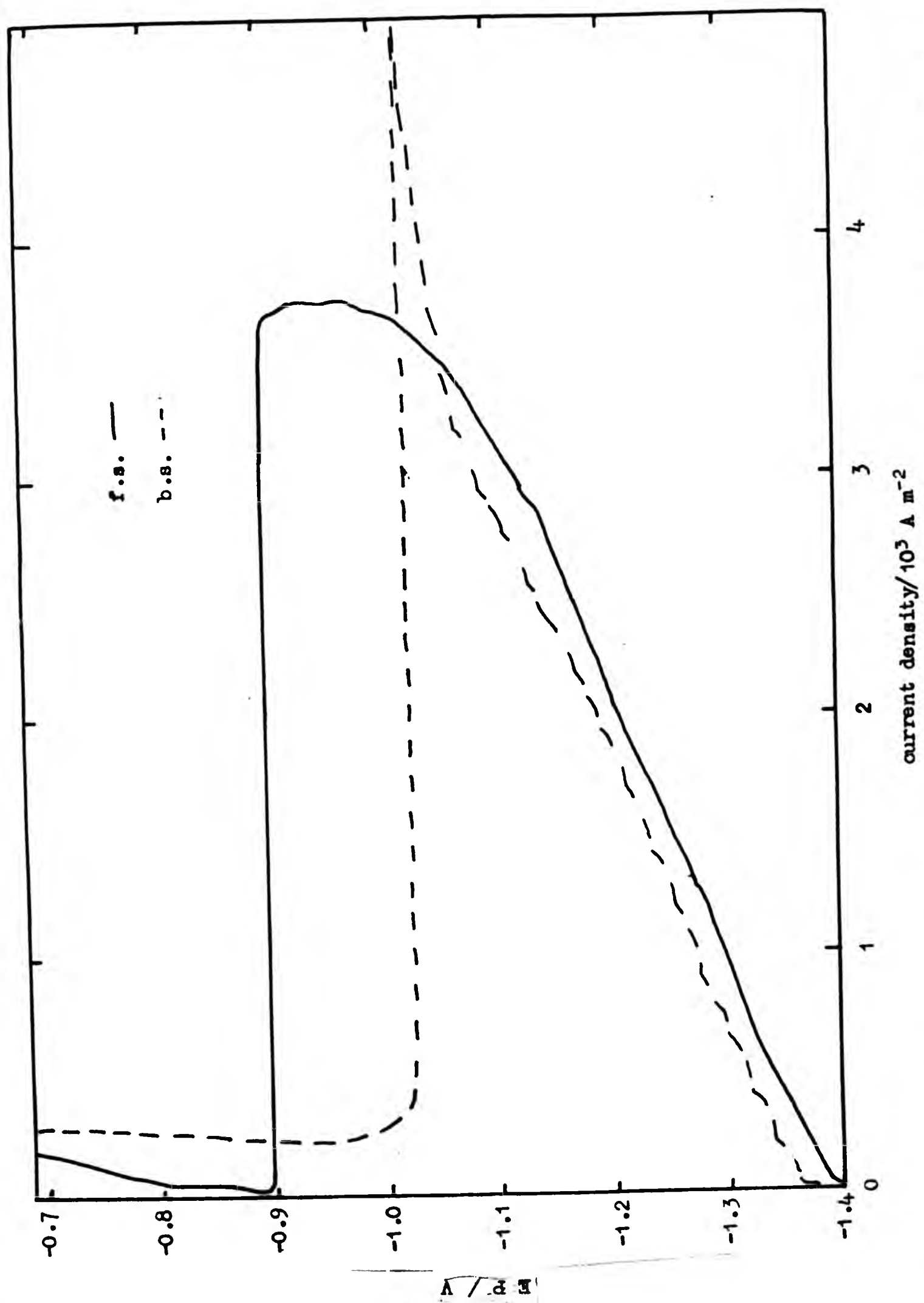


Figure 162. Anodic polarisation curves for Zn-0.05 Cd alloy in ZnO saturated 6 mol dm⁻³ KOH at 10 rad s⁻¹ rotation speed.

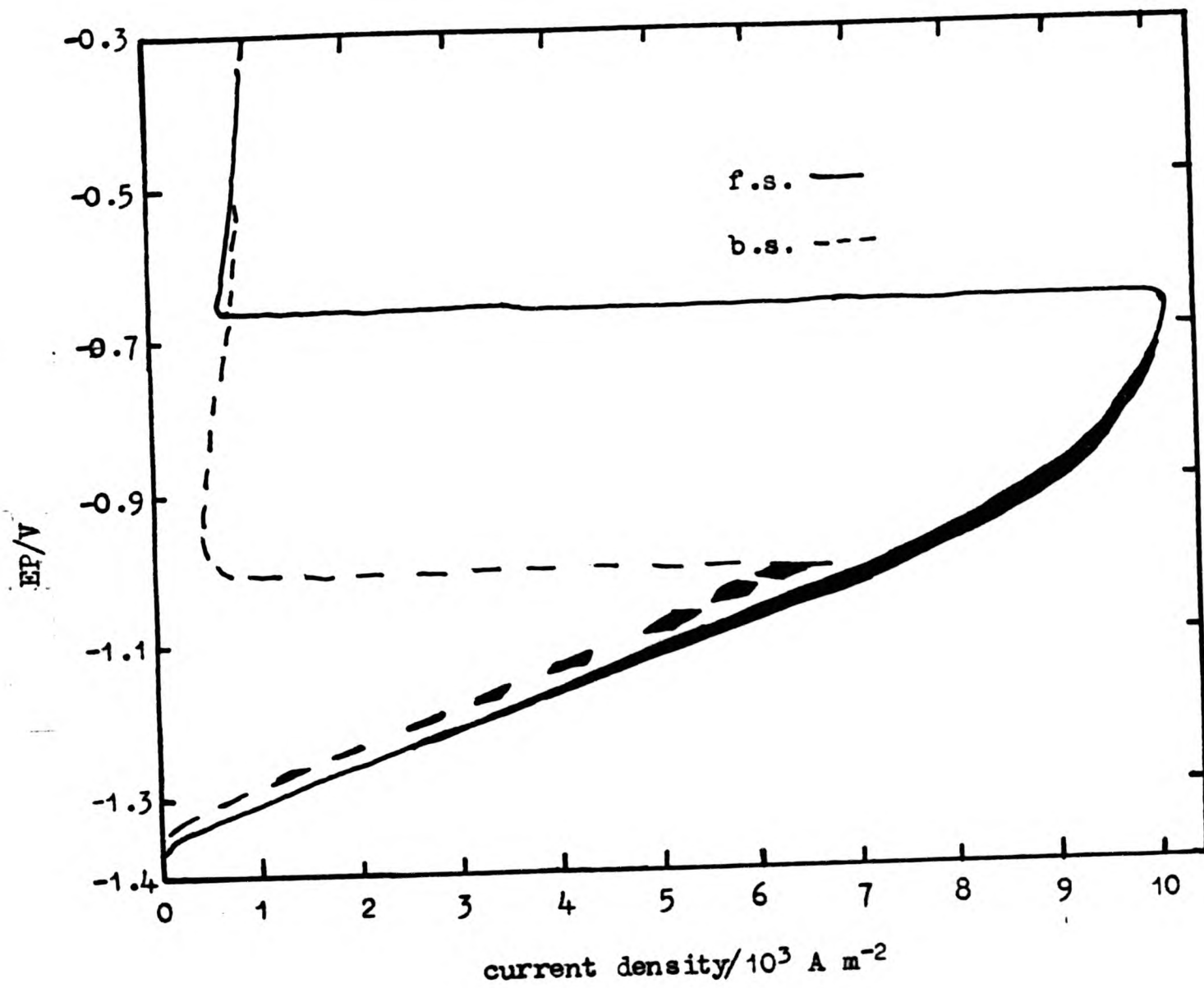


Figure 164. Anodic polarisation curves for Zn-.05 Cd alloy in ZnO saturated in 6 mol dm⁻³ KOH at 100 rad s⁻¹ rotation speed.

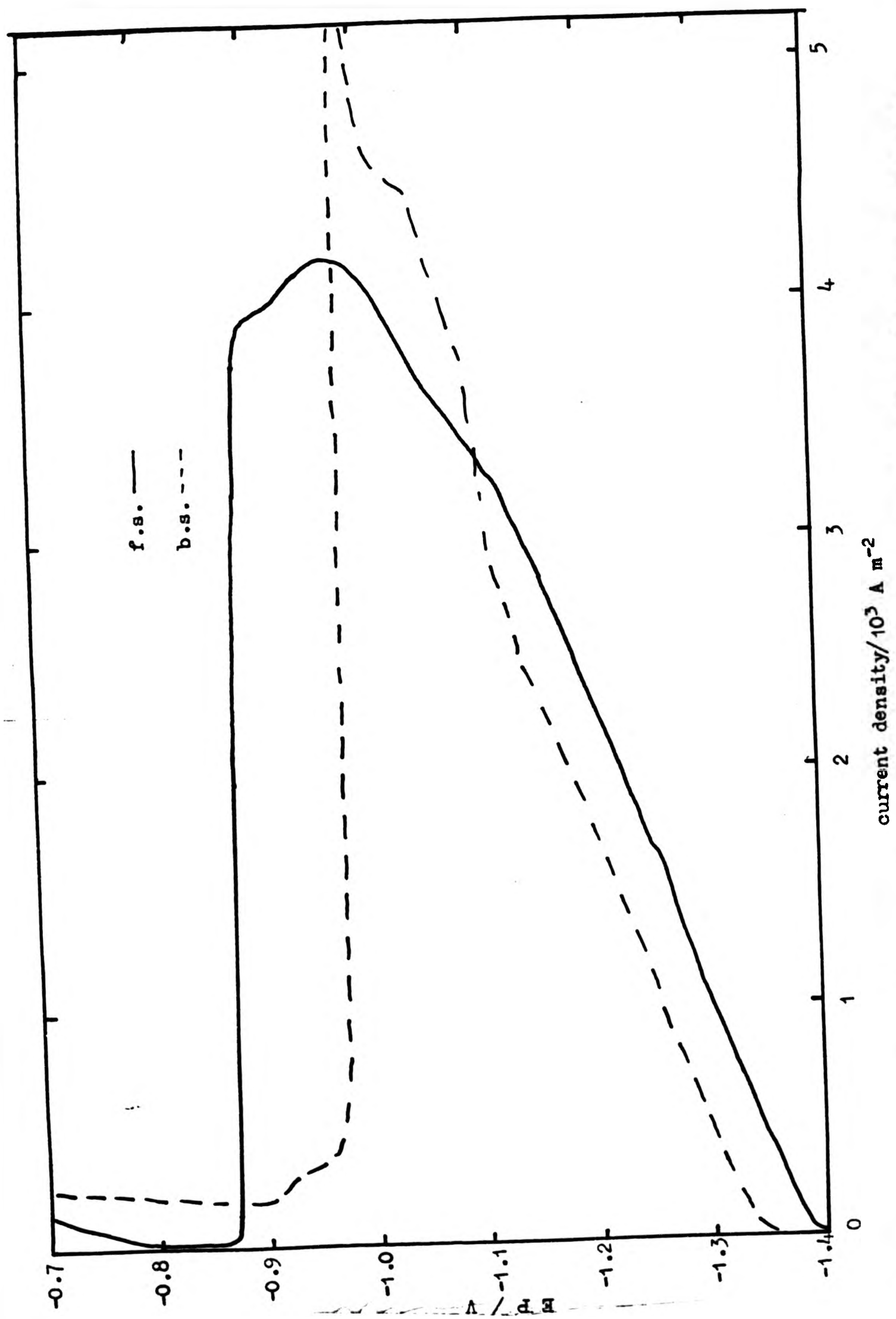


Figure 165. Anodic polarisation curves for Zn-2 Cd alloy in ZnO saturated 6 mol dm⁻³ KOH on a stationary electrode.

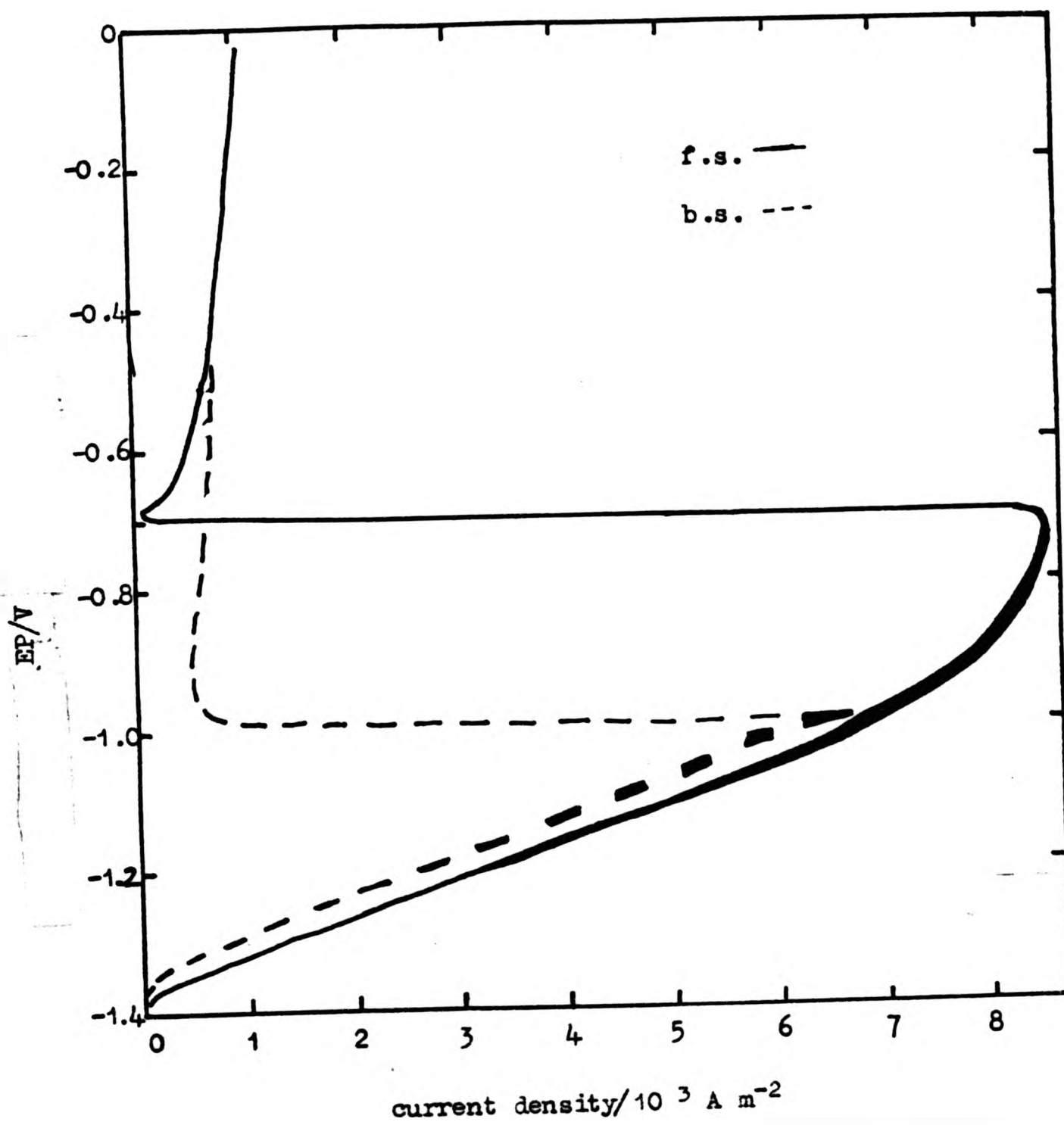


Figure 167. Anodic polarisation curves for Zn-.2 Cd alloy in ZnO saturated 6 mol dm⁻³ KOH at 50 rad s⁻¹ rotation speed.

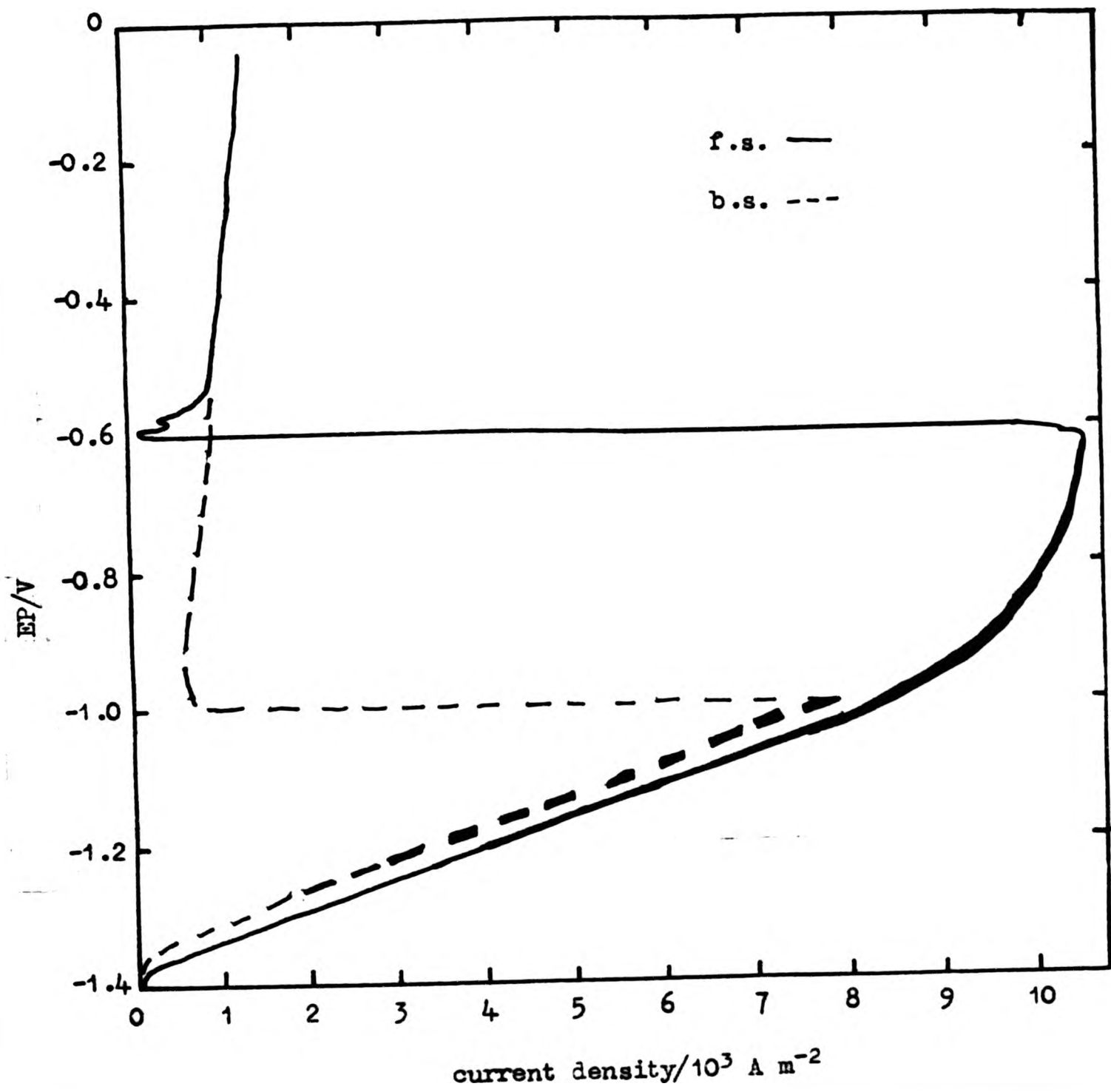


Figure 168. Anodic polarisation curves for Zn-.2 Cd alloy in ZnO saturated 6 mol dm⁻³ KOH at 100 rad s⁻¹ rotation speed.

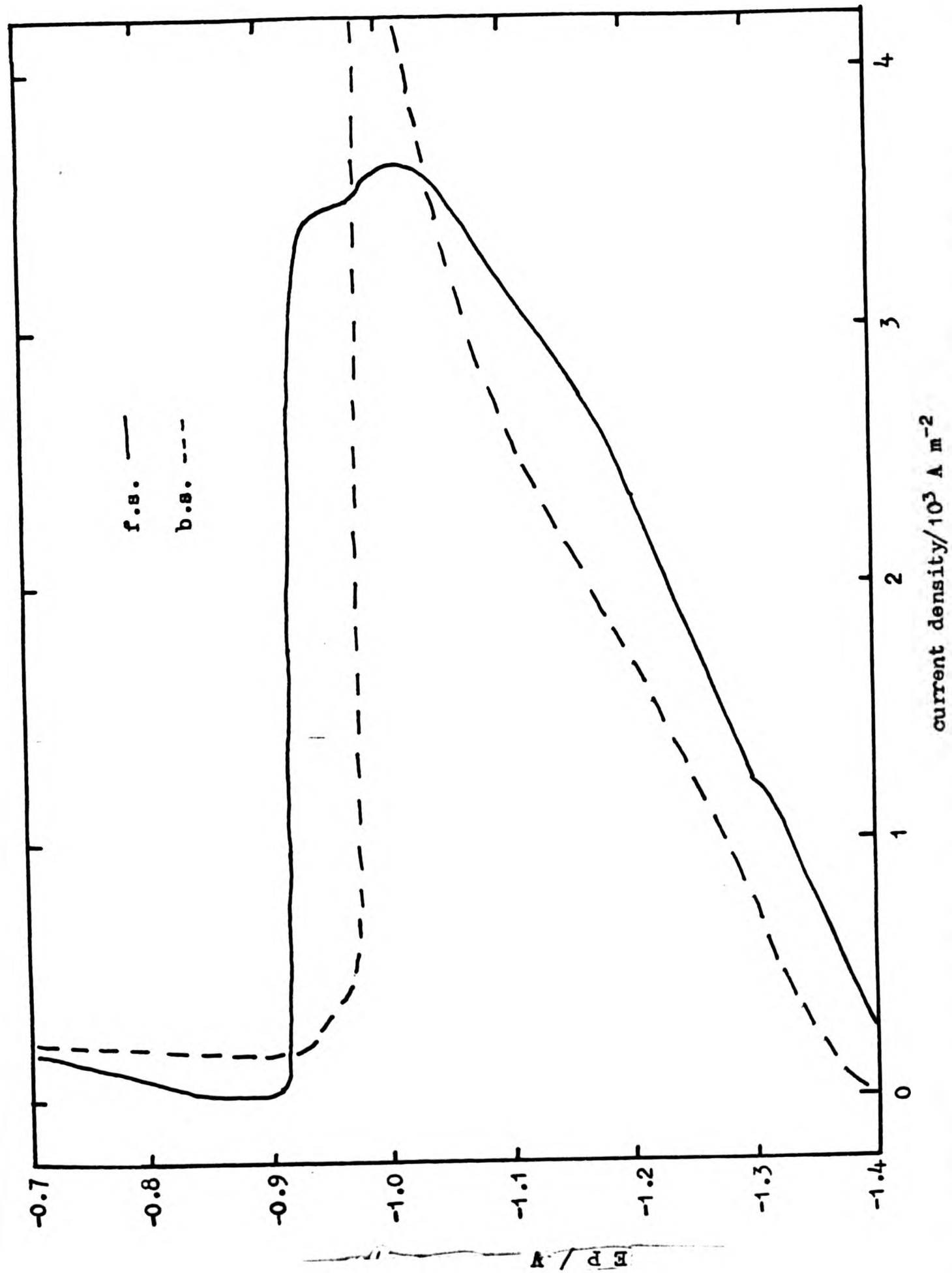


Figure 169. Anodic polarisation curves for Zn-1 Cd alloy in ZnO saturated 6 mol dm⁻³ KOH on a stationary electrode.

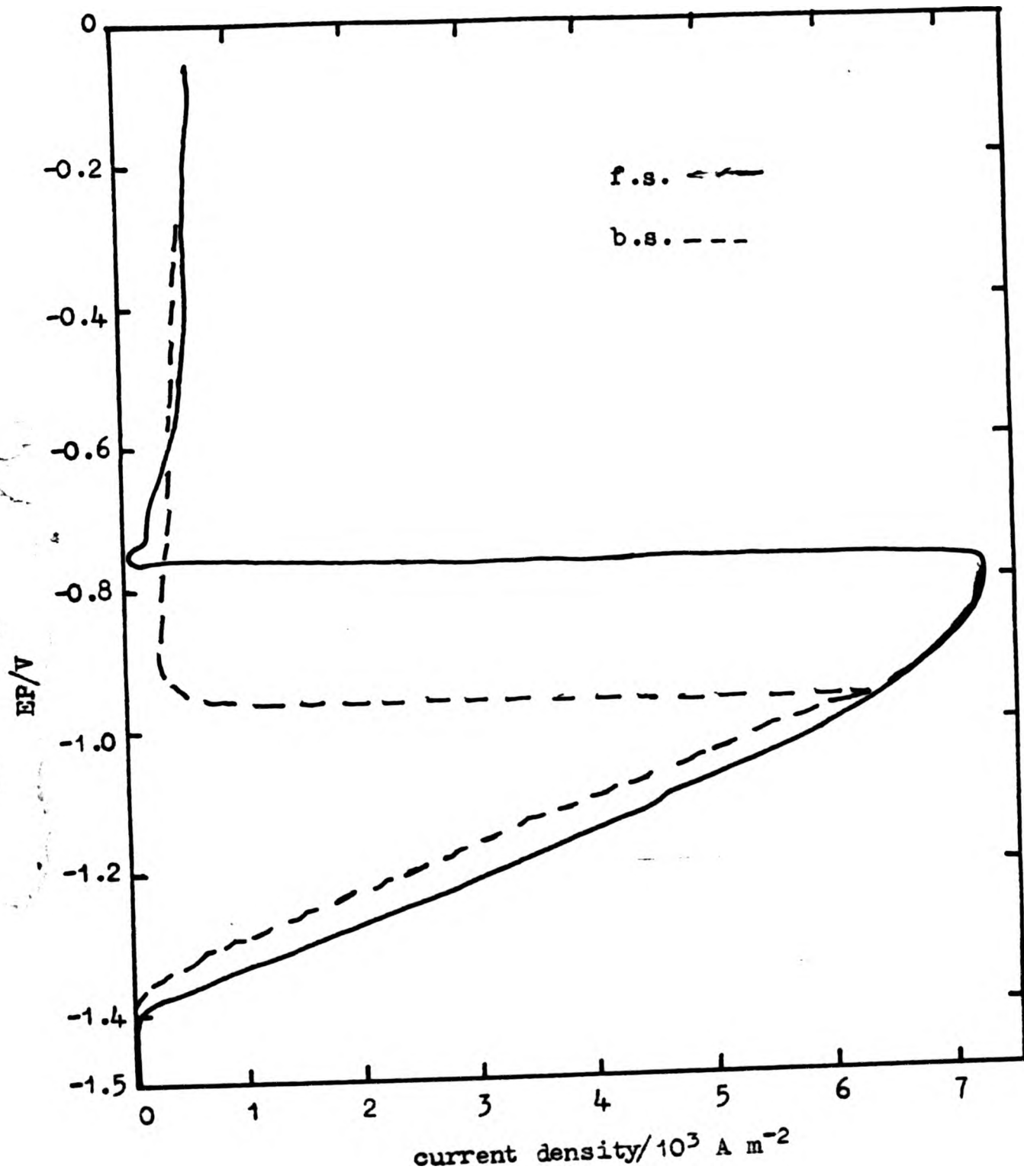


Figure 171. Anodic polarisation curves for Zn-1 Cd alloy in ZnO saturated 6 mol dm⁻³ KOH at 50 rad s⁻¹ rotation speed.

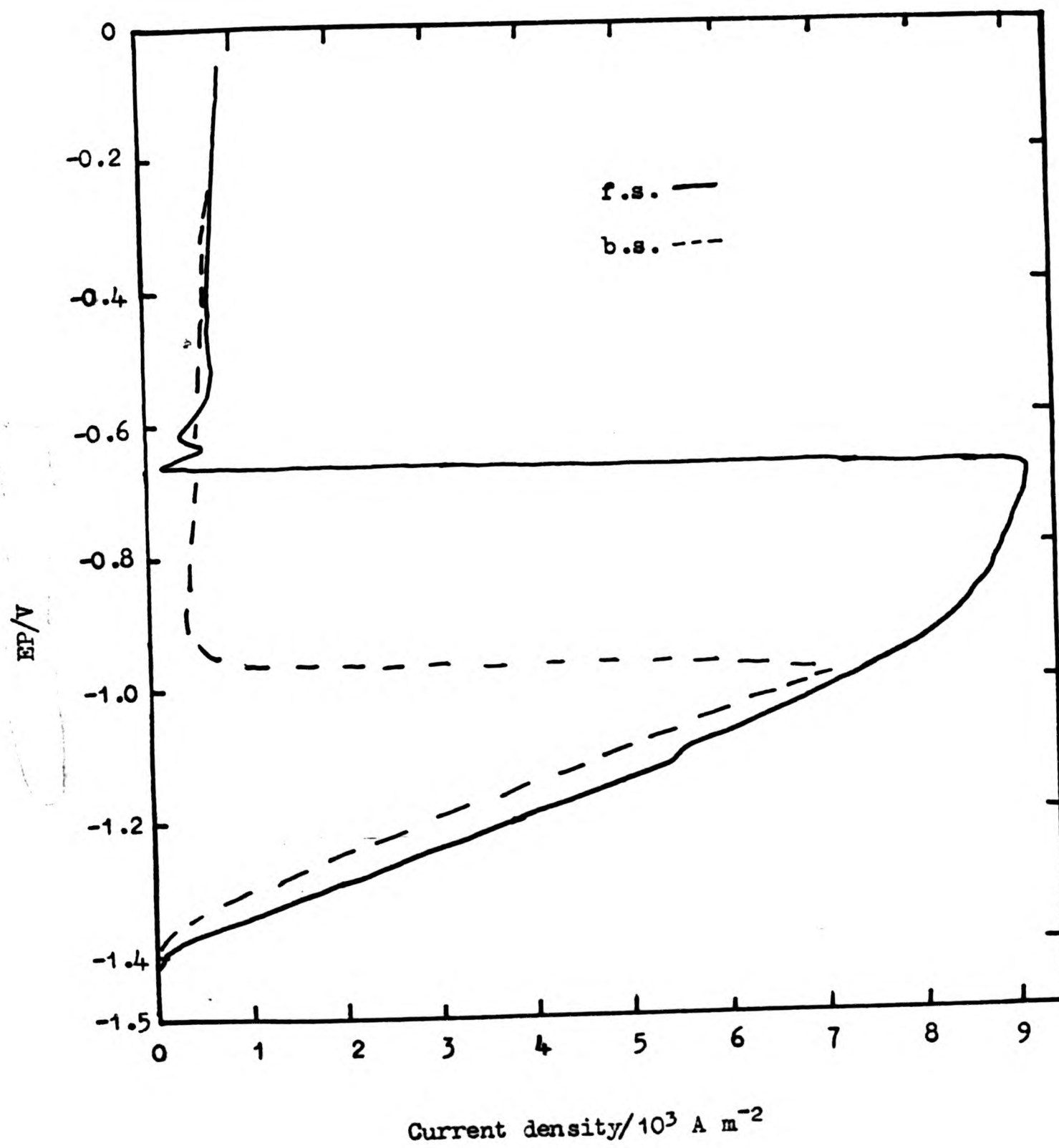


Figure 172. Anodic polarisation curves for Zn-1 Cd alloy in ZnO saturated 6 mol dm⁻³ KOH at 100 rad s⁻¹ rotation speed.

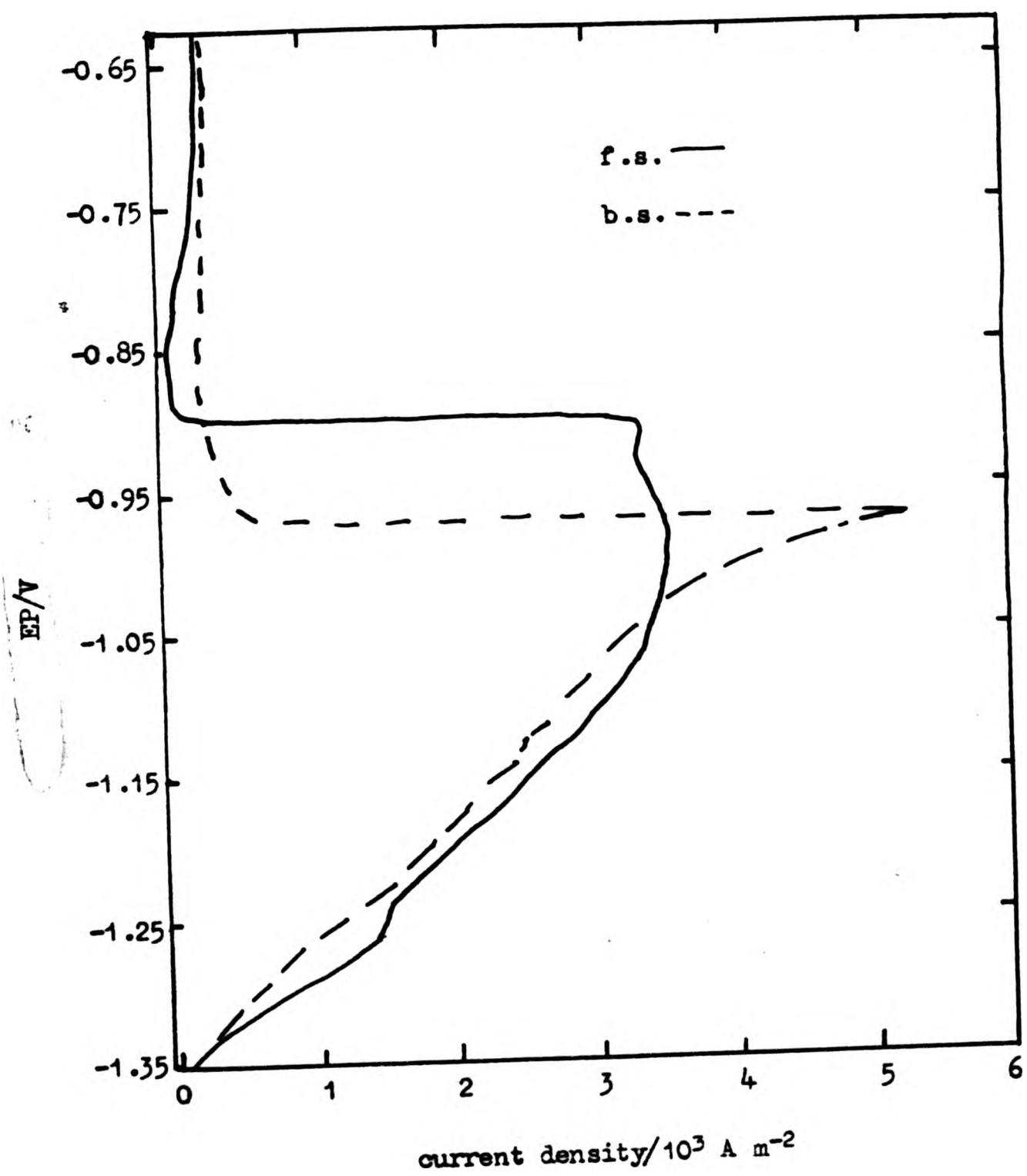


Figure 173. Anodic polarisation curves for Zn-2 Cd alloy in ZnO saturated 6 mol dm⁻³ KOH on a stationary electrode.

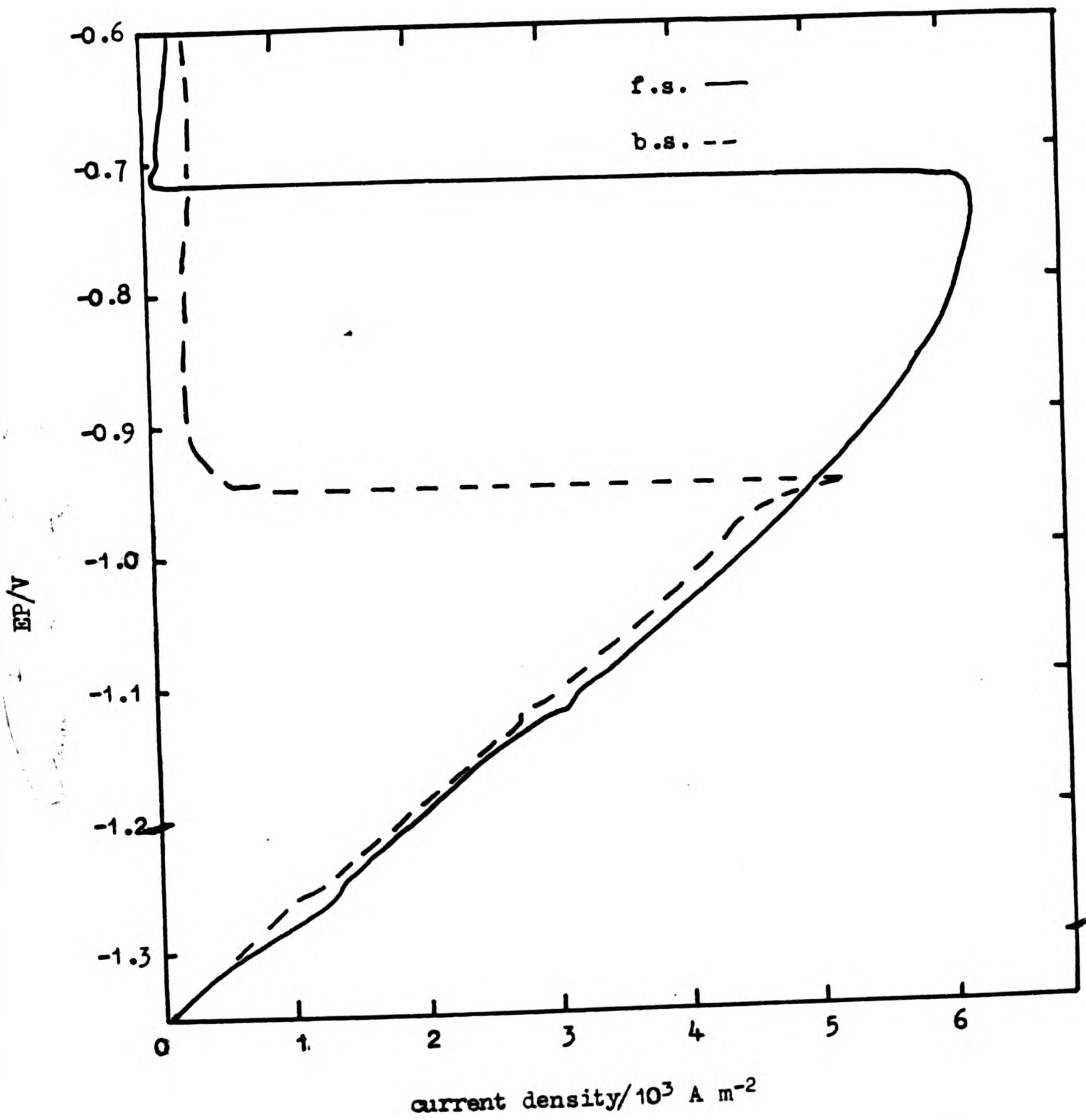


Figure 175. Anodic polarisation curves for Zn-2 Cd alloy in ZnO saturated 6 mol dm⁻³ KOH at 50 rad s⁻¹ rotation speed.

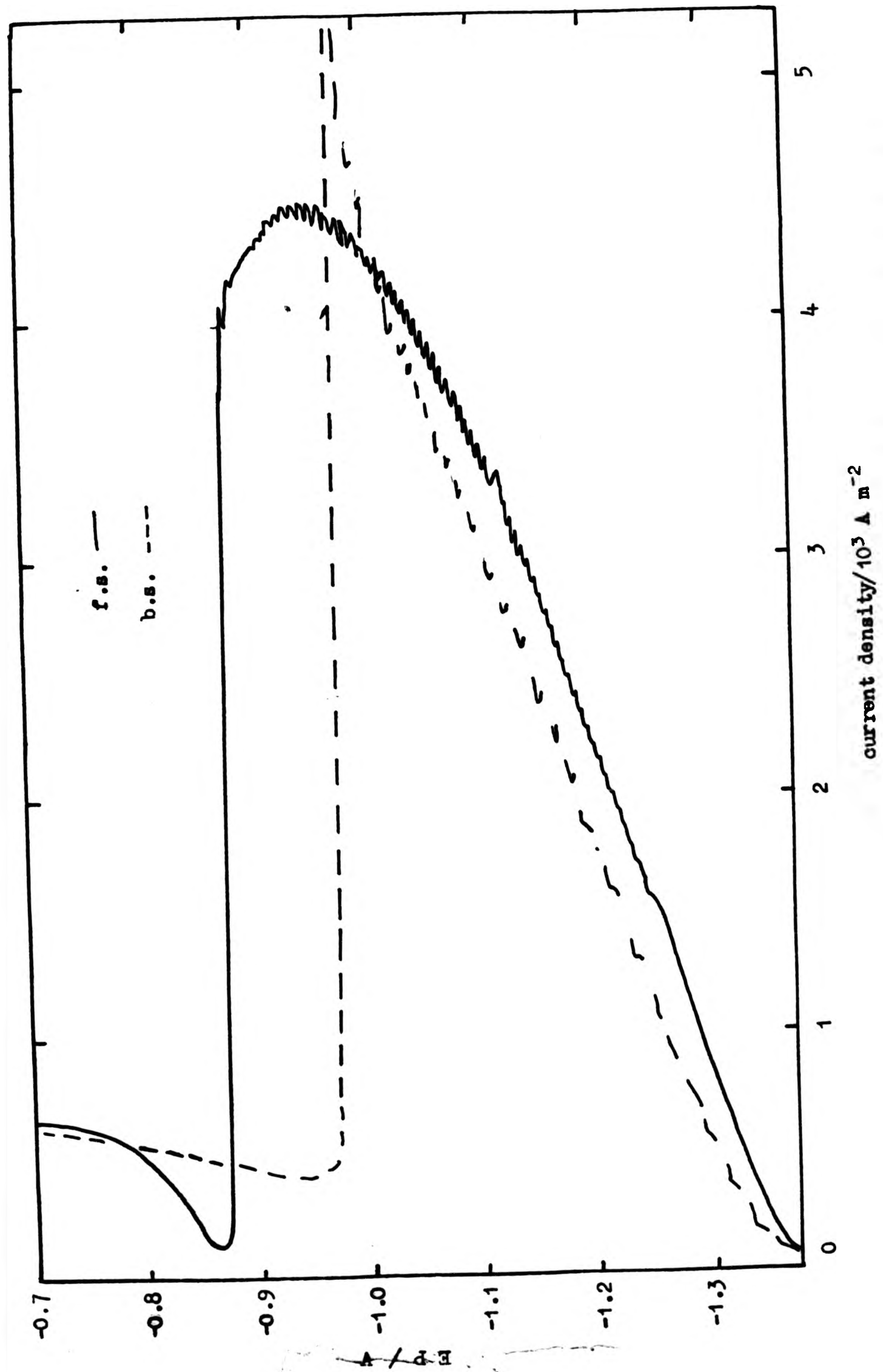


Figure 177. Anodic polarisation curves for Zn-5 Cd alloy in ZnO saturated 6 mol dm⁻³ KOH at 10 rad s⁻¹ rotation speed.

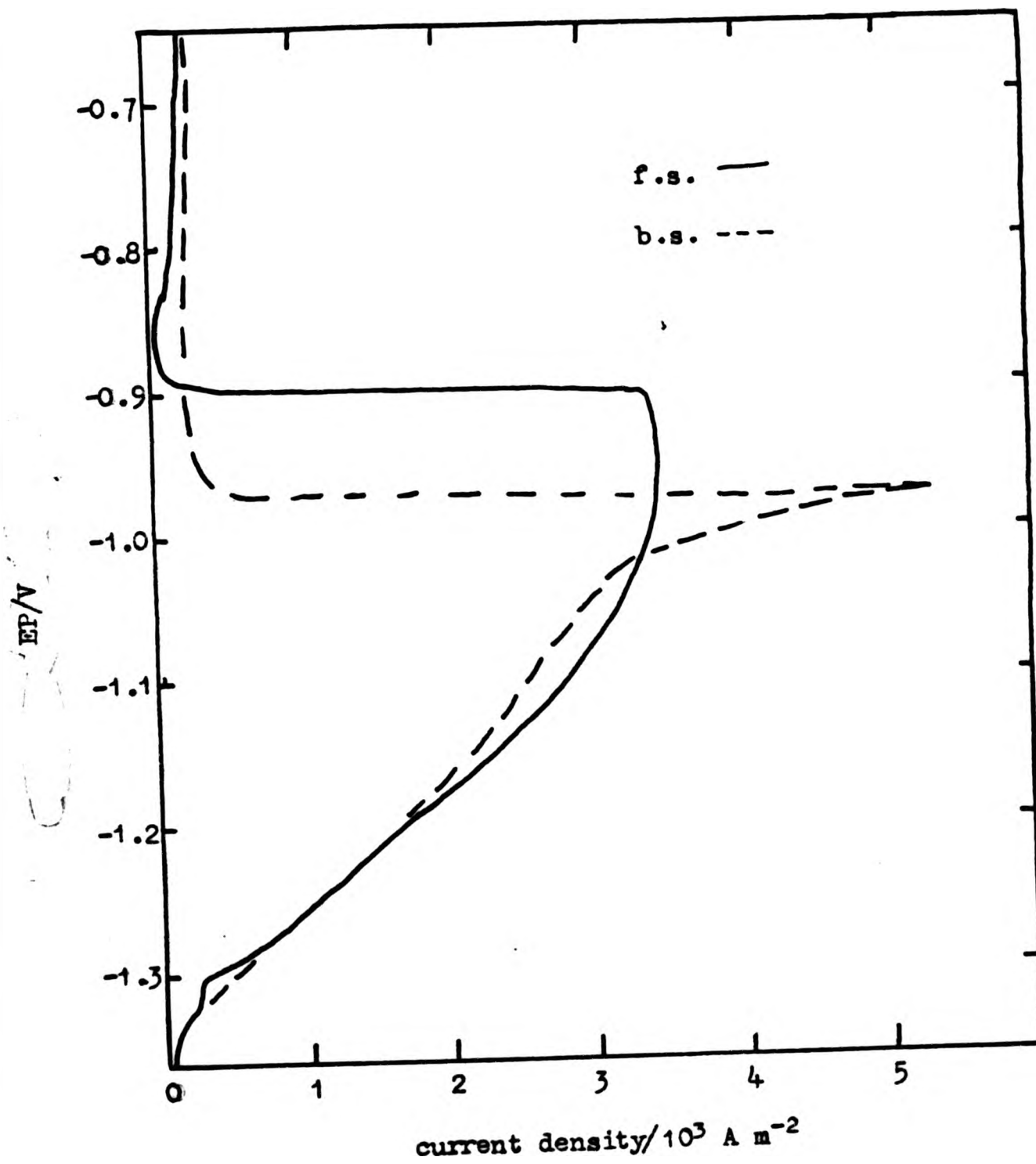


Figure 178. Anodic polarisation curves for the Zn-10 Cd alloy in ZnO saturated 6 mol dm⁻³ KOH on a stationary electrode.

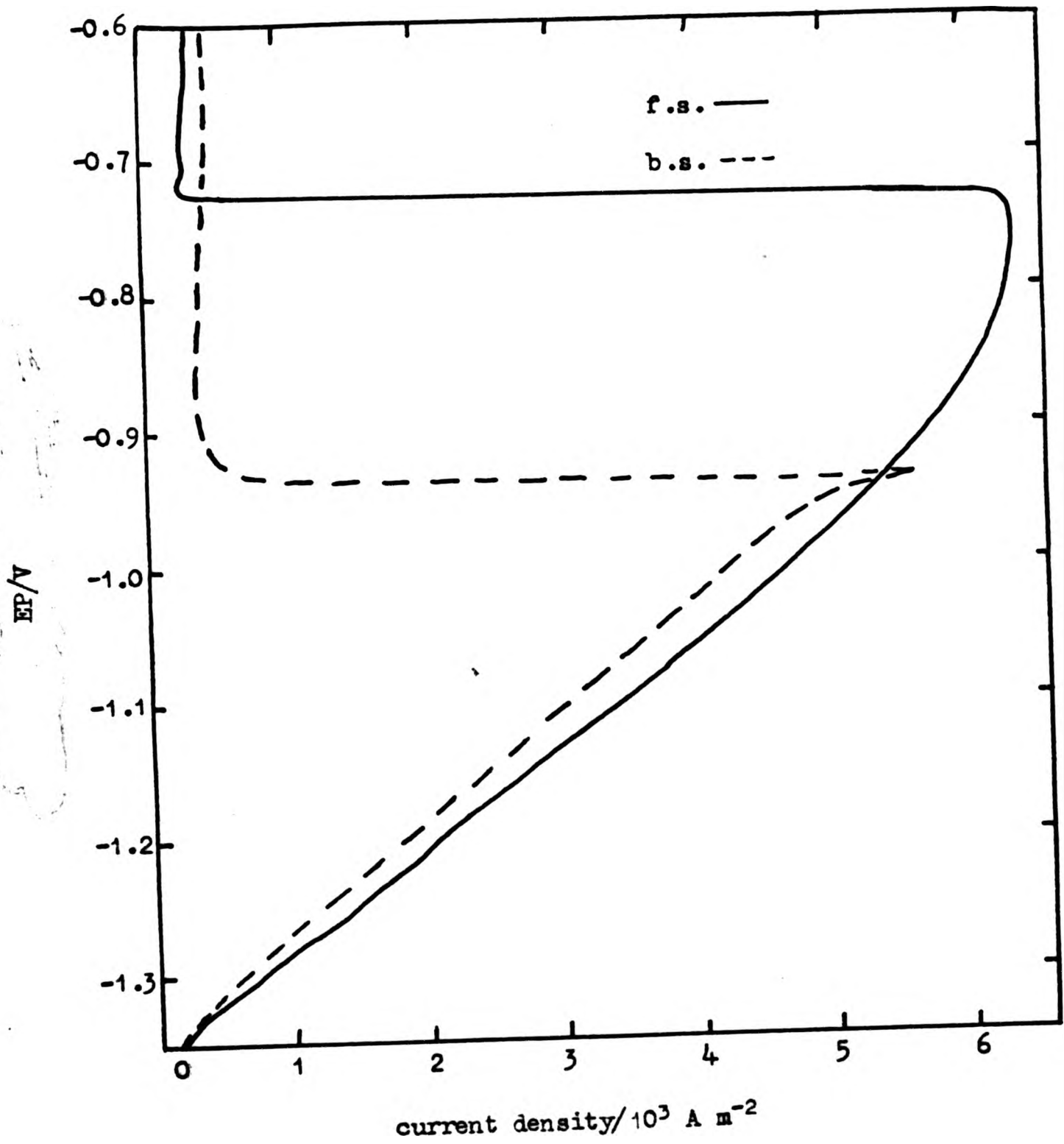


Figure 180. Anodic polarisation curves for Zn-10 Cd alloy in ZnO saturated 6 mol dm⁻³ KOH at 50 rad s⁻¹ rotation speed.

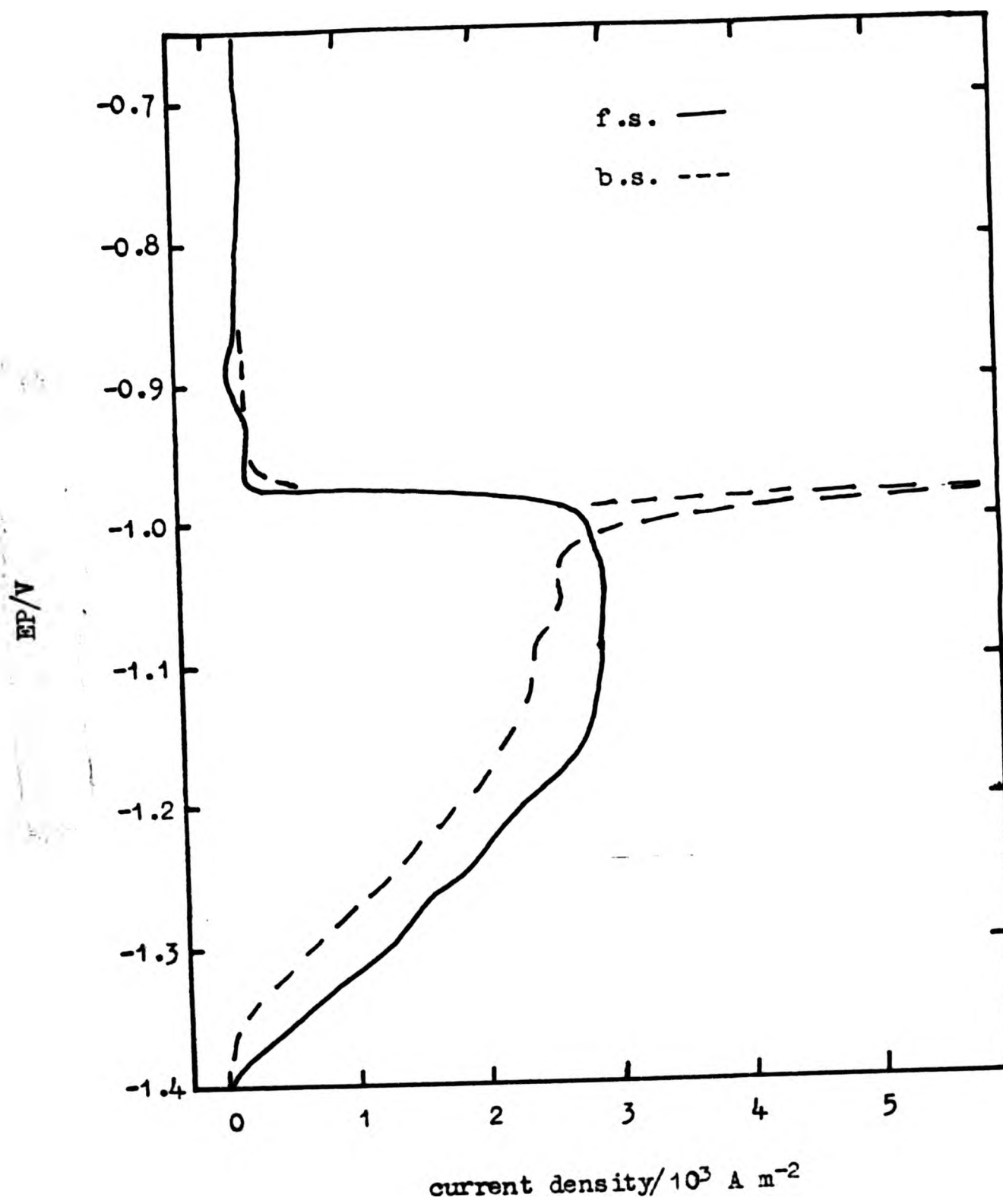


Figure 182. Anodic polarisation curves for Zn-25 Cd alloy in ZnO saturated 6 mol dm⁻³ KOH on a stationary electrode.

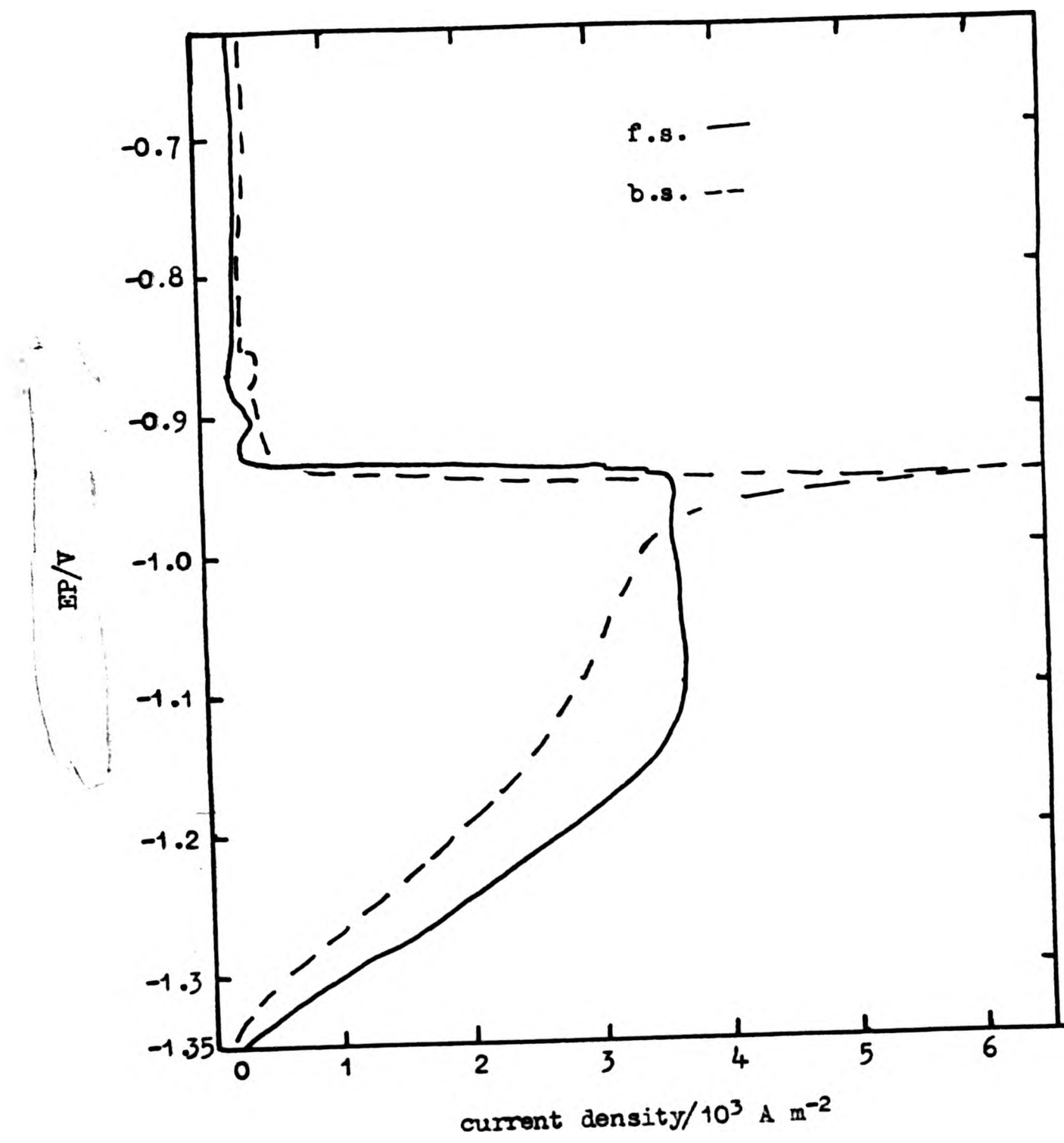


Figure 183. Anodic polarisation curves for the Zn-25 Cd alloy in ZnO saturated 6 mol dm⁻³ KOH at 10 rad s⁻¹ rotation speed.

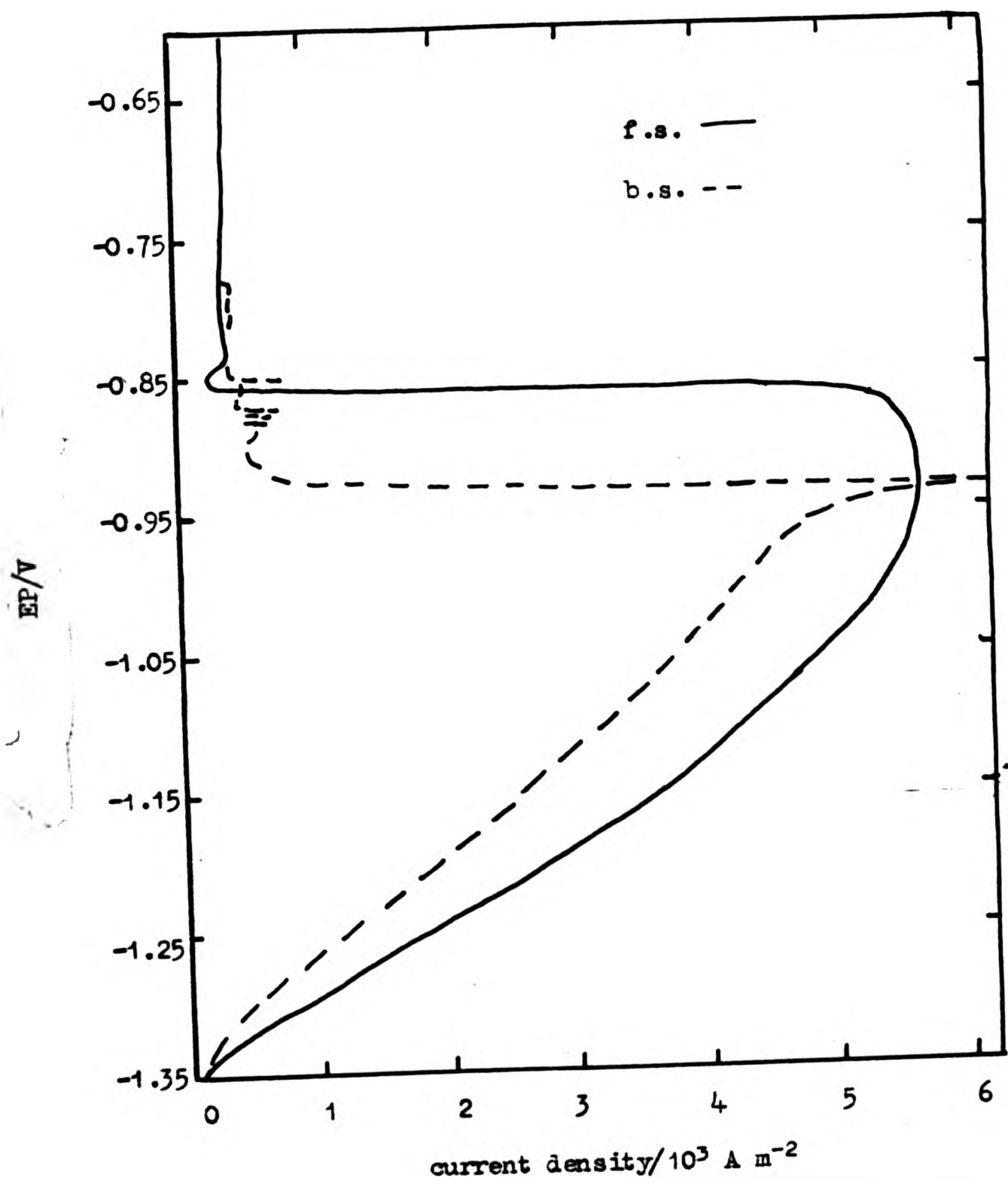


Figure 184. Anodic polarisation curves for the Zn-25 Cd alloy in ZnO saturated 6 mol dm⁻³ KOH at 50 rad s⁻¹ rotation speed.

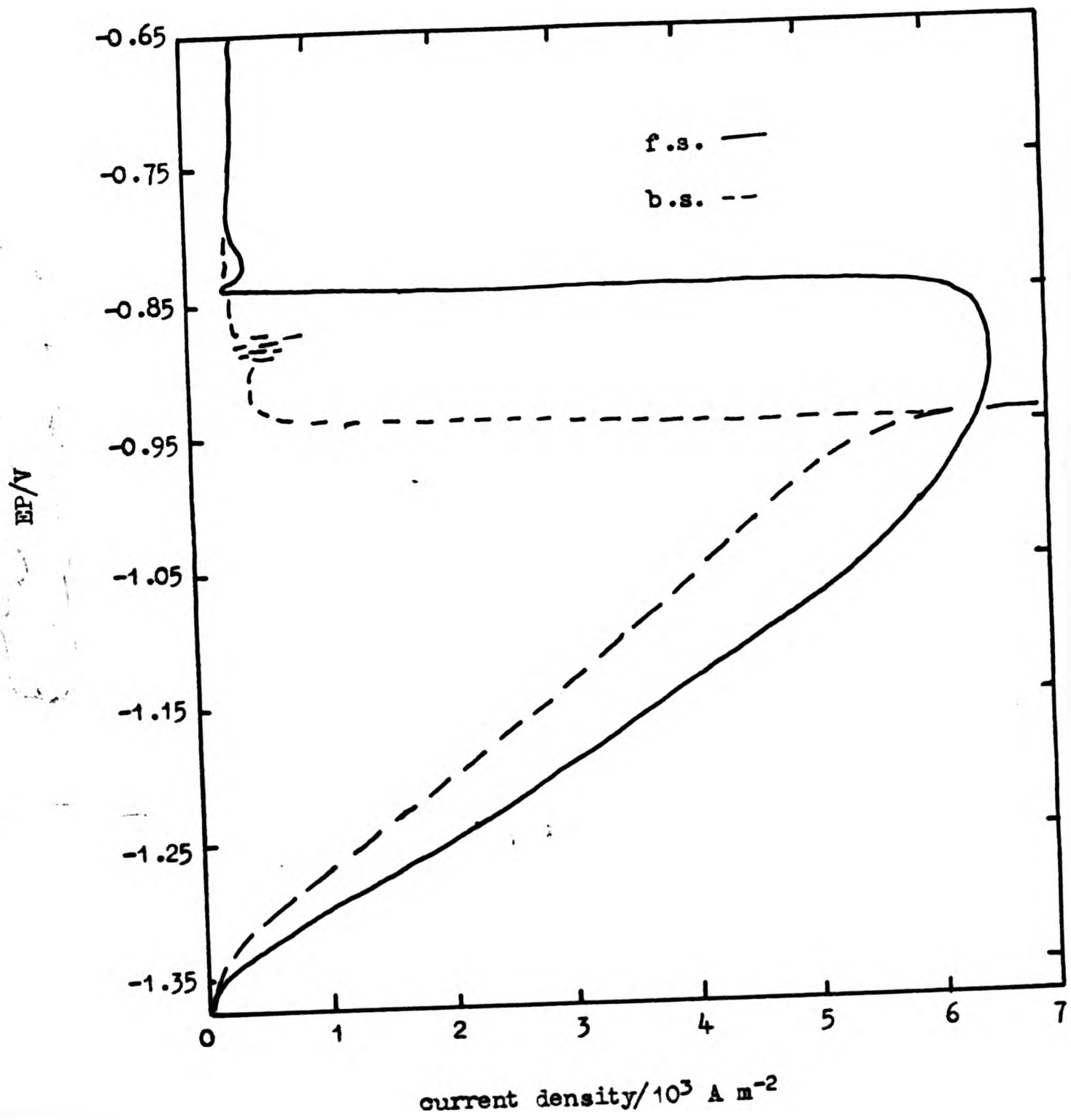


Figure 185. Anodic polarisation curves for the Zn-25 Cd alloy in ZnO saturated 6 mol km⁻³ KOH at 100 rad s⁻¹ rotation speed.

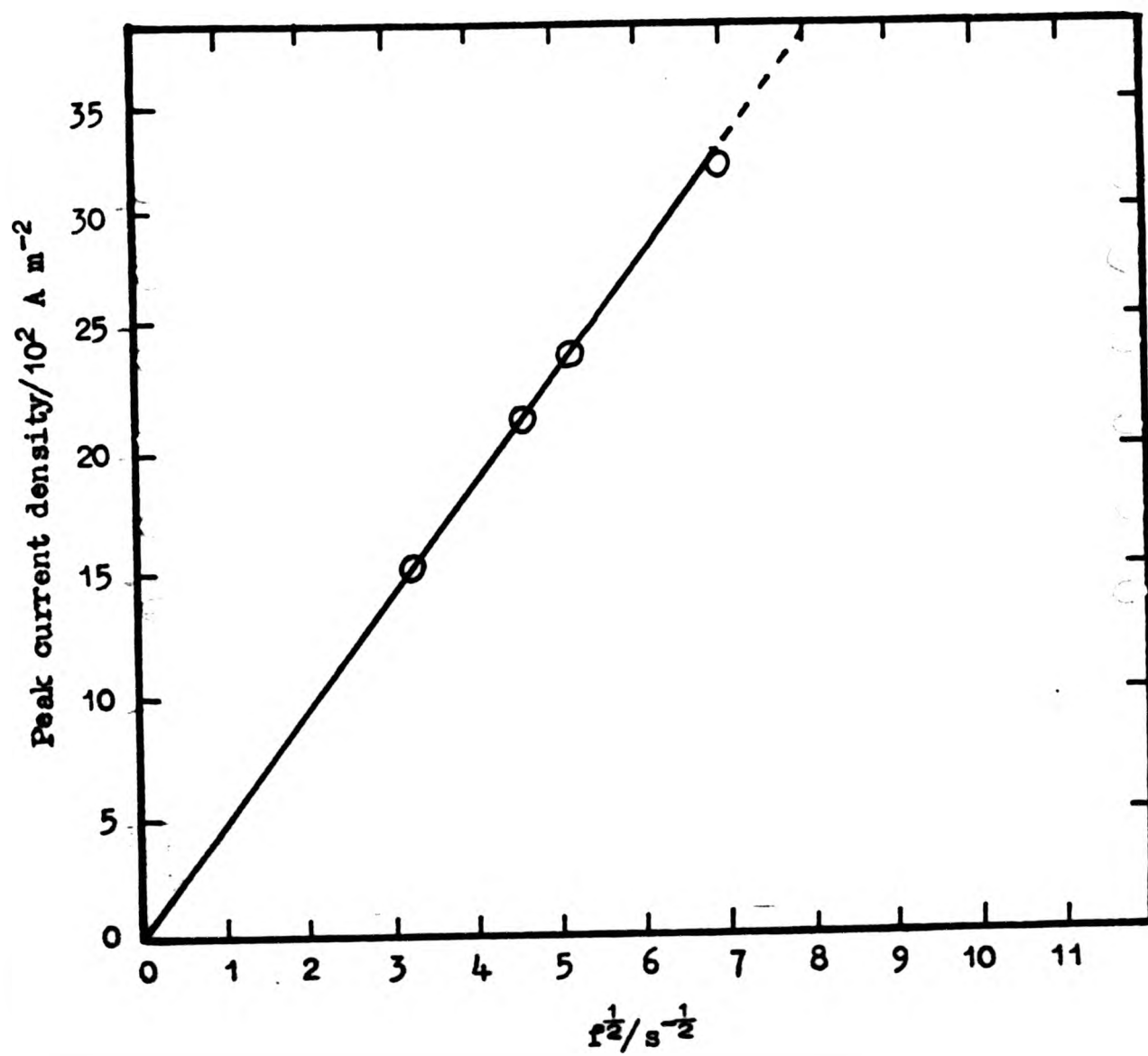


Figure 186. Relationship between peak current density and the rotation speed of rotating disc electrode of flared shape. Verification of Levich theory.

4.5 DISCUSSION

In the active dissolution region unhindered dissolution of the alloy takes place. This can take place up to a certain current density which, in corrosion-related contexts, is often referred to as the critical current density for passivation. When this peak value is exceeded, the insoluble products of corrosion begin to form on the surface. These first nucleate at suitable points, then grow gradually into clumps, finally forming a continuous film up to 100 nm thick. This film is many molecular layers thick. This acts as a barrier layer, through which the dissolving zinc and cadmium ion travel in one direction and the hydroxyl ions in the other. Thus the rate of dissolution and hence the current diminishes considerably for a given applied potential. From here on, even if a higher potential is applied, the current is still very low. After a certain value of potential the current increases suddenly, where oxygen evolution reaction takes place. The passive layer is formed by adsorption of the hydroxyl ions, which is directly formed on the alloy electrode surface, once a critical potential and current is reached. Further dissolution of the electrode is then determined by the thickness and the rate at which transport processes can occur within this layer. The thickness of this layer decreases with the increase in the rotation speed and so does the resistance of the film. The rate controlling step is the diffusive transport of the cadmate and zincate ion into the bulk of the electrolyte and not the transport of ions across the surface film under the action of the local electrical field existing across the film. In the case of the plain KOH electrolyte the rate controlling step is the diffusive transport of the hydroxyl ion. The absence of oscillations in the case of amalgam electrodes and zinc oxide saturated electrolyte shows that the nature and conductivity of the film does not change. Oscillations in current are observed in the plain electrolyte with some alloys, indicating that the nature and conductivity of the film is changing, resulting in dissolution and reformation of the insoluble corrosion product.

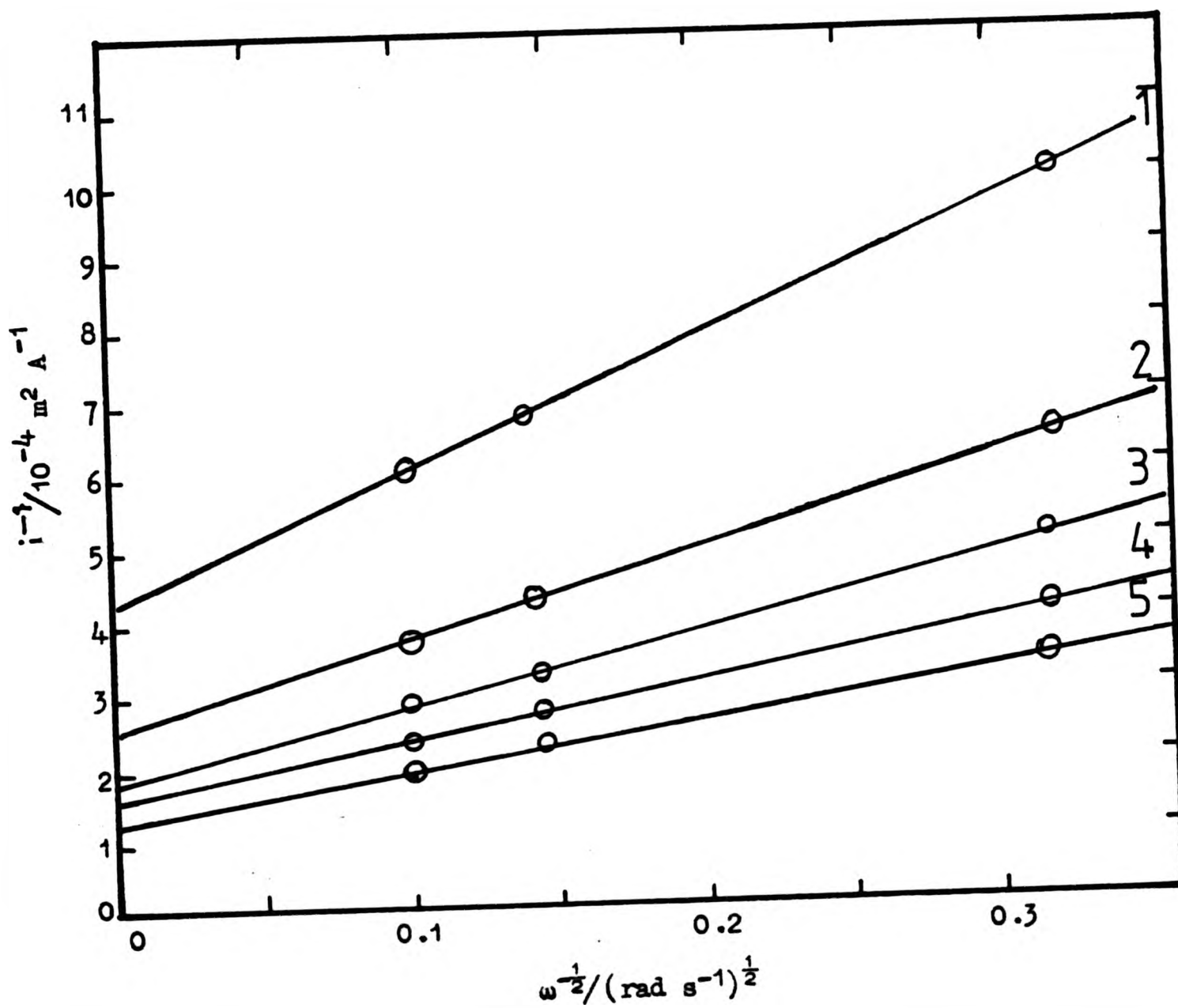


Figure 187. Plot of i^{-1} vs. $\frac{1}{\omega^{1/2}}$ at -1.40 V .

1. Zn in KOH slope 42 mV dec^{-1}
2. Zn-Cd alloys in KOH slope 33 mV dec^{-1}
3. " " " " saturated with ZnO slope 30 mV dec^{-1}
4. Zn-Cd-Hg " " " slope 26 mV dec^{-1}
5. " " " " saturated with ZnO slope 20 mV dec^{-1}

$$i_{\infty} = nF K_b C^s$$

or

$$\frac{i_{\infty}}{nF K_b} = C^s = C^{E^0} \exp \left[\frac{(E - E^0) nF}{RT} \right]$$

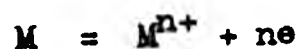
where K_b is rate constant for the reduction reaction,
 C^s is the concentration at the electrode surface.

See reference 121.

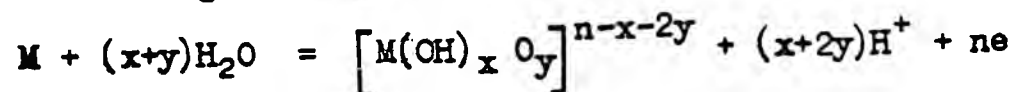
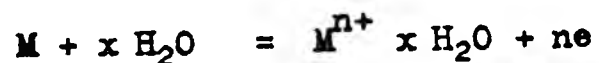
A plot of i^{-1} vs. $1/\omega^{1/2}$ should give an intercept of $1/i_{\infty}$ and hence a slope of 40 mV dec^{-1} for Zn-Cd alloys and 25 mV dec^{-1} for Zn-Cd-Hg alloys in plain electrolyte; whereas in ZnO saturated electrolyte for Zn-Cd alloys 30 mV dec^{-1} and 18 mV dec^{-1} for Zn-Cd-Hg alloys. A test of the above equation is shown in Figure 187 where i^{-1} is plotted against $\omega^{-1/2}$. These values are indicated by the Zn-Cd alloys in plain and ZnO saturated KOH and also by Zn-Cd-Hg alloys in plain KOH within the limits of experimental error.

In the active and passive regions the dissolution current is found to be a function of rotation speed. Thus the reaction is reversible under diffusion control. The diffusing ions are OH^- and $\text{Zn}(\text{OH})_4^{2-}$. The passivating film is monomolecular over a considerable range of potentials and at most up to 10 nm thick (several layers), which is the stable form as there is always a balance between formation and dissolution. Long term galvanostatic discharge studies (see chapter 6) indicate that if sufficient time is allowed a thick film eventually dissolves to leave a transparent film of thickness not more than 70 layers or of the order of 10 nm thick.⁴⁹ The passive film has appreciable electronic conductivity. The growth of the film from a monolayer to many molecular layers probably follows a parabolic law,⁶² from which deviations are observed when a crack, fold or fissure occurs. The parabolic growth law is consistent with the assumption that the necessary electron transfer process in the growth of cadmium and zinc hydroxide occurs at the metal oxide interface. Metal ions go into solution and later deposit on the metal surface as an hydrated hydroxide,

oxides or hydroxyl anions and metal cations. The passivation process involves the formation of a new phase, in steps that include adsorption as an important intermediate stage. Here metal dissolution is most responsible for the magnitude of the current represented by a reaction of the type:



Formation of an anodic film may be represented by any of the following types of reactions:



The presence of water is a necessary factor for the appearance of passivity. The OH^-/H_2O ratio at the interface is significant. At low ratios the electrode may behave according to the appropriate Pourbaix diagram (see section 1.4.2). At higher ratios anodic brightening occurs.

The passive films may be characterised by their thickness, composition and structure, and conductivity. Film thickness increases with both time and potential, depends inversely on the dissolution current and electronic conductivity of the film. Coulometric and ellipsometric evidence¹²³ suggests that the thickness varies from a monolayer in the active region to up to 10 nm in the passive region.

Furthermore, in the present programme of investigations the application of the rotating disc technique suggests that the passivation process is diffusion dependent, which implies that a dissolution-precipitation mechanism is operating. The passivation is partly because of coverage of the electrode surface by anodic products and partly because of their adverse effect on the kinetics of the anodic dissolution of the metal. The anodic products are non-stoichiometric, electronically conductive and non-protective, but nevertheless bring about a significant decrease in the dissolution current.

X-ray powder diffraction carried out on a 1 w/o Cd-Zn binary alloy yielded information on the composition of the passive film. The film was composed of metal dissolution products such as CdO, Zn(OH)₂, ZnO and Cd(OH)₂. The hydroxide of zinc and oxide of cadmium were present in larger quantities compared to that of oxide of zinc and hydroxide of cadmium. Cadmium being in small quantity in the alloy metal, it was present in a proportional amount in the anodic products.

4.6 CONCLUSIONS

The following conclusions can be drawn from the anodic polarisation studies described above.

- 4.6.1 In the active and passive regions the current is dependent on the rotation speed. As the speed of rotation increases the critical/peak current required for passivation also increases.
- 4.6.2 This rotation speed dependence of current indicates the processes are under diffusion control.
- 4.6.3 The ions involved in diffusion are OH⁻ and Zn(OH)₄²⁻, and cadmate, but initially Zn²⁺ and Cd²⁺ cations are involved.
- 4.6.4 The active region Tafel slope varies from 18 to 40 mV with an experimental error of ±5 mV. This difference in Tafel slope is an indication of a change in the value of the transfer coefficient 'α' and therefore of a change in mechanism. The interpretations given by others workers have not led to a clear understanding of the phenomena.
- 4.6.5 Passivity is due to the formation of a phase monolayer on the electrode surface. The reversible potential of film formation is about 100 mV more anodic than the Zn/ZnO electrode.

4.6.14 Since the film thickness does not vary linearly with the potential one can assume a constant film to solution potential difference and an independence of the free energy of activation (for the passage of zinc ions through the film) on the potential. The qualitative physical meaning of this is a tightening of the monolayer film on the surface with increase in the anodic potential.

4.6.15 Due to reversibility of film dissolution the steady state current and the film thickness are functions of the convective conditions at the electrode surface.

CHAPTER FIVE

HYDROGEN OVERPOTENTIAL ON THE ALLOYS IN ALKALINE SOLUTIONS5.1 INTRODUCTION

Data on hydrogen overvoltage on the anodes of the alkaline battery is both of theoretical as well as practical importance. Despite this, the scientific literature does not contain much information. Zhoulodev and Stender¹¹⁰ measured hydrogen overvoltage on a number of metals in 6 mol dm^{-3} sodium hydroxide in an open vessel. Jofa and co-workers⁴⁶ measured this on a zinc surface in different concentrations of potassium hydroxide solutions. Vorkapic and co-workers⁴⁹ measured this on pure and amalgamated zinc in concentrated potassium hydroxide solutions by galvanostatic polarisation. T.S. Lee¹¹¹ measured this on pure zinc, zinc containing a known amount of impurities and some zinc alloys for example zinc-lead, zinc-iron etc. in 9 mol dm^{-3} potassium hydroxide. The purpose of this work is to report measurements of hydrogen overvoltage on zinc-cadmium alloys in 6 mol dm^{-3} potassium hydroxide solution.

5.2 EXPERIMENTAL

The cell used for these experiments is the same as that used for the anodic polarisation studies. The cell is a closed system with a slightly positive gas pressure to prevent air entry. Anode and cathode have separate compartments. A stream of high purity gas is bubbled through both the compartments. The counter electrode was chosen from a large platinum gauze. The working electrode was prepared as described earlier. The experiments were carried out with the rotating disc electrode apparatus. A mercury-mercuric oxide reference electrode was used, as before. The method of electrolyte preparation and alloy preparation is as previously described. The electrolyte was pre-electrolysed for several days before the actual measurements were carried out. To eliminate the risk of dissolution of active metal into the electrolyte, the working and counter

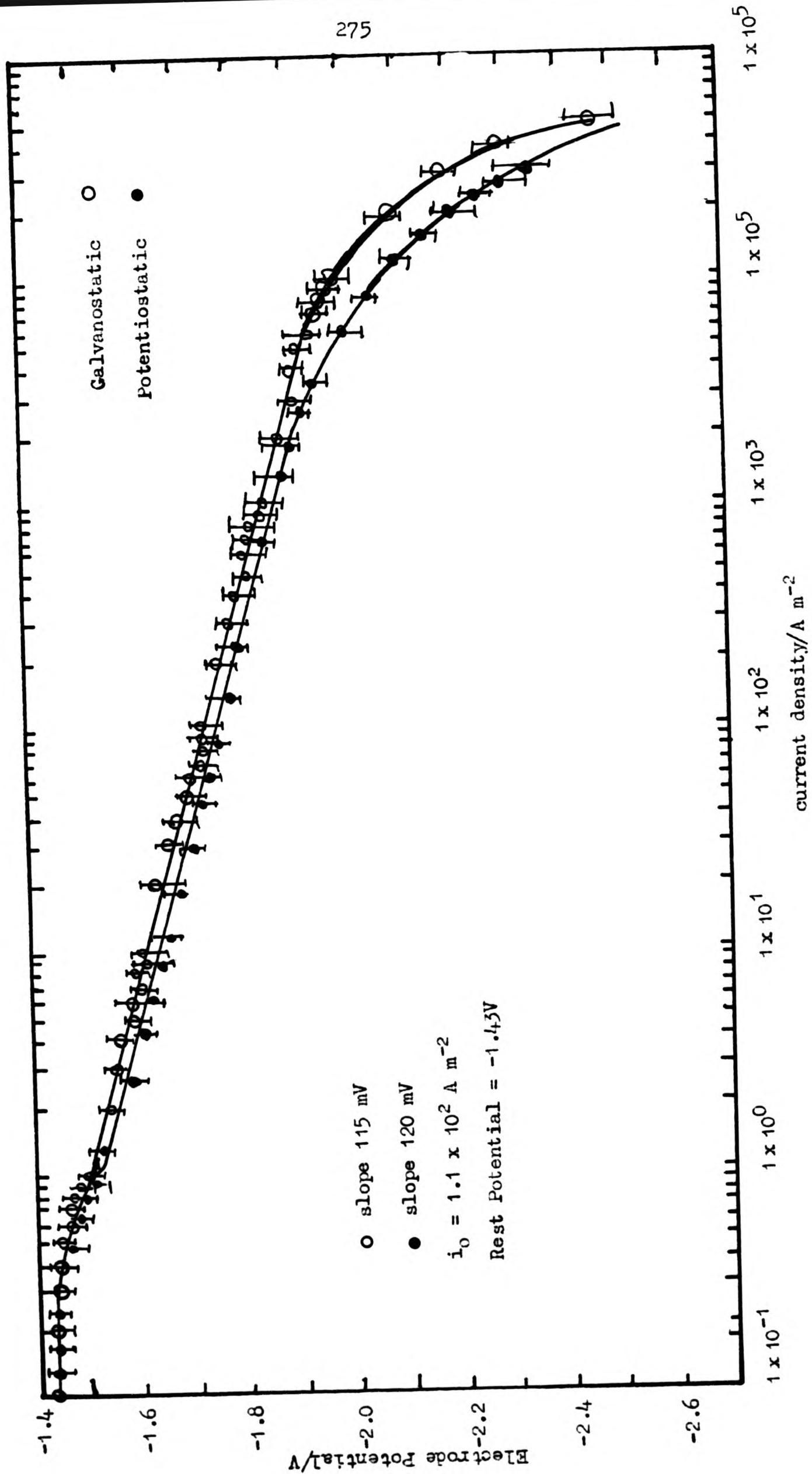


Figure 188. Cathodic polarisation curve for pure zinc at 25°C in 6 mol dm⁻³ KOH at 200 r.p.s.

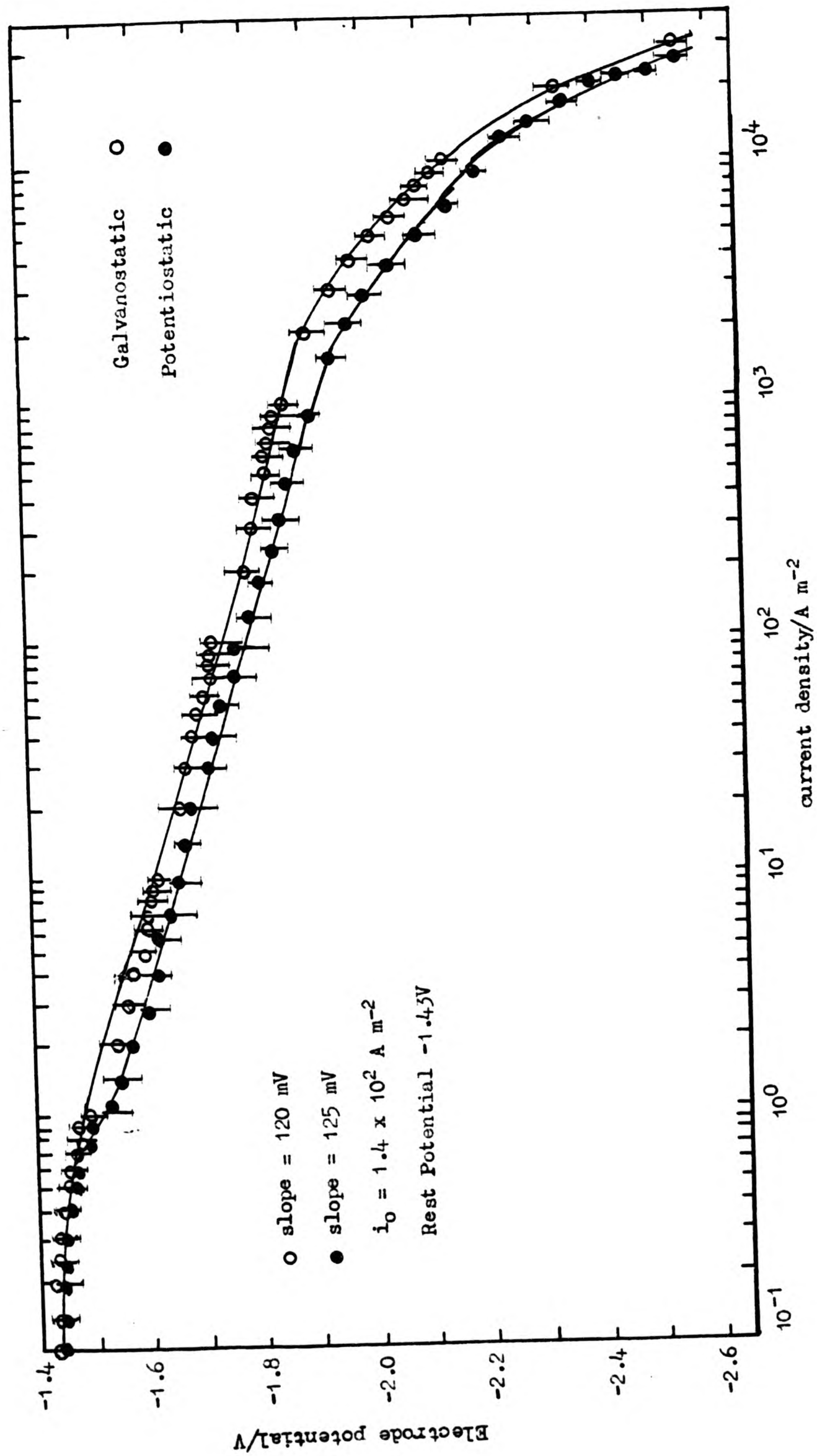


Figure 190. Cathodic polarisation curve for 0.20 w/o Cd alloy at 25°C in 6 mol dm⁻³ KOH at 200 r.p.s.

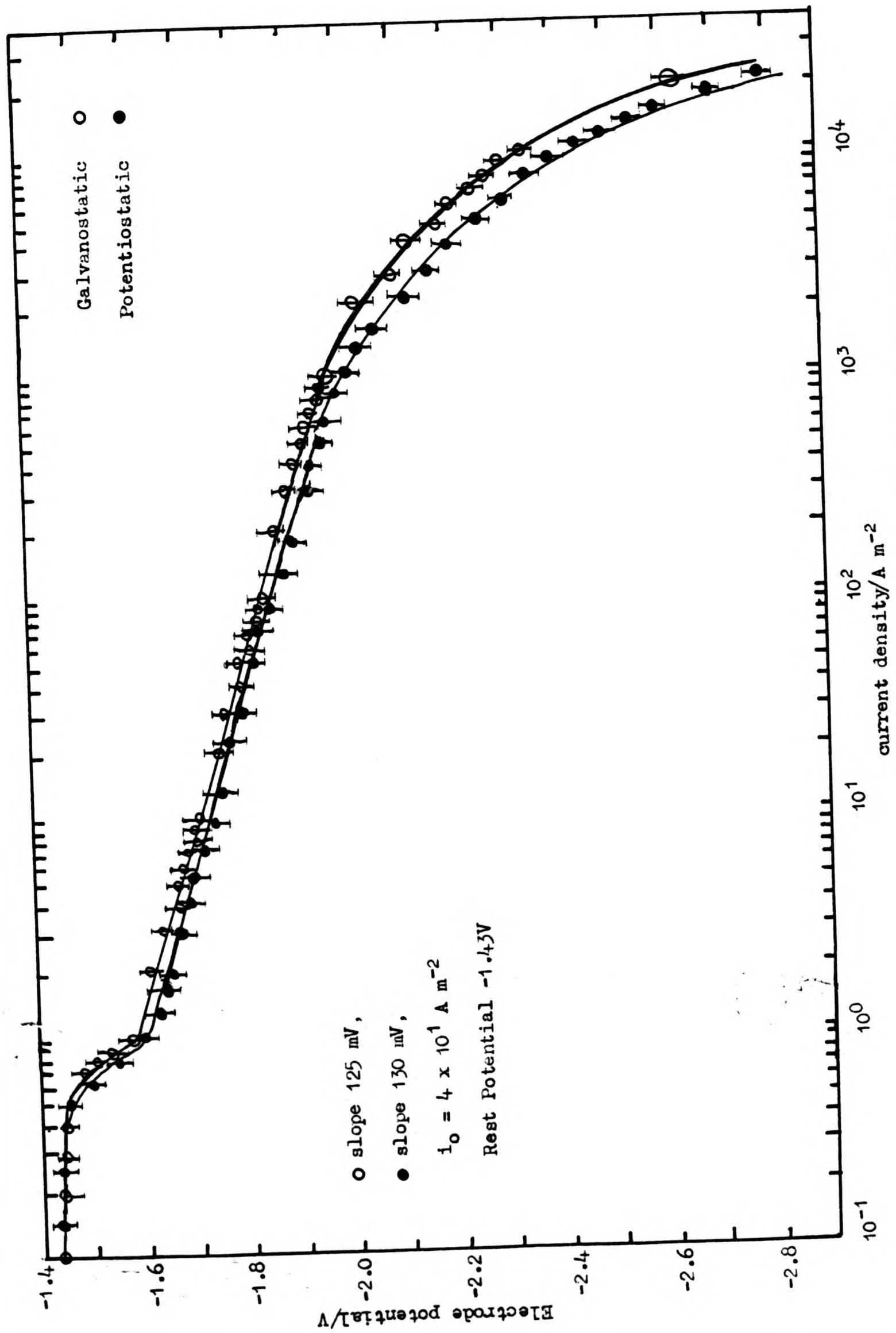


Figure 191. Cathodic polarisation curve for 1.0 w/o Cd alloy at 25°C in 6 mol dm⁻³ KOH at 200 r.p.s.

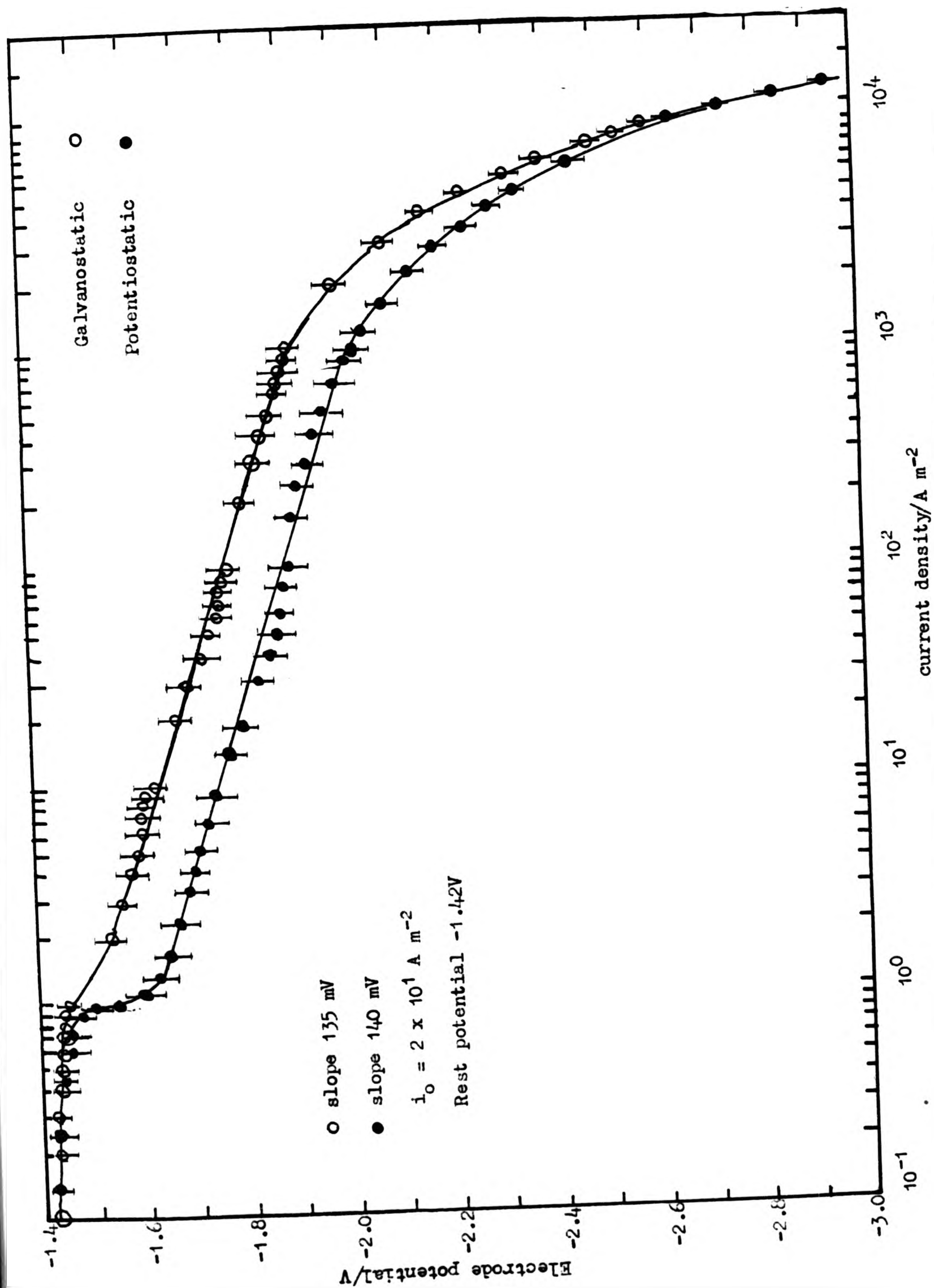


Figure 193. Cathodic polarisation curve for 5.0 w/o Cd alloy at 25°C in 6 mol dm⁻³ KOH at 200 r.p.s.

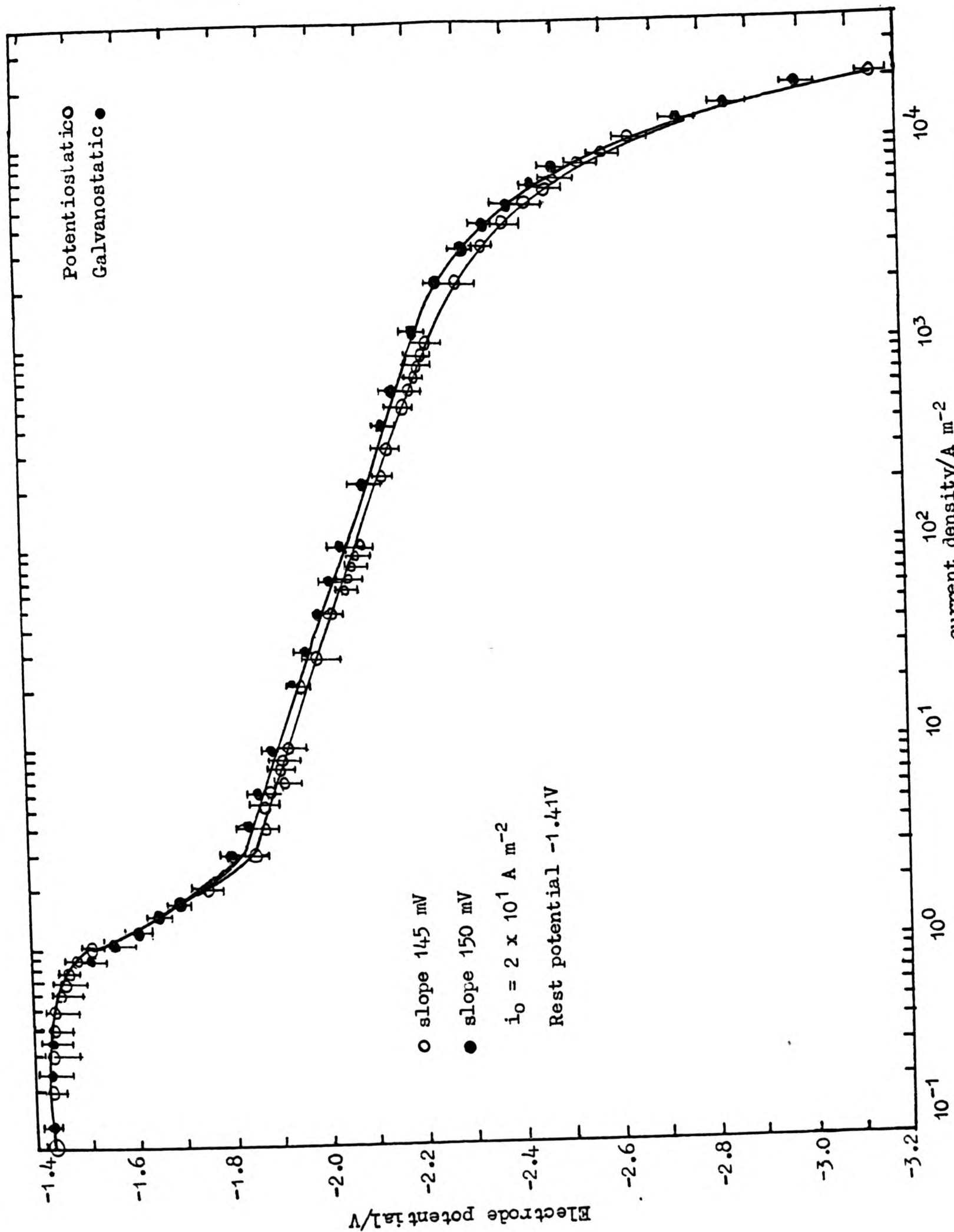


Figure 195. Cathodic polarisation curve for 25.0 w/o Cd alloy at 25°C in 6 mol dm⁻³ KOH at 200 r.p.s.

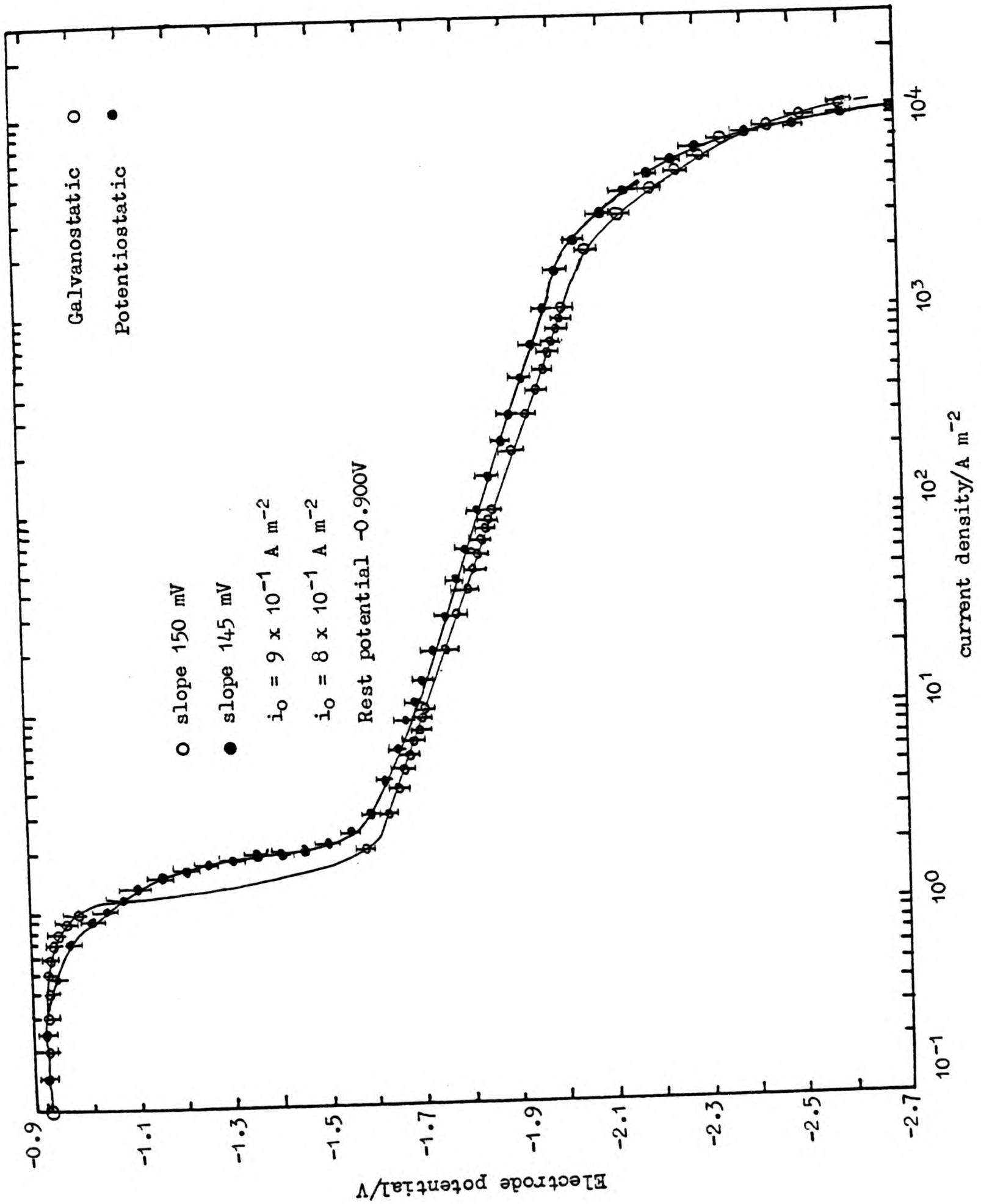


Figure 196. Cathodic polarisation curve for Cd at 25°C in 6 mol dm⁻³ KOH at 200 r.p.s.

electrodes were connected to the potentiostats before the entry. Wenking polarisation assembly described earlier was used as a source of constant potential for potentiostatic measurements and as a source of constant current for galvanostatic measurements. The potentials were measured with a Sinclair digital voltmeter DM450 and the currents by Avo Meter Model 8. The measurements were carried out from the high current density end to the low current density region and back again, this process was then repeated. The steady potential was recorded at each current density for galvanostatic measurements and steady current was recorded for each potential, in potentiostatic measurements. Variations of a few millivolts were observed in steady potentials in each direction. However, these were reproducible. Experiments were repeated until reproducible data was obtained. This required an average of three runs. The temperature of the cell was maintained at $25^{\circ}\text{C} \pm 0.1^{\circ}\text{C}$.

Zinc oxide saturated electrolyte could not be used in these experiments because the hydrogen evolution and zinc deposition potentials practically coincide, thus current drawn would mainly be due to zinc deposition, masking the current due to hydrogen evolution.

5.3 RESULTS AND DISCUSSION

The electrode potentials and the logarithm of current density plots for Zn, Cd and their alloys in $6 \text{ mol dm}^{-3}\text{KOH}$ at 25°C are shown in Figures 188-196. The transfer coefficients α , and the exchange current densities i_0 , for the hydrogen discharge reaction were obtained from these plots. These parameters are listed in Table 20. Figure 197 shows the Tafel curves (linear regions) of the hydrogen evolution reaction curves for the metals plotted together on the same paper.

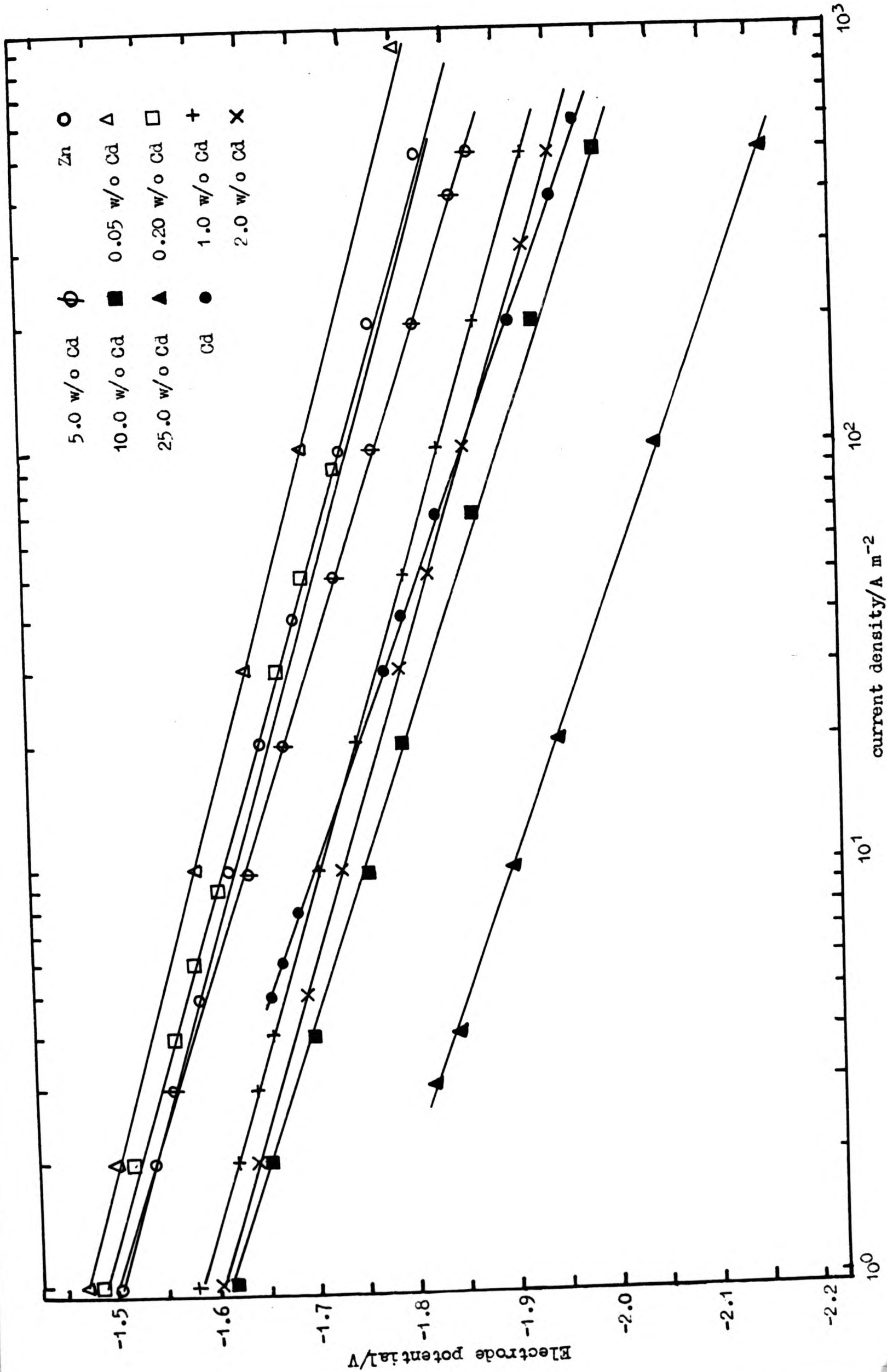


Figure 197. A plot of electrode potential vs. current density for various alloys

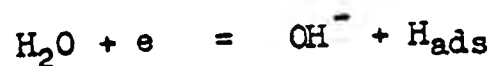
Table 20. Electrochemical parameters for the hydrogen evolution process in 6 mol dm⁻³ KOH at 25°C

Metal	Potentiostatic Method			Galvanostatic Method		
	b mV dec ⁻¹	a	i ₀ Am ⁻²	b mV dec ⁻¹	a	i ₀ Am ⁻²
Zn	115	0.51	1.1 x 10 ²	120	0.49	1.1 x 10 ²
0.05 w/v Cd	115	0.51	2.7 x 10 ²	120	0.49	2.7 x 10 ²
0.20 "	115	0.51	1.4 x 10 ²	120	0.49	1.4 x 10 ²
1.0 "	120	0.49	4 x 10 ¹	125	0.47	4 x 10 ¹
2.0 "	125	0.47	4 x 10 ¹	130	0.45	4 x 10 ¹
5.0 "	130	0.45	2 x 10 ¹	135	0.44	2 x 10 ¹
10.0 "	135	0.44	4 x 10 ¹	140	0.42	4 x 10 ¹
25.0 "	145	0.42	2 x 10 ¹	150	0.39	2 x 10 ¹
Cd	145	0.41	8 x 10 ⁻¹	150	0.39	9 x 10 ⁻¹

The overall reaction for the hydrogen evolution process in alkaline medium may be written as:



It is well known that this is a multistage process. As a first step, water molecules accept an electron to breakdown into hydroxyl ion and an hydrogen atom. The hydrogen atom being very reactive bonds on to a metal atom, forming an M-H bond, and is said to be adsorbed. Thus



Here it is obvious that the adsorption energy of hydrogen on metal, the electron work function of the metal, the metal to solution potential difference, and the ψ_1 potential are important parameters. Loss of hydrogen from H₂O molecule involves stretching of the O-H bond. The hydrogen ion or the proton behaves, not in a classical manner, but its behaviour is essentially of quantum mechanical in nature. The hydrogen

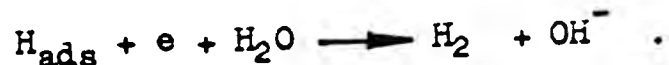
ion can not exist as H^+ in the aqueous solutions. It is surrounded by four H_2O molecules, which occupy corners of a tetrahedron, H^+ being in the centre. The least complicated, acceptable structure is H_3O^+ which represents a weak hydrogen bond. On metals readily adsorbing hydrogen, the absorption occurs practically instantaneously. Such metals are arsenic, steels, Pt, Pd, etc. The adsorption energy would be exothermic in nature. For metals adsorbing hydrogen poorly, the adsorption energy would be endothermic, and activation energy required would practically be equal to the adsorption heat, and the activation energy of the recombination would be close to zero. The nature of the metal and the solution are clearly important factors.

The desorption of adsorbed hydrogen atoms can take place via two routes. The chemical desorption, in which two adsorbed hydrogen atoms combine together to form an H_2 molecule because the first shell is stable when there are two electrons with opposite spins. After all, hydrogen atoms cannot exist, but molecules can and are more stable; the combination releasing an exothermic bond energy. The reaction can be written as:



This is more likely with metals whose M-H bond energy is very low, where the discharge activation energy is independent of electron work function of the metal. Examples of such metals are Pt, Pd, Rh, etc.

The recombination can also take place by electrochemical desorption i.e.



Electrochemical desorption is most likely to occur for metals with lowest adsorption heat e.g. Zn, Cd, Hg, Pb, Sn, Ga etc.

The mechanism of hydrogen evolution at very negative overpotentials (than their equilibrium values) depends not so much on the ratio of exchange currents as on the ratio of reaction rate constants. The dependence of the latter on the hydrogen adsorption heat would be determined by

the effect of adsorption heat on the activation energy. Rate constant rises with rising bond energy for H^+ discharge but falls for the desorption and recombination. The ratio of the rate constants for slow discharge and electrochemical desorption is taken as a criterion for the choice of rate determining step. For metals like Zn, Cd, Hg and amalgams a slow barrierless discharge with electrochemical desorption is a most likely mechanism.

A small amount of Cd in Zn does not change the slope 'b' or i_0 much one way or the other. As the Cd content increases, these parameters change to values approaching those of Cd.

The hydrogen evolution through anodic dissolution, on the other hand, depends on the corrosion current in the region of active dissolution. Thus the rate of hydrogen evolution will be a measure of corrosion current. Upon increasing the potential in a positive direction, passivity sets in when precipitation of insoluble anodic products hinders the kinetic dissolution of metal and the corrosion current falls to a constant low value, which is independent of the potential. This is reflected in the rate of hydrogen evolution.

The anodic reaction of zinc dissolution in alkaline solution can be represented by curve 'a', which will not vary under a given condition. The cathodic reaction of hydrogen evolution can be represented by curve 'b', which will vary depending on the metal surface i.e. whether it is Zn-Cd alloy or Zn-Cd-Hg alloy or pure Zn etc. Thus a family of curves can be drawn. The intersection of curves 'a' and 'b' defines corrosion potential and corrosion current. Thus lower slope of curve 'b' or shifting it to the left will result in a decrease in the corrosion current. The MnO_2 and HgO depolarisers and amalgamation do this. Additions of Cd also have this same effect as found through the present investigations. This is illustrated in Figure 198.

CHAPTER SIX

CONSTANT CURRENT DISCHARGE BEHAVIOUR6.1 INTRODUCTION

The previous work⁷⁴ carried out by the author in this direction consisted of applying a current step and studying the potential-time behaviour of the alloy (see section 1.4.3.5). The chronopotentiograms were obtained for current densities ranging from 30 A m^{-2} to 2100 A m^{-2} for approximately two minutes. These experiments were carried out at different temperatures namely 25, 35 and 45°C . The chart recorder used was a Bryans X-Y 26000/A-4 with a time base facility. The time base could provide various sweep rates. At the lowest sweep rate the maximum time interval available was 12 minutes. The specimens were repolished after each run, i.e. each chronopotentiogram obtained was on a fresh surface. The working electrode, during these experiments, was held vertically at the wall of the electrochemical cell. It is because of these differences that strict comparison of this work with the present studies has severe limitations. In assessing the results of this series of experiments, it was realised that:

- a) The tests were not carried out for a sufficiently long period of time.
- b) The current densities used were very high. This was so because of a very short test duration of 2 minutes. Only high current densities could lead to a transition time of this order.
- c) Long term tests with electrodes, remaining in constant contact with the electrolyte, should be able to simulate the cell performance more closely in the conditions under which cell electrodes discharge. The work described below was undertaken to extend the range of assessment of this anodic discharge behaviour, bearing in mind the limitations outlined above.

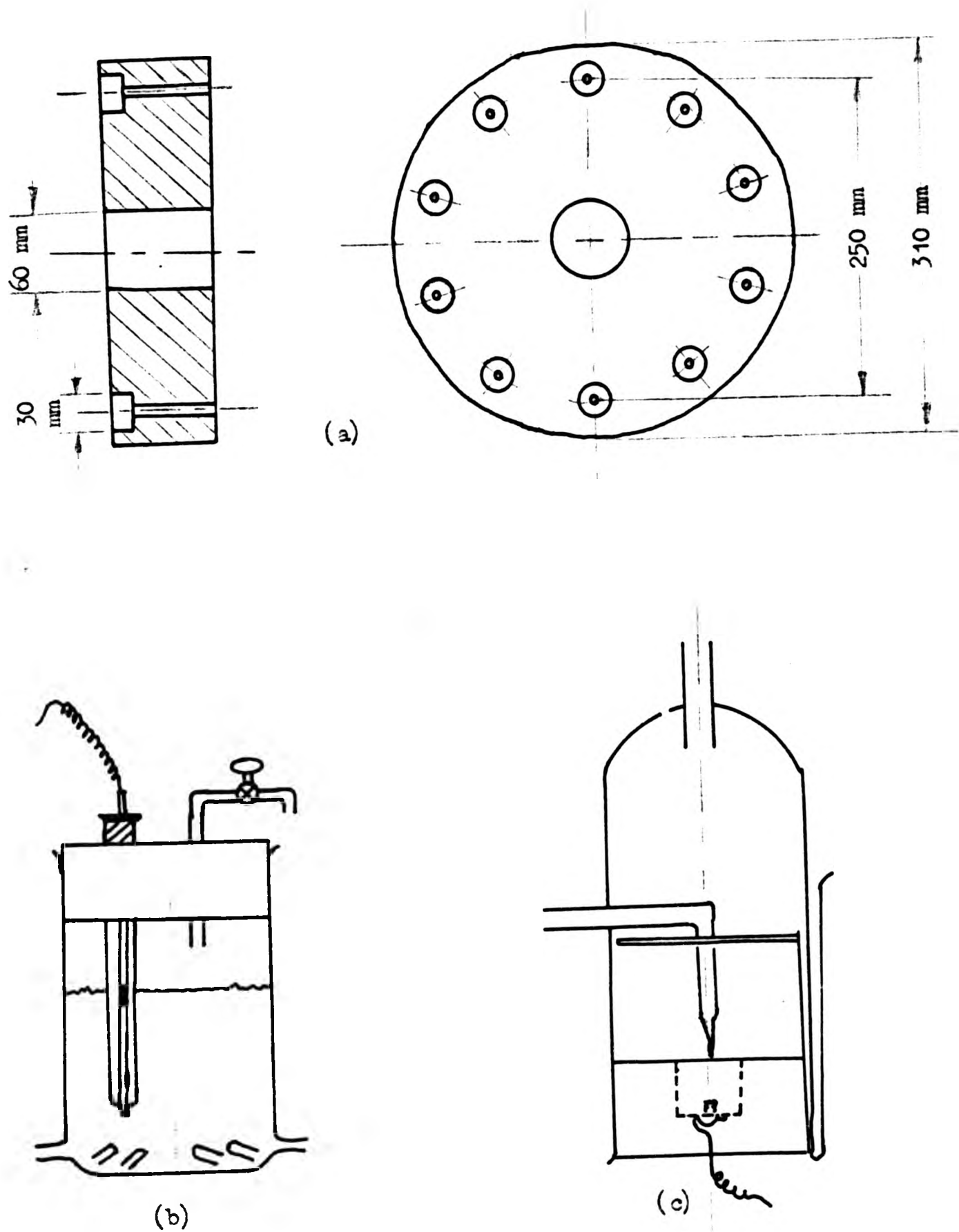


Figure 199. Details of construction of parts required for the chronopotentiometric experiments.

(a) Perspex mounting plate.

(b) Electrolyte reservoir holding Hg-HgO reference electrode.

(c) Polarisation cell assembly showing nickel counter electrode, specimen, and Luggin probe in position.

acted as a reservoir of electrolyte. The level of electrolyte inside the electrochemical cells was controlled by adjusting the height of the container with respect to the cells. By partially opening or closing the stopcock the pressure of the inert gas, coming through the other end, was changed to obtain additional help in controlling the level of electrolyte in the cells. The nitrogen supply was distributed to individual cells through a main glass tube with several side arms similar to the one shown in Figure 55, but much smaller in size. Figure 199-b shows the drawing of this container.

The electrochemical cells were mounted on a thick circular Perspex plate made to the drawing shown in Figure 199-a. The cells were arranged along the periphery of a circle 250 mm diameter. A maximum of ten cells could be accommodated. The plate was 310 mm in diameter. A circular hole 60 mm in diameter was cut through the centre to take up the electrolyte reservoir. The cells sat in recessed holes of 30 mm diameter. The plate-stand was fitted with four legs of suitable length made out of Perspex rods of suitable diameter. The legs were glued on by Tensol cement, and between an adjacent pair a Perspex plate was fixed. This plate served as a mount for a two gang single pole single throw switch used to connect each cell at a time to the galvanostat. The experimental set up described is shown in Figure 200.

The reference electrode was connected directly to the galvanostat because it was common to all probes. The counter electrodes were connected to one gang of poles and the working electrode leads to the second gang. The cells and the poles were marked for identification. Thus at each position of the switch only one of the cells was connected to the galvanostat, the others being on open circuit. There was an "off" position in which all the cells were on open circuit. The Wenking facility was used as a galvanostat. An Avometer Model 8 was used to measure currents and a Sinclair Model DM 450 digital voltmeter was used to measure potentials. A Bryans 28000 x-t chart recorder was used to record the chronopotentiograms.

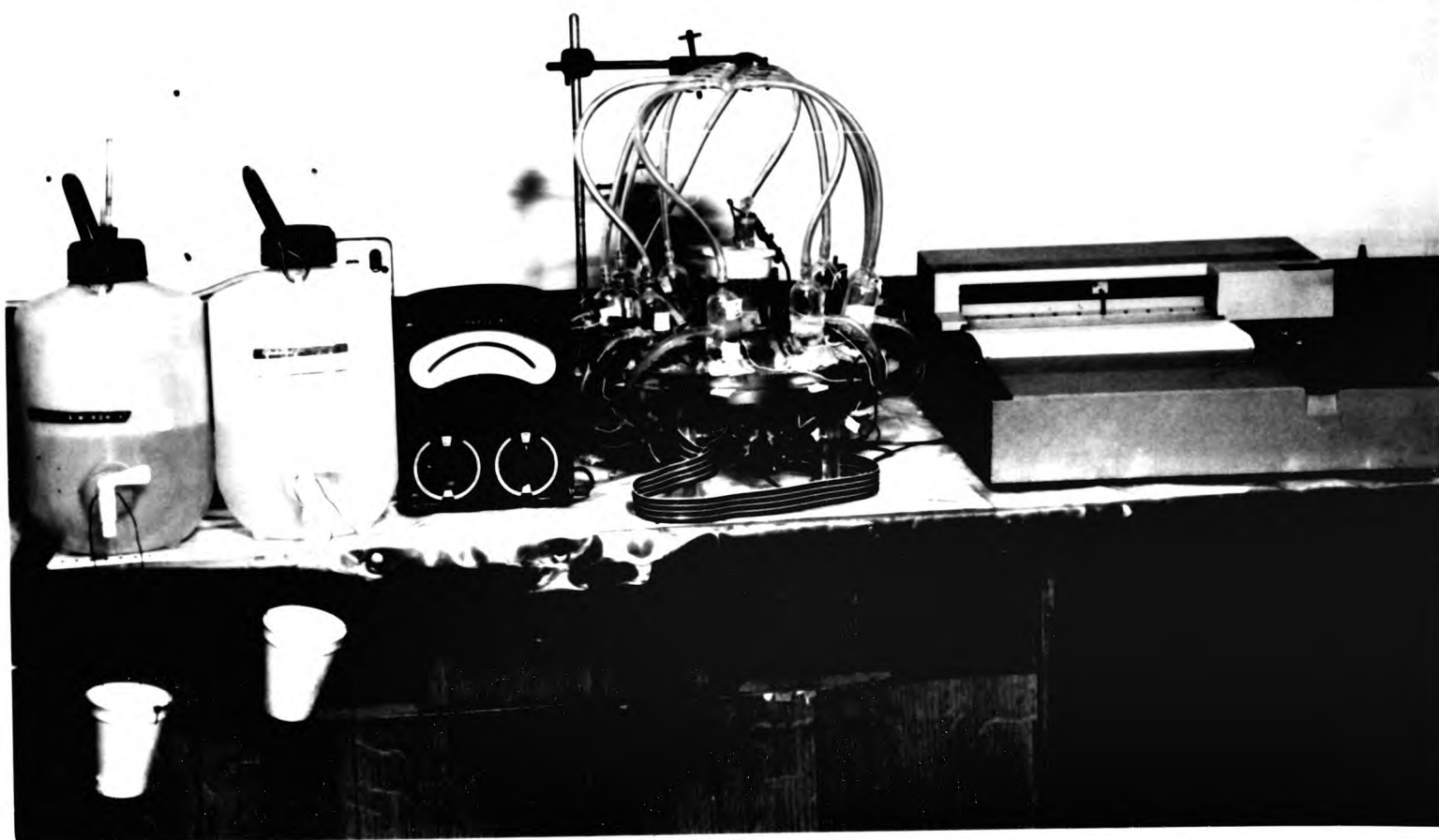


Figure 200. Arrangement of apparatus for the galvanostatic long term discharge experiments

Experiments were conducted at regular intervals when the cells were discharged galvanostatically. For the rest of the time they were left on open circuit. In these experiments the area of the electrodes was 0.40 cm^2 and the volume of electrolyte used was 14 cm^3 , therefore the ratio of volume to area was 35 cm.

The apparatus and pieces of equipment were assembled and connected. The cells were purged with nitrogen. The reservoir was filled with the electrolyte and the level in each cell was adjusted by the means described earlier. Stirring or bubbling with gas was avoided in order to simulate the quiescent conditions of a battery cell. The chart recorder time base was selected to give a suitable chart speed and the measured potential of the working electrode was applied to the x-axis. Thus when a given current was supplied by the galvanostat a chronopotentiogram was recorded on the chart recorder. The chart recorder was capable of measuring a wide range of time intervals, thus passivation time " t_p " and therefore transition time could be determined for various values of current densities. This was not possible on the chart recorder used previously, where the maximum time interval that could be measured was 12 minutes. At very high current densities the passivation is very fast. On the other hand, at very low current densities the passivation time may be so long that it is not practicable to measure it and it could be said that the specimen does not passivate. The values of current densities selected were such that they were neither very high, nor very low but 'moderate' so that the passivation times obtained were more realistic. These 'moderate' current density values would also be more near to the values encountered in practical battery usage.

Potential-time curves were recorded over a range of current densities until the electrodes passivated. Only ten alloys could be used for these experiments. Because of lack of time and the problems encountered with leakage in the electrochemical cells while the experiments were in progress more work could not be undertaken. To extend the time scale of these experiments a new design of cells (such as one incorporating sealed glass joints) with freedom from leakage would be

required. In view of the aggressiveness of concentrated KOH solution, any new design should be proved first by running dummy tests before actual experiments could begin. This was not possible due to shortage of time available. Experiments had to be terminated when sufficient data of significance had been obtained on the ten alloys, four of which were 2.5 w/o Hg amalgams.

6.3 RESULTS AND DISCUSSION

Figures 201-208 represent the chronopotentiograms obtained earlier on fresh, clean and vertical surfaces at 25°C in 6 mol dm⁻³ KOH saturated with ZnO under quiescent conditions.⁷⁴ As can be seen from the time axis these tests were for a short duration and therefore transition times could only be measured at high current densities, where this was less than or equal to two minutes. Figures 209-214 represent chronopotentiograms for ten alloys, including four amalgams, used during the present experiments. Here the electrodes were horizontal, facing upwards and the surfaces were always in contact with the electrolyte. The electrolyte used was the same as before, namely 6 mol dm⁻³ KOH saturated with ZnO.

Table 21 lists the values of steady state electrode potentials at various current densities for these alloys as obtained from the chronopotentiograms. The data in Table 21 is plotted in Figure 215. In this plot, in the interest of clarity, the 0.2 w/o Cd and its 2.5 w/o Hg amalgam have been represented by the same symbol. The same is true for 1.0 w/o Cd and 2.0 w/o Cd alloys and their 2.5 w/o Hg amalgam. This is so because the plotted points are almost coincidental to each other. Different symbols could, however, be chosen for 5.0 w/o Cd and its 2.5 w/o Hg amalgam because the plots are quite distinct. For 0.05 w/o Cd, 0.2 w/o Cd, 1.0 w/o Cd and their amalgams the points at initial current densities are crowded together and therefore for the sake of clarity these have been displaced horizontally and vertically.

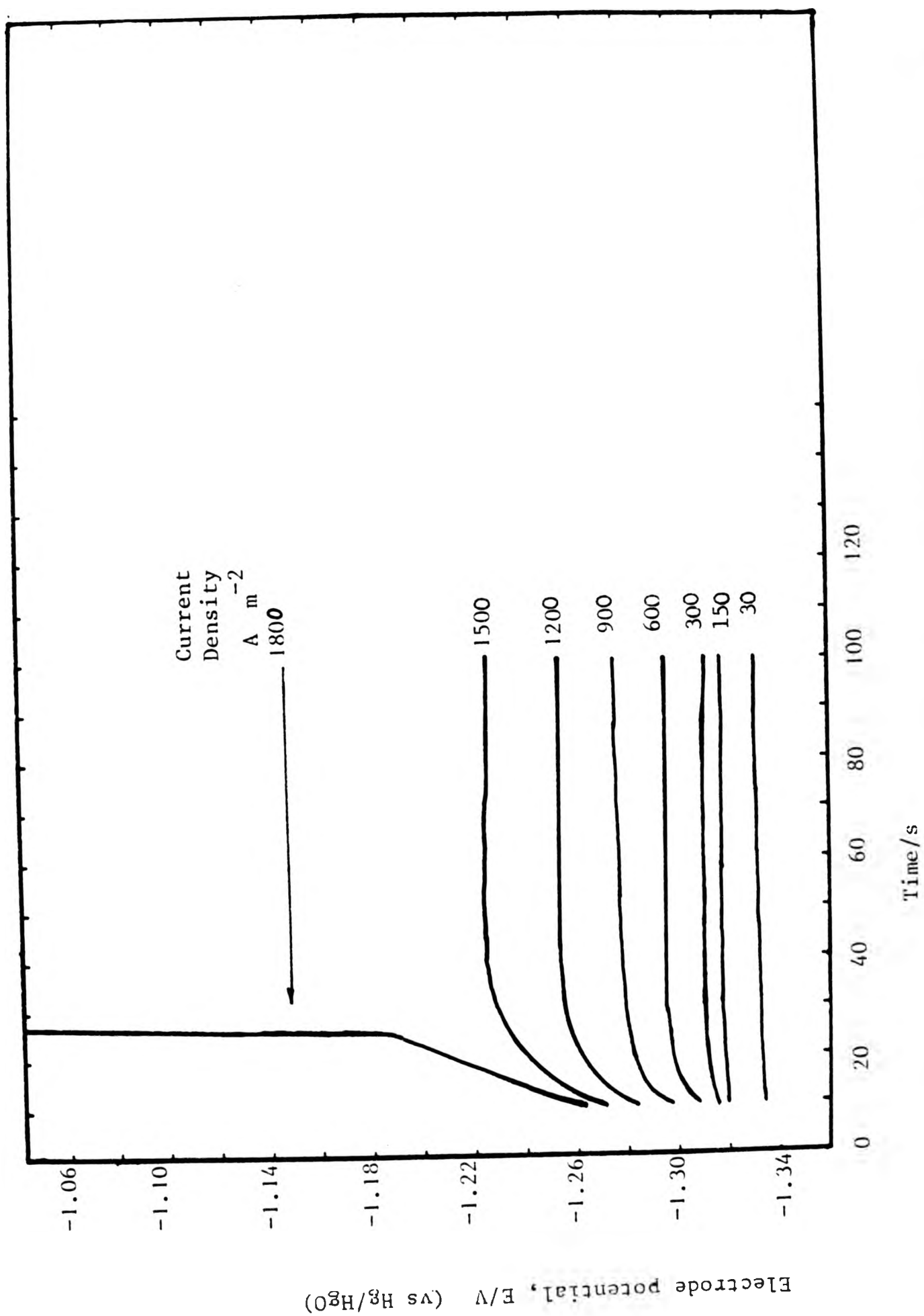


Figure 201. Chronopotentiograms for pure zinc in ZnO saturated $6 \text{ mol dm}^{-3} \text{ KOH}$ at 25°C

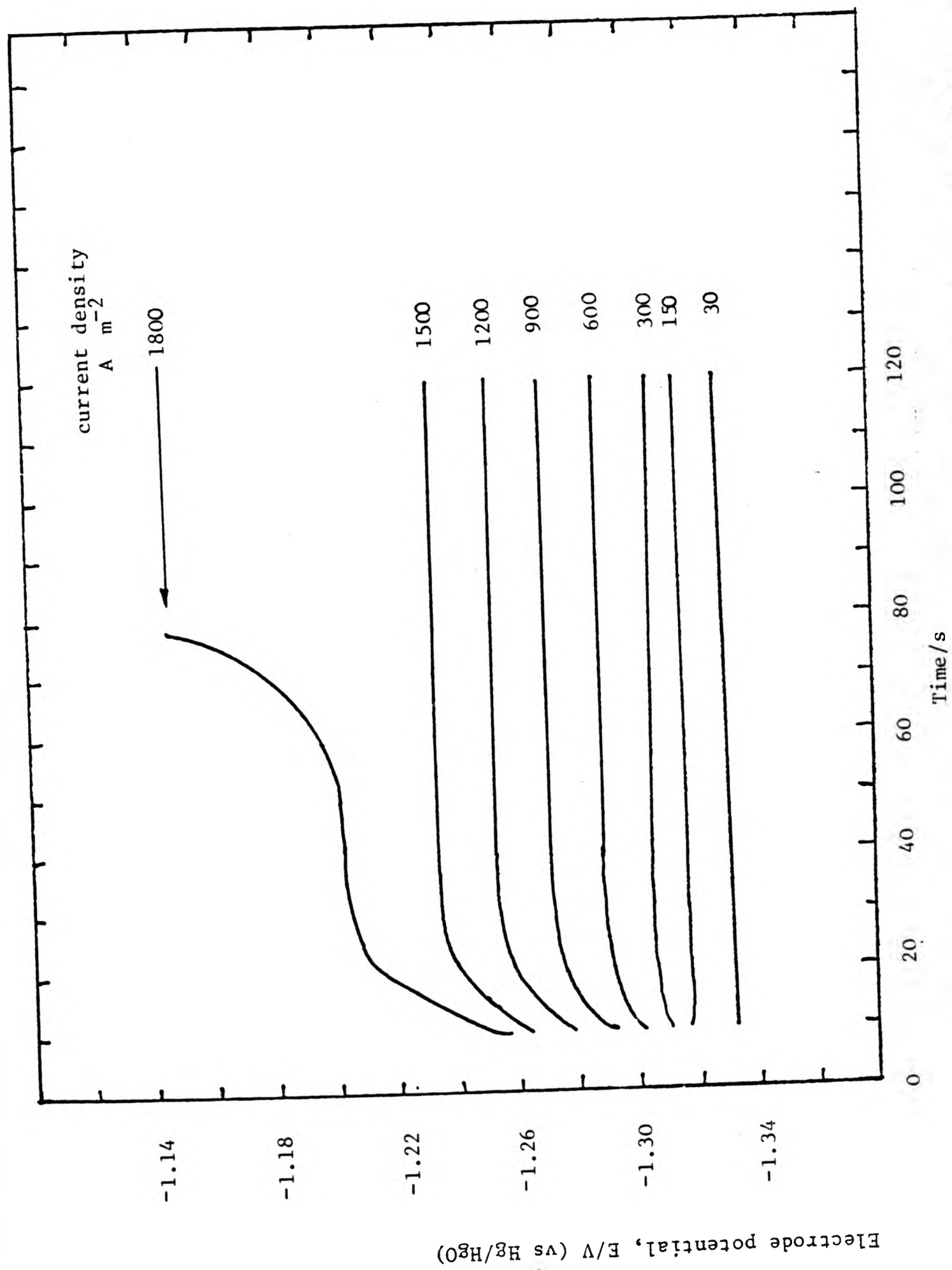


Figure 203. Chronopotentiograms for Zn-0.05 Cd alloy in ZnO saturated 6 mol dm⁻³ KOH at 25°C.

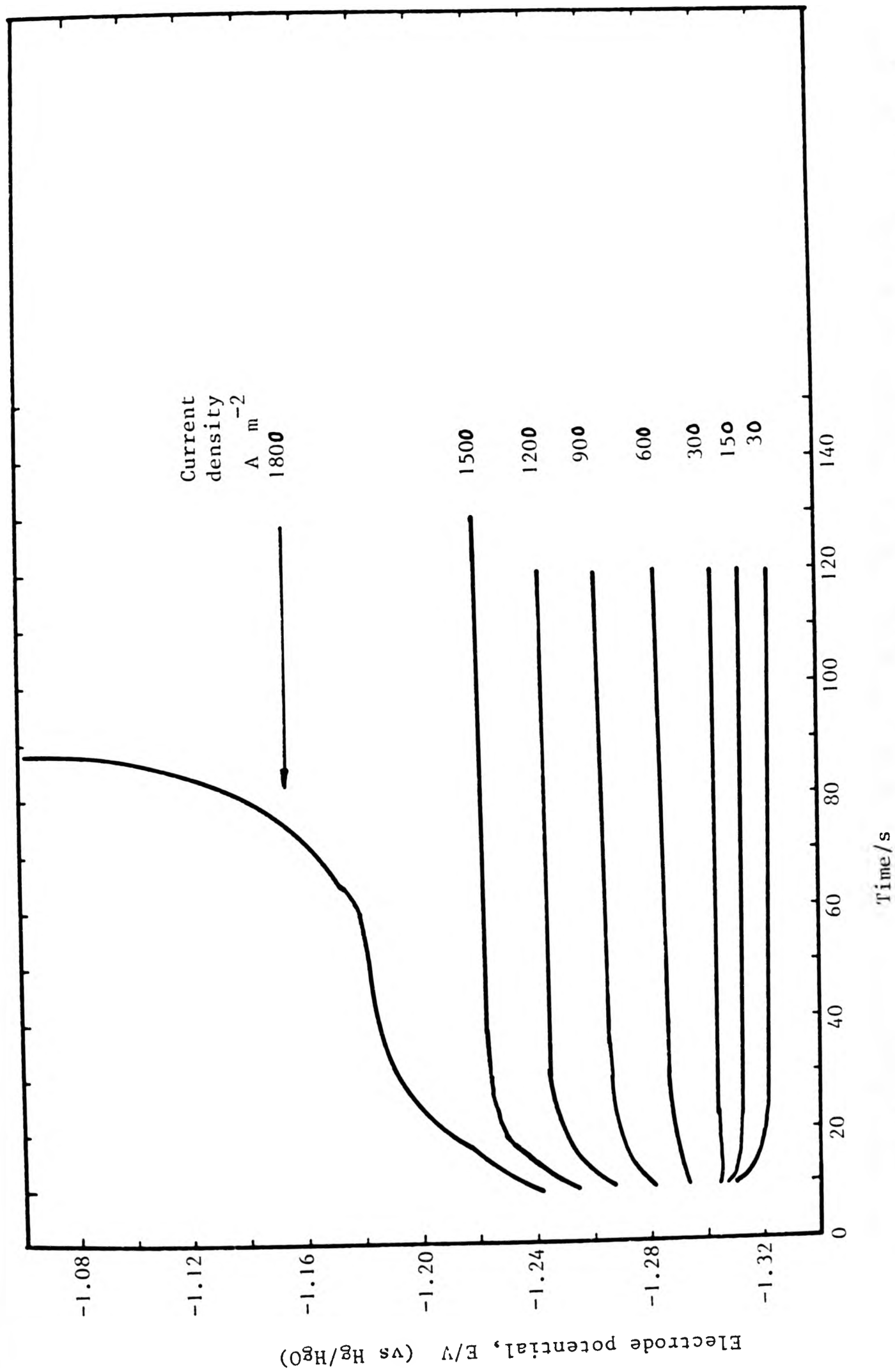


Figure 205. Chronopotentiograms for Zn-1.0 Cd alloy in ZnO saturated 6 mol dm^{-3} KOH at 25°C .

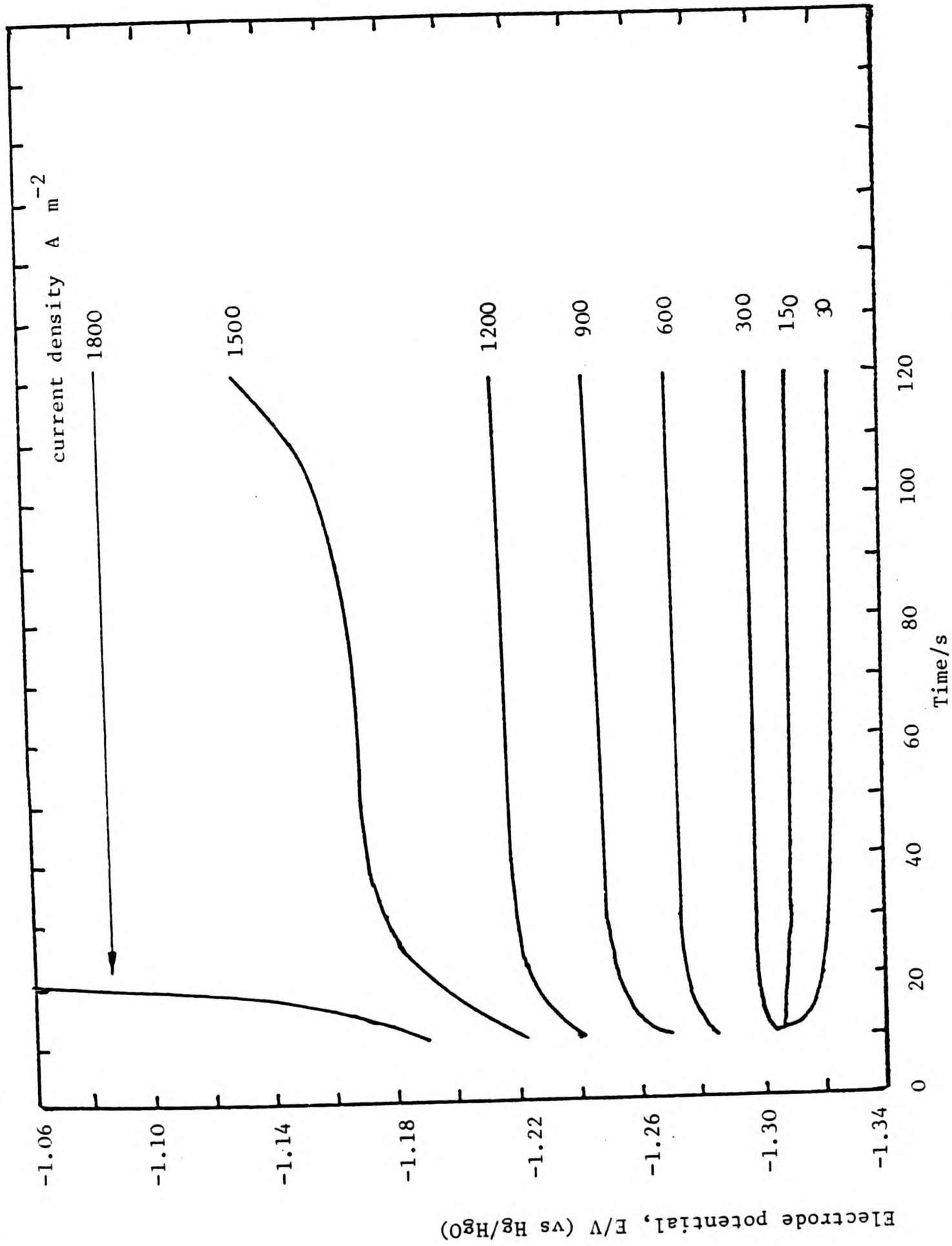


Figure 207. Chronopotentiograms for Zn-5.0 Cd alloy in ZnO saturated 6 mol dm⁻³ KOH at 25°C.

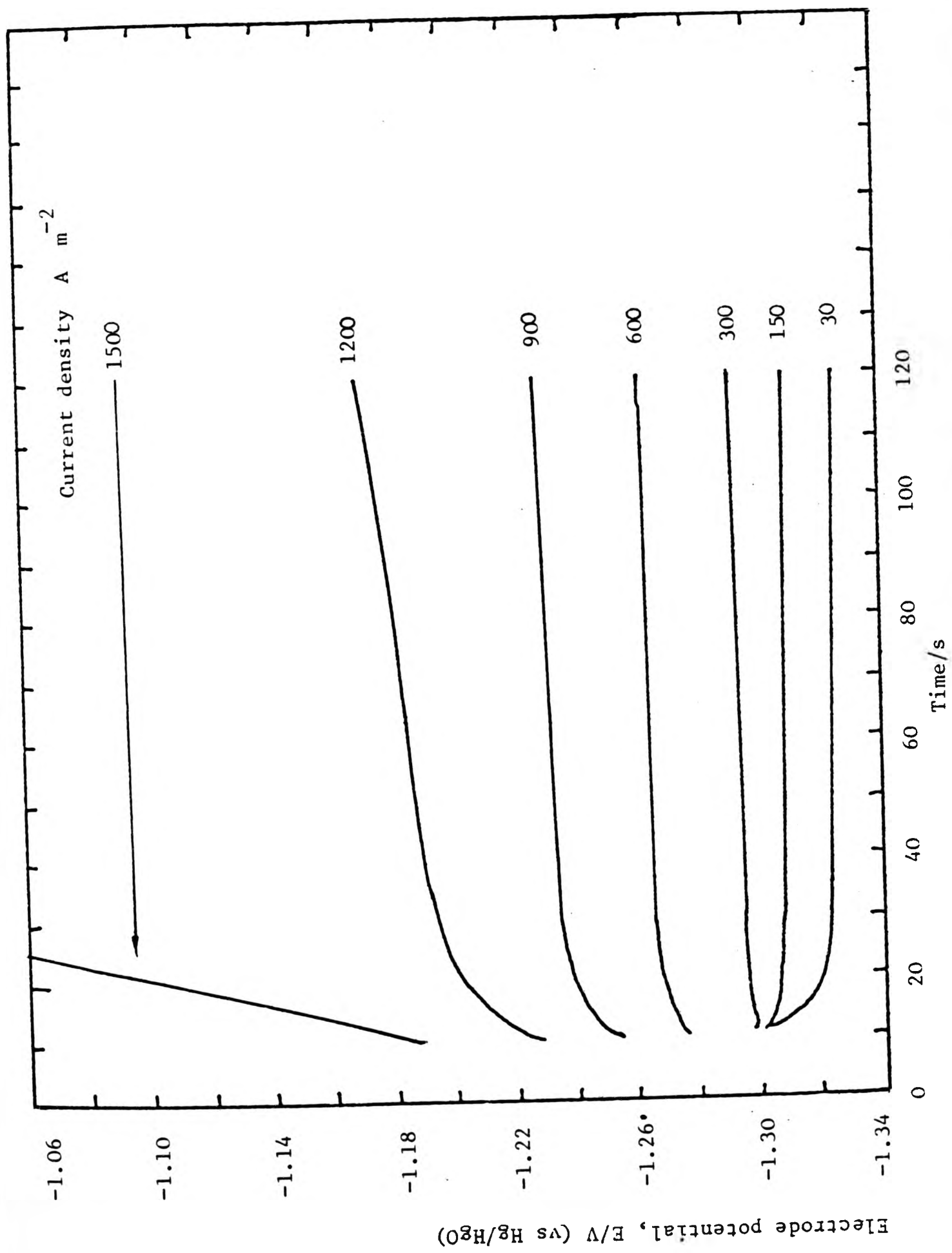


Figure 208. Chronopotentiograms for Zn-25 Cd alloy in ZnO saturated 6 mol dm³ KOH at 25°C.

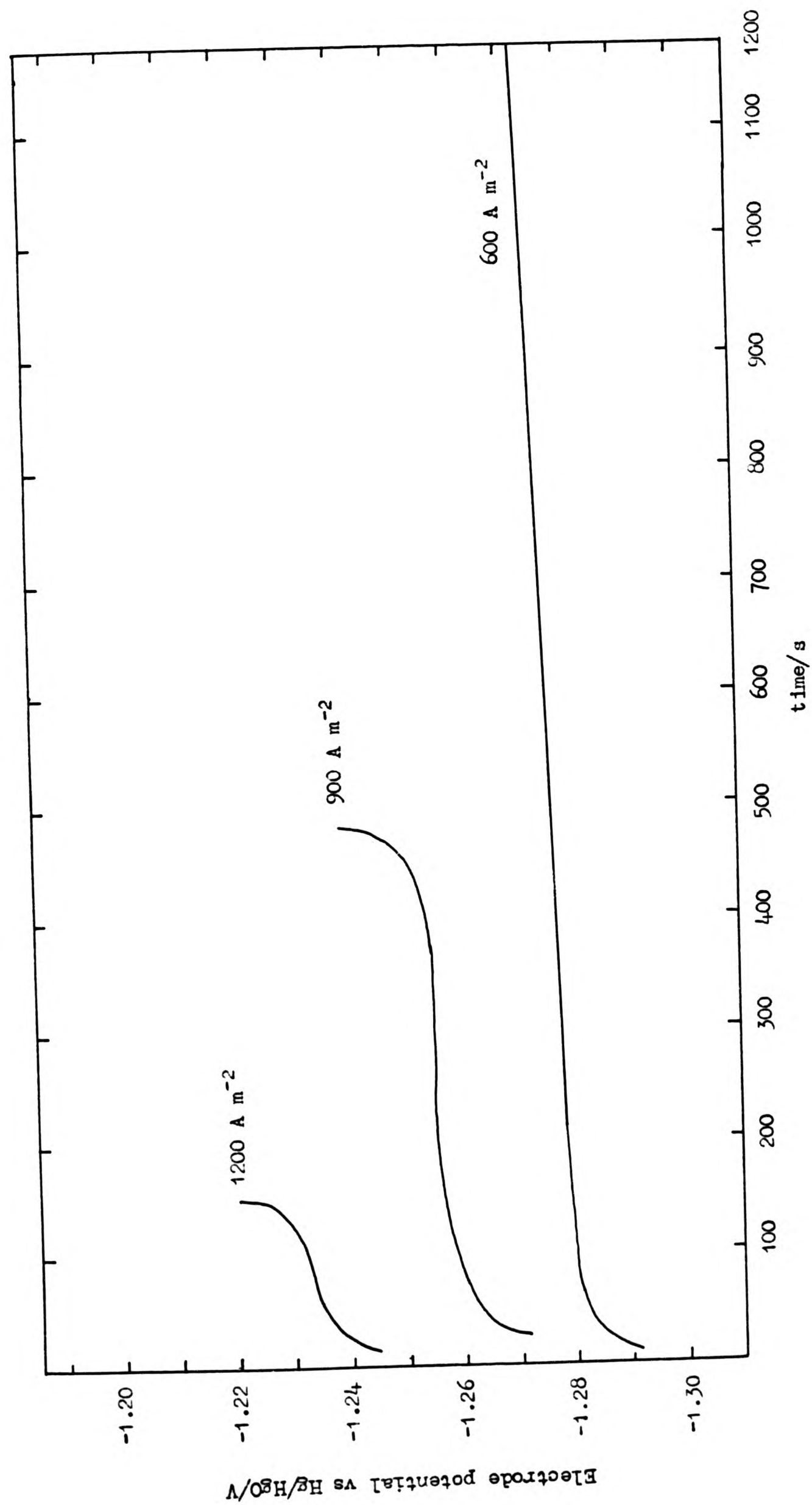


Figure 210. Chronopotentiograms for Zn 0.20 w/o Cd alloy in ZnO saturated 6 mol dm⁻³ KOH at 25°C.

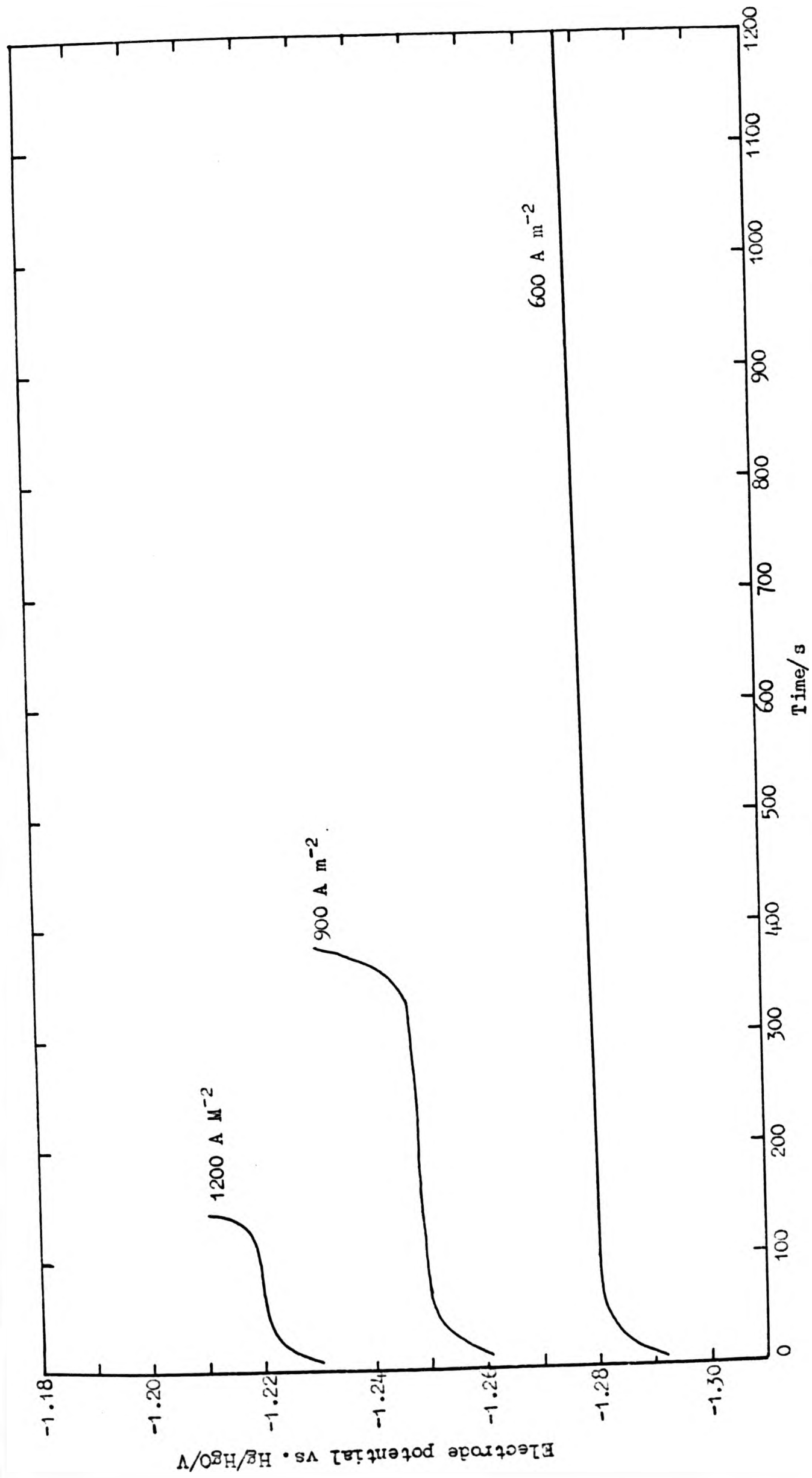


Figure 211. Chronopotentiograms for Zn-1.0 w/o Cd alloy in ZnO saturated 6 mol dm⁻³ KOH at 25°C.

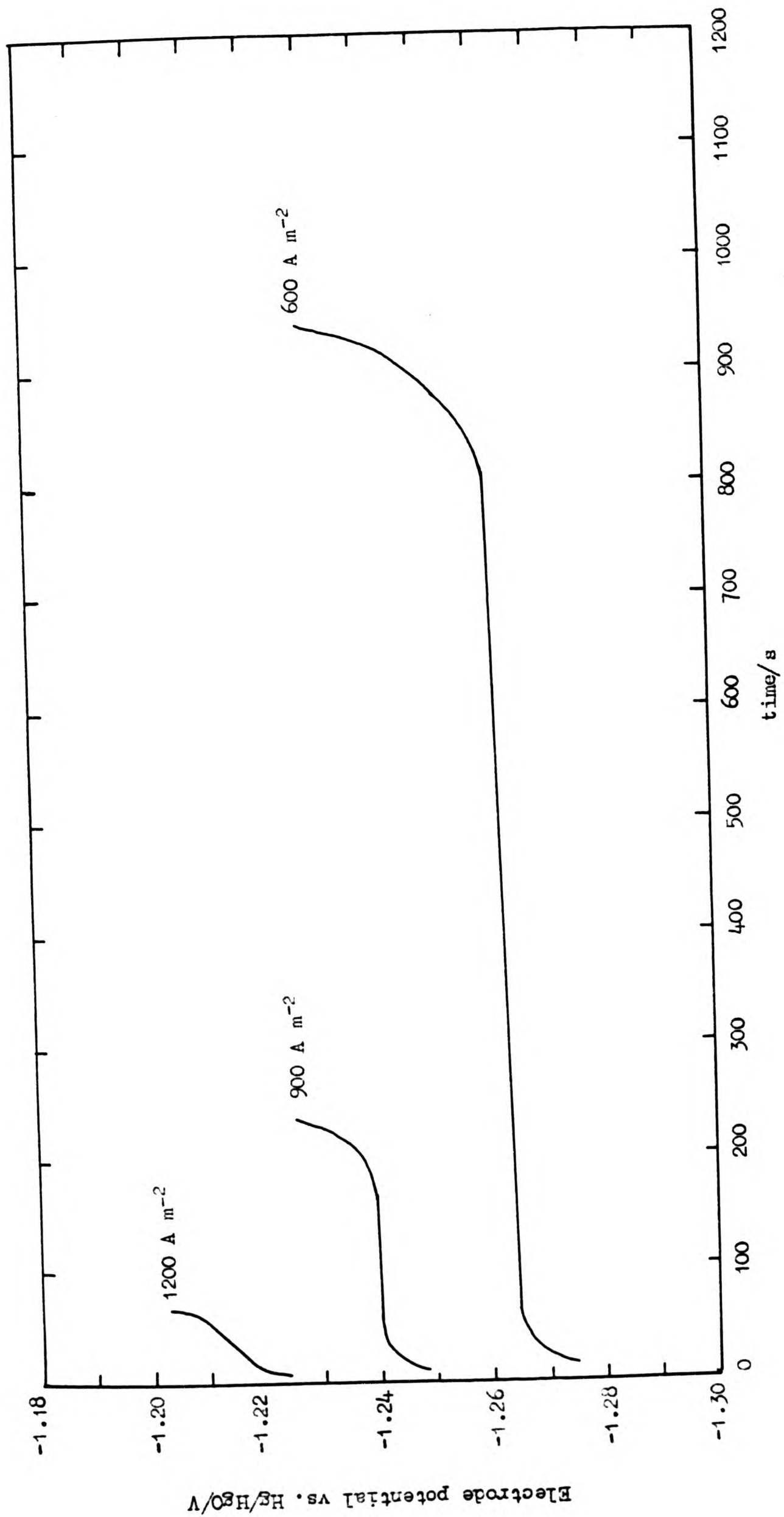


Figure 212. Chronopotentiograms for Zn-2.0 w/o Cd alloy in ZnO saturated 6 mol dm⁻³ KOH at 25°C.

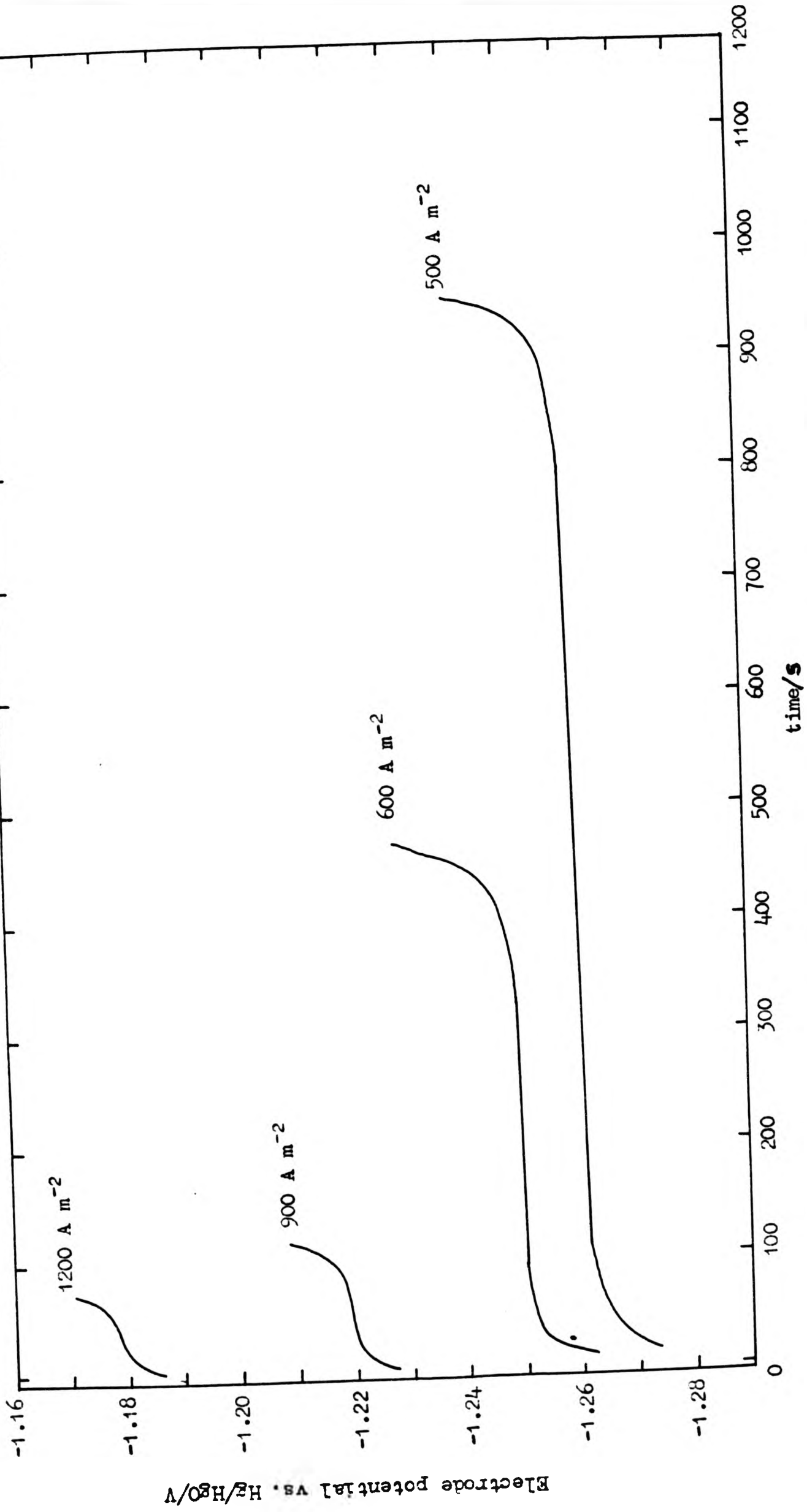


Figure 213. Chronopotentiograms for Zn-5.0 w/o Cd alloy in ZnO saturated 6 mol dm⁻³ KOH at 25°C.

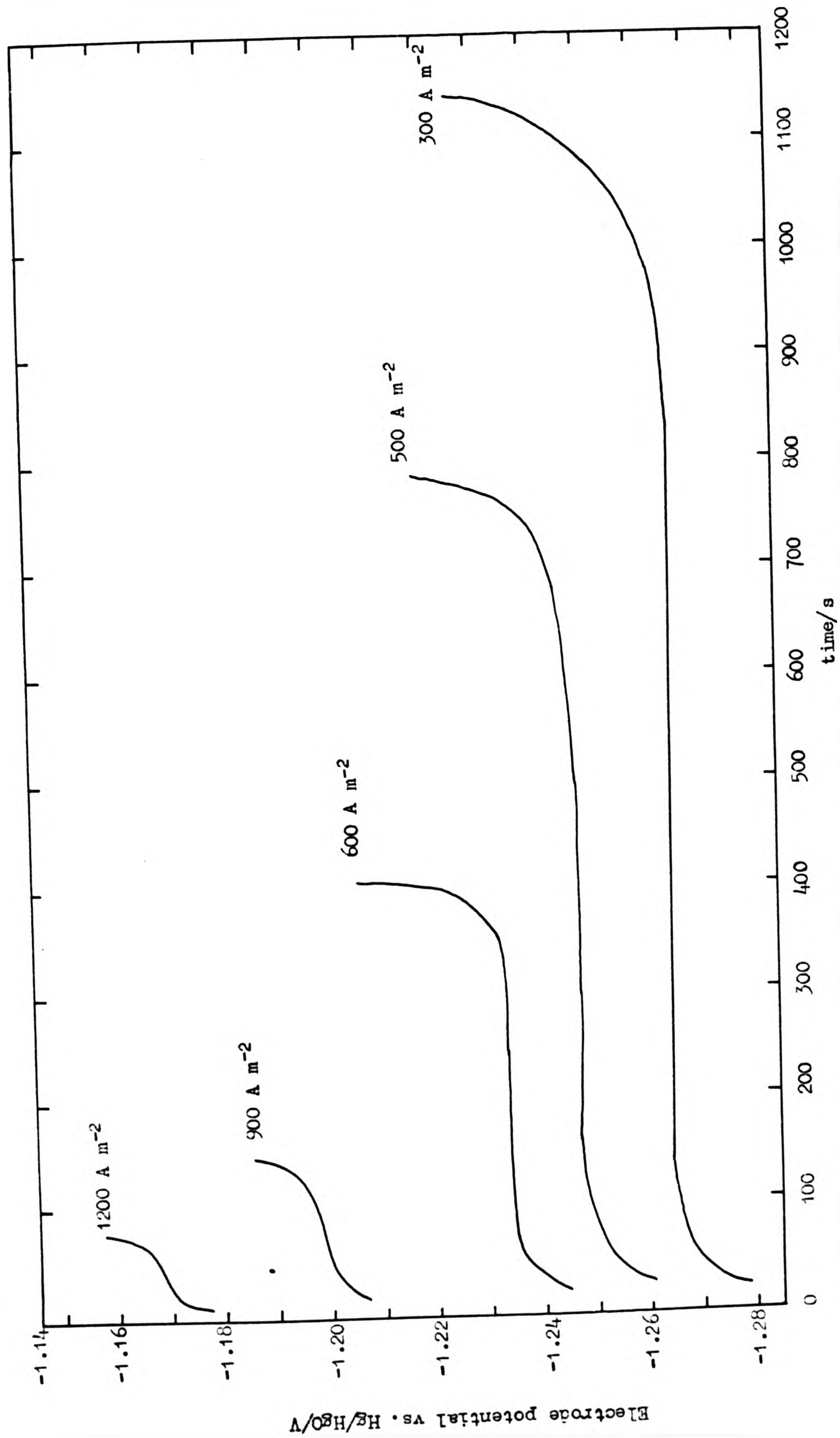


Figure 214. Chronopotentiograms for Zn-25.0 w/o Cd alloy in ZnO saturated 6 mol dm⁻³ KOH at 25°C.

Table 21. Values of steady state electrode potentials for the alloys at various current densities at 25°C for horizontal electrodes facing upwards and in long term contact with 6 mol dm⁻³ KOH saturated with ZnO

Alloy w/o Cd	Steady state potential, negative vs.Hg-HgO reference/V					
	Current Density A m ⁻²					
nominal	150	300	600	900	1200	1500
0.05	1.320	1.310	1.290	1.270	1.250	1.235
0.20	1.320	1.310	1.290	1.265	1.240	1.235
1.00	1.320	1.300	1.290	1.250	1.230	1.225
2.00	1.315	1.301	1.275	1.250	1.220	1.213
5.00	1.307	1.294	1.264	1.236	1.196	1.180
25.00	1.295	1.278	1.248	1.218	1.180	1.168
0.2+2.5 w/o Hg	1.325	1.315	1.290	1.265	1.235	1.230
1.0+2.5 w/o Hg	1.325	1.310	1.291	1.260	1.229	1.217
2.0+2.5 w/o Hg	1.315	1.298	1.272	1.250	1.220	1.214
5.0 2.5 w/o Hg	1.310	1.292	1.260	1.230	1.200	1.180

The slopes of curves in Figure 215* have been compared with the slopes of potentiodynamic curves reported in Chapter 4. These values are set out in Table 22. This shows that although electrode configuration, mass transport conditions and the electrode area to electrolyte volume ratios are different, the values of the slopes are comparable.

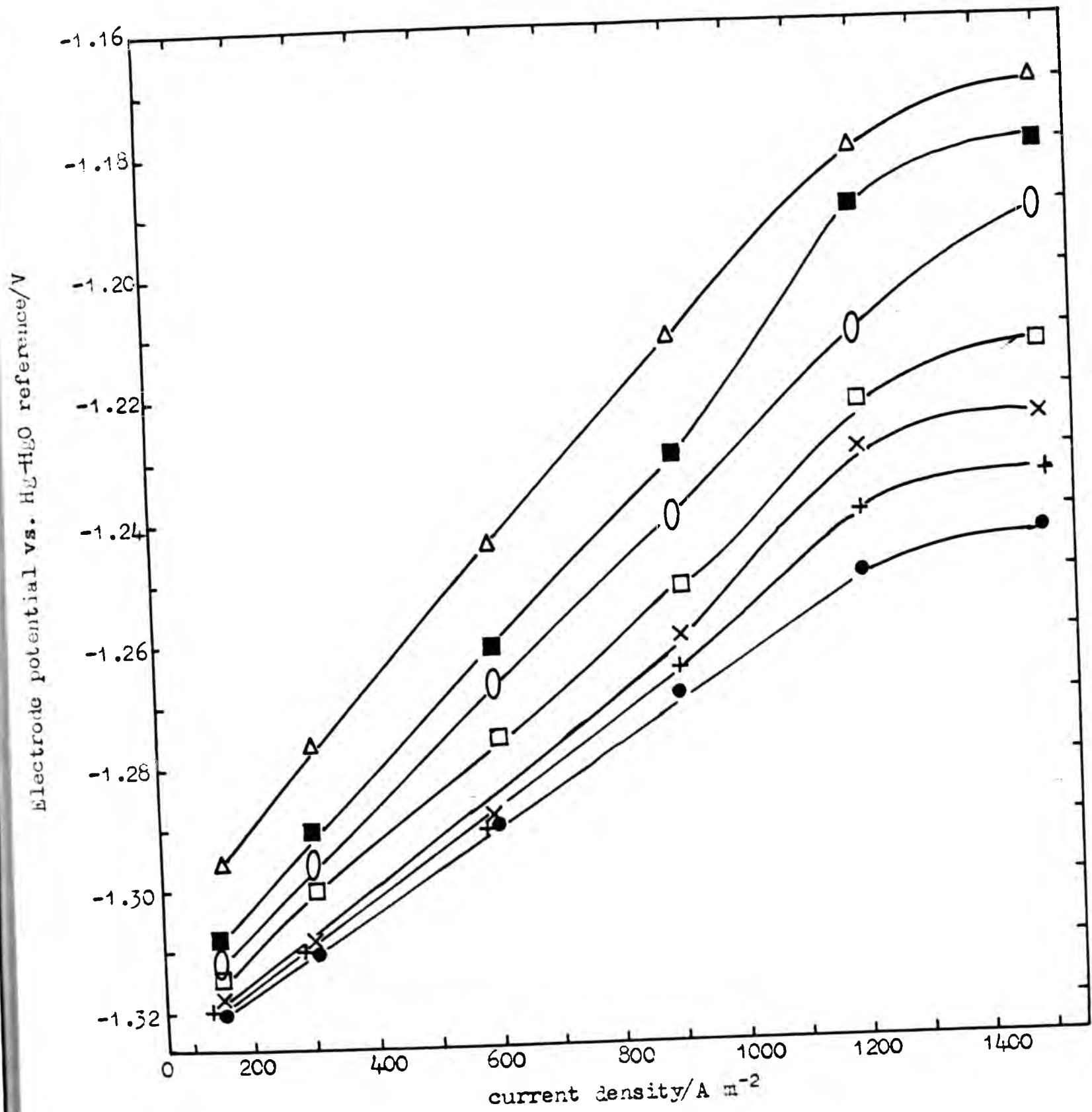


Figure 215. Derived potential-current density curves for the alloys in 6 mol dm^{-3} KOH saturated with ZnO at 25°C . on horizontal electrodes.

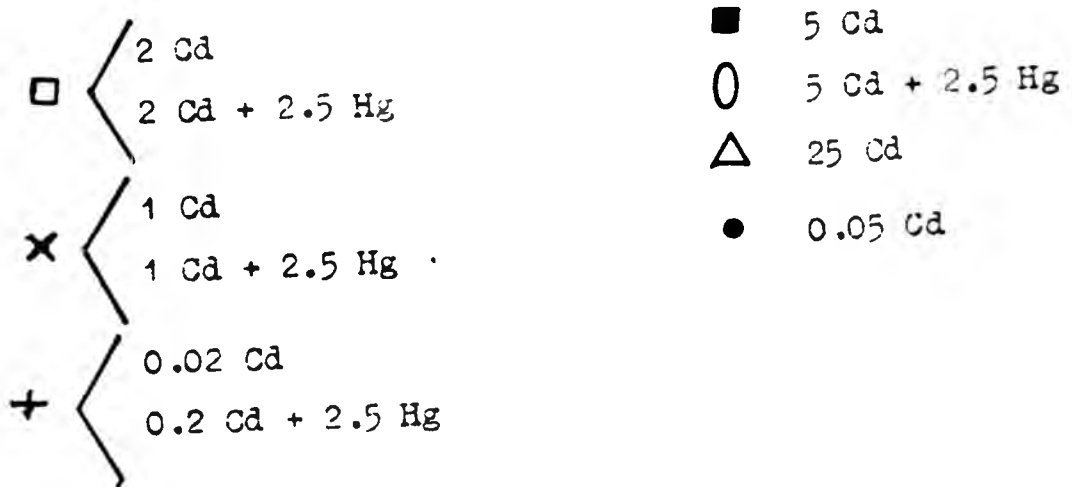


Table 22. Comparison of the slopes of the i-E curves

Alloy w/o Cd Nominal	Potentiodynamic method horizontal face down	*Galvanostatic method horizontal face up	Galvanostatic method vertical electrode
0.05	7.75	6.7	6.0
0.20	8.10	7.5	6.5
1.0	9.4	8.7	7.7
2.0	9.75	9.5	8.9
5.0	9.8	9.7	9.7
25.0	8.5	10.0	10.3
0.20 + 2.5 w/o Hg	8.4	8.3	not available
1.0 + "	8.8	8.4	"
2.0 + "	8.06	8.0	"
5.0 + "	6.7	9.3	"

Table 23. Values of steady state electrode potentials for the alloys at various current densities at 25°C for vertical electrodes using fresh surfaces in 6 mol dm⁻³ KOH saturated with ZnO⁷⁴

Alloy w/o Cd nominal	Steady State Potential, negative vs. Hg-HgO reference/V current density/A m ⁻²							
	30	150	300	600	900	1200	1500	1800
0.05	1.334	1.320	1.310	1.294	1.274	1.254	1.234	1.204
0.20	1.328	1.317	1.308	1.292	1.272	1.255	1.234	1.204
1.00	1.326	1.316	1.304	1.290	1.268	1.248	1.220	1.180
2.00	1.324	1.313	1.300	1.286	1.264	1.243	1.218	1.190
5.00	1.324	1.310	1.298	1.272	1.246	1.216	1.180	1.184
25.00	1.324	1.308	1.292	1.262	1.230	1.180	1.167	1.180

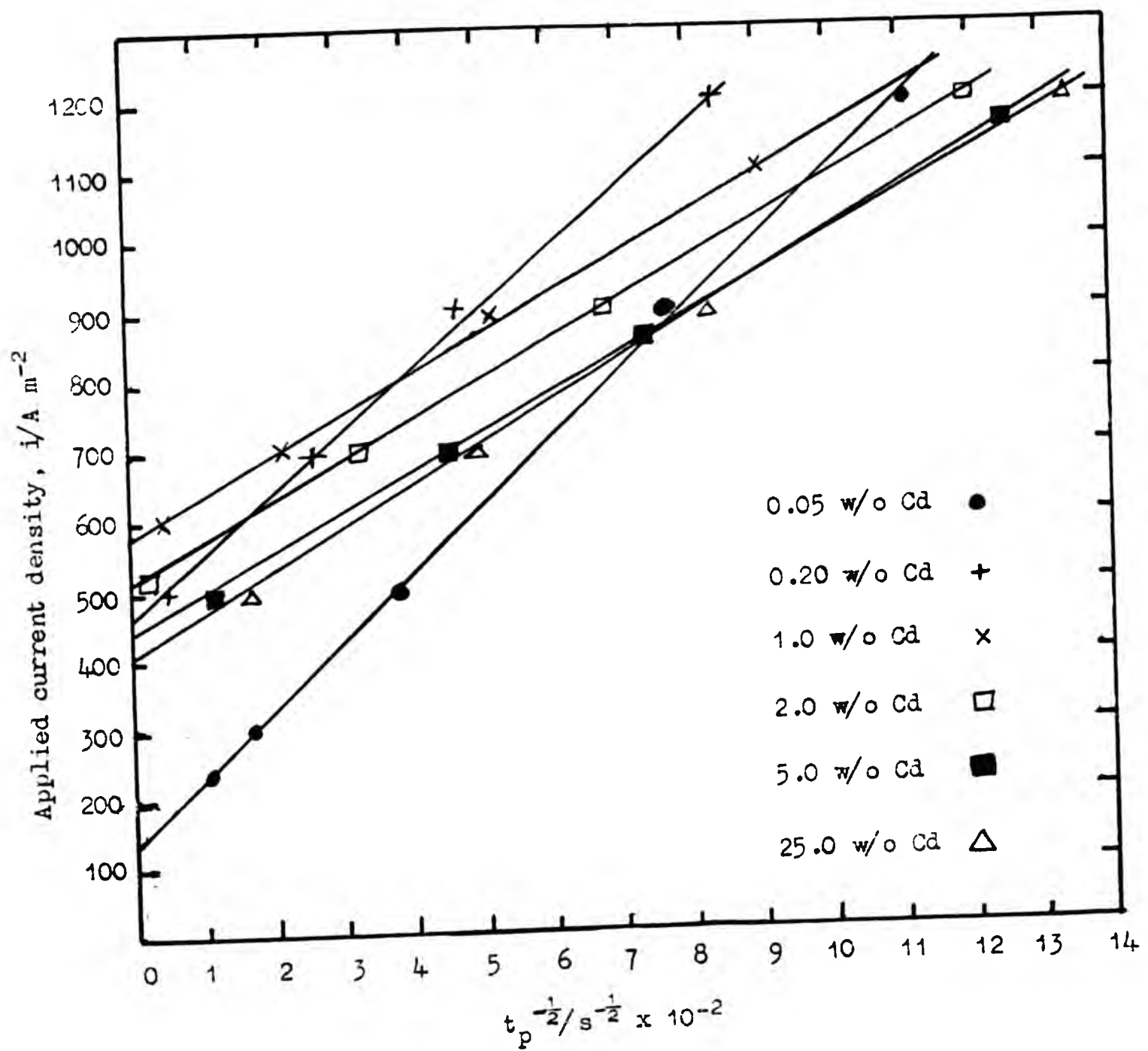


Figure 216. A plot of applied current density vs. inverse of square root of passivation time on horizontal electrodes facing upward at 25°C in 6 mol dm⁻³ KOH saturated with ZnO.

It should be noted that the electrodes in these experiments were horizontal facing upwards, thus the natural convection was assisted by this configuration. The variation of slopes and the distribution of values is quite scattered as the values were obtained experimentally and therefore subject to experimental errors and the effect of long term contact with the electrolyte.

Table 25 lists calculated transition times for the alloys for some current densities at 25°C on vertical electrodes under quiescent conditions. This data was obtained from previous work.⁷⁴ The transition times obtained experimentally were at very high current densities so that all values were less than 2 minutes. These measurements represented single experiments on fresh vertical surfaces.

Table 25. Calculated values of transition time for the alloys on vertical electrodes with fresh surface, at 25°C, at various current densities⁷⁴

Alloy w/o Cd	Current density A m ⁻²	Transition time/s						
		300	600	900	1200	1500	1800	2100
0.05		2450	625	287	152	100	74	49
0.20		3850	1100	566	330	198	144	110
2.00		1011	236	104	62	39	30	20
5.00		2750	216	356	204	126	83	59
25.00		400	97	46	26	18	v.short	v.short

This data has been plotted in Figure 217. The transition time was calculated assuming that it is inversely proportional to the square of the current density. The curves pass through the origin for this reason. It was assumed that the concept of a "threshold" current density does not apply in the case of gravity balancing the natural convection in the case of vertical

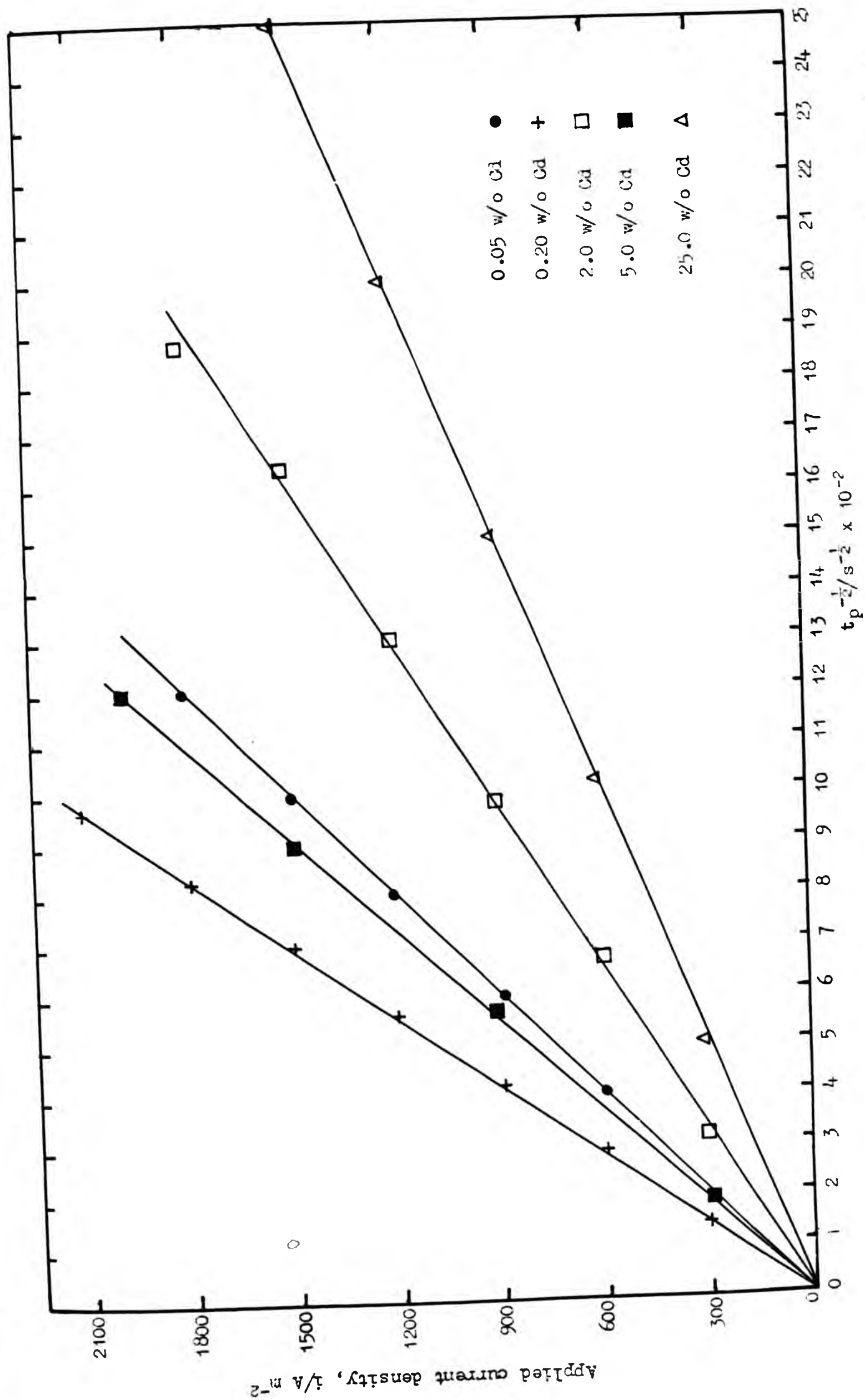


Figure 217. A plot of applied current density vs. calculated inverse of square root of passivation time on vertical electrodes starting with a fresh surface, in 6 mol dm^{-3} KOH saturated with ZnO.

allowed sufficient time for the thick passive film to redissolve so that the surface became bright again covered only with a transparent anodic film. In this state the electrodes regain their ability to repassivate at a higher current density and after a longer time. The electrode potentials are not affected by these factors to any significant extent.

6.4 CONCLUSIONS

- 6.4.1 At low and moderate current densities the electrode potential assumes a steady state value after a very short time.
- 6.4.2 At high current densities the electrode potential becomes more anodic continuously until passivation sets in, whence the potential rises very steeply.
- 6.4.3 At lower current densities the transition time is longer and at higher current densities the transition time is much shorter. A plot of i vs. $t^{-\frac{1}{2}}$ resulting in a straight line confirms the relationship mentioned in section 1.4.3.5.
- 6.4.4 For horizontal electrodes, where convection assists ionic movement in the electrolyte, the electrodes do not passivate below a certain "threshold" value of current density.
- 6.4.5 For low cadmium alloys the transition times are much longer than those for high cadmium alloys.
- 6.4.6 Higher cadmium alloys passivate at lower current densities than do low cadmium alloys.
- 6.4.7 The presence of mercury does not make any difference to the passivation properties of the Zn-Cd alloys.
- 6.4.8 For a given current density, electrode potentials become less negative or more anodic with increasing cadmium content.

- 6.4.9 With increasing current density the electrode potential increases in the anodic direction. The tendency to passivate increases with increasing cadmium content.
- 6.4.10 The anodic slopes of i - E curves obtained by either the potentiodynamic or galvanostatic method are comparable. Thus the differences in the electrode geometry, mass transport conditions and the electrolyte volume to electrode surface area ratio does not seem to have much effect on this parameter.
- 6.4.11 For low Cd contents the slopes of i vs. $t_p^{1/2}$ straight lines are likely to be similar to that of Zn, while at 1 w/o or higher Cd content the slopes decrease from $100 \text{ A m}^{-2} \text{ s}^{1/2}$ to $60 \text{ A m}^{-2} \text{ s}^{1/2}$ and probably approach values closer to that for Cd. This modification by Cd is corroborated by the RDE studies where a secondary passivation peak is observed at higher Cd contents.
- 6.4.12 A change in slope of these lines could be indicative of a change in mechanism or of a significant influence of presence of Cd to change the value of critical concentration of anodic products at the surface required for passivation.
- 6.4.13 The straight lines of i vs. $t_p^{1/2}$ plot do not show any connection between the Cd content and the slope. This may be due to the slight inhomogeneity of the thermally prepared alloys.

CHAPTER SEVEN

STUDIES ON ELECTRODEPOSITION OF Zn-Cd, Zn-Cd-Hg ALLOYS7.1 INTRODUCTION

To study further the electrochemical properties of the zinc-cadmium alloys it was considered worthwhile to pursue the possibilities of using material in powder form comparable to existing commercial practice, e.g. Mallory products. Prospects with gas blown powder from molten state as practised with the production of powdered zinc, were not promising with these alloys. The powder particles when examined under the microscope were shaped like a "frozen falling drop" - an elongated pear shape with a very smooth surface. An alternative proposal to prepare material by electro-deposition was thought to be a more viable prospect. It was known that Crompton-Parkinson make an encapsulated sealed Cd-HgO cell on a commercial scale in which the cadmium electrode is electroformed on a nickel gauze. It was also established that the principle of the electrodeposition of alloys by a simultaneous discharge of the cations of two or more metals on a suitable substrate was well documented.¹¹⁷

7.2 PRACTICAL CONSIDERATIONS IN ALLOY ELECTRODEPOSITION

7.2.1 Thermodynamic Aspects. The standard reduction potentials of zinc, cadmium and mercury are $E_{\text{Zn}^{2+}/\text{Zn}}^{\ominus} = -0.763 \text{ V}$, $E_{\text{Cd}^{2+}/\text{Cd}}^{\ominus} = -0.403 \text{ V}$ and $E_{\text{Hg}^{2+}/\text{Hg}}^{\ominus} = +0.789 \text{ V}$, all measured with reference to the standard hydrogen electrode. However these can be taken only as a rough guide to predict the possibility of codeposition of two metals. These values are based on thermodynamic equilibrium, while in practice electrode polarisation causes these values to shift in the negative direction. When complex ions are used more negative potentials occur. Therefore methods are required for bringing potentials closer together. Static standard potentials can be brought together by changing the concentrations of the salts in the solution or by

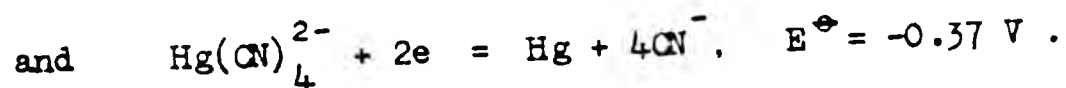
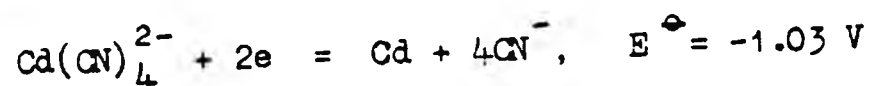
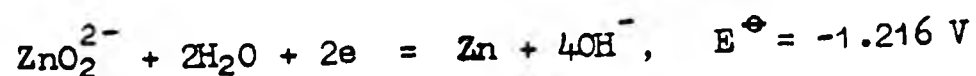
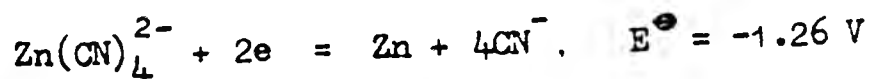
using complex ion formation. However dilution does not result in sufficient change in potential for most pairs of metals to make co-deposition practicable. The equilibrium potential at an activity a_{Mn+} of dissolved ions of valency 'n' at 298 K is given by the Nernst equation:

$$E = E^{\ominus} - \frac{0.059}{n} \log (a_{Mn+})$$

(with usual meanings for the notation)

A hundredfold decrease in the concentration of a divalent salt of the more noble metal would make the potential of the electrode only about 0.06 V more negative. Furthermore, the use of a dilute solution of the more noble metal in an alloy bath is impracticable because when the concentration of the more noble metal is less than 1% that of the other, the concentration changes so rapidly during deposition that alloys of reproducible composition cannot be obtained. However, this method of varying the ratio of ions is suitable when the equilibrium potentials of the metals being deposited are initially comparable, whence it is used to control the composition of the alloy being deposited and is commonly employed for this purpose.

7.2.2. Complex Formation. A much more effective method of displacing the equilibrium potentials of metals in order to bring the deposition potentials closer together is by the method of complex formation. Thus for:



The potentials can be brought together further by either using different complexes for each ion and/or by increasing the concentration of free complexing ligand.

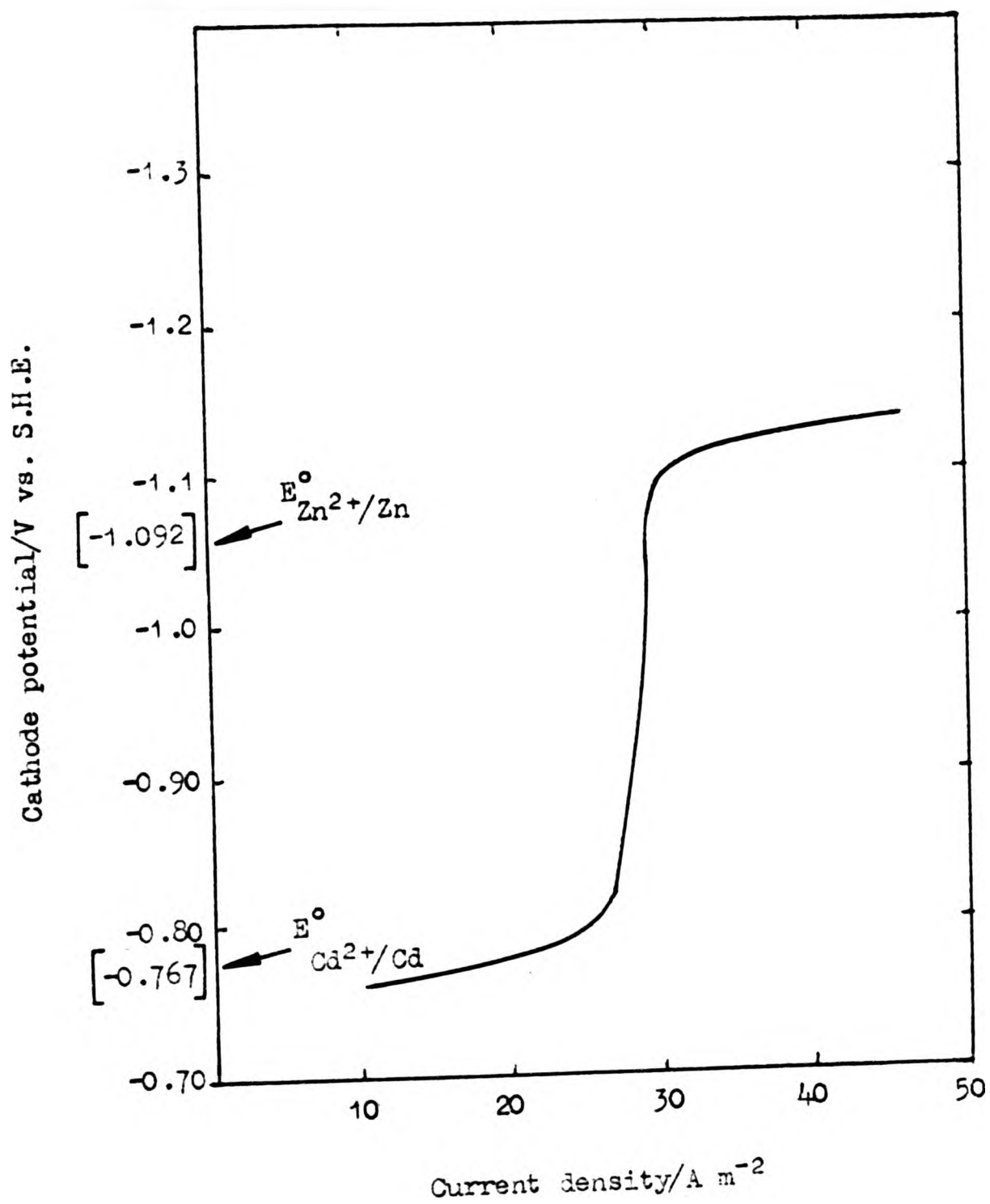


Figure 218. Influence of cathode current density on the co-deposition of Zn and Cd. Uncorrected values of $E_{\text{Zn}^{2+}/\text{Zn}}^{\circ}$ and $E_{\text{Ca}^{2+}/\text{Cd}}^{\circ}$ are indicated. (After Vagramyan¹¹⁸)

7.2.3 Influence of Current Density. The simultaneous deposition of two different metals can be achieved by using the limiting current attained for the more noble metal. As the cathode over potential of the electrode increases, the discharge of ions of the less noble metal becomes possible. Figure 218 shows the relation between current density and cathode potential for a $2 \text{ mol dm}^{-3} \text{ Zn SO}_4$ and $0.1 \text{ mol dm}^{-3} \text{ Cd SO}_4$ solution. The limiting current density under these conditions for cadmium is about 25 A m^{-2} after which simultaneous deposition of Zn and Cd begins. However the practical application of this does not always give good results, because the quality of deposit may be unsatisfactory.

7.2.4 Addition Agents. Different surface active materials may have a marked effect on the rate of discharge of ions retarding or accelerating the discharge rate of one ion while having no effect on other ions. This behaviour makes it possible in some cases to achieve the simultaneous discharge of ions of metals having widely different normal potentials. This phenomenon can be explained on the basis of adsorption of the surface active material on the cathode. Thus addition agents can bring about co-deposition by bringing the deposition potentials closer. Small concentration changes of addition agents can produce large changes in the composition of the deposits. The concentration of an addition agent required to produce an appreciable effect is much smaller than that of a complexing agent. In the presence of an addition agent the composition of the deposit may often rapidly approach a limiting value. Addition agents are usually most effective in simple ion baths, the content of the less noble metal being increased by the incorporation of the addition agent.

7.3 EXPERIMENTAL

7.3.1 Apparatus and Circuit Diagram. The apparatus used consists of a 100 V D.C. power supply which could supply up to 10 Amps. A 500 ohm, 2 Amps rheostat was used as a potential divider to give a controlled voltage and

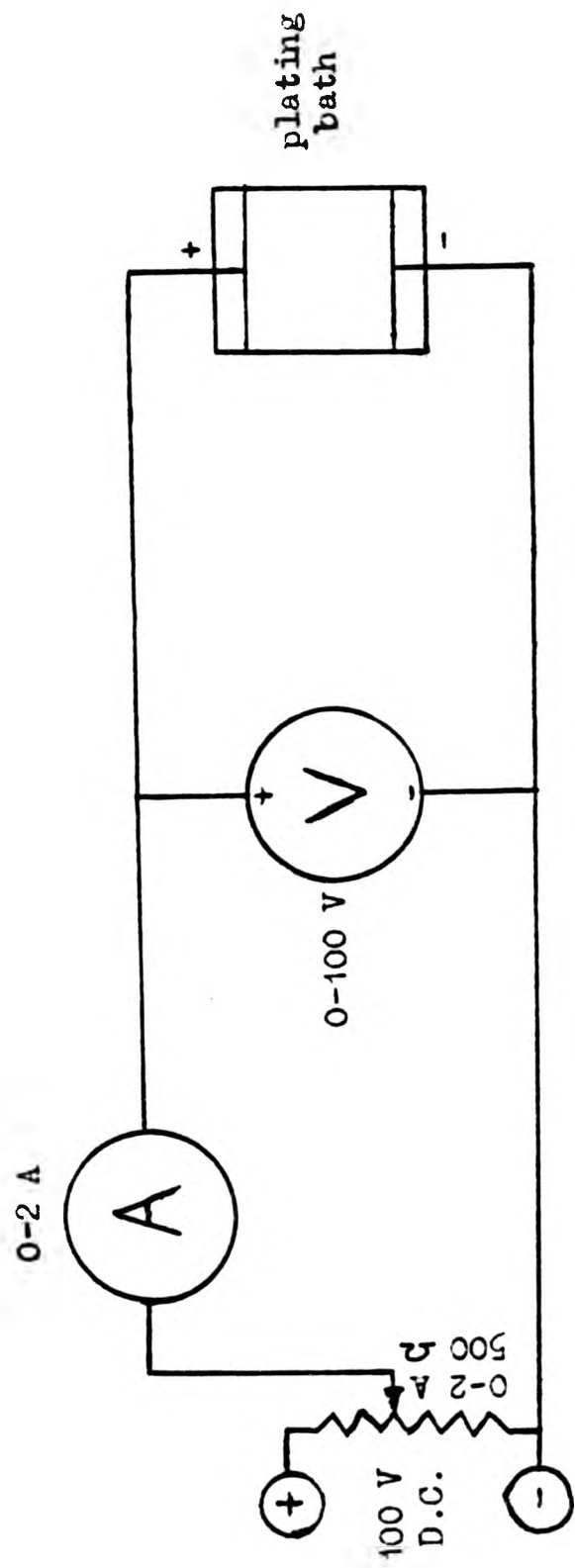


Figure 219. Schematic diagram of the plating circuit.

bath composition over long periods which could be achieved by using two soluble anodes of different areas of immersion controlled independently by two circuits or by adding metal salts in a fixed ratio at regular intervals.

7.3.4 Bath Composition. A composition based on the sulphate bath is given below in Table 26.

Table 26. A typical Zn-Cd alloy bath

Constituent	Concentration g dm ⁻³	Metal ion concentration g dm ⁻³
Zn SO ₄ · 7 H ₂ O	70	15.9
3Cd SO ₄ · 8H ₂ O	5	2.19
Al ₂ (SO ₄) ₃ · 16H ₂ O	30	-
Gelatin	0.1-0.2	-

pH of bath 3.6-3.8, temperature 25°C, current density 100-500 A m⁻², depending upon the type of deposit required, increasing current density leading to coarser crystallinity, while low current density gives rise to fine, coherent, bright deposits. To observe the influence of bath composition on the composition of the electrodeposited alloy, the cadmium content of the bath was varied while the zinc content was kept constant.¹¹⁹

Table 27. Variation in Cd salt content to provide various Zn-Cd bath ratios

Concentration of 3 Cd SO ₄ · 8H ₂ O g dm ⁻³	Concentration of cadmium g dm ⁻³	Ratio Zn:Cd
5	2.19	7.25:1
4	1.75	9.08:1
3	1.31	12.14:1
2	0.88	18.07:1
1	0.44	36.14:1

Since the deposit required should be in the form of coarse crystals it was not essential to resort to cyanide baths or employ a variety of addition agents. For ternary alloys a further modification is indicated in Table 28 below:

Table 28. A typical bath composition for Zn-Cd-Hg alloys

Constituent	Concentration g dm ⁻³	M ⁿ⁺ concentration g dm ⁻³
Zn SO ₄ · 7H ₂ O	70	15.90
3 Cd SO ₄ · 8H ₂ O	2	0.88
Hg(NO ₃) ₂ · H ₂ O	1.71	1.0
Al ₂ (SO ₄) ₃ · 16H ₂ O	30	-
gelatin	0.1-0.2	-

The temperature of the bath was maintained at 25°C. The current density may be varied from 100-500 $\frac{A}{m^2}$ depending upon the type and composition of the deposit required. The mercury content is varied as indicated in Table 29, while zinc and cadmium contents are kept constant.

Table 29. Mercury concentration in Zn/Cd bath

Concentration of Hg(NO ₃) ₂ · H ₂ O g dm ⁻³	Mercury concentration g dm ⁻³
0.427	0.25
0.854	0.50
1.281	0.75
1.710	1.00
2.564	1.50
3.418	2.00

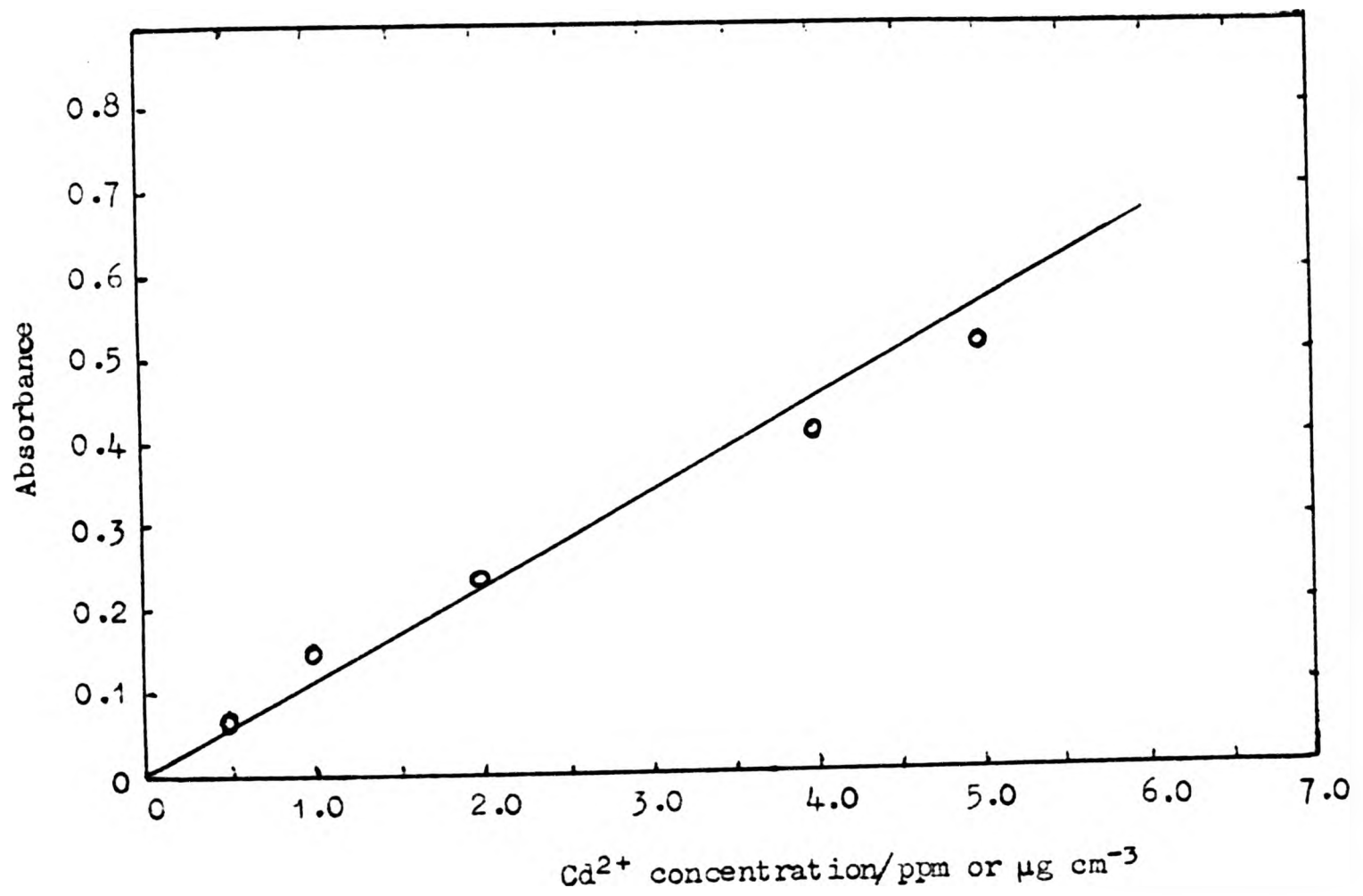


Figure 220. Calibration curve for the chemical analysis of cadmium by atomic absorption spectrometry.

7.3.5 Analysis of Electrodeposited Alloys. Zinc-cadmium alloys do not lend themselves to the conventional analytical techniques because of their almost identical chemical nature. However it is possible to analyse the alloys by colorimetry using dithizone as a complexing agent. This is a lengthy process. A much simpler technique is atomic absorption spectrometry. A representative sample of the alloy is dissolved in dilute HCl and the volume made up to one litre. After calibrating the instrument with standard solutions of known concentration, a known amount of the alloy was dissolved in a minimum quantity of 1 w/o HCl acid and the volume was made to 1.0 dm^3 . This solution would be far too concentrated to be used in measuring absorbances. This was therefore diluted until such time as it gave absorbance reading within the linear region of the curve. By using this procedure the metal content of an unknown sample was calculated. The technique is quite accurate except for the errors involved in dilution. The measurements were repeated several times until reproducible results were obtained. Figures 220-222 show the calibration curves used to analyse unknown samples.

7.4 RESULTS

7.4.1 Influence of Addition Agent. Using a bath containing 70 g dm^{-3} $\text{Zn SO}_4 \cdot 7\text{H}_2\text{O}$, 5 g dm^{-3} $3 \text{ Cd SO}_4 \cdot 8\text{H}_2\text{O}$, and 30 g dm^{-3} $\text{Al}_2(\text{SO}_4)_3 \cdot 16\text{H}_2\text{O}$, i.e. a Zn to Cd ratio of approximately 7:1 and a soluble anode of zinc foil, a deposit of 17 to 20 w/o Cd was obtained at current densities of 300 A m^{-2} and over. When $0.2-0.25 \text{ g dm}^{-3}$ gelatin was added the same bath composition gave a 7 to 8 w/o Cd-Zn alloy. If the amount of addition agent (gelatin) was varied the deposit composition varied accordingly. This is illustrated in Table 30.

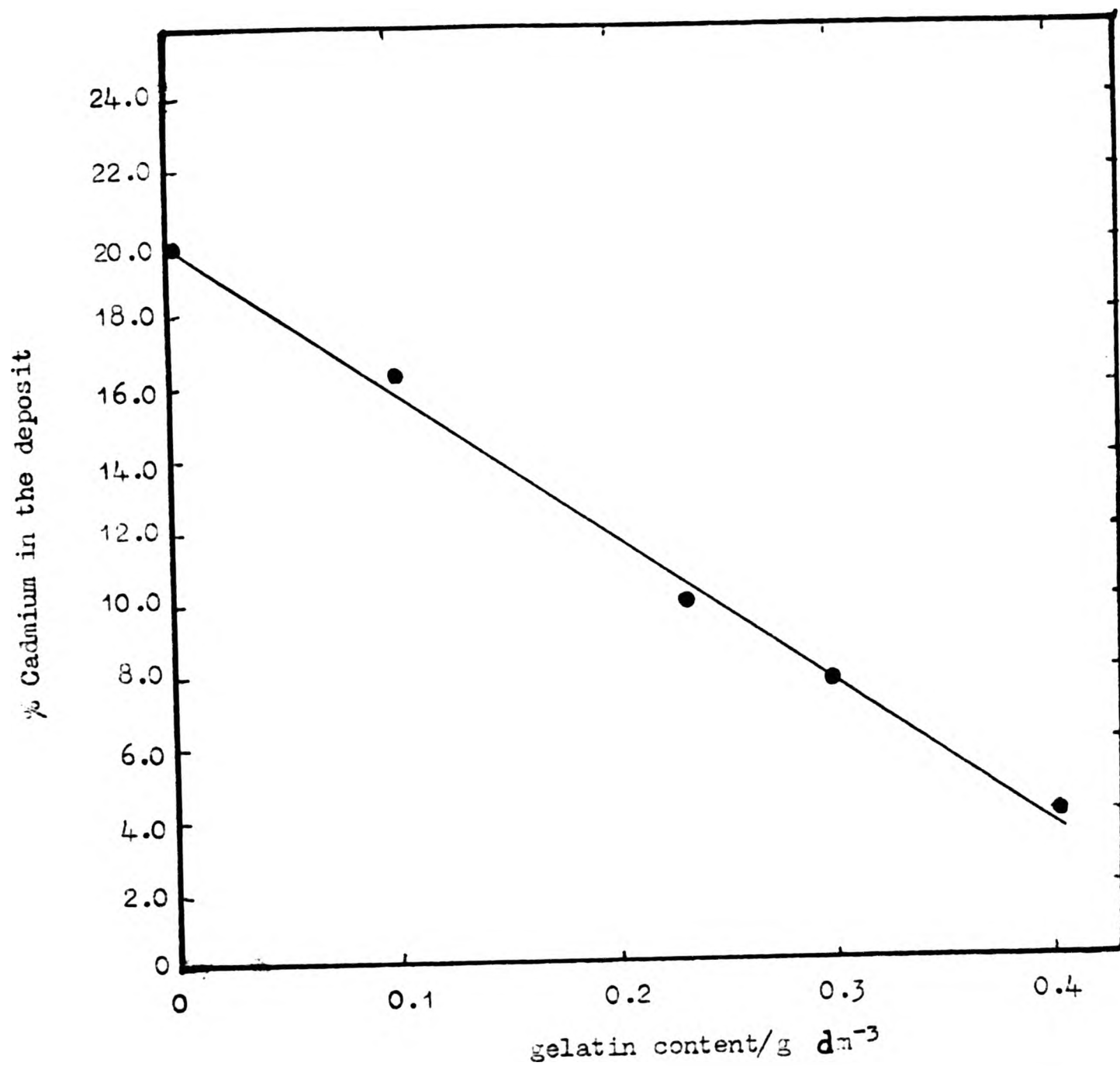


Figure 223. Variation of cadmium content in the deposit with the variation in the gelatin content of the bath.

Table 30. Variation of the deposit composition with gelatin content of the bath

Gelatin content g dm ⁻³	w/o Cd in the deposit
0	20.0
0.1	16.1
0.2	10.2
0.3	7.9
0.4	4.0

Figure 223 depicts this relation graphically.

7.4.2 Influence of current density. A series of plating experiments were carried out at various current densities whilst the bath composition, temperature and the pH were maintained constant. The data are reported in Table 31 and the progressive variation of composition with current density is evident.

Table 31. Influence of current density on the composition of the deposit

c.d./A m ⁻²	100	200	300	400	500	600	700
w/o Cd in the deposit	3.70	4.10	4.80	5.10	5.50	6.20	6.80

Figure 224 depicts this relation graphically. Figure 229 shows the influence of current density on the mercury content in the deposit, for the electrodeposition of the ternary alloys containing Zn, Cd and Hg. See section 7.4.6.

7.4.3 Influence of pH. Another series of experiments was carried out to establish the influence of bath pH on the composition of the deposit while maintaining other factors such as bath composition, temperature and current density constant. This data is shown in Table 32, from which it is seen that pH influences the composition only slightly over the pH range of 1 to 5.

Table 32. Influence of pH on the composition of the deposit

pH	1.0	2.0	3.0	4.0	5.0
w/o Cd	1.0	1.0	1.1	1.2	1.3

This is expected because the simple ions, used here, are not sensitive to pH variations. The state of the chemical combination of the simple ions is not affected by the changes in pH. Figure 225 is a graphical representation of the pH dependence of the deposit composition.

7.4.4 Influence of Metal Content of Bath. Cadmium is a far more readily depositable metal than zinc. As the Cd content of the bath increases the Cd content of the deposit also increases as shown in Table 33.

Table 33. Variation of the deposit composition with Cd content of the bath

w/o Cd in the bath	0	0.44	0.88	1.31	1.75	2.19
w/o Cd in the deposit	0	1.30	2.85	4.75	5.60	7.3

A clear rectilinear relation is evident between the two parameters indicating a 3.24 w/o Cd in deposit per 1 w/o change in Cd of the bath. This is shown in Figure 226. The relation between the Cd content of the deposit with total metal ($Zn^{2+} + Cd^{2+}$) content of the bath is depicted in Figure 227. This curve features a narrow band of the bath metal content in which the deposit composition is more or less constant. As mentioned later on Figure 228 shows the effect of Hg content in the bath on the Hg content of the deposit for the electrodeposition of the ternary alloys containing Zn, Cd and Hg.

7.4.5 Influence of Temperature. It was found that both the binary and ternary deposits could be obtained satisfactorily at ambient temperatures of 12-25°C. This feature is very welcome from an economic point of view, since it is desirable for any process to be performed satisfactorily at room temperature so that savings in energy and therefore money could be made. Some experiments were performed at elevated temperatures. The general

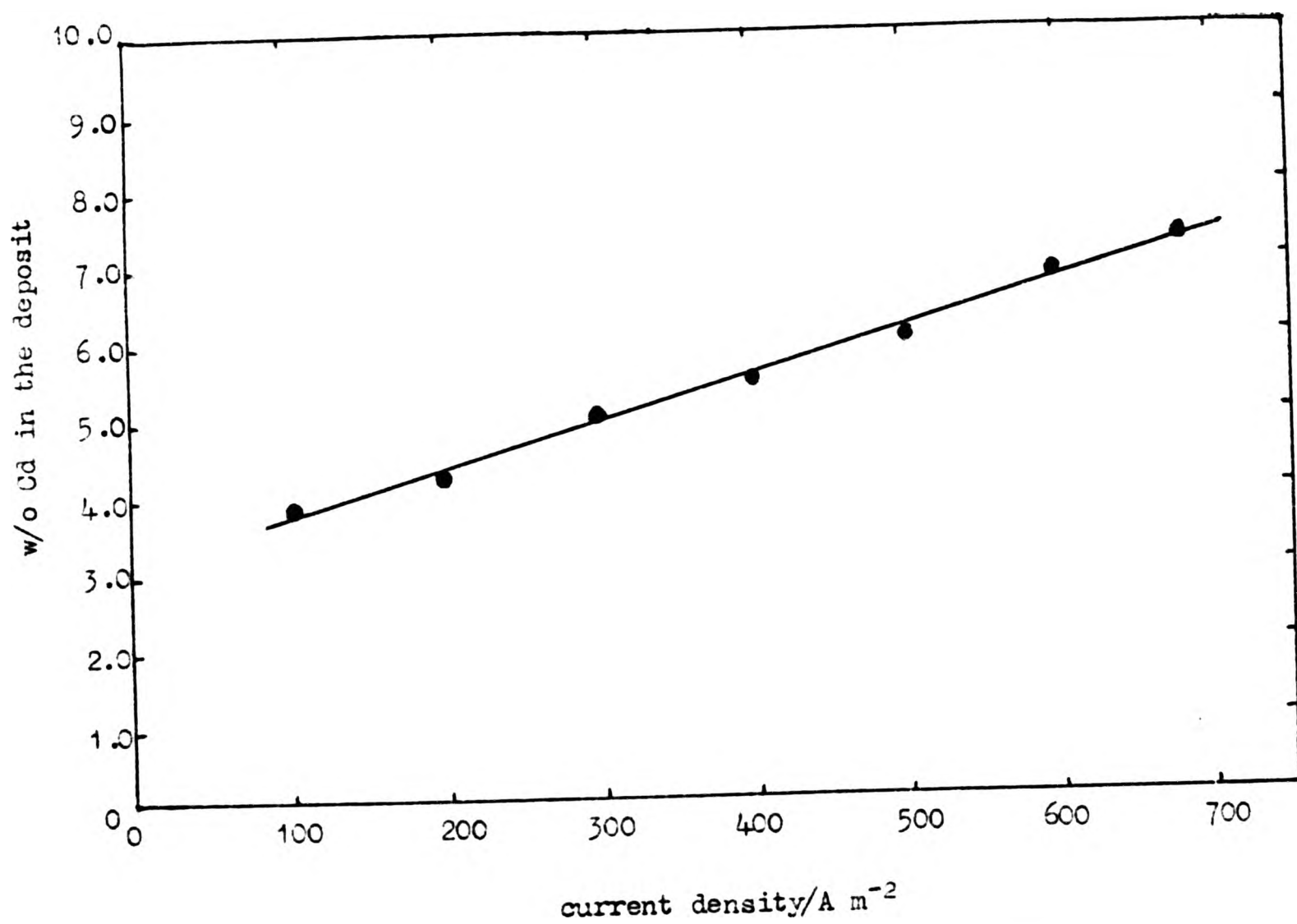


Figure 22A. Influence of current density on the composition of the deposit.

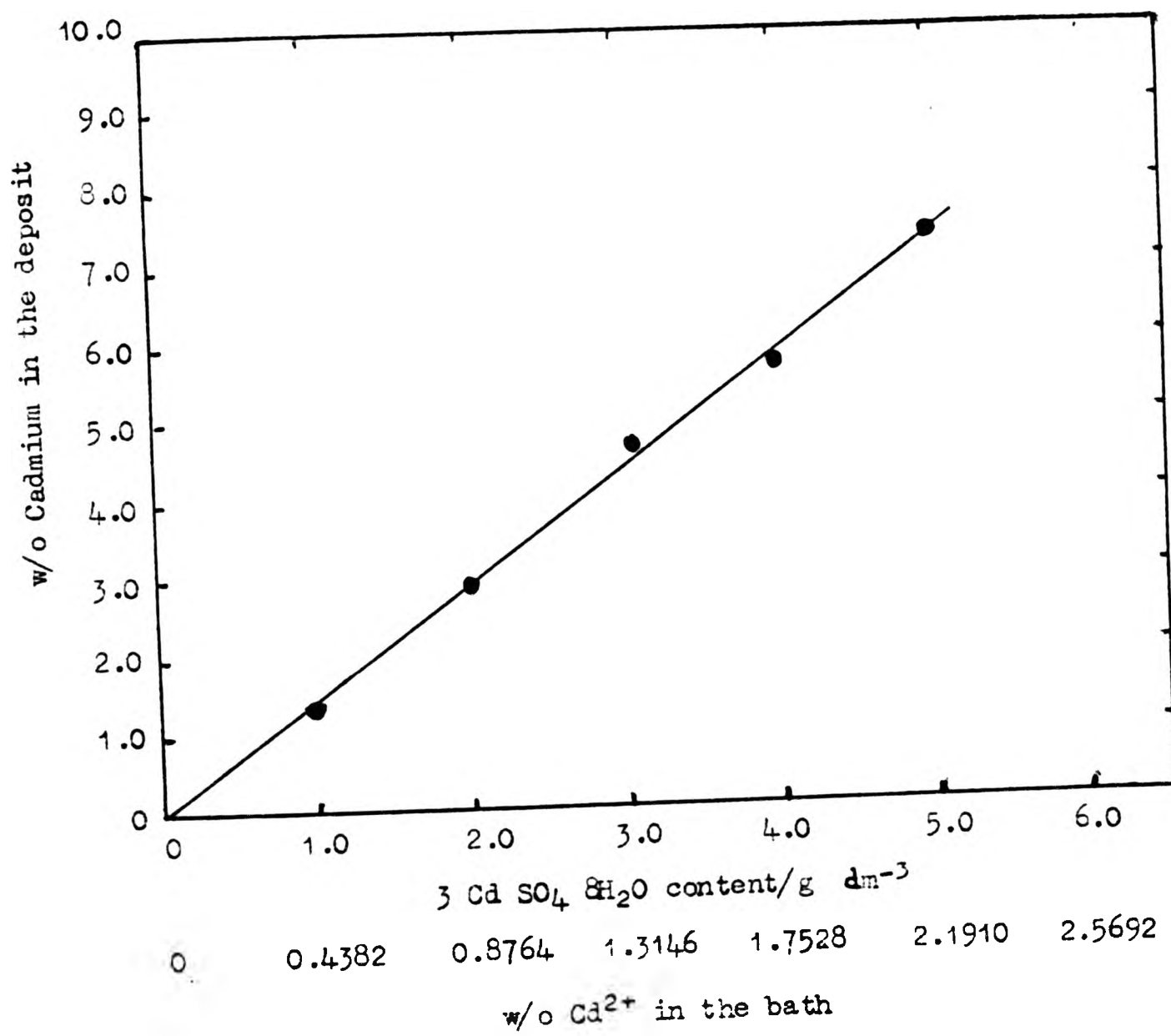


Figure 226. Relation between cadmium content of the bath and the cadmium content of the deposit.

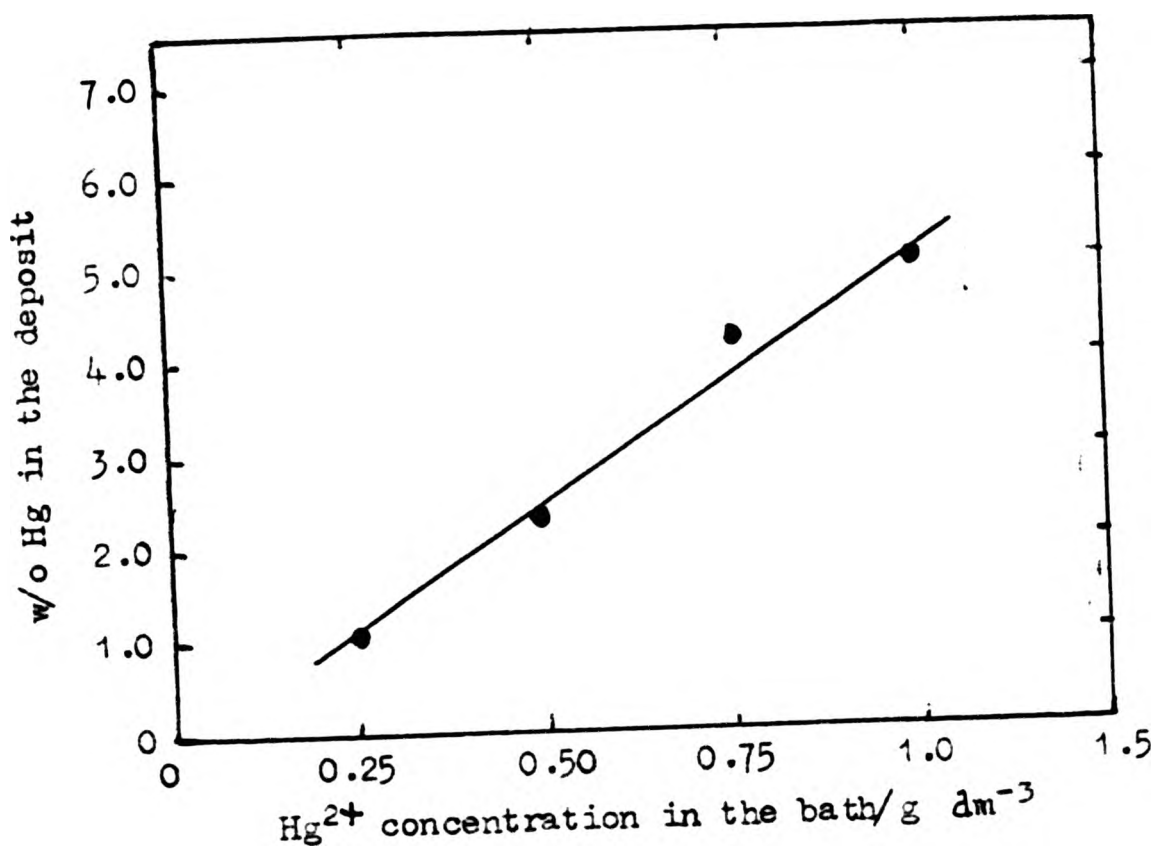


Figure 228. Effect of mercury content of the bath on the composition of the deposit.

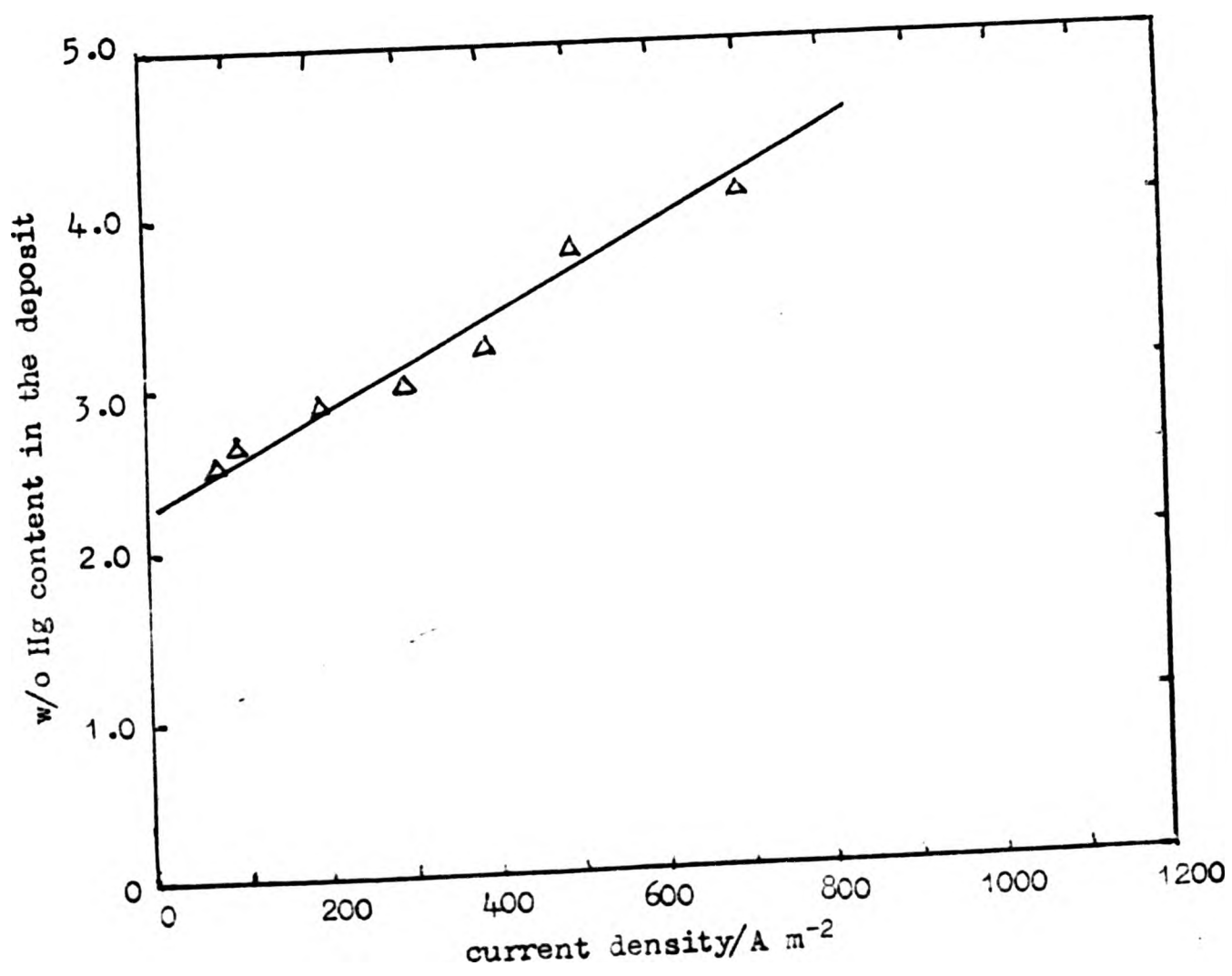


Figure 229. Influence of current density on the deposit composition.

effect of temperature rise was to enhance the rate of deposition, but the quality was not affected to any extent. Two experiments were performed at higher temperatures, one at 40°C and the other at 80°C. These showed that there was a decrease in the zinc content - all other factors being constant.

7.4.6 Influence of mercury ion concentration and the current density on the deposit composition for ternary baths. A series of experiments were conducted to find out the influence of changing concentration of mercury in the bath and the applied current density on the composition of the deposit. The results are plotted in Figures 228 and 229. It is clearly evident that a direct relation exists between these parameters and the composition of the deposit.

7.5 X-RAY DIFFRACTION STUDIES

7.5.1 General. Atomic absorption spectrometry proved that the powders obtained by electrodeposition contained the desired elements. To decide whether an alloy or just an intimate mechanical mixture was obtained, X-ray diffraction studies were carried out. These studies helped to determine the size of crystallites deposited and proved that an alloy has been obtained rather than an intimate mixture.

A Philips X-ray powder diffractometer was used to obtain the diffraction patterns by counting the diffracted intensities point by point. The measurements of these profiles with sufficient precision for crystallite size calculations taxed the capabilities of the spectrometer for several reasons, including:

- (1) the weak peak intensities encountered in this work,
- (2) the relatively high background counting rate,
- (3) b/B ratios are too large to give good precision.

Adjustment of the instrument for good resolution was possible by employing 1° divergence slit and 0.025° receiving slit and correcting for the dead time of the Geiger counter. X-ray beam size is 2 cm x 1 cm. For more accurate work an evacuated camera can be used to eliminate scattering due

(2) Other intensities are much lower than those given in the index card.

(3) The 'd' values are in excellent agreement.

Using the Bunn charts and rechecking the results through the use of the formulae $\sin^2\theta = (\lambda^2/4a^2)(h^2 + hk + k^2) + (\lambda^2/4c^2)l^2$ and $\lambda = 2d \sin \theta$, c/a ratio was calculated to be 1.857 which compares with the listed value 1.856. The other listed values for zinc are:

hexagonal close packed structure

$$a = 2.6585 \times 10^{-1} \text{ nm}$$

$$c = 4.9342 \times 10^{-1} \text{ nm}$$

$$c/a = 1.856$$

The crystallite size was calculated on the (101) reflection:-

$$\begin{aligned} N_{101} &= \frac{0.89 \lambda}{\beta_{\frac{1}{2}} \cos \theta} \times 57.3 \\ &= \frac{0.89 \times .15421 \times 57.3}{0.185 \times \cos(43.28/2)} \\ &= 46 \text{ nm} \end{aligned}$$

Pure electrodeposited cadmium gave the following diffraction results presented in Table 35.

Table 35. Measurements from X-ray diffractograms

2θ °	I/I ₀	$d = \lambda/2 \sin \theta$ 10 ⁻¹ nm	Reflection (hkl)
31.85	4	2.808	(002)
34.75	50	2.580	(100)
38.40	100	2.345	(101)
47.85	12	1.899	(102)
61.20	10	1.515	(103)
62.35	45	1.490	(110)
71.80	17	1.316	(112)
73.25	4	1.290	(200)
75.60	17	1.258	(201)
82.10	4	1.174	(202)

- Remarks:- (1) Zn (101) plane gives the maximum reflected intensity.
- (2) Cd (101) plane gives a maximum reflected intensity which is half that of zinc.
- (3) 'd' values when compared with those for pure elements indicate that neither pure zinc nor pure cadmium is present. The "distortion" in the values has been confirmed beyond doubt.
- (4) The maximum intensities do not occur for the same crystal planes as they would in pure components.
- (5) Corresponding reflection intensities have decreased considerably.
- (6) Application of Vegard's Law suggests that zinc and cadmium are in a state of combination that is crystalline in nature. The crystallite size was calculated for the (100) reflection,

$$N_{\text{alloy}}^{100} = \frac{0.89 \times .1542 \times 57.3}{0.302 \cos 38.945/2}$$

$$= 27.6 \text{ nm}$$

for (101) reflection:

$$N_{\text{alloy}}^{101} = \frac{0.89 \times 0.15421 \times 57.3}{0.305 \cos 43.167/2}$$

$$= 27.7 \text{ nm}$$

Table 37 below lists the values 'c', 'a' and ratio 'c/a' for some alloys. Corresponding values for Zn and Cd alone have also been listed for the sake of comparison. These values were calculated using the equation $\sin^2\theta = (\lambda^2/4a^2)(h^2 + hk + k^2) + (\lambda^2/4c^2)l^2$ observing that for certain reflections $h = k = 0$ and $l = 1$, and also $h = k = 1$, and $l = 0$, thus allowing 'c' and 'a' to be calculated from a single equation.

Table 37. Crystallographic data for some Zn-Cd alloys

w/o Cd in Zn	a nm	c nm	c/a
0	0.26585	0.49342	1.856
100	0.2973	0.5606	1.886
0.60	0.23156	0.48855	2.1098
1.00	0.23130	0.49571	2.1430
4.00	0.23041	0.49510	2.1522

The increase in c/a ratio indicates a substitutional solid solution type of alloying.

7.5.3 Discussion. X-ray diffraction provides a means of measuring changes in lattice parameters taking place due to the presence of a substitutional element in the matrix of another element. In this case the variation is linear with the proportion of the atoms of the substituting metal. In some instances the deposit showed a preferred orientation with a crystal axis aligned with that of the substrate metal. However this epitaxy was confined to first few molecular layers. A thick deposit did not show such an orientation. The preferred orientation is indicated on the count profile by a coincidence of the maximum intensities of the substrate and the deposit. Thus it was found that Cd (110) deposited on Cu (111) preferentially. This preference was also revealed in the Debye-Scherrer photographs by the lack of uniformity of the rings. If a random orientation exists then the rings are of uniform intensity.

The X-ray diffraction measurements thus prove that electrodeposited alloys have been produced which are homogeneous and of very fine size and therefore of large surface area.

7.6 ELECTRON MICROSCOPY

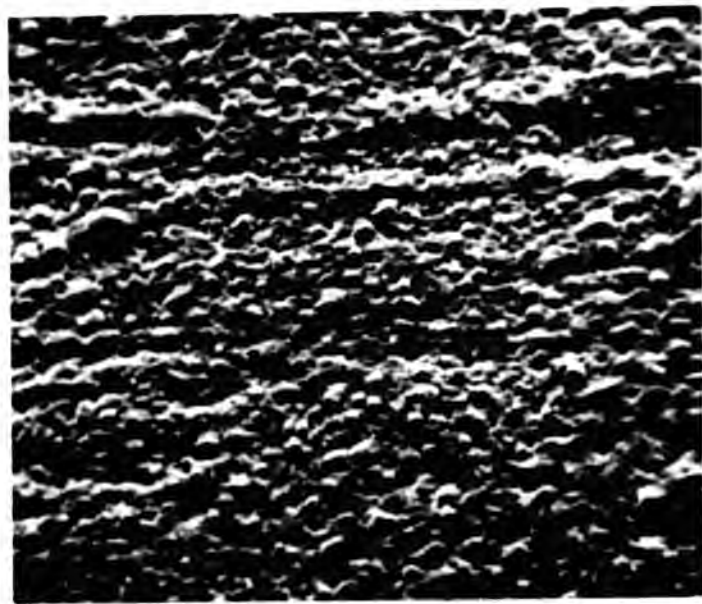
The electrodeposited alloys were examined under an optical microscope but it was not possible to obtain a well defined image because of extreme depth of field required. A scanning electron microscope provided better resolution and well defined images. The specimens were cut from the plated substrates of size 6 x 6 mm and glued to aluminium stubs which act as specimen holders. An air setting conducting silver 'paint' was used as a glue. This provided a current conducting path for the electron beam impinging on the deposit. The accelerating voltage was 15-20 keV. The beam current was $1.5-2.0 \times 10^{-7}$ A. A lithium fluoride crystal at $41^{\circ}42'$ was used to detect zinc; a mica crystal at $23^{\circ}01'$ was used to detect cadmium; and a lithium fluoride crystal at $35^{\circ}54'$ was used to detect mercury.

The electron images show the topographical features of the deposits. The deposits are either crystalline or nodular. Electron microprobe analysis and the distribution pictures for zinc, cadmium and mercury indicate clearly that the individual elements are uniformly distributed. The distributions were also recorded using a chart recorder and a line scan photograph. These show that distribution is uniform (after allowing for the non-smooth surface of the deposit). Figures 231-235 represent some of the photographs obtained during electron microscopy.

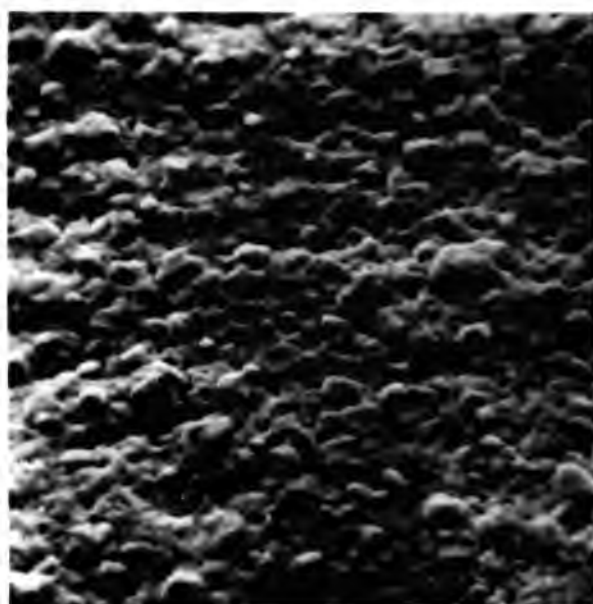
7.7 DISCUSSION

The investigation of the variables for producing Zn and Cd electrodeposits has indicated that a satisfactory procedure based on a mixed sulphate bath may be optimised by the use of a suitable addition agent, selection of pH and choice of current density.

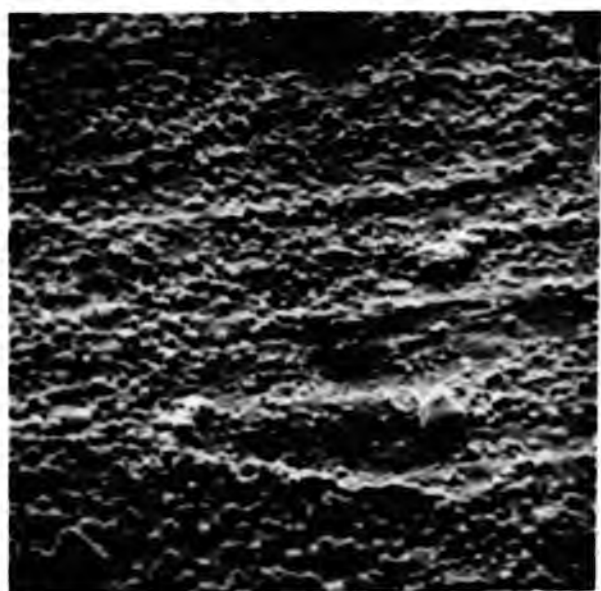
There are a few suitable addition agents specific to cadmium deposition such as liquorice, caffeine, aloin and gelatin. Of these, aloin and gelatin were found to be better, whereby an improvement was obtained by using small quantities of the compound. The improvement was in terms of the appearance, quality and the composition of the deposit. Without the



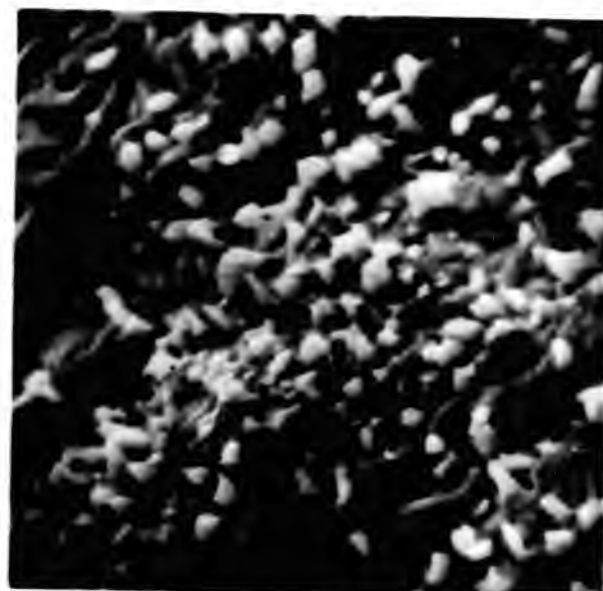
(a)



(b)



(c)



(d)

Figure 231. Scanning electronmicrographs of Zn-Cd binary alloy electrodeposited in the absence of gelatin in the bath

(a) Backscattered electron image at x 1000 at a current density of 400 A m^{-2}

(b) Backscattered electron image at x 2000 at a current density of 400 A m^{-2}

(c) Backscattered electron image at x 1000 at a current density of 700 A m^{-2}

(d) Backscattered electron image at x 5000 at a current density of 700 A m^{-2}

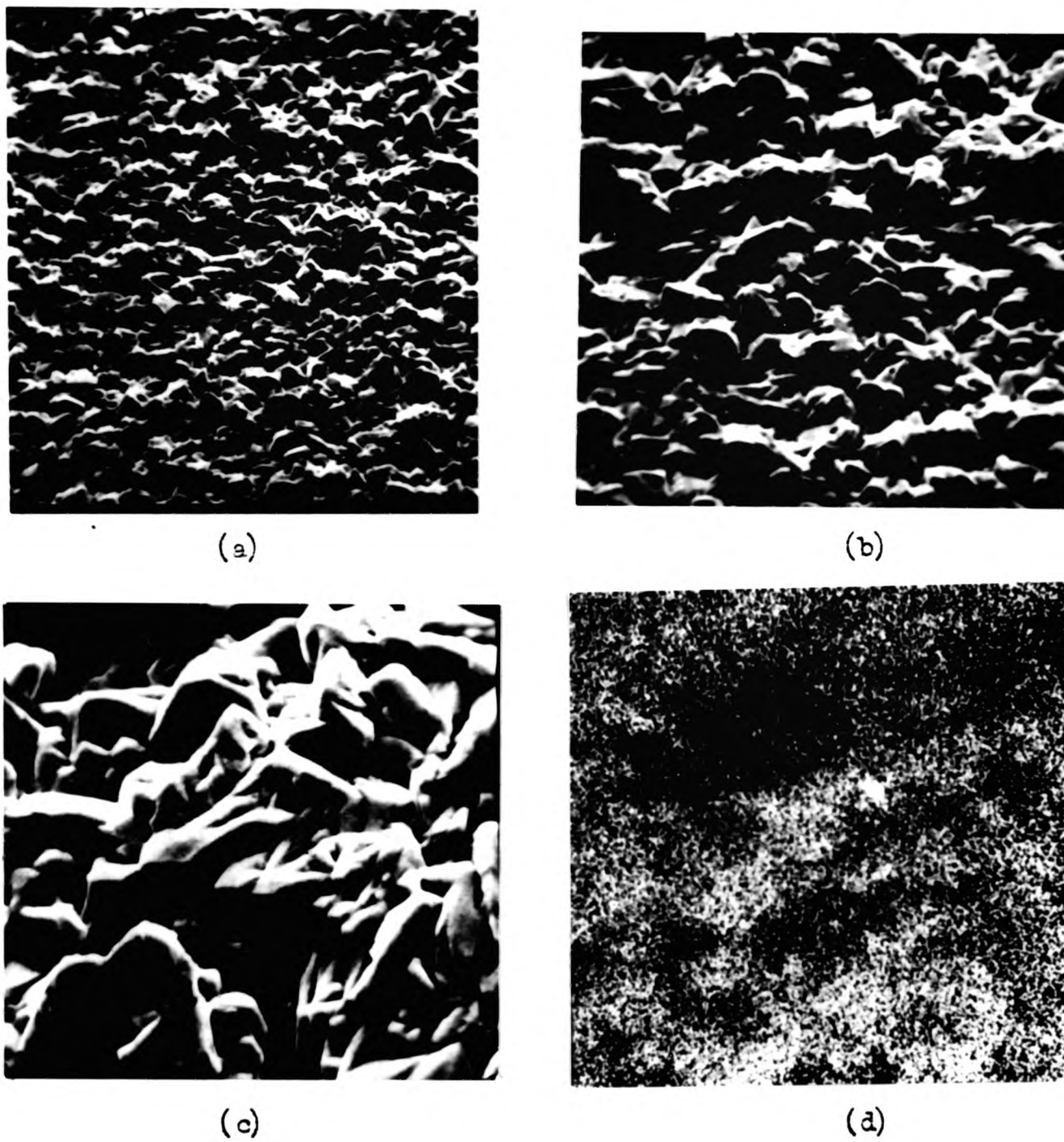


Figure 232. Scanning electronmicrographs of electrodeposited Zn-Cd binary alloy. Current density 300 A m^{-2} . Bath containing 0.2 w/o gelatin.

- (a) Backscattered electron image at x 1000
- (b) Backscattered electron image at x 2000
- (c) Backscattered electron image at x 5000
- (d) Cd distribution at x 1000

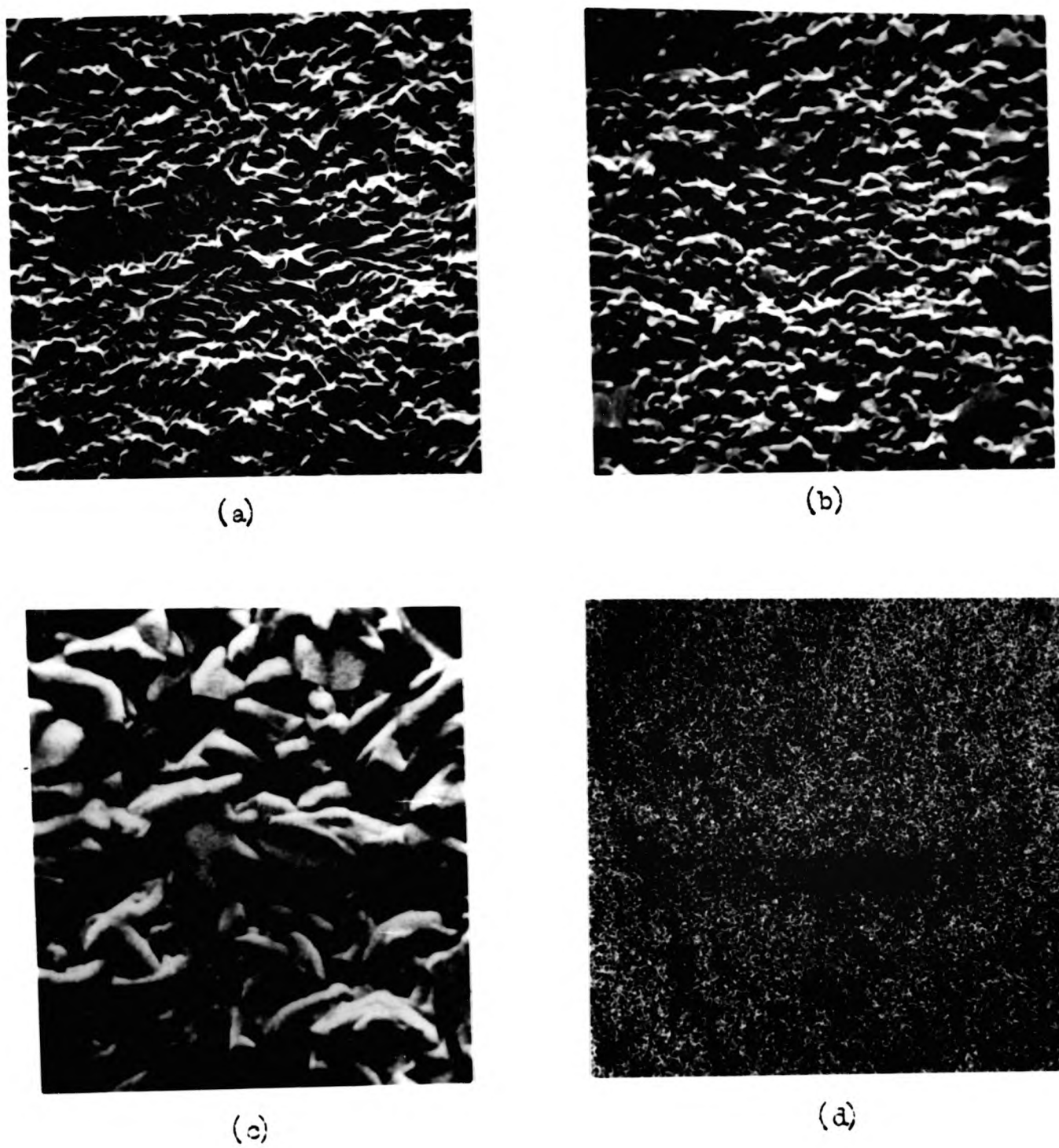


Figure 233. Scanning electron micrographs of electrodeposited Zn-Cd binary alloy. Current density 500 A m^{-2} . Bath containing 0.2 w/o gelatin.

- (a) Backscattered electron image at x 1000
- (b) Backscattered electron image at x 2000
- (c) Backscattered electron image at x 5000
- (d) Cd distribution at x 1000

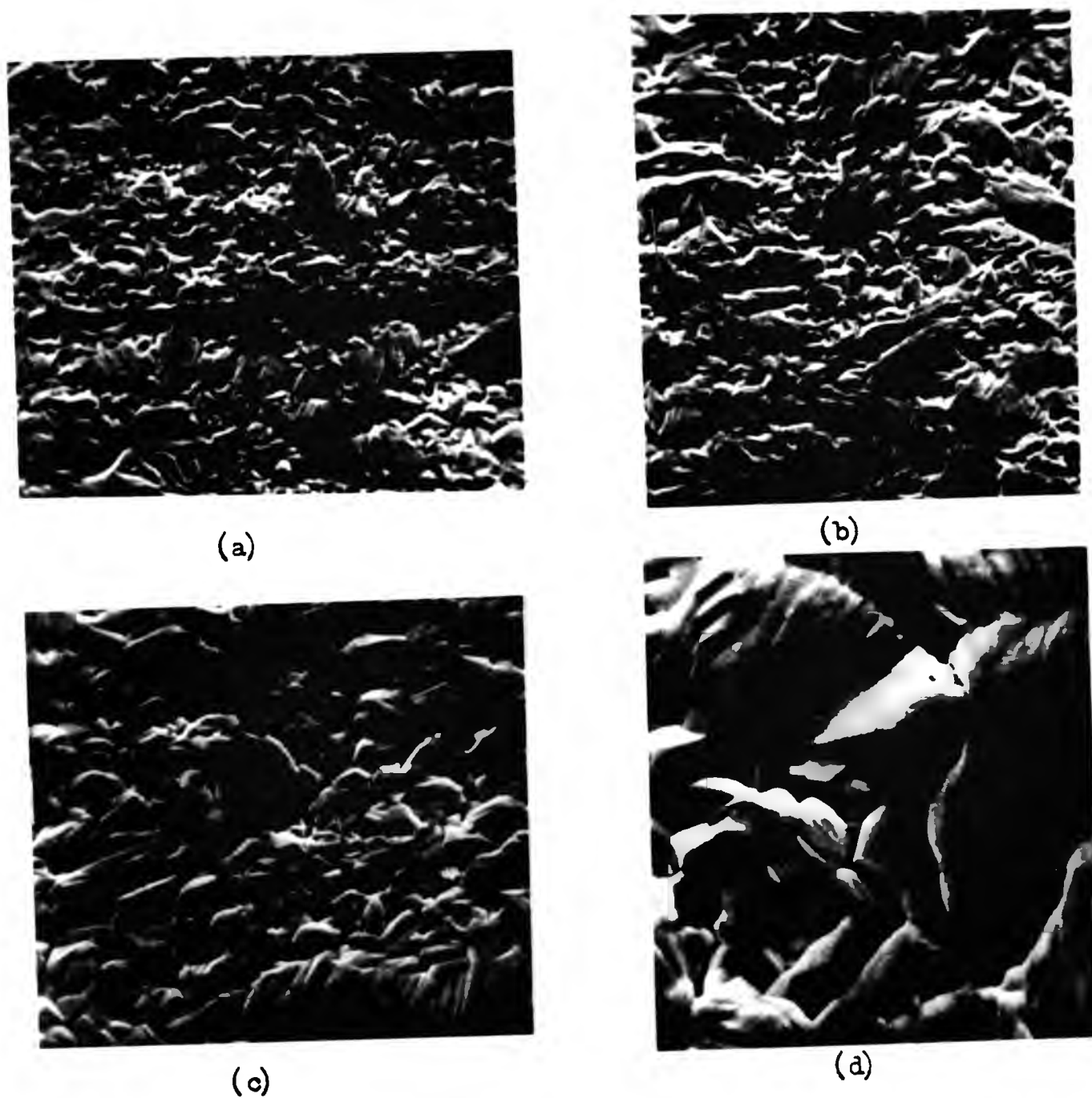


Figure 234. Scanning electronmicrographs of electrodeposited Zn-Cd-Hg ternary alloy. Current density 300 A m^{-2} . Bath containing 0.2 w/o gelatin.

- (a) Backscattered electron image at x 1000
- (b) Backscattered electron image at x 2000
- (c) Backscattered electron image at x 5000
- (d) Backscattered electron image at x 5000 of a central area

addition agent the deposit was always high in cadmium. The use of an addition agent helped the aim of getting a low Cd deposit. Aloin eliminated gassing to a greater extent at the cathode than did gelatin, but whereas gelatin baths kept longer without deteriorating, the aloin baths suffered from decomposition manifested by a gradual change in colour, probably associated with the anodic oxidation of aloin. The value of addition agents is well recognised in practical electrodeposition technology, and this especially so with respect to zinc and cadmium codeposition from simple ionic salt baths. Small additions of gelatin produced a welcome decrease in the cadmium content of the deposit. Without an addition agent the bath would require, for a given deposit composition, a much lower cadmium salt concentration than is practically desirable.

Another important parameter of the process of electrodeposition is the current density. The influence of a given current density is reflected in the rate of deposition and the physical and chemical characteristics of the deposit. With this work the effect of current density on the composition of the deposit was of principal interest. There is a preferential cadmium deposition with little zinc codeposition below the limiting current density, which is a function of metal salt concentration and the activities of the ions. If the applied current density exceeds this limiting value, then increasing amounts of zinc codeposit. As the current density increases beyond this point the cadmium content of the deposit also increases gradually. For the range of current densities investigated there is a direct relationship between these two parameters.

The influence of the total metal ion content of the bath and the zinc to cadmium ratio is also similar. Since cadmium is a far more readily depositable metal than zinc, any increase in the amount of cadmium salt in the bath would naturally increase the amount of cadmium in the deposit.

The deposition process and the deposition rate was adequate at room temperature. Both the binary and the ternary deposits could be obtained in an ambient temperature range of 12-25°C. Elevation of temperature to

higher values such as up to 80°C caused a slight increase in zinc content of the deposit. There would not be any economic advantage gained by heating the bath because any increase in the rate of deposition and improvement in the quality of the deposit will have to be offset against the additional cost of heating the bath and replenishing the water lost through evaporation.

Variation of the pH does have a slight effect on the composition of the deposit, but this is not significant. As the sulphates of Zn and Cd are acidic the pH of the prepared bath was always below 4.0. Mercuric nitrate was added to the bath for deposition of ternary alloys. This lowered the pH to 1.0 because acidification was required to dissolve the mercuric nitrate. As expected, the simple ion baths were only slightly sensitive to the changes in pH because the state of chemical combination of metal ions in solution is not altered. In contrast to this it is known that the pH has a significant effect on the composition of alloys deposited from baths in which the parent metals are present as complex ions with large instability constants.

With the standard plating cell arrangement it was not easy to investigate the influence of stirring thoroughly. To establish the diffusion dependence of the process of electrodeposition of zinc-cadmium alloys redesigning of the apparatus would be required involving a new cell and cathode in the form of a rotating disc electrode. Two types of stirring methods were used, namely using a magnetic stirrer - follower at various speeds and the to and fro motion of a glass/Teflon rod in front of the cathode. Medium to high speeds of magnetic stirrer were found to be detrimental. Low speeds and glass rod stirring, at best, helped to dislodge gas bubbles from the surface of the cathode. On the whole it can be said that this kind of stirring did not produce any remarkable difference.

A further evidence of the optimal conditions was obtained by examining the deposit under the electronmicroprobe analyser, where the electron images would differentiate between a fine crystalline deposit and

CHAPTER EIGHT

GENERAL DISCUSSION AND CONCLUSIONS

In the previous chapters of this thesis, opportunity has been taken to discuss and draw conclusions from individual aspects of the experimental programme. The purpose of this concluding chapter is to summarise in a more general way the overall investigation, to draw specific conclusions and to make recommendations for future work.

In Chapter 1 a survey of the historical background to the development of primary cells and to the literature on the basic electrochemistry of the system emphasised the importance of the zinc-alkali system which has been subject to continuous improvement. Zinc anodes function quite successfully in primary cells as evident from their use in a variety of systems. The self corrosion during storage and the tendency to passivate at high discharge rate prevent full utilisation of the available capacity. To improve anode performance for a specific application requires an appraisal to determine the relative importance of shelf life and high discharge rate capability, since these two factors impose conflicting requirements on the system. The present work shows that improvements are possible in both directions.

Metallurgical studies carried out on thermally prepared alloys in Chapter 2 indicate that inhomogeneity of Cd distribution in Zn-Cd alloys and that of Hg and Cd in Zn-Cd-Hg alloys will remain a problem. Although Zn and Cd are completely soluble in the liquid state, they are not miscible in the solid state. The solubility decreases rapidly with temperature. At the eutectic temperature about 2% Cd can dissolve in Zn. With rapid cooling (quenching) a greater amount of Cd can dissolve in Zn resulting in a single phase structure. However, even upon quenching, a two phase structure cannot be avoided if the Cd content is around 25 w/o. Quenching results in a metastable structure which tends to recrystallise

after mechanical working. Hg dissolves more Cd and Zn and therefore the Cd-rich phase becomes a Hg-rich phase also. Thus amalgamated alloy must be homogeneous and single phase before amalgamation.

Self-corrosion studies on the alloys, in Chapter 3, proved that two phase alloys should have a comparatively short shelf life compared to pure zinc or single phase alloys. Pure Cd would have the longest shelf life. Amalgamation of alloys or addition of ZnO to the electrolyte considerably reduced the self-discharge. On the basis of 1000 hour exposure tests the alloys may be arranged in the increasing order of corrodibility as follows:

Cd, Zn-0.05 Cd, Zn-0.2 Cd, Zn-1 Cd, Zn-2 Cd, Zn,
Zn-25 Cd, Zn-5 Cd.

The amount of self-corrosion suffered by the 0.2 w/o Cd and 1 w/o Cd alloys is nearly half of that suffered by Zn. The general reduction of corrosion of single phase Zn-Cd alloys may be expected because Cd could, if distributed homogeneously, impart its corrosion resistant properties, increase the hydrogen overvoltage, and alter the cathodic Tafel slope favourably, while not affecting the exchange current density.

The anodic polarisation studies employing rotating disc electrode technique, described in Chapter 4, show that the nature of the E-i curves is similar to that of pure zinc, but the two phase alloys show a secondary passivation peak due to Cd at 0.8-0.9 V vs. Hg-HgO reference electrode. These are attributed to the two phase nature of high Cd alloys associated with the changes in the nature of the film in plain electrolyte. The ZnO saturated electrolyte does not show any. With rotating disc electrodes oscillations were observed at higher speeds with all alloys and both electrolytes, indicating that these were due to the vibration of the Luggin probe. These studies established that the passivation process is diffusion controlled and a dissolution-precipitation mechanism of film formation applies. Another peculiar property of the passive film is the presence of

excess Zn metal in the thick film indicating that it is the outward diffusion of Zn atoms through the solid anodic product layers which is responsible for the growth of passive layers. This is also corroborated by galvanostatic discharge studies, which show that under certain conditions the film is easily dissolved away. The following conclusions were drawn from the anodic polarisation studies in addition to those already stated earlier:

- i) The active region Tafel slopes vary from 18-40 mV per decade. This difference is indicative of a change in activation energies of discharge, diffusion and adsorption. The interpretations given by other workers do not lead to a clear understanding of the phenomenon.
- ii) At low speeds the active-passive transition shows two peaks. These are associated with adsorption of OH^- and incorporation of water of hydration and subsequent actual monolayer film tightening.
- iii) A hysteresis effect is observed in the forward and backward sweep of the anodic E-i curves at high rotation speeds.
- iv) Upon increasing the rotation speed passivation occurs at more anodic potentials, breakdown of passivation is at less anodic potentials, critical current density increases to a great extent, indicating that if mass transport is increased the anode can be fully discharged long before the onset of passivity.
- v) Since the film thickness does not vary linearly with the potential we can assume a constant film to solution potential and an independence of the free energy of activation of the passage of ions through the film on the potential.

In Chapter 5, a study of hydrogen overpotential on the alloys indicated that the presence of Cd in Zn does not decrease the exchange current density to a significant extent and at the same time it increases the overpotential bringing it near to that of Cd, while the cathodic Tafel slope approaches that of pure Cd. These factors favourably improve the

Zn SO ₄ · 7 H ₂ O	70	g dm ⁻³
3 Cd SO ₄ · 8 H ₂ O	2	"
Hg(NO ₃) ₂ · H ₂ O	1.71	"
Al ₂ (SO ₄) ₃ · 16 H ₂ O	30	"
Gelatin	0.2	"
Temperature	25	°C
Current density	500	A m ⁻²

This is a regular bath containing simple ions having the advantage of producing a deposit composition insensitive to the influence of pH, stirring or temperature. Further, it has every prospect of providing economic production on the commercial scale.

In the light of these discussions it may be concluded that:

- a) Cd can provide a low cost replacement for Hg in binary Zn-Hg alloys,
- b) Cd, in conjunction with Hg, may provide an equally acceptable ternary Zn-Cd-Hg alloy for particular purposes.

Alloying with Cd will definitely reduce the amount of Hg required, say from the normal 10 w/o to 1.0 w/o. Alloys containing 0.2 to 1 w/o Cd strike an excellent compromise between long shelf life and high discharge rate capabilities. In this respect they are superior to pure zinc, pure cadmium or two phase alloys.

Recommendations for Further Work

It has become apparent during the present investigations that single phase, homogeneous, microcrystalline and larger surface area alloys can be produced by electrodeposition. This method is superior in various respects to traditional melting and casting. Porous electrodes with large surface areas and therefore high rate discharge capability can thus be constructed for certain applications. Electroformed or compacted alloys are amenable to such types of electrochemical studies as have been made on the more massive cast alloys. Thus the self corrosion behaviour, anodic polarisation

characteristics on rotating disc electrodes and the determination of cathodic kinetic parameters, together with constant current anodic discharge studies could be carried out on these alloys to complete a final assessment. These should prove to be of value in establishing an improved anode material for primary alkaline cell development.

As far as more detailed studies of the mechanism of anodic processes on alloy systems is concerned, the use of a ring disc and/or a split ring disc modification to the rotating disc electrode technique could provide valuable information on the nature of intermediate species involved in the overall reaction scheme.

Subsequently, it would be necessary to evaluate the economic and production aspects of adopting such a modified cell for commercial exploitation.

REFERENCES

- 1(a). Vinal G.W., "Primary Batteries", John Wiley and Sons, New York, 1950.
- 1(b). Heise G.W. and Cahoon N.C., "The Primary Battery, Vol.I, E.C.S., John Wiley, 1971.
2. Daniell J.F., Philosophical Magazines III, 8, 421 (1836).
 " Philosophical Transactions 126, 106, 125-129 (1836).
 " ibid. 127, 141-150, (1837).
3. Grove W.R., Philosophical Magazines III, 13, 430 (1838).
 " ibid. 14, 388 (1839).
 " " 15, 287 (1839).
4. Poggendorff, J., Pogg. Ann. Phys., 57, 101 (1842).
5. Rive, de la, Id. Ann. Chim., 61, 40 (1843).
6. de Lalande F. and Chaperon G., U.S. Pat. 274110 (1883).
7. Leclanche G., French Patent 71865 (1866).
8. Gassner, C., U.S. Patent 373064 (1887).
9. Bobker R.V., Lucas Group Research Report No. GR 90698 (1973).
- 10(a). Kemp K.T., Edinburgh New Phil. J., 6, 70-77 (1828).
- 10(b). Johnson W.M., Trans. Electrochem. Soc., 1, 187 (1902).
11. Milner P.C., J. Electrochem. Soc., 107, 1 (1960).
- 12(a). Evans G.E., Proceedings 13th Annual Power Sources Conference, U.S.A.S.R.D.L. (1959).
- 12(b). Chambers and Tantrum, "Fuel Cells", Reinhold Publishing Corp., N.Y. (1960).
- 12(c). Clark M.B. et al., 18th Annual Power Sources Conference, U.S.A.S.R.D.L. (1964).
- 12(d). Haldeman R.G. et al., "Fuel Cell Systems", Advances in Chemistry Series, American Chemical Society (1965).
- 12(e). Lurie R.M. et al., J. Electrochem. Soc., 110, 1173 (1963).
- 13(a). Elmore G.V. and Tanner H.A., J. Electrochem. Soc., 108, 669 (1961).

- 13(b). Heibronner H.H. et al., Final Report, Contract No. DA-44009-AMC-756
V.S.G.D. of Commerce (1965).
14. Acker R.F., Developments in Industrial Biology, 6, 260 (1964).
15. Waddington T.C., Editor, "Non-aqueous solvent systems",
Academic Press, New York (1965).
16. Robinson P., U.S. Patent 2786088 (1957).
17. Pauli W.J., U.S. Patent 2851510 (1958).
18. Schwartz M. and Frenklin P.J., U.S. Patent 2895000 (1959).
19. Harding M.S., U.S. Patent 2831045 (1958).
20. Grubb W.T., Proc. Eleventh Annual Battery R and D Conf., Fort
Monmouth, N. J, p.5 (1957);
J. Electrochem. Soc., 106, 275 (1959);
U.S. Patent 2861116, U.S. Patent 2933547 (1960).
21. van der Grinten W.J. and Mohler D., U.S. Patent 2928890 (1960).
22. Ruben S., U.S. Patent 2852591 (1958).
23. Richter E.W. et al., U.S. Patent 3004093 (1961).
24. Lieb H.C., U.S. Patent 2930830 (1960).
25. Smyth D.M. and Shirn G.A., U.S. Patent 2905740 (1959).
26. Perrot M. and Sator A., Compt. rend., 234, 1883 (1952).
27. Moulton C.W., Hacskaylo M. and Feldman C., "The Electrochemistry
of Thin Films", presented at Toronto Meeting, Electrochemical
Society (May 1964).
28. Hacskaylo M. and Foley R.T., J. Electrochemical Society, 113, 1231,
(1966).
29. Vouros P. and Masters J.I., J. Electrochemical Society, 116, 880
(1969).
30. Perrott C.M. and Fletcher N.H., J. Chem. Phys., 48, 2143 (1968).
31. Latimer W.M., "Oxidation Potentials" Prentice-Hall (1952).
32. Pourbaix M., "Atlas of Electrochemical Equilibria in Aqueous
Solutions". Cebelcor, Brussels (1966).
33. Schikorr G., Korrosion und Metallschutz, 16, 181 (1940).

**PAGE
MISSING**

REFERENCES

- 1(a). Vinal G.W., "Primary Batteries", John Wiley and Sons, New York, 1950.
- 1(b). Heise G.W. and Cahoon N.C., "The Primary Battery, Vol.I, E.C.S.", John Wiley, 1971.
2. Daniell J.F., Philosophical Magazines III, 8, 421 (1836).
 " Philosophical Transactions 126, 106, 125-129 (1836).
 " ibid. 127, 141-150, (1837).
3. Grove W.R., Philosophical Magazines III, 13, 430 (1838).
 " ibid. 14, 388 (1839).
 " " 15, 287 (1839).
4. Poggendorff, J., Pogg. Ann. Phys., 57, 101 (1842).
5. Rive, de la, Id. Ann. Chim., 61, 40 (1843).
6. de Lalande F. and Chaperon G., U.S. Pat. 274110 (1883).
7. Leclanche G., French Patent 71865 (1866).
8. Gassner, C., U.S. Patent 373064 (1887).
9. Bobker R.V., Lucas Group Research Report No. GR 90698 (1973).
- 10(a). Kemp K.T., Edinburgh New Phil. J., 6, 70-77 (1828).
- 10(b). Johnson W.M., Trans. Electrochem. Soc., 1, 187 (1902).
11. Milner P.C., J. Electrochem. Soc., 107, 1 (1960).
- 12(a). Evans G.E., Proceedings 13th Annual Power Sources Conference, U.S.A.S.R.D.L. (1959).
- 12(b). Chambers and Tantrum, "Fuel Cells", Reinhold Publishing Corp., N.Y. (1960).
- 12(c). Clark M.B. et al., 18th Annual Power Sources Conference, U.S.A.S.R.D.L. (1964).
- 12(d). Haldeman R.G. et al., "Fuel Cell Systems", Advances in Chemistry Series, American Chemical Society (1965).
- 12(e). Lurie R.M. et al., J. Electrochem. Soc., 110, 1173 (1963).
- 13(a). Elmore G.V. and Turner H.A., J. Electrochem. Soc., 108, 669 (1961).

34. Kolthoff I.M. and Kameda T., *J.Amer.Chem.Soc.*, 53, 832, 42 (1931).
35. Gmelins Handbuch der anorganischen Chemie, Zink.S.N.32. Verlag Chemie, GmbH Weinheim, 1956.
36. A. Ya. Chatalov, *Doklad.Akad.,Nauk. S.S.S.R.*, 86, 775-7 (1952).
37. Deltombe, E. and Pourbaix M., Technical Report RT3 CEBELCOR (1953).
38. Charlot G., *Qualitative Analysis of reactions in solutions*, 4th ed. Masson, Paris.
39. Ives D. and Janz G., "Reference Electrodes", Academic Press, New York (1961).
40. Rùetschi P. and Delahay P., *J.Chem.Phys.*, 23, 556 (1955).
41. Handbook of Chemistry and Physics, 42nd Edition, Chemical Rubber Publishing Co. (1960).
42. International Critical Tables, Vol.5, p.68.
43. Milner P.C. and Thomas U.B., in "Advances in Electrochemistry and Electrochemical Engineering", Vol.5, Interscience Publishers, New York (1967).
44. Snyder R.N. and Lander J.J., *Electrochem.Technol.*, 3, 161 (1965).
45. Rùetschi P., *J.Electrochem.Soc.*, 114, 301 (1967).
46. Jofa Z.A. et al., *Zh.Fiz.Khim.*, 35, 1571 (1961).
47. Dirkse T.P. and Trimmer R., *J.Electrochem.Soc.*, 116, 102 (1969).
48. Gregory D.P. et al., *J.Electrochem.Soc.*, 119, 1268 (1972).
49. Vorkapic L.Z., Drazic D.M. and Despic A.R., *J.Electrochem.Soc.*, 121, 1385 (1974).
50. Moshtev R.V. and Stoicheva R., *J.Applied Electrochem.*, 6, 163 (1976).
51. De Pauli C., De Rosa O. and Giordano M.C., *J.Electroanalytical Chem.*, 13, 105 (1976).
52. Vozdvizhenskii G.S. and Kochman E.D., *Zh.Fiz.Khim.*, 39, 347 (1965).
53. Powers R.W. and Breiter M.W., *J.Electrochem.Soc.*, 116, 719 (1969).
54. Shaikh A. Salam, M.Sc. Report, 20 January (1978). City of London Polytechnic.
55. Breiter M.W., *Electrochim.Acta.*, 16, 1169 (1971).

79. Armstrong R.D. et al., *J.Appl.Electrochem.*, 2, 265 (1972).
80. Armstrong R.D. and West G.D., *J.Electroanalyt.Chem. and Interfacial Electrochem.*, 30, 385 (1971).
81. Kági J. and Vallee B., *J.Biol.Chem.*, 236, 2435 (1961).
82. Orvini E. et al., *Anal.Chem.*, 46, 1294 (1974).
83. Crossman S.T. and Dean J., *Anal.Chim.Acta*, 75, 421 (1975).
84. Ben-Bassat A. et al., *Anal.Chem.*, 47, 534 (1975).
85. Coloros C. et al., *Anal.Chim.Acta*, 64, 457 (1973).
86. Beyer M.E. et al., *Anal.Chem.*, 47, 479 (1975).
87. Nakamura K. and Ozawa T., *Anal.Chim.Acta*, 86, 147 (1976).
88. "Analytical methods for Atomic Absorption Spectrophotometry",
Perkin Elmer Corporation, May 1966.
89. Clinton O.E., "Static vapour apparatus for the determination of mercury by flameless atomic absorption", *Laboratory Practice* (December 1974).
90. Wendt R.H. and Fassel V.A., *Anal.Chem.*, 22, 667 (1950).
91. Goleb J. and Brody J., *Anal.Chim.Acta.*, 28, 457 (1963).
92. Adcock J., *J.Inst.Metals*, 26, 361 (1921).
93. ASTM Special Technical Publication No.285, "Methods of Metallographic Specimen Preparation", (1960).
94. Zholudev M.D. and Stender V.V., *Ukr.Fiz.Khim.*, 23, 200 (1957).
95. Adams R.N., "Electrochemistry at Solid Electrodes", Marcel Dekker, N.Y. (1969).
96. Azim S. and Riddiford A.C., *Anal.Chem.*, 34, 1023 (1962).
97. Blurton K.F. et al., *J.Electrochem.Soc.*, 10, 457 (1965).
98. Levich V.G., "Physicochemical Hydrodynamics", Prentice Hall, N.J. (1962).
99. Eucken A., *Z.Electrochem.*, 38, 341 (1932).
100. Newman J., *Journal Phys.Chem.*, 70, 1327 (1966).
101. Kassner T.F., *J.Electrochem.Soc.*, 114, 689 (1967).
102. Pleskov and Filinovskii, "The Rotating Disc Electrode", Plenum Press (1976).

103. Newman J., J.Electrochem.Soc., 113, 501 (1966).
104. Angell D.H. et al., Electrochim.Acta, 13, 120 (1968).
105. Alberry W.J., Trans.Farad.Soc., 67, 2408 (1971).
106. Alberry W.J. et al., Electrochim.Acta., 13, 281 (1968).
107. Bruckenstein S. and Miller B., J.Electrochem.Soc., 117, 1044 (1970).
108. Marathe V. and Newman J., J.Electrochem.Soc., 116, 1704 (1969).
109. Newman J., J.Electrochem.Soc., 113, 1235 (1966).
110. Zholoudev M. and Stender V., Zh.Prikl.Khim., 31, 711 (1958).
111. Lee T.S., J.Electrochem Soc., 120, 707 (1973).
 ibid. 122, 171 (1975).
 ibid. 118, 1278 (1971).
112. Davies C.W., "Electrochemistry", George Newnes, London (1967).
113. Krishtalik L.I., in "Advances in Electrochemistry and Electro-chemical Engineering". Editors Delahay P. and Tobias C.W., Vol.7, John Wiley (1970).
114. Frumkin A.N., in ibid., Vol.1, John Wiley (1961).
115. Bockris J. et al., J.Chim.Phys., 49, C70 (1952).
116. Kapzan O. and Jofa S., Zhur.Fiz.Khim., 26, 193-201 (1952).
117. Brenner A., "Electrodeposition of Alloys". Vols.1 and 2, Academic Press, 1963.
118. Vagramyan A. and Solovirea Z., "Technology of Electrodeposition", Robert Draper (English Translation), 1961.
119. Fink G.G. and Young C., Trans.Electrochem.Soc., 67, 311-336 (1935).
120. Thirsk H.R., Editor, Electrochemistry Vol.No.4, Specialist Periodical Reports, The Chemical Society (1974).
121. Macdonald D.D., "Transient Techniques in Electrochemistry", Plenum Press (1977).
122. Gilroy D. and Mayne J., J.Appl.Chem., 12, 382 (1962).
123. Bruslic V., "Oxide and Oxide Films", Editor, Diggle J.W., Marcel Dekker (1972).
124. Vetter K.J., "Electrochemical Kinetics", Academic Press, New York (1967).

ACKNOWLEDGEMENTS

The author wishes to express his gratitude to his supervisor, Dr. C.J.L. Booker, of the Department of Metallurgy and Materials at the City of London Polytechnic, for guidance and helpful advice in this work. Thanks are also due to Dr. T.J. Sinclair of the Royal Armament Research and Development Establishment for his support and helpful discussions.

I am deeply indebted to the Science Research Council and the Procurement Executive of the Ministry of Defence for the sponsorship of this work. My sincere thanks are due to the members of the Department at the Sir John Cass School of Science and Technology for their help and cooperation.

Last, but not least, I should pay my tributes to the selfless patience, understanding and support of my wife Nafees throughout the progress of this work.

Attention is drawn to the fact that the copyright of this thesis rests with its author.

This copy of the thesis has been supplied on condition that anyone who consults it is understood to recognise that its copyright rests with its author and that no quotation from the thesis and no information derived from it may be published without the author's prior written consent.

V

D39229'82

END